# Functional Gold Nanoparticles for Biomedical Applications

**Dissertation**

zur Erlangung des Doktorgrades
der Naturwissenschaften
(Dr. rer. nat.)

dem
Fachbereich Physik
der Philipps-Universität Marburg

vorgelegt von

**Dominik Hühn**

aus
Marburg

Marburg, 2013

Vom Fachbereich Physik der Philipps-Universität (Hochschulkennziffer 1180)
als Dissertation angenommen am: 17.03.2014

| | |
|---|---|
| Erstgutachter: | Prof. Dr. Wolfgang J. Parak |
| Zweitgutachter: | Prof. Dr. Martin Koch |
| Prüfer: | Prof. Dr. Reinhard M. Noack |
| Prüfer: | Prof. Dr. Wolfram Heimbrodt |

Tag der mündlichen Prüfung: 25.03.2014

Die vorliegende Arbeit wurde am Fachbereich Physik
der Philipps-Universität Marburg unter der Anleitung von

Herrn Prof. Dr. Wolfgang J. Parak

in der Zeit von August 2010 bis Oktober 2013 angefertigt.

# Abstract

Subjects of the present dissertation are the synthesis, the functionalization and the characterization of colloidal gold nanoparticles. The employed nanoparticles consist of an inorganic Au core of approximately 5 nm diameter, which is stabilized by hydrophobic surface molecules. To transfer the nanoparticles to aqueous environments (an indispensable necessity for biomedical applications) they are coated with an amphiphilic polymer, which generates water solubility and moreover gives the ability for further functionalization. The physico-chemical properties of such nanoparticles are verified within different purposes:

First, several fundamental intrinsic surface properties are quantified, including the establishment of pH titration as characterization tool. It is found that the carboxylic groups, responsible for the colloidal stabilization, partly have different properties (like their $pK_a$) compared to free standing carboxylic acids. These findings are crucial for the colloidal stabilization of nanoparticles as well as for their further functionalization.

Secondly, two species of fluorescently labeled nanoparticles, which differed in first order only in the net surface charge, are employed to study charge dependent interaction of nanoparticles with biological systems, including proteins as well as living cells. The main finding is, that a so called protein corona forms around nanoparticles, what has far-reaching impacts on cell internalization abilities. Moreover it is found that positively charged nanoparticles show a higher cell association as well as a higher toxicity.

Thirdly, nanoparticles are modified towards sensing applications by surface functionalization with ion sensitive dyes. Positively charged nanoparticles are modified with a $Cl^-$ sensitive dye and negatively charged nanoparticles are modified with a $Zn^{2+}$ sensitive dye.

The goals of the dissertation can be synoptically depicted as:
1) Extension of the existing techniques for nanoparticle functionalization, particularly regarding new types of functional polymers.
2) A fundamental and comprehensive characterization of nanoparticles ranging from the verification of intrinsic, physico-chemical properties to biomedical applications.

# Zusammenfassung

Die Thematik der vorliegenden Arbeit umfasst die Synthese, die Funktionalisierung und die Charakterisierung von kolloidalen Gold-Nanopartikeln. Die verwendeten Nanopartikel bestehen aus einem anorganischen Au Kern von ungefähr 5 nm Durchmesser, der durch hydrophobe Moleküle an der Oberfläche stabilisiert wird. Um die Nanopartikel in wässrige Umgebungen zu überführen (eine unverzichtbare Notwendigkeit für biomedizinische Anwendungen), werden sie mit einem amphiphilen Polymer ummantelt, das zum einen Wasserlösligkeit generiert und zum anderen die Möglichkeit zur weiteren Funktionalisierung eröffnet. Die physikochemischen Eigenschaften solcher Nanopartikel werden unter verschiedenen Gesichtspunkten verifiziert:

Zunächst werden einige fundamentale intrinsische Oberflächeneigenschaften quantifiziert, was die Etablierung der pH-Titration als Charakterisierungsmethode einschließt. Es wird gezeigt, dass Carboxygruppen, die für die kolloidale Stabilisierung sorgen, teilweise verschiedene Eigenschaften (etwa ihr $pK_s$-Wert), verglichen mit freien Carbonsäuren, besitzen. Diese Erkenntnisse sind bedeutend für die kolloidale Stabilisierung von Nanopartikeln wie auch für ihre weitere Funktionalisierung.

Des weiteren werden zwei Typen von fluoreszent markierten Nanopartikeln, die sich in erster Ordnung nur in ihrer Netto-Oberflächenladung unterscheiden, verwendet, um die ladungsabhängige Interaktion von Nanopartikeln mit biologischen Systemen, einschließlich Proteinen und lebenden Zellen, zu untersuchen. Eine wesentliche Erkenntnis ist, dass sich um die Nanopartikel eine sogenannte Protein-Corona ausbildet, was weitreichende Auswirkungen auf die zelluläre Internalisierung hat. Darüber hinaus wird gezeigt, dass positiv geladene Nanopartikel stärker mit Zellen assoziieren, was mit einer höheren Toxizität verbunden ist.

Zuletzt werden Nanopartikel an der Oberfläche mit ionensensitiven Farbstoffen funktionalisiert um Sensor-Anwendungen zu ermöglichen. Positiv geladene Nanopartikel werden mit einem $Cl^-$-sensitiven Farbstoff modifiziert und negativ geladene Nanopartikel mit einem $Zn^{2+}$-sensitiven Farbstoff.

Die Ziele der Dissertation können wie folgt zusammenfassend dargestellt werden:

1) Erweiterung der bestehenden Techniken für die Nanopartikel-Funktionalisierung, speziell in Bezug auf neue Typen von funktionalen Polymeren.

2) Eine fundamentale und umfassende Charakterisierung von Nanopartikeln, die von der Verifizierung intrinsischer, physikochemischer Eigenschaften bis hin zu biomedizinischen Anwendungen reicht.

# Acknowledgement

I would like to address many thanks to Wolfgang Parak, for giving me the opportunity to work in his group and moreover for motivating me always with his fair and kind attitude.

As well I would like to thank Jose Maria Montenegro Martos for his kind supervision and simply for having him as friend. Without his input this work wouldn't have been possible, especially regarding all issues of chemical nature.

I'm very grateful for all the support I got from the current and past members of the biophotonics group. Special thanks go to Moritz, Christian, Raimo, Karsten, Markus, and Dorleta for great times not only regarding the work together.

For proof reading this work I would like to thank (again) Jose Maria, Beatriz, and my brother Jonas. Especially I thank Jonas for help with the chemical drawings and all the support during his time as lab student.

For all the help and constructive discussions I thank the colleagues with whom I was working within collaborative projects. Special thanks go to: Gaelle Charron (Université Paris Diderot) for our joint pH titration study, Christian Geidel (Max Planck Institute for polymer research, Mainz) for providing the amphiphilic polymers, Stefan Brandholt (Karlsruhe Institute for Technology) for the FCS measurements, and Stefaan Soenen (Ghent University) for the cytotoxicity and FACS experiments.

I express deep thanks to my whole family and friends, especially to my parents, my brother Jonas and Anne, who always are standing by my side. You whisper the right words advisedly through all the noise and it feels like they are my sextant and compass – applause, applause!

# Table of Contents

# Preface

The present work is written in a cumulative way; hence the publications in the field of nanobiotechnology, to which the author contributed, are summarized and integrated to form a coherent story. In chapter 1 a general introduction is given, in which the state of the art, comprising nanoparticles (NPs) and their functionalization towards biological applications, is reviewed. Herein a focus is set on the NP systems, which are relevant for the experimental work of this dissertation. Chapter 2 embeds the author's experimental work into the topics given in the introduction. In this context the published studies regarding functional NPs are summarized. In chapter 3 the main results are summarized and an outlook section gives an overview about perspectives and future ideas concerning the presented results. All publications[1-10] and the contained contributions by the author are briefly summarized in chapter 4. The whole articles can be found in the appendix. Please be aware, that some of the references are not yet in their final shape. As the state of reference [3] was too premature to be depicted in the appendix, a patent applications, which contains the relevant data as well, was attached instead.

# 1 Introduction

In the recent decades the number of applications involving nanotechnology for biomedical purposes increased enormously.[11, 12] Two main reasons might be responsible for this huge expansion: 1) The attribute that physico-chemical properties change entirely when downscaling a material to the order of magnitude of a few to a few hundreds of nanometers and 2) the opportunity to equip a single nano-device with more than only one functionality. This great opening of new fields of research enables not only advanced functions in nano-medicine[8], but also brings the duty to deal with safety aspects.[13] Herein the study of environmental as well as health effects has to go hand in hand with the development of new functional materials.

In the introduction a focus will be set on gold nanoparticles (Au NPs), comprising their physico-chemical properties and their potential use for biomedical purposes. Finally aspects like the interaction of NPs with biological materials will be discussed.

## 1.1 Physico-chemical properties of gold nanoparticles

Nowadays Au NPs are one of the most important subjects of the rapidly growing field of nanotechnology with all its sub areas and applications towards biology and technology.[14-18] This great importance can be attributed to the unique electronic, magnetic or optical properties of Au NPs. But unexpectedly Au NPs are employed as building blocks even since ancient times mainly as staining agent for glass or ceramics. One of the most impressive examples, that directly goes back to quantum size related optical properties, is the Lycurgus Cup (4$^{th}$ century, Figure 1). In case the glass is front-lit with white light (light source outside) it appears green, and in case it is back-lit (light source inside) it appears red. The reason is a net absorption in the green part of the electromagnetic spectrum what causes transmittance of red light. These optical properties originate from Au and Ag NPs that are embedded in the glass. In contrast to bulk Au or Ag, these NPs (size ~50 nm) strongly absorb light of a certain wavelength, what is a direct result of the quantum size.[19-22] It goes back to the fact that noble metals are excellent electrical conductors with the ability to show collective oscillations of the present electron gas, known as plasmons. These oscillations can be excited at optical frequencies. In case an oscillation is located at a surface or interface the associated oscillation and electromagnetic fields are called surface plasmon polariton (SPP). These propagate alongside the surface in form of an evanescent wave while losing energy.

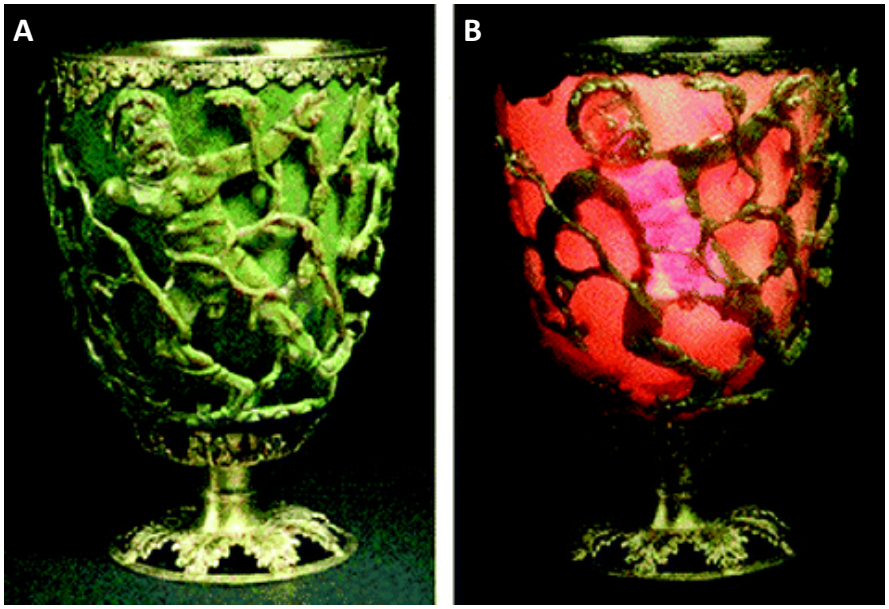


Figure 1: The Lycurgus Cup appears green (A) when front-lit and red (B) when back-lit (light source inside the cup). This phenomenon is directly related to the presence of Au NPs embedded in the glass. Source: http://someinterestingfacts.net/what-is-plasmons/.

The energy loss is due to absorption by the metal on the one hand and radiation into free space on the other hand. In case the frequency of the excitation light matches with the natural frequency of the electrons oscillating against the positively charged atomic nuclei, the resonant case is given, called surface plasmon resonance (SPR). Upon downscaling of the material to the order of magnitude of the mean free path of electrons in the metal this resonance is even enhanced and highly localized. Hence this phenomenon is denoted as localized surface plasmon resonance (LSPR). For Au NPs with diameters between approximately 1-100 nm this coupling occurs in the visible (Vis) to near infrared (NIR) and with increasing diameter the LSPR shifts to the red. Thus the color of a colloidal Au NP suspension appears in the complementary of the LSPR: Red for smaller NPs and purple/bluish for bigger NPs. As the location of the LSPR depends strongly on changes of the local dielectric environment, *e. g.* by adsorption of molecules onto the NP surface, LSPR spectroscopy and surface-enhanced Raman scattering (SERS) represent very sensitive techniques enabling the detection of such changes.[22-24] Moreover agglomeration of Au NPs leads to a coupling of the electronic wave functions and thus to a red shift of the LSPR, what is the starting point of many colorimetric detection applications.[25-28] Additionally the spectroscopic characteristic of the LSPR depends sensitively on the shape of the NPs. Thus, *e. g.* Au nanorods (NRs), hence NPs with different longitudinal and transverse dimension show two LSPR peaks with their location and magnitude depending on the aspect ratio.[19, 29-31]

Upon excitation of Au NPs at their LSPR, one observes, that parts of the energy is transferred to the atomic nuclei resulting in lattice oscillations, hence phonons. These oscillations usually are the source of heat, what leads to temperature increase in the Au NP itself as well as of the close environment.[32] The fact, that Au NPs are excellent light to heat converters is the starting point for the field of photothermal applications. Herein two main purposes are of great interest: 1) Photothermal therapies (*e. g.* cancer treatment) and 2) photothermal release of materials whether bound to the NPs or accumulated in higher order structures as cargo.[15, 33-37] Regarding photothermal applications in which the excitation light has to pass through tissue to reach a certain site, at which absorption centers are located, one has to consider an important circumstance: The light gets absorbed by tissue to a certain extent and the transmittance is highest in the so called NIR window.[38] Hence, absorption centers in the NIR region are desired. Unfortunately small (5-50 nm) spherical Au NPs possess a LSPR

around 520 nm, hence in the green part of the visible spectrum. Thus for life science applications very often Au NRs or agglomerated Au NPs are the material of choice.[5, 30, 39] But also more individual constructs like nanoshells, nanocages, or nanoprisms are under investigation.[40-42]

Regarding the synthesis of colloidal Au suspensions several techniques are established. An early one is the method by Turkevich *et al.* which delivers citrate capped and thus readily water soluble Au NPs with sizes around 15 nm.[43] The Brust method takes place in organic solvents and the result are hydrophobically capped Au NPs with diameters around 5 nm.[44] Thus for biomedical applications these NPs have to be coated by polymers that mediate water solubility or have to undergo a ligand exchange. Both methods are based on the reduction of $HAuCl_4$, what finally leads to the formation of small Au seeds, which initiate the formation of nanocrystals. There exist plenty more methods which can be seen as extensions of the mentioned ones as they make use of the same reduction principle.[45, 46] What they all have in common is, that they follow a bottom-up approach, hence the final NP is the result of the fusion of smaller building blocks (Au atoms in the present case). An established method that follows a top-down approach is mediated by laser ablation.[47] Here colloidal Au NPs are seceded from a piece of bulk gold with a laser beam.

## 1.2 Other inorganic nanoparticles

A short chapter will be dedicated to other types of inorganic NPs. Although they are not part of the experimental core part of this dissertation, they play an important role for getting a complete understanding of the possible opportunities inorganic NPs offer.

Ag NPs as second type of noble metal NPs besides Au NPs already play an important role in daily life products, mainly due to their antimicrobial properties.[48, 49] But there is still a lack in understanding how and to which extend these NPs are hazardous when released to the environment or getting in contact with the human body.[50] Regarding biomedical applications the areas of usage of Ag NPs are very much similar to those of Au NPs. They can for example serve as carriers for biomolecules,[51] or as sensor platform due to their plasmonic properties.[52, 53] A rather novel field of application of noble metal NPs is the usage as fluorescent probes. When downscaling the material (Au or Ag) to the sub 2 nm region (then

they are commonly called clusters) they show fluorescent properties.[54, 55] Many synthetic routes for Ag NPs are established, but the most common ones are, similar to those of Au NPs, based on the reduction of salts of silver.[56, 57]

Another class of inorganic NPs, nanocrystals consisting of semiconductors, are so called quantum dots (QDs).[58] In contrast to metals, semiconductors possess a band gap between valence and conduction band. Thus, depending on the material, an excitation at optical frequencies can lead to the formation of an exciton, hence a bound state consisting of an electron that is shifted to the conduction band and an electron hole that remains in the valence band. Recombination thus can lead to the emission of a photon. Quantum mechanically an exciton can be described within a formalism, which is similar to that of a hydrogen atom. Thus a kind of Bohr radius can be derived, although with lower binding energy and higher spatial extension compared to a H atom due to screening effects. If the spatial dimensions of the material are decreased down to the order of magnitude of the Bohr radius the effect of quantum confinement comes into play: The exciton gets "squeezed", what results in an increased potential energy, hence the energy gap between ground state and excited state is increased the smaller the particle gets. The situation is comparable with the model of a "particle in a box". Thus by adjusting the dimension (usually in the sub 10 nm region) of the material, the optoelectronic behavior of the QD is highly tunable. In other words, the emission wavelength of an excited QD undergoes a blue shift when decreasing the diameter. Due to their fluorescence properties QDs are widely used as optical tracers, often in a functionalized form to address individual biomedical purposes.[59-61] Compared to conventional fluorescence markers like organic dyes, QDs possess the advantage of a rather narrow emission peak paired with a broad absorption profile, what qualifies them as excellent Förster resonance energy transfer (FRET) donors.[62] Besides, QDs are much less subject of photo bleaching compared to organic dyes.[63] The synthetic routes for QDs include lithographic, epitaxic and wet chemistry methods. QDs can be composed of a single material or of compositions like chalcogenides (sulfides, selenides) of metals like Zn or Cd. A feasible method for improving the optical properties (quantum yield and brightness) of QDs is to use a core-shell architecture, in which a shell of a semiconductor with higher band gap compared to the core is assembled around the latter. In this way non-radiative exciton recombination is minimized in the core. A common combination is *e. g.* CdSe/ZnS.[63]

By varying the thickness ratio between core and shell and by varying the composition ratio between the components in alloyed QDs, it is possible to tune the emission wavelength under maintenance of the total diameter, a beneficial feature for size restricted applications.[64]

Also magnetic NPs attracted great attention in the recent decade due to their potential use in biomedicine.[65-68] The applications range from drug delivery systems, hyperthermia, magnetic resonance imaging (MRI) to magnetic separation and bio sensing and are more or less all related to the superparamagnetic properties and thus the response to an external magnetic field. Established material classes are metal oxides, like magnetite ($Fe_3O_4$) or maghemite ($\gamma$-$Fe_2O_3$), or metals (Fe, Ni, Co) that are further passivated by a layer of a metal oxide, a noble metal, a polymer or other surfactants. The most common synthetic routes involve methods like co-precipitation (iron oxides), thermal decomposition, or thermal spraying (passivated metals).

## 1.3 Colloidal stabilization – phase transfer

An indispensible need that a NP suspension must possess is colloidal stability. Otherwise NPs would start to agglomerate and there could be no talk of individual objects, hence particles. Moreover the physico-chemical properties could change entirely. As agglomeration would be the result of an attractive interaction (*e. g.* van der Waals forces) between the surfaces of individual NPs, it can be prevented by modification of the surface. This modification can act in different manner and induce repulsion, either by electrostatics or steric exclusion. Often the modification itself, *i. e.* surfactant molecules or passivating layers, are already involved in the assembly process of the NP core and are desired for a later functionalization. This is, why the topics of synthesis, stabilization and functionalization go hand in hand and often are attained by the employment of only one type of surface modification. The attachment of such surfactants usually is achieved *via* electrostatic and/or hydrophobic interaction or covalent binding. In the case of noble metal NPs the most common strategy is to covalently attach a molecule with a thiol bearing end group.[69, 70] The part of the surfactant pointing towards the solvent consequently determines the hydrophilic character of the NP. A possibility to achieve directly water soluble NPs, is to choose a carboxyl bearing end group, like given in thioglycolic acid (TGA), mercaptopropionic acid (MPA), or mercaptoundecanoic

acid (MUA). Also heterofunctional polyethylene glycol (PEG) derivatives are a feasible choice in case long surfactants are desired. In the case of PEG as surfactant also steric exclusion effects come into play due to the space filling conformation of PEG. In all cases the functional end group bears a charge and ensures electrostatic repulsion between individual NPs. For electrostatically stabilized NPs it is obvious that the suspension is sensitive to ionic strength (including pH) due to screening of the surface charge. In case the isoelectric point is reached due to charge screening, what is equivalent to neutralization of the surface charge, agglomeration would occur. Much more resistant to these charge screening effects are NPs stabilized *via* steric exclusion.[71] In many other cases the synthesis of the NPs involves hydrophobic side chains which appear as surfactant molecules after crystallization. To achieve water solubility, these surfactants can either be exchanged by a desired one ("ligand exchange") or an amphiphilic polymer can serve as coat.[72, 73] Such a polymer comprises in the simplest case two domains: One bearing a charge, hence providing water solubility, and another one comprising hydrophobic side chains. In case the latter show a conformational similarity (at least comparable length) they can intercalate with the hydrophobic surfactants of the NP surface. If the hydrophilic domains, located at the polymer backbone, are pointing outward and the initial organic solvent is exchanged against an aqueous buffer the polymer forms a dense shell around the NP core. Colloidal stability is maintained by electrostatic repulsion of the charged groups.

## 1.4 Functionalization towards biological applications

To equip water soluble NPs with further functionality, a feasible method is, to covalently attach desired molecules to the outermost surface of the NPs. Very often an anchor point for such a functionalization is given by the stabilizing groups themselves, *e. g.* carboxylic groups, either part of individual surfactant molecules (like in TGA, MPA, MUA, etc.) or of the backbone of an amphiphilic polymer. A good overview about established conjugation strategies between NPs and a certain substrate is given in the literature.[74] By these a functionality of interest, like organic dyes for imaging and sensing, biomolecules for biological recognition/targeting, or chelators for the complexation of metals, can be introduced to the NP.[72, 75-78] Another possibility to introduce functionality to a NP system is to embed additional monomers in a coating polymer, for example to achieve a terpolymer.[2]

In the following a variety of such (core + organic shell) functional NP systems (extended by some other examples) will be reviewed. A focus will be set on sensing, being one of the purposes of the present dissertation. Already in 2004 an immense emergence of improvements and developments according to the use of nanocrystals in terms of applications in life sciences was predicted, concisely their use in ion and molecular sensing.[79] During the last decade these considerations became more than true with look to multiplexed sensing, not only according to the exploited properties of NPs but also to nanostructures of higher dimension and the variety of pertinent analytes. This automatically demands for a classification of different techniques like optical / electrical / magnetic detection and their extensions to electrochemical sensing or more specific methods like SERS. Also a classification considering the types of most interesting analytes could be a meaningful route to verify the made predictions. These include single ions and molecular probes such as deoxyribonucleic acid (DNA), cancer cells (also comprising bio markers for those) and hazardous materials but also physico-chemical parameters like temperature, polarity, etc. Above all one has to consider one of the main acquisitions nanotechnology introduced to sensing capabilities, that is the opportunity to combine different techniques giving the possibility to crosscheck observations and to expand the applicability of a system.

This opportunity was reflected by Cheon and Lee on the basis of multimodal imaging probes consisting of magnetic NPs decorated with further functionalities, *i. e.* radionuclides enabling positron emission tomography (PET), fluorescent moieties for optical tracking or anchor molecules like antibodies / peptides / DNA / RNA giving the possibility to address specific targets.[80] By their message, that "synergistically" acting properties give the possibility for multimodal diagnosis and even for therapeutic functions (drug delivery, hyperthermia, etc.), the authors come straight to the point. How advantageous a magnetic NP based multimodal system can be, is also shown by Liong *et al.*[77] In their study they are dealing with multifunctional iron oxide – mesoporous silica NPs, which are detectable optically and by MRI. It is shown that the particles are suitable for live cell imaging and therapeutic purposes by addressing them specifically to human cancer cells. Moreover, an important advantage of using NPs as carrier system is pointed out, that is the transfer of hydrophobic anti cancerous drugs (or other molecules) into cells, as the nature of the NP surface generates the water solubility of the whole system, including incorporated molecules on the one hand and covalently bound molecules on the other hand. A comparable trimodal imaging system

comprising MRI (iron oxide core), PET (chelator ligand complexing the radiotracer $Cu^{64}$) and fluorescence (Vivotag-680) enabling *in vivo* studies concerning detection of macrophage markers was investigated by Nahrendorf *et al.* with regard to the detection of inflammatory atherosclerosis.[81] Due to the low required concentration of NPs and a higher target-to-background ratio the authors claim the high relevance for clinical perspectives.
An overview and several promising applications concerning magnetic NPs are given by Jun *et al.*[82] Besides the synthesis and further use in cellular MRI the authors report in their review about the use of magnetic NPs in terms of multimodal probes comprising possibilities like hybrid "core-satellite" constructs with a fluorescent core and magnetic NPs attached, enabling a higher MRI contrast compared to individual magnetic NPs.

Regarding other core materials as starting point for the investigation of multimodal sensing devices it is inevitable to mention gold nano-structures.[83] The excellent range of possibilities for tuning optical properties or surface chemistry and the fact of chemical inertness of the starting material make it a versatile platform for the purpose of biomedical applications comprising a huge variety of sensing applications.[84, 85] Concerning sensing of ions one special class of material is of particular interest, that is substances like heavy metals which are hazardous for the human health and the environment. Having this in mind, Lin *et al.* discuss thoroughly possible routes to sense potentially toxic metal ions like $Hg^{2+}$, $Pb^{2+}$, $Cu^{2+}$.[86] In summary, they present a collection of gold NP based probes with sensitivities that are two orders of magnitude lower compared to the current legislative limits. Two further approaches to detect $Hg^{2+}$, one comprising gold NP-oligonucleotide hybrids and another one comprising a DNA-based machine, reached detection sensitivities of 2 ppb and 0.2 ppb, respectively.[87] However, Li *et al.* admit, that the measurements are made in clean aqueous solutions and potential cross talk signals in environmental samples still have to be evaluated. A big advantage of the shown system is certainly the colorimetric signaling as it enables instrument-free and thus rapid analysis of $Hg^{2+}$ contaminations as was also pointed out by Xue *et al.*[88] That sensing of mercury is of essential importance does not at least owe the fact that many countries in northern Europe demand for stronger laws or even a total prohibition. Thus it is not surprising that a lot of improvements with promising sensing capabilities are subject of the recent research.[89, 90] Besides hazardous materials also biological analytes are topic of recent sensing approaches. Especially the detection of DNA

and the diagnosis of cancerous cells are truly representing the main focus of biological sensing applications based on NPs. In this purpose Bunz and Rotello succeeded in a sensitive distinction between different proteins, bacteria and cells (especially healthy and cancerous cells) based on the efficient fluorescence quenching of fluorophores, when adsorbed to gold NPs, although the concrete mechanism of quenching is not yet understood completely.[91] An approach, dealing with the indirect detection of cancer, hence the detection of protein bio markers for it, was presented in an immunoassay by Liu *et al.*[92] The assay is based on antibody labeled Au NPs and Au NRs specific for an antigen of interest. The buildup of dimers/trimers/oligomers and the associated changes in dynamic light scattering (DLS) signals served as sensitive basis for the measurements. Again a colorimetric assay based on aptamer-conjugated Au NPs was developed by Medley *et al.* avoiding time and money consuming sensing techniques for cancer detection.[93] Regarding the motivation of a multiplexed sensing device colorimetric assays have the advantage of a simple by-eye-verification besides spectroscopic methods. The recent efforts concerning colorimetric Au NP assays for a variety of analytes was summarized by Zhao *et al*.[94] Besides sensing systems within colloidal solutions also immobilized Au NPs have been used mainly in terms of electrochemical approaches leading to interesting applications considering enzyme or DNA detection, but also other analytes.[95] Regarding capillary electrophoresis–mass spectrometry (CE-MS) gold NPs can play an increasing role for molecular sensing, as was shown for the detection of heroin and related compounds with the purpose of forensic studies or illicit drug control.[96]

Although some of the presented approaches considering sensing assays based on gold NPs partly do not comprise multiple analysis techniques, they are bearing a great potential towards those.

However, the verification of illicit drugs can serve for the passing towards other sensing systems for those. Thus, Zhang and Johnson reported about an aptamer functionalized QD assay for a very sensitive detection of cocaine with possible extensions to other molecules (proteins, DNA, single ions, etc.) in the future.[97] The study is based on FRET, a commonly exploited phenomenon for biosensing purposes, in particular considering QDs as donor or acceptor probe.[62, 98] A label-free study for the detection of the cocaine metabolite benzoylecgonine was presented by Sanles-Sobrido *et al.* based on SERS supported by Ag NP

decorated carbon nanotubes (CNTs) as substrate.[99] As can be seen from this example, the fact, that NP assisted SERS operates even at detection sensitivities on the single molecule level, one has to endow a particular compliance to this versatile technique.[100-102] Recent advantages and limitations of SERS in terms of biosensing are summarized by Alvarez-Puebla and Liz-Marzán.[103] However, also for the detection of DNA or *in vivo* tumor targeting SERS acquired vogue for promising sensors.[104, 105]

## 1.5 Health and environmental aspects

Besides the potential applications nanomaterials offer, great importance has to be addressed towards safety aspects, including health as well as environmental issues.[13] Regarding cytotoxicity, it is obvious, that potentially toxic chemical substances, like cadmium (*e. g.* part of CdSe based QDs), can cause cell death due to release of $Cd^{2+}$ ions.[106] The mentioned strategy to encapsulate the NP core in a polymer shell could be a route to 1) lower the release of parts of the core material and 2) minimize the direct interaction of the core material with biological compounds ("the surface determines the chemical identity"), compared to only ligated NP cores. But also chemically inert materials like gold can cause toxic effects if scaled down to a certain size so that mechanical interaction with cell compartments comes into play.[107] Besides the size also shape and surface chemistry certainly are crucial parameters determining toxicity related properties.[108-110] In general one can say, that the evaluation of toxicity of nanomaterials depends entirely on the verified nanomaterial (including all physico-chemical parameters), the cell type and further external conditions. As these differ enormously throughout the literature, there can be no talk of coherent or convergent evidence. But recently comparative studies came up, which are the starting point for such a comprehensive understanding.[111]

Findings on a cellular level can be largely assigned to tissue but also aspects like distribution, degradation or excretion of nanomaterials in organisms demand for extensive evaluation. In many studies the liver and spleen are found to be the major collecting sites.[112] Surface modifications like PEGylation promise to reduce toxic effects, *e. g.* due to reduced interaction with biological compounds like proteins.[113] NP uptake pathways *via* the lung or the skin are also important topics of research, that contribute to a greater understanding, how NPs in daily life can affect organisms.[114, 115] Surface modification can also contribute

indirectly to a reduced cytotoxicity, whilst addressing the NPs towards specific sites, like tumor cells, accompanied by drug delivery purposes.[116] Even the possibility to cross the blood-brain barrier by a transferring modification was reported.[117]

Also environmental aspects can be source of significant drawbacks regarding engineered NPs.[118] Air/water pollution and/or interaction with plants could be challenging problems, which call the use of NPs on industrial scale into question.[119]

# 2 Synthesis and characterization of functional nanoparticles towards biological applications

This chapter is assigned to the author's experimental work regarding functional NPs.[1-3] The intention is to give an overview about the relevant publications in this field and to associate them. For a reproduction of experiments the reader may be additionally referred to the publications. First some general procedures and methods, that to a certain extent are similar for the different studies regarding synthesis and purification of NPs will be discussed in chapters 2.1 to 2.3. Thereafter the studies themselves will be presented in chapters 2.4 to 2.6.

## 2.1 Synthesis of inorganic gold nanoparticles

Regarding the main experimental parts, which are relevant in terms of functionalized Au NPs, a certain type of this kind of NPs was employed throughout the whole studies. The Au NPs are synthesized following the Brust method.[44] Briefly, from an aqueous solution of chloroauric acid ($HAuCl_4$, 1 eq) $AuCl_4^-$ is transferred to toluene forming an ionic pair with tetraoctylammonium bromide (TOAB, 4.5 eq), which later also acts as stabilizing agent. In the organic phase sodium borohydride ($NaBH_4$, 10 eq) is added to reduce $Au^{3+}$ to $Au^0$, what subsequently leads to the formation of colloidal Au crystals. After several washing steps Ostwald ripening occurs during an incubation step over night, what supports the evolution of a rather monodisperse suspension. TOAB as surfactant molecule has two disadvantages: One is the relatively weak binding strength and secondly the geometry of the NPs including the surfactants is expected to be not perfectly spherical due to the potentially pyramidal appearance of TOAB at the surface. Thus a ligand exchange against 1-dodecanethiol (47.5 eq) is performed, what diminishes these findings. The result are hydrophobically capped Au NPs with a core diameter of approximately 4 nm, which do not show any sign of stability loss even over several months. Figure 2 exemplifies some properties of the Au NPs. In the transmission electron microscopy (TEM) image (Figure 2 A) the Au cores appear as grey spots with high contrast. The intermediate space between NPs indicates the presence of dodecanethiol surfactants, which prevent the Au cores from agglomeration. The core diameter $d_c$ is determined from TEM images using the public domain software ImageJ in

combination with a "particle size analyzer" macro freely available on the web (http://code.google.com/p/psa-macro/).

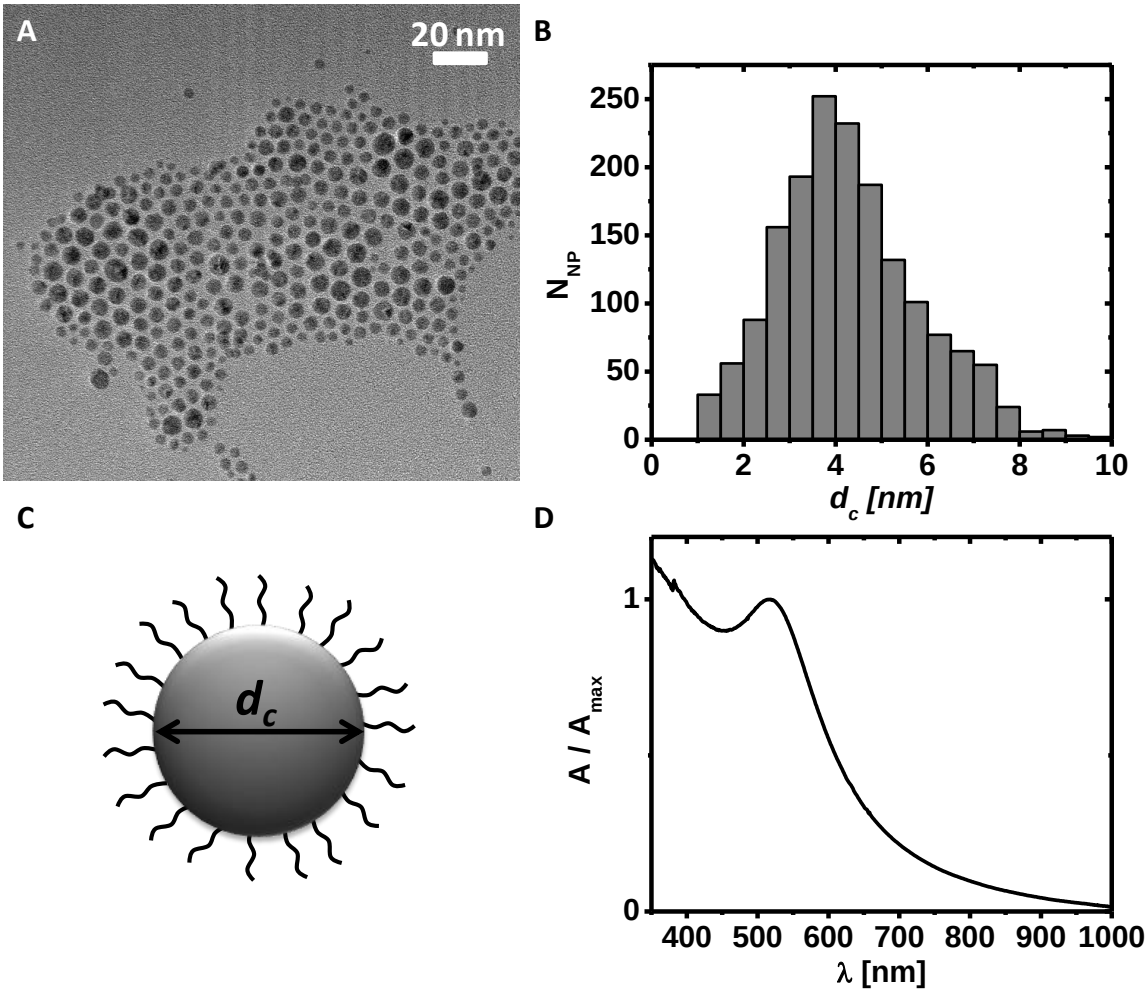


Figure 2: A) TEM image of dodecanethiol stabilized Au NPs. B) Histogram of the size distribution of Au NPs as determined from TEM images. In the present case the core diameter is $d_c$ = (4 ± 1.3) nm. C) Schematic illustration of the Au core capped with dodecanethiol surfactants (approximately drawn to scale). D) Extinction spectrum of dodecanethiol stabilized Au NPs in chloroform. The graph is normalized at the LSPR at approximately 520 nm. The figure is adopted from reference [3].

Figure 2 D shows an extinction spectrum of Au NPs in chloroform. A clear peak around 520 nm indicates the presence of a LSPR. For the concentration determination of Au NPs the Lambert-Beer law (Equations 1a – 1c) is applied for the extinction at the LSPR.

$$I_1 = I_0 \cdot \mathrm{e}^{-\varepsilon^* c d} \tag{1a}$$

$$A = \log\left(\frac{I_0}{I_1}\right) = \varepsilon \cdot c \cdot d \tag{1b}$$

$$\varepsilon = \log(\mathrm{e}) \cdot \varepsilon^* \tag{1c}$$

Here $I_1$ is the intensity of the excitation light after having passed a certain distance $d$ (in practice the length of the cuvette) through the absorbing medium. $I_0$ represents the original intensity, $\varepsilon^*$ the molar extinction coefficient and $c$ the molar concentration of the absorbing compounds. Furthermore $A$ is the extinction and $\varepsilon$ the molar decadic extinction coefficient, which is often used in practice instead of $\varepsilon^*$. The relevant molar decadic extinction coefficients are determined in the work of Liu *et al.*, in which $\varepsilon$ is correlated with the core size of Au NPs (Equation 2).[120]

$$\ln(\varepsilon \cdot \mathrm{M} \cdot \mathrm{cm}) = k \cdot \ln\left(\frac{d_c}{\mathrm{nm}}\right) + a \tag{2}$$

Here $\varepsilon$ is the molar decadic extinction coefficient in $M^{-1}cm^{-1}$, $d_c$ the core diameter in nm, and $k$ = 3.32111 and $a$ = 10.80505 are fitting parameters.

## 2.2 Phase transfer

For biomedical applications it is essential, that NPs possess water solubility. Especially cell associated experiments would suffer from hydrophobic moieties as they would lead to agglomeration and subsequently to a loss of functionality or intangible fate in a cell. Anyway, the transfer to an aqueous environment would already lead to colloidal instability. As many types of NPs are capped with hydrophobic surfactants, a phase transfer has to be carried out. If a certain type of NPs is stabilized with hydrophobic molecules, depends entirely on the way of synthesis. Regarding Au NPs the simple method established by Turkevich *et al.* provides for example hydrophilic NPs in contrast to the already mentioned Brust method (chapter 2.1).[43] But desired properties like size, shape, or monodispersity often oblige to assign to a synthesis providing hydrophobic NPs.

The strategy for an efficient phase transfer from organic to aqueous solvents utilized throughout this work is based on a polymer coating mechanism. In the course of this, amphiphilic polymers are used to encase the inorganic NP core. The polymer has to possess two crucial properties: 1) Hydrophobic side chains, which have conformational similarity compared to the hydrophobic surfactants of the NP core and 2) polar or charged groups at the polymer backbone that provide a net charge once the coated NP is transferred to an aqueous solvent. For the coating process the two components (NP cores and amphiphilic polymer) are merged in an organic solvent, usually chloroform, and stirred for several minutes at T > room temperature (RT = 20°C). During this step the hydrophobic side chains of the polymer are believed to intercalate with the hydrophobic surfactants of the NP core due to their conformational similarity. After evaporation of the solvent under reduced pressure the dried film is re-dissolved in chloroform and another round of stirring is performed. This procedure is usually repeated three times. After the last evaporation step the dried solid can be diluted in an aqueous buffer as the hydrophobic parts are facing each other and thus ensure a dense packing. Moreover the hydrophilic sites at the polymer backbone provide colloidal stability due to electrostatic repulsion. Figure 3 illustrates how the coating process can be understood. It is kept in a very schematic appearance as throughout this work various types of polymers are employed regarding their conformation and physico-chemical properties. What they all have in common is the possession of hydrophobic and hydrophilic parts, hence an amphiphilic nature, and anchor points for an

attachment of further functional molecules, indicated by the blue and red letters "F" in the scheme.

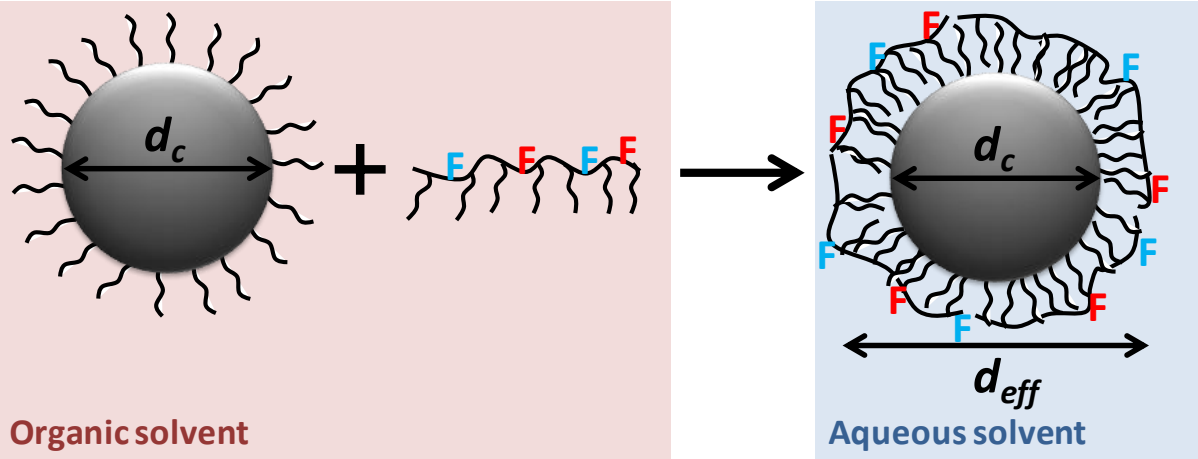


Figure 3: Schematic depiction of the coating process for the transfer of inorganic NPs capped with hydrophobic surfactants from an organic to an aqueous solvent. An amphiphilic polymer intercalates with the hydrophobic surfactants to form a dense shell, which provides hydrophilic groups at the entire backbone. Further functionalities can be mounted to the polymer (blue and red letters "F"). The inner core diameter is denoted as $d_c$, the effective diameter comprising the core and the polymer shell is denoted as $d_{eff}$. The figure is adopted from reference [3].

Another common ground the various polymer types used to coat inorganic NPs have, is the way of calculation of the ratio of NPs and polymer to merge. It is assigned to the number of hydrophobic monomer units of the polymer that are employed per surface area regarding the effective diameter $d_{eff}$ (Figure 3). Equation 3 is used to calculate the required volume of polymer solution $V_P$:

$$V_P = \frac{n_P}{c_P} = \frac{A \cdot R_P}{N_A \cdot c_P} = \frac{c \cdot V \cdot \pi \cdot d_{eff}^2 \cdot R_P}{c_P} \quad (3)$$

Here $n_P$ is the molar amount of hydrophobic monomers in the polymer solution of molar concentration $c_P$ of hydrophobic monomers. $A$ refers to the total surface area present in the NP suspension, $R_P$ to the number of hydrophobic monomers employed per unit area and $N_A$ to the Avogadro constant. $A$ can be calculated from the known molar concentration of the NP suspension $c$, the employed volume of the NP suspension $V$ and the effective diameter $d_{eff}$. Usually $d_{eff}$ is depicted in nm so that $R_P$ in most of the cases is between 50 $nm^{-2}$ and 100 $nm^{-2}$ for an efficient coating process. The term "efficient coating process" means, that

after addition of the aqueous solvent a transparent solution with as less agglomerates as possible is present. In case agglomerates are observed, an increased value of $R_P$ could lead to an improvement, although too high values of $R_P$, *i. e.* a huge excess of polymer, should be avoided as it could impede a later purification of the NP suspension from unbound polymer material. The thickness of the polymer shell, comprising the layer of surfactants and the outer polymer backbone, is estimated to be approximately 1 nm so that $d_{eff}$ is calculated from the core diameter determined by TEM: $d_{eff} = d_c + 2$ nm.

Several advantages of the presented coating strategy have to be mentioned: 1) In principle it works regardless of the composition of the inorganic core material as only the conformational similarity of the core surface and the hydrophobic part of the polymer determines the coating ability. 2) The resulting physico-chemical surface properties of the readily coated NPs are in first order only determined by the polymer backbone. 3) Thus intrinsic core properties can be compared under equal circumstances regarding the surface properties. This is especially advantageous with regard to the reduction of cytotoxicity. 4) Finally, the polymers can be modified in a way, so that they are ideally suitable for the attachment of further functionalities.

In the following chapters this general procedure will be communicated within several examples regarding various types of polymers. The objective of some examples is, to study the physico-chemical properties themselves or with regard to the interaction with biological systems. Some other examples aim on the functionalization of NPs towards sensing applications.

## 2.3 Colloidal characterization and purification of nanoparticles

In the style of the last chapters (2.1 and 2.2) a general description of several techniques regarding characterization and purification of NPs will be discussed. These two issues will be communicated within one section as they often are correlated. Deviations from this general description will be mentioned at the specific examples.

Once NPs are coated with an amphiphilic polymer and transferred to an aqueous solvent, remaining agglomerates often can be resolved employing ultrasonication. Afterwards in a first purification step, NPs are filtered within a 0.22 µm syringe filter to get rid of bigger agglomerates.

After concentration in a centrifuge filter a gel electrophoresis step is applied for both purification from free polymer material and other molecules and colloidal characterization of the NP suspension. Therefore the NP suspension is loaded into a 2% agarose gel (UltraPure$^{TM}$ Agarose) placed in an electrophoresis chamber (Bio-Rad Laboratories) within 0.5% tris(hydroxymethyl)aminomethane-borate-ethylenediamintetraacetic acid (Tris-borate-EDTA = TBE) buffer. A voltage of 100 V is applied (length of the gel: 10 cm → 10 V/cm) for at least 1 hour. This ensures a migration of NPs through the gel and an efficient separation from free polymer material. The free polymer material is believed to form micelle like structures that migrate faster through the gel matrix due to a bigger charge to size ratio compared to the coated NPs. Figure 4 shows an illustrative gel electrophoresis result. The presented system comprising Au NPs coated with a negatively charged and dye (a $Zn^{2+}$ sensitive dye and cresyl violet (CV)) modified polymer will be discussed particularly in chapter 2.6. The example is chosen as the empty polymer micelles can be observed by fluorescence and a plain, unmodified polymer wouldn't be visible. After a certain migration time the two bands regarding coated NPs and micelles are retarded enough, to be extracted separately. Although the Au NPs in the example are equipped with fluorescent moieties, no fluorescence is visible in the more retarded band by eye, as the micelle band has a much higher content of dye molecules. At the edges of the gels commercial 10 nm Au NPs are used as internal standard for comparison between different batches. The original citrate shell is exchanged by bis(p-sulfonatophenyl)phenylphosphine dehydrate dipotassium salt. The retarded bands can be cut out of the whole gel bed with a scalpel. After transfer of each gel band into a dialysis membrane (MWCO = 50 kDa) and replenishment with TBE buffer the

different species can be drawn out of the gel matrix under the same voltage and migration direction. As neither the NPs nor the micelles are able to pass through the dialysis membrane they can be efficiently collected followed by concentration *via* centrifugation.

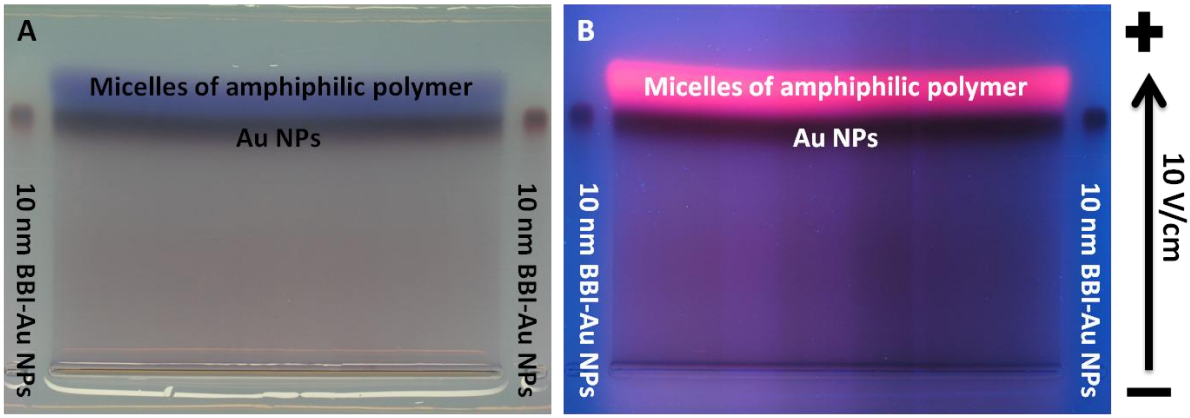


Figure 4: Purification of Au NPs *via* gel electrophoresis. The NPs are coated with a negatively charged polymer, which is pre-modified with two fluorescent dyes (for details see chapter 2.6). A) and B) show a top view on the gel with visible and ultraviolet (UV) illumination. First the NP suspension is loaded into a gel pocket at the bottom of the images. Then an electric field of 10 V/cm is applied for 1 hour. After a migration towards the anode (+) two separated bands can be observed. The slow band (dark red) corresponds to the coated Au NPs and the faster band (purple in A) and fluorescing in B)) represents the micelle band. At the edges commercial 10 nm Au NPs are used as internal control standard. The figure is adopted from reference [3].

Besides the purpose of purification of NPs from unbound polymer also information about the colloidal properties can be extracted from gel electrophoresis experiments: The migration distance gives information about the charge to size ratio and can thus verify if a certain molecule is attached to the NPs and to which extent. The width of a band represents the homogeneity, hence the monodispersity, of a sample. In case an unexpected retardation is observed, the coating procedure probably has been unfavorable and parameters like $R_P$ have to be rescheduled.

After gel electrophoresis usually another purification step with a 0.22 µm syringe filter is performed.

A further level of purification and colloidal characterization is applied *via* size exclusion chromatography (SEC). Therefore a high-performance liquid chromatography (HPLC) system from Agilent Technologies is employed. Herein the stationary phase routinely consists of self packed gel matrices: Sephacryl S-300 HR for negatively charged NPs and Sephadex G-25 Superfine for positively charged NPs. The mobile phase consists of a certain buffer: Phosphate buffered saline (PBS) or sodium borate buffered saline (SBBS) at neutral to basic

pH for negatively charged NPs, and 0.1 M NaCl (pH = 3.3 adjusted with 0.1 M HCl) for positively charged NPs. Due to interactions with the gel matrix, smaller molecules (like unbound polymer strands) remain longer in the column and can thus be separated from the NP suspension. Absorbance and emission (for fluorescent samples) profiles of the flowing sample give information about content and homogeneity. Figure 5 illustrates for two examples how the separation of NPs from free polymer material can be observed in the various absorbance and/or emission channels. Collection of a narrow part of the NP suspension fraction ensures a homogeneous sample for further processing. Besides excess polymer material also other bigger or smaller (compared to NPs) impurities are removed.

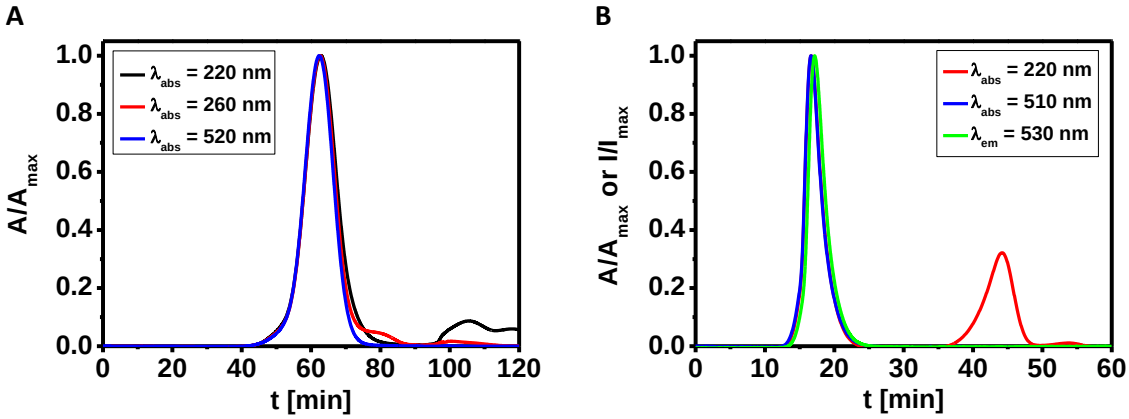


Figure 5: Illustrative SEC profiles: A) Au NPs coated with a negatively charged polymer are run through a Sephacryl S-300 HR matrix with SBBS (pH = 9) as eluent. The NP fraction passes between 50-70 min. At 220 nm as well as at 260 nm the Au cores and the polymer shell contribute to the net absorbance. At 520 nm only the Au cores contribute due to their LSPR. Hence the detected absorbance for $t \gtrsim 80$ min can be ascribed to excess polymer material. B) QDs coated with a positively charged polymer are run through a Sephadex G-25 Superfine matrix with 0.1 M NaCl (pH = 3.3) as eluent. Here the absorbance at 220 nm is induced by the QD core and the polymer shell. The blue and the green line represent absorbance and emission at specific wavelengths for the green fluorescing QDs. Hence a fraction of polymer material (peak at 45 min) can be separated from the sample. The elution times in A) and B) are different due to different column sizes.

After SEC usually an additional purification step is performed. Therefore the NP suspension is run through a disposable PD-10 desalting column (Sephadex G-25 Medium). Desalting is of particular importance in case the NPs are equipped with ion sensitive dyes as various ionic species in the suspension can influence the distribution of the analyte ions around NPs. Moreover ionic residues originating from TBE and the SEC eluent are removed. Afterwards the suspension can be further washed or transferred to a desired buffer *via* centrifugal filtration.

## 2.4 Characterization of nanoparticles *via* pH titration

When employing NPs for biomedical purposes noble metals as core material have attracted great interest.[15, 18] Not least because of the chemical inertness of these materials in contrast to hazardous materials like in QDs. But two main aspects put a ceiling on this advantage:[121] 1) "Size matters" – the size and the shape of a certain material can lead to unexpected effects and thus interactions with biological systems. 2) The surface chemistry of the NP shell has to be considered as crucial parameter regarding interaction with the environment, stability and functionalization ability. These findings demand for a thorough characterization of the physico-chemical surface properties of NPs. A feasible, time and cost effective method to do so is pH titration.[1] In an illustrative study, pH titration in combination with hydrodynamic diameter and zeta potential measurements is applied to characterize Au NPs coated with a carboxyl bearing polymer. The used polymer is of particular interest as it provides great value throughout this thesis as well as according to previous studies.[3, 72, 122] The polymer consists of a backbone of poly(isobutylene-*alt*-maleic anhydride) (PMA, $M_W$ = 6 kDa), which is modified with dodecylamine. Usually 75% of the maleic acid anhydride rings are reacted with dodecylamine so that after the coating procedure (chapter 2.2), and the transfer to an aqueous buffer, carboxylic moieties provide a net charge at the entire polymer backbone and are anchor points for further functionality. As every anhydride ring contributes two carboxylic groups and 75% of rings are reacted at one site the coating terminates in 1.25 × n carboxylic groups in case n monomers are present. Figure 6 A shows a NP after the coating has occurred but before the transfer into SBB (sodium borate buffer) at pH = 12, *i. e.* before the maleic acid anhydride rings are opened. In Figure 6 B a fraction of the polymer after coating is depicted with protonated carboxylic groups. Depending on pH a deprotonation of those provides a net charge and colloidal stability of the system. Thus a basic pH is preferred. But for a feasible functionalization strategy, namely N-(3-dimethylaminopropyl)-N'-ethylcarbodiimide (EDC) activated coupling, the optimum pH is in the range 3.5 to 4.5.[123] Herein an amide bond is formed between a carboxylic site and a primary amine of a certain molecule. Under usual circumstances regarding the $pK_a$ of aliphatic carboxylic acids ($pK_a$ = 4-5) an EDC coupling reaction is therefore practicable as enough charge is maintained to achieve colloidal stability. But in a series of titration experiments in which a colloidal suspension of polymer coated Au NPs is titrated against an

acid entirely higher $pK_a$ values are found.[1] The employed Au NPs are synthesized with a slightly different method compared to that presented in chapter 2.1 (for details see the supporting information of [1]) providing other sizes but the same surface properties.[124] For 7 nm core diameter the $pK_a$ is 7.2 and for 2 nm core diameter even a polybasic behavior (6.2 and 8.3) is observed. Apart from the latter, which might be related to curvature dependence, the higher $pK_a$ values compared to plain carboxylic acids of approximately 3 pH units is the crucial finding here. It prevents from working in an ideal environment for the further attachment of molecules *via* EDC chemistry as agglomeration is induced by van der Waals forces in case the pH is dropped under the given $pK_a$. A simple explanation for the higher $pK_a$ and also for a polybasic behavior is the formation of hydrogen bonds between specific sites at the polymer backbone (Figure 6 C).

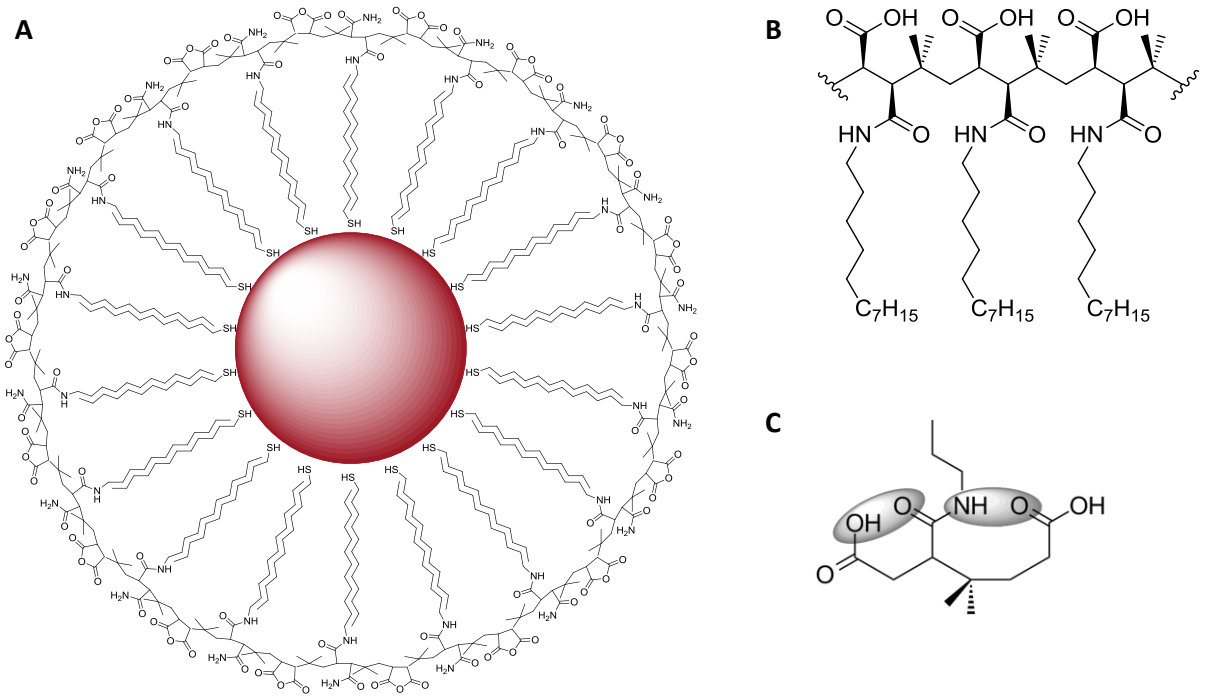


Figure 6: A) Scheme of a polymer coated NP before the transfer to an aqueous buffer indicated by the closed maleic acid anhydride rings. The hydrophobic dodecylamine side chains of the polymer intercalate with the hydrophobic dodecanethiol surfactants of the NP core. The scheme is not drawn to scale; the polymer is overexpressed for clarity. B) A fraction of the polymer backbone after transfer to an aqueous buffer. The carboxylic groups ensure a negative surface charge. As not all carboxylic groups are equivalent (some have an amide bond as counterpart and some another carboxylic group) a polybasic behavior can be observed. C) The explanation for a higher $pK_a$ compared to plain carboxylic acids goes back to the formation of hydrogen bonds at specific sites of the polymer, which also occur for the plain polymer without a NP core. The bonds show typical geometric parameters regarding bonding length and angles as determined by density functional theory (DFT) calculations. The figure is adopted and modified from reference [1].

One of the main intentions of the presented study is moreover to establish other methods to confirm the findings regarding the higher $pK_a$ values. Therefore the hydrodynamic diameter ($d_h$) and the zeta potential (ζ) are the parameters of choice and measured while titrating a Au NP suspension against an acid. The measurements are performed within a Malvern Zetasizer Nano ZS with integrated MPT-2 Autotitrator *via* DLS for $d_h$ and laser Doppler anemometry (LDA) for ζ. First the pH of the Au NP suspension is adjusted to approximately pH = 12 with a NaOH solution within several washing steps. The concentration of the NaOH solution is adjusted according to the number of carboxylic groups in the solution. As this number is beyond the knowledge of the experimenter the maximum number of present carboxylic groups, regarding the added polymer amount during the coating, is used. This ensured a full deprotonation of carboxylic groups. Incidentally the number of carboxylic groups present in the suspension can be estimated from a routine pH titration as mentioned above from the width of the buffer plateau. The NP suspension is then titrated against HCl and $d_h$ and ζ are monitored. Regarding the zeta potential measurement the following expectation can be drawn with respect to the $pK_a$: Having in mind the Henderson-Hasselbalch equation (Equation 4)

$$\mathrm{pH} = \mathrm{pK_a} + \log\left(\frac{f}{1-f}\right) \tag{4}$$

in which *f* is

$$f = \frac{[\mathrm{COO^-}]}{[\mathrm{COO^-}] + [\mathrm{COOH}]} \tag{5}$$

and thus represents the fraction of deprotonated carboxylic groups $[COO^-]$ in relation to all carboxylic groups present $[COO^-] + [COOH]$ (Equation 5). The terms in square brackets are standing for molar concentrations. Moreover the entire surface charge *Q* is then given by the maximum charge $Q_{max}$ ([COOH] ~ minimal) times the fraction *f* (Equation 6).

$$Q = Q_{max} \cdot f = Q_{max} \cdot \frac{1}{1 + 10^{\mathrm{pK_a} - \mathrm{pH}}} \tag{6}$$

Assuming a fictitious charge $Q_{max}$ of -1 C and a $pK_a$ of 7, the log(-$Q$/C) would show a linear behavior towards low (acidic) and high (basic) pH, see Figure 7. Then the asymptotes of the acidic and basic regime would have their intersection point at the given $pK_a$.

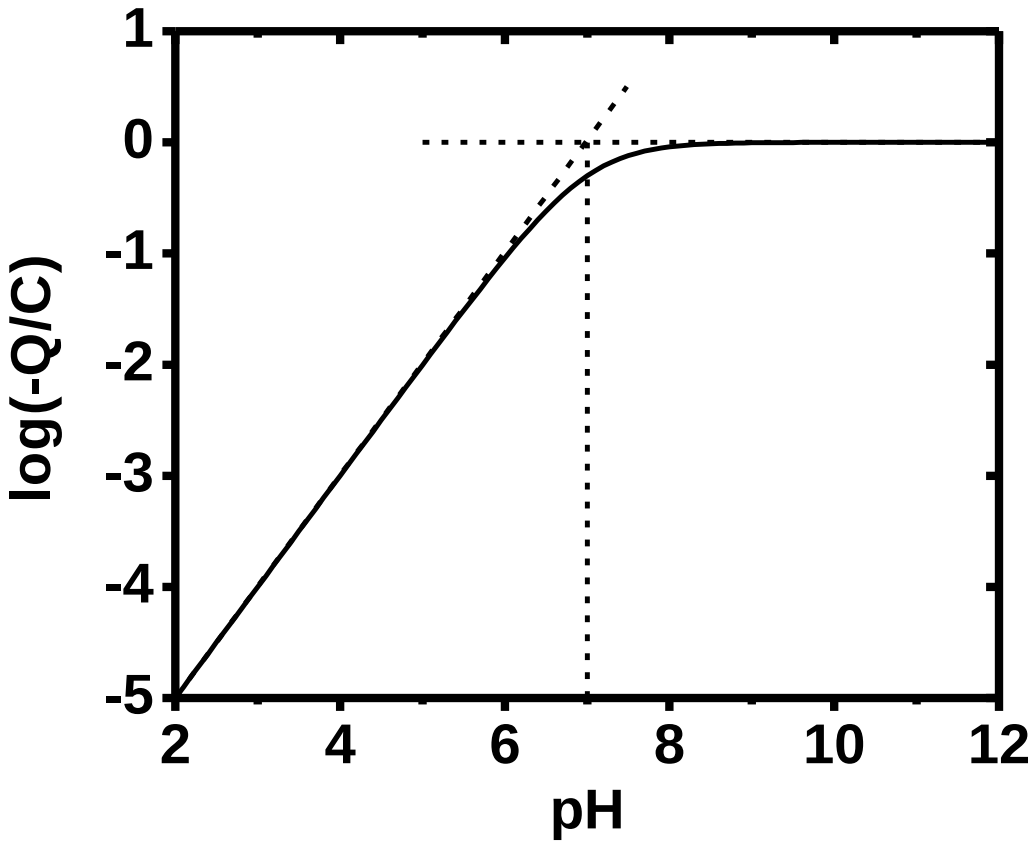


Figure 7: Fictitious behavior of log(-$Q$/C) following the Henderson-Hasselbalch equation (Equations 4-6) for $Q_{max}$ = -1 C and $pK_a$ = 7. The figure is adopted and modified from reference [1].

Assuming now, that the log(-ζ/mV) shows a similar behavior regarding the curve profile an estimate for the $pK_a$ can be drawn out of the titration experiment. Of course the zeta potential is not the same like the present surface charge but can be seen as a measure for it. The higher the entire surface charge the higher the electrostatic potential at the slipping plane of the ambient ionic cloud present at the NP surface in an aqueous buffer. Figure 8 shows on the one hand the zeta potential recorded at different pH values and on the other hand the log(-ζ/mV) for 7 nm and 2 nm core diameter, polymer coated Au NPs. In each case $pK_a$ values between 6 and 7 are estimated ($pK_{a,\zeta}$(7 nm) ≈ 6.3 and $pK_{a,\zeta}$(2 nm) ≈ 6.8). This is somewhat lower compared to the findings of the volumetric titration, considering the average $pK_a$ for 2 nm Au NPs ($pK_{a,V}$(7 nm) ≈ 7.2 and $pK_{a,V}$(2 nm) ≈ 7.3). However, the

increased $pK_a$ compared to plain carboxylic acids can be also verified by zeta potential measurements, although the method might not have the same accuracy and higher error in $pK_a$. But it supplements the opportunities to get a better understanding of the physico-chemical surface properties of the employed NPs by an easy, time and cost effective method.

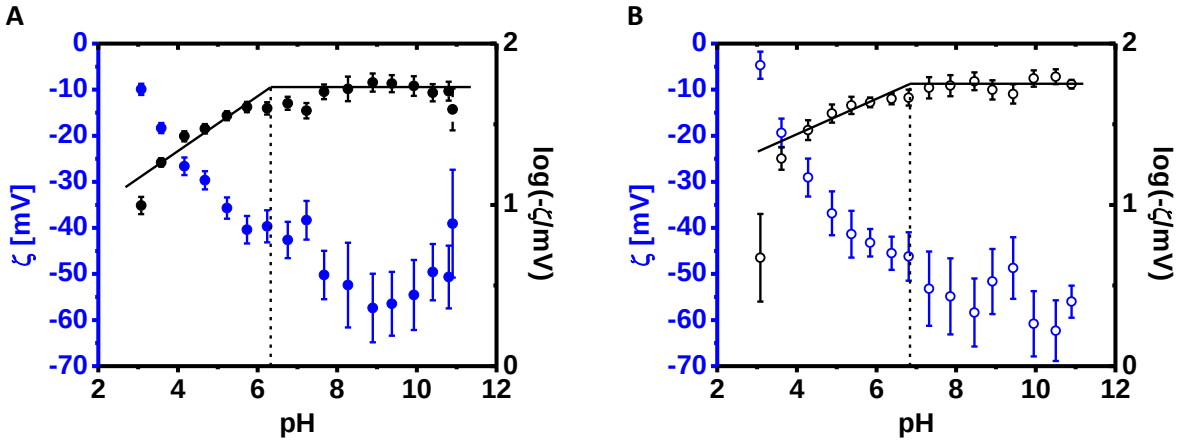


Figure 8: Zeta potential measurements (left/blue y-axis) for A) 7 nm and B) 2 nm core diameter, polymer coated Au NPs at different pH values. The present $pK_a$ of each sample is estimated from the log(-ζ/mV) at the site with the biggest curvature between the basic and acidic linear regimes (indicated by a dashed line). Each data point consists of three individual measurements. The figure is adopted and modified from reference [1].

Besides the zeta potential, which allows for a direct statement about the ionization state of the NP surface, also the hydrodynamic diameter $d_h$ can serve as characteristic parameter. In case a sufficient surface charge is not present accompanied by a low absolute zeta potential, van der Waals forces might overcome the electrostatic repulsion between individual NPs and thus lead to agglomeration. This agglomeration obviously should be verifiable by a significant increase in $d_h$ at varying pH. Figure 9 shows such a titration measurement (starting from basic pH) for 7 nm and 2 nm core diameter, polymer coated Au NPs. The arrows display from which pH on a significant increase of $d_h$ is observed indicating agglomeration. It is assumed that the $pK_a$ is located in the same pH region. Again this region is found to be around pH ≈ 7, hence significantly higher compared to the $pK_a$ of plain carboxylic acids, what confirms the previous findings. That the increase of $d_h$ occurs to a greater extent for the smaller 2 nm core diameter NPs cannot be explained at this point. A possible reason could be the higher $pK_a$ that leads to an "earlier" agglomeration. More time between the pH adjustment and the $d_h$ measurement should lead to a reversed observation.

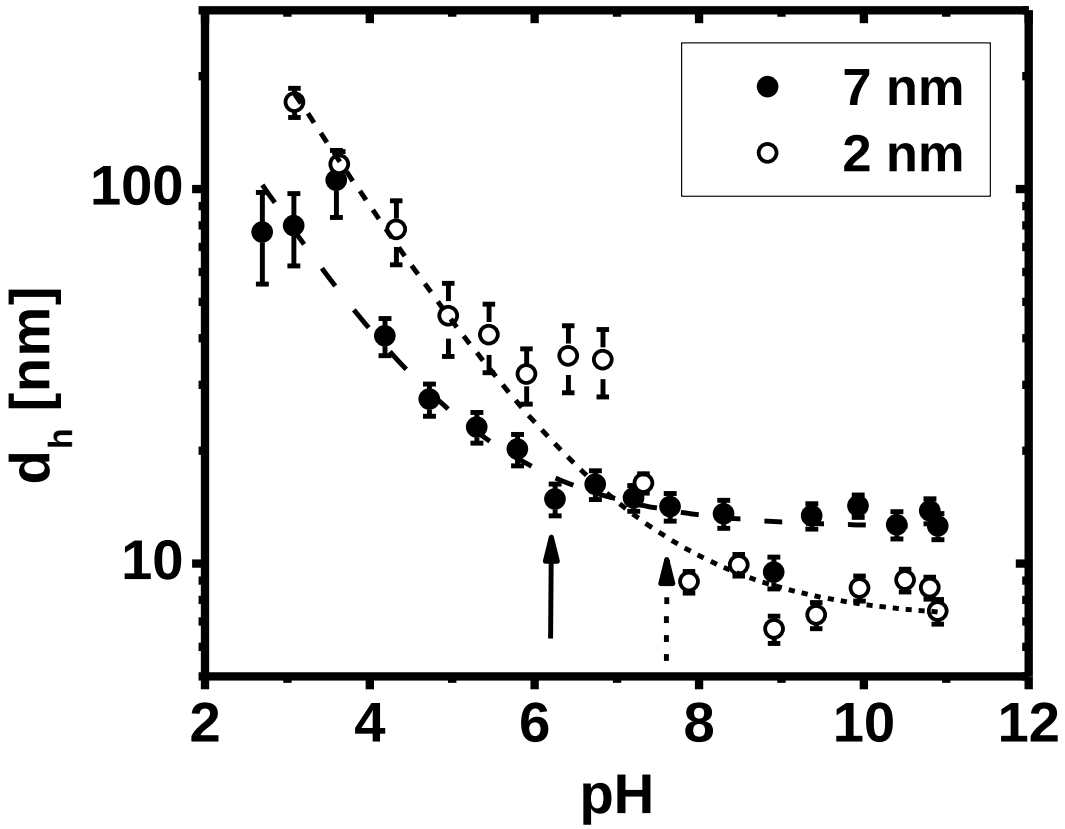


Figure 9: DLS measurement for 7 nm and 2 nm core diameter, polymer coated Au NPs. A significant increase of $d_h$ is indicated by the arrows. The lines are guides to the eye. Each data point consists of three individual measurements. The figure is adopted and modified from reference [1].

In summary one can say that, by the presented DLS and LDA methods, usual volumetric titration measurements can be verified and supported. The gained data have great value for developing an understanding of the true physico-chemical properties of the NP surface. This is of particular importance for estimating the colloidal stability or the functionalization ability of the NP system. For example the attachment of certain molecules like PEG *via* peptide coupling demand for a meticulous estimation and testing of the added amount of EDC.[72, 125, 126] But as it is not possible to work in the optimum pH range for EDC chemistry compromises have to be implemented, *e. g.* in which EDC is added once a while during the conjugation procedure.

## 2.5 Charge dependent interaction of nanoparticles with biological systems

In chapter 2.4 some insights into the physico-chemical properties of NPs, coated by a soft polymer shell, are given. It becomes clear that the state of colloidal stability or functionalization ability depend on environmental parameters like pH or more general, the ionic strength. With look to biological applications it is even more crucial to understand how the colloidal properties of NPs depend on the interaction with biological components. That is for example the colloidal stability within protein containing media, like cell culture media, or the interaction with cells themselves. It is a known feature that a so called protein corona is formed around NPs when contained in the surrounding medium or during cell uptake.[127-132] This protein corona can have far-reaching effects as on the one hand it can influence the colloidal properties of NPs and on the other hand it attributes a biological identity to NPs, what is decisive for the uptake and further processing by cells.

Thus in an exemplary study the interaction of two species of NPs, namely negatively and positively charged NPs, with biological systems is investigated.[2] Herein the surface charge is in first order the only variable parameter. An additional intention of the study is simply to enlarge the toolkit regarding polymers suitable for coating NPs with desired properties. The employed polymers are depicted in Figure 10 (for details regarding the synthesis see the supporting information of reference [2]). Each polymer consists of charged, hydrophobic and potentially functional monomers.

For the negatively charged polymer poly((2-(methacryloyloxy)ethyl)phosphonic acid)$_x$-*stat*-poly(lauryl methacrylate)$_y$-*stat*-poly(propargyle methacrylate)$_z$ (PMAPHOS-*stat*-PLMA-*stat*-PgMA) the charge is generated by the deprotonated phosphonic acid part. For the positively charged polymer poly(*N*,*N*,*N*-trimethylammonium-2-ethyl methacrylate iodide)$_x$-*stat*-poly(lauryl methacrylate)$_y$-*stat*-poly(propargyle methacrylate)$_z$ (PTMAEMA-*stat*-PLMA-*stat*-PgMA) the charge is generated by a trimethylammonium group. In both cases the hydrophobic part consists of PLMA similar to the dodecylamine modified PMA (chapter 2.4). These compounds ensured an efficient coating of NPs and transfer to aqueous solvents. One has to bear in mind, that a sufficient percentage of hydrophobic parts have to be present to ensure the coating of NPs, but as soon as the hydrophobic proportion rises too high, no colloidal stability in aqueous buffers can be maintained. The third monomer (z) is an optional one and contains the fluorescent dye perylene tetracarboxylic diimide (PDI) as functionality.

For attachment the dye is azide-modified and linked to the polymer *via* click chemistry. Depending on the characterization methodologies employed in the following, fluorescence can be necessary or a hindrance, what will become clear at the specific sites. First, optimum parameters regarding molecular weight and composition (x : y : z) have to be determined. Herein two criteria are of particular interest: 1) The polymer should be soluble in chloroform so that a homogeneous mixture with the hydrophobically capped NPs is possible. 2) The transfer to an aqueous buffer should lead to a colloidally stable suspension. Some experience from a previous study[73] regarding these requirements paved the way to find the final parameters as depicted in Table 1.

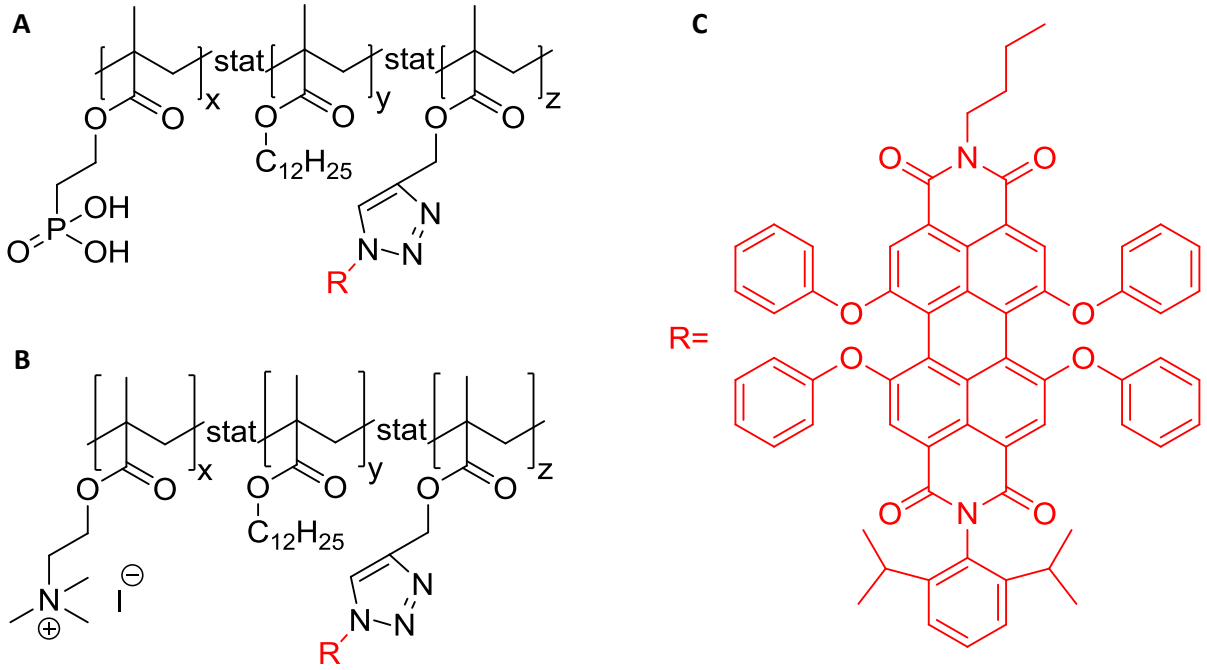


Figure 10: Structural formulas of the employed polymers. A) Negatively charged terpolymer. B) Positively charged terpolymer. C) Fluorescent dye PDI. The figure is adopted and modified from reference [2].

Table 1: Composition of the employed amphiphilic co- and terpolymers.

| **Charge** | **Functionality** | **Composition of the polymer** | | | | ***M*$_n$** |
|---|---|---|---|---|---|---|
| | | TMAEMA (x) [mol-%] | MAPHOS (x) [mol-%] | LMA (y) [mol-%] | PgMA (z) [mol-%] | [g mol$^{-1}$] |
| neg. | - | - | 40 | 60 | - | 9000 |
| pos. | - | 53 | - | 47 | - | 16300 |
| neg. | PDI | - | 52 | 42 | 6 | 9500 |
| pos. | PDI | 48 | - | 48 | 4 | 17800 |

The employed Au NPs in this study are of the same nature as depicted in Figure 2. For the transfer to aqueous solvents and for the purification *via* SEC, 0.1 M NaCl (pH = 3.3, adjusted with 0.1 M HCl) is used in case of the positively charged polymer in contrast to the already mentioned SBB at pH = 12 for the negatively charged polymer (chapter 2.4, PMA). After the routine purification processes (chapter 2.3) the coated Au NPs are thoroughly characterized. Just one exception regarding purification has to be mentioned at this point: A purification of positively charged NPs *via* gel electrophoresis with agarose gel is not possible, probably due to an interaction of the ammonium sites with the agarose matrix. However, by the even more accurate SEC and the additional desalting column and centrifugal filtration a sufficient purification is achieved.

The concentration determination of Au NPs that contain the dye PDI in their shell is not as straight forward as in case no dye is present as the dye absorbance overlaps with the LSPR peak (Figures 11 A and B). Thus a simple approach is applied, in which a linear combination of the dye and the Au core absorbance is assumed. Herein the total absorbance of the sample $A_S$ is given by Equation 7:

$$A_s = x \cdot A_{ref} + y \cdot A_p \tag{7}$$

Here $A_{ref}$ is the known absorbance of a reference Au NP sample coated with a copolymer without dye (Figure 11 C) and $A_p$ is the absorbance of the plain polymer with PDI (Figure 11 D). The parameters *x* and *y* are varied until a combination fits best to the terpolymer coated Au NP sample (Figures 11 E and F). Thus *x* determines the true Au NP concentration in the sample from the reference concentration. Of course this method is a thorough simplification of the complex system consisting of Au core and polymer shell, but with respect to the considerable matching of the spectra it can be treated as a viable approach. Moreover, the amount of dye in the sample can be estimated. It might vary, as the molar ratio of dye molecules per polymer varied and as different amounts of polymer strands might be attached to the Au cores. For sure also impurities regarding empty polymer micelles might contribute to the dye absorbance. But for the later microscopic analysis regarding cellular uptake a normalization factor is applied, which considers differences of intrinsic fluorescence intensities.

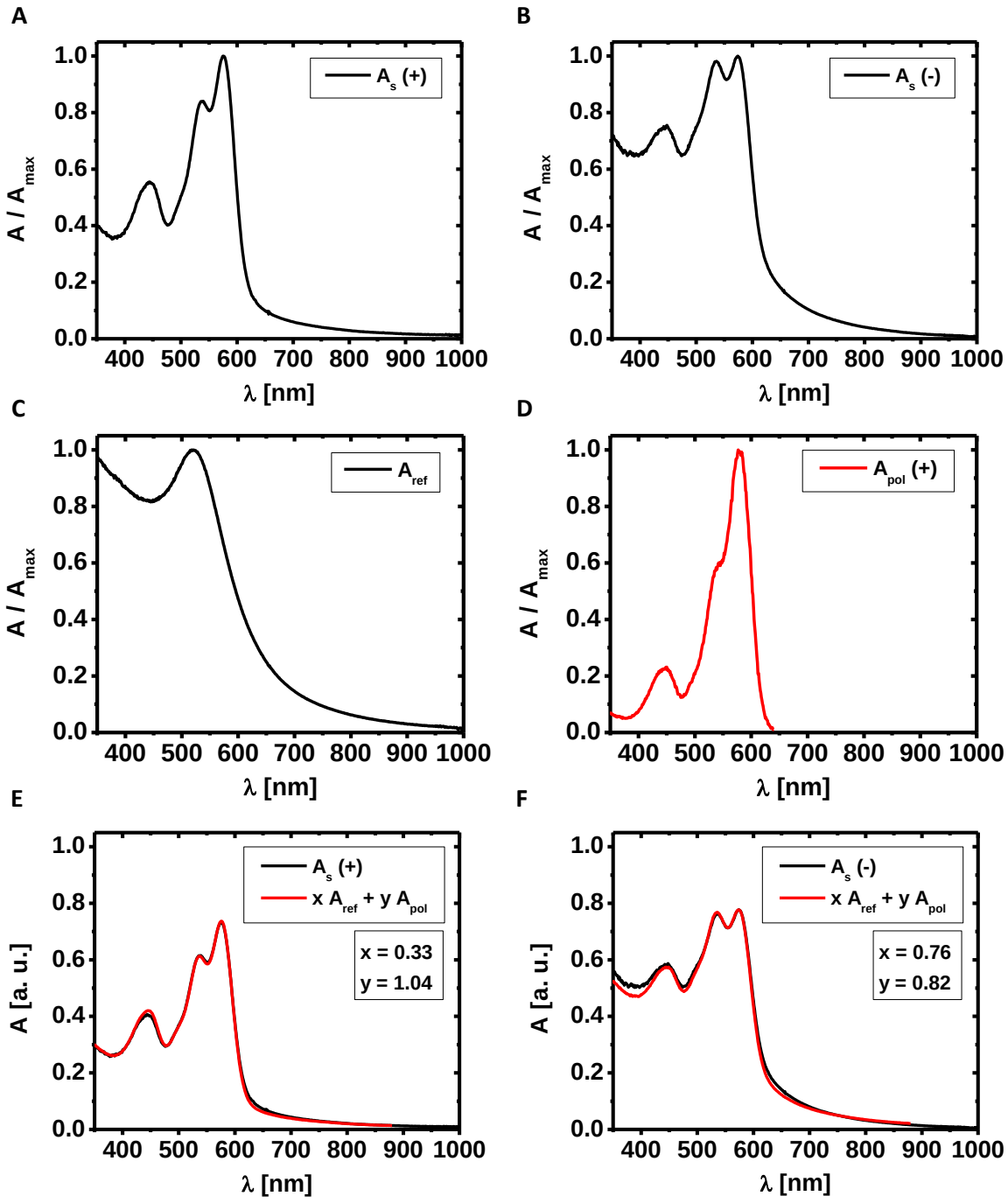


Figure 11: Extinction spectra of A) positively charged and B) negatively charged Au NPs with dye in their shell normalized at the maximum absorbance in the region of the LSPR. C) Normalized extinction spectrum of Au NPs coated with dodecylamine modified PMA as reference. D) Normalized extinction spectrum of the plain positively charged terpolymer $A_p$ showing the specific absorbance of PDI. The absorbance of the negatively charged polymer is not shown here as it does not differ from that of the positively charged one. Anyway, the absorbance by the polymers themselves is located in the UV part of the spectrum and the shown peak corresponds to PDI only. E) and F) show the same spectra like in A) and B) before normalization (black line) and each best fit according to the linear combination (Equation 7) of the dye absorbance $A_p$ and the absorbance of a reference sample without dye in the shell $A_{ref}$ (red line). The determined parameters $x$ and $y$ for each best fit are depicted in the graphs. The figure is adopted and modified from reference [2].

The fluorescence properties of Au NPs coated with positively and negatively charged co- and terpolymers as well as of a plain terpolymer are depicted in Figure 12.

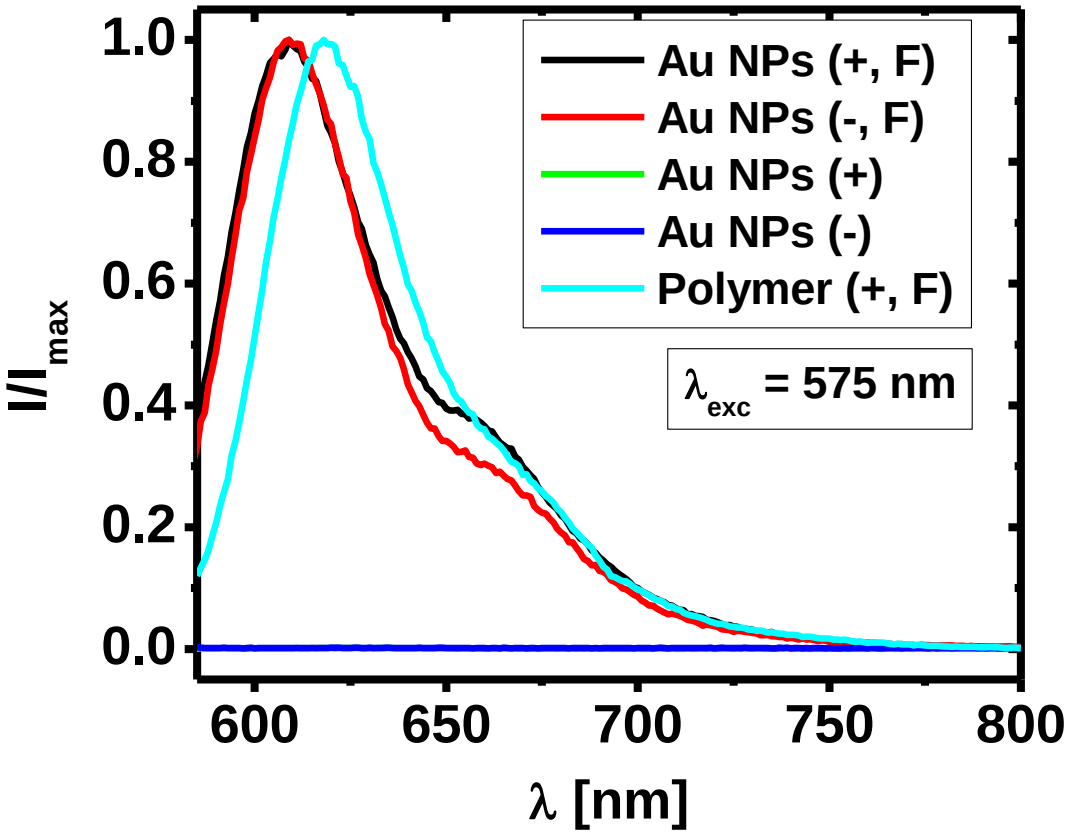


Figure 12: Fluorescence spectra of Au NPs coated with positively (+, F) or negatively (-, F) charged terpolymers with PDI in their shell. The spectra differ only within a small shoulder between 650 nm and 675 nm. The location of the maximum fluorescence is blue shifted by approximately 10 nm compared to the plain positively charged terpolymer with PDI (+, F), what might be related to changes of the micro-environment of the dye after coating. The fluorescence of the plain negatively charged terpolymer with PDI is not shown as it did not differ from that of the positively charged one. The fluorescence of Au NPs coated with positively (+) or negatively (-) charged copolymers without PDI is zero as expected. The figure is adopted from reference [2].

Fluorescent NPs are required for a characterization *via* fluorescence correlation spectroscopy (FCS) and fluorescence microscopy. Non fluorescent NPs are used for a characterization *via* DLS and LDA, here the fluorescence emission would interfere with the operating laser. The quantum yield of fluorescent Au NPs is determined *via* the method suggested by Horiba Jobin Yvon.[133] For different concentrations of Au NPs absorbance and emission spectra are recorded. The slope of the linear relation between the absorbance at

575 nm and the integrated emission ($\lambda_{exc}$ = 575 nm) delivers the quantum yield following Equation 8:

$$\Phi_s = \Phi_{ref}\left(\frac{Grad_s}{Grad_{ref}}\right)\left(\frac{\eta_s}{\eta_{ref}}\right)^2 \quad (8)$$

Here $\Phi_s$ and $\Phi_{ref}$ are the quantum yields, $Grad_s$ and $Grad_{ref}$ the slopes of the mentioned relation, and $\eta_s$ and $\eta_{ref}$ the refractive indices each of the sample and of a reference dye. Figure 13 shows the recorded extinction and emission profiles as well as the linear relations between absorbance and integrated fluorescence intensity. The reference dye is cresyl violet perchlorate (CVP) diluted in methanol with a quantum yield of $\Phi_{ref}$ = 0.54 ± 0.03.[134] The slopes are $Grad_{ref}$ = (227.4 ± 5.9) · $10^8$ cps, $Grad_s$(+) = (23.6 ± 0.4) · $10^8$ cps, and $Grad_s$(-) = (22.2 ± 0.3) · $10^8$ cps (note that the values of ΣI in Figure 13 are divided by $10^8$ for a more convenient depiction). For the refractive indices $\eta_s$ = 1.333 (water) and $\eta_{ref}$ = 1.3288 (methanol) are used. Thus quantum yields of $\Phi_s$(+) = 0.057 ± 0.004 and $\Phi_s$(-) = 0.053 ± 0.003 can be determined for positively and negatively charged Au NPs. The errors are determined *via* the Gaussian error propagation.

Furthermore the Au NPs are characterized regarding their hydrodynamic diameter and zeta potential. Therefore Au NPs which do not contain PDI in their shell are employed. Measurements with PDI are performed, but high fluctuations leave doubts about the reliability. DLS measurements are carried out in water and PBS. However, LDA measurements are carried out in water only, as too salty media are not compatible with the used cuvettes due to undesirable deposition effects at the electrodes. In Table 2 the determined values for $d_h$ in water and PBS and for ζ in water are depicted. The higher absolute zeta potential of negatively charged Au NPs is believed to do not limit the comparative study regarding charge dependent uptake, as a potential or surface charge has to be treated as a relative parameter compared to those of the cell membrane, which itself carries a net negative charge. But the higher absolute zeta potential of negatively charged Au NPs is believed to be responsible for the higher hydrodynamic diameter in PBS. Due to the ionic content an ionic cloud of greater extent is probably formed due to the higher net charge.[135]

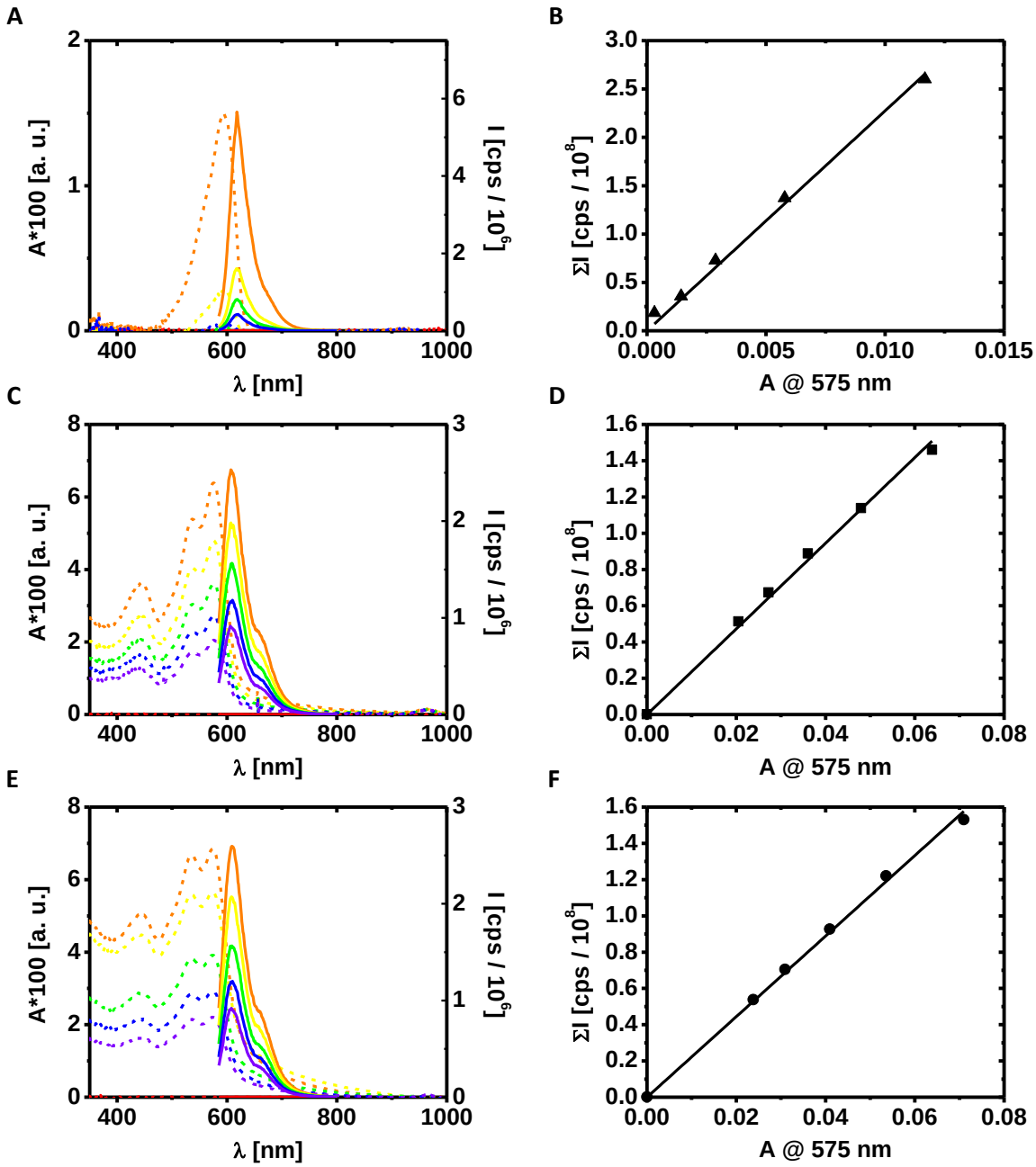


Figure 13: Quantum yield determination for fluorescent Au NPs. Graphs in the left column (A), C), E)) show the absorbance (left y-axis) and emission (right y-axis, $\lambda_{exc}$ = 575 nm) profiles of CVP, positively and negatively charged Au NPs. Graphs in the right column (B), D), F)) show the relation between integrated (588 – 800 nm) fluorescence intensity ΣI and absorbance at 575 nm. The figure is adopted from reference [2].

Table 2: Hydrodynamic diameter and zeta potential of positively and negatively charged Au NPs as determined *via* DLS and LDA. Every value consists of three individual measurements. $d_h$ was extracted from the number distribution.

| NP charge | $d_h$(water) [nm] | $d_h$(PBS) [nm] | ζ(water) [mV] |
|---|---|---|---|
| + | 13.0 ± 3.0 | 10.1 ± 0.6 | 9.7 ± 8.9 |
| - | 10.9 ± 3.2 | 14.5 ±1.0 | -39.8 ± 10.0 |

That $d_h$ in water shows a counterintuitive behavior and moreover a higher fluctuation between individual measurements (higher error) can be due to a diminished equilibrium in the NP system. In case no or little salt is present the dimension of ionic clouds formed around NPs might vary more compared to an excess of ions like in PBS.

FCS yields comparable results regarding the hydrodynamic diameter in PBS: $d_h(+)$ = 10.2 ±0.2 nm and $d_h(-)$ = 15.8 ±0.4 nm. As PDI bearing polymers are employed for FCS measurements the similar values indicate, that the dye itself might have at best little influence on the colloidal properties. Due to the hydrophobicity of the plain PDI it can also be assumed, that it might tend to the hydrophobic sites of the surface. That it is not sticking away from the NP surface in a radial manner is also supported by previous results, in which the location of a polarity sensitive dye is found to be in the hydrophobic part of the coating.[136] Figure 14 shows the result of the FCS measurement.

Additionally to plain PBS also different concentrations of human serum albumin (HSA) are added to map the adsorbance of proteins *via* an increase of $d_h$ (or as shown the hydrodynamic radius $r_h = 0.5\ d_h$). The values given above for plain PBS correspond to the asymptote of $r_h(0)$ considering the Hill model.[137] With increasing HSA concentration $r_h$ increases in a sigmoidal manner until saturation is reached indicating the formation of a protein corona. [128, 129] Here it becomes clear, that the difference in $d_h$ for positively and negatively charged NPs is not crucial regarding the comparability. As soon as proteins attach to the NP surface the difference in ζ and thus the difference in $d_h$ aligns to an almost negligible extent. Within the given uncertainty one can estimate that the hydrodynamic diameters of the NPs possessing a protein corona are approximately 20 nm.

DLS measurements within protein containing media unfortunately do not deliver reliable results. In case proteins are present in physiological conditions (*e. g.* within growth medium for cell culture) only the plain proteins are detected.

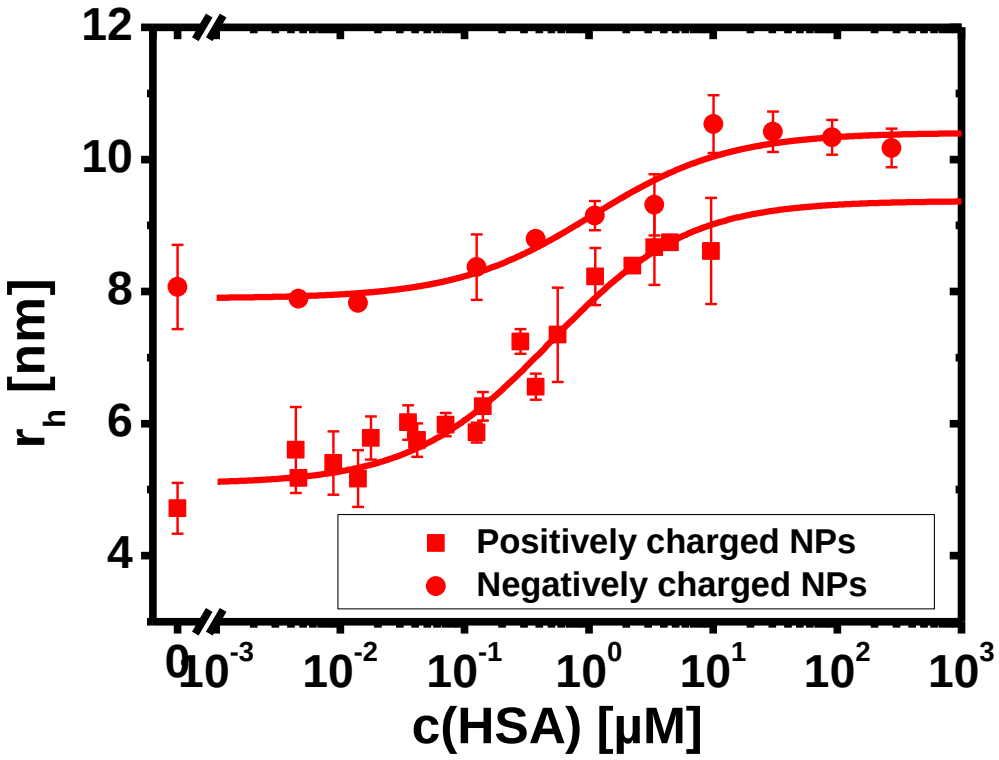


Figure 14: The hydrodynamic radius $r_h$ of positively and negatively charged Au NPs as recorded *via* FCS in PBS with increasing concentration of HSA. Every data point consists of three independent measurements. The figure is adopted from reference [2].

Thus, regarding the interaction of NPs with biological media, especially protein containing media, another method is applied, namely UV-Vis spectrometry. It is a known feature that ions or other content can attach to the NP surface and screen the entire surface charge.[138, 139] This screening can lead to an attraction of NPs *via* van der Waals forces and thus to agglomeration. In case individual Au NPs agglomerate their LSPR peak is no longer resolved clearly due to a coupling of the electronic wave functions, *i. e.* it flattens/broadens and can undergo a red shift.[140] Thus, changes in the LSPR peak can be attributed to interaction with ingredients of the medium. The media of interest, in which extinction spectra are recorded are specified in Table 3. Extinction spectra of Au NPs without PDI in their shell are recorded after a blank spectrum of the entire medium is taken. Spectra are taken every 5 minutes for 1 hour starting 1 minute after addition of the Au NPs into the medium. The maximum net absorbance located at the LSPR peak is extracted and plotted against the time after addition of the Au NPs into the medium. Surprisingly, changes of the absorbance are observed in protein containing media but without indications that allow for a conclusion in the direction of agglomeration (Figure 15).

Table 3: List of media employed for stability tests.

| Medium # | | | | | | | |
|---|---|---|---|---|---|---|---|
| **1** | **2** | **3** | **4** | **5** | **6** | **7** | **8** |
| Water[a] | PBS[b] | DMEM[c] | PBS | DMEM | PBS | DMEM | DMEM |
| - | - | - | 1% P/S[d] | 1% P/S | - | 1% P/S | 1% P/S |
| - | - | - | 1% L-Glu[e] | 1% L-Glu | - | 1% L-Glu | 1% L-Glu |
| - | - | - | - | | 800 µM BSA[f] | 800 µM BSA | 10% FBS[g] |

[a] Fresh Milli-Q water
[b] Phosphate buffered saline
[c] Dulbecco's modified Eagle's medium
[d] Penicillin/streptomycin
[e] L-glutamin
[f] Bovine serum albumin
[g] Fetal bovine serum

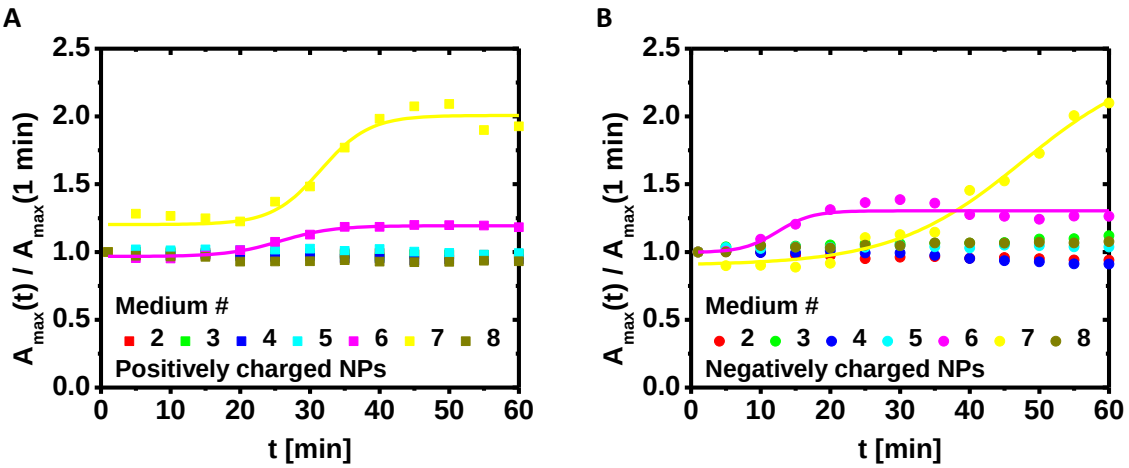


Figure 15: Time evolution of the maximum net absorbance of A) positively and B) negatively charged Au NPs at their LSPR peak in different media. The pure medium serves as blank and the indicated numbers correspond to the compositions as depicted in Table 3. 1 minute after the addition of Au NPs into the medium the first extinction spectrum is taken, then every 5 minutes for 1 hour. The added volume of Au NP suspension is 10 times lower compared to the volume of present medium, so that the physico-chemical properties of the medium are believed to be maintained. The absorbance is normalized to that after 1 minute. A significant change of the absorbance is only observed for BSA containing media (#6 and #7). The figure is adopted from reference [2].

Although the net absorbance is increasing by time for BSA containing media no red shift is observed. Thus it can be concluded that an interaction of NPs with BSA takes place which influences the absorbance and/or scattering characteristics of NPs but does not lead to agglomeration. Indeed a sigmoidal behavior can be attributed to the evolution within media #6 and #7 in accordance to the FCS results (Figure 14), although HSA is employed in this case, indicating the formation of a protein corona. In both cases the increase in the net absorbance is even stronger for the DMEM based medium #7. The concentration of 800 µM BSA in media #6 and #7 ensures similar protein content in these media compared to medium

#8 in which FBS provides the proteins. Thus, it can be concluded, that the NPs might have an increased affinity towards albumin compared to other proteins as no significant change in the absorbance profiles in medium #8 is observed, although albumin is the most abundant protein in serum. The other media (#2-#5) whether based on PBS or DMEM do not show any significant change in the absorbance profiles, what indicates that P/S and L-Glu do not influence the absorbance/scattering characteristics of the Au NPs.

Charge dependent cell internalization experiments are also performed in protein containing and protein free media, #5, #7 and #8 (Table 3), to monitor how a potential protein corona affects on uptake abilities. Therefore 3T3 fibroblast cells are incubated with positively or negatively charged Au NPs with PDI in their shell. The amount of internalized Au NPs is quantified by verification of the cell associated red fluorescence at various time points (Figure 16). Moreover the fluorescence intensity is normalized considering the different amounts of fluorophores per polymer strand, the differences of the quantum yields as well as of the brightness of a droplet of plain Au NPs under the microscope. Thus, the graphs in Figure 16 allow for a quantitative comparison of internalization efficiency. It is found, that positively charged Au NPs are taken up faster and to a greater extent. This is in line with other studies dealing with charge dependent NP internalization.[141-144] The difference in the uptake rate can be explained with the net negative surface charge the cell membrane possesses.[145-147] Both negatively and positively charged Au NPs have in common, that protein associated uptake (media #7 and #8) is diminished compared to a protein free incubation (medium #5). Also this finding is in line with previous studies,[129, 148, 149] and probably can be explained by an increased hydrodynamic diameter accompanied by a reduced surface charge due to screening effects. The latter assumption is not proven here.

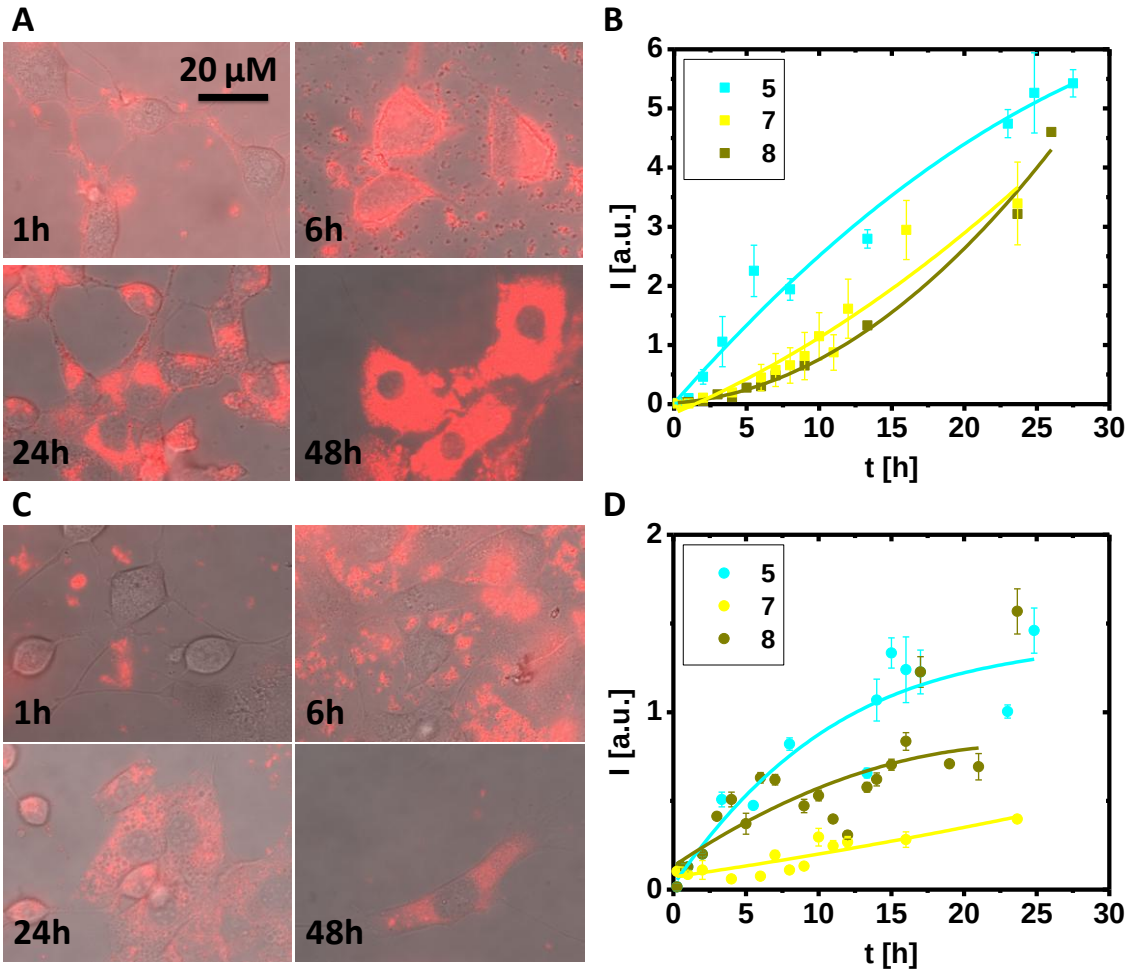


Figure 16: Illustrative fluorescence microscopy images of 3T3 fibroblast cells incubated with A) positively and C) negatively charged Au NPs at various time points in medium #8 (c(Au NPs) = 5 nM). After normalization and background correction the cell associated fluorescence intensity is verified and plotted against the incubation time. B) and D) show the uptake evolution for positively and negatively charged Au NPs with quantitatively comparable intensity axes in different incubation media (#5, #7 and #8 according to Table 3). The uptake efficiency is higher for positively charged NPs and for protein free medium #5 regardless of the charge. The lines in graphs B) and D) are guides to the eye. The figure is adopted from reference [2].

To further verify these findings, murine C17.2 neural progenitor cells (NPCs) and human umbilical vein endothelial cells (HUVECs) are incubated with positively and negatively charged Au NPs and uptake affinities are analyzed by fluorescence-activated cell sorting (FACS). Figure 17 confirms, that positively charged Au NPs are taken up to a greater extent whether after 2 h (A) or after 24 h (B) of incubation for both cell types. One has to note, that FACS cannot distinguish between Au NPs which are internalized or adhered at the outer cell membrane, thus all cell associated NPs are taken into account. Moreover it is found, that more NPs are associated with C17.2 NPCs than with HUVECs for both NP charges, although this difference is greater for the positively charged NPs. The cell type dependent uptake

affinities may not only be attributed to the cell type itself, but also reflect differences in the composition of the growth media. The NPs might be colloidally more stable in the medium used for HUVECs with less serum content as compared to NPCs. Thus, agglomeration might lead to the higher cell association observed for NPCs.

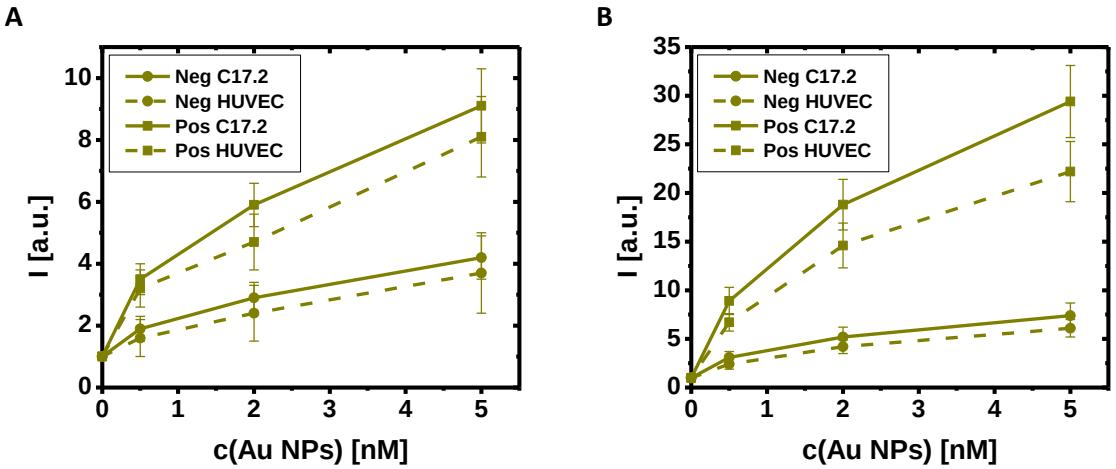


Figure 17: Uptake affinities as quantified with FACS for two different cell types (C17.2 NPCs and HUVECs) after A) 2 h and B) 24 h of incubation with positively and negatively charged fluorescent Au NPs at various NP concentrations. The fluorescence intensity I is normalized to that without NPs added (c(Au NPs) = 0 nM). The figure is adopted from reference [2].

In conclusion one can say, that cell uptake abilities depend clearly on the NP surface charge being in first order the only variable physico-chemical parameter of the evaluated NP system. Also the growth medium composition plays a crucial role as the formation of a protein corona around NPs may influence the uptake dynamics not least due to the biological identity NPs hence possess. Regarding cytotoxic effects the positively charged NPs show a clearer trend towards reduced cell viability compared to negatively charged NPs probably due to increased oxidative stress.[2] The orders of magnitude of the NP concentration from which these observations come into effect are 5 nM for positively charged and 20 nM for negatively charged NPs. One has to note, that these are the extracellular NP concentrations the cells are exposed to. But for an evaluation of cytotoxicity the intracellular NP concentration is the crucial parameter. Thus, it is a consistent finding that higher cytotoxicity for positively charged NPs correlates with a higher uptake rate.

## 2.6 Nanoparticles for ion sensing

In the previous chapters 2.4 and 2.5 the route from the characterization of the physico-chemical properties of polymer coated Au NPs towards their interaction with biological systems is depicted. So far Au NPs are not being discussed with respect to possible applications. In the following they will be presented as a feasible platform for sensing abilities. Herein the Au NPs serve as a carrier system for ion-sensitive fluorophores, which are covalently linked to the NP surface.

That Au NPs are an excellent platform as carrier system for biological purposes, is verified in a couple of studies.[16, 150, 151] This suitability is mainly related to the chemical inertness of gold, the ease of synthesis of Au NPs of various sizes, the means of functionalization abilities, and the well understood and tunable physico-chemical properties.[14] Regarding the detection of molecules or ions in solution, the immobilization of the analyte sensitive fluorophore at the NP surface has two outstanding advantages compared to the free dye: 1) The possibility to operate with intrinsically hydrophobic dyes as water solubility is mainly determined by the NP surface and 2) the ability to immobilize several dyes or other functions at the NP surface enabling the simultaneous detection of various specimens or introducing a normalization entity (*e. g.* a reference dye). Several studies provide insights into the NP/nanodevice based sensing of ions within fluorescent probes.[152-154] But experimental studies regarding ion sensitive fluorophores attached to a NP surface very often neglect an inevitable fact, that is, that the NP, and especially its surface, influences the physical conditions in close proximity. Herein the major factor is the charge of the surface as it directly influences the distribution of ions around a NP. An ion sensitive fluorophore directly attached to the surface thus generates a fluorescence signal, which is different from the signal the free dye would generate. In other words, the dye always represents its local environment regarding the distribution, hence concentration, of ions. Actually this fact has to be considered, *e. g.* in a way, that the local concentration of ions around a charged sphere is determined theoretically and compared with the readout signal of the dye. Theoretical models include calculations based on the solution of the Poisson-Boltzmann equation[155-157] or more accurate tools based on the classical DFT.[158-160] However, there is still a lack of synergy between those theoretical models and recent experimental studies.

A possible method to partly overcome the influence of the NP surface on ion distribution around NPs is, to use cross linker molecules that serve as spacer between the NP surface and the dye molecule. Hence the distance between NP surface and dye molecule is increased, so that the vicinity of the dye is more similar to the bulk conditions regarding ion concentration. This strategy is effectively carried out for the case of a negatively charged NP surface and the $Cl^-$ sensitive dye 2-[2-(6-methoxyquinolinium chloride)ethoxy]-ethanamine hydrochloride (amino-MQAE) in a previous study.[76] Herein the charge is generated by carboxylic groups which are part of the PMA based amphiphilic polymer which is already mentioned in chapter 2.4. The carboxylic groups also serve as anchor points for efficient attachment of the dye molecules, whether directly linked to the surface or with a spacer molecule in-between *via* amide bond formation. It is shown that the fluorescence intensity, which is quenched with increasing $Cl^-$ concentration, is lowered by a factor of 10 for the free dye in case the bulk $Cl^-$ concentration is increased from 0 µM to 140 µM. Whereas the fluorescence intensity of the same dye linked directly to the polymer backbone at the Au NP surface is lowered by a factor of approximately 1.7 for the same bulk conditions regarding $Cl^-$ concentration. This is due to a lower local $Cl^-$ concentration in close proximity to the NP surface due to electrostatic repulsion. In case a spacer molecule, here PEG of varying molecular weight (*i. e.* length), is mounted in-between the dye and the NP surface, the factor by which the fluorescence is lowered increases with increasing length of the spacer molecule.

To verify if the used sensor dye is also applicable with a positively charged NP surface Au NPs are coated with an amphiphilic PTMAEMA-stat-PLMA based polymer similar to the earlier mentioned click modified polymer (Figure 10). The anchor points (functionality z) are now represented by sulfhydril groups and the dye is attached using the cross linker molecule sulfosuccinimidyl-4-(*N*-maleimidomethyl)cyclohexane-1-carboxylate (sulfo-SMCC), see Figure 18.

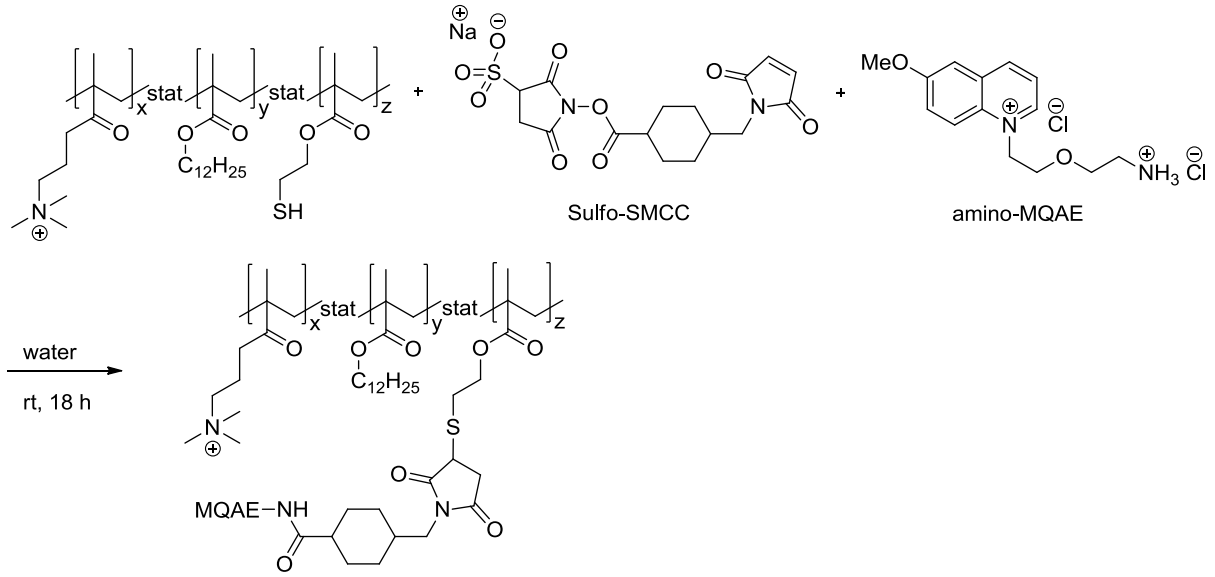


Figure 18: Reaction scheme for the functionalization of a positively charged amphiphilic polymer with amino-MQAE using the cross linker molecule sulfo-SMCC. 1 eq SH groups are stirred with 10 eq sulfo-SMCC and 100 eq amino-MQAE for 18 h at RT in water. After the conjugation, in which the maleimide group reacts with the SH group of the polymer and the *N*-hydroxysuccinimid (NHS) residue is released under an amide bond formation with the amino function of the dye, the polymer is purified from unreacted cross linker and dye molecules *via* centrifugation. After transfer of the polymer to chloroform it is readily usable for the coating of Au NPs. The scheme is adopted from reference [3].

The length of the SMCC molecule can be assumed to be approximately 0.83 nm, what results in an average distance of the dye to the NP surface of 0.5·0.83 nm ≈ 0.4 nm. In this case the fluorescence intensity is lowered by a factor of approximately 1.7 for the same bulk $Cl^-$ concentration as compared to the negatively charged Au NPs (Figure 19). As for the latter case the same factor is gained for a distance of 0 it can be assumed that the same local $Cl^-$ concentration is present. This fact and the finding, that no saturation is reached in the relevant bulk $Cl^-$ concentration region, lead to the conclusion, that the present $Cl^-$ ions accumulate around the surface and that the ion concentration decreases rapidly with increasing distance to the surface. To verify this assumption positively charged Au NPs are equipped with the same dye but a spacer molecule of approximately the double length (1.76 nm), namely succinimidyl-([*N*-maleimidopropionamido]-2ethyleneglycol) ester ($SM(PEG)_2$), see Figure 20. The fluorescence intensity is lowered by a factor of approximately 1.3 and much higher $Cl^-$ bulk concentrations are needed to reach a plateau (Figure 21). This finding supports the conclusion made above, as a significantly lower local $Cl^-$ concentration must be present for the latter case with a longer spacer.

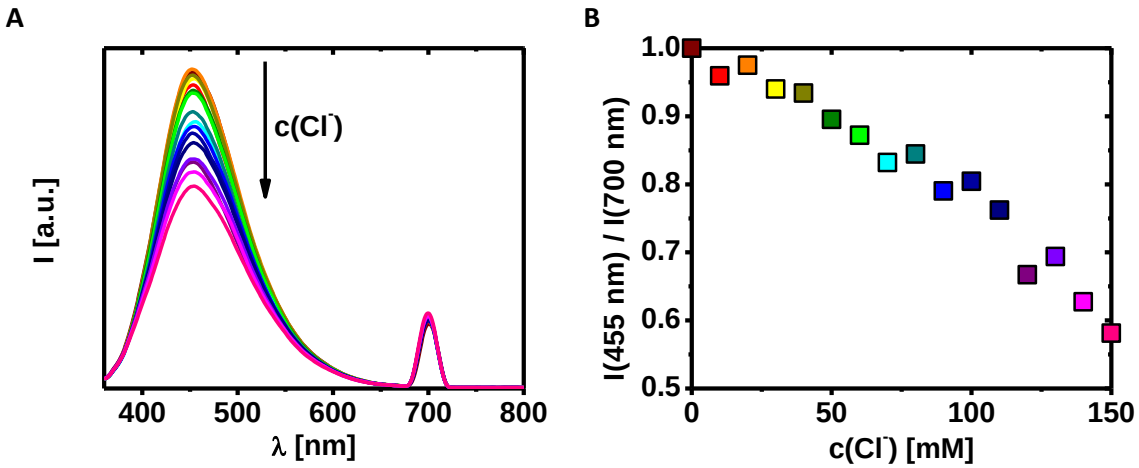


Figure 19: A) Fluorescence intensity I of positively charged Au NPs functionalized with amino-MQAE *via* SMCC suspended in water for various $Cl^-$ concentrations. The arrow indicates the direction of increasing $Cl^-$ concentration, $\lambda_{exc}$ = 350 nm, c(Au NPs) = 0.1 µM. The emission peak of amino-MQAE appears at approximately 455 nm (15 nm red shifted compared to the free dye). The $2\cdot\lambda_{exc}$ peak at 700 nm serves for normalization. B) The maximum intensities at approximately 455 nm (averaged from 450 nm to 460 nm) are plotted against the corresponding $Cl^-$ concentration. First the intensities are divided by the corresponding $2\cdot\lambda_{exc}$ peak intensity at 700 nm, then the data points are normalized in a way, that the value 1 corresponds to 0 mM $Cl^-$. Thus, an intensity quenching by a factor of approximately 1.7 is observed. The sensitive region extends over the whole set of evaluated $Cl^-$ concentrations. The figure is adopted from reference [3].

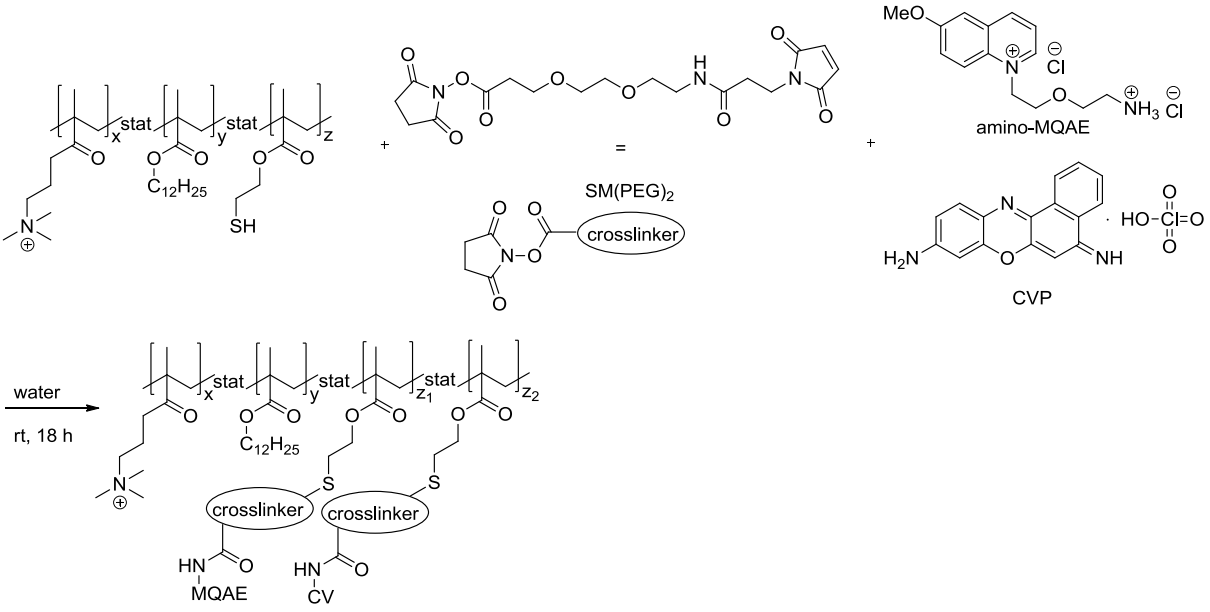


Figure 20: Reaction scheme for the functionalization of a positively charged amphiphilic polymer with amino-MQAE using the cross linker molecule $SM(PEG)_2$. 1 eq SH groups are stirred with 10 eq $SM(PEG)_2$, 90 eq amino-MQAE and 10 eq CVP for 18 h at RT in PBS / ethanol (1:2). CV serves as intrinsic fluorescent normalization probe. The remaining procedure is the same as compared to the conjugate with sulfo-SMCC (Figure 18). The scheme is adopted from reference [3].

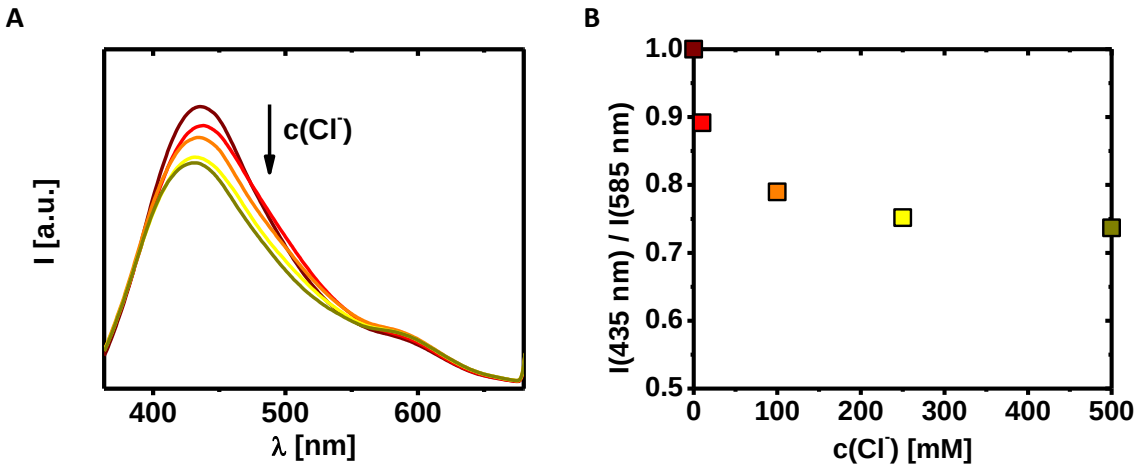


Figure 21: A) Fluorescence intensity I of positively charged Au NPs functionalized with amino-MQAE and CV *via* $SM(PEG)_2$ suspended in water for various $Cl^-$ concentrations. The arrow indicates the direction of increasing $Cl^-$ concentration, $\lambda_{exc}$ = 350 nm, c(Au NPs) = 0.1 µM. The emission peak of amino-MQAE appears at approximately 435 nm (5 nm blue shifted compared to the free dye) and the emission peak of CV appears as shoulder at approximately 585 nm. Although the emission of CV is partly overlapping with the emission of amino-MQAE it serves as a suitable control for normalization. B) The maximum intensities at approximately 435 nm (averaged from 430 nm to 440 nm) are plotted against the corresponding $Cl^-$ concentration. First the intensities are divided by the corresponding CV intensity at 585 nm (averaged from 580 nm to 590 nm), then the data points are normalized in a way, that the value 1 corresponds to 0 mM $Cl^-$. Thus, an intensity quenching by a factor of approximately 1.3 is observed. The figure is adopted from reference [3].

The presented effect, that ions in solution are attracted or repulsed by colloidal NPs depending on the sign of charge, does not compellingly have to be a disadvantage. It offers the possibility to tune the sensitivity of fluorescent dyes linked to NPs regarding the local concentration of ions. This is shown in a previous study for the dye seminaphtharhodafluor (SNARF), which responds with a change in its emission profile with changing pH.[75] Once linked to the surface of negatively charged Au NPs with spacer molecules of various lengths, the dye responds to its local pH, *i. e.* to the local concentration of hydronium ions. As the analyte is attracted by the NP surface, a low pH is suggested by SNARF molecules linked with a short spacer. Employment of a long spacer results in a read out signal similar to that of the free dye. Thus the sensitive region of the sensor device can be tuned to be in a certain range of pH.

To verify the influence of a charged NP surface on the distribution of ions with valence 2 a $Zn^{2+}$ sensitive dye is attached to negatively charged NPs. Moreover, Zn is an important metabolic trace element, what motivates its detection in biological systems. The derivative **11** of reference [161], in the following denoted as 4-aminomethyl-*N*-(6-methoxy-quinolin-8-yl)-

benzenesulfonamide (AMQB), is chosen as it possesses a primary amino group for an effective attachment to the above mentioned PMA based carboxyl bearing amphiphilic polymer (Figure 22).

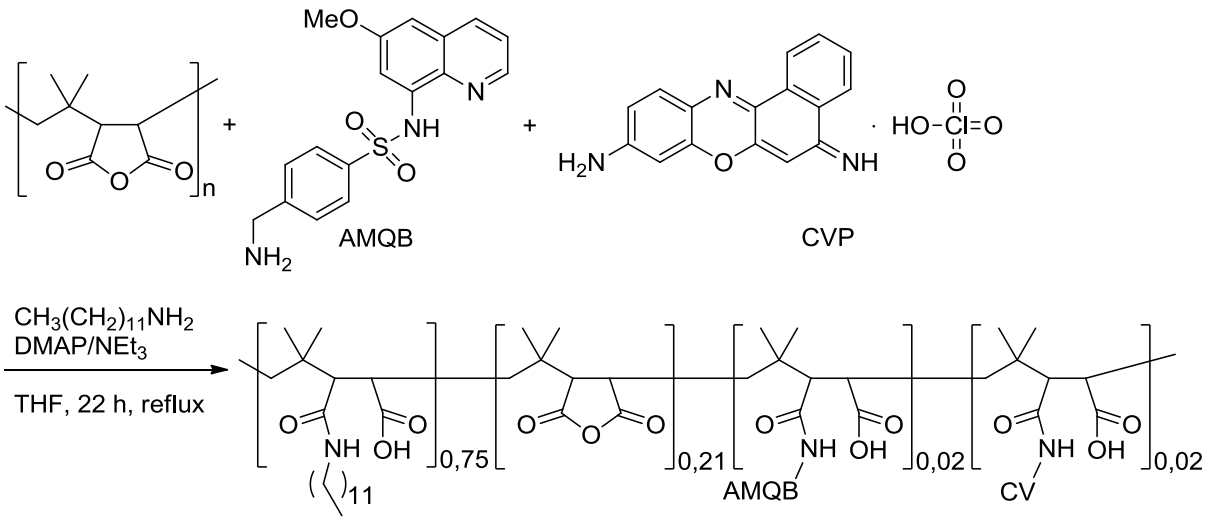


Figure 22: Reaction scheme for the functionalization of a negatively charged amphiphilic polymer with AMQB. 1 eq maleic acid anhydride rings (monomers of PMA, $M_W$ = 6 kDa) are stirred with 0.75 eq dodecylamine, 0.02 eq AMQB, 0.02 eq CVP, 0.1 eq 4-(dimethylamino)pyridine (DMAP) and 0.12 eq triethylamine (TEA) for 22 h at 80°C under reflux in tetrahydrofuran (THF). After the conjugation, in which the amino groups of AMQB and CV form amide bonds with the carboxylic groups of the polymer, the solvent is evaporated and the dry film dissolved in chloroform. The polymer is used for coating without further purification. The scheme is adopted from reference [3].

The fluorescence intensity of the free dye is amplified by a factor ≥ 50 with increasing $Zn^{2+}$ concentration, whereas the NP-dye conjugate shows an increased intensity by a factor of 6.5 (Figure 23), what may be related to the number of present dye molecules. Moreover a plateau is reached for much smaller concentrations in case of the NP-dye conjugate, what goes hand in hand with the assumption that the $Zn^{2+}$ ions are attracted by the NP surface, gaining a much higher local concentration at the surface compared to the bulk. Hence, a state of saturation is reached for smaller bulk concentrations.

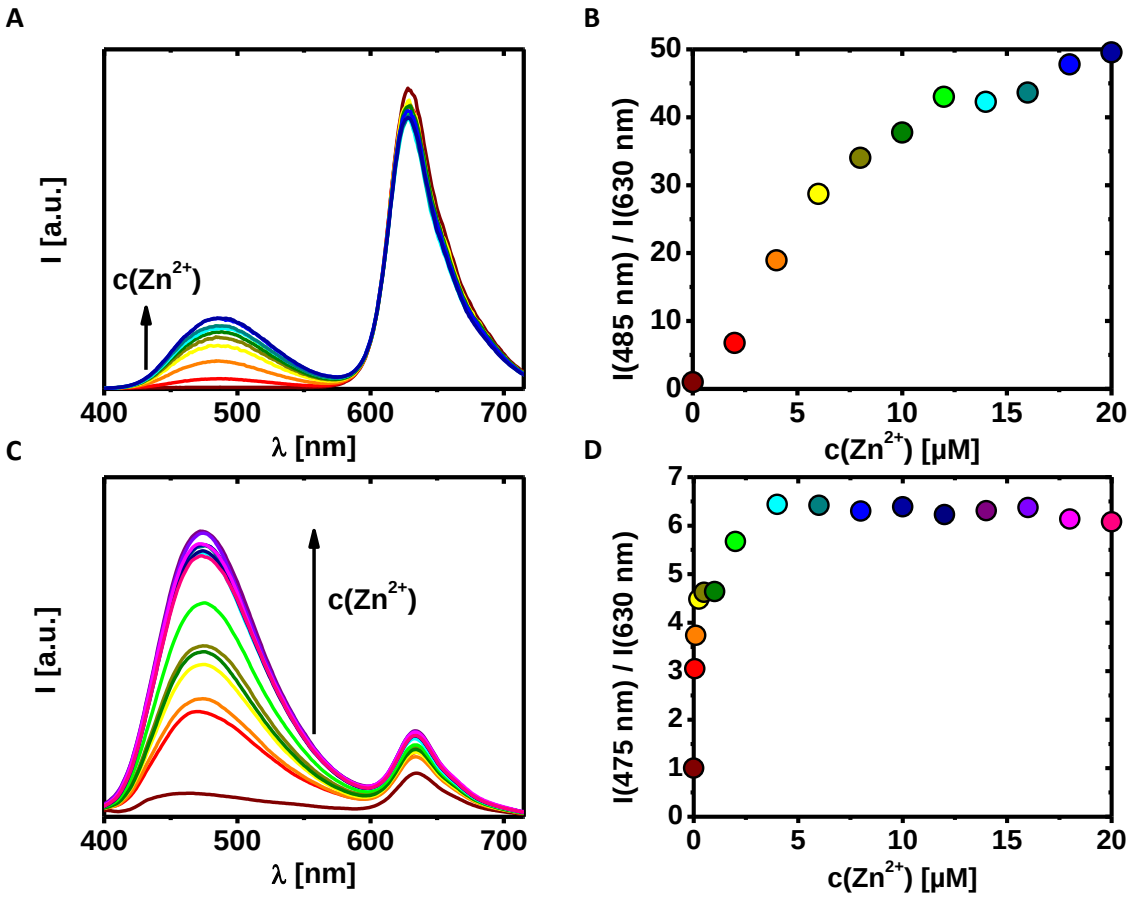


Figure 23: A) Fluorescence intensity I of free AMQB and CVP diluted in water/ethanol (1:1) for various $Zn^{2+}$ concentrations. The arrow indicates the direction of increasing $Zn^{2+}$ concentration, $\lambda_{exc}$ = 340 nm. B) The maximum intensities at approximately 485 nm (averaged from 480 nm to 490 nm) are plotted against the corresponding $Zn^{2+}$ concentration. First the intensities are divided by the corresponding CVP intensity at 585 nm (averaged from 580 nm to 590 nm), then the data points are normalized in a way, that the value 1 corresponds to 0 µM $Zn^{2+}$. Thus, an amplification of the intensity by a factor of ≥ 50 times is observed. The sensitive region extends over the whole set of evaluated $Zn^{2+}$ concentrations. C) Fluorescence intensity I of negatively charged Au NPs functionalized with AMQB and CV suspended in water for various $Zn^{2+}$ concentrations. The arrow indicates the direction of increasing $Zn^{2+}$ concentration, $\lambda_{exc}$ = 365 nm, c(Au NPs) = 0.175 µM. The emission peak of AMQB appears at approximately 475 nm (10 nm blue shifted compared to the free dye) and the emission peak of CV appears at approximately 630 nm. Although the emission of CV is partly overlapping with the emission of AMQB, it serves as a suitable control for normalization. D) The maximum intensities at approximately 475 nm (averaged from 470 nm to 480 nm) are plotted against the corresponding $Zn^{2+}$ concentration. First the intensities are divided by the corresponding CV intensity at 630 nm (averaged from 625 nm to 635 nm), then the data points are normalized in a way, that the value 1 corresponds to 0 µM $Zn^{2+}$. Thus, an amplification of the intensity by approximately 6.5 times is observed. The sensitive region extends over 0 µM to 5 µM. The figure is adopted from reference [3].

# 3 Conclusions and outlook

In the present work functional Au NPs were synthesized and investigated within different purposes. First, several general procedures regarding synthesis, surface modification, and purification were described. Herein the as synthesized Au NPs capped by hydrophobic ligands needed to be transferred into aqueous solution, what was gained by a coating procedure, in which the inorganic Au core gets enclosed within an amphiphilic polymer shell. Different scenarios regarding the functionalization ability of the polymer backbone were introduced based on the covalent attachment of molecules to one of the monomer groups. Additionally several purification steps including gel electrophoresis and SEC were introduced. Afterwards three individual studies were presented ranging from the physico-chemical characterization and the verification of interactions with biological systems to sensing applications.

pH titration was investigated as feasible method to characterize the physico-chemical surface properties of polymer coated colloidal Au NPs. It was found that the amphiphilic polymer, employed for the phase transfer of Au NPs, shows a polybasic behavior due to the formation of hydrogen bonds. Moreover the $pK_a$ values were found to be entirely higher compared to free standing carboxylic acids. This finding is crucial, to guarantee, that the conditions of a NP system are kept in a manner, so that colloidal stability is ensured (mainly regarding pH). Moreover, it allows for an estimation of optimum conditions suitable for peptide coupling reactions (like EDC coupling). As colloidal stability and EDC coupling are competing purposes, in the present case a characterization *via* pH titration can be a good strategy, to find a compromise between functionalization and stability.

Regarding the interaction of polymer coated Au NPs with biological systems, a study, in which two species of NPs were synthesized was set up. The fluorescently labeled Au NPs differed in first order only in the net surface charge, what was verified by a thorough purification and characterization. The interaction with proteins in biological media was quantified within several techniques including UV-Vis spectrometry and FCS. It was found, that a protein corona forms around NPs, a phenomenon that entirely influences the behavior of NPs in biological systems due to the different physical (size, shape) and biological

properties (the protein corona attributes a biological identity to the surface). Cell uptake experiments showed, that positively charged NPs get internalized more efficiently compared to negatively charged NPs, probably mainly driven by the net negative charge of the cell membrane. The greater uptake efficiency was accompanied by greater cytotoxicity due to a higher intracellular NP concentration of positively charged NPs.

Additionally it was shown that Au NPs are a feasible platform for sensing applications. Positively charged NPs were equipped with a $Cl^-$ sensitive dye and negatively charged NPs were equipped with a $Zn^{2+}$ sensitive dye. It can be advantageous, to use NPs as template instead of the free dyes as also hydrophobic dyes can be employed and moreover the possibility for the implementation of further functionality is given (*e. g.* additional dyes as normalization). Furthermore, the NP core itself can carry certain functionality. Though a quantitative interpretation of the data seems premature, sensitivity was evidenced. These difficulties are also related to the lacking theory regarding ion distribution around colloidal NPs. Existing theories are representing scenarios, which might be too idealized to be able to render the complex NP system given.

In summary one can say that the presented studies are a further building block for gaining a more complete understanding of the nature of colloidal NP suspensions and their potential applications. However, the power certainly lies in the well purified and characterized NP systems - a feature that often is undervalued. This statement simultaneously can be understood as a demand for more standardization in the field of nanobiotechnology. The evaluated systems regarding *e. g.* different NP types and different cell types have to be comparable so that a convergence can be drawn on the way to save nanomaterials with minimum undesired risks for health and environment.

The outlook to ongoing and future work mainly focuses on the transfer of the gained knowledge also to other NP systems instead of Au NPs. QDs for example offer great possibilities in fluorescence based studies. To study the interaction and uptake of NPs by cell nuclei could be one of those purposes. NPs could be potential candidates to study nuclear organization in space and time.

Another purpose is to develop further multifunctional NP platforms in order to combine different physico-chemical properties opening various options for detection and therapy. A desired objective would be, to be able, to combine any function (like magnetism, fluorescence, plasmon related properties, or radioactivity) with any other in one and the same object. This could happen within multiple functionalized NPs or within higher order integrated systems like polyelectrolyte microcapsules.[162, 163] Here NPs of various functions can be embedded in-between the walls of the capsules besides further functionality present as cargo in the inner cavity.

# 4 Publications

As the present thesis is written in a cumulative way, the studies that are related to a publication in the field of nanobiotechnology are mentioned in this chapter. A short description gives an overview about the intentions and results of the publications. Therefore they are ordered thematically and some additional notes behind the respective reference reflect the specific contributions by the author. The full papers can be found in the appendix. As the attachment of the supporting information of each manuscript, in which all experimental details are noted, would lead to an overloaded manuscript they are omitted, but are available online following the respective journal webpage. The studies concerning layer-by-layer (LBL) assemblies (chapter 4.2) were partly started during the author's diploma thesis and partly continued/finished during the experimental phase of the present dissertation. Hence they are not part of the central chapters of this thesis, which are dealing with functional NPs.

## 4.1 Functional nanoparticles

- [A1][1] Charron, G.; Hühn, D.; Perrier, A.; Cordier, L.; Pickett, C. J.; Nann, T.; Parak, W. J., On the Use of pH Titration to Quantitatively Characterize Colloidal Nanoparticles. *Langmuir* **2012**, *28*, 15141-15149.
    - Synthesis and phase transfer of Au NPs with an amphiphilic polymer
    - Characterization of Au NPs *via* UV-Vis spectrometry, DLS and LDA measurements at varying pH (autotitration)

An indispensable requirement that NPs must fulfill for biological applications is water solubility. As inorganic NPs very often possess hydrophobic surfactant molecules after their synthesis, amphiphilic polymers can serve as coating agents enabling the phase transfer to an aqueous solvent and give the possibility for further functionalization. An example, which is often used throughout the present thesis, is a polymer that possesses hydrophobic side chains on the one hand, which can intercalate with the surfactants of the NPs, and carboxylic groups at the entire backbone on the other hand, which generate a net negative charge and represent anchor points for the attachment of further molecules. To characterize the

physico-chemical properties of the surface of such coated NPs several techniques are applied, like gel electrophoresis, size exclusion chromatography, UV-Vis spectrometry, DLS and LDA. To expand the common techniques by another characterization tool, pH titration is established. The main intention is, to determine $pK_a$ values of carboxylic groups present at NP surfaces. They can deliver useful information about the composition of the NP shell, the stability of the colloidal suspension or the purity. Moreover it is an important parameter that determines functionalization abilities for example *via* EDC activated coupling and its reproducibility. As the $pK_a$ value depends on the entire microenvironment of the present carboxylic groups, *e. g.* due to the formation of hydrogen bonds, it is found that it is higher compared to free standing carboxylic acids. Herein simple pH measurements are combined with DLS and zeta potential measurements.

- [A2][2] Hühn, D.*; Kantner, K.*; Geidel, C.; Brandholt, S.; De Cock, I.; Soenen, S. J. H.; Rivera Gil, P.; Montenegro, J.-M.; Braeckmans, K.; Müllen, K.; Nienhaus, G. U.; Klapper, M.; Parak, W. J., Polymer-Coated Nanoparticles Interacting with Proteins and Cells: Focusing on the Sign of the Net Charge. *ACS Nano* **2013**, *7*, 3253-3263.
    - Synthesis, phase transfer and purification of Au NPs
    - Characterization of coated Au NPs with UV-Vis and fluorescence spectrometry, DLS, LDA, stability tests in biological media
    - Data evaluation

    *Both authors contributed equally

To be able, to adjust the physico-chemical surface properties of NPs, the toolkit of amphiphilic polymers is extended by several new polymers. The principle of surface coating is the same as described before: Hydrophobic monomers are intercalating with the hydrophobic surfactants of the NPs and charged monomers are gaining colloidal stability. As functionality a third monomer contained an alkyne residue, which enables the functionalization *via* click chemistry. In this way an organic fluorophore is attached to be able to optically track the NPs. Regarding the charged monomers two different polymer types are designed, which differ in their sign of charge. The intention here is, to compare quantitatively, how the interaction of Au NPs with biological systems depends on the surface charge being in first order the only variable parameter. This requires a thorough

characterization and purification of Au NPs coated with the amphiphilic polymers. The evaluated biological systems are on the one hand solutions of different composition regarding the ingredients which are relevant in cell culture media. Especially the protein content is of importance as NPs are often covered with a so called protein corona in protein containing environments. On the other hand cell uptake studies are performed *in vitro* and show that positively charged NPs are taken up more efficiently than negatively charged NPs. Moreover it is shown that, in case proteins are present in the cell culture medium during the NP uptake, the uptake rate is slowed down due to the protein corona. A higher uptake rate is also correlating with higher cytotoxicity, what is consistent with the expectation.

- [A3][3] Jimenez de Aberasturi, D.*; Hühn, D.*; Hühn, J.; Beqa, L.; Ruiz de Larramendi, I.; Pinedo, R.; Rojo, T.; Montenegro, J.-M.; Carregal-Romero, S.; Geidel, C.; Dommershausen, F.; Schütte, J.; Klapper, M.; Koert, U.; Müllen, K.; Parak, W. J., et al., Ion Selective Ligands - How Colloidal Nano- and Microparticles Introduce New Functionality. *To be submitted*.
    - Preparation and characterization of $Cl^-$ and $Zn^{2+}$ sensitive Au NPs

    *Both authors contributed equally

In an application-oriented study the potential use of NPs as platform for sensing experiments is evaluated. Herein Au NPs are employed as carrier for ion sensitive fluorophores. The fluorophores are covalently attached to amphiphilic polymers which enable the transfer of Au NPs from an organic to an aqueous environment as described before. Two species of NPs are examined: Positively charged NPs equipped with a $Cl^-$ sensitive dye and negatively charged NPs equipped with a $Zn^{2+}$ sensitive dye. Moreover the employed positively charged amphiphilic polymer is a novel investigation to enlarge the available toolkit for NP coatings and functionalization abilities. Two main ideas constitute the intention to use NPs as a sensor platform: 1) The possibility to employ also hydrophobic fluorophores, as water solubility is mainly determined by the composition of the NP surface and 2) to provide potential multifunctionality, whether anchored within the NP core or by additional molecules mounted to the shell. It is shown, that for both cases the NPs are sensitive for the respective ion species, although a quantitative interpretation of the data is challenging. One has to reflect, that the NP surface itself influences the distribution of ions

around the NP due to electrostatic repulsion or attraction. A dye, whether attached directly to the polymer backbone or with a spacer molecule of a certain length in-between, always maps the local ion concentration in its immediate environment. This fact has to be considered for a correct interpretation but can also be a useful circumstance as it allows for tunability of the sensitivity. A comprehensive theoretic approach, which quantitatively describes the ion distribution around NPs while correctly matching with recent, experimental results is still missing, not least due to the complexity of the system involving a charged spherical surface and potentially several ionic species in solution. Moreover volume displacement effects can play a role in case large molecules like PEG spacers are involved. The so called DFT is perhaps the most promising example of an appropriate description.
As the state of reference [3] was too premature to be depicted in the appendix, a patent applications, which contains the relevant data as well, was attached instead.

- [A4][4] Cywinski, P. J.; Hammann, T.; Hühn, D.; Parak, W. J.; Löhmannsröben, H.-G., Long-Decaying Quantum Dot-Europium Complex Conjugates as Luminescent Probes for Time-Resolved Fluoroassays. *To be submitted*.
    - Contribution to sample preparation, purification and characterization

In case two fluorophores get into close proximity ($\lesssim$ 10 nm) the phenomenon of FRET can be observed. It is a non radiative process, in which energy is transferred from an excited donor molecule to an acceptor molecule. As the efficiency of the process is distance dependent, it can serve as distance measure or as indication of proximity at all. QDs equipped with dye molecules represent a feasible FRET platform. In the more common case of using QDs as donor due to their sharp emission profile, the QDs get excited, energy is transferred to the acceptor (possessing a net absorption overlapping with the QD emission) and finally an acceptor emission can be observed, although not excited by the original excitation light. In case QDs function as acceptor, they usually get excited directly by the excitation light as well as by the FRET donor due to their broad absorption profile. But the two emission species can be distinguished within time-resolved fluorescence measurements. Two characteristic fluorescence life times can be observed in this scenario at the QD emission wavelength: 1) The natural life time of the QD emission (around 20 ns) and 2) the life time of the donor molecule imposed by FRET. In this study a QD-europium complex conjugate suitable for

time-resolved fluoroassays is prepared. The europium complex is therefore covalently linked to the backbone of an amphiphilic polymer as described before. $Eu^{3+}$ ions are complexed and serve as donor possessing a rather long fluorescence decay time. *Via* time-resolved fluorescence measurements the $Eu^{3+}$ fluorescence lifetime could be verified at the QD emission wavelength. By the additional attachment of biotin to the surface the QDs get biologically active and the conjugate could serve as a potential fluoroassay platform with the FRET efficiency as measure.

## 4.2 Layer-by-layer assemblies

- [A5][5] Hühn, D.; Govorov, A.; Rivera Gil, P.; Parak, W. J., Photostimulated Au Nanoheaters in Polymer and Biological Media: Characterization of Mechanical Destruction and Boiling. *Adv. Funct. Mater.* **2012**, *22*, 294-303.
    - All experimental work and data evaluation

The LBL technique is a simple self assembly method to achieve thin layers of polyelectrolytes. Herein oppositely charged polyelectrolytes are assembled on a substrate in a manner, that anionic and cationic monomers form ion pairs. For the assembly a substrate with a net surface charge is dipped into an aqueous solution of an oppositely charged polyelectrolyte. After a certain incubation time ion pairing and dissolution urge of polyelectrolytes are in equilibrium and excess polyelectrolyte can be removed in a washing step. Then the sample is dipped into an aqueous solution of the contrarily charged polyelectrolyte to restore the original charge. By repetition a desired architecture can be achieved. Additional functional molecules like organic fluorophores, proteins or NPs can be assembled in-between polyelectrolyte layers in case they possess a net charge. The purpose can be the assembly of functional surfaces/interfaces or drug release systems. In the present case clusters formed of Au NPs and fluorescein 5-isothiocyanate (FITC) labeled BSA as optical tracer were embedded in-between layers formed of poly(allylamine hydrochloride) (PAH, positively charged) and poly(sodium 4-styrenesulfonate) (PSS, negatively charged). Due to the plasmon resonance of Au clusters in the NIR region they can be efficiently heated by an appropriate laser. Thereby the LBL matrix can be locally destroyed and furthermore heat is

transported to the surrounding medium, what can be observed by the formation of vapor bubbles due to superheating. This destruction and the heat transport were studied under various conditions, comprising solvents of different physical properties and biological media.

- [A6][6] Khalid, W.; Göbel, G.; Hühn, D.; Montenegro, J. M.; Rivera Gil, P.; Lisdat, F.; Parak, W. J., Light Triggered Detection of Aminophenyl Phosphate with a Quantum Dot Based Enzyme Electrode. *J. Nanobiotechnol.* **2011**, *9*, 46.
    - Preparation of samples with LBL deposited polyelectrolytes and ALP

In another approach the LBL deposition technique is employed to immobilize the enzyme alkaline phosphatase (ALP). It converts *p*-aminophenyl phosphate (*p*APP, substrate) to 4-aminophenol (4AP, product). For an efficient oxidation an electron transport has to be present which is generated by illumination of QDs, which are fixed on a gold substrate underneath the immobilized ALP. The sensing ability for *p*APP in this photobioelectrochemical sensor is verified with immobilized ALP versus ALP in solution (without LBL fixation). An immobilization can provide a higher local enzyme concentration but permeability of the polyelectrolytes has to be given. *p*APP is detected within the range of 25 µM – 1 mM.

- [A7][7] Carregal-Romero, S.; Rinklin, P.; Schulze, S.; Schäfer, M.; Ott, A.; Hühn, D.; Yu, X.; Wolfrum, B.; Weitzel, K.-M.; Parak, W. J., Ion Transport Through Polyelectrolyte Multilayers. *Macromol. Rapid Commun.* **2013**, In press.
    - Preparation of planar LBL samples on copper substrates with and without Au NPs

A promising application of LBL deposited polyelectrolyte matrices are so called polyelectrolyte multilayer (PEM) capsules. Here the polyelectrolytes are assembled around a spherical template, which can be diluted afterwards, so that a hollow capsule is formed. The inner cavity as well as the walls of the capsules can carry certain types of functionalities, *e. g.* analyte sensitive fluorophores or NPs. Many approaches deal with ion sensitive dyes, which are deposited in the inner cavity and covalently bound to macromolecules, like dextrans, to prevent them from diffusion to the exterior. For a thorough understanding of the sensing

abilities of these kinds of capsules, it is important, to verify the transport dynamics regarding ionic species through PEMs. Thus, the transport of ions is studied within several scenarios: 1) By quantifying the sensing ability of the pH sensitive dye SNARF located in the cavity under changing environmental conditions regarding protein content. 2) By dynamically mapping the diffusion of protons into SNARF modified capsules within a flow channel system, which allows for setting a pH gradient. 3) By the bombardment induced ion transport (BIIT) technique, in which planar PEMs assembled on a copper substrate are bombarded with a potassium beam and the current-voltage characteristics give information about the ion transport abilities. The latter experiments are performed with and without Au NPs in-between the polyelectrolytes. Without Au NPs a linear current-voltage behavior is observed whereas Au NPs caused non-linear effects indicating various transport mechanisms or even electronic conductivity in addition to ionic conductivity.

## 4.3 Reviews

- [A8][8] Rivera Gil, P.; Hühn, D.; del Mercato, L. L.; Sasse, D.; Parak, W. J., Nanopharmacy: Inorganic Nanoscale Devices as Vectors and Active Compounds. *Pharmacol. Res.* **2010**, *62*, 115-125.

In this review article the current state regarding the function of pharmaceuticals based on or supplemented by nanomaterials (especially inorganic NPs) is reflected. The review is mainly addressed to pharmacists to show up potential features coming along with those functional nanomaterials of which some are already in clinical practice and some in pre-clinical phases. A focus is set on NPs made of iron oxides (magnetic resonance, hyperthermia), gold (plasmonic properties, hyperthermia), hafnium oxides (reducing agent), and calcium phosphate (delivery and imaging).

- [A9][9] Carregal-Romero, S.; Caballero-Diaz, E.; Beqa, L.; Abdelmonem, A. M.; Ochs, M.; Hühn, D.; Suau, B. S.; Valcarcel, M.; Parak, W. J., Multiplexed Sensing and Imaging with Colloidal Nano- and Microparticles. *Annu. Rev. Anal. Chem.* **2013**, *6*, 53-81.

Another review article deals with multifunctional nano- and microparticle based systems. Multifunctionality as such is one of the biggest motivations and goals for doing research in nanotechnology at all. Herein this keypoint is reflected in terms of sensing of different analytes or imaging of different labels each in parallel. The main properties and sensing abilities of materials discussed in this manner are fluorescent, magnetic and plasmonic features. Systems in which NPs are free in suspension, immobilized on a substrate, or incorporated in higher dimensional constructs like polyelectrolyte microcapsules are discussed.

- [A10][10] Pfeiffer, C.; Rehbock, C.; Hühn, D.; Carrillo, C.; Jimenez de Aberasturi, D.; Merk, V.; Barcikowski, S.; Parak, W. J., Interaction of Colloidal Nanoparticles with their Local Environment - the (Ionic) Nanoenvironment Around Nanoparticles is Different from Bulk and Determines the Physico-Chemical Properties of the Nanoparticles. *J. R. Soc., Interface*, In press.

For colloidal NPs their interaction with the local environment is of crucial importance for their function. On the one hand the local environment, especially ionic or protein content can interact with the surface of NPs in a manner (*e. g.* by chemi- and/or physisorption), so that physico-chemical surface properties are influenced. On the other hand the surface of NPs itself influences the local environment, *e. g.* in terms of ion distribution around the NP – a charged surface leads to an accumulation of oppositely charged ionic species. This review addresses this topic within several scenarios regarding the surface appearance of NPs (*e. g.* ligand free and ligand coated NPs).

# Chemicals and materials

Enlisted are all chemicals and materials with certain significance (no solvents or routine lab materials), first ordered according to their appearance in the text and secondly alphabetically (next page).

Logical order:

| **Material** | **Supplier** | **Order number** |
|---|---|---|
| Chloroauric acid | Alpha Aesar | 42803 |
| TOAB | Sigma-Aldrich | 294136 |
| Sodium borohydride | Sigma-Aldrich | 452882 |
| 1-Dodecanethiol | Sigma-Aldrich | 471364 |
| UltraPure™ Agarose | Invitrogen | 16500500 |
| TBE | Sigma-Aldrich | T3913 |
| Au NPs (10 nm colloidal gold) | British Biocell International | EM.GC10 |
| Bis(p-sulfonatophenyl)phenylphosphine dihydrate dipotassium salt | Strem Chemicals | 15-0463 |
| Dialysis membrane (MWCO = 50 kDa) | Roth | 1893.1 |
| Sephacryl S-300 HR | GE Healthcare Life Sciences | 17-0599-01 |
| Sephadex G-25 Superfine | GE Healthcare Life Sciences | 17-0031-01 |
| Disposable PD-10 desalting column | GE Healthcare Life Sciences | 17-0851-01 |
| PMA | Sigma-Aldrich | 531278 |
| Dodecylamine | Sigma-Aldrich | 325163 |
| CVP | Sigma-Aldrich | 255246 |
| PBS | Biochrom | L 1825 |
| DMEM | Sigma-Aldrich | D5796 |
| P/S | Sigma-Aldrich | P4333 |
| L-Glu | Sigma-Aldrich | G8540 |
| BSA | Sigma-Aldrich | A9647 |
| FBS | Biochrom | S 0615 |
| Sulfo-SMCC | Thermo Scientific | 22322 |
| $SM(PEG)_2$ | Thermo Scientific | 22102 |
| DMAP | Sigma-Aldrich | 522805 |
| TEA | Sigma-Aldrich | T0886 |

Alphabetic order:

| **Material** | **Supplier** | **Order number** |
|---|---|---|
| 1-Dodecanethiol | Sigma-Aldrich | 471364 |
| Au NPs (10 nm colloidal gold) | British Biocell International | EM.GC10 |
| Bis(p-sulfonatophenyl)phenylphosphine dihydrate dipotassium salt | Strem Chemicals | 15-0463 |
| BSA | Sigma-Aldrich | A9647 |
| Chloroauric acid | Alpha Aesar | 42803 |
| CVP | Sigma-Aldrich | 255246 |
| Dialysis membrane (MWCO = 50 kDa) | Roth | 1893.1 |
| Disposable PD-10 desalting column | GE Healthcare Life Sciences | 17-0851-01 |
| DMAP | Sigma-Aldrich | 522805 |
| DMEM | Sigma-Aldrich | D5796 |
| Dodecylamine | Sigma-Aldrich | 325163 |
| FBS | Biochrom | S 0615 |
| L-Glu | Sigma-Aldrich | G8540 |
| P/S | Sigma-Aldrich | P4333 |
| PBS | Biochrom | L 1825 |
| PMA | Sigma-Aldrich | 531278 |
| Sephacryl S-300 HR | GE Healthcare Life Sciences | 17-0599-01 |
| Sephadex G-25 Superfine | GE Healthcare Life Sciences | 17-0031-01 |
| $SM(PEG)_2$ | Thermo Scientific | 22102 |
| Sodium borohydride | Sigma-Aldrich | 452882 |
| Sulfo-SMCC | Thermo Scientific | 22322 |
| TBE | Sigma-Aldrich | T3913 |
| TEA | Sigma-Aldrich | T0886 |
| TOAB | Sigma-Aldrich | 294136 |
| UltraPure™ Agarose | Invitrogen | 16500500 |

# Abbreviations

| | | |
|---|---|---|
| 4AP | - | 4-aminophenol |
| Amino-MQAE | - | 2-[2-(6-methoxyquinolinium chloride)ethoxy]-ethanamine hydrochloride |
| ALP | - | alkaline phosphatase |
| AMQB | - | 4-aminomethyl-*N*-(6-methoxy-quinolin-8-yl)-benzenesulfonamide |
| BIIT | - | bombardment induced ion transport |
| BSA | - | bovine serum albumin |
| CE-MS | - | capillary electrophoresis–mass spectrometry |
| CNT(s) | - | carbon nanotube(s) |
| CVP | - | cresyl violet perchlorate |
| CV | - | cresyl violet |
| DFT | - | density functional theory |
| DLS | - | dynamic light scattering |
| DMAP | - | 4-(dimethylamino)pyridine |
| DMEM | - | Dulbecco's modified Eagle's medium |
| DNA | - | deoxyribonucleic acid |
| EDC | - | N-(3-dimethylaminopropyl)-N'-ethylcarbodiimide |
| EDTA | - | ethylenediamintetraacetic acid |
| FACS | - | fluorescence-activated cell sorting |
| FBS | - | fetal bovine serum |
| FITC | - | fluorescein 5-isothiocyanate |
| FRET | - | Förster resonance energy transfer |
| HPLC | - | high-performance liquid chromatography |
| HSA | - | human serum albumin |
| HUVEC(s) | - | human umbilical vein endothelial cell(s) |
| LDA | - | laser Doppler anemometry |
| LBL | - | layer-by-layer |
| L-Glu | - | L-glutamin |
| LSPR | - | localized surface plasmon resonance |
| MPA | - | mercaptopropionic acid |
| MRI | - | magnetic resonance imaging |
| MUA | - | mercaptoundecanoic acid |
| NHS | - | *N*-hydroxysuccinimid |
| NIR | - | near infrared |
| NP(s) | - | nanoparticle(s) |
| NPC(s) | - | neural progenitor cell(s) |
| PAH | - | poly(allylamine hydrochloride) |
| *p*APP | - | *p*-aminophenyl phosphate |
| PBS | - | phosphate buffered saline |

| | | |
|---|---|---|
| PDI | - | perylene tetracarboxylic diimide |
| PEG | - | polyethylene glycol |
| PEM(s) | - | polyelectrolyte multilayer(s) |
| PET | - | positron emission tomography |
| PgMA | - | poly(propargyle methacrylate) |
| PLMA | - | poly(lauryl methacrylate) |
| PMA | - | poly(isobutylene-*alt*-maleic anhydride) |
| PMAPHOS | - | poly((2-(methacryloyloxy)ethyl)phosphonic acid) |
| P/S | - | penicillin/streptomycin |
| PSS | - | poly(sodium 4-styrenesulfonate) |
| PTMAEMA | - | poly(*N*,*N*,*N*-trimethylammonium-2-ethyl methacrylate iodide) |
| QD(s) | - | quantum dot(s) |
| RT | - | room temperature |
| SEC | - | size exclusion chromatography |
| SERS | - | surface-enhanced Raman scattering |
| SMCC | - | succinimidyl-4-(*N*-maleimidomethyl)cyclohexane-1-carboxylate |
| $SM(PEG)_2$ | - | succinimidyl-([*N*-maleimidopropionamido]-2ethyleneglycol) ester |
| SNARF | - | seminaphtharhodafluor |
| SPP | - | surface plasmon polariton |
| SPR | - | surface plasmon resonance |
| TBE | - | Tris-borate-EDTA |
| TEA | - | triethylamine |
| TEM | - | transmission electron microscopy |
| TGA | - | thioglycolic acid |
| THF | - | tetrahydrofuran |
| TOAB | - | tetraoctylammonium bromide |
| Tris | - | tris(hydroxymethyl)aminomethane |
| UV | - | ultra violet |
| Vis | - | visible |

# Bibliography


1. Charron, G.; Hühn, D.; Perrier, A.; Cordier, L.; Pickett, C. J.; Nann, T.; Parak, W. J., On the Use of pH Titration to Quantitatively Characterize Colloidal Nanoparticles. *Langmuir* **2012**, *28*, 15141-15149.
2. Hühn, D.; Kantner, K.; Geidel, C.; Brandholt, S.; De Cock, I.; Soenen, S. J. H.; Rivera Gil, P.; Montenegro, J.-M.; Braeckmans, K.; Müllen, K.; Nienhaus, G. U.; Klapper, M.; Parak, W. J., Polymer-Coated Nanoparticles Interacting with Proteins and Cells: Focusing on the Sign of the Net Charge. *ACS Nano* **2013**, *7*, 3253-3263.
3. Jimenez de Aberasturi, D.; Hühn, D.; Hühn, J.; Beqa, L.; Ruiz de Larramendi, I.; Pinedo, R.; Rojo, T.; Montenegro, J.-M.; Carregal-Romero, S.; Geidel, C.; Dommershausen, F.; Schütte, J.; Klapper, M.; Koert, U.; Müllen, K.; Parak, W. J., Ion Selective Ligands - How Colloidal Nano- and Microparticles Introduce New Functionality. *To be submitted*.
4. Cywinski, P. J.; Hammann, T.; Hühn, D.; Parak, W. J.; Löhmannsröben, H.-G., Long-Decaying Quantum Dot-Europium Complex Conjugates as Luminescent Probes for Time-Resolved Fluoroassays. *To be submitted*.
5. Hühn, D.; Govorov, A.; Rivera Gil, P.; Parak, W. J., Photostimulated Au Nanoheaters in Polymer and Biological Media: Characterization of Mechanical Destruction and Boiling. *Adv. Funct. Mater.* **2012**, *22*, 294-303.
6. Khalid, W.; Göbel, G.; Hühn, D.; Montenegro, J.-M.; Rivera Gil, P.; Lisdat, F.; Parak, W. J., Light Triggered Detection of Aminophenyl Phosphate with a Quantum Dot Based Enzyme Electrode. *J. Nanobiotechnol.* **2011**, *9*, 46.
7. Carregal-Romero, S.; Rinklin, P.; Schulze, S.; Schäfer, M.; Ott, A.; Hühn, D.; Yu, X.; Wolfrum, B.; Weitzel, K.-M.; Parak, W. J., Ion Transport Through Polyelectrolyte Multilayers. *Macromol. Rapid Commun.* **2013**, In press.
8. Rivera Gil, P.; Hühn, D.; del Mercato, L. L.; Sasse, D.; Parak, W. J., Nanopharmacy: Inorganic Nanoscale Devices as Vectors and Active Compounds. *Pharmacol. Res.* **2010**, *62*, 115-125.
9. Carregal-Romero, S.; Caballero-Diaz, E.; Beqa, L.; Abdelmonem, A. M.; Ochs, M.; Hühn, D.; Suau, B. S.; Valcarcel, M.; Parak, W. J., Multiplexed Sensing and Imaging with Colloidal Nano- and Microparticles. *Annual Review of Analytical Chemistry* **2013**, *6*, 53-81.
10. Pfeiffer, C.; Rehbock, C.; Hühn, D.; Carrillo, C.; Jimenez de Aberasturi, D.; Merk, V.; Barcikowski, S.; Parak, W. J., Interaction of Colloidal Nanoparticles with their Local Environment - the (Ionic) Nanoenvironment Around Nanoparticles is Different from Bulk and Determines the Physico-Chemical Properties of the Nanoparticles. *J. R. Soc., Interface*, In press.
11. Goesmann, H.; Feldmann, C., Nanoparticulate Functional Materials. *Angew. Chem. Int. Ed.* **2010**, *49*, 1362-1395.
12. Pelaz, B.; Jaber, S.; Jimenez de Aberasturi, D.; Wulf, V.; de la Fuente, J. M.; Feldmann, J.; Gaub, H. E.; Josephson, L.; Kagan, C. R.; Kotov, N. A.; Liz-Marzán, L.; Mattoussi, H.; Mulvaney, P.; Murray, C. B.; Rogach, A. L.; Weiss, P. S.; Willner, I.; Parak, W. J., The State of Nanoparticle-Based Nanoscience and Biotechnology: Progress, Promises, and Challenges. *ACS Nano* **2012**, *6*, 8468–8483.
13. Maynard, A. D.; Aitken, R. J.; Butz, T.; Colvin, V.; Donaldson, K.; Oberdörster, G.; Philbert, M. A.; Ryan, J.; Seaton, A.; Stone, V.; Tinkle, S. S.; Tran, L.; Walker, N. J.; Warheit, D. B., Safe Handling of Nanotechnology. *Nature* **2006**, *444*, 267-269.
14. Daniel, M. C.; Astruc, D., Gold Nanoparticles: Assembly, Supramolecular Chemistry, Quantum-Size-Related Properties, and Applications toward Biology, Catalysis, and Nanotechnology. *Chem. Rev.* **2004**, *104*, 293-346.

15. Jain, P. K.; Huang, X. H.; El-Sayed, I. H.; El-Sayed, M. A., Noble Metals on the Nanoscale: Optical and Photothermal Properties and Some Applications in Imaging, Sensing, Biology, and Medicine. *Acc. Chem. Res.* **2008**, *41*, 1578-1586.
16. Sperling, R. A.; Rivera Gil, P.; Zhang, F.; Zanella, M.; Parak, W. J., Biological Applications of Gold Nanoparticles. *Chem. Soc. Rev.* **2008**, *37*, 1896-1908.
17. Dreaden, E. C.; Alkilany, A. M.; Huang, X.; Murphy, C. J.; El-Sayed, M. A., The Golden Age: Gold Nanoparticles for Biomedicine. *Chem. Soc. Rev.* **2012**, *41*, 2740-2779.
18. Doria, G.; Conde, J.; Veigas, B.; Giestas, L.; Almeida, C.; Assuncao, M.; Rosa, J.; Baptista, P. V., Noble Metal Nanoparticles for Biosensing Applications. *Sensors* **2012**, *12*, 1657-1687.
19. Link, S.; El-Sayed, M. A., Spectral Properties and Relaxation Dynamics of Surface Plasmon Electronic Oscillations in Gold and Silver Nanodots and Nanorods. *J. Phys. Chem B* **1999**, *103*, 8410-8426.
20. Moores, A.; Goettmann, F., The Plasmon Band in Noble Metal Nanoparticles: An Introduction to Theory and Applications. *New J. Chem.* **2006**, *30*, 1121-1132.
21. Eustis, S.; El-Sayed, M. A., Why Gold Nanoparticles are More Precious than Pretty Gold: Noble Metal Surface Plasmon Resonance and its Enhancement of the Radiative and Nonradiative Properties of Nanocrystals of Different Shapes. *Chem. Soc. Rev.* **2006**, *35*, 209-217.
22. Willets, K. A.; Van Duyne, R. P., Localized Surface Plasmon Resonance Spectroscopy and Sensing. In *Annu. Rev. Phys. Chem.*, 2007; Vol. 58, pp 267-297.
23. Nie, S. M.; Emery, S. R., Probing Single Molecules and Single Nanoparticles by Surface-Enhanced Raman Scattering. *Science* **1997**, *275*, 1102-1106.
24. Kneipp, K.; Wang, Y.; Kneipp, H.; Perelman, L. T.; Itzkan, I.; Dasari, R.; Feld, M. S., Single Molecule Detection Using Surface-Enhanced Raman Scattering (SERS). *Phys. Rev. Lett.* **1997**, *78*, 1667-1670.
25. Elghanian, R.; Storhoff, J. J.; Mucic, R. C.; Letsinger, R. L.; Mirkin, C. A., Selective Colorimetric Detection of Polynucleotides Based on the Distance-Dependent Optical Properties of Gold Nanoparticles. *Science* **1997**, *277*, 1078-1081.
26. Liu, J.; Lu, Y., A Colorimetric Lead Biosensor Using DNAzyme-Directed Assembly of Gold Nanoparticles. *J. Am. Chem. Soc.* **2003**, *125*, 6642-6642.
27. Slocik, J. M.; Zabinski, J. S.; Phillips, D. M.; Naik, R. R., Colorimetric Response of Peptide-Functionalized Gold Nanoparticles to Metal Ions. *Small* **2008**, *4*, 548-551.
28. Chah, S.; Hammond, M. R.; Zare, R. N., Gold Nanoparticles as a Colorimetric Sensor for Protein Conformational Changes. *Chemistry & Biology* **2005**, *12*, 323-328.
29. Sau, T. K.; Murphy, C. J., Seeded High Yield Synthesis of Short Au Nanorods in Aqueous Solution. *Langmuir* **2004**, *20*, 6414-6420.
30. Skirtach, A. G.; Karageorgiev, P.; De Geest, B. G.; Pazos-Perez, N.; Braun, D.; Sukhorukov, G. B., Nanorods as Wavelength-Selective Absorption Centers in the Visible and Near-Infrared Regions of the Electromagnetic Spectrum. *Adv. Mater.* **2008**, *20*, 506-510.
31. Jo, W.; Freedman, K.; Yi, D. K.; Bose, R. K.; Lau, K. K. S.; Solomon, S. D.; Kim, M. J., Photon to Thermal Response of a Single Patterned Gold Nanorod Cluster Under Near-Infrared Laser Irradiation. *Biofabrication* **2011**, *3*, 1-7.
32. Govorov, A. O.; Richardson, H. H., Generating Heat with Metal Nanoparticles. *Nano Today* **2007**, *2*, 30-38.
33. Huang, X.; El-Sayed, I. H.; Qian, W.; El-Sayed, M. A., Cancer Cell Imaging and Photothermal Therapy in the Near-Infrared Region by Using Gold Nanorods. *J. Am. Chem. Soc.* **2006**, *128*, 2115-2120.
34. Alkilany, A. M.; Thompson, L. B.; Boulos, S. P.; Sisco, P. N.; Murphy, C. J., Gold Nanorods: Their Potential for Photothermal Therapeutics and Drug Delivery, Tempered by the Complexity of their Biological Interactions. *Adv Drug Deliv Rev* **2012**, *64*, 190-199.

35. Bakhtiari, A. B. S.; Hsiao, D.; Jin, G. X.; Gates, B. D.; Branda, N. R., An Efficient Method Based on the Photothermal Effect for the Release of Molecules from Metal Nanoparticle Surfaces. *Angew. Chem. Int. Ed.* **2009**, *48*, 4166-4169.
36. Skirtach, A. G.; Dejugnat, C.; Braun, D.; Susha, A. S.; Parak, W. J.; Möhwald, H.; Sukhorukov, G. B., The Role of Metal Nanoparticles in Remote Release of Encapsulated Materials. *Nano Lett.* **2005**, *5*, 1371-1377.
37. Muñoz Javier, A.; del Pino, P.; Bedard, M. F.; Skirtach, A. G.; Ho, D.; Sukhorukov, G. B.; Plank, C.; Parak, W. J., Photoactivated Release of Cargo from the Cavity of Polyelectrolyte Capsules to the Cytosol of Cells. *Langmuir* **2008**, *24*, 12517-12520.
38. Weissleder, R., A Clearer Vision for in Vivo Imaging. *Nat. Biotechnol.* **2001**, *19*, 316–317.
39. Huschka, R.; Zuloaga, J.; Knight, M. W.; Brown, L. V.; Nordlander, P.; Halas, N. J., Light-Induced Release of DNA from Gold Nanoparticles: Nanoshells and Nanorods. *J. Am. Chem. Soc.* **2011**, *133*, 12247-12255.
40. Hirsch, L. R.; Stafford, R. J.; Bankson, J. A.; Sershen, S. R.; Rivera, B.; Price, R. E.; Hazle, J. D.; Halas, N. J.; West, J. L., Nanoshell-Mediated Near-Infrared Thermal Therapy of Tumors Under Magnetic Resonance Guidance. *Proc. Natl. Acad. Sci. U. S. A.* **2003**, *100*, 13549-13554.
41. Chen, J.; Wang, D.; Xi, J.; Au, L.; Siekkinen, A.; Warsen, A.; Li, Z. Y.; Zhang, H.; Xia, Y.; Li, X., Immuno Gold Nanocages with Tailored Optical Properties for Targeted Photothermal Destruction of Cancer Cells. *Nano Lett.* **2007**, *7*, 1318-1322.
42. Pelaz, B.; Grazu, V.; Ibarra, A.; Magen, C.; del Pino, P.; de la Fuente, J. M., Tailoring the Synthesis and Heating Ability of Gold Nanoprisms for Bioapplications. *Langmuir* **2012**, *28*, 8965-8970.
43. Turkevich, J.; Stevenson, P. C.; Hillier, J., A Study of the Nucleation and Growth Processes in the Synthesis of Colloidal Gold. *Discuss. Faraday Soc.* **1951**, *11*, 55 - 75.
44. Brust, M.; Walker, M.; Bethell, D.; Schiffrin, D. J.; Whyman, R., Synthesis of Thiol-Derivatized Gold Nanoparticles in a 2-Phase Liquid-Liquid System. *J. Chem. Soc., Chem. Commun.* **1994**, 801-802.
45. Perrault, S. D.; Chan, W. C. W., Synthesis and Surface Modification of Highly Monodispersed, Spherical Gold Nanoparticles of 50-200 nm. *J. Am. Chem. Soc.* **2009**, *131*, 17042-17043.
46. Sakai, T.; Alexandridis, P., Mechanism of Gold Metal Ion Reduction, Nanoparticle Growth and Size Control in Aqueous Amphiphilic Block Copolymer Solutions at Ambient Conditions. *J. Phys. Chem. B* **2005**, *109*, 7766-7777.
47. Mafune, F.; Kohno, J.; Takeda, Y.; Kondow, T.; Sawabe, H., Formation of Gold Nanoparticles by Laser Ablation in Aqueous Solution of Surfactant. *J. Phys. Chem. B* **2001**, *105*, 5114-5120.
48. Rai, M.; Yadav, A.; Gade, A., Silver Nanoparticles as a New Generation of Antimicrobials. *Biotechnol. Adv.* **2009**, *27*, 76-83.
49. Morones, J.; Elechiguerra, J.; Camacho, A.; Holt, K.; Kouri, J.; Ram, J.; Yacaman, M., The Bactericidal Effect of Silver Nanoparticles. *Nanotechnology* **2005**, *16*, 2346-2352.
50. Wijnhoven, S. W. P.; Peijnenburg, W. J. G. M.; Herberts, C. A.; Hagens, W. I.; Oomen, A. G.; Heugens, E. H. W.; Roszek, B.; Bisschops, J.; Gosens, I.; Van de Meent, D.; Dekkers, S.; De Jong, W. H.; Van Zijverden, M.; Sips, A.; Geertsma, R. E., Nano-Silver - a Review of Available Data and Knowledge Gaps in Human and Environmental Risk Assessment. *Nanotoxicology* **2009**, *3*, 109-138.
51. Ravindran, A.; Chandran, P.; Khan, S. S., Biofunctionalized Silver Nanoparticles: Advances and Prospects. *Colloids Surf., B* **2013**, *105*, 342-352.
52. Haes, A. J.; Van Duyne, R. P., A Nanoscale Optical Biosensor: Sensitivity and Selectivity of an Approach Based on the Localized Surface Plasmon Resonance Spectroscopy of Triangular Silver Nanoparticles. *J. Am. Chem. Soc.* **2002**, *124*, 10596-10604.
53. McFarland, A. D.; Van Duyne, R. P., Single Silver Nanoparticles as Real-Time Optical Sensors with Zeptomole Sensitivity. *Nano Lett.* **2003**, *3*, 1057-1062.
54. Duan, H. W.; Nie, S. M., Etching Colloidal Gold Nanocrystals with Hyperbranched and Multivalent Polymers: A New Route to Fluorescent and Water-Soluble Atomic Clusters. *J. Am. Chem. Soc.* **2007**, *129*, 2412-2413.

55. Huang, S.; Pfeiffer, C.; Hollmann, J.; Friede, S.; Chen, J. J.-C.; Beyer, A.; Volz, K.; Heimbrodt, W.; Montenegro Martos, J. M.; Chang, W.; Parak, W. J., Synthesis and Characterization of Colloidal Fluorescent Silver Nanoclusters. *Langmuir* **2012**, *28*, 8915−8919.
56. Sun, Y.; Xia, Y., Shape-Controlled Synthesis of Gold and Silver Nanoparticles. *Science* **2002**, *298*, 2176-2179.
57. Panacek, A.; Kvitek, L.; Prucek, R.; Kolar, M.; Vecerova, R.; Pizurova, N.; Sharma, V. K.; Nevecna, T.; Zboril, R., Silver Colloid Nanoparticles: Synthesis, Characterization, and their Antibacterial Activity. *J. Phys. Chem. B* **2006**, *110*, 16248-16253.
58. Alivisatos, A. P., Semiconductor Clusters, Nanocrystals, and Quantum Dots. *Science* **1996**, *271*, 933-937.
59. Chan, W. C. W.; Nie, S., Quantum Dot Bioconjugates for Ultrasensitive Nonisotopic Detection. *Science* **1998**, *281*, 2016-2018.
60. Michalet, X.; Pinaud, F. F.; Bentolila, L. A.; Tsay, J. M.; Doose, S.; Li, J. J.; Sundaresan, G.; Wu, A. M.; Gambhir, S. S.; Weiss, S., Quantum Dots for Live Cells, in Vivo Imaging, and Diagnostics. *Science* **2005**, *307*, 538-544.
61. Medintz, I. L.; Uyeda, H. T.; Goldman, E. R.; Mattoussi, H., Quantum Dot Bioconjugates for Imaging, Labelling and Sensing. *Nat. Mater.* **2005**, *4*, 435-446.
62. Medintz, I. L.; Clapp, A. R.; Mattoussi, H.; Goldman, E. R.; Fisher, B.; Mauro, J. M., Self-Assembled Nanoscale Biosensors Based on Quantum Dot FRET Donors. *Nat. Mater.* **2003**, *2*, 630-638.
63. Gerion, G.; Pinaud, F.; Williams, S. C.; Parak, W. J.; Zanchet, D.; Weiss, S.; Alivisatos, A. P., Synthesis and Properties of Biocompatible Water-Soluble Silica-Coated CdSe/ZnS Semiconductor Quantum Dots. *J. Phys. Chem. B* **2001**, *105*, 8861-8871.
64. Vastola, G.; Zhang, Y. W.; Shenoy, V. B., Experiments and Modeling of Alloying in Self-Assembled Quantum Dots. *Curr. Opin. Solid State Mater. Sci.* **2012**, *16*, 64-70.
65. Pankhurst, Q. A.; Connolly, J.; Jones, S. K.; Dobson, J., Applications of Magnetic Nanoparticles in Biomedicine. *J. Phys. D: Appl. Phys.* **2003**, *36*, R167-R181.
66. Gupta, A. K.; Gupta, M., Synthesis and Surface Engineering of Iron Oxide Nanoparticles for Biomedical Applications. *Biomaterials* **2005**, *26*, 3995-4021.
67. Lu, A. H.; Salabas, E. L.; Schuth, F., Magnetic Nanoparticles: Synthesis, Protection, Functionalization, and Application. *Angew. Chem. Int. Ed.* **2007**, *46*, 1222-1244.
68. Laurent, S.; Forge, D.; Port, M.; Roch, A.; Robic, C.; Vander Elst, L.; Muller, R. N., Magnetic Iron Oxide Nanoparticles: Synthesis, Stabilization, Vectorization, Physicochemical Characterizations, and Biological Applications. *Chem. Rev.* **2008**, *108*, 2064-2110.
69. Weisbecker, C. S.; Merritt, M. V.; Whitesides, G. M., Molecular Self-Assembly of Aliphatic Thiols on Gold Colloids. *Langmuir* **1996**, *12*, 3763-3772.
70. Love, J. C.; Estroff, L. A.; Kriebel, J. K.; Nuzzo, R. G.; Whitesides, G. M., Self-Assembled Monolayers of Thiolates on Metals as a Form of Nanotechnology. *Chem. Rev.* **2005**, *105*, 1103-1169.
71. Sakura, T.; Takahashi, T.; Kataoka, K.; Nagasaki, Y., One-Pot Preparation of Mono-Dispersed and Physiologically Stabilized Gold Colloid. *Colloid. Polym. Sci.* **2005**, *284*, 97-101.
72. Lin, C.-A. J.; Sperling, R. A.; Li, J. K.; Yang, T.-Y.; Li, P.-Y.; Zanella, M.; Chang, W. H.; Parak, W. J., Design of an Amphiphilic Polymer for Nanoparticle Coating and Functionalization. *Small* **2008**, *4*, 334-341.
73. Geidel, C.; Schmachtel, S.; Riedinger, A.; Pfeiffer, C.; Müllen, K.; Klapper, M.; Parak, W. J., A General Synthetic Approach for Obtaining Cationic and Anionic Inorganic Nanoparticles *via* Encapsulation in Amphiphilic Copolymers. *Small* **2011**, *7*, 2929–2934.
74. Erathodiyil, N.; Ying, J. Y., Functionalization of Inorganic Nanoparticles for Bioimaging Applications. *Acc. Chem. Res.* **2011**, *44*, 925-935.
75. Zhang, F.; Ali, Z.; Amin, F.; Feltz, A.; Oheim, M.; Parak, W. J., Ion and pH Sensing with Colloidal Nanoparticles: Influence of Surface Charge on Sensing and Colloidal Properties. *ChemPhysChem* **2010**, *11*, 730-735.

76. Riedinger, A.; Zhang, F.; Dommershausen, F.; Röcker, C.; Brandholt, S.; Nienhaus, G. U.; Koert, U.; Parak, W. J., Ratiometric Optical Sensing of Chloride Ions with Organic Fluorophore - Gold Nanoparticle Hybrids: A Systematic Study of Distance Dependency and the Influence of Surface Charge. *Small* **2010**, *6*, 2590-2597.
77. Liong, M.; Lu, J.; Kovochich, M.; Xia, T.; Ruehm, S. G.; Nel, A. E.; Tamanoi, F.; Zink, J. I., Multifunctional Inorganic Nanoparticles for Imaging, Targeting, and Drug Delivery. *ACS Nano* **2008**, *2*, 889-896.
78. Ali, Z.; Abbasi, A. Z.; Zhang, F.; Arosio, P.; Lascialfari, A.; Casula, M. F.; Wenk, A.; Kreyling, W.; Plapper, R.; Seidel, M.; Niessner, R.; Knoll, J.; Seubert, A.; Parak, W. J., Multifunctional Nanoparticles for Dual Imaging. *Anal. Chem.* **2011**, *83*, 2877-2882.
79. Alivisatos, P., The Use of Nanocrystals in Biological Detection. *Nat. Biotechnol.* **2004**, *22*, 47-51.
80. Cheon, J.; Lee, J.-H., Synergistically Integrated Nanoparticles as Multimodal Probes for Nanobiotechnology. *Acc. Chem. Res.* **2008**, *41*, 1630-1640.
81. Nahrendorf, M.; Zhang, H. W.; Hembrador, S.; Panizzi, P.; Sosnovik, D. E.; Aikawa, E.; Libby, P.; Swirski, F. K.; Weissleder, R., Nanoparticle PET-CT Imaging of Macrophages in Inflammatory Atherosclerosis. *Circulation* **2008**, *117*, 379-387.
82. Jun, Y. W.; Lee, J. H.; Cheon, J., Chemical Design of Nanoparticle Probes for High-Performance Magnetic Resonance Imaging. *Angew. Chem. Int. Ed.* **2008**, *47*, 5122-5135.
83. Cobley, C. M.; Chen, J. Y.; Cho, E. C.; Wang, L. V.; Xia, Y. N., Gold Nanostructures: A Class of Multifunctional Materials for Biomedical Applications. *Chem. Soc. Rev.* **2011**, *40*, 44-56.
84. Boisselier, E.; Astruc, D., Gold Nanoparticles in Nanomedicine: Preparations, Imaging, Diagnostics, Therapies and Toxicity. *Chem. Soc. Rev.* **2009**, *38*, 1759-1782.
85. Wang, Z. X.; Ma, L. N., Gold Nanoparticle Probes. *Coord. Chem. Rev.* **2009**, *253*, 1607-1618.
86. Lin, Y. W.; Huang, C. C.; Chang, H. T., Gold Nanoparticle Probes for the Detection of Mercury, Lead and Copper Ions. *Analyst* **2011**, *136*, 863-871.
87. Li, D.; Wieckowska, A.; Willner, I., Optical Analysis of $Hg^{2+}$ Ions by Oligonucleotide-Gold-Nanoparticle Hybrids and DNA-Based Machines. *Angew. Chem. Int. Ed.* **2008**, *47*, 3927-3931.
88. Xue, X. J.; Wang, F.; Liu, X. G., One-Step, Room Temperature, Colorimetric Detection of Mercury ($Hg^{2+}$) Using DNA/Nanoparticle Conjugates. *J. Am. Chem. Soc.* **2008**, *130*, 3244-3245.
89. Wang, H.; Wang, Y. X.; Jin, J. Y.; Yang, R. H., Gold Nanoparticle-Based Colorimetric and "Turn-On" Fluorescent Probe for Mercury(II) Ions in Aqueous Solution. *Anal. Chem.* **2008**, *80*, 9021-9028.
90. Xie, J. P.; Zheng, Y. G.; Ying, J. Y., Highly Selective and Ultrasensitive Detection of Hg(2+) Based on Fluorescence Quenching of Au Nanoclusters by Hg(2+)-Au(+) Interactions. *Chem. Commun.* **2010**, *46*, 961-963.
91. Bunz, U. H. F.; Rotello, V. M., Gold Nanoparticle-Fluorophore Complexes: Sensitive and Discerning "Noses" for Biosystems Sensing. *Angew. Chem. Int. Ed.* **2010**, *49*, 3268-3279.
92. Liu, X.; Dai, Q.; Austin, L.; Coutts, J.; Knowles, G.; Zou, J. H.; Chen, H.; Huo, Q., A One-Step Homogeneous Immunoassay for Cancer Biomarker Detection Using Gold Nanoparticle Probes Coupled with Dynamic Light Scattering. *J. Am. Chem. Soc.* **2008**, *130*, 2780-2782.
93. Medley, C. D.; Smith, J. E.; Tang, Z.; Wu, Y.; Bamrungsap, S.; Tan, W. H., Gold Nanoparticle-Based Colorimetric Assay for the Direct Detection of Cancerous Cells. *Anal. Chem.* **2008**, *80*, 1067-1072.
94. Zhao, W.; Brook, M. A.; Li, Y. F., Design of Gold Nanoparticle-Based Colorimetric Biosensing Assays. *ChemBioChem* **2008**, *9*, 2363-2371.
95. Pingarron, J. M.; Yanez-Sedeno, P.; Gonzalez-Cortes, A., Gold Nanoparticle-Based Electrochemical Biosensors. *Electrochim. Acta* **2008**, *53*, 5848-5866.
96. Zhang, Z. X.; Yan, B.; Liu, K. L.; Liao, Y. P.; Liu, H. W., CE-MS Analysis of Heroin and its Basic Impurities Using a Charged Polymer-Protected Gold Nanoparticle-Coated Capillary. *Electrophoresis* **2009**, *30*, 379-387.

97. Zhang, C. Y.; Johnson, L. W., Single Quantum-Dot-Based Aptameric Nanosensor for Cocaine. *Anal. Chem.* **2009**, *81*, 3051-3055.
98. Jares-Erijman, E. A.; Jovin, T. M., FRET Imaging. *Nat. Biotechnol.* **2003**, *21*, 1387-1395.
99. Sanles-Sobrido, M.; Rodriguez-Lorenzo, L.; Lorenzo-Abalde, S.; Gonzalez-Fernandez, A.; Correa-Duarte, M. A.; Alvarez-Puebla, R. A.; Liz-Marzan, L. M., Label-Free SERS Detection of Relevant Bioanalytes on Silver-Coated Carbon Nanotubes: The Case of Cocaine. *Nanoscale* **2009**, *1*, 153-158.
100. Qian, X. M.; Nie, S. M., Single-Molecule and Single-Nanoparticle SERS: From Fundamental Mechanisms to Biomedical Applications. *Chem. Soc. Rev.* **2008**, *37*, 912-920.
101. Li, J. F.; Huang, Y. F.; Ding, Y.; Yang, Z. L.; Li, S. B.; Zhou, X. S.; Fan, F. R.; Zhang, W.; Zhou, Z. Y.; Wu, D. Y.; Ren, B.; Wang, Z. L.; Tian, Z. Q., Shell-Isolated Nanoparticle-Enhanced Raman Spectroscopy. *Nature* **2010**, *464*, 392-395.
102. Lim, D. K.; Jeon, K. S.; Kim, H. M.; Nam, J. M.; Suh, Y. D., Nanogap-Engineerable Raman-Active Nanodumbbells for Single-Molecule Detection. *Nat. Mater.* **2010**, *9*, 60-67.
103. Alvarez-Puebla, R. A.; Liz-Marzan, L. M., SERS-Based Diagnosis and Biodetection. *Small* **2010**, *6*, 604-610.
104. Cao, Y. C.; Jin, R.; Mirkin, C. A., Nanoparticles with Raman Spectroscopic Fingerprints for DNA and RNA Detection. *Science* **2002**, *297*, 1536-1540.
105. Qian, X. M.; Peng, X. H.; Ansari, D. O.; Yin-Goen, Q.; Chen, G. Z.; Shin, D. M.; Yang, L.; Young, A. N.; Wang, M. D.; Nie, S. M., In Vivo Tumor Targeting and Spectroscopic Detection with Surface-Enhanced Raman Nanoparticle Tags. *Nat. Biotechnol.* **2008**, *26*, 83-90.
106. Kirchner, C.; T., L.; Kudera, S.; Pellegrino, T.; Muñoz Javier, A.; Gaub, H. E.; Stölzle, S.; Fertig, N.; Parak, W. J., Cytotoxicity of Colloidal CdSe and CdSe/ZnS Nanoparticles. *Nano Lett.* **2005**, *5*, 331-338.
107. Tsoli, M.; Kuhn, H.; Brandau, W.; Esche, H.; Schmid, G., Cellular Uptake and Toxicity of $Au_{55}$ Clusters. *Small* **2005**, *1*, 841-844.
108. Powers, K. W.; Palazuelos, M.; Moudgil, B. M.; Roberts, S. M., Characterization of the Size, Shape, and State of Dispersion of Nanoparticles for Toxicological Studies. *Nanotoxicology* **2007**, *1*, 42-51.
109. Schmid, G., The Relevance of Shape and Size of $Au_{55}$ Clusters. *Chem. Soc. Rev.* **2008**, *37*, 1909-1930.
110. Albanese, A.; Tang, P. S.; Chan, W. C. W., The Effect of Nanoparticle Size, Shape, and Surface Chemistry on Biological Systems. In *Annual Review Of Biomedical Engineering, Vol. 14*, Annual Reviews: Palo Alto, 2012; Vol. 14, pp 1-16.
111. Lewinski, N.; Colvin, V.; Drezek, R., Cytotoxicity of Nanoparticles. *Small* **2008**, *4*, 26-49.
112. De Jong, W. H.; Hagens, W. I.; Krystek, P.; Burger, M. C.; Sips, A. J.; Geertsma, R. E., Particle Size-Dependent Organ Distribution of Gold Nanoparticles After Intravenous Administration. *Biomaterials* **2008**, *29*, 1912-9.
113. Gref, R.; Lück, M.; Quellec, P.; Marchand, M.; Dellacherie, E.; Harnisch, S.; Blunk, T.; Müller, R. H., 'Stealth' Corona-Core Nanoparticles Surface Modified by Polyethylene Glycol (PEG): Influences of the Corona (PEG Chain Length and Surface Density) and of the Core Composition on Phagocytic Uptake and Plasma Protein Adsorption. *Colloids Surf., B* **2000**, *18*, 301-313.
114. Baroli, B.; Ennas, M. G.; Loffredo, F.; Isola, M.; Pinna, R.; Lopez-Quintela, M. A., Penetration of Metallic Nanoparticles in Human Full-Thickness Skin. *J. Invest. Dermatol.* **2007**, *127*, 1701-1712.
115. Limbach, L. K.; Wick, P.; Manser, P.; Grass, R. N.; Bruinink, A.; Stark, W. J., Exposure of Engineered Nanoparticles to Human Lung Epithelial Cells: Influence of Chemical Composition and Catalytic Activity on Oxidative Stress. *Environ. Sci. Technol.* **2007**, *41*, 4158-4163.
116. Perrault, S. D.; Walkey, C.; Jennings, T.; Fischer, H. C.; Chan, W. C. W., Mediating Tumor Targeting Efficiency of Nanoparticles Through Design. *Nano Lett.* **2009**, *9*, 1909-1915.
117. Ulbrich, K.; Hekmatara, T.; Herbert, E.; Kreuter, J., Transferrin- and Transferrin-Receptor-Antibody-Modified Nanoparticles Enable Drug Delivery Across the Blood-Brain Barrier (BBB). *Eur. J. Pharm. Biopharm.* **2009**, *71*, 251-256.

118. Nowack, B.; Bucheli, T. D., Occurrence, Behavior and Effects of Nanoparticles in the Environment. *Environ. Pollut.* **2007**, *150*, 5-22.
119. Moore, M. N., Do Nanoparticles Present Ecotoxicological Risks for the Health of the Aquatic Environment? *Environ. Int.* **2006**, *32*, 967-976.
120. Liu, X. O.; Atwater, M.; Wang, J. H.; Huo, Q., Extinction Coefficient of Gold Nanoparticles with Different Sizes and Different Capping Ligands. *Colloids Surf., B* **2007**, *58*, 3-7.
121. Nel, A. E.; Madler, L.; Velegol, D.; Xia, T.; Hoek, E. M. V.; Somasundaran, P.; Klaessig, F.; Castranova, V.; Thompson, M., Understanding Biophysicochemical Interactions at the Nano-Bio Interface. *Nat. Mater.* **2009**, *8*, 543-557.
122. Pellegrino, T.; Manna, L.; Kudera, S.; Liedl, T.; Koktysh, D.; Rogach, A. L.; Keller, S.; Rädler, J.; Natile, G.; Parak, W. J., Hydrophobic Nanocrystals Coated with an Amphiphilic Polymer Shell: A General Route to Water Soluble Nanocrystals. *Nano Lett.* **2004**, *4*, 703-707.
123. Nakajima, N.; Ikada, Y., Mechanism of Amide Formation by Carbodiimide for Bioconjugation in Aqueous Media. *Bioconjugate Chem.* **1995**, *6*, 123-130.
124. Jana, N. R.; Peng, X., Single-Phase and Gram-Scale Routes toward Nearly Monodisperse Au and Other Noble Metal Nanocrystals. *J. Am. Chem. Soc.* **2003**, *125*, 14280-14281.
125. Sperling, R. A.; Pellegrino, T.; Li, J. K.; Chang, W. H.; Parak, W. J., Electrophoretic Separation of Nanoparticles with a Discrete Number of Functional Groups. *Adv. Funct. Mater.* **2006**, *16*, 943-948.
126. Lin, C.-A. J.; Yang, T.-Y.; Lee, C.-H.; Huang, S. H.; Sperling, R. A.; Zanella, M.; Li, J. K.; Shen, J.-L.; Wang, H.-H.; Yeh, H.-I.; Parak, W. J.; Chang, W. H., Synthesis, Characterization, and Bioconjugation of Fluorescent Gold Nanoclusters toward Biological Labeling Applications. *ACS Nano* **2009**, *3*, 395-401.
127. Cedervall, T.; Lynch, I.; Lindman, S.; Berggård, T.; Thulin, E.; Nilsson, H.; Dawson, K. A.; Linse, S., Understanding the Nanoparticle-Protein Corona Using Methods to Quantify Exchange Rates and Affinities of Proteins for Nanoparticles. *Proc. Natl. Acad. Sci. U. S. A.* **2007**, *104*, 2050-2055.
128. Röcker, C.; Pötzl, M.; Zhang, F.; Parak, W. J.; Nienhaus, G. U., A Quantitative Fluorescence Study of Protein Monolayer Formation on Colloidal Nanoparticles. *Nat. Nanotechnol.* **2009**, *4*, 577-580.
129. Jiang, X.; Weise, S.; Hafner, M.; Röcker, C.; Zhang, F.; Parak, W. J.; Nienhaus, G. U., Quantitative Analysis of the Protein Corona on FePt Nanoparticles Formed by Transferrin Binding. *J. R. Soc., Interface* **2010**, *7*, S5-S13.
130. Monopoli, M. P.; Walczyk, D.; Campbell, A.; Elia, G.; Lynch, I.; Bombelli, F. B.; Dawson, K. A., Physical-Chemical Aspects of Protein Corona: Relevance to in Vitro and in Vivo Biological Impacts of Nanoparticles. *J. Am. Chem. Soc.* **2011**, *133*, 2525-2534.
131. Lundqvist, M.; Stigler, J.; Cedervall, T.; Berggard, T.; Flanagan, M. B.; Lynch, I.; Elia, G.; Dawson, K., The Evolution of the Protein Corona around Nanoparticles: A Test Study. *ACS Nano* **2011**, *5*, 7503-7509.
132. Safi, M.; Courtois, J.; Seigneuret, M.; Conjeaud, H.; Berret, J. F., The Effects of Aggregation and Protein Corona on the Cellular Internalization of Iron Oxide Nanoparticles. *Biomaterials* **2011**, *32*, 9353-9363.
133. Williams, A. T. R.; Winfield, S. A.; Miller, J. N., Relative Fluorescence Quantum Yields Using a Computer-controlled Luminescence Spectrometer. *Analyst (Cambridge, U. K.)* **1983**, *108*, 1067-1071.
134. Magde, D.; Brannon, J. H.; Cremers, T. L.; Olmsted, J., Absolute Luminescence Yield of Cresyl Violet - Standard for the Red. *J. Phys. Chem.* **1979**, *83*, 696-699.
135. Brown, W.; Zhao, J. X., Adsorption of Sodium Dodecyl-Sulfate on Polystyrene Latex-Particles Using Dynamic Light-scattering and Zeta-Potential Measurements. *Macromolecules* **1993**, *26*, 2711-2715.
136. Amin, F.; Yushchenko, D. A.; Montenegro, J. M.; Parak, W. J., Integration of Organic Fluorophores in the Surface of Polymer-Coated Colloidal Nanoparticles for Sensing the Local Polarity of the Environment. *ChemPhysChem* **2012**, *13*, 1030-1035.

137. Müller, C. B.; Loman, A.; Pacheco, V.; Koberling, F.; Willbold, D.; Richtering, W.; Enderlein, J., Precise Measurement of Diffusion by Multi-Color Dual-Focus Fluorescence Correlation Spectroscopy. *Europhys. Lett.* **2008**, *83*, 46001.
138. Loeb, J., The Influence of Electrolytes on the Cataphoretic Charge of Colloidal Particles and the Stability of their Suspensions. I. Experiments with Collodion Particles. *J. Gen. Physiol.* **1922**, *5*, 109-126.
139. Puertas, A. M.; de las Nieves, F. J., Colloidal Stability of Polymer Colloids with Variable Surface Charge. *J. Colloid Interface Sci.* **1999**, *216*, 221-229.
140. Casals, E.; Pfaller, T.; Duschl, A.; Oostingh, G. J.; Puntes, V. F., Time Evolution of the Nanoparticle Protein Corona. *ACS Nano* **2010**, *4*, 3623-3632.
141. Jiang, X.; Dausend, J.; Hafner, M.; Musyanovych, A.; Röcker, C.; Landfester, K.; Mailander, V.; Nienhaus, G. U., Specific Effects of Surface Amines on Polystyrene Nanoparticles in their Interactions with Mesenchymal Stem Cells. *Biomacromolecules* **2010**, *11*, 748-753.
142. Jiang, X.; Musyanovych, A.; Röcker, C.; Landfester, K.; Mailander, V.; Nienhaus, G. U., Specific Effects of Surface Carboxyl Groups on Anionic Polystyrene Particles in their Interactions with Mesenchymal Stem Cells. *Nanoscale* **2011**, *3*, 2028-2035.
143. Bartneck, M.; Keul, H. A.; Wambach, M.; Bornemann, J.; Gbureck, U.; Chatain, N.; Neuss, S.; Tacke, F.; Groll, J.; Zwadlo-Klarwasser, G., Effects of Nanoparticle Surface Coupled Peptides, Functional Endgroups, and Charge on Intracellular Distribution and Functionality of Human Primary Reticuloendothelial Cells. *Nanomedicine (New York, NY, U. S.)* **2012**, *8*, 1282-1292.
144. Bhattacharjee, S.; Ershov, D.; van der Gucht, J.; Alink, G. M.; Rietjens, I. M. C. M.; Zuilhof, H.; Marcelis, A. T. M., Surface Charge-Specific Cytotoxicity and Cellular Uptake of Tri-Block Copolymer Nanoparticles. *Nanotoxicology* **2013**, *7*, 71-84.
145. Jung, T.; Kamm, W.; Breitenbach, A.; Kaiserling, E.; Xiao, J. X.; Kissel, T., Biodegradable Nanoparticles for Oral Delivery of Peptides: Is there a Role for Polymers to Affect Mucosal Uptake? *Eur. J. Pharm. Biopharm.* **2000**, *50*, 147-160.
146. Rabinovich-Guilatt, L.; Couvreur, P.; Lambert, G.; Dubernet, C., Cationic Vectors in Ocular Drug Delivery. *J. Drug Targeting* **2004**, *12*, 623-633.
147. Harush-Frenkel, O.; Rozentur, E.; Benita, S.; Altschuler, Y., Surface Charge of Nanoparticles Determines their Endocytic and Transcytotic Pathway in Polarized MDCK Cells. *Biomacromolecules* **2008**, *9*, 435-443.
148. Muñoz Javier, A.; Kreft, O.; Piera Alberola, A.; Kirchner, C.; Zebli, B.; Susha, A. S.; Horn, E.; Kempter, S.; Skirtach, A. G.; Rogach, A. L.; Rädler, J.; Sukhorukov, G. B.; Benoit, M.; Parak, W. J., Combined Atomic Force Microscopy and Optical Microscopy Measurements as a Method to Investigate Particle Uptake by Cells. *Small* **2006**, *2*, 394-400.
149. Lesniak, A.; Fenaroli, F.; Monopoli, M. R.; Aberg, C.; Dawson, K. A.; Salvati, A., Effects of the Presence or Absence of a Protein Corona on Silica Nanoparticle Uptake and Impact on Cells. *ACS Nano* **2012**, *6*, 5845-5857.
150. Ghosh, P.; Han, G.; De, M.; Kim, C. K.; Rotello, V. M., Gold Nanoparticles in Delivery Applications. *Adv Drug Deliv Rev* **2008**, *60*, 1307-1315.
151. Giljohann, D. A.; Seferos, D. S.; Daniel, W. L.; Massich, M. D.; Patel, P. C.; Mirkin, C. A., Gold Nanoparticles for Biology and Medicine. *Angew. Chem. Int. Ed.* **2010**, *49*, 3280-94.
152. Wallace, K. J., Molecular Dyes Used for the Detection of Biological and Environmental Heavy Metals: Highlights from 2004 to 2008. *Supramol. Chem.* **2009**, *21*, 89-102.
153. Aragay, G.; Pons, J.; Merkoci, A., Recent Trends in Macro-, Micro-, and Nanomaterial-Based Tools and Strategies for Heavy-Metal Detection. *Chem. Rev.* **2011**, *111*, 3433-3458.
154. Sumalekshmy, S.; Fahrni, C. J., Metal-Ion-Responsive Fluorescent Probes for Two-Photon Excitation Microscopy. *Chem. Mater.* **2011**, *23*, 483-500.
155. Ohshima, H.; Healy, T. W.; White, L. R., Accurate Analytic Expressions for the Surface-Charge Density Surface-Potential Relationship and Double-Layer Potential Distribution for a Spherical Colloidal Particle. *J. Colloid Interface Sci.* **1982**, *90*, 17-26.

156. Lopez-Garcia, J. J.; Horno, J.; Grosse, C., Numerical Solution of the Poisson-Boltzmann Equation for Suspended Charged Particles Surrounded by a Charged Permeable Membrane. *Phys. Chem. Chem. Phys.* **2001**, *3*, 3754-3760.
157. Ohshima, H., Donnan Potential and Surface Potential of a Spherical Soft Particle in an Electrolyte Solution. *J. Colloid Interface Sci.* **2008**, *323*, 92-97.
158. Wu, J. Z.; Li, Z. D., Density-Functional Theory for Complex Fluids. In *Annu. Rev. Phys. Chem.*, Annual Reviews: Palo Alto, 2007; Vol. 58, pp 85-112.
159. Wu, J. Z., Density Functional Theory for Chemical Engineering: From Capillarity to Soft Materials. *AlChE J.* **2006**, *52*, 1169-1193.
160. Yu, Y. X.; Wu, J. Z.; Gao, G. H., Density-Functional Theory of Spherical Electric Double Layers and Zeta Potentials of Colloidal Particles in Restricted-Primitive-Model Electrolyte Solutions. *J. Chem. Phys.* **2004**, *120*, 7223-7233.
161. Teolato, P.; Rampazzo, E.; Arduini, M.; Mancin, F.; Tecilla, P.; Tonellato, U., Silica Nanoparticles for Fluorescence Sensing of Zn-II: Exploring the Covalent Strategy. *Chem. Eur. J.* **2007**, *13*, 2238-2245.
162. Rivera Gil, P.; del Mercato, L. L.; del Pino, P.; Muñoz-Javier, A.; Parak, W. J., Nanoparticle-Modified Polyelectrolyte Capsules. *Nano Today* **2008**, *3*, 12-21.
163. del Mercato, L. L.; Rivera Gil, P.; Abbasi, A. Z.; Ochs, M.; Ganas, C.; Zins, I.; Sönnichsen, C.; Parak, W. J., LbL Multilayer Capsules: Recent Progress and Future Outlook for their Use in Life Sciences. *Nanoscale* **2010**, *2*, 458-467.

# Appendix

# Wissenschaftlicher Lebenslauf

### Persönliche Angaben

| | |
|---|---|
| Name | Dominik Hühn |
| Geburtsdatum | 24. Mai 1985 in Marburg (Lahn) |
| Staatsangehörigkeit | Deutsch |

### Ausbildung

| | |
|---|---|
| Seit 08/2010 | **Promotion**<br>Arbeitsgruppe Biophotonik (Prof. W. J. Parak), Fachbereich Physik, Philipps-Universität Marburg<br><br>Thema: *Functional Gold Nanoparticles for Biomedical Applications* |
| 03/2005 - 07/2010 | **Studium der Physik**<br>Philipps-Universität Marburg<br>Abschluss als **Diplom-Physiker**<br><br>Titel der Diplomarbeit (AG Biophotonik, Prof. W. J. Parak):<br>*Light-triggered Heating of Gold Clusters in a Polyelectrolyte Film for Remote Release of Molecules* |
| 06/2004 | **Abitur**<br>Stiftsschule St. Johann, Amöneburg |

### Wissenschaftliche Veröffentlichungen

[A1] Charron, G.; Hühn, D.; Perrier, A.; Cordier, L.; Pickett, C. J.; Nann, T.; Parak, W. J., On the Use of pH Titration to Quantitatively Characterize Colloidal Nanoparticles. *Langmuir* **2012**, *28*, 15141-15149.

[A2] Hühn, D.*; Kantner, K.*; Geidel, C.; Brandholt, S.; De Cock, I.; Soenen, S. J. H.; Rivera Gil, P.; Montenegro, J.-M.; Braeckmans, K.; Müllen, K.; Nienhaus, G. U.; Klapper, M.; Parak, W. J., Polymer-Coated Nanoparticles Interacting with Proteins and Cells: Focusing on the Sign of the Net Charge. *ACS Nano* **2013**, *7*, 3253-3263.

[A3] Jimenez de Aberasturi, D.*; Hühn, D.*; Hühn, J.; Beqa, L.; Ruiz de Larramendi, I.; Pinedo, R.; Rojo, T.; Montenegro, J.-M.; Carregal-Romero, S.; Geidel, C.; Dommershausen, F.; Schütte, J.; Klapper, M.; Koert, U.; Müllen, K.; Parak, W. J., Ion Selective Ligands - How Colloidal Nano- and Microparticles Introduce New Functionality. *To be submitted*.

[A4] Cywinski, P. J.; Hammann, T.; Hühn, D.; Parak, W. J.; Löhmannsröben, H.-G., Long-Decaying Quantum Dot-Europium Complex Conjugates as Luminescent Probes for Time-Resolved Fluoroassays. *To be submitted*.

[A5] Hühn, D.; Govorov, A.; Rivera Gil, P.; Parak, W. J., Photostimulated Au Nanoheaters in Polymer and Biological Media: Characterization of Mechanical Destruction and Boiling. *Adv. Funct. Mater.* **2012**, *22*, 294-303.

[A6] Khalid, W.; Göbel, G.; Hühn, D.; Montenegro, J.-M.; Rivera Gil, P.; Lisdat, F.; Parak, W. J., Light Triggered Detection of Aminophenyl Phosphate with a Quantum Dot Based Enzyme Electrode. *J. Nanobiotechnol.* **2011**, *9*, 46.

[A7] Carregal-Romero, S.; Rinklin, P.; Schulze, S.; Schäfer, M.; Ott, A.; Hühn, D.; Yu, X.; Wolfrum, B.; Weitzel, K.-M.; Parak, W. J., Ion Transport Through Polyelectrolyte Multilayers. *Macromol. Rapid Commun.* **2013**, In press.

[A8] Rivera Gil, P.; Hühn, D.; del Mercato, L. L.; Sasse, D.; Parak, W. J., Nanopharmacy: Inorganic Nanoscale Devices as Vectors and Active Compounds. *Pharmacol. Res.* **2010**, *62*, 115-125.

[A9] Carregal-Romero, S.; Caballero-Diaz, E.; Beqa, L.; Abdelmonem, A. M.; Ochs, M.; Hühn, D.; Suau, B. S.; Valcarcel, M.; Parak, W. J., Multiplexed Sensing and Imaging with Colloidal Nano- and Microparticles. *Annual Review of Analytical Chemistry* **2013**, *6*, 53-81.

[A10] Pfeiffer, C.; Rehbock, C.; Hühn, D.; Carrillo, C.; Jimenez de Aberasturi, D.; Merk, V.; Barcikowski, S.; Parak, W. J., Interaction of Colloidal Nanoparticles with their Local Environment - the (Ionic) Nanoenvironment Around Nanoparticles is Different from Bulk and Determines the Physico-Chemical Properties of the Nanoparticles. *J. R. Soc., Interface*, In press.

**Patente**

Parak, W. J.; Hühn, D.; Hühn, J.; Jimenez de Aberasturi, D.; Montenegro Martos, J. M.; Carrillo Carrion, C.; Koert, U.; Schütte, Use of nanoparticles with variable surface charge / polarity and spacer length for tuning the working point of analyte-sensitive fluorophores, which are attached *via* molecular spacers to the surface of the nanoparticles. *To be submitted.*

*Gleichberechtigte Erstautorenschaft

Marburg, 28.03.2014

# Erklärung

Hiermit versichere ich, dass ich meine Dissertation

# Functional Gold Nanoparticles for Biomedical Applications

selbständig, ohne unerlaubte Hilfe angefertigt und mich dabei keiner anderen als der von mir ausdrücklich bezeichneten Quellen und Hilfen bedient habe.

Die Dissertation wurde in der jetzigen oder einer ähnlichen Form noch bei keiner Hochschule eingereicht und hat noch keinem sonstigen Prüfungszweck gedient.

Name, Vorname: Hühn, Dominik

Marburg, 28.03.2014 .....

(Unterschrift)

Langmuir

Article

pubs.acs.org/Langmuir

# On the Use of pH Titration to Quantitatively Characterize Colloidal Nanoparticles

Gaëlle Charron,*[,†,‡] Dominik Hühn,[§] Aurélie Perrier,[†] Laure Cordier,[∥] Christopher J. Pickett,[‡] Thomas Nann,[⊥] and Wolfgang J. Parak*[,§]

[†]Univ Paris Diderot, Sorbonne Paris Cité, ITODYS, UMR CNRS 7086, 15 rue J-A de Baïf, 75205 Paris Cedex 13, France

[‡]School of Chemistry, Energy Materials Lab., University of East Anglia, NR47TJ − Norwich, United Kingdom

[§]Fachbereich Physik and WZMW, Philipps Universität Marburg, Marburg, Germany

[∥]Univ Paris Diderot, Sorbonne Paris Cité, IPGP, UMR 7154, CNRS, F-75205 Paris, France

[⊥]Ian Wark Research Institute, University of South Australia, Adelaide, SA 5095, Australia

Supporting Information

**ABSTRACT:** Functional nanoparticles (NPs) for bioapplications have been achieved, thanks to synthesis providing high quality nanocrystals, efficient procedures for transfer in water, and further conjugation of (bio)active molecules. However, these nanomaterials are still subjected to batch-to-batch variability and investigations of their physicochemical properties and chemical reactivity are still in their infancy. This may be due to lack of a routine, cost-effective, and readily available quantitative method for characterizing functional NPs. In this work, we show that pH titrations can be a powerful tool for investigating the surface properties of charged NPs and quantifying their surface functionalities. We demonstrate how this method can be useful in characterizing the colloidal and chemical stability, composition, and purity of the nanomaterial. The method also shows potential for the optimization of conjugation conditions.

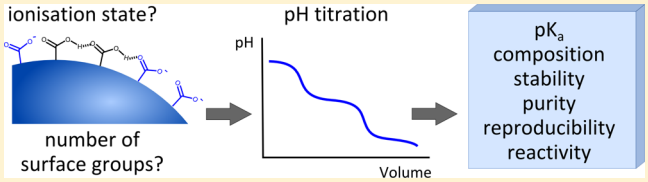


## INTRODUCTION

There are nowadays plenty of robust methods to synthesize high quality colloidally stable nanoparticles (NPs) with various sizes, shapes, and compositions.[1,2] Their use in bioapplications has been widely documented, thanks to the development of efficient strategies for providing colloidal stability in water, through either steric or electrostatic repulsion.[3−10] In many cases, the terminal groups are functional and can be used as anchoring points for further conjugation using classical bioconjugation methods inherited from the modification of proteins, such as peptide coupling or reductive amination.[11]

There is a wide range of techniques to assess that a (bio)functionalization procedure has been successful. However, more often than not, those techniques require costly instrumentation (X-ray photoelectron spectroscopy, energy dispersive X-ray analysis) and might therefore not be done routinely, are not quantitative in the sense that they do not easily provide absolute quantification of the functionalities (FTIR, NMR), or may necessitate large amounts of material with regard to the scale of the nanomaterial synthesis (thermogravimetric or microanalysis).

Moreover, most of the time, further conjugation reactions of colloidal NPs are performed without control of the reaction parameters and performance, such as precise NP concentration, number of reactive groups per NP and reagents stoichiometry, purity of NPs, reaction efficiency, and so forth. In addition, NPs are generally assumed to react in the same way as the proteins for which the reaction was initially developed do. This lack of quantification and mechanistic insights may be one of the reasons for which efficient controlled conjugation of NPs with biological molecules still remains a challenge to this day.

The first step in optimizing (bio)functionalization reactions regarding the yields or batch-to-batch reproducibility is to enable facile quantitative characterization of NPs, that is, easy quantification of their surface functionalities and assessment of their physicochemical properties. Here, we aim at showing that pH titration, a readily available bench technique, can be a powerful and convenient tool for the quantitative characterization of functional NPs. Both its ability to quantify the number of surface functionalities and the information it provides about the surface physicochemical properties can have important spin-off effects on the quality and reproducibility of the functional nanomaterial. Moreover, we suggest that pH titration could help optimize reaction conditions.

We illustrate the advantages of pH titration on carboxylate-bearing gold NPs. Two types of NPs were selected as examples. The first one consists of gold NPs protected by aliphatic thiol ligands bearing terminal carboxyl moieties (self-assembled monolayer (SAM)-coated NPs).[12,13] In the second one, gold NPs are covered (in an idealized picture) with a monolayer of amphiphilic polymer strands encompassing repeating carboxyl units, according to previously published protocols (Schemes 1

**Received:** June 25, 2012
**Revised:** August 29, 2012
**Published:** October 17, 2012

**Scheme 1. Surface Groups of SAM Protected (left) and Polymer Coated (right) NPs**

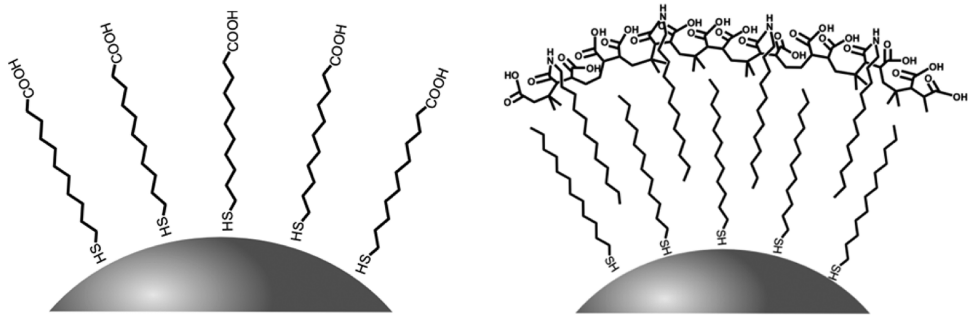

and 2, and Supporting Information S1).[14] pH titrations of these systems will lead to the determination of two key parameters:

**Scheme 2. Structure of the Amphiphilic Polymer**

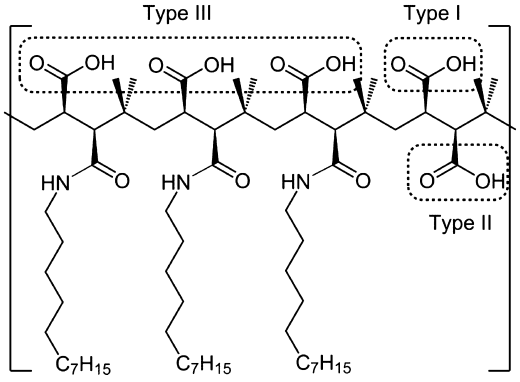


the p$K_a$ of the surface carboxylates and their concentration in the sample. This information will in turn lead to estimations of their colloidal stability, purity, and stability of the organic coating and also potential reactivity in a classical bioconjugation scheme.

## EXPERIMENTAL SECTION

**NP Synthesis and NP Concentration Estimation.** Self-assembled monolayer protected and polymer coated gold NPs with core diameters of roughly 2 nm and 5−7 nm were prepared according to previously reported procedures with minor alterations.[12−14] The size distribution of the metallic core diameter ($d_c$) (Scheme 3) was

**Scheme 3. Nomenclature for the Various Diameters**

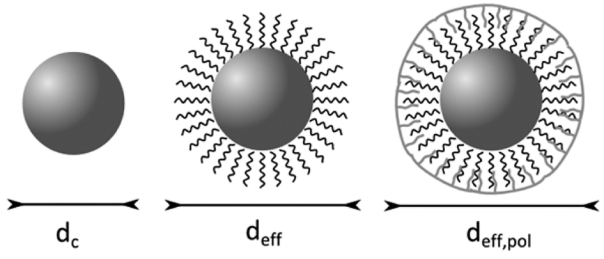


estimated by transmission electron microscopy (TEM) imaging along with image analysis using CellProfiler software. The total gold concentration of each sample was determined by inductively coupled plasma atomic emission (ICP-AES) measurements. Experimental details are provided in the Supporting Information (SI).

**pH Potentiometric Titrations.** Prior to each titration, the pH-meter was calibrated using pH 7.02 and pH 10.02 standards. For each titration, the initial pH of the analyte solution and the titrant concentration needed to be optimized in order to obtain the sharpest possible features.[15] In a typical experiment, a given amount of purified NPs bearing roughly 5 $\mu$mol of carboxyl groups was dispersed in 6 mL of a 50 mM NaOH solution to ensure full deprotonation. The resulting solution was filtered with Amicon tubes ($M_w$ cutoff of 30 kDa) and redispersed in a 1.5 mM NaOH in Millipore water stock. Two more steps of filtration and redispersion in 1.5 mM NaOH stock were performed. The last redispersion was completed using a freshly prepared NaOH solution in Millipore water having a resistivity of 18 MΩ·cm to achieve a final volume of 10 mL. To avoid carbonate interference, the titration was performed within 30 min after solution preparation (see the SI for details). After each addition of 50 $\mu$L titrant (HCl, 23−25 mM depending on the experiment), the solution was stirred magnetically for 1 min and the pH was recorded. The titration was repeated on a second NP sample to check for reproducibility.

**Dynamic Light Scattering (DLS)/Zeta Potential versus pH Titrations.** A solution of polymer coated NPs identical to the one used for pH titration was diluted to 10 mL of a solution roughly 0.5 mM in carboxyl groups in 1.0 mM NaOH. The solution was placed in the reservoir of a Malvern ZetaSizer Autotitrator and connected to a disposable clear zeta cell. The solution was titrated using 25 mM HCl. Three size measurements and three zeta measurements were recorded after each pH step.

**Density Functional Theory (DFT) Calculation Method.** Hydrogen bonding patterns within the polymer used for polymer coating were investigated using DFT ($\omega$B97X-D/aug-cc-pVDZ) on a dimeric fraction of the polymer strand. The choices of polymeric fragment, functional and basis set are detailed in the SI.[16−22]

## RESULTS AND DISCUSSION

The p$K_a$ of surface carboxylic acids is related to the extent of deprotonation of COOH groups attached to a molecular residue R at a given pH through the Henderson−Hasselbalch equation (eq 1).[15]

$$\mathrm{pH} = \mathrm{p}K_a + \log(f/1-f), \quad \text{with } f = [\mathrm{RCOO^-}]/([\mathrm{RCOOH}] + [\mathrm{RCOO^-}]) \tag{1}$$

Aliphatic carboxylic acids generally have p$K_a$ values around 4−5.[23] Let us analyze the theoretical potentiometric titration curve of NPs bearing carboxyl moieties with a surface p$K_a$ of 5 (Figure 1). The titration starts at high pH to ensure full deprotonation of the carboxyl moieties and colloidal stability, that is, in the presence of excess hydroxide ions. The curve displays three domains. At first, the reaction between hydroxide and hydronium ions is predominant. Hence, the first plateau corresponds to the titration of excess hydroxide ions. The first equivalence point is evidenced by a pH jump. As soon as it is reached, titration of surface carboxylates begins and gives rise to a second plateau (buffer plateau). Addition of excess titrant after the second equivalence, or second pH jump, leads to a


dx.doi.org/10.1021/la302570s | Langmuir 2012, 28, 15141−15149
[A1]2

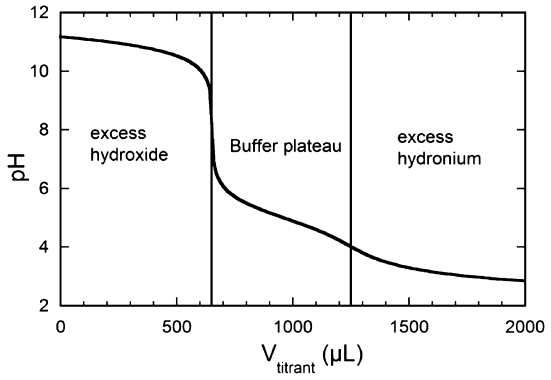


**Figure 1.** Theoretical titration curve of a 1.4 mM solution of carboxylate bearing a p$K_a$ of 5.0 in 1.5 mM NaOH with 23 mM HCl.

third plateau at low pH. The height of the second plateau allows for an estimation of the p$K_a$. Indeed, according to the Henderson−Hasselbalch equation,

$$f = 1/2 \Rightarrow \mathrm{pH} = \mathrm{p}K_a \quad (2)$$

Hence, the p$K_a$ can be estimated from the pH halfway through the second plateau.

**Investigation of the p$K_a$.** *Self Assembled Monolayer (SAM) Protected NPs.* We synthesized mercaptoundecanoic acid (MUA) protected gold NPs with average core metallic diameters ($d_c$, see Scheme 3) of 2.4 and 5.2 nm (∼2 and 5 nm), as determined by TEM analysis (SI Figure S10). Similarly, we synthesized 3-mercaptopropanoic acid (MPA) protected gold NPs with comparable core diameters of 2.5 and 5.7 nm on average (rounded to 2 and 6 nm for convenience). The NPs with various sizes and different coating were purified (see the SI) and subsequently titrated by HCl using a calibrated pH-meter.

A p$K_a$ titration curve of 5 nm MUA protected gold NPs is given in Figure 2 (and SI Figure S2). It displays the three

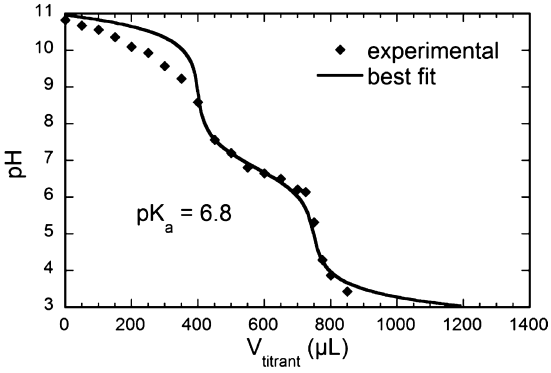


**Figure 2.** Experimental titration curve of 5 nm core, MUA coated gold NPs dispersed in 1.1 mM NaOH by 25 mM HCl and corresponding best fit.

characteristic domains mentioned above. The height of the buffer plateau is around pH = 7, which suggests a p$K_a$ about 2 pH units higher than that of the free, unbound MUA (p$K_a$ = 4.8; $\Delta \mathrm{p}K_a$ = +2). Simulations of the titration curve were performed using the p$K_a$ and the buffer concentration as adjustable parameters. A good agreement between the experimental and simulated curve was reached for a p$K_a$ value of 6.8. This observation evidence that MUA moieties adsorbed on gold NPs have acid/base properties that differ markedly from their free-standing counterpart, with the adsorbed molecule being around 100 = $10^2$ = $10^{\Delta \mathrm{p}K_a}$ times harder to deprotonate than the free one.

We performed additional pH titrations on 2 nm MUA protected gold NPs and on 2 and 6 nm MPA protected gold NPs. Table 1 sums up the p$K_a$ values extracted by simulation of the experimental curves. The experimental data and the corresponding fits are shown in the SI (Figures S3−S5). All four types of NPs display a positive p$K_a$ shift of at least 2 units compared to the free-standing molecules, with higher p$K_a$ shift corresponding to the shorter MPA ligand.

*Origin of the p$K_a$ Shift.* Such an observation is consistent with past studies of terminal carboxyl bearing thiols assembled on planar gold substrates,[24,25] and with a more recent study by Wang et al.[26] In their work, the authors demonstrated that the increase in p$K_a$ of MUA coated gold NPs stems from an unfavorable accumulation of negative charges on the surface, as carboxyl moieties get deprotonated. The authors also observed and explained a variation of the p$K_a$ shift as a function of NPs curvature. As the NP radius decreases, the distance between the charges increases (cf. Scheme 1). Accordingly, the electrostatic repulsion between carboxylates decreases. Hence, smaller NPs have smaller shift in p$K_a$. One could extend this reasoning to the influence of the length of the ligand carbon chain. With the curvature radius kept constant, ligands bearing shorter chains should develop a more intense electrostatic repulsion with each other.

In our case, the p$K_a$ shifts for 5 nm MUA and 6 nm MPA-protected NPs are significantly smaller than the ones reported by Wang et al. ($\Delta \mathrm{p}K_a$ =+2 vs. $\Delta \mathrm{p}K_a$ > 4 for 5 or 7 nm MUA-coated NPs). With a p$K_a$ of 7.0 and 6.7, respectively, 6 and 2 nm MPA-coated NPs display similar p$K_a$ shifts when compared to the free MPA molecules (p$K_a$ = 4.3, as determined by pH-titration). Similarly, both 2 and 5 nm MUA protected NPs display close p$K_a$ shifts (7.2 and 6.8, respectively). Those differences in p$K_a$ shifts with varying curvature radius are close to the error margin of our method, in contrast with the difference in p$K_a$ of 0.7 to 1 observed in the case of 7 and 4 nm MUA-protected NPs by Wang et al.[26] One possible explanation for these observations lies in the fact that we used sodium hydroxide to bring the NP solution to a basic starting pH. In their original study, Wang et al. have used tetramethylammonium hydroxide instead and have shown that the smaller the counterions of the carboxylates, the smaller the shift in p$K_a$. This may be understood in terms of the different charge screening powers of the various counterions. A sodium cation is "harder" than an ammonium cation according to the "Hard and Soft Acid and Base Theory",[27] because its radius is smaller while the net charge is the same. In other words, sodium has a higher volume charge density compared to ammonium, and thus its charge screening abilities are greater. Sodium ions then lead to reduced electrostatic repulsion and weaker p$K_a$ shifts compared to bulkier ions. This screening effect could also be responsible for the leveling up of all the apparent p$K_a$ in our experiments, although for MPA-protected NPs the similar p$K_a$ shifts were to be expected. As MPA has a shorter chain compared to MUA, carboxylates might be just as close to one another on a 2 nm NP than on a 6 nm one, which would lead to similar electrostatic interactions regardless of the curvature radius.

We conclude that all investigated SAM-protected NPs bearing terminal carboxyl groups display a p$K_a$ shift of roughly


dx.doi.org/10.1021/la302570s | *Langmuir* 2012, 28, 15141−15149

Table 1. Diameters, Surface p$K_a$, and Surface Group Densities of the SAM and Polymer Coated NPs[a]

| | MUA | | MPA | | Polymer | |
|---|---|---|---|---|---|---|
| $d_c$ (nm) | 2.4 | 5.2 | 2.5 | 5.7 | 2.4 | 6.9 |
| $d_{eff}$ (nm) | 4.4 | 7.2 | 3.2 | 6.4 | 4.4 | 8.9 |
| $d_{eff,pol}$ (nm) | - | – | – | – | [4.4–6.4] | [8.9–10.9] |
| p$K_a$ of free molecule | 4.8 | | 4.3 | | 7.0 and 8.8 | |
| surface p$K_a$ | 7.2 | 6.8 | 6.7 | 7.0 | 7.3 | 7.2 |
| no. of carboxyls/NP (molecules/nm$^2$) | 249 | 1088 | 180 | – | 1295 | – |
| density of functionalities (groups/nm$^2$) | 4 | 7 | 5 | – | 22/10 | – |
| thiol coverage density (groups/nm$^2$) | 14 | 13 | 8 | – | – | – |

[a]See SI for TEM analysis of the diameter distributions and determination of the density of functionalities and thiol coverage densities. For polymer coated NPs, the density of functionalities was calculated using either $d_{eff,pol}$ (right figure) or $d_{eff}$ (left figure), assuming that the dodecanethiol shell was 1 nm thick.

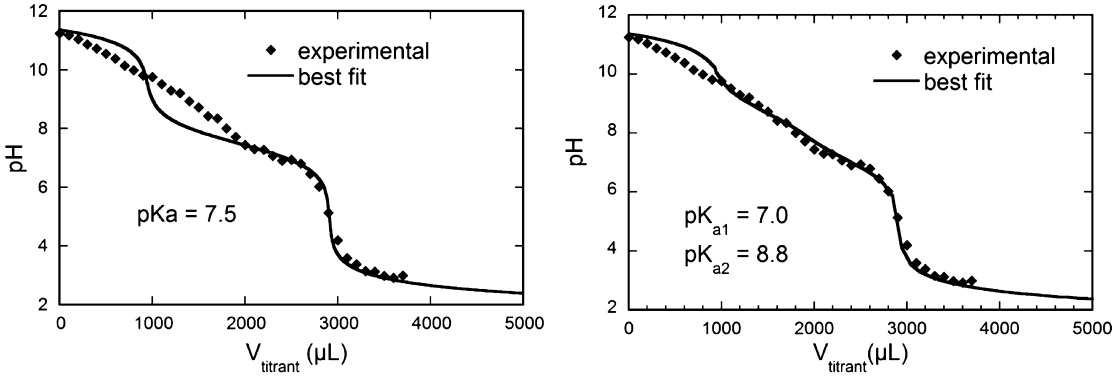


**Figure 3.** Experimental titration curve of 20.5 mL of a 4.8 mM polymer solution (expressed as monomer units) in 2.3 mM NaOH by 50 mM HCl and best fits using an only set (left) or two sets of carboxyl functions (right).

$\Delta pK_a$ = 2–2.5 compared to the free ligand molecules, regardless of the chain length or radius of curvature (within the ranges investigated here). The coated NPs will therefore have a different chemical reactivity than that of the starting material. For instance, carboxylic acids are weak nucleophiles when ionized. They will in this case exert their nucleophilicity at different pH when free in solution or when supported on NPs. In such simple functionalization cases, models like the one developed by Wang et al. may be available to predict the extent of variation in physicochemical properties of the NPs with regard to the free molecules. In order to develop functional NPs for bioapplications, it is likely that more chemical complexity will be needed in the functionalization of the NPs, through introduction of orthogonal anchoring groups or more stable biocompatible ligand chains, for instance. For this purpose, modeling of the origin of a possible p$K_a$ shift would be useful to improve the design of the ligand. However, for large or complex molecules, complex parameters, such as conformational effects, will need to be taken into account, and it is likely that simulation will become tedious.

*Polymer Coated NPs.* Polyelectrolyte molecules are an interesting group of surface capping agents to this regard because they are likely to undergo less drastic p$K_a$ changes once anchored on the surface of NPs than simple molecules. The resilience of their properties stems from the fact that as free-standing molecules they encompass already all the effects that one can foresee on the surface of a NP, namely, close spatial proximity of the charges and complex conformational structure. We investigated such a resilience effect on NPs coated with an amphiphilic polymer bearing multiple carboxyl functions (Schemes 1 and 2). The synthesized NPs had core diameters of 2.4 and 6.9 nm on average, as determined by TEM analysis (~2 and 7 nm) (SI Figure S10).

Extraction of the p$K_a$ of the free-standing polymer proved to be less straightforward than for the SAM-coated NPs. Simulation of the curve using the method mentioned above led to a poorer agreement with the experimental data than in the previous cases. This is due to the distorted shape of the buffer plateau. This distortion evidences a polybasic behavior, namely, a distribution of p$K_a$ on the surface. By including two sets of carboxyl groups with distinct p$K_a$ values, we were able to fit the experimental data with a good agreement. According to the simulation, the free-standing polymer bears two families of carboxylic acids with p$K_a$'s of 7.0 and 8.8, respectively (Figure 3). The existence of the two distinct sets of carboxyl moieties is within our experimental setup a reproducible fact. These values are markedly higher than those of classic carboxylic acids.

We investigated the origin of this high average p$K_a$. The chemical structure of the amphiphilic polymer encompasses three types of carboxylates (I–III, Scheme 2). If $x$ represents the amount of monomer units engaged in the sample, the amount of carboxyl moieties bearing an amide function in $\alpha$ position (type III) is 0.80$x$ to 0.85$x$ and the amount of carboxyl moieties bearing another carboxyl moiety in $\alpha$ position (types I and II) is 0.15$x$ to 0.20$x$ for each type. The total number of functionalities whose buffering behavior is potentially solved in the titrations we performed is 1.15$x$ to 1.20$x$ (SI Table S1).

We first analyze the two p$K_a$ values of the carboxylic acids adjacent to one another (types I and II). The free-standing polymer most likely adopts a micelle conformation in water due to its amphiphilic nature.[14] The conformation of the strands maintains both carboxylic acids in close proximity. The overall moiety therefore resembles maleic acid, in which both acids


dx.doi.org/10.1021/la302570s | *Langmuir* 2012, 28, 15141–15149

face each other due to the cis-configuration of the alkene. The two p$K_a$ values of maleic acid are 1.9 and 6.2.[23] The first deprotonation is eased up by the formation of a hydrogen bond between the carboxylic acid (type II) and its neighboring carboxylate (type I) and gives rise to a low lying first p$K_a$. This very low p$K_a$ precludes the titration of this type of carboxyl moieties within the frame of our experimental set up. Consequently, the amount of carboxylates still available for titration is 1.00$x$ and therefore accounts for exactly the amount of engaged monomer units. The second p$K_a$ (type II) is higher than that of a typical carboxylic acid because the second deprotonation goes through breaking of the hydrogen bond and unfavorable accumulation of negative charges. This value of 6.0 is likely to increase in the macromolecule due to additional charge accumulation. The titration of type II acids, which represent 0.15$x$−0.20$x$, is therefore embedded in the unique buffer plateau observed experimentally.

Second, we modeled the p$K_a$ of the carboxylic acid bearing an adjacent amide group (type III), which accounts for 0.80$x$−0.85$x$. DFT calculations were performed on a dimeric fraction of the polymer (see the SI). The resulting optimized geometry displays a hydrogen bond between the OH donor group of the carboxylic acid and the carbonyl of the neighboring amide function, with the functions being arranged in a 7-membered ring (Figure 4 and SI Figure S12). A N−H···O bonding scheme

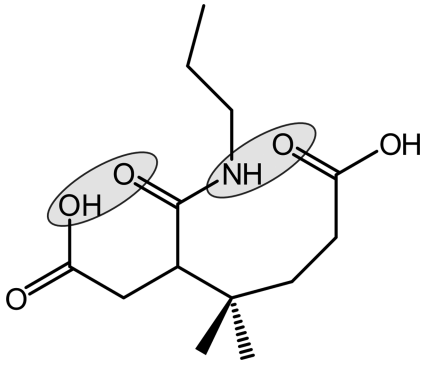


**Figure 4.** Representation of the monomer unit.

is also obtained between the amide group and the carbonyl function of the nearby carboxylic acid, rigidifying the overall conformation. Both hydrogen bonds increase the strength of the bonding of protons to the polymer and are therefore responsible for the high observed p$K_a$.

The micelle-like conformation of the polymer, and the associated acid−base behavior, should be retained on the NPs due to the interdigitation of the polymer hydrophobic chains and the aliphatic ligands (Scheme 1). A good fit of the experimental titration curve of 7 nm core polymer coated gold NPs was obtained using one set of carboxylates bearing a p$K_a$ of 7.2 (Figure 5 and SI Figure S6). From this simulation, two conclusions can be drawn: (i) the p$K_a$ of carboxyl functions on the NPs (p$K_a$ = 7.2) is actually lower than that in the free macromolecules (average p$K_a$ of 7.9, with two sets of carboxyl functions with p$K_a$ of 7.0 and 8.8). This is an unprecedented situation which emphasizes the fact that for complex molecules, for which no simulation tools are available, pH titration is an excellent way to get insights into surface physicochemical properties. (ii) The p$K_a$ is only about 0.7 pH units apart from the average p$K_a$ of the free-standing polymer. It means that, as expected, carboxyl functions remain mostly unchanged because

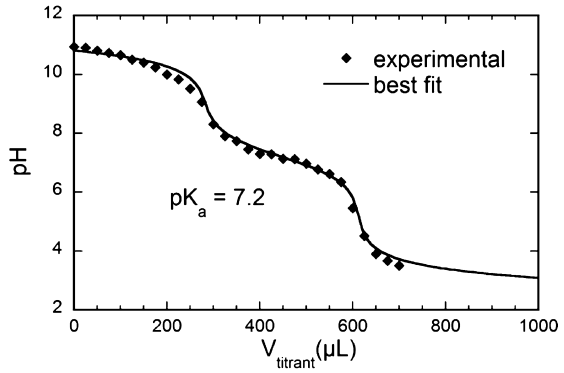


**Figure 5.** Experimental titration curve of 7 nm core, polymer coated gold NPs dispersed in 0.7 mM NaOH by 23 mM HCl and best fit.

the conformations of the carboxyl moieties are mostly retained after adsorption on the NPs. The lowering of the p$K_a$, as well as the fact that only one p$K_a$ was needed to fit the curve, could arise from minor conformational distortions that would lead to variations in the hydrogen bonds. Similarly to the free-standing polymer, fitting of the experimental titration curve of 2 nm polymer coated NPs required the use of two sets of carboxylates with distinct p$K_a$ (Figure 6 and SI Figure S7). A good agreement was reached for p$K_a$ values of 6.2 and 8.3. Once again, the average p$K_a$ (7.25) is close to that of the pure polymer but lower.

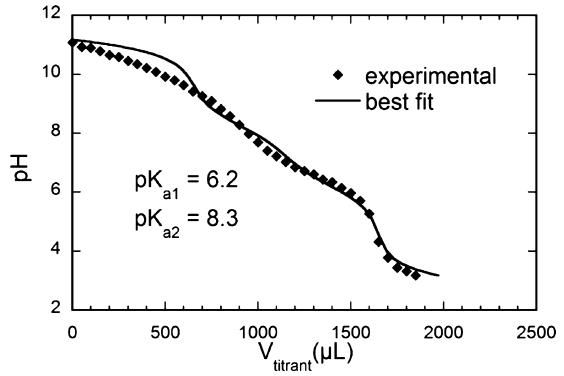


**Figure 6.** Experimental titration curve of 2 nm core, polymer coated gold NPs dispersed in 1.5 mM NaOH by 23 mM HCl and best fit using two sets of carboxyl functions.

**Investigation of Colloidal Stability.** An important consequence of the Henderson−Hasselbalch equation is that, at a given pH, the net charge of NPs depends on the pH. Hence, the colloidal stability strongly depends on the p$K_a$, with the lowest p$K_a$ providing the widest pH range where NPs bear a net negative charge, and thus the widest pH range of colloidal stability.

DLS and zeta potential measurements are two common methods to investigate colloidal stability, although their indications are mostly qualitative due to rather large irreproducibility for small particles. We performed DLS and zeta potential versus pH titrations on the polymer coated NPs and observed that the colloidal stability trends they indicate qualitatively reflects the p$K_a$ values measured by pH potentiometric titrations. Indeed, a pH dependent agglomeration phenomenon was observed in the hydrodynamic diameter $d_h$ versus pH titration curves (Figure 7). The hydrodynamic


dx.doi.org/10.1021/la302570s | Langmuir 2012, 28, 15141−15149

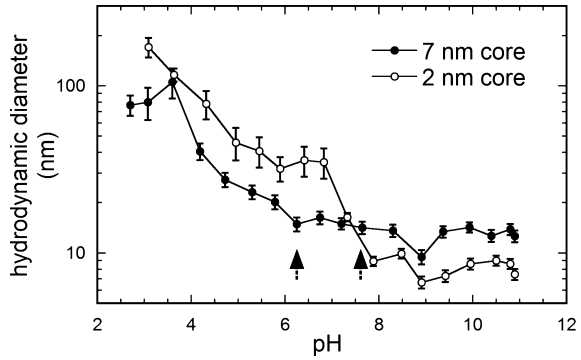


**Figure 7.** Experimental hydrodynamic diameter vs pH titration curves plots for 2 and 7 nm core polymer coated gold NPs.

diameter significantly increased at pH below approximately 7.6 and 6.2 for 2 and 7 nm core NPs, respectively, evidencing that charge repulsion no longer compensates van der Waals attraction. This is consistent with the p$K_a$ values of 7.25 and 7.2 extracted from the pH potentiometric titrations.

The zeta potential is often taken as the potential at the limit of the so-called Stern double layer. Briefly, it can be seen as the potential created by the surface charge $Q$ and screened by a double layer of ions. As such, one should expect it to roughly follow the trends of $Q$. Similarly to the hydrodynamic diameter, the zeta potential varies significantly around pH 7, in good agreement with the p$K_a$ determined by potentiometric pH titrations (Figures S8 and S9 and and text in SI for discussion of the curve interpretation). In principle, the p$K_a$ could also be estimated from zeta potential versus pH titrations. However, the zeta potential is of complex nature and is not a simple reflection of the surface charge as it strongly depends on the surrounding electrolyte. Moreover, one has to point out that, practically speaking, zeta potential versus pH curves have fewer data points than classical titration curves, which in turn leads to lower accuracy.

From these measurements, we conclude that pH titrations can give a reasonable picture of the pH range of colloidal stability, provided that the ionic strength is not so high that electrostatic repulsions are strongly screened. Moreover, pH titrations have the added advantage compared to zeta potential measurements of providing the ionization state at a given pH with appreciable accuracy. This may be of interest for tuning the reactivity of the surface groups in further functionalization reactions, as will be discussed later on.

Finally, the comparison of the p$K_a$ shifts observed for SAM coated and polymer coated NPs triggers some remarks about the prediction of the colloidal stability when designing a water-soluble material. Polymer coated NPs have surface p$K_a$ values very close to that of the free-standing polymer, whereas alkanethiols experience p$K_a$ shifts of at least 2 units when assembled on the NPs. This evidence a fundamental difference between functionalization schemes based on small molecules and on macromolecules. Indeed, polyelectrolyte molecules encompass already all the electrostatic effects at play on the surface of NPs. Provided that the conformation of the macromolecule is not drastically disturbed, its physicochemical properties, and in particular its p$K_a$ or isoelectric point, should be mostly retained on the NPs. Some deviations are expected but to a smaller extent than with simple molecules. This means that the pH range of colloidal stability can be derived in a straightforward way from the physicochemical properties of the macromolecule. pH titrations are a simple, time-efficient, and low cost means to probe them and to optimize the colloidal system, without wasting high value nanocrystals.

**Determination of the Surface Density of Functionalities Using pH Titrations.** *Method.* In addition to the p$K_a$, other important information can be extracted from the buffer plateau of pH titration curves. Knowing the concentration of the titrant, its width gives the concentration of carboxyl groups $c_{carboxyl}$ (Figure 1). When combined with the NP concentration ($c_{NPs}^{tot}$), the average number of functional groups per NP ($N_{carboxyl}$) can be determined according to eq 3. Alternatively, the surface density of functionalities $\sigma_{carboxyl}$ can be calculated with regards to the effective specific area $A_{eff}$ (the specific area defined by the effective sphere comprising the metallic core and the organic shell, i.e., calculated using $d_{eff}$, Scheme 3). Likewise, the coverage density of thiols on gold in the case of SAM coated NPs ($\sigma_{thiol}$) can be calculated with regards to the metallic core specific area $A_c$ (i.e., calculated using $d_c$), according to eq 4.

$$N_{carboxyl} = \frac{c_{carboxyl}}{c_{NPs}^{tot}} \tag{3}$$

$$\sigma_{carboxyl} = \frac{c_{carboxyl} V_{tot}}{A_{eff}}; \quad \sigma_{thiol} = \frac{c_{carboxyl} V_{tot}}{A_c} \tag{4}$$

where $V_{tot}$ is the total volume of the sample.

From the simulation of the experimental titration curves, we extracted the concentrations of carboxyl species within our samples ($c_{carboxyl}$). The determination of specific NP area ($A_{eff}$ and $A_c$) were obtained by coupling the determination of the total gold concentration by ICP-AES ($c_{Au}^{tot}$) and the estimation of the NP size distribution by TEM analysis (Figures S10 and S11 and associated methods in the SI).

*SAM-Coated NPs.* The numbers of carboxyl moieties per NP, per unit (nm$^2$) of effective specific area and the numbers of thiol per nm$^2$ of gold surface are summed up in Table 1. One needs to stress that these figures have been derived from the titrations of colloidally stable dispersions of NPs (not sedimenting). The 6 nm MPA coated NPs were not considered for this analysis since the sample had become colloidally unstable by the time the ICP-AES measurements were performed. The thiol coverage densities were on the same order of magnitude within the SAM-coated NP family and varied from 8 to 14 thiols per nm$^2$ of metal core. These thiol coverage densities were higher on average than the reference value of around 5 molecules/nm$^2$ reported by Strong and Whitesides for docosylthiol on planar gold films, following electron diffraction experiments.[28] Murray et al. previously observed thiol coverage densities on 2 nm dodecanethiol-stabilized gold NPs two times higher than that on gold planar surfaces.[29] They were attributed to the presence of excess "defect sites", namely, edge and corner gold atoms, on highly curved NPs compared to planar surfaces. However, some of the densities we observed are even higher, suggesting an excess of ligands in equilibrium with the thiol-coated gold surface. Interestingly, the ligands in excess seem to be somehow bound to the NPs and not free-standing in the solution. Indeed, if a substantial amount of unbound ligands remained within the SAM coated samples after purification, those should appear in the corresponding pH titration curves as a buffer plateau with a height equal to the p$K_a$ of the free ligand (4.3 and 4.8 for MPA and MUA, respectively) and a width corresponding to the


dx.doi.org/10.1021/la302570s | *Langmuir* 2012, 28, 15141−15149

excess ligands with regards to the reference coverage density of 5 molecules/nm$^2$. For all four types of SAM-coated NPs, the titration curves display a single buffer plateau at heights of between 6.7 and 7.2. This single p$K_a$ suggests that the excess thiol is bound to the NPs. Two hypothesis can then be foreseen to account for the discrepancy in thiol coverage densities between our values and that of Strong and Whitesides or Murray et al.

The first possibility stems from the method used to prepare the samples for ICP-AES analysis. Assuming that NPs smaller than 10 nm would be fully shattered in the plasma, no predigestion step in aqua regia was performed to convert the gold NPs into tetrachloroauric acid molecules. Instead, aliquots of colloidally stable NPs solutions were dispersed in 2% nitric acid by sonication. It is conceivable that agglomeration occurs, which could induce sedimentation on the time scale of the ICP-AES measurements and in turn lead to underestimated gold concentration.

In the second possibility, the excess thiol is bound to the NPs even if it is not bound directly onto the gold surface. While noncoordinating, those excess ligands are affected by the same charge effects than the coordinating ligands and must therefore experience a positive p$K_a$ shift with regard to the free molecule. Excess ligands might be bound to coordinating ones through hydrophobic interactions between aliphatic chains. Hydrophobic interactions between long alkyl chains and alkylthiols on the surface of NPs have been demonstrated previously. These interactions have been exploited in the water transfer of NPs synthesized in organic media through their wrapping in amphiphilic polymers or intercalation with fatty acids derivatives.[14,30,31] They are all the more likely to occur with weakly hydrosoluble ligands, such as MUA. Indeed the balance between stabilization by hydrophobic interactions within the organic shell and interaction of the alkyl chains of the ligands with water may be unfavorable to the release of excess ligand in solution. Further experiments, such as diffusion ordered NMR (DOSY) or cross-referencing ICP-AES with gas chromatography coupled to mass spectrometry, would be needed to gain structural insights about this ligand excess but were beyond the scope of the present study.

*Polymer Coated NPs.* For the sake of simplicity, the method of polymer coating we employed is often depicted as giving rise to a monolayer of amphiphilic polymer wrapped around the NP, with the long aliphatic chains in hydrophobic interaction with the aliphatic ligands, although arrangements will be less ordered in reality. One can foresee two extreme arrangements in which the polymer chains adopt an extended conformation and are either fully intercalated with the ligands or sitting on top of them in a lipidic bilayer fashion. Assuming a chain length of roughly 1 nm both for dodecanethiol and dodecylamine, we therefore calculated the surface density of functionality using effective diameters after polymer coating $d_{eff,pol}$ of $d_c$+2 or $d_c$+4 (in nm) (Table 1).

The 2 nm NPs were coated using 200 monomer units per nm$^2$ of effective specific area (core + ligand shell). The resulting density of functionalities was determined to be between 10 and 22 carboxylates per nm$^2$ of effective polymer-coated specific area. As previously established, 1 equiv of titrated carboxylate is associated with 1 equiv of monomer. According to our DFT calculations, one monomer unit has a projected area on the sphere of roughly 0.33 nm$^2$. If the polymer is wrapped around the NP as a perfect flat monolayer, then the maximal surface coverage density should be of 3 monomer units/nm$^2$. The experimental density is much higher and suggests a rough polymer layer, possibly bearing dangling polymer strands.

**Practical Applications of pH Titrations in the Preparation of Functional NPs.** *Stability of the Coating.* pH titrations, when coupled to a NP quantification technique (e.g., visible absorption spectroscopy or ICP-AES), could be used to assess the stability of the ligand layer. As an example, we investigated the stability of the SAM on the MUA-coated 5 nm gold NPs toward isolation and redispersion in fresh solvent. Figure S2 in the SI depicts two pH titration curves recorded on a purified sample of MUA-coated 5 nm NPs before and after an additional washing step on an ultracentrifugational filter using 20 mL of 5 mM NaOH solution and redispersion in 1 mM NaOH. The concentration in terms of carboxyl moieties of the extra-purified sample was found to be 95% of that of the mother sample. This result indicates that the "excess" thiols are actually tightly bound to the NP and resilient to purification in water. More generally, pH titrations could be used to assess the stability of ligand layers toward time, precipitation−redispersion, or exposure to other species.

*Monitoring and Optimizing Purification Procedures.* Following the same principle, pH titrations can enable monitoring and optimization of purification procedures. For instance, the 7 nm NPs were coated using an excess of polymer of 600 monomer units per nm$^2$ of effective specific area. To achieve the thinnest possible coating, the NPs were purified by several runs of size exclusion chromatography. After three runs of size exclusion chromatography designed to remove the excess polymer, the density of functionalities was still between 102 and 153 carboxylates/nm$^2$, therefore evidencing that the organic shell encompassed multilayers of polymer. To investigate whether the purification could be further improved, we performed pH titrations before and after the last purification step on aliquots of NPs having the same volume and same optical density (SI Figure S6). Comparison of both measurements indicates that about half of the polymer was removed on the column, even after two purifications had been performed. Therefore purification could be further improved. One could set as a criterion to achieve optimal purity to have the carboxyl concentration constant (the optical density being constant) before and after a purification step.

*Monitoring of Reaction Yields.* The quantification of surface functionalities by pH titration could be an important step in the routine determination of reaction yields. For instance, the yield of coupling of a protected peptide on carboxylated NP could be estimated by comparing the number of carboxylates per NP before and after reaction. Routine estimation of surface reaction yields would pave the way to optimization of the reaction and reasonable use of expensive (bio/nano)reagents.

*Potential Optimization of Surface Reactions.* We hypothesize that pH titrations could be of help to optimize reactions for which the ionization state of the surface functions and/or the stoichiometry are critical. We illustrate this potential on the attachment of $NH_2$-bearing molecules on gold nanoparticles (NPs) bearing $COO^-$ groups via *N*-(3-dimethylaminopropyl)-*N*′-ethylcarbodiimide (EDC) activated peptide coupling. This reaction is known to be tedious and has been the subject of a recent study by Bartczak and Kanaras.[32] By systematically varying the relative concentrations of all reagents, they demonstrated that there is an optimal amount of EDC with regards to the amount of NPs that maximizes the yield of conjugation, with fewer or more activating reagents leading to poorer yields.

In a comprehensive study, Nakajima and Ikada shed light onto the sharp dependence on the pH of EDC activity toward carboxyl groups in water (SI Scheme S2), with the optimal pH zone ranging from 3.5 to 4.5.[33] From the suggested mechanism, three golden rules can be drawn to ensure a successful EDC activated amide bond formation in water: (i) the amount of EDC needs to be finely adjusted to avoid producing dead-end species (N-acylurea); (ii) there needs to be protons in the reaction medium; (iii) there needs to be a fair proportion of deprotonated carboxyl moieties. Finally, the use of NPs imposes an additional rule: the reaction pH should be compatible with colloidal stability in order to ensure maximum contact between the reactants.

The first rule agrees well with the observation made by Bartczak and Kanaras of a nonmonotonic behavior of the reaction yield with the amount of EDC.[32] A sufficient amount of EDC enables total activation of the carboxylates but an excess may lead to the degradation of the reactive species by attack by another EDC molecule. The fine-tuning of the EDC amount may be performed by titrating the carboxylates prior to activation. Standard peptide coupling protocols recommend to use one equivalent of EDC compared to carboxylates.[34]

There is a substantial amount of protons in solution only if the pH is lower than 7. In addition, the majority of carboxyl groups are deprotonated if the pH is superior to $pK_a + 1$, which is also a pH at which the NPs should be colloidal stable. Hence, regarding the proton and carboxylate concentrations, there is only a narrow range of pH favorable to the amide bond formation ($pK_a + 1 < pH < 7$). The knowledge of the $pK_a$ of the carboxyl groups may therefore help predict the efficiency of an EDC coupling. One should not overlook that the amine to be coupled should be nucleophilic and therefore nonionized. Primary amines generally have a $pK_a$ around 9−10 which seems unfavorable, but this value is subjected to large variations in multifunctional molecules, such as biomolecules. The effect of an unfavorable amine $pK_a$ can also be overcome by using an excess of molecule to be coupled. However, a discussion on the properties of the biomolecules is beyond the scope of this paper.

Following these guidelines, a graphical representation of the pH ranges where protons and carboxylates are the major species of their respective acid−base couples helps qualitatively predict the efficiency of an EDC activated bond formation (Figure 8). For instance, there is no pH range over which the proton and carboxylate domains of predominance overlap for polymer coated NPs. Accordingly, EDC couplings will be of low efficiency on this type of NPs. For SAM coated NPs, the overlapping window is narrow. Hence, the EDC couplings will also be quite unfavorable. However Wang et al. observed that the apparent surface $pK_a$ decreases when the solution is rich in screening electrolyte.[26] By carefully selecting an electrolyte-rich medium that brings the $pK_a$ around 6 as a reaction medium, such as tetramethylammonium chloride 200 mM with 4 nm NPs (see reference paper of Wang et al.[26]), one should enable efficient EDC couplings.

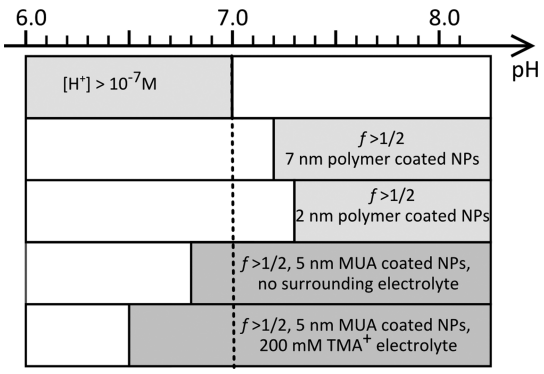


**Figure 8.** Favorable pH ranges for EDC-activated amide bond formation on MUA protected and polymer coated gold NPs. $TMA^+$ = tetramethylammonium cation.

## CONCLUSION

In this work, we used pH titrations to illustrate how the $pK_a$ of species adsorbed on NPs can markedly differ from those of the free molecules and the consequences on the colloidal stability. Importantly, macromolecules are more likely to retain their physicochemical properties once assembled onto NPs than small molecules. We suggest that pH titration of macromolecules could help predict the colloidal stability of functional nanomaterial and avoid wasting of quality nanocrystals.

We demonstrated that pH titrations can be used to quantify the surface functionalities of NPs and their surface density when coupled to a method for quantifying the number of NPs. This method could pave the way to work quantitatively with functional material, through monitoring the stability of the functional coating, the efficiency of purification procedures or the yield of surface reactions.

We hypothesize that this convenient and cost-effective methodology could enable the optimization of challenging surface reactions, such as EDC-activated amide bond formation, through the careful control of the relative stoichiometry and speciation of the reactive functionalities. Importantly, the methodology can be generalized to other types of NP cores, such as quantum dots (QDs) or magnetic NPs (SPIONs) and other types of acid−base functionalities (amines, phosphates, etc.).

## ASSOCIATED CONTENT

### Supporting Information

Synthetic details, measurement protocols (pH titration, DLS and zeta potential titration, TEM, ICP-AES), additional titration curves, method for DFT calculation, and overview of EDC mechanism. This material is available free of charge via the Internet at http://pubs.acs.org.

## AUTHOR INFORMATION

### Corresponding Author

*E-mail: gaelle.charron@univ-paris-diderot.fr (G.C.); wolfgang.parak@physik.uni-marburg.de (W.J.P.).

### Notes

The authors declare no competing financial interest.

## ACKNOWLEDGMENTS

The authors are grateful to Dr. Jose Maria Montenegro Martos for helpful discussions. Part of this work was supported by the EC (project Nanognostics to W.J.P.), the DFG (project PA794/11-1), and the SolarCAP grant (EPSRC).

## REFERENCES

(1) Scher, E. C.; Manna, L.; Alivisatos, A. P. Shape control and applications of nanocrystals. *Philos. Trans. R. Soc. A* **2003**, *361*, 241−257.

(2) Parak, W. J. Complex Colloidal Assembly. *Science* **2011**, *334*, 1359−1360.
(3) Mout, R.; Moyano, D. F.; Rana, S.; Rotello, V. M. Surface functionalization of nanoparticles for nanomedicine. *Chem. Soc. Rev.* **2012**, *41*, 2539−2544.
(4) Hildebrandt, N. Biofunctional Quantum Dots: Controlled Conjugation for Multiplexed Biosensors. *ACS Nano* **2011**, *5*, 5286−5290.
(5) Basiruddin, S.; Saha, A.; Pradhan, N.; Jana, N. R. Advances in Coating Chemistry in Deriving Soluble Functional Nanoparticle. *J. Phys. Chem. C* **2010**, *114*, 11009−11017.
(6) Guerrero-Martínez, A.; Pérez-Juste, J.; Liz-Marzán, L. M. Recent Progress on Silica Coating of Nanoparticles and Related Nanomaterials. *Adv. Mater.* **2010**, *22*, 1182−1195.
(7) Sperling, R. A.; Parak, W. J. Surface functionalization of nanoparticles for nanomedicine. *Philos. Trans. R. Soc. A* **2010**, *368*, 1333−1383.
(8) Schneider, G.; Decher, G. Functional Core/Shell Nanoparticles via Layer-by-Layer Assembly. Investigation of the Experimental Parameters for Controlling Particle Aggregation and for Enhancing Dispersion Stability. *Langmuir* **2008**, *24*, 1778−1789.
(9) Mei, B. C.; Susumu, K.; Medintz, I. L.; Delehanty, J. B.; Mountziaris, T. J.; Mattoussi, H. Modular poly(ethylene glycol) ligands for biocompatible semiconductor and gold nanocrystals with extended pH and ionic stability. *J. Mater. Chem.* **2008**, *18*, 4949−4958.
(10) Medintz, I. L.; Uyeda, H. T.; Goldman, E. R.; Mattoussi, H. Quantum dot bioconjugates for imaging, labelling and sensing. *Nat. Mater.* **2005**, *4*, 435−446.
(11) Hermanson, G. T. *Bioconjugate Techniques*, 2nd ed.; Academic Press: London, 2008.
(12) Jana, N. R.; Peng, X. Single-Phase and Gram-Scale Routes toward Nearly Monodisperse Au and Other Noble Metal Nanocrystals. *J. Am. Chem. Soc.* **2003**, *125*, 14280−14281.
(13) Laaksonen, T.; Ahonen, P.; Johans, C.; Kontturi, K. Stability and Electrostatics of Mercaptoundecanoic Acid-Capped Gold Nanoparticles with Varying Counterion Size. *ChemPhysChem* **2006**, *7*, 2143−2149.
(14) Lin, C.-A. J.; Sperling, R. A.; Li, J. K.; Yang, T.-Y.; Li, P.-Y.; Zanella, M.; Chang, W. H.; Parak, W. J. Design of an Amphiphilic Polymer for Nanoparticle Coating and Functionalization. *Small* **2008**, *4*, 334−341.
(15) Skoog, D. A.; West, D. M.; Holler, F. J.; Crouch, S. R. *Fundamentals of Analytical Chemistry*, 8th ed.; Brooks/Cole: Belmont, CA, 2003.
(16) Frisch, M. J.; Trucks, G. W.; Schlegel, H. B.; Scuseria, G. E.; Robb, M. A.; Cheeseman, J. R.; Scalmani, G.; Barone, V.; Menucci, B.; Petersson, G. A.; Nakatsuji, H.; Caricato, M.; Li, X.; Hratchian, H. P.; Izmaylov, A. F.; Bloino, J.; Zheng, G.; Sonnenberg, J. L.; Hada, M.; Ehara, M.; Toyota, K.; Fukuda, R.; Hasegawa, J.; Ishida, M.; Nakajima, T.; Honda, Y.; Oxx Kitao; Nakai, H.; Vreven, T.; Montgomery, J. A.; Peralta, J. E.; Ogliaro, F.; Bearpark, M.; Heyd, J. J.; Brothers, E.; Kudin, K. N.; Staroverov, V. N.; Kobayashi, R.; Normand, J.; Raghavachari, K.; Rendell, A.; Burant, J. C.; Iyengar, S. S.; Tomasi, J.; Cossi, M.; Rega, N.; Millam, J. M.; Klene, M.; Knox, J. E.; Cross, J. B.; Bakken, V.; Adamo, C.; Jaramillo, J.; Gomperts, R.; Stratmann, R. E.; Yazyev, O.; Austin, A. J.; Cammi, R.; Pomelli, C.; Ochterski, J. W.; Martin, R. L.; Morokuma, K.; Zakrzewski, V. G.; Voth, G. A.; Salvador, P.; Dannenberg, J. J.; Dapprich, S.; Daniels, A. D.; Farkas, O.; Foresman, J. B.; Ortiz, J. V.; Cioslowski, J.; Fox, D. J. *Gaussian 09*; Gaussian Inc.: Wallingford, CT, 2009.
(17) Chai, J.-D.; Head-Gordon, M. Long-range corrected hybrid density functionals with damped atom−atom dispersion corrections. *Phys. Chem. Chem. Phys.* **2008**, *10*, 6615−6620.
(18) Chai, J.-D.; Head-Gordon, M. Systematic optimization of long-range corrected hybrid density functional. *J. Chem. Phys.* **2008**, *128*, 084106.
(19) Dunning, T. H. Gaussian basis sets for use in correlated molecular calculations. I. The atoms boron through neon and hydrogen. *J. Chem. Phys.* **1989**, *90*, 1007−1023.
(20) Thanthiriwatte, K. S.; Hohenstein, E. G.; Burns, L. A.; Sherrill, C. D. Assessment of the Performance of DFT and DFT-D Methods for Describing Distance Dependence of Hydrogen-Bonded Interactions. *J. Chem. Theory Comput.* **2011**, *7*, 88−96.
(21) Kendall, R. A.; Dunning, T. H.; Harrison, R. J. Electron affinities of the first-row atoms revisited. Systematic basis sets and wave functions. *J. Chem. Phys.* **1992**, *96*, 6796−6806.
(22) Gavezzotti, A.; Filippini, G. Geometry of the Intermolecular X−H···Y (X, Y = N, O) Hydrogen Bond and the Calibration of Empirical Hydrogen-Bond Potentials. *J. Phys. Chem.* **2011**, *98*, 4831−4837.
(23) *CRC Handbook of Chemistry and Physics*, 90th ed.; Lide, D. R., Ed.; CRC Press: Boca Raton, FL, 2010.
(24) Creager, S. E.; Clarke, J. Contact-Angle Titrations of Mixed ω-Mercaptoalkanoic Acid/Alkanethiol Monolayers on Gold. Reactive vs Nonreactive Spreading, and Chain Length Effects on Surface pKa Values. *Langmuir* **1994**, *10*, 3675−3683.
(25) Kane, V.; Mulvaney, P. Double-Layer Interactions between Self-Assembled Monolayers of ω-Mercaptoundecanoic Acid on Gold Surfaces. *Langmuir* **1998**, *14*, 3303−3311.
(26) Wang, D.; Nap, R. J.; Lagzi, I.; Kowalczyk, B.; Han, S.; Grzybowski, B. A.; Szleifer, I. How and Why Nanoparticle's Curvature Regulates the Apparent p$K_a$ of the Coating Ligands. *J. Am. Chem. Soc.* **2011**, *133*, 2192−2197.
(27) Miessler, G. L.; Tarr, D. A. *Inorganic Chemistry*, 3rd ed.; Prentice Hall: Upper Saddle River, NJ, 1991.
(28) Strong, L.; Whitesides, G. M. Structures of self-assembled monolayer films of organosulfur compounds adsorbed on gold single crystals: electron diffraction studies. *Langmuir* **1988**, *4*, 546−558.
(29) Hostetler, M. J.; Wingate, J. E.; Zhong, C.-J.; Harris, J. E.; Vachet, R. W.; Clark, M. R.; Londono, J. D.; Green, S. J.; Stokes, J. J.; Wignall, G. D.; Glish, G. L.; Porter, M. D.; Evans, N. D.; Murray, R. W. Alkanethiolate Gold Cluster Molecules with Core Diameters from 1.5 to 5.2 nm: Core and Monolayer Properties as a Function of Core Size. *Langmuir* **1998**, *14*, 17−30.
(30) Ducongé, F.; Pons, T.; Pestourie, C.; Hérin, L.; Thézé, B.; Gombert, K.; Mahler, B.; Hinnen, F.; Kühnast, B.; Dollé, F.; Dubertret, B.; Tavitian, B. Fluorine-18-Labeled Phospholipid Quantum Dot Micelles for in Vivo Multimodal Imaging from Whole Body to Cellular Scales. *Bioconjugate Chem.* **2008**, *19*, 1921−1926.
(31) Wu, H.; Zhu, H.; Zhuang, J.; Yang, S.; Liu, C.; Cao, Y. C. Water-Soluble Nanocrystals Through Dual-Interaction Ligands. *Angew. Chem., Int. Ed.* **2008**, *47*, 3730−3734.
(32) Bartczak, D.; Kanaras, A. G. Preparation of Peptide-Functionalized Gold Nanoparticles Using One Pot EDC/Sulfo-NHS Coupling. *Langmuir* **2011**, *27*, 10119−10123.
(33) Nakajima, N.; Ikada, Y. Mechanism of Amide Formation by Carbodiimide for Bioconjugation in Aqueous Media. *Bioconjugate Chem.* **2011**, *6*, 123−130.
(34) Chan, W.; White, P. D. *Fmoc Solid Phase Peptide Synthesis: A Practical Approach*; Oxford University Press: New York, 2000.

# Polymer-Coated Nanoparticles Interacting with Proteins and Cells: Focusing on the Sign of the Net Charge

**Dominik Hühn,[†,⊗] Karsten Kantner,[†,⊗] Christian Geidel,[‡] Stefan Brandholt,[§] Ine De Cock,[⊥] Stefaan J. H. Soenen,[⊥] Pilar Rivera_Gil,[†] Jose-Maria Montenegro,[†] Kevin Braeckmans,[⊥] Klaus Müllen,[‡] G. Ulrich Nienhaus,[§,∥,#] Markus Klapper,[‡,*] and Wolfgang J. Parak[†,▽,*]**

[†]Department of Physics, Philipps-University Marburg, Marburg, Germany, [‡]Max Planck Institute for Polymer Research, Mainz, Germany, [§]Institute of Applied Physics and Center for Functional Nanostructures (CFN), Karlsruhe Institute of Technology (KIT), Karlsruhe, Germany, [⊥]Faculty of Pharmaceutical Sciences, Ghent University, Ghent, Belgium, [∥]Institute of Toxicology and Genetics, Karlsruhe Institute of Technology (KIT), Karlsruhe, Germany, [#]Department of Physics, University of Illinois at Urbana-Champaign, Urbana, Illinois 61801, United States, and [▽]CIC biomaGUNE, San Sebastián, Spain. [⊗]Both authors contributed equally to this work.

**ABSTRACT** To study charge-dependent interactions of nanoparticles (NPs) with biological media and NP uptake by cells, colloidal gold nanoparticles were modified with amphiphilic polymers to obtain NPs with identical physical properties except for the sign of the charge (negative/positive). This strategy enabled us to solely assess the influence of charge on the interactions of the NPs with proteins and cells, without interference by other effects such as different size and colloidal stability. Our study shows that the number of adsorbed human serum albumin molecules per NP was not influenced by their surface charge. Positively charged NPs were incorporated by cells to a larger extent than negatively charged ones, both in serum-free and serum-containing media. Consequently, with and without protein corona (*i.e.*, in serum-free medium) present, NP internalization depends on the sign of charge. The uptake rate of NPs by cells was higher for positively than for negatively charged NPs. Furthermore, cytotoxicity assays revealed a higher cytotoxicity for positively charged NPs, associated with their enhanced uptake.

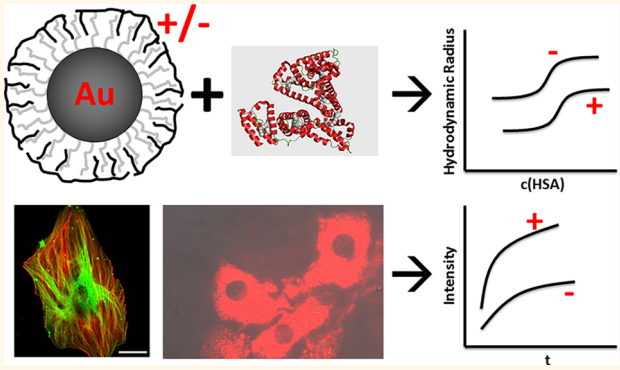


**KEYWORDS:** colloidal gold nanoparticles · surface charge dependence · protein corona · uptake by cells · cytotoxicity

Although cytotoxicity of colloidal nanoparticles (NPs) is currently under intensive research, we are not yet at the point where we understand how cytotoxic effects are related to key physicochemical parameters of the NPs such as colloidal stability, size, surface charge, *etc.*[1,2] This is partly due to the fact that some of these properties are hard to control and study individually. In fact, it is challenging to prepare a set of NPs for which only a single property is varied because they are often interrelated.[1]

Charge is a key parameter of NPs known to influence their cellular uptake as well as cytotoxicity.[3−11] In studies of charge-dependence, negative or positive net surface charge is often introduced *via* surfactants bearing $-COO^-$ or $-NH_3^+$ groups, respectively. However, the protonation state of these groups and, therefore, the net charge depend on the surrounding pH. Moreover, changes in net charge can drastically affect colloidal stability. pH is a very important factor because it changes along the internalization pathway from slightly alkaline in the cell medium (7.4−7.0) to highly acidic in intracellular vesicles (5.0−4.6).[12] Limitations in colloidal stability can be partly avoided by using proteins or polyethylene glycol (PEG) terminated with $-COO^-$ or $-NH_3^+$ groups as ligands.[13,14,15] In this work, we introduce charge by enshrouding the NP with an amphiphilic diblock-copolymer containing blocks of monomers with a long, hydrophobic alkyl side chain and blocks of monomers that carry charge (Figure 1). Phosphonate ($-PO(OH)_2$) and trimethylammonium ($-N(CH_3)_3$) groups provide a permanent negative and positive charge,

* Address correspondence to wolfgang.parak@physik.uni-marburg.de, klapper@mpip-mainz.mpg.de.

Received for review December 21, 2012 and accepted March 26, 2013.

**Published online March 26, 2013**
10.1021/nn3059295

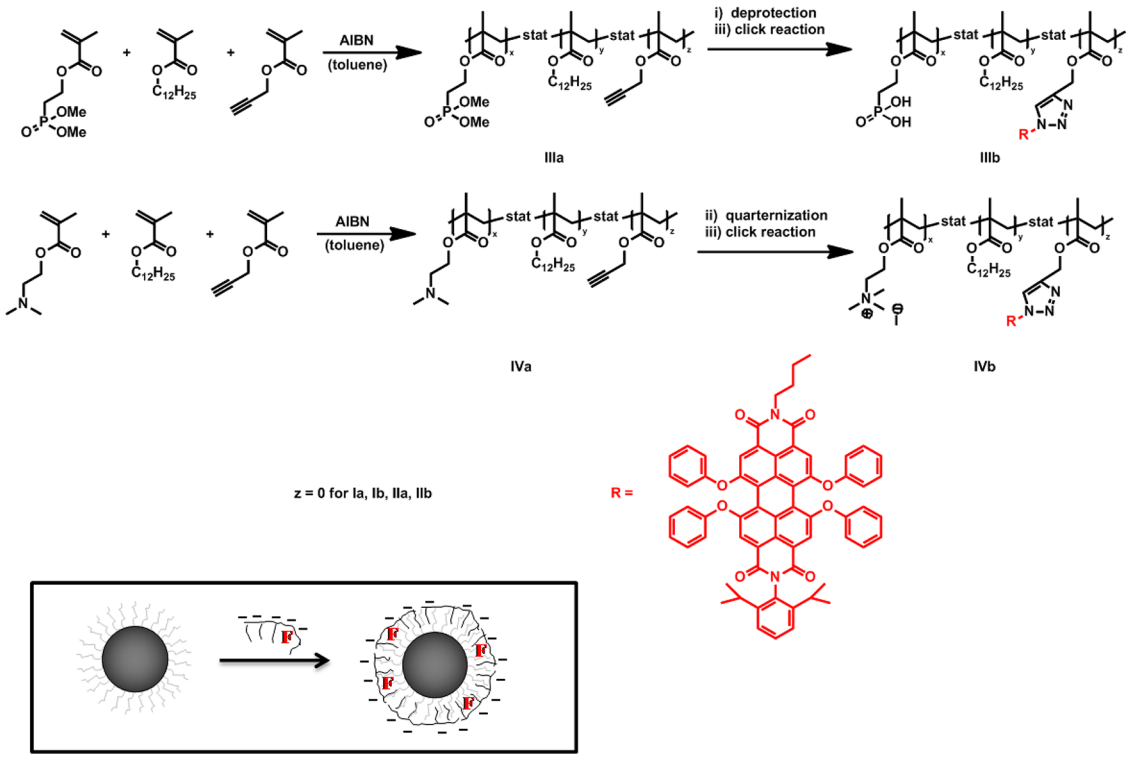


**Figure 1. Copolymers and fluorophore-functionalized terpolymers for coating the hydrophobic Au NPs. A detailed description is given in the Supporting Information. (i) Deprotection with trimethylsilyl bromide in dichloromethane; (ii) quaternization of the amino function with methyliodide in dichloromethane; (iii) click reaction with dye-azide (PDI-$N_3$), CuI, and *N*,*N*,*N*′,*N*′,*N*″-pentamethyldiethylenetriamine in toluene. IIIa and IVa refer to the negatively and positively charged terpolymers with an alkyne residue. IIIb and IVb refer to the negatively and positively charged fluorescent terpolymers. For the nonfluorescent copolymers (Ia/Ib = negatively charged; IIa/IIb = positively charged), the alkyne comprising monomer has to be neglected in each case ($z = 0$). Box: Scheme of the polymer coating procedure. Au NPs were capped with hydrophobic surfactants (dodecanethiol). An amphiphilic polymer with monomers comprising hydrophobic side-chains, monomers comprising polar groups, and optionally monomers comprising a fluorophore (F) can be wrapped around the NP driven by hydrophobic interaction. Upon exposure of the polar groups on the surface, the NPs can be suspended in water. Negatively or positively charged NPs are obtained, depending on the polar group of the polymer.**

respectively. The first $pK_a$ value of the $-PO(OH)_2$ ($pK_{a1} = 2.4$) is low enough to provide a negative charge under all pH conditions that NPs may experience outside and inside cells, *cf.* Figure 1.[16] For negatively as well as for positively charged NPs, the charged groups are situated at the same polymer backbone, so that the surface properties of the NPs are—to a very good approximation—identical except for the sign of the charge. The polymer is wrapped around the surface of dodecanethiol-capped Au NPs.[16] The hydrophobic side chains of the polymer intercalate with the hydrophobic dodecyl chains on the Au cores, and the charged blocks point toward the surrounding solution so as to provide excellent colloidal stability in an aqueous environment (Figure 1). The resulting NPs are very well-defined and enable a detailed analysis of their physicochemical parameters.

We hypothesized that the different charge on the NPs may affect cellular uptake and their subsequent cytotoxicity along two different routes. On the one hand, charge could directly influence the interaction with cells. On the other hand, charge could change the protein corona around the NP surface, which would indirectly modify cell-NP interactions. To resolve these issues, we have investigated both, the charge dependence of the protein corona as well as the charge dependence on NPs uptake under serum-containing (*i.e.*, in the presence of a protein corona) and under serum-free conditions (*i.e.*, in the absence of a protein corona). In addition, the charge-dependence of the cytotoxicity was studied using a variety of methods. Notably, due to the high colloidal stability of the NPs, the effects of charge could be examined without interference by changes in NP size or colloidal stability.

## RESULTS AND DISCUSSION

**Physicochemical Characterization.** The charge on the as-synthesized NPs was determined by ζ-potential measurements on NPs without fluorophores in in Milli-Q water (medium #1) to be $-39.8 \pm 10.0$ mV and $+9.7 \pm 8.9$ mV for the negatively and positively charged NPs (*cf.* Table 1 and Figure 1 about their surface chemistry), respectively. Hydrodynamic diameters of NPs were recorded in phosphate-buffered saline (PBS) (medium #2) with dynamic light scattering (DLS, as determined from the number distribution) and with fluorescence

**TABLE 1. Composition of the Amphiphilic Co- and Terpolymers**

| | composition of the polymer[a] | | | | | |
|---|---|---|---|---|---|---|
| polymer | TMAEMA [mol %] | MAPHOS [mol %] | LMA [mol %] | PgMA [mol %] | $M_n$[b] [g mol$^{-1}$] | PDI[c] |
| **Ib** | - | 40 | 60 | - | 9000 | 2.0 |
| **IIb** | 53 | - | 47 | - | 16300 | 1.8 |
| **IIIb** | - | 52 | 42 | 6 | 9500 | 2.1 |
| **IVb** | 48 | - | 48 | 4 | 17800 | 2.0 |

[a] Determined *via* $^1$H NMR-spectroscopy. [b] Molecular weights were determined by GPC in THF *versus* PMMA standard after the initial reaction step (polymerization of the protected/neutral monomers; **Ia** – **IVa**). The presented $M_n$ values were recalculated for the final polymers (**Ib** – **IVb**). [c] PDI: polydispersity index.

correlation spectroscopy (FCS). While a fluorescent polymer shell was required for FCS, fluorescence would have interfered with DLS. Thus, DLS measurements were performed with NPs without fluorophores in the polymer shell. Hydrodynamic diameters, $d_h$, of negatively and positively charged NPs were determined as 14.5 ± 1.0 nm (DLS) and 15.8 ± 0.4 nm (FCS), and 10.1 ± 0.6 nm (DLS) and 10.2 ± 0.2 nm (FCS), respectively, *cf.* Table 2. Within the experimental errors, DLS and FCS yielded comparable results, however, FCS results had smaller errors and, in our hands, were better reproducible. The negatively charged NPs are slightly bigger than the positively charged ones. This might be due to a charge effect, so that a higher ζ-potential results in a further extended Stern double layer. Consequently, the hydrodynamic diameter correlates with the magnitude of the ζ-potential.[17] As the magnitude of the ζ-potential of negatively charged NPs was approximately four times higher than that of the positively charged NPs, the difference in hydrodynamic diameter is consistent with this interpretation.

It is well-known that counterions can screen the charge of the NPs and, thereby, cause instability of colloidal properties.[18,19] To examine this effect, colloidal stability was probed using 5 nM NP suspensions in the following solutions which are relevant as cell culture media (water as Medium #1 was used as reference): Medium #2, PBS; Medium #3, Dulbecco's modified Eagle's medium (DMEM); Medium #4, PBS + 1% penicillin/streptomycin (P/S) + 1% L-glutamine (L-Glu); Medium #5, DMEM + 1% P/S + 1% L-Glu; Medium #6, PBS + 800 μM bovine serum albumin (BSA); Medium #7, DMEM + 1% P/S + 1% L-Glu + 800 μM BSA; Medium #8, DMEM + 1% P/S + 1% L-Glu + 10% fetal bovine serum (FBS). Colloidal stability was first probed *via* UV/vis spectroscopy by recording changes in the normalized absorbance (*cf.* Figures 2a,b) at the surface plasmon resonance (SPR) of Au NPs. The idea was to attribute changes in absorbance to reduced colloidal stability. Typically, when Au NPs agglomerate, their plasmon peak broadens and shifts to the red,

**TABLE 2. Results of the FCS Data[a]**

| NP charge | $r_h(0)$ [nm] | $r_h(N_{max})$ [nm] | $\Delta r_h$ [nm] | $N_{max}$ | $K_d$ [μM] | $n$ |
|---|---|---|---|---|---|---|
| negative | 7.9 ± 0.2 | 10.4 ± 0.3 | 2.5 ± 0.2 | 32 ± 4 | 1.5 ± 0.8 | 0.8 ± 0.3 |
| positive | 5.1 ± 0.1 | 9.4 ± 0.4 | 4.3 ± 0.4 | 35 ± 3 | 1.0 ± 0.3 | 0.8 ± 0.3 |

[a] $r_h(0)$ is the hydrodynamic radius of bare NPs without protein corona (as determined at a HSA concentration of $1 \times 10^{-4}$ μM and $2 \times 10^{-5}$ μM for negatively and positively charged NPs, respectively), $r_h(N_{max})$ is the hydrodynamic radius of the NPs saturated with HSA, $\Delta r_h = r_h(N_{max}) - r_h(0)$ the thickness of the protein corona, $N_{max}$ is the maximum number of adsorbed HSA molecules per NP, $K_d$ is the apparent binding constant, and $n$ *is* the Hill coefficient. We noted that the positively charged NPs started to agglomerate at HSA concentrations above 3 μM, as inferred from the increasing molecular brightness (see Supporting Information).

which would give rise to a reduced absorbance at the wavelength of the original plasmon peak.[20] For the incubation experiments in Figure 2, DMEM without the pH indicator phenol red was used. In case phenol red is present in DMEM (media #3, #5, #7), the absorption of the dye itself changes over time and thus may lead to misinterpretation, *cf.* the Supporting Information. As second indicator for colloidal stability, changes in the hydrodynamic diameter $d_h$ upon incubation in the different media were recorded with DLS (*cf.* Figure 2c,d). However, these measurements were possible only in the media without proteins (media #2, #3, #4, #5), as proteins themselves contributed to light scattering and thus interfered with determination of $d_h$, *cf.* the Supporting Information. The results obtained with UV/vis spectroscopy (*cf.* Figures 2a,b) indicate that incubation in media without BSA (media #2, #3, #4, #5, #8) did not lead to changes in the absorption profile. Especially noteworthy is the colloidal stability of Au NPs in medium #8, the most relevant one for cell culture and uptake experiments. Presence of BSA as the only protein (media #6, #7), however, led to changes (increase of the relative absorbance) at the surface plasmon peak over time for negatively and positively charged NPs, although the plasmon peak was still resolved without significant broadening. Thus, these changes may not result from the formation of (large) agglomerates, but from adsorption of BSA proteins, which changes the absorbance behavior while maintaining colloidal stability. However, this effect was the same for both polarities, and therefore, the effect on the NPs of opposite charge on cells is comparable. DLS data (Figure 2c,d) indicate a different situation. No change in $d_h$ over time was found for positively charged NPs in all media without protein component (media #2, #3, #4, #5), whereas $d_h$ was constant over time only for negatively charged NPs immersed in medium #2. In the other media (#3, #4, #5), agglomeration of negatively charged Au NPs was observed directly after addition of the medium. Interestingly, even the small content of P/S and L-Glu, whether in PBS (medium #4) or in DMEM (medium #5), had a pronounced and reproducible effect. These data

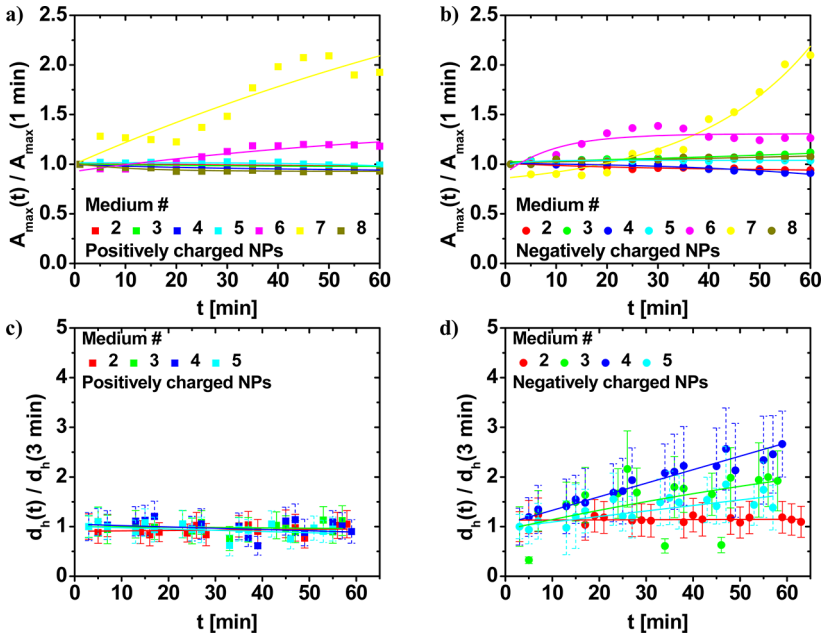


**Figure 2. Stability tests in different media (#2, PBS; #3, DMEM; #4, PBS + 1% P/S + 1% L-Glu; #5, DMEM + 1% P/S + 1% L-Glu; #6, PBS + 800 $\mu$M BSA; #7, DMEM + 1% P/S + 1% L-Glu + 800 $\mu$M BSA; #8, DMEM + 1% P/S + 1% L-Glu + 10% FBS). (a and b) The time dependent evolution of the absorbance $A_{max}(t)$ at the surface plasmon peak normalized to absorbance at the surface plasmon peak after 1 min of incubation, $A_{max}(1\ min)$, for positively and negatively charged Au NPs without fluorophore in the shell. The spectra and a UV/vis series including DMEM with pH indicator for Au NPs with and without fluorophore in the shell are shown in the Supporting Information. The pure medium always served as blank. (c and d) The time dependent evolution of the hydrodynamic diameter $d_h(t)$ normalized to the hydrodynamic diameter after 3 min of incubation, $d_h(3\ min)$, for positively and negatively charged Au NPs without fluorophore in the shell as recorded by DLS. The absolute hydrodynamic diameters are provided in the Supporting Information. For a–d, the type of the medium is indicated in color, the charge of the NPs by the symbol (square, positively charged NPs; circle, negatively charged NPs). The lines are drawn to guide the eye.**

suggest that our negatively charged NPs are colloidally less stable than the positively charged ones. This is further supported by the optical microscopy data (*cf.* Figure 4), which qualitatively suggest the presence of more agglomerates for negatively charged NPs. We note, however, that FCS data showed more agglomerates for positively charged NPs at high protein concentrations (*cf.* the Supporting Information).

In summary, our data indicate that colloidal stability in complex media cannot be trivially assessed, and different methods show different sensitivity. Changes in the UV/vis spectra are less sensitive to the formation of small agglomerates than changes in the hydrodynamic diameter as detected by DLS. However, as the size of the present NPs is at the lower detection limit of the used DLS instrument, those results also have to be interpreted with care. We conclude that the negatively charged NPs used in this study show the tendency to form (small) agglomerates in the media used for cell culture. Bigger agglomerates would have been visible in the UV/vis spectra and thus are not predominantly formed. No effect on the different media on their colloidal stability has been observed for the positively charged NPs. Thus, differences in colloidal stability between the negatively and the positively charged NPs upon their interaction with cells need to be considered.

**Investigation of Protein Adsorption.** NPs in biological media are coated by a so-called protein corona,[21,22] which may influence both the colloidal stability of NPs and NP uptake by cells.[23] To probe the charge dependence of the protein corona, we used serum albumin as a model protein (bovine: BSA, human: HSA) with a similar concentration as the FBS proportion of medium #8. Because serum albumin is the most abundant protein in blood serum, a detailed study was performed with this protein using FCS. Because of compatibility reasons with previous studies, HSA was used instead of BSA.[24] The hydrodynamic radius of the Au NPs increased with increasing HSA concentration due to adsorption of HSA, and saturated for HSA concentrations around 10 $\mu$M, *cf.* Figure 3. Fitting of the results with the Hill model yielded the hydrodynamic radii of the NPs without and with saturated protein corona, the maximum number of adsorbed HSA molecules per NP, the apparent binding constant, and the Hill coefficient, *cf.* Table 2.

In summary, the adsorption of HSA showed the same qualitative behavior on the negatively and positively charged NPs. For both, the best fit yields a slightly anti-cooperative behavior, the adsorbed proteins form a monolayer on the NP surface, and a similar number of HSA molecules is adsorbed per NP.[25] Compared to the results with FePt NPs coated with a similar negatively charged reference polymer,[24] the binding affinity is

decreased by a factor three for the negatively and by a factor five for the positively charged NPs. For the negatively charged NPs, this discrepancy may result from the fact that the negatively charged polymer used in this study had a lower charge density than the negatively charged reference polymer.[16] However, our data are not sensitive to the conformation of the adsorbed HSA molecules, which may differ in both cases. We note that our protein adsorption study utilizes a single, well-defined model protein, HSA. However, serum contains a huge number of proteins which all may be involved in protein corona formation.[26] It was shown that HSA may be displaced from the NP surface by other proteins,[27] which resulted in differences in the protein corona around negatively and positively charged NPs.[11,22] Furthermore, the amount of adsorbed proteins per NP also depends on their type and conformational properties.[28] Taken together, although we are not sensitive to conformational changes of the adsorbed HSA on negatively and positively charged NPs, our data clearly reveal that the amount of adsorbed HSA on our NPs is not strongly affected by the sign of the charge.

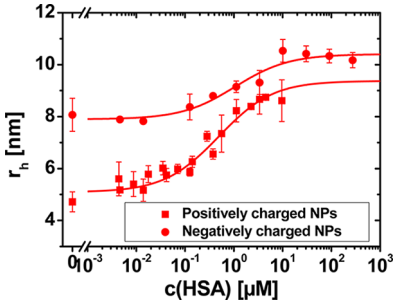


**Figure 3. HSA concentration dependent increase of the hydrodynamic radius $r_h$ of positively and negatively charged Au NPs as recorded in PBS (medium #2). Each data point represents an average from three independent measurements.**

**Charge-Dependent Uptake of Nanoparticles.** 3T3 fibroblast cells were incubated in different media with negatively and positively charged NPs with red fluorophores in the shell. As cell media, we selected buffers without proteins (medium #5) and buffers supplemented with 800 $\mu$M BSA (medium #7) or with 10% FBS (medium #8), to take into account effects of the protein corona. NPs were incorporated by cells, as concluded by the accumulation of red fluorescence inside the cells (*cf.* Figure 4). Granular distribution suggests the presence of the NPs in intracellular vesicles such as endosomes and lysosomes, in accordance with the literature.[8,29−33] Fluorescence originating from internalized NPs was quantified from microscopy images (transmission and red fluorescence channel) and is plotted in Figure 4 as fluorescence intensity *versus* time. The intensities were corrected for background and intrinsic differences of the fluorescence behavior

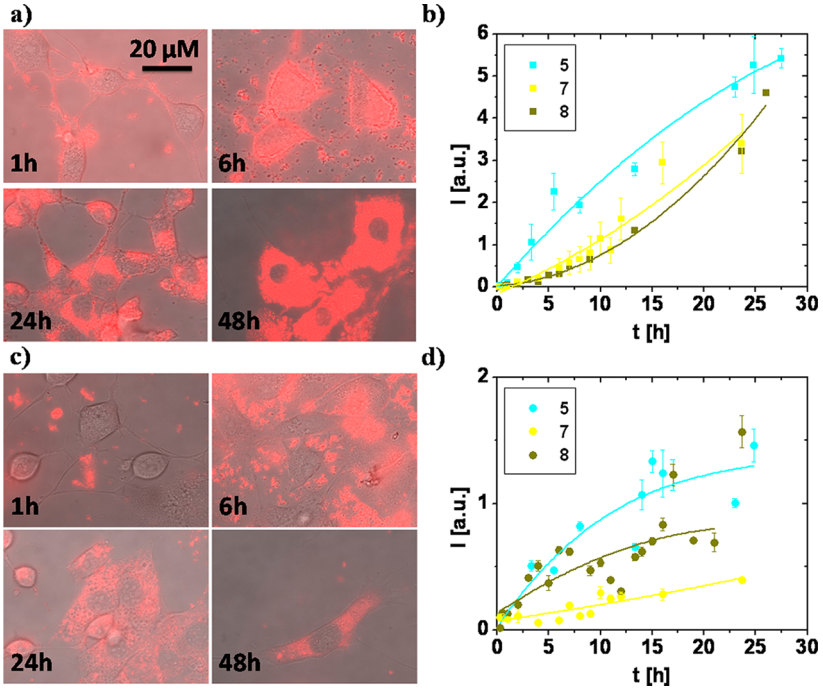


**Figure 4. 3T3 fibroblasts were incubated with (a) positively and (c) negatively charged Au NPs in different culture media. The images show the cells at different times (as indicated in each panel) after incubation in medium #8 (dark field overlaid with fluorescence channel). Brightness differs slightly due to environmental influences (day light); the data were background-corrected for further analysis (see Supporting Information). The average fluorescence intensity ($I$) per cell (background corrected) for (b) positively and (d) negatively charged NPs is plotted *versus* incubation time for media #5, #7 and #8. The uptake rate of positively charged Au NPs was significantly higher compared to negatively charged Au NPs. The scale of the fluorescence intensity axes is arbitrary but chosen so as to enable a quantitative comparison. Lines are drawn to guide the eye.**

of negatively and positively charged NPs (a detailed description of the data correction is part of the Supporting Information). A significant difference between the uptake rates of negatively and positively charged NPs was observed; uptake of positively charged NPs was significantly faster (*cf.* the slope of fluorescence intensity). Already 1 h after incubation, attachment of positively charged NPs to the outer cell membrane (which is overall negatively charged) can be observed. This difference is likely explained by electrostatic attraction of the positively charged NPs toward the negatively charged cell membrane.[34−36] After two days, significantly more positively charged NPs were internalized per cell than negatively charged NPs (absolute fluorescence intensity). Our data analysis hereby allowed for distinction between adherent and incorporated NPs (*cf.* Supporting Information). Differences in uptake are in agreement with other studies in which enhanced uptake of positively charged NPs has been reported.[37−40] Our data also allow for analyzing the dependence of uptake from the presence of the protein corona. As has been demonstrated above, both negatively and positively charged NPs in media #7 and #8 are assumed to be saturated with proteins on their surface (*cf.* also Figure 3), whereas no proteins are present in medium #5. As can be seen from Figure 4, the presence of proteins slows the uptake of NPs independent of their charge.[41,42] This behavior is in accordance with other studies, however, the extent of that difference is not as pronounced in our study.[43]

The observed differences in uptake yield clearly depend on the employed cell media.[23] However, because both, negatively and positively charged NPs have been incubated with the same media, the charge dependence of the uptake in the different media can be analyzed. To further investigate the differences in uptake levels of the negatively and positively charged NPs in relation to differences in medium composition and cell type, the NPs were used to label murine C17.2 neural progenitor cells (NPCs) and human umbilical vein endothelial cells (HUVECs). Afterward, their fluorescence intensities were recorded by flow cytometry (*cf.* Figure 5a,b). Standard fluorescence measurements by using FACS cannot distinguish well between internalized NPs and NPs adhering to the outer cell membrane,[44] despite washing. Thus, the FACS data quantify the overall amount of cell-associated NPs. The data clearly show higher levels of cell-associated positively charged NPs for both cell types, at both 2 and 24 h of incubation (*cf.* Figure 5a,b). This is in accordance with data obtained using the microscopy analysis in this study for 3T3 fibroblasts and with literature data.[45] Furthermore, uptake levels of negatively charged NPs were similar for the two cell types, whereas positively charged NPs were associated much more with the NPC than with the HUVECs, demonstrating clear cell type-dependent uptake characteristics that are most pronounced for the positively charged NPs. The latter may reflect differences in the media composition used for the two cell types, where the positively charged NPs may form agglomerates in the serum-rich media used for the NPCs, whereas the NPs are more stable in the serum-low media used for the HUVECs. Alternatively, differences in the plasma membrane composition of the cell types and intrinsic differences in the cellular endocytosis levels and mechanisms of either cell type may further contribute to these differences.

In summary, cellular uptake experiments clearly demonstrate enhanced internalization of positively charged NPs compared to negatively charged ones. Presence of proteins in the media reduces NP uptake regardless of the charge of the NPs.

**Charge-Dependent Cytotoxicity of Nanoparticles.** Mechanistic explanations of enhanced toxicity by positively charged NPs are still under discussion.[46] For this reason, we directly compared NPs with negative and positive net charge that were otherwise essentially identical. HUVECs and C17.2 cells were exposed to various concentrations of the Au NPs to examine differences in cytotoxic effects of the NPs related to their surface charge. Multiple parameters typically associated with the cytotoxic profile of engineered NPs were tested, including cell viability, induction of oxidative stress, cell morphology and stem cell functionality.[6,47] The data show a clear concentration-dependent decrease in cell viability for the positively charged NPs, whereas no effects were observed for the negatively charged NPs up to a concentration of 50 nM (*cf.* Figure 5c). Interestingly, the observed decrease in cell viability for positively charged NPs correlated well with increased oxidative stress in both cell types (*cf.* Figure 5d), suggesting an important role of oxidative stress in the cytotoxic effects of the positively charged NPs, which is in line with available literature data.[48,49] To further evaluate possible effects of the NPs on cell homeostasis, alterations in the morphology of HUVECs cells at non-cytotoxic NP concentrations were assessed. The results show, that despite the absence of cytotoxic effects, both types of NPs display concentration-dependent decreases in cell spreading and effects on the actin cytoskeleton (*cf.* Figure 5e). Such effects of Au NPs on cellular cytoskeleton architecture have been described in a few reports.[50,51] We also evaluated the differentiation potential of C17.2 NPC cells upon exposure to Au NPs at non-cytotoxic concentrations. Figure 5f shows a clear diminution of cell differentiation for cells exposed to the positively charged Au NPs at 5 nM or above, in contrast to the negatively charged NPs, which did not induce any effects at concentrations up to at least 20 nM.

Upon internalization, NPs subsequently translocate to different cellular compartments until they reach their final destination.[52] Thus, cytotoxic effects also need to be seen in the context of the intracellular

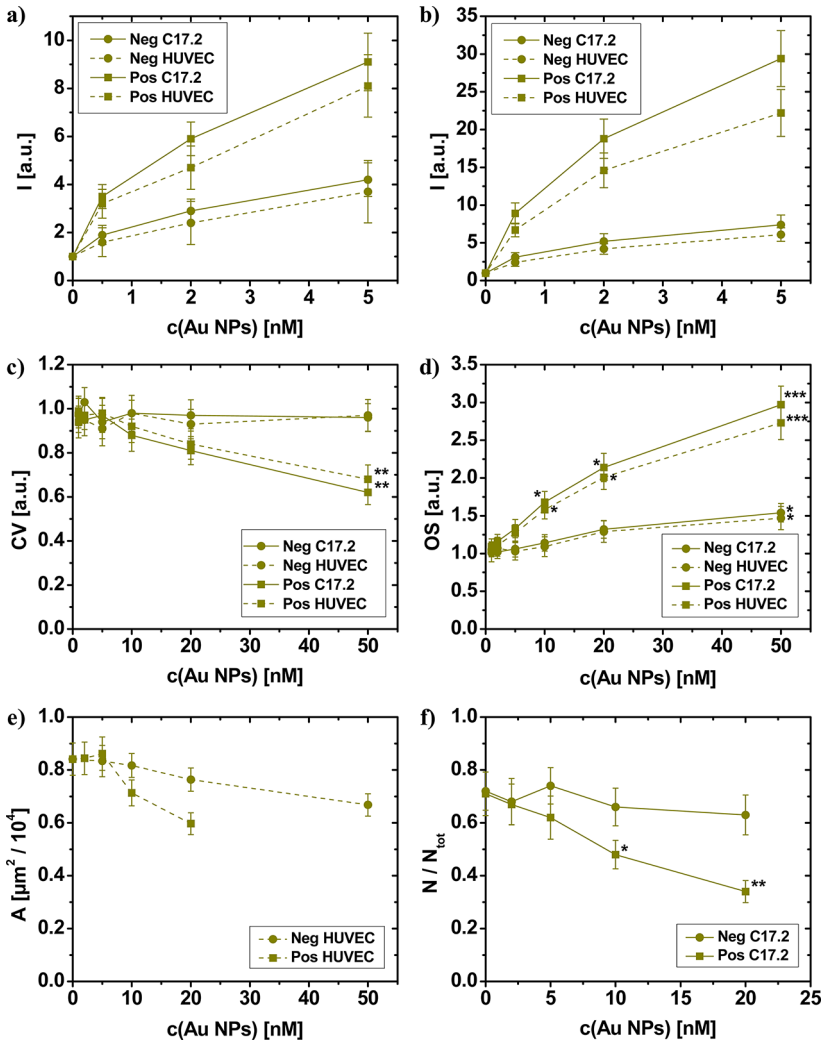


**Figure 5. Fluorescence-activated cell sorting (FACS) results (*I* = fluorescence intensity) for (a) 2 h and (b) 24 h of incubation in medium similar to medium #8 (*cf.* Supporting Information). Data are normalized to *I* at *c*(Au NPs) = 0 nM. (c) Cell viability (CV) for C17.2 neural progenitor cells and primary HUVEC cells as assessed by an Alamar blue assay after 24 h incubation. Data are expressed relative to untreated control cells as mean ± standard deviation (SD; *n* = 4). A value of 1.0 corresponds to 100%. (d) Levels of oxidative stress (OS) for C17.2 neural progenitor cells and primary HUVEC cells as assessed by $H_2$DCFDA after 24 h incubation. Data are expressed relative to untreated control cells as mean ± SD (*n* = 3). A value of 1.0 corresponds to 100%. (e) The average cell areas (*A*) of HUVEC cells after 24 h incubation. (f) Quantitative analysis of differentiation efficacy expressed as the number of TuJ-1 positive cells (*N*) over total cell population ($N_{tot}$) for C17.2 cells after 24 h of incubation. Data are expressed as mean ± SD for at least 500 cells per condition (*n* = 4). The degree of significance between treated samples and control samples are indicated when appropriate (**p* < 0.05; ***p* < 0.01; ****p* < 0.001). In a–f, solid lines correspond to C17.2 neural progenitor cells and dotted lines correspond to primary HUVEC cells. Squares correspond to positively charged NPs and circles to negatively charged NPs.**

location of the NPs. In particular, it is important to differentiate between the concentration of NPs that is externally applied and the concentration of the NPs within the cell. Our uptake data demonstrate that, at equivalent extracellular NP concentration, the concentration of internalized NPs is greater for positively than for negatively charged NPs. Although the precise nature of the cytotoxic effects observed in our study remains elusive, the data obtained here indicate that they are related to the intracellular NP level rather than to the concentration of NPs to which the cells were exposed, in agreement with earlier reports on various types of NPs.[23,53,54]

Taking together all our cytotoxicity data, the concentrations above which adverse effects are observable can be defined as 20 nM for the negatively charged NPs and 5 nM for the positively charged ones, indicating a clear effect of the NP surface charge on cytotoxicity, mainly driven by their higher cellular uptake.

## CONCLUSIONS

Our data indicate that positively charged NPs are incorporated faster than negatively charged NPs by several cell lines, while they also possess higher cytotoxic potential. Similar findings have been reported before, *i.e.*, there have been claims that higher cytotoxic potential of positively charged NPs is predominantly related with higher cellular uptake of these NPs. However, by using highly defined and well characterized

NPs, our study contributes further insights into the charge-dependent interaction of these NPs with cells. Our study points to the problem that several physicochemical parameters are entangled. Despite symmetric surface chemistry of our negatively and positively charged NPs, the negatively charged NPs used in this study had a lower colloidal stability than their positively charged counterparts. This may well affect cellular uptake, which is known to be size dependent. The key point of the present study is the use of NPs with good colloidal stability, thereby keeping the effective size (hydrodynamic diameter) constant and avoiding formation of large agglomerates, so that the effect of the net surface charge is decoupled from the effects NP size and agglomeration.

Parallel to the analysis of the colloidal stability and the formation of the protein corona, the uptake kinetics of the NPs by cells were recorded. Many studies report that uptake of NPs is mainly influenced by the protein corona. Protein adsorption relies on interaction with charged spots on the proteins.[25] If the charge on the NP is reverted, proteins may adsorb to the NPs such that the charge on the outside of the corona will be reverted. In our experiments, the qualitative formation of the protein corona (as determined from the amount of adsorbed HSA proteins upon exposure to HSA) was similar for negatively and positively charged NPs, though their uptake behavior by cells differed drastically. It has to be pointed out, however, that our FCS data are sensitive only to changes in the size of the adsorbed protein (HSA) corona, but do not give information about the internal structure of the proteins. In fact, with or without the presence of a protein corona, clear differences depending on the surface charge are visible. As differences in cellular uptake were also observed in media without proteins, we conclude that the sign of the charge (and eventually associated changes in colloidal stability) is also a direct parameter which determines quantitative uptake of NPs. Associated changes in the structure of the protein corona will play an additional role compared to the direct charge effect. There is also a clear correlation between uptake of NPs and their corresponding toxic effects on cells, which in both cases are higher for positively than for negatively charged NPs.

## MATERIALS AND METHODS

**NP Synthesis.** Colloidal Au NPs were synthesized in organic solvents according to standard procedures.[55] Transmission electron microscopy (TEM) analysis indicated an inorganic core diameter of $d_c$ = 4.6 ± 1.1 nm. To transfer the NPs into an aqueous solution, they were enshrouded by an amphiphilic polymer shell.[56] Negatively and positively charged co- and terpolymers of type poly((2-(methacryloyloxy)ethyl)phosphonic acid)$_x$-*stat*-poly(lauryl methacrylate)$_y$-*stat*-poly(propargyle methacrylate)$_z$ (PMAPHOS-*stat*-PLMA-*stat*-PgMA) and poly(*N*,*N*,*N*-trimethylamonium-2-ethyl methacrylate iodide)$_x$-*stat*-poly(lauryl methacrylate)$_y$-*stat*-poly(propargyle methacrylate)$_z$ (PTMAEMA-*stat*-PLMA-*stat*-PgMA) which contained charged monomers (phosphonate or trimethylammonium groups, respectively) and monomers with hydrophobic side chains ($-C_{12}H_{25}$) were synthesized similar to a previously described protocol,[16] *cf.* Figure 1 and Table 1. The ratios of charged ($x$) to hydrophobic ($y$) monomers and the molecular weights were $x$:$y$ = 40:60 ($z$ = 0) and $M_n$ = 9000 g/mol, and $x$:$y$ = 53:47 ($z$ = 0) and $M_n$ = 16 300 g/mol for the negatively and positively charged copolymers, respectively. Both polymers thus had comparable molecular weights and compositions. They were selected on the basis of a prior study in which optimal conditions for colloidal stability were determined.[16] For the terpolymers, an additional monomer with an alkyne residue (PgMA) was added. The ratios of charged ($x$), hydrophobic ($y$), and functional ($z$) units and the molecular weights were $x$:$y$:$z$ = 52:42:6 and $M_n$ = 9500 g/mol, and $x$:$y$:$z$ = 48:48:4 and $M_n$ = 17 800 g/mol for the negatively and positively charged terpolymers, respectively. Monomers were assembled statistically. The red azide-modified fluorophore perylene tetracarboxylic diimide (PDI-$N_3$) was attached to the monomers carrying the alkyne function *via* the azide group using click chemistry.[57] The quantitative conversion was verified by UV/vis and $^1$H NMR spectroscopy (see Supporting Information). The dye provided the fluorescence contrast employed for cellular uptake studies. Recent investigations using the same polymer-coating technique with a different fluorophore demonstrated that the hydrophobic fluorophores were located inside the polymer shell rather than pointing toward the solution.[58] Consequently, we expect that the fluorophore in the polymer shell has only minimal, if any, influence on the NP interaction with cells. Polymers were added to the hydrophobic Au NPs, the organic solvent (chloroform) was evaporated, and the NPs became water-soluble upon addition of alkaline sodium borate buffer (SBB, pH = 12) and 0.1 M NaCl solution (pH = 3.3, adjusted with HCl) for negatively and positively charged polymers, respectively, following standard procedures.[16,56] The NPs were extensively purified by size exclusion chromatography and/or gel electrophoresis (the latter worked only for negatively charged NPs), leading to pure NP suspensions.[16] The effective quantum yields ($\Phi_s$) of the negatively and positively charged NPs (with fluorophore in their polymer shell) in water were $\Phi_s(-) = 0.053 \pm 0.003$ and $\Phi_s(+) = 0.057 \pm 0.004$, respectively (see Supporting Information). These "effective" quantum yields (= number of emitted photons emitted by PDI per number of incident photons reaching the Au-PDI hybrid particle) are significantly smaller than the quantum yield of PDI in solution because a significant fraction of incident light is absorbed by the Au NPs and not by PDI. A detailed description and all raw data are given in the Supporting Information.

**Physicochemical Characterization.** Extinction spectra of negatively and positively charged NPs with and without fluorophore were measured in different media (#2 to #8). In each case, the pure medium served as a blank. After addition of NPs at a concentration of 5 nM, an extinction spectrum was taken at different time points within 1 h. The added volume of NP solution was 2 orders of magnitude lower compared to the present volume of medium to maintain the physical conditions of the medium. The maximum absorbance between 500 and 600 nm comprising the surface plasmon peak and the dye absorbance (in case a fluorophore was present) was plotted against the time after addition of the NP solution.

**Investigation of Protein Adsorption in Different Media.** FCS measurements were performed on a homemade confocal microscope with single-molecule sensitivity similar to those reported previously.[59,60] The setup is based on an inverted microscope frame (Axiovert 135 TV, Zeiss, Oberkochen, Germany) and equipped with a home-made acousto-optical beam splitter (AOBS). A 532-nm laser excitation (power 6 $\mu$W) was focused onto the sample by a water immersion objective

(UPLAPO 60x/1.2w, Olympus, Hamburg, Germany). The emitted light was collected by the same objective and focused onto a 50 $\mu$m-diameter pinhole, passed through a 532 nm notch filter and 50/50 beam splitter cube and was detected by two avalanche photo diodes (SPCM-AQR 14, Perkin-Elmer, Boston, MA). Cross-correlation functions from the two detector outputs were calculated by a digital correlator (ALV 5000/E, ALV, Langen, Germany). All measurements were performed at 23 °C. NP suspensions were diluted to 4 nM with PBS buffer; HSA was diluted to the desired concentrations with PBS (medium #2) at room temperature (23 °C) and mixed in equal volumes with the dilute NP solution. Samples were incubated for 10 min just prior to the measurements. The autocorrelation functions were fitted with a model function for free diffusion with a three-dimensional Gaussian volume to obtain diffusional correlation times,[61] which can be converted into diffusion coefficients. Rhodamine 6G was used as a reference sample (diffusion coefficient $D = 4.14 \pm 0.05$ cm$^2$/s)[62] to calculate the hydrodynamic radii of the Au NPs. Diffusion coefficients were converted into hydrodynamic radii by the Stokes−Einstein equation. The change in hydrodynamic radius by concentration dependent adsorption of proteins on surfaces was fitted with a simple binding model[24,42] using

$$r_h = r_h(0)\left(1 + \frac{V_{HSA}}{\frac{4}{3}\pi r_h(0)^3} N_{max} \frac{1}{1 + (K_d/c(HSA))^n}\right)^{1/3} \quad (1)$$

Here, $r_h$ and $r_h(0)$ are the hydrodynamic radii of the protein-coated and bare NPs, respectively, $V_{HSA}$ and $c$(HSA) represent the molecular volume and concentration of HSA, respectively. Protein binding to the Au NPs is governed by three parameters, the maximum number of proteins bound per NP, $N_{max}$, the `apparent' binding coefficient, $K_d$, and the Hill coefficient, $n$.[62]

**Charge-Dependent Uptake of Nanoparticles.** 3T3 cells were incubated with negatively and positively charged Au NPs (with PDI-$N_3$ in their polymer shell) in different media (#5, #7 and #8). The experiments were carried out in different culture media in micro-8-well plates at 5% $CO_2$ atmosphere and 37 °C. The samples were analyzed with an Axiovert 200 M widefield microscope (Zeiss, Germany) with attached incubator stage at different time points of incubation. The obtained images (dark field + red fluorescence of fluorophore in NP shell) were analyzed with ImageJ. The mean intensity of a number of regions of interest (ROIs) inside the cell body and cell membrane excluding the nucleus was determined for around 30 cells per specimen. In all experiments, the background intensity was subtracted, and data were corrected for intrinsic differences in the fluorescence emission of Au NPs (see Supporting Information).

**Charge-Dependent Cytotoxicity of Nanoparticles.** The cytotoxic effects of the nanoparticles was investigated on primary human umbilical vein endothelial cells (HUVECs) and murine neural progenitor cells (C17.2). Essentially, these experiments were performed in serum-containing media, similar to medium #8. Cell viability was measured in both cell types for a range of nanoparticles concentrations (1−50 nM) after 24 h by an Alamar Blue assay (Molecular Probes, Invitrogen, Merelbeke, Belgium) according to the manufacturer's protocol. For the same concentration range, cell viability was qualitatively examined by means of Calcein AM/Ethidium homodimer co-incubation as described previously.[63] Oxidative stress was evaluated by means of the 5-(and-6)-chloromethyl-2′,7′-dichlorodihydrofluorescein diacetate, acetyl ester (CM-$H_2$DCFDA; Molecular Probes, Invitrogen, Merelbeke, Belgium) assay as described previously.[8] The effects of the nanoparticles on HUVEC morphology and C17.2 cell functionality were assessed as described elsewhere.[6,53] A detailed description can also be found in the Supporting Information.

*Conflict of Interest:* The authors declare no competing financial interest.

*Acknowledgment.* S.J.H.S. is a postdoctoral fellow from FWO-Vlaanderen. Financial support from FWO-Vlaanderen (Krediet aan Navorsers to S.J.H.S.), the Centre for Nano- and Biophotonics (Ghent University), and the Deutsche Forschungsgemeinschaft (DFG, SPP1313 and CFN) are gratefully acknowledged.

*Supporting Information Available:* Full methodology and additional data are available free of charge *via* the Internet at http://pubs.acs.org.

## REFERENCES AND NOTES

1. Rivera_Gil, P.; Jimenez de Aberasturi, D.; Wulf, V.; Pelaz, B.; del Pino, P.; Zhao, Y.; de la Fuente, J.; Ruiz de Larramendi, I.; Rojo, T.; Liang, X.-J.; et al. The Challenge to Relate the Physicochemical Properties of Colloidal Nanoparticles to Their Cytotoxicity. *Acc. Chem. Res.* **2013**, *46*, 743–749.
2. Rivera_Gil, P.; Oberdorster, G.; Elder, A.; Puntes, V. F.; Parak, W. J. Correlating Physico-Chemical with Toxicological Properties of Nanoparticles: The Present and the Future. *ACS Nano* **2010**, *4*, 5527–5531.
3. Tanguay, R. L.; Harper, S. L.; Carriere, J. L.; Miller, J. M.; Hutchison, J. E.; Maddux, B. L. S. Systematic Evaluation of Nanomaterial Toxicity: Utility of Standardized Materials and Rapid Assays. *ACS Nano* **2011**, *5*, 4688–4697.
4. Asati, A.; Santra, S.; Kaittanis, C.; Perez, J. M. Surface-Charge-Dependent Cell Localization and Cytotoxicity of Cerium Oxide Nanoparticles. *ACS Nano* **2010**, *4*, 5321–5331.
5. Verma, A.; Stellacci, F. Effect of Surface Properties on Nanoparticle-Cell Interactions. *Small* **2010**, *6*, 12–21.
6. Soenen, S. J. H.; Himmelreich, U.; Nuytten, N.; De Cuyper, M. Cytotoxic Effects of Iron Oxide Nanoparticles and Implications for Safety in Cell Labelling. *Biomaterials* **2011**, *32*, 195–205.
7. Schweiger, C.; Hartmann, R.; Zhang, F.; Parak, W. J.; Kissel, T.; Rivera_Gil, P. Quantification of the Internalization Patterns of Superparamagnetic Iron Oxide Nanoparticles with Opposite Charge. *J. Nanobiotechnol.* **2012**, *10*, 28.
8. Soenen, S. J. H.; Demeester, J.; De Smedt, S. C.; Braeckmans, K. The Cytotoxic Effects of Polymer-Coated Quantum Dots and Restrictions for Live Cell Applications. *Biomaterials* **2012**, *33*, 4882–4888.
9. Ojea-Jiménez, I.; García-Fernández, L.; Lorenzo, J.; Puntes, V. F. Facile Preparation of Cationic Gold Nanoparticle-Bioconjugates for Cell Penetration and Nuclear Targeting. *ACS Nano* **2012**, *6*, 7692–7702.
10. Goodman, C. M.; McCusker, C. D.; Yilmaz, T.; Rotello, V. M. Toxicity of Gold Nanoparticles Functionalized with Cationic and Anionic Side Chains. *Bioconjugate Chem.* **2004**, *15*, 897–900.
11. Hirsch, V.; Kinnear, C.; Moniatte, M.; Rothen-Rutishauser, B.; Clift, M. J. D.; Fink, A. Surface Charge of Polymer Coated SPIONs Influences the Serum Protein Adsorption, Colloidal Stability and Subsequent Cell Interaction in Vitro. *Nanoscale* **2013**, 10.1039/C2NR33134A.
12. Tycko, B.; Maxfield, F. R. Rapid Acidification of Endocytic Vesicles Containing Alpha-2-Macroglobulin. *Cell* **1982**, *28*, 643–651.
13. Yu, W. W.; Chang, E.; Falkner, J. C.; Zhang, J. Y.; Al-Somali, A. M.; Sayes, C. M.; Johns, J.; Drezek, R.; Colvin, V. L. Forming Biocompatible and Nonaggregated Nanocrystals in Water Using Amphiphilic Polymers. *J. Am. Chem. Soc.* **2007**, *129*, 2871–2879.
14. Yu, W. W.; Chang, E.; Sayes, C. M.; Drezek, R.; Colvin, V. L. Aqueous Dispersion of Monodisperse Magnetic Iron Oxide Nanocrystals through Phase Transfer. *Nanotechnology* **2006**, *17*, 4483–4487.
15. Chanana, M.; Rivera_Gil, P.; Correa-Duarte, M. A.; Liz-Marzán, L. M.; Parak, W. J. Physicochemical Properties of Protein-Coated Gold Nanoparticles in Biological Fluids and Cells Before and After Proteolytic Digestion. *Angew. Chem., Int. Ed. Engl.* **2013**, DOI: 10.1002/anie.201208019.s.
16. Geidel, C.; Schmachtel, S.; Riedinger, A.; Pfeiffer, C.; Müllen, K.; Klapper, M.; Parak, W. J. A General Synthetic Approach for Obtaining Cationic and Anionic Inorganic Nanoparticles *via* Encapsulation in Amphiphilic Copolymers. *Small* **2011**, *7*, 2929–2934.
17. Brown, W.; Zhao, J. X. Adsorption of Sodium Dodecyl-Sulfate on Polystyrene Latex-Particles Using Dynamic

Light-scattering and Zeta-Potential Measurements. *Macromolecules* **1993**, *26*, 2711–2715.
18. Loeb, J. The Influence of Electrolytes on the Cataphoretic Charge of Colloidal Particles and the Stability of their Suspensions. I. Experiments with Collodion Particles. *J. Gen. Physiol.* **1922**, *5*, 109–126.
19. Puertas, A. M.; de las Nieves, F. J. Colloidal Stability of Polymer Colloids with Variable Surface Charge. *J. Colloid Interface Sci.* **1999**, *216*, 221–229.
20. Casals, E.; Pfaller, T.; Duschl, A.; Oostingh, G. J.; Puntes, V. F. Time Evolution of the Nanoparticle Protein Corona. *ACS Nano* **2010**, *4*, 3623–3632.
21. Cedervall, T.; Lynch, I.; Lindman, S.; Berggård, T.; Thulin, E.; Nilsson, H.; Dawson, K. A.; Linse, S. Understanding the Nanoparticle-Protein Corona Using Methods to Quantify Exchange Rates and Affinities of Proteins for Nanoparticles. *Proc. Natl. Acad. Sci. U.S.A.* **2007**, *104*, 2050–2055.
22. Lundqvist, M.; Stigler, J.; Elia, G.; Lynch, I.; Cedervall, T.; Dawson, K. A. Nanoparticle Size and Surface Properties Determine the Protein Corona with Possible Implications for Biological Impacts. *Proc. Natl. Acad. Sci. U.S.A.* **2008**, *105*, 14265–14270.
23. Maiorano, G.; Sabella, S.; Sorce, B.; Brunetti, V.; Malvindi, M. A.; Cingolani, R.; Pompa, P. P. Effects of Cell Culture Media on the Dynamic Formation of Protein-Nanoparticle Complexes and Influence on the Cellular Response. *ACS Nano* **2010**, *4*, 7481–7491.
24. Röcker, C.; Pötzl, M.; Zhang, F.; Parak, W. J.; Nienhaus, G. U. A Quantitative Fluorescence Study of Protein Monolayer Formation on Colloidal Nanoparticles. *Nat. Nanotechnol.* **2009**, *4*, 577–580.
25. Maffre, P.; Nienhaus, K.; Amin, F.; Parak, W. J.; Nienhaus, G. U. Characterization of Protein Adsorption onto FePt Nanoparticles Using Dual-Focus Fluorescence Correlation Spectroscopy. *Beilstein J. Nanotechnol.* **2011**, *2*, 374–383.
26. Tenzer, S.; Docter, D.; Rosfa, S.; Wlodarski, A.; Kuharev, J.; Rekik, A.; Knauer, S. K.; Bantz, C.; Nawroth, T.; Bier, C.; et al. Nanoparticle Size is a Critical Physicochemical Determinant of the Human Blood Plasma Corona: A Comprehensive Quantitative Proteomic Analysis. *ACS Nano* **2011**, *5*, 7155–67.
27. Monopoli, M. P.; Aberg, C.; Salvati, A.; Dawson, K. A. Biomolecular Coronas Provide the Biological Identity of Nanosized Materials. *Nat. Nanotechnol.* **2012**, *7*, 779–786.
28. Lesniak, A.; Campbell, A.; Monopoli, M. P.; Lynch, I.; Salvati, A.; Dawson, K. A. Serum Heat Inactivation Affects Protein Corona Composition and Nanoparticle Uptake. *Biomaterials* **2010**, *31*, 9511–9518.
29. Harford, C. G.; Hamlin, A.; Parker, E. Electron Microscopy of HeLa Cells after the Ingestion of Colloidal Gold. *J. Biophys. Biochem. Cytol.* **1957**, *3*, 749–756.
30. Muller-Borer, B. J.; Collins, M. C.; Gunst, P. R.; Cascio, W. E.; Kypson, A. P. Quantum Dot Labeling of Mesenchymal Stem Cells. *J. Nanobiotechnol.* **2007**, *5*, 1–9.
31. Derfus, A. M.; Chan, W. C. W.; Bhatia, S. N. Intracellular Delivery of Quantum Dots for Live Cell Labeling and Organelle Tracking. *Adv. Mater. (Weinheim, Ger.)* **2004**, *16*, 961–966.
32. Brandenberger, C.; Mühlfeld, C.; Ali, Z.; Lenz, A.-G.; Schmid, O.; Parak, W. J.; Gehr, P.; Rothen-Rutishauser, B. Quantitative Evaluation of Cellular Uptake and Trafficking of Plain and Polyethylene Glycol-Coated Gold Nanoparticles. *Small* **2010**, *6*, 1669–1678.
33. Jiang, X.; Röcker, C.; Hafner, M.; Nienhaus, G. U. Endo- and Exocytosis of Zwitterionic Quantum Dot Nanoparticles by Living Cells. *ACS Nano* **2010**, *4*, 6787–6797.
34. Harush-Frenkel, O.; Rozentur, E.; Benita, S.; Altschuler, Y. Surface Charge of Nanoparticles Determines their Endocytic and Transcytotic Pathway in Polarized MDCK Cells. *Biomacromolecules* **2008**, *9*, 435–443.
35. Jung, T.; Kamm, W.; Breitenbach, A.; Kaiserling, E.; Xiao, J. X.; Kissel, T. Biodegradable Nanoparticles for Oral Delivery of Peptides: Is there a Role for Polymers to Affect Mucosal Uptake? *Eur. J. Pharm. Biopharm.* **2000**, *50*, 147–160.
36. Rabinovich-Guilatt, L.; Couvreur, P.; Lambert, G.; Dubernet, C. Cationic Vectors in Ocular Drug Delivery. *J. Drug Targeting* **2004**, *12*, 623–633.
37. Bartneck, M.; Keul, H. A.; Wambach, M.; Bornemann, J.; Gbureck, U.; Chatain, N.; Neuss, S.; Tacke, F.; Groll, J.; Zwadlo-Klarwasser, G. Effects of Nanoparticle Surface Coupled Peptides, Functional Endgroups, and Charge on Intracellular Distribution and Functionality of Human Primary Reticuloendothelial Cells. *Nanomedicine (New York, NY, U.S.)* **2012**, *8*, 1282–1292.
38. Bhattacharjee, S.; Ershov, D.; van der Gucht, J.; Alink, G. M.; Rietjens, I. M. C. M.; Zuilhof, H.; Marcelis, A. T. M. Surface Charge-Specific Cytotoxicity and Cellular Uptake of Tri-Block Copolymer Nanoparticles. *Nanotoxicology* **2013**, *7*, 71–84.
39. Jiang, X.; Musyanovych, A.; Röcker, C.; Landfester, K.; Mailander, V.; Nienhaus, G. U. Specific Effects of Surface Carboxyl Groups on Anionic Polystyrene Particles in their Interactions with Mesenchymal Stem Cells. *Nanoscale* **2011**, *3*, 2028–2035.
40. Jiang, X.; Dausend, J.; Hafner, M.; Musyanovych, A.; Röcker, C.; Landfester, K.; Mailander, V.; Nienhaus, G. U. Specific Effects of Surface Amines on Polystyrene Nanoparticles in their Interactions with Mesenchymal Stem Cells. *Biomacromolecules* **2010**, *11*, 748–753.
41. Muñoz Javier, A.; Kreft, O.; Piera Alberola, A.; Kirchner, C.; Zebli, B.; Susha, A. S.; Horn, E.; Kempter, S.; Skirtach, A. G.; Rogach, A. L.; et al. Combined Atomic Force Microscopy and Optical Microscopy Measurements as a Method to Investigate Particle Uptake by Cells. *Small* **2006**, *2*, 394–400.
42. Jiang, X.; Weise, S.; Hafner, M.; Röcker, C.; Zhang, F.; Parak, W. J.; Nienhaus, G. U. Quantitative Analysis of the Protein Corona on FePt Nanoparticles Formed by Transferrin Binding. *J. R. Soc., Interface* **2010**, *7*, S5–S13.
43. Lesniak, A.; Fenaroli, F.; Monopoli, M. R.; Aberg, C.; Dawson, K. A.; Salvati, A. Effects of the Presence or Absence of a Protein Corona on Silica Nanoparticle Uptake and Impact on Cells. *ACS Nano* **2012**, *6*, 5845–5857.
44. Semmling, M.; Kreft, O.; Muñoz Javier, A.; Sukhorukov, G. B.; Käs, J.; Parak, W. J. A Novel Flow-Cytometry-based Assay for Cellular Uptake Studies of Polyelectrolyte Microcapsules. *Small* **2008**, *4*, 1763–1768.
45. Soenen, S. J. H.; Brisson, A. R.; Jonckheere, E.; Nuytten, N.; Tan, S.; Himmelreich, U.; De Cuyper, M. The Labeling of Cationic Iron Oxide Nanoparticle-Resistant Hepatocellular Carcinoma Cells Using Targeted Magnetoliposomes. *Biomaterials* **2011**, *32*, 1748–1758.
46. Bexiga, M. G.; Varela, J. A.; Wang, F. J.; Fenaroli, F.; Salvati, A.; Lynch, I.; Simpson, J. C.; Dawson, K. A. Cationic Nanoparticles Induce Caspase 3-, 7- and 9-Mediated Cytotoxicity in a Human Astrocytoma Cell Line. *Nanotoxicology* **2011**, *5*, 557–567.
47. Soenen, S. J. H.; Rivera_Gil, P.; Montenegro, J. M.; Parak, W. J.; De Smedt, S. C.; Braeckmans, K. Cellular Toxicity of Inorganic Nanoparticles: Common Aspects and Guidelines for Improved Nanotoxicity Evaluation. *Nano Today* **2011**, *6*, 446–465.
48. Nel, A. E.; Madler, L.; Velegol, D.; Xia, T.; Hoek, E. M. V.; Somasundaran, P.; Klaessig, F.; Castranova, V.; Thompson, M. Understanding Biophysicochemical Interactions at the Nano-Bio Interface. *Nat. Mater.* **2009**, *8*, 543–557.
49. Pan, Y.; Leifert, A.; Ruau, D.; Neuss, S.; Bornemann, J.; Schmid, G.; Brandau, W.; Simon, U.; Jahnen-Dechent, W. Gold Nanoparticles of Diameter 1.4 nm Trigger Necrosis by Oxidative Stress and Mitochondrial Damage. *Small* **2009**, *5*, 2067–2076.
50. Mironava, T.; Hadjiargyrou, M.; Simon, M.; Jurukovski, V.; Rafailovich, M. H. Gold Nanoparticles Cellular Toxicity and Recovery: Effect of Size, Concentration and Exposure Time. *Nanotoxicology* **2010**, *4*, 120–137.
51. Pernodet, N.; Fang, X. H.; Sun, Y.; Bakhtina, A.; Ramakrishnan, A.; Sokolov, J.; Ulman, A.; Rafailovich, M. Adverse Effects of Citrate/Gold Nanoparticles on Human Dermal Fibroblasts. *Small* **2006**, *2*, 766–773.
52. Shapero, K.; Fenaroli, F.; Lynch, I.; Cottell, D. C.; Salvati, A.; Dawson, K. A. Time and Space Resolved Uptake Study of Silica Nanoparticles by Human Cells. *Mol. BioSyst.* **2011**, *7*, 371–378.

53. Soenen, S. J. H.; Nuytten, N.; De Meyer, S. F.; De Smedt, S. C.; De Cuyper, M. High Intracellular Iron Oxide Nanoparticle Concentrations Affect Cellular Cytoskeleton and Focal Adhesion Kinase-Mediated Signaling. *Small* **2010**, *6*, 832–842.
54. Soenen, S. J. H.; De Meyer, S. F.; Dresselaers, T.; Velde, G. V.; Pareyn, I. M.; Braeckmans, K.; De Cuyper, M.; Himmelreich, U.; Vanhoorelbeke, K. I. MRI Assessment of Blood Outgrowth Endothelial Cell Homing Using Cationic Magnetoliposomes. *Biomaterials* **2011**, *32*, 4140–4150.
55. Brust, M.; Walker, M.; Bethell, D.; Schiffrin, D. J.; Whyman, R. Synthesis of Thiol-Derivatized Gold Nanoparticles in a 2-Phase Liquid-Liquid System. *J. Chem. Soc., Chem. Commun.* **1994**, 801–802.
56. Lin, C.-A. J.; Sperling, R. A.; Li, J. K.; Yang, T.-Y.; Li, P.-Y.; Zanella, M.; Chang, W. H.; Parak, W. J. Design of an Amphiphilic Polymer for Nanoparticle Coating and Functionalization. *Small* **2008**, *4*, 334–341.
57. Kolb, H. C.; Finn, M. G.; Sharpless, K. B. Click Chemistry: Diverse Chemical Function from a Few Good Reactions. *Angew. Chem., Int. Ed.* **2001**, *40*, 2004–2021.
58. Amin, F.; Yushchenko, D. A.; Montenegro, J. M.; Parak, W. J. Integration of Organic Fluorophores in the Surface of Polymer-Coated Colloidal Nanoparticles for Sensing the Local Polarity of the Environment. *ChemPhysChem* **2012**, *13*, 1030–1035.
59. Schenk, A.; Ivanchenko, S.; Röcker, C.; Wiedenmann, J. R.; Nienhaus, G. U. Photodynamics of Red Fluorescent Proteins Studied by Fluorescence Correlation Spectroscopy. *Biophys. J.* **2004**, *86*, 384–394.
60. Kobitski, A. Y.; Nierth, A.; Helm, M.; Jaschke, A.; Nienhaus, G. U. $Mg^{2+}$-Dependent Folding of a Diels-Alderase Ribozyme Probed by Single-Molecule FRET Analysis. *Nucleic Acids Res.* **2007**, *35*, 2047–2059.
61. Elson, E. L.; Magde, D. Fluorescence Correlation Spectroscopy. 1. Conceptual Basis and Theory. *Biopolymers* **1974**, *13*, 1–27.
62. Müller, C. B.; Loman, A.; Pacheco, V.; Koberling, F.; Willbold, D.; Richtering, W.; Enderlein, J. Precise Measurement of Diffusion by Multi-Color Dual-Focus Fluorescence Correlation Spectroscopy. *Europhys. Lett.* **2008**, *83*, 46001.
63. Soenen, S. J. H.; De Cuyper, M. How to Assess Cytotoxicity of (Iron Oxide-Based) Nanoparticles. A Technical Note Using Cationic Magnetoliposomes. *Contrast Media Mol. Imaging* **2011**, *6*, 153–164.

**Inventors from the Philipps Universität Marburg:**

- Wolfgang J. Parak (42%) Neustadt 2, 35037 Marburg, Germany
- Dominik Hühn (20%) Lilienstraße 3, 35043 Marburg, Germany
- Jonas Hühn (7%) Lilienstraße 3, 35043 Marburg, Germany
- Dorleta Jimenez de Aberasturi Arranz (7%) Santa Lucia 7-3C, 01003 Vitoria-Gasteiz, Spain
- Jose Maria Montenegro Martos (7%) C/ Paseo de los Tilos 69, 4°A, 29006 Malaga, Spain
- Carolina Carrillo Carrion (7%) C/ Escultor Ramon Barba 42, 14012 Cordoba, Spain
- Ulrich Koert (5%) Hopfengarten 12, 35043 Marburg, Germany
- Julia Schütte (5%) Hofstatt 11, 35037 Marburg, Germany

**Title of invention:**

Use of nanoparticles with variable surface charge / polarity and spacer length for tuning the working point of analyte-sensitive fluorophores which are attached *via* molecular spacers to the surface of the nanoparticles.

**State of the art:**

Small analyte molecules, such as in particular ions can be detected with analyte-sensitive fluorophores (F). In general, upon binding of the analyte to the analyte-sensitive fluorophore the fluorescence emission of the fluorophore changes. In ratiometric measurements a second (reference) fluorophore (R) can be added, of which the emission intensity does not depend on presence of the analyte, see Figure 1. Thus, the ratio of the emission of the analyte-sensitive fluorophore and the emission of the reference fluorophore depends on the concentration of the analyte. Some examples are shown in Figures 2-5.

Linkage of the fluorophores to the surface of colloidal nanoparticles (NPs) changes the response of the fluorophores to the presence of analyte molecules [1-3]. This effect will be discussed in the following for ion-sensitive fluorophores in which ions are the analyte molecules to be detected. The NPs are coated with an organic coating which bears charged moieties (C), see Figure 1. These charged moieties stabilize the NPs in aqueous solution by electrostatic repulsion [4]. However, they also attract counter ions from solution, an effect which is known as Debye-Hückel screening. In case the NP surface is charged negatively, positively charged ions from the surrounding solution will be locally attracted, while negatively charged ones will be locally repelled. In the case of positively charged NPs the effect is reverse: the will be local attraction and repulsion of negatively and positively charged ions, respectively. In this way the charged NP surface creates a local nanoenvironment close to the NP surface in which

the local concentrations of ions are different from bulk concentrations [5]. Screening is in general non-specific to the chemical nature of the ions and in first order depends only on their charge.

The ion-sensitive fluorophores (F) can be linked to the NP surface *via* molecular spacers (S) of variable length (the "shortest" length hereby corresponds to no spacer), see Figure 1. Thus, in case the ion-sensitive fluorophores are linked directly to the NP surface (none or very short molecular spacers used for attachment), they will sense the local ion concentration close to the NP surface. On the other hand, in case the ion-sensitive fluorophores are far away from the NP surface (long molecular spacers used for their attachment), they will sense bulk ion concentrations [1-3]. In other words, attachment of ion-sensitive fluorophores to the surface of charged NPs changes their response to the presence of the ions to be detected, whereby the response depends on the distance of the fluorophores to the NP surface. The reference fluorophores (R) can be directly linked to the NP surface or also *via* spacers, whereby there distance to the NP surface is of no importance. In Figures 2-5 four examples are described.

Besides for ion-sensitive fluorophores, the influence of the NP surface to the local environment has also been demonstrated for polarity-sensitive fluorophores [6].

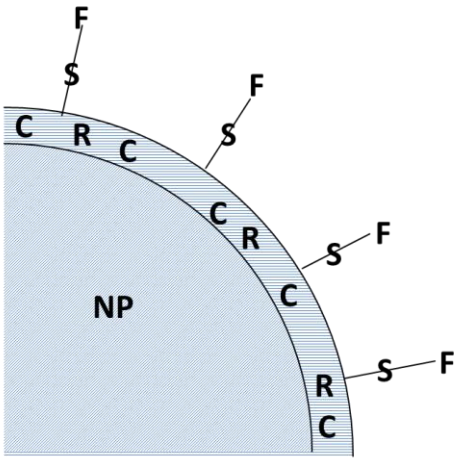


Figure 1: A nanoparticle (NP) is surrounded by a (in general semi-permeable) organic coating which comprises charged groups (C) and reference fluorophores (R). Analyte-sensitive fluorophores (F) are linked *via* molecular spacers (S) to the surface of the NP.

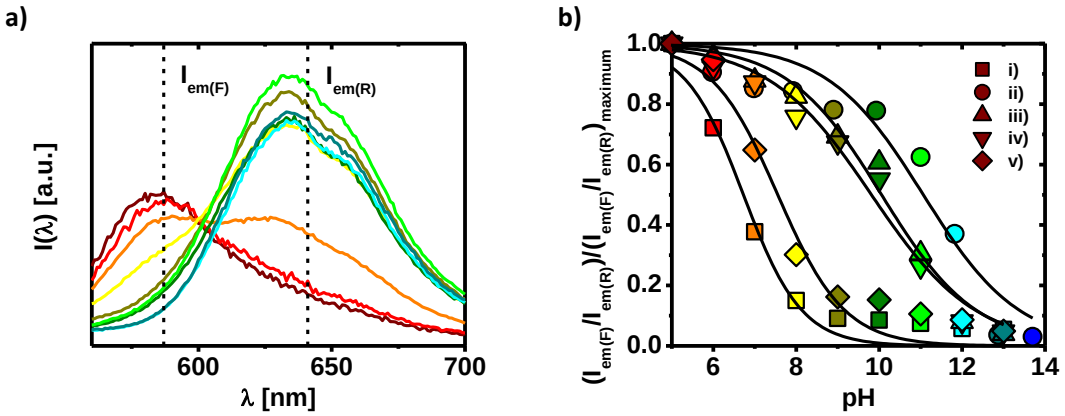


Figure 2. a) Fluorescence emission spectrum I(λ) of then free $H^+$-sensitive fluorophore seminaphtharhodafluor (SNARF) conjugated to 2 kDa polyethyleneglycol (PEG) in dependence of the bulk $H^+$ concentration $c(H^+)$ [M] (given as pH = -log($c(H^+)$/M)), upon excitation at $\lambda_{ex}$ = 540 nm. SNARF is a ratiometric fluorophore (F) which (in a simplified way of description) integrates the reference fluorophore (R) in the ion-sensitive fluorophore (F). Two emission peaks can be distinguished: $I_{em(F)}$ at $\lambda_{em(F)}$ = 587 nm and $I_{em(R)}$ at $\lambda_{em(R)}$ = 641 nm. b) The response to bulk pH is given as ratio $I_{em(F)}/I_{em(R)}$. The normalized response $(I_{em(F)}/I_{em(R)})/(I_{em(F)}/I_{em(R)})_{maximum}$ is shown for the following geometries: SNARF not bound to NPs (i), and SNARF linked to the NP surface with PEG spacers (S) to the surface of negatively charged NPs with spacers of molecular weight 0.1 kDa (ii), 2 kDa (iii), 6 kDa (iv), 10 kDa (v). These data are adopted from Zhang *et al.* [1].

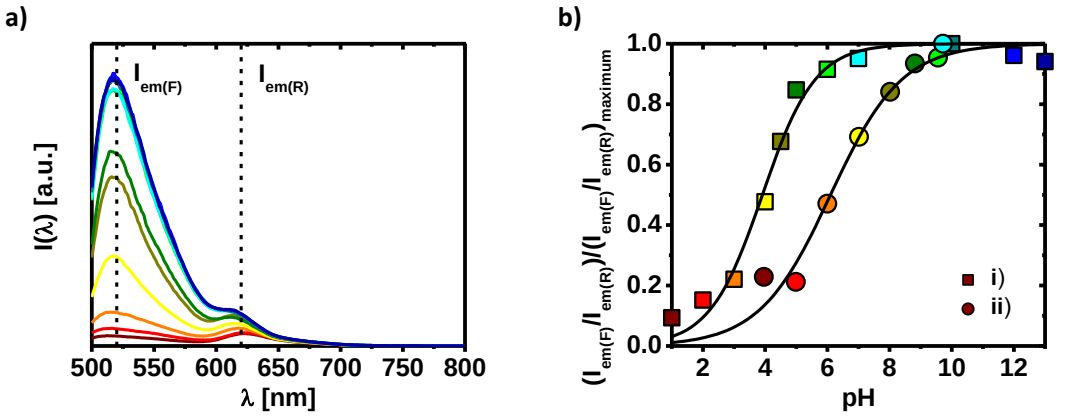


Figure 3. a) Fluorescence emission spectrum I(λ) of the $H^+$-sensitive fluorophore Oregon Green (F) mixed together with the reference fluorophore (R) ATTO-590 in dependence of the bulk $H^+$ concentration $c(H^+)$ [M] (given as pH = -log($c(H^+)$/M)), upon excitation at $\lambda_{ex}$ = 488 nm. Two emission peaks originating from Oregon Green and ATTO-590 can be distinguished with $I_{em(F)}$ at $\lambda_{em(F)}$ = 520 nm and $I_{em(R)}$ at $\lambda_{em(R)}$ = 620 nm, respectively. b) The response to bulk pH is given as ratio $I_{em(F)}/I_{em(R)}$. The normalized response $(I_{em(F)}/I_{em(R)})/(I_{em(F)}/I_{em(R)})_{maximum}$ is shown for the following geometries: Mixture of Oregon Green and ATTO-590 not bound to NPs (i), and Oregon

Green and ATTO-590 linked without spacers (S) directly to the surface of negatively charged NPs (ii). These data are adopted from Zhang *et al.* [3].

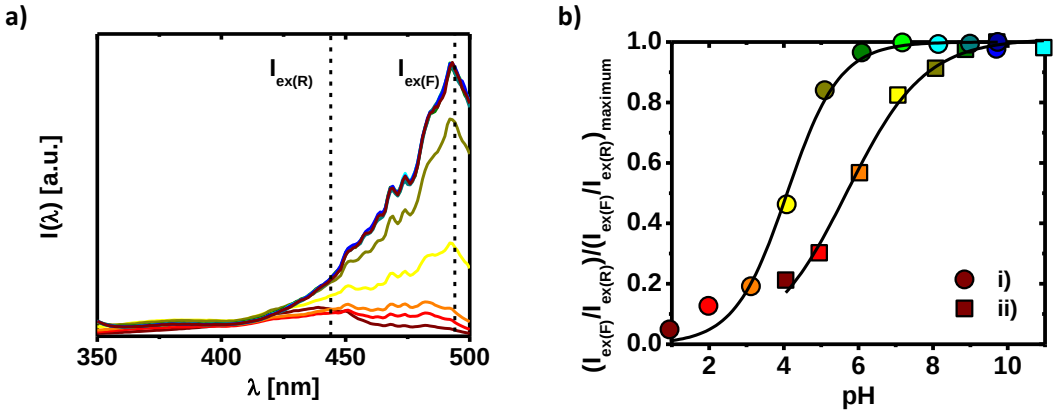


Figure 4. a) Fluorescence excitation spectrum I(λ) of the $H^+$-sensitive fluorophore Oregon Green (F) in dependence of the bulk $H^+$ concentration c($H^+$) [M] (as given as pH = -log(c($H^+$)/M)), upon recording the emission at $\lambda_{em}$ = 518 nm. This demonstrates that sensing can be performed not only *via* emission but also *via* excitation spectra. Oregon green is a ratiometric fluorophore which (in a simplified way of description) integrates the reference fluorophore (R) in the ion-sensitive fluorophore (F). Two excitation peaks can be distinguished with $I_{ex(F)}$ at $\lambda_{ex(F)}$ = 494 nm and $I_{ex(R)}$ at $\lambda_{ex(R)}$ = 444 nm, respectively. b) The response to bulk pH is given as ratio $I_{ex(F)}$ /$I_{ex(R)}$. The normalized response $(I_{ex(F)}/I_{ex(R)})/(I_{ex(F)}/I_{ex(R)})_{maximum}$ is shown for the following geometries: Oregon Green not bound to NPs (i), and Oregon Green linked without spacer (S) directly to the surface of negatively charged NPs (ii). These data are adopted from Zhang *et al.* [3].

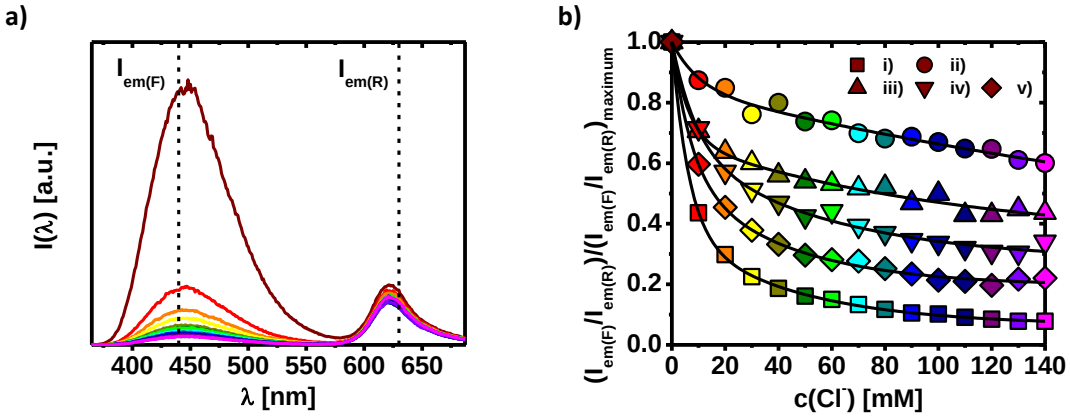


Figure 5. a) Fluorescence emission spectrum I(λ) of the $Cl^-$-sensitive fluorophore 2-[2-(6-methoxyquinolinium chloride)ethoxy]-ethanamine hydrochloride (amino MQAE) (F) mixed together with the reference fluorophore (R) cresyl violet in dependence of the bulk $Cl^-$ concentration c($Cl^-$), upon excitation at $\lambda_{ex}$ = 350 nm. Two emission peaks originating from amino MQAE and cresyl violet can be distinguished with $I_{em(F)}$ at

$\lambda_{em(F)}$ = 440 nm and $I_{em(R)}$ at $\lambda_{em(R)}$ = 630 nm, respectively. b) The response to bulk $Cl^-$ is given as ratio $I_{em(F)}$ /$I_{em(R)}$. The normalized response $(I_{em(F)}/I_{em(R)})/(I_{em(F)}/I_{em(R)})_{maximum}$ is shown for the following geometries: Mixture of amino MQAE and cresyl violet not bound to NPs (i), amino MQAE linked without spacer (S) directly to the surface of negatively charged NPs (ii) and amino MQAE linked with polyethyleneglycol spacers (S) to the surface of negatively charged NPs with spacers of molecular weight 3 kDa (iii), 5 kDa (iv), 10 kDa (v), together with cresyl violet linked without spacers. These data are adopted from Riedinger *et al.* [2].

Linkage of the fluorophores (F, R) to the NPs can be achieved by using different strategies. For example, fluorophores can be embedded in a porous nanoscale matrix, attached covalently to the NP surface, or integrated in an amphiphilic polymer coating [1, 2, 7-20]. For the data shown in Figures 2-5 the polymer coating approach was used. An example for this linking chemistry for embedding fluorophores in the amphiphilic polymer is depicted in Figure 6. Most important, multiple fluorophores can be attached per NP, which increases their local concentration and, concomitantly, the detection efficiency. Linkage of multiple fluorophores in general is also required for ratiometric detection schemes. In general the surface chemistry of the NPs after their modification with fluorophores is mainly governed by the NPs themselves and is only minimally—if at all—affected by the presence of the few fluorophores.

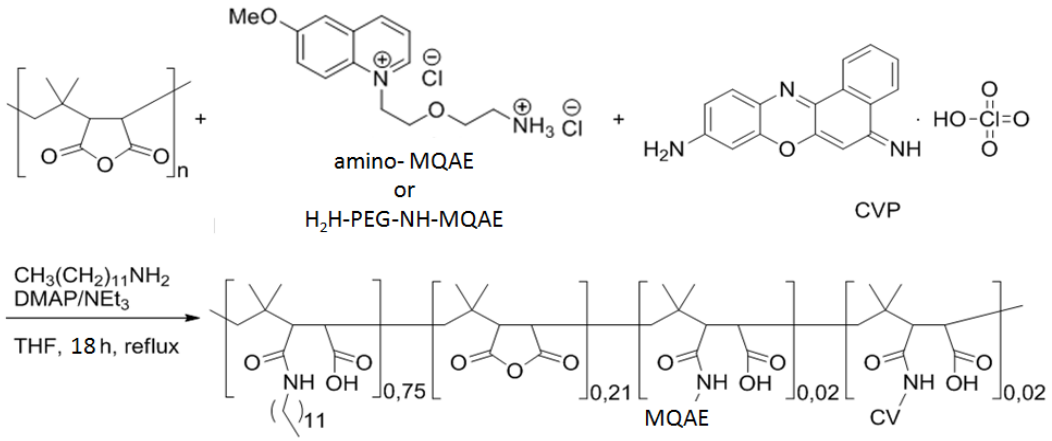


Figure 6: Reaction scheme for the functionalization of a negatively charged amphiphilic polymer with amino MQAE or amino-PEG-modified amino MQAE [2]. 1 eq maleic acid anhydride rings (monomers of poly(isobutylene-*alt*-maleic anhydride) PMA, $M_W$ = 6 kDa) are stirred with 0.75 eq dodecylamine, 0.02 eq amino MQAE, 0.02 eq cresyl violet perchlorate (CVP), 0.1 eq 4-(dimethylamino)pyridine (DMAP) and 0.12 eq triethylamine (TEA) for 18 h at 80 °C under reflux in tetrahydrofuran (THF). After the conjugation, in which the amino groups of MQAE and CVP form amide bonds with the carboxylic groups of the polymer, the solvent is evaporated and the dry film dissolved in chloroform.

**Summary of the invention:**

In the state-of-the art it was described how the presence of a NP surface close to analyte-sensitive fluorophores can change their response to the analyte. So far, this fact has been considered as a drawback or a potential source of error in the field of sensors based on NPs, which had to be corrected properly in the calibration curve. The idea of our invention now is to exploit this effect to improve the analytical performance of analyte-sensitive fluorophores. The idea of our invention is to control the working range / the sensitivity of analyte-sensitive fluorophores by linking them to the surface of NPs controlling the following parameters: The polarity of the NP surface (sign of charge, charge density, hydrophilic/hydrophobic behavior), and the distance of the fluorophore (F) to the NP surface as mediated by molecular spacer molecules (S). In this way, the charged NP would act not as a simple passive carrier, but as an active element in the sensing system. In the case of ion-sensitive fluorophores sensitivity can be tuned by the sign of the surface charge of the NPs. In case the NP is oppositely charged in general the local concentration of the ion to be detected will be increased at the NP surface and sensitivity in detection is reduced, *i. e.* the NP surface allows for (nonspecific) preconcentration of oppositely charged ions. In the opposite direction, in case the working range should be extended, linkage of the ion-sensitive fluorophore to a NP surface with opposite charge will lead to local (nonspecific) depletion of the ions to be detected and thus to intentionally reduced sensitivity. The effect can be further modulated by the charge density of the NP surface (the bigger the charge density, the higher the effect) and the distance of the fluorophore to the NP surface (the closer the fluorophore, the higher the effect). It is important to point out that so far it is not possible to quantitatively predict the tuning or the working point of ion-sensitive fluorophores by attaching them to the surface of NPs, thus that the details rely on experimental fine-tuning. Besides local preconcentration / depletion of ions in the context of ion-sensitive fluorophores the same effect can also be used for local preconcentration / depletion of polar molecules, by changing the hydrophilicity/hydrophobicity of the NP surface. The less polar the NP surface, the higher the preconcentration effect of apolar analytes will be (note that solvents need to be chosen appropriately in order to maintain colloidal stability of the NPs).

A wide range of nanoparticles (NPs) can be used as carrier and preconcentration element of the system, such as Au NPs, Ag NPs, magnetic NPs, quantum dots, etc., and thus the approach is highly general. The charge of the NPs (density and sign) will be determined by the type and number of ligands used for their functionalization and solubilization. The ligand molecules on the NP surface can be introduced directly in the synthetic process or later by a ligand exchange method or a polymer coating process (which is the case in our examples). Depending on the molecule used as ligand, positive or negative charge is provided to the NPs. The polymer coating as used in our examples is highly suitable because it leads to a high colloidal stability of the NPs. The distance between the organic fluorophore and the underlying NP can be easily varied attaching the fluorophore directly linked to the NP surface or by using spacer molecules (S) such as polyethylene glycol (PEG) of varying molecular weight (*i. e.* length). The distance

between the fluorophore and the NP surface can for example be estimated by fluorescence correlation spectroscopy (FCS) measurements and semiempirical calculations [2].

**Example 1: Extending the working range of a $Cl^-$-sensitive fluorophore by attachment to positively charged NPs.**

Several $Cl^-$-sensitive fluorophore – Au NP hybrids have been synthesized by attaching the fluorophore to Au NPs with different charge and at varying distances from the NP surface. Then, the effect of the charge of the NP and the distance of the fluorophore to the NP surface concerning preconcentration and detection of $Cl^-$ ions has been evaluated. As $Cl^-$-sensitive amino MQAE was used (see also Figures 5, 6), which was fist linked to positively charged Au NPs. The Au NPs were coated with an amphiphilic poly(N,N,N-trimethylammonium-2-ethyl methacrylate iodide)$_x$-*stat*-poly(lauryl methacrylate)$_y$ (PTMAEMA-stat-PLMA) based polymer leading to a positive charge at the NP surface [21]. On the one hand, the dye was attached using the cross linker molecule sulfosuccinimidyl-4-(*N*-maleimidomethyl)cyclohexane-1-carboxylate (sulfo-SMCC) through the sulfhydryl groups of the polymer (Figure 7). In this case the fluorophore is really close to the NP surface. The length of the SMCC molecule can be assumed to be approximately 0.83 nm which results in an average distance of the dye to the NP surface of 0.5·0.83 nm ≈ 0.4 nm. On the other hand, and with the aim to investigate the effect of the fluorophore-NP distance, the $Cl^-$-sensitive dye was then attached to the NP by means of a spacer molecule of approximately the double length (1.76 nm), namely succinimidyl-([*N*-maleimidopropionamido]-2ethyleneglycol) ester (SM(PEG)$_2$) (Figure 8).

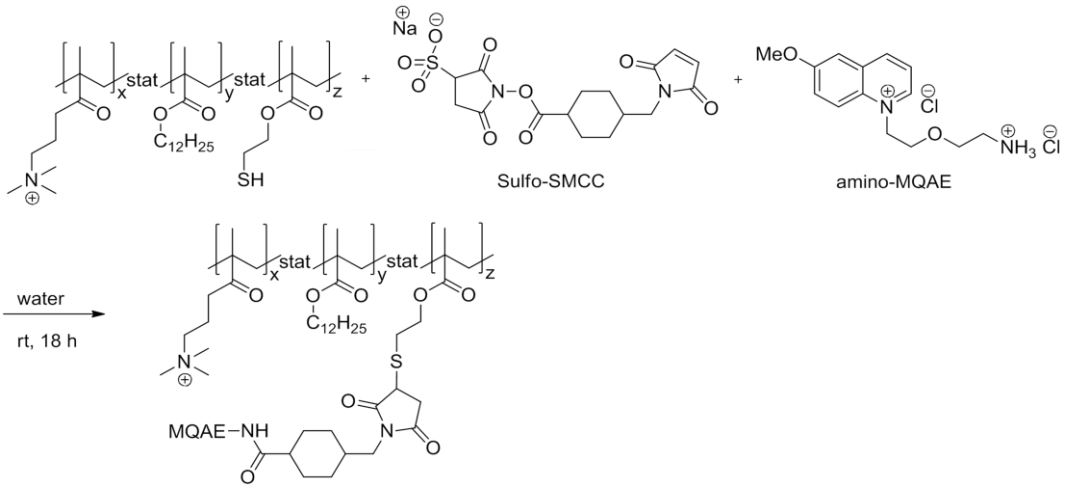


Figure 7: Reaction scheme for the functionalization of a positively charged amphiphilic polymer with MQAE using the cross linker molecule sulfo-SMCC. 1 eq SH groups are stirred with 10 eq sulfo-SMCC and 100 eq amino MQAE for 18 h at room temperature (RT) in water. After the conjugation, in which the maleimide group reacts with the SH group of the polymer and the *N*-hydroxysuccinimide (NHS) residue is released under an

amide bond formation with the amino function of the dye, the polymer is purified from unreacted cross linker and dye molecules *via* centrifugation. After transfer of the polymer to chloroform it is readily usable for the coating of Au NPs.

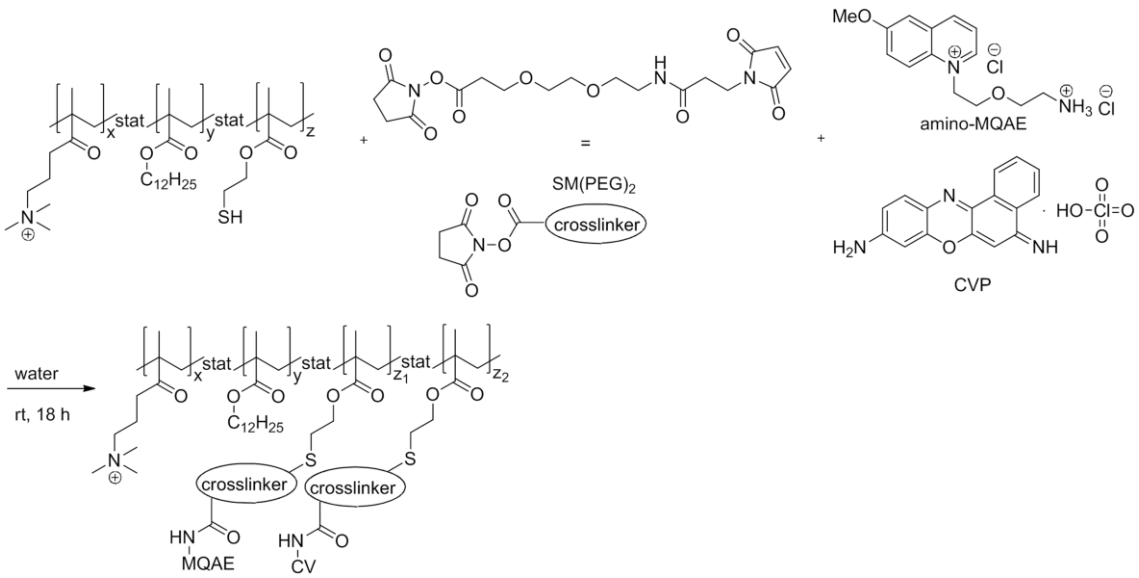


Figure 8: Reaction scheme for the functionalization of a positively charged amphiphilic polymer with MQAE using the cross linker molecule $SM(PEG)_2$. 1 eq SH groups are stirred with 10 eq $SM(PEG)_2$, 90 eq amino MQAE and 10 eq CVP for 18 h at RT in phosphate buffered saline (PBS) / ethanol (1:2). CVP serves as intrinsic fluorescent normalization probe. The remaining procedure is the same as compared to the conjugate with sulfo-SMCC (Figure 7).

The response of both fluorophore-NP hybrids for increasing $Cl^-$-concentrations was studied through the changes of their fluorescence emission. The comparison of both responses (Figure 9) showed clearly that the first hybrid (Figure 7, with short spacer molecule) is much more sensitive to low $Cl^-$ concentrations as a higher fluorescence decrease was observed for the same $Cl^-$ bulk concentration. This fact and the finding, that no saturation is reached in the relevant bulk $Cl^-$ concentration region, leads to the conclusion that the present $Cl^-$ ions accumulate around the surface and that the ion concentration decreases rapidly with increasing distance to the surface. This fact can be explained because the positive charge of the NP attracts the $Cl^-$ anions, and thus, preconcentrates them close to their surface. The NP acts here not only as a carrier for the dye but also as a preconcentrator unit to increase the amount of $Cl^-$ ions around the responsive dye (in the case of the first hybrid, Figure 7). In contrast in the second hybrid (Figure 8), which has the dye far away from the NP surface, significantly lower local $Cl^-$ concentration must be present around the responsive dye.

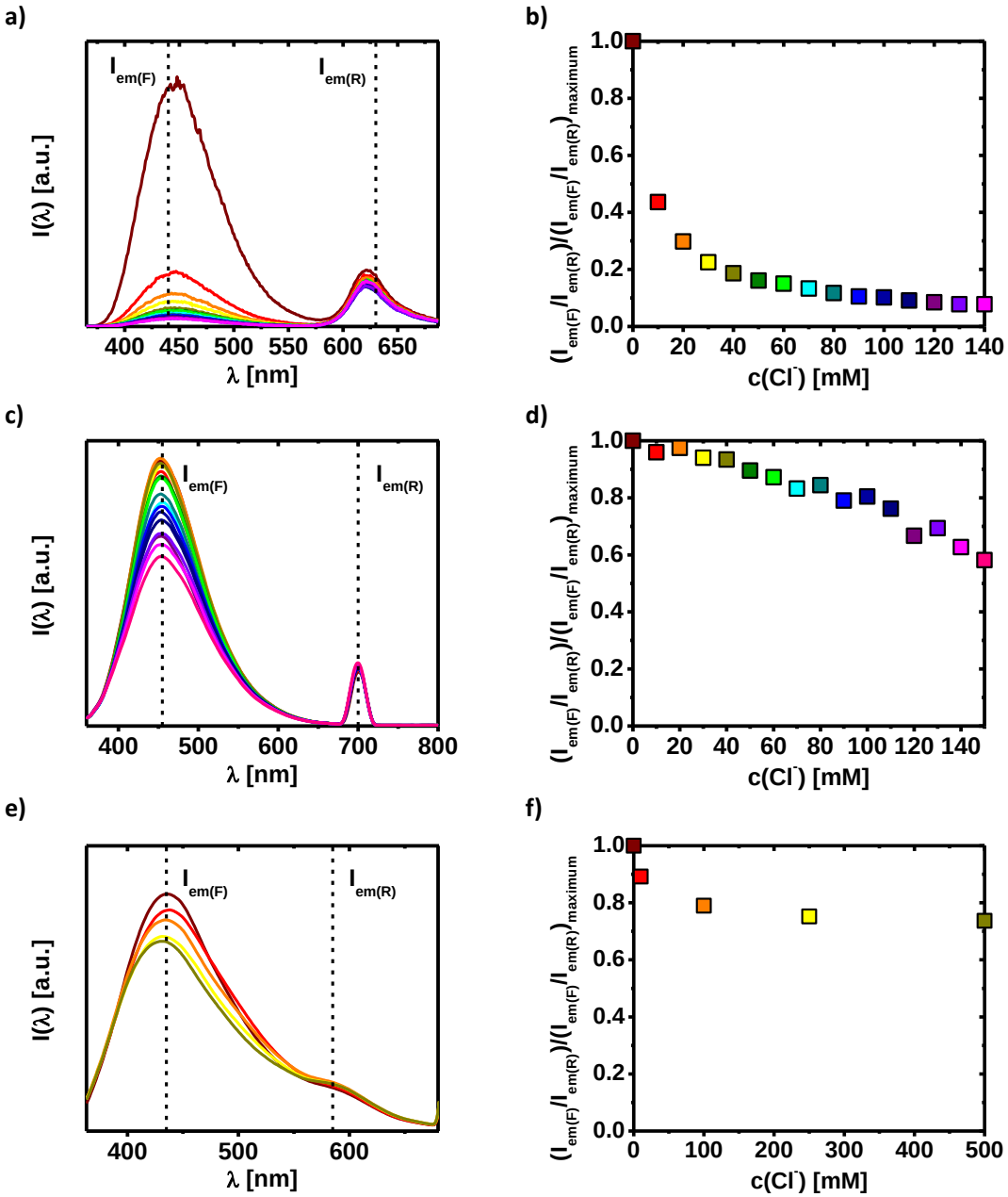


Figure 9: a) Fluorescence emission spectrum I(λ) of the $Cl^-$-sensitive fluorophore amino MQAE (F) mixed together with the reference fluorophore (R) cresyl violet in dependence of the bulk $Cl^-$ concentration c($Cl^-$), upon excitation at $\lambda_{ex}$ = 350 nm. Two emission peaks originating from amino MQAE and cresyl violet can be distinguished with $I_{em(F)}$ at $\lambda_{em(F)}$ = 440 nm and $I_{em(R)}$ at $\lambda_{em(R)}$ = 630 nm, respectively. b) The response to bulk $Cl^-$ is given as ratio $I_{em(F)}$ /$I_{em(R)}$. The normalized response $(I_{em(F)}/I_{em(R)})/(I_{em(F)}/I_{em(R)})_{maximum}$ is shown for a mixture of free amino MQAE and cresyl violet, which are not bound to NPs. c) Fluorescence intensity I(λ) of positively charged Au NPs functionalized with amino MQAE *via* SMCC suspended in water for various $Cl^-$ concentrations. $\lambda_{exc}$ = 350 nm, c(Au NPs) = 0.1 µM. The emission peak of amino MQAE appears at $\lambda_{em(F)}$ = 455 nm (15 nm red shifted compared to the free dye). The $2\cdot\lambda_{exc}$ scattering peak at $\lambda_{sc(R)}$ = "$\lambda_{em(R)}$" = 700 nm served for normalization. d) The response to bulk $Cl^-$ is given as ratio $I_{em(F)}$ /$I_{em(R)}$. The normalized response

$(I_{em(F)}/I_{em(R)})/(I_{em(F)}/I_{em(R)})_{maximum}$ is shown. An intensity quenching by a factor of approximately 1.7 was observed. The sensitive region extends over the whole set of evaluated $Cl^-$ concentrations. e) Fluorescence intensity I(λ) of positively charged Au NPs functionalized with amino MQAE and cresyl violet *via* $SM(PEG)_2$ suspended in water for various $Cl^-$ concentrations. $\lambda_{exc}$ = 350 nm, c(Au NPs) = 0.1 μM. The emission peak of amino MQAE appears at $\lambda_{em(F)}$ = 435 nm (5 nm blue shifted compared to the free dye) and the emission peak of cresyl violet appears as shoulder at $\lambda_{em(R)}$ = 585 nm. Although the emission of cresyl violet is partly overlapping with the emission of amino MQAE it serves as a suitable control for normalization. f) The response to bulk $Cl^-$ is given as ratio $I_{em(F)}$ /$I_{em(R)}$. The normalized response $(I_{em(F)}/I_{em(R)})/(I_{em(F)}/I_{em(R)})_{maximum}$ is shown. An intensity quenching by a factor of approximately 1.3 was observed. While one would have expected a steeper response of the $Cl^-$-sensitive fluorophore upon attachment to the positively charged NPs the experimental data demonstrate that this is not the case. However, Figure 9 clearly demonstrates that upon conjugation to the surface of positively charged NPs the working range of the $Cl^-$-sensitive fluorophore is extended. While the free fluorophore is most sensitive (biggest slope in the response curve) to changes in the $Cl^-$ concentrations between *ca.* 0 - 40 mM, the most sensitive range of operation for the $Cl^-$-sensitive fluorophore attached to the NPs is for $Cl^-$ concentrations. between 40 and 150 mM. Thus, while the effect of attaching the the $Cl^-$-sensitive fluorophore to the surface of positively charged NPs could not be quantitatively predicted, is still clearly allows for shifting the working point, *i.e.* the concentration range of highest sensitivity.

**Example 2: Increasing the sensitivity of a $Zn^{2+}$-sensitive fluorophore by attachment to negatively charged NPs.**

In this example a $Zn^{2+}$-sensitive fluorophore, named 4-aminomethyl-N-(6-methoxy-quinolin-8-yl)-benzenesulfonamide (AMQB), has been attached to negatively charged Au NPs in order to study the influence of a charged NP surface on the preconcentration of divalent ions. The Au NPs were coated with an amphiphilic PMA based polymer which has carboxylic groups to provide a negative charge to the NP surface [19, 22]. The primary amino group of the AMQB dye was used for the effective attachment to the carboxylic groups of the PMA polymer *via* amide bond formation (Figure 10). The response of the synthesized fluorophore-NP hybrid for increasing $Zn^{2+}$ ion concentrations was studied through the changes of its fluorescence emission. In this case, an increase of the fluorescence of the hybrid was observed after binding the ions. The sensing response of the hybrid was compared with the behavior of the free dye (Figure 11). As can be seen a plateau is reached for much smaller concentrations in case of the fluorophore-NP hybrid, what goes hand in hand with the assumption that the $Zn^{2+}$ ions are attracted by the NP surface gaining a much higher local concentration at the surface compared to the bulk. Hence a state of saturation is reached for smaller bulk concentrations. This example proves that when the $Zn^{2+}$-sensitive dye is placed close to

the negatively charged NP surface, the sensitivity of the system increases significantly due to the preconcentration effect of the negatively charged NP on the sensed cations.

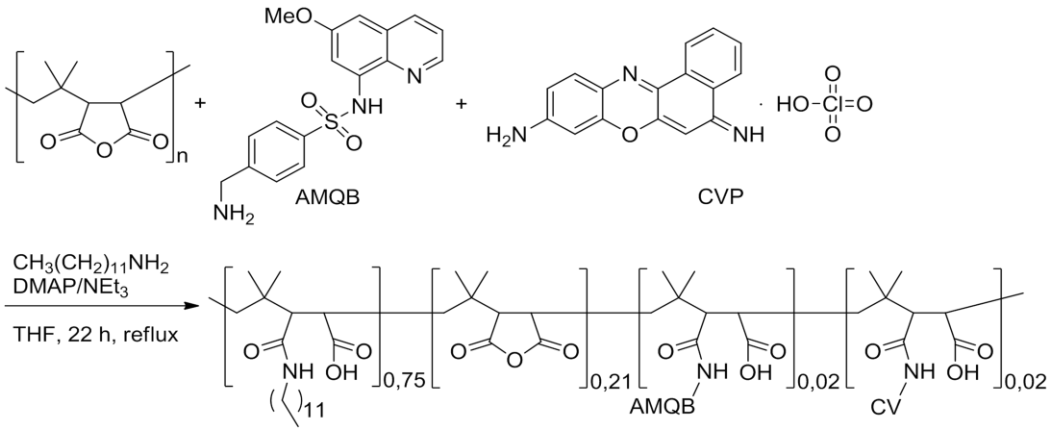


Figure 10: Reaction scheme for the functionalization of a negatively charged amphiphilic polymer with AMQB. 1 eq maleic acid anhydride rings (monomers of PMA, MW = 6 kDa) are stirred with 0.75 eq dodecylamine, 0.02 eq AMQB, 0.02 eq CVP, 0.1 eq 4-(dimethylamino)pyridine (DMAP) and 0.12 eq triethylamine (TEA) for 22 h at 80 °C under reflux in tetrahydrofuran (THF). After the conjugation, in which the amino groups of AMQB and CV form amide bonds with the carboxylic groups of the polymer, the solvent is evaporated and the dry film dissolved in chloroform. The polymer is used for coating without further purification.

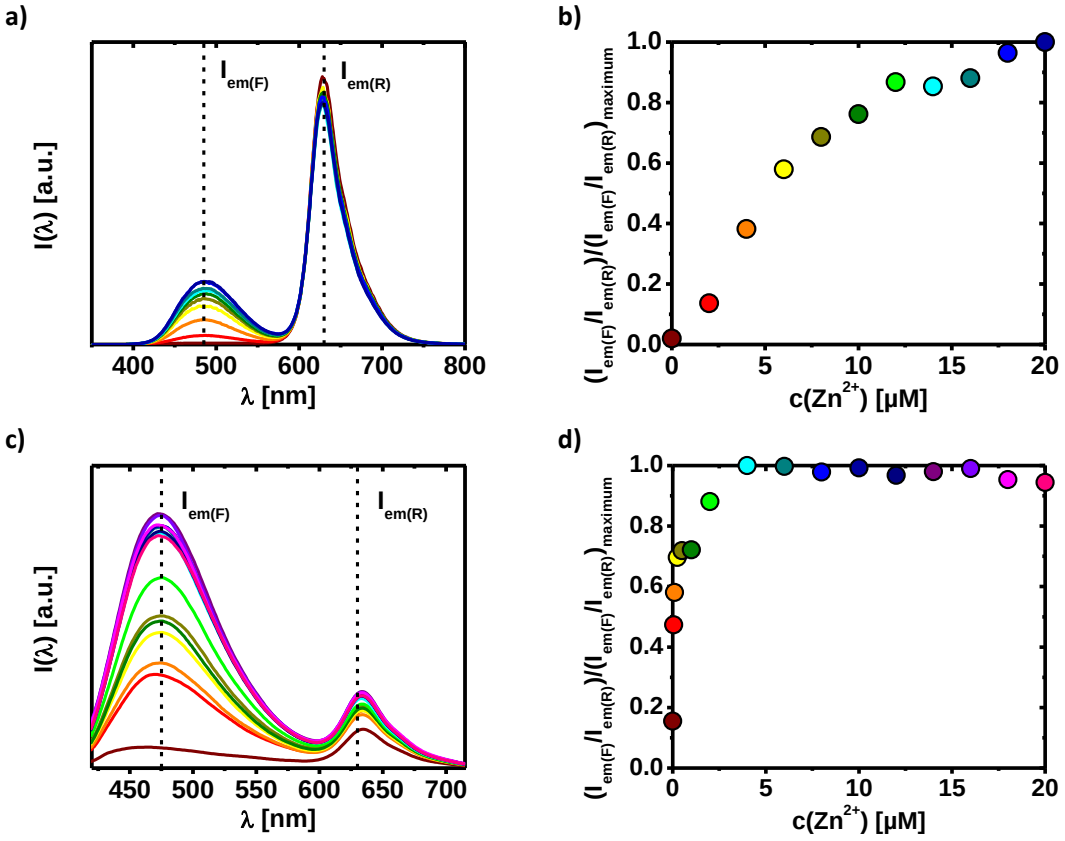

Figure 11: a) Fluorescence emission spectrum I(λ) of the $Zn^{2+}$-sensitive fluorophore AMQB (F) mixed together with the reference fluorophore (R) cresyl violet in water/ethanol (1:1) in dependence of the bulk $Zn^{2+}$ concentration c($Zn^{2+}$), upon excitation at $\lambda_{ex}$ = 340 nm. Two emission peaks originating from AMQB and cresyl violet can be distinguished with $I_{em(F)}$ at $\lambda_{em(F)}$ = 485 nm and $I_{em(R)}$ at $\lambda_{em(R)}$ = 630 nm, respectively. b) The response to bulk $Zn^{2+}$ is given as ratio $I_{em(F)}$ /$I_{em(R)}$. The normalized response $(I_{em(F)}/I_{em(R)})/(I_{em(F)}/I_{em(R)})_{maximum}$ is shown for a mixture of amino AMQB and cresyl violet not bound to NPs. An amplification of the intensity by a factor of ≥ 50 times is observed. The sensitive region extends over the whole set of evaluated $Zn^{2+}$ concentrations. c) Fluorescence intensity I(λ) of negatively charged Au NPs functionalized with AMQB and cresyl violet suspended in water for various $Zn^{2+}$ concentrations. $\lambda_{exc}$ = 365 nm, c(Au NPs) = 0.175 µM. The emission peak of AMQB appears at $\lambda_{em(F)}$ = 475 nm (15 nm blue shifted compared to the free dye) and the emission peak of CVP appears at $\lambda_{em(R)}$ = 630 nm. Although the emission of CVP is partly overlapping with the emission of AMQB it serves as a suitable control for normalization. d) The response to bulk $Cl^-$ is given as ratio $I_{em(F)}$ /$I_{em(R)}$. The normalized response $(I_{em(F)}/I_{em(R)})/(I_{em(F)}/I_{em(R)})_{maximum}$ is shown. An amplification of the intensity by approximately 6.5 times is observed. The sensitive region extends over 0 µM to 5 µM.

## Claims

By attaching analyte-sensitive fluorophores (F) to the surface of NPs, by varying the charge (C) of the NP surface and by varying the distance between the fluorophore and the NP surface *via* molecular spacers (S) the working point (*i.e*. the concentration range of the analyte at which the fluorophore responds with the highest changes in optical output signal) can be experimentally tuned.

## References


1. Zhang, F., et al., *Ion and pH Sensing with Colloidal Nanoparticles: Influence of Surface Charge on Sensing and Colloidal Properties.* ChemPhysChem, 2010. **11**: p. 730-735.
2. Riedinger, A., et al., *Ratiometric Optical Sensing of Chloride Ions with Organic Fluorophore - Gold Nanoparticle Hybrids: A Systematic Study of Distance Dependency and the Influence of Surface Charge.* Small, 2010. **6**(22): p. 2590-2597.
3. Zhang, F., et al., *Polymer-Coated Nanoparticles: A Universal Tool for Biolabelling Experiments.* SMALL, 2011. **7**: p. 3113-3127.
4. Pellegrino, T., et al., *On the Development of Colloidal Nanoparticles towards Multifunctional Structures and their Possible Use for Biological Applications.* Small, 2005. **1**(1): p. 48-63.
5. Rivera Gil, P., et al., *The Challenge to Relate the Physicochemical Properties of Colloidal Nanoparticles to Their Cytotoxicity.* Accounts of Chemical Research, 2013. **46**(3): p. 743-749.
6. Amin, F., et al., *Integration of Organic Fluorophores in the Surface of Polymer-Coated Colloidal Nanoparticles for Sensing the Local Polarity of the Environment.* ChemPhysChem, 2012. **13**(4): p. 1030-1035.

7. Lee, Y.E.K., R. Smith, and R. Kopelman, *Nanoparticle PEBBLE Sensors in Live Cells and In Vivo.* Annual Review Of Analytical Chemistry, 2009. **2**: p. 57-76.
8. Brasuel, M., et al., *Production, Characteristics and Applications of Fluorescent PEBBLE Nanosensors: Potassium, Oxygen, Calcium and pH Imaging Inside Live Cells.* Sensors And Materials, 2002. **14**(6): p. 309-338.
9. Snee, P.T., et al., *A Ratiometric CdSe/ZnS Nanocrystal pH Sensor.* Journal Of The American Chemical Society, 2006. **128**(41): p. 13320-13321.
10. Dulkeith, E., et al., *Fluorescence Quenching of Dye Molecules Near Gold Nanoparticles: Radiative and Nonradiative Effects.* Physical Review Letters, 2002. **89**(20): p. 203002-1 - 202002-4.
11. Dulkeith, E., et al., *Gold Nanoparticles Quench Fluorescence by Phase Induced Radiative Rate Suppression.* Nanoletters, 2005. **5**(4): p. 585-589.
12. Fu, Y. and J.R. Lakowicz, *Modification of Single Molecule Fluorescence Near Metallic Nanostructures.* Laser & Photonics Reviews, 2009. **3**(1-2): p. 221-232.
13. Bae, S.H., et al., *Single-Layered Films of Diblock Copolymer Micelles Containing Quantum Dots and Fluorescent Dyes and Their Fluorescence Resonance Energy Transfer.* Chemistry Of Materials, 2008. **20**(13): p. 4185-4187.
14. Ren, T., et al., *A Simple and Versatile Route to Stable Quantum Dot-Dye Hybrids in Nonaqueous and Aqueous Solutions.* Journal Of The American Chemical Society, 2008. **130**(51): p. 17242-17243.
15. Suzuki, M., et al., *Quantum Dot FRET Biosensors that Respond to pH, to Proteolytic or Nucleolytic Cleavage, to DNA Synthesis, or to a Multiplexing Combination.* J. Am. Chem. Soc., 2008. **130**(17): p. 5720-5725.
16. Dubach, J.M., D.I. Harjes, and H.A. Clark, *Ion-Selective Nano-Optodes Incorporating Quantum Dots.* J. Am. Chem. Soc., 2007. **129**(27): p. 8418-8419.
17. Yakovlev, A.V., et al., *Wrapping Nanocrystals with an Amphiphilic Polymer Preloaded with Fixed Amounts of Fluorophore Generates FRET-Based Nanoprobes with a Controlled Donor/Acceptor Ratio.* Langmuir, 2009. **25**(5): p. 3232-3239.
18. Debye, P. and E. Hückel, *Zur Theorie der Elektrolyte.* Physikalische Zeitschrift, 1923. **24**(9): p. 185 - 206.
19. Lin, C.-A.J., et al., *Design of an Amphiphilic Polymer for Nanoparticle Coating and Functionalization.* Small, 2008. **4**(3): p. 334-341.
20. Fernández-Argüelles, M.T., et al., *Synthesis and Characterization of Polymer-Coated Quantum Dots with Integrated Acceptor Dyes as FRET-based Nanoprobes.* Nano Lett., 2007. **7**(9): p. 2613-2617.
21. Hühn, D., et al., *Polymer-Coated Nanoparticles Interacting with Proteins and Cells: Focusing on the Sign of the Net Charge.* ACS Nano, 2013. **7**(4): p. 3253-3263.
22. Pellegrino, T., et al., *Hydrophobic Nanocrystals Coated with an Amphiphilic Polymer Shell: A General Route to Water Soluble Nanocrystals.* Nano Lett., 2004. **4**(4): p. 703-707.

# Long-decaying quantum dot-europium complex conjugates as luminescent probes for time-resolved fluoroassays

Piotr J. Cywiński[1,§,*], Tommy Hammann[1,§], Dominik Hühn[2], Wolfgang J. Parak[2], Hans-Gerd Löhmannsröben[1]

[1]*Department of Physical Chemistry, Institute of Chemistry, University of Potsdam, Karl-Liebknecht-Str. 24-25, 14476 Potsdam-Golm, Germany*

[2]*Fachbereich Physik, Philipps-Universität Marburg, Renthof 7, 35032 Marburg, Germany*

[§] *Present address:*
*NanoPolyPhotonics, Fraunhofer Institute for Applied Polymer Research, Geiselbergstr. 69, 14476 Potsdam-Golm Germany*

* Corresponding author:
Dr. Piotr Cywinski
Fraunhofer Institute for Applied Polymer Research (IAP)
NanoPolyPhotonics
Geiselbergstr. 69
14476 Potsdam-Golm, Germany
Phone: +49 331 568-3332
Fax: +49 331 568-3000
e-mail: piotr.cywinski@iap.fraunhofer.de

**Abstract:**

Novel long-decaying nanobioconjugates have been synthesized using cadmium selenide quantum dots (QDs), europium complexes (EuC), and biotin. In those conjugates long time emission is provided by the europium complexes, which due to close proximity to the QDs, transfer efficiently energy to the QDs via Förster Resonance Energy Transfer (FRET). In result, the conjugates have an emission spectrum characteristic for QDs combined with the long decay time characteristic for europium complexes. The nanobioconjugate synthesis strategy and photophysical properties are described as well as its performance in a time-resolved streptavidin-biotin fluoroassay. In order to prepare the QD-EuC-biotin conjugates, first, an amphiphilic polymer has been functionalized with the EuC and biotin. Then, the polymer has been brought onto the surface of QDs (either QD655 or QD705) to provide functionality and to make the QDs water dispersible. Due to a very short distance between EuC and QD (estimated to be less than 4 nm), an efficient FRET can be observed. Additionally, the functionality of the QD-EuC-biotin conjugates has been demonstrated in a fluoroassay yielding good signal discrimination, both from auto-fluorescence and directly excited QDs. Those newly synthesized QD-EuC-biotin conjugates expand the class of highly sensitive analytical tools for bioanalytical methods such as time-resolved fluoroimmunoassays (TR-FIA) or luminescent imaging (LI).

## 1. Introduction

Quantum dots (QDs) are fluorescent semiconductor nanocrystals that, due to the quantum confinement effect and their macromoleular size, combine unique photophysical features, such as broad, strong absorption, and size-dependent, efficient fluorescence.[1] The mobility in liquid phases, high surface-to-volume ratio, and effective methods established for their bioconjugation make QDs promising objects for bioanalytics and fluoroimmunoassays in particular.[2] Noticeably, QDs have a reduced tendency for fluorescence self-quenching and photobleaching, which are common drawbacks observed for organic dyes or fluorescent proteins.[3] This improved resistance against photodegradation effects also enables high sensitivity and usability in high-throughput molecular diagnostics.[4] Over the last two decades QDs have attracted considerable attention as universal luminescent nanoobjects for numerous fields including medicine[5], pharmacy[6], or chemical sensing.[7] In recent years, various QDs have been used in biological and biomedical applications, such as multiplexed systems for DNA[8], biomarker sensing[9, 10], luminescent immunoassays[11], optical coding[12, 13, 14], protein concentration determination[15], drug tracking[16], single molecule tracking[17], photodynamic therapy[18], and intracellular imaging[19, 20]. Continuously, new various QD-based nanosystems are appearing and new application fields are growing very dynamically.

In recent years, numerous systems have been presented, in which QDs are combined with organic fluorescent moieties to achieve additional properties beyond those provided solely by QDs. In this selection, a wide variety of systems can be found including a combination of nanorods and dyes[21], pyrene-functionalized nanoparticles to detect nitroaromatic compounds such as nitroanilines and nitrobenzenes[22], CdSe QDs functionalized with a naphthalimide dye to yield unconventional QD quenching, graphene QDs combined with europium ions to recognize phosphates[23], quantum dot-carbon nanotube conjugates for photoacoustic and fluorescence detection of circulating cells with flow cytometry *in-vivo*[24], doxorubicin-QD conjugates for photocontrolled drug delivery[25], and QD-europium ion conjugates to detect nucleoside triphosphates. A QD-Lucigenin conjugate sensor has been developed to sense chloride anions in aqueous environment with sensitivity down to around 300 nM[26]. Recently an interesting example of fluorescent QD-based conjugates has been presented, in which specific assembly allowed for a cascade FRET from a conjugated polymer to a QD and then to an organic dye.[27] Very recently, CdTe quantum dots functionalized with a naphthyridine dye were developed to detect guanosine nucleotides in aqueous environment. Due to specific and selective naphthyridine-nucleotide interaction

combined with the optical properties of the QDs, those conjugates showed improved sensitivity in comparison to naphthyridine or polystyrene nanoparticle-based sensors[28] and were able to detect cyclic 3'5' guanosine monophosphate (cGMP) down to 70 ng/mL.[29]

FRET is a non-radiative energy transfer from an emitting moiety (donor) to another energy-receiving moiety (acceptor). In fundamental considerations, FRET is a dipole-dipole interaction and it requires both (1) permanent donor-acceptor spatial positioning and (2) a spectral overlap between donor emission and acceptor absorption. In a standard time-resolved FRET (TR-FRET) assay, a donor is usually a long-living entity, typically a $Eu^{3+}$ or $Tb^{3+}$ complex, while an acceptor can be an organic fluorescent dye or a QD. The lanthanide complexes have many advantages for their application in fluoroimmunoassays including large Stokes' shift or well-defined and narrow emission peaks. However, their emission is limited to peaks typical for forbidden f-f transitions.[30, 31] Under certain circumstances, this constrained emission can be an unwanted limitation. In this view, the long-decaying QD-EuC-biotin conjugates bypass the gap between QD and lanthanides making the occurrence of a long-decaying and efficient emission possible, also at wavelengths between the emission lines typical for lanthanides. Apart from medical applications, such QD-based conjugates can find their application in display technologies, where long-living emissions at freely-selected and well-defined wavelengths are highly desirable properties.

In this contribution, we present a novel QD-based conjugate architecture combining an emission spectrum typical for a QD and a decay time typical for a europium complex. The preparation strategy, photophysical evaluation and the performance in biotin-streptavidin fluoroassays are also described. Our study shows that in the chosen architecture, the energy transfer can be very efficient with significantly limited direct excitation of QDs. The QD-EuC-biotin conjugates have high potential to be applied for, but not limited to, routine application in fluoroimmunoassays and cellular imaging.

## 2. Materials and Methods

### Materials

Hydrophobically capped quantum dots in decane, Qdot® 655 ITK™ (QD655), Qdot® 705 ITK™ (QD705) and biotinylated water-dispersible Qdot® 655 (QD655-biotin) were purchased from Life Technologies GmbH (Darmstadt, Germany). Sodium [4'-(4'-Amino-4-biphenylyl)-2,2':6',2''-terpyridine-6,6''-diylbis(methyliminodiacetato)]europate(III) (EuC) was purchased from TCI Deutschland GmbH (Eschborn, Germany). Amine-$PEG_3$-Biotin and 1 M Sodium Borate Buffer (SBB12) were purchased from Thermo Fisher Scientific GmbH (Ulm,

Germany). Poly(isobutylene-*alt*-maleic anhydride) (PMA, $M_w \approx 6$ kDa, 531278), Dodecylamine (DAM), Triethylamine ($NEt_3$), and 4-Dimethylaminopyridine (DMAP) were purchased from Sigma Aldrich (Taufkirchen bei München, Germany). Streptavidin was purchased from Promega GmbH (Mannheim, Germany). Biotin-free Bovine Serum Albumin (BSA) was purchased from Carl Roth GmbH + Co. KG (Karlsruhe, Germany). Double distilled water (G = 0.055 µS), used during fluoroassay experiments, was prepared using an Arium® Comfort water purification system (Sartorius AG, Göttingen, Germany). All chemicals were used without further purification.

## Methods

### Preparation of QD-EuC-biotin nanoconjugates

*Preparation of the PMA-Eu-biotin*

The QD655/705-EuC conjugates have been prepared according to the following general protocol. The PMA preparation procedure has been described in detail elsewhere.[32] Briefly, 1 eq. (related to the number of monomer units) of PMA, 0.75 eq. of DAM, 0.77 eq. of $NEt_3$, 0.1 eq of DMAP, 0.02 eq. of EuC and 0.02 eq. of PEG-biotin were dissolved in THF and stirred under reflux for 24 h (80 °C). NEt3 and DMAP serve as nucleophilic compounds, which promote the opening of maleic acid anhydride rings and thus the formation of an amide bond. This formation occurs as the opened rings provide two carboxylic groups each which can react with the primary amines of DAM, EuC, or PEG-biotin. By this procedure 75% of monomer units were reacted with DAM (hydrophobic side chains), 2% with EuC and 2% with PEG-biotin. The rest of the anhydride rings was believed to remain unreacted. Thus in total 22.8% of unreacted monomer units and one carboxylic group per reacted/opened ring were available for further functionalization or could serve for the later colloidal stabilization of QDs. After the conjugation reaction the solvent was evaporated to dryness and the remaining solid was redissolved in chloroform to a 50 mM solution (related to the number of PMA monomer units). After preparation, the polymer excitation and emission spectra stayed in good agreement with the spectra typical for EuC. Marginal terpyridine emission was observed as parts of the europium ions were removed from antenna chelates during polymer preparation. Additionally, for EuC attached on the polymer, the excitation spectrum was shifted of about 15 nm to the red and the relative relation between emission peaks has changed reflecting the change in immediate vicinity of the complex. The EuC emission and

excitation spectra taken before and after EuC conjugation to the PMA are shown in Figure 1 in the Supporting Information (SI).

*QD coating with PMA-Eu-biotin*

The QDs, originally delivered in decane, were transferred to chloroform according to the flocculation protocol provided by the manufacturer (precipitation with the 4-fold volume of a 75/25 methanol/isopropanol mixture *via* centrifugation and redissolution in chlorophorm). Then, the QDs were mixed with PMA-EuC-biotin solution also in chloroform.[32] The amount of added polymer was chosen in a way to assure a defined number $R_{P/Area}$ of the monomers per $nm^2$ of the effective QD surface (see formula for $R_{P/Area}$ in the SI of reference [32]). The effective QD surface refers to the effective diameter $d_{eff}$, which is composed of the core diameter $d_c$ and the thickness of the surface capping $d_p$ ($d_{eff} = d_c + 2 \cdot d_p$). In each case, the surface capping thickness was estimated to be $d_p = 1$ nm and the core diameters for QD655 and QD705 were $d_c = (9.6 \pm 0.6)$ nm and $d_c = (9.4 \pm 0.7)$ nm, respectively. As the QD shape was found to be partly rod like (see TEM images in the SI), $d_c$ refers to the diameter of a spherical QD that would lead to the same surface area like a rod with length $d_{c,1}$ and width $d_{c,2}$ (see formula for $d_c$ in the SI). Regarding the employed amount of polymer for QD655 or QD705, $R_{P/Area}$ was 125 $nm^{-2}$ or 130 $nm^{-2}$, respectively. The mixture was heated to 45 °C for 10-15 min and the solvent was then subsequently evaporated under reduced pressure. Then the solid was redissolved in approximately 1 mL chloroform. This heating-evaporating procedure was repeated three times. Afterwards, the dry QDs were dissolved in 50 mM Sodium Borate Buffer, pH=12 (SBB12). Then a syringe filter (0.22 µm, Carl Roth, P818.1) was used to remove QD agglomerates and residual cross-linked polymer aggregates. The filtrated solution was concentrated with 100 kDa centrifugation filters (Sartorius, VS2042) and purified via gel electrophoresis in 2% Agarose / 0.5× Tris Borate EDTA (TBE) buffer (pH ≈ 8.0) to remove remaining empty polymer micelles and unreacted reagents.[32, 33] Further purification was done in double distilled water with 100 kDa centrifugation filters (five times). The sample concentration has been determined from absorption measurements. The extinction coefficient values at the excitonic peak equal to $0.9 \cdot 10^6$ $M^{-1}$ $cm^{-1}$ for QD 655 and $0.5 \cdot 10^6$ $M^{-1}$ $cm^{-1}$ for QD705 were taken for the concentration determination.

**Fluoroassay using QD-Eu-biotin**

1, 2 and 3 µg/mL Streptavidin solutions in phosphate buffered saline (PBS) were incubated overnight at 4° C in selected wells of a microtiter plate (high-binding Lumitrac 600 plate). A well filled only with PBS was used to provide a reference zero value. For each Streptavidin concentration three wells were filled. Then, the Streptavidin solution was removed. Next, in order to reduce non-specific interaction between QD-EuC-biotin and the plate surface, the wells were blocked for 1 h with 2% BSA solution in PBS. Then, the BSA solution was removed and 50 µL of 50 nM QD-EuC-biotin conjugates solution in PBS were added to the Streptavidin-modified wells and incubated for 1 h at room temperature. Then, the nanoconjugate solution was removed and the wells were washed three times with PBS. After a final washing step, the wells have been filled with 150 µL PBS and the fluorescence decays were collected. The decays were integrated over the 200-2000 µs timeframe to receive the final analytical values.

**Photoluminescence Measurements**

Steady-state photoluminescence emission and excitation spectra were recorded using a FluoroMax 4 (Horiba, Jobin Yvon GmbH, Unterhaching, Germany) spectrophotometer working with a continuous 450 W Xe lamp. The samples were excited at 337 nm to provide the same excitation conditions as for time-resolved spectroscopy. The spectra were collected at 2 nm bandpass and an integration time equal to 0.5 s. Additionally, a 390 nm cut-off filter was used to eliminate the second order artifacts. All spectra were corrected for the instrumental response.

The time-resolved luminescence measurements were carried out on a Nanoscan photoluminescence multifunctional immunoassay reader (IOF Innovative Optische Messtechnik GmbH, Berlin. Germany). A nitrogen laser ($\lambda_{ex}$ = 337 nm, PRR = 20 Hz) was used as an excitation source. The luminescence signals were collected in an 8 ms time window using two photomultipliers with bandpass filters around the emission spectrum of the donor ((488 ± 10) nm) and around the emission spectrum of the acceptor ((665 ± 13) nm for the QD655 and (740 ± 13) nm for the QD705) channel. The luminescence of the QDs and the EuC were also measured separately to estimate the background signal.

## 3. Results and Discussion

Hyrophobically capped QDs were transferred to aqueous solution using overcoating with an amphiphilic polymer, which has advantages and disadvantages compared to standard ligand-exchange protocols.[20,34, 35] Depending on the method several properties can be varied: The distance between attached ligands and the QD surface, non-specific ligand-QD surface interaction, and colloidal stability.[34, 35] Prior to the practical applications this consideration should be taken into account and the method to transfer initially hydrophobic QDs into aqueous solution needs to be selected upon the particular requirements of the application. In our present case we desired QDs with high colloidal stability and thus opted for coating them with an amphiphilic polymer.[32]

The polymer prepared within this study and its arrangement on a QD is shown in Figure 1. Firstly, the octyl chains of trioctylphosphine oxide (TOPO), which are present on the hydrophobic QDs as supplied by the vendor, intercalate in organic solvent with the dodecyl chains of the amphiphilic polymer (by hydrophobic interaction) to form a hydrophobic buffering shell around the QD.[32] The hydrolysis of maleic anhydride rings of the backbone of the polymer upon presence of aqueous solution results in a large number of carboxylic moieties on the QD surface to provide the QDs with colloidal stability. The maleic anhydride rings facilitate also uncomplicated coupling of amine-containing molecules to the polymer through amide bond formation, which in the present cases has been used to pre-modify the polymer (before coating the QDs with it) with EuC and PEG-biotin.[32] After transfer of the polymer-coated QDs to aqueous solution the carboxylic moieties would also facilitate an uncomplicated polymer post-functionalization in aqueous environment, *e. g. via* 1-Ethyl-3-(3-dimethylaminopropyl)carbodiimide (EDC) coupling.

In our system, highly efficient FRET is observed due to close spatial proximity between EuC donors in the polymer shell and the QD acceptors. A rough distance estimation based on assuming a distance of the EuC to the inorganic QD surface of ~ 30 single C-C bonds (each with a length of 0.12-0.15 nm) yields a distance of 3-5 nm, assuming the dodecyl chains in their extended form. For calculation of FRET efficiencies one naturally needs to take into account the distance from the QD's surface to its center corresponding to the dipole center, the core radius $r_c$ (= $d_c$/2) which is around $r_c$ = 3-5 nm for both kinds of QDs (see TEM images in SI). Noteworthy, the Förster radius for the EuC-QD655 system has been calculated to be equal to 10 nm.[15] Therefore, a highly efficient FRET is expected in this system, particularly at donor-acceptor distances equal to or below 5 nm. Förster radius is a theoretical value, which depends on (1) donor quantum yield in the absence of an acceptor,

(2) overlap between the donor's emission and the acceptor’s absorption, (3) the orientation factor between both dipoles and (4) refractive index of the medium.

Time-gated detection in time-resolved spectroscopy allows for minimizing the undesired background effects coming from directly excited QDs and lanthanide complexes. Under UV light excitation at 337 nm, the QDs are excited both directly and indirectly through FRET. In a detection timeframe starting from 100 μs, fluorescence coming from directly excited QDs is no longer observed and solely the emission coming from sensitized QDs can be observed (the QD decay time is 20 ns and the full emission timeframe is 200 ns). Additionally, the directly excited EuC, which do not contribute to the energy transfer, can be observed both in steady-state and time resolved spectroscopy. This effect, however, can be minimized by the use of a bandpass filter, which passes light at a QD-characteristic wavelength and blocks all other emissions. In time resolved spectroscopy Eu can also be seen marginally at the QD-specific wavelengths. In our case, the crosstalk of the EuC emission to the acceptor channel was found to be 5% (at 655 nm) and 1% (at 740 nm) of the initial counts (cps) value collected in the donor channel at 620 nm. Additionally, no large EuC emission peaks were observed in the steady-state spectra supporting the assumption of effective energy transfer to QDs.

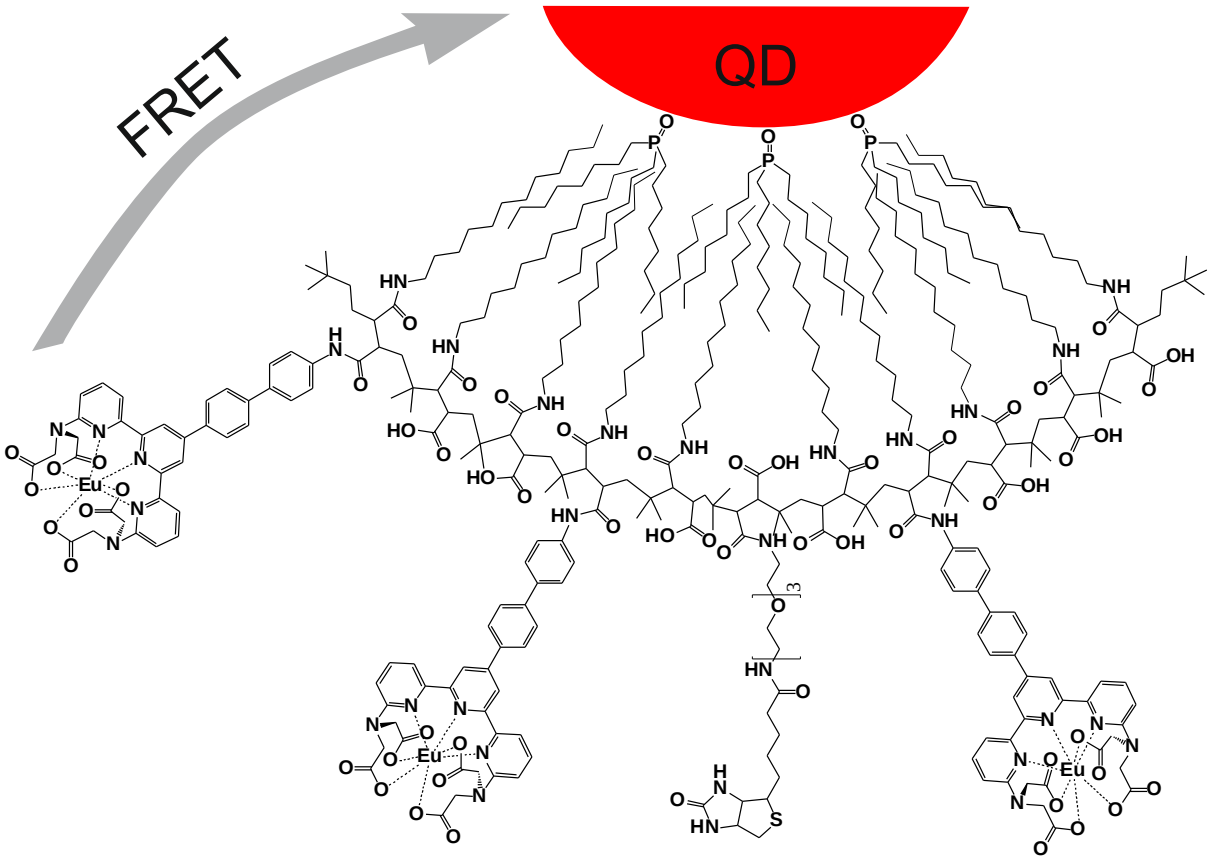


**Figure 1.** The assembly of the functional polymer on the QD surface. The QD is surrounded by trioctylphosphine oxide chains (coming from QD preparetion) assembled with the dodecyl chains of the amphiphilic polymer. Biotin (to facilitate binding to streptavidin) and EuC (to pump QD with long-living emission) were incorporated to the polymer prior to its assembly on the QD. The remaining carboxylic moieties facilitate stability and solubility of such construct in aqueous solutions.

Luminescence steady-state emission spectra of QD655-EuC-biotin and QD705-EuC-biotin conjugates upon light excitation at 337 nm are shown in Figure 2. Initially, after coating the QDs with the polymer, the steady-state spectrum shows two well-separated emission peaks. First, in the range 400-500 nm there is a spectrum typical for terpyridine present in the EuC organic antenna. The second peaking either at around 655 nm or 705 nm represents the emission of QD655 or QD705, respectively. Since the antenna emission can be seen in the spectrum, it supports the presumption that some $Eu^{3+}$ ions were washed out from the chelating antenna during the purification using gel electrophoresis. Before coating the polymer on the QDs no antenna emission was observed in the polymer emission (see SI). Additionally, at around 610 nm, at a wavelength typical for the $Eu^{3+}$ main peak characteristic of the $^5D_0 \rightarrow {}^7F_2$ transition, a marginal sharp peak coming from directly excited EuCs that do not participate in FRET can be seen. In order to stimulate re-complexation of $Eu^{3+}$ into empty

europium chelating pockets (terpyridines), we added $EuCl_3$ solution to the solution of nanoconjugates. The addition of $Eu^{3+}$ ions yielded in a considerable decrease in terpyridine emission (supporting successful $Eu^{3+}$ association into chelating pockets) simultaneously associated with a significant, around 5 times for QD655 and 3 times for QD705, increase in the QD emission intensity (See Figure 2). Noticeably, the emission, characteristic for europium, was no longer observed supporting the assumption of highly efficient energy transfer from the donor complex to the acceptor QD. No further increase was observed after further addition of $EuCl_3$, supporting the full complexation for most of accessible chelates on QDs. The marginal terpyridine emission can be explained by the existence of antennas hindered in the hydrophobic shell, and therefore, weakly accessible for $Eu^{3+}$ ions. A similar effect has also been observed for QD705 (Figure 2b). Such enriched nanobioconjugates were used for studies in fluoroassays.

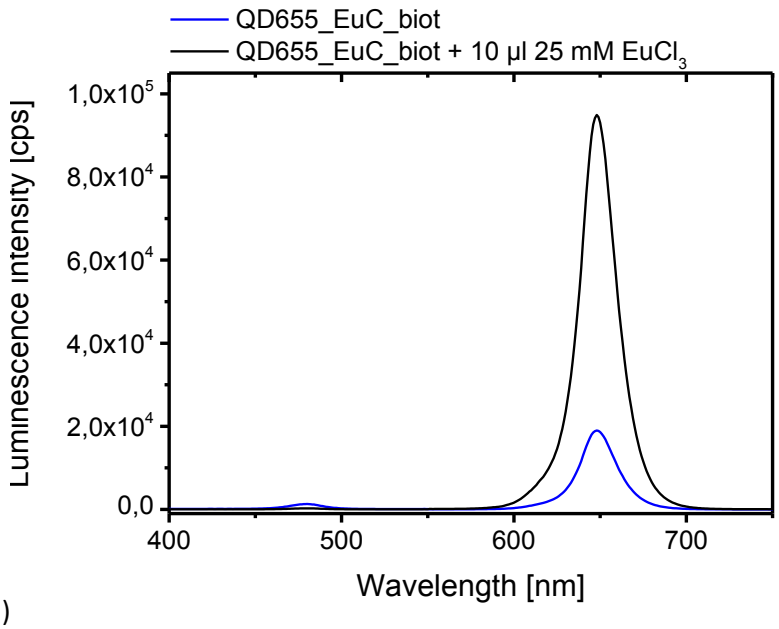


(a)

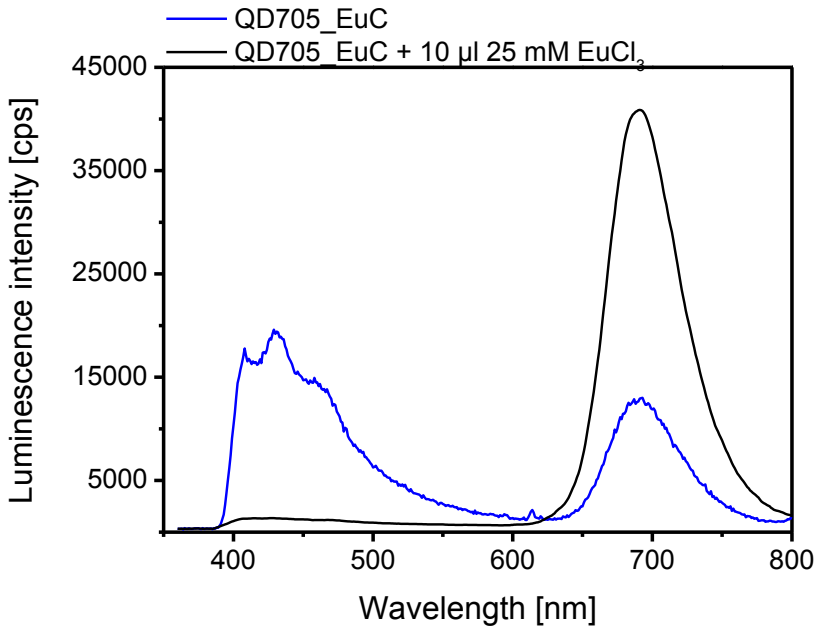


(b)

**Figure 2.** Luminescence emission spectra ($\lambda_{ex}$ = 337nm) of QD655-EuC–biotin (a) and QD705-EuC–biotin (b) nanoconjugates before (blue) and after addition of 10 µL (black) of 25 mM $EuCl_3$ in 50 mM citric acid, pH = 4. A 390 nm cut-off filter was placed in the emission path to remove second order artifacts.

The effect observed in steady-state spectroscopy was also observed in time-resolved fluorescence spectroscopy. The luminescence decays for QD655, EuC and QD655-EuC-biotin are shown in Figure 3.

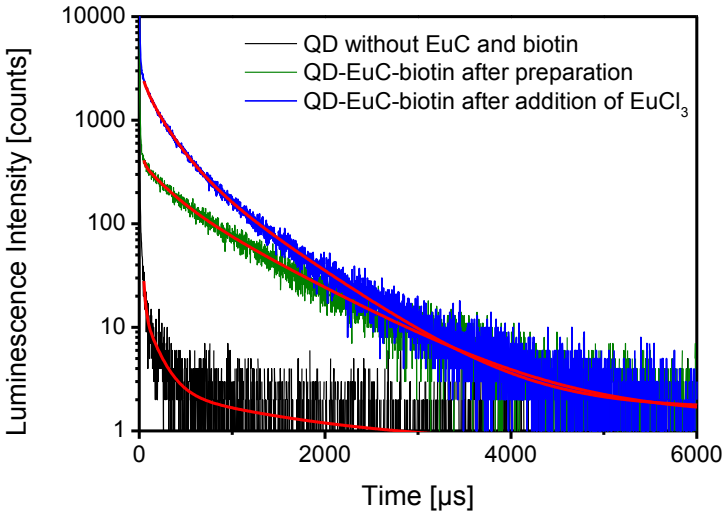


**Figure 3.** Luminescence decays of QD655 without EuC and biotin (black curve), QD655-Eu-biotin before (green curve) and after (blue curve) the addition of 10 µL of 25 mM $EuCl_3$ in

50 mM citric acid, pH = 4. ($\lambda_{exc}$ = 337 nm, emission bandpass filter – (665 ± 13) nm). The red curves correspond to fits with a triexponential function.

Similarly to steady-state measurements, an increase in QD fluorescence is observed upon $EuCl_3$ addition to the nanoconjugate solution. In contrast to steady-state measurements, when using time-resolved spectroscopy, we were able to estimate the FRET process quantitatively. To do so, the functional nanobioconjugates' luminescence decays have been fitted with a triexponential function (Equation 1):[36]

$$I(t) = A_1 \exp\left(-\frac{t}{\tau_1}\right) + A_2 \exp\left(-\frac{t}{\tau_2}\right) + A_3 \exp\left(-\frac{t}{\tau_3}\right) \quad (1)$$

Here $A_1$, $A_2$ and $A_3$ are amplitudes and $\tau_1$, $\tau_2$ and $\tau_3$ are the respective decay times corresponding to each decay contribution. Fitting with a triexponential function assumes the co-existence of three emissive species, namely from, (1) directly-excited fast-decaying acceptor QDs, (2) directly-excited long-decaying donor EuCs, and (3) QD-EuC-biotin conjugates sensitized through FRET. The directly-excited long-decaying donor EuCs must be considered in the fitting in the acceptor channel since there is a crosstalk between EuC and QD emission due to background emission of EuC. Usually this crosstalk is smaller than 10% of the intensity observed in the donor channel. The decay times obtained from decays presented in Figure 3 for QD655-EuC-biotin conjugates before and after adding $EuCl_3$ are summarized in Table 1. The decay times determined from decays collected for solutions containing EuC or QD655 only have been added for comparison. Luminescence decay either of QDs or EuC has been fitted with a monoexponential function assuming the existence of one species in solution.

The luminescence decay contributions with a decay time $\tau_1$ can be attributed to the directly excited fast-decaying acceptor QDs and the associated detector response. The decay time $\tau_2$ is associated with directly excited EuC complexes. After adding 10 µL 25 mM $EuCl_3$ to 3 mL of nanobiosensors solution a tremendous change in the emission contributions can be observed. The contribution $A_1$ corresponding to directly-excited QDs has been reduced by 40% (from 0.47 to 0.29) and the contribution $A_2$ of long-decaying EuC by around 50% (from 12% to 22%). Simultaneously, the contribution $A_3$ (conjugates) has increased by 100% (from 31 % to over 60 %) of the whole decay. This result supports our assumption of a very efficient energy transfer between EuC and QDs that occurs in QD-EuC-biotin conjugates.

Table 1. The decay times $\tau_i$ and corresponding amplitudes $A_i$ obtained from fitting luminescence decays in Figure 3 using equation (1). The QD655- EuC-biotin (1) corresponds to the sample resulting from nanobioconjugate preparation and QD655- EuC-biotin (2) to the sample after addition 10µL of $EuCl_3$.

| | $\tau_1$ [µs] | $A_1$ [-] | $\tau_2$ [µs] | $A_2$ [-] | $\tau_3$ [µs] | $A_3$ [-] |
|---|---|---|---|---|---|---|
| QD655- EuC-biotin (1) | 26.5 | 0.47 | 910 | 0.22 | 238 | 0.31 |
| QD655- EuC-bioitn (2) | 26.9 | 0.29 | 770 | 0.12 | 220 | 0.61 |
| EuC | - | - | 1020 | 1 | - | - |
| QD655 | 27.5 | 1 | - | - | - | - |

Based on the decay time values presented in Table 1, the transfer efficiency has been determined to be equal to 76%. Taking into account this high FRET efficiency and Förster radius for QD655- EuC donor-acceptor pair equal to 10 nm, the physical donor-acceptor distance was estimated to be 6.8 nm. The formulae used both for calculating FRET efficiency and physical donor-acceptor distance can be found in the SI.

**Fluoroimmunoassay**

Biotin-streptavidin interaction is often used in immunoassays due to the highest binding affinity constant ($10^{-14}$ mol/L) known for non-covalent interactions. Due to a strong biotin-streptavidin interaction, biotin is a convenient chemical group to test the usability of our complexes for subsequent bioconjugation in an uncomplicated way. In our study, the PEG-biotin has been attached to the amphiphilic polymer to provide biotin functionality to the QD655-EuC-biotin. Microtiter plate wells covered with different streptavidin concentrations (1, 2, 3 µg/mL) have been exposed to 50 nM QD655-EuC-biotin solutions in PBS. The fluoroassay results are presented in Figure 4. One can observe an increase in the luminescence signal with an increased streptavidin concentration. This result demonstrates the binding of biotin to streptavidin, and therefore, the potential of our nanobioconjugates for their use in fluoroimunnoassays. For example, in a heterogeneous assay a catcher antibody is usually adsorbed first at the well surfaces. After the passivation, usually with BSA, such a prepared surface is exposed to a sample containing analyte, *i. e.* antigen. Then, in order to visualize the antigens bound to the catcher antibodies, a second antibody – a detector – is usually added. Very often this detector antibody is functionalized either with biotin or with streptavidin. If the detection antibody is conjugated with streptavidin, a biotinylated label can facilitate the

uncomplicated, antigen concentration dependent detection even done to femtomolar concentrations. Apart from the use in fluoroimmunoassays, the nanobiosensors can be used in each system utilizing the biotin-streptavidin interaction. A similar effect was observed for QD705-Eu-biotin. The presented nanobioconjugates represent a reliable approach for developing applications based on long-decay and bright species in bioanalysis, but they still require further optimization to improve the polymer composition, the coating assembly, and the resulting energy transfer efficiency. Apart from the use in immunoassay such long-decaying constructs can find their application in other fields such as imaging or display technologies.

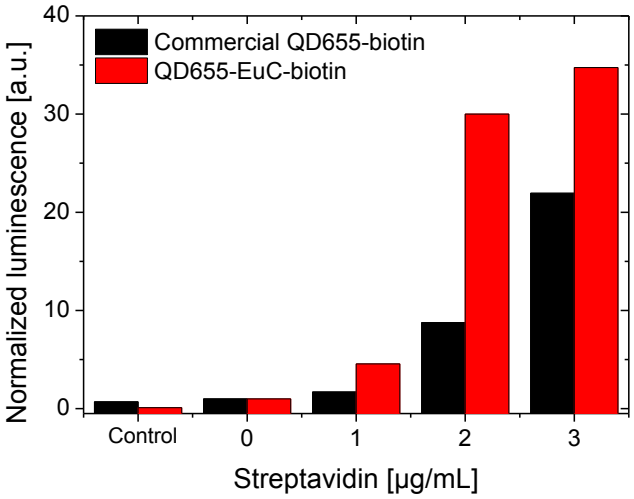


Figure 4. Luminescence signal (integrated over 1800 µs (200-2000 µs) of QD655-EuC-biotin and commercial biotinylated QD655 (integrated over 180 ns (20-200 ns)) collected in microtiter plate wells covered with 1, 2 and 3 µg/mL of streptavidin. The signals were normalized to 1 corresponding to 0 µg/mL streptavidin. A well only with BSA without streptavidin (0 µg/mL) has been added to test non-specific interactions. The control corresponds to a signal from a well, in which no BSA and no streptavidin was present.

## 4. Conclusions

In our paper, we presented a method to design nanobioconjugates that constitute a new approach for novel long-decaying luminescent QDs, which at the used wavelengths, normally are hard to achieve, solely by integrating $Eu^{3+}$ complexes. The presented long-decaying QDs extend the range of materials that can be applied in fluoroimmunoassays, imaging, flow cytometry applications or microfluidic optical sensing systems. In floroimmunoassays or biomaging the conjugates can improve signal-to-noise ratio, when compared to short living QDs. Additionally with longer lifetimes, less QDs are needed for studies when compared to systems with QDs only. Thus our system constitutes a novel approach towards efficient long-decaying fluorescent species.

## 5. Acknowledgements

This research was supported by the Marie Curie European Reintegration Grant $QUANTUM_{DOT}IMPRINT$ (PERG05-GA-2009-247825), the German Research Foundation (DFG, project PA 794/11-1) and the European Commission (project Namdiatream).

## 6. References

1. Alivisatos, A. P., Semiconductor clusters, nanocrystals, and quantum dots. *Science* 1996, 271, 933-937.
2. Hildebrandt, N.; Charbonniere, L. J.; Beck, M.; Ziessel, R. F.; Lohmannsroben, H. G., Quantum dots as efficient energy acceptors in a time-resolved fluoroimmunoassay. *Angew. Chem.-Int. Edit.* 2005, 44, 7612-7615.
3. Resch-Genger, U.; Grabolle, M.; Cavaliere-Jaricot, S.; Nitschke, R.; Nann, T., Quantum dots versus organic dyes as fluorescent labels. *Nat. Methods* 2008, 5, 763-775.
4. Jain, K. K., Nanodiagnostics: application of nanotechnology in molecular diagnostics. *Expert Rev. Mol. Diagn.* 2003, 3, 153-161.
5. Michalet, X.; Pinaud, F. F.; Bentolila, L. A.; Tsay, J. M.; Doose, S.; Li, J. J.; Sundaresan, G.; Wu, A. M.; Gambhir, S. S.; Weiss, S., Quantum dots for live cells, in vivo imaging, and diagnostics. *Science* 2005, 307, 538-544.
6. Geszke-Moritz, M.; Moritz, M., Quantum dots as versatile probes in medical sciences: Synthesis, modification and properties. *Mater. Sci. Eng. C-Mater. Biol. Appl.* 2013, 33, 1008-1021.
7. Costa-Fernandez, J. M.; Pereiro, R.; Sanz-Medel, A., The use of luminescent quantum dots for optical sensing. *Trac-Trends Anal. Chem.* 2006, 25, 207-218.
8. Ai, X.; Ma, Q.; Su, X., Multiplex DNA sensor for BRAF and BRCA detection. *Analytical biochemistry* 2013, 438, 22-8.
9. Algar, W. R.; Malanoski, A. P.; Susumu, K.; Stewart, M. H.; Hildebrandt, N.; Medintz, I. L., Multiplexed Tracking of Protease Activity Using a Single Color of Quantum Dot Vector and a Time-Gated Forster Resonance Energy Transfer Relay. *Analytical chemistry* 2012, 84, 10136-10146.

10. Freeman, R.; Girsh, J.; Jou, A. F.-j.; Ho, J.-a. A.; Hug, T.; Dernedde, J.; Willner, I., Optical Aptasensors for the Analysis of the Vascular Endothelial Growth Factor (VEGF). *Analytical Chemistry* 2012, 84, 6192-6198.
11. Geißler, D.; Charbonnière, L. J.; Ziessel, R. F.; Butlin, N. G.; Löhmannsröben, H.-G.; Hildebrandt, N., Quantum Dot Biosensors for Ultrasensitive Multiplexed Diagnostics. *Angewandte Chemie International Edition* 2010, 49, 1396-1401.
12. Han, M.; Gao, X.; Su, J. Z.; Nie, S., Quantum-dot-tagged microbeads for multiplexed optical coding of biomolecules. *Nat Biotech* 2001, 19, 631-635.
13. del Mercato, L. L.; Abbasi, A. Z.; Ochs, M.; Parak, W. J., Multiplexed Sensing of Ions with Barcoded Polyelectrolyte Capsules. *Acs Nano* 2011, 5, 9668-9674.
14. Fournier-Bidoz, S.; Jennings, T. L.; Klostranec, J. M.; Fung, W.; Rhee, A.; Li, D.; Chan, W. C. W., Facile and rapid one-step mass preparation of quantum-dot barcodes. *Angewandte Chemie-International Edition* 2008, 47, 5577-5581.
15. Härmä, H.; Pihlasalo, S.; Cywinski, P. J.; Mikkonen, P.; Hammann, T.; Löhmannsröben, H.-G.; Hänninen, P., Protein Quantification Using Resonance Energy Transfer between Donor Nanoparticles and Acceptor Quantum Dots. *Analytical chemistry* 2013, 85, 2921-2926.
16. Chakravarthy, K. V.; Davidson, B. A.; Helinski, J. D.; Ding, H.; Law, W.-C.; Yong, K.-T.; Prasad, P. N.; Knight, P. R., Doxorubicin-conjugated quantum dots to target alveolar macrophages and inflammation. *Nanomedicine: Nanotechnology, Biology and Medicine* 2011, 7, 88-96.
17. Clarke, S.; Pinaud, F.; Beutel, O.; You, C.; Piehler, J.; Dahan, M., Covalent Monofunctionalization of Peptide-Coated Quantum Dots for Single-Molecule Assays. *Nano Letters* 2010, 10, 2147-2154.
18. Bakalova, R.; Ohba, H.; Zhelev, Z.; Nagase, T.; Jose, R.; Ishikawa, M.; Baba, Y., Quantum dot anti-CD conjugates: Are they potential photosensitizers or potentiators of classical photosensitizing agents in photodynamic therapy of cancer? *Nano Lett.* 2004, 4, 1567-1573.
19. Delehanty, J. B.; Mattoussi, H.; Medintz, I. L., Delivering quantum dots into cells: strategies, progress and remaining issues. *Anal. Bioanal. Chem.* 2009, 393, 1091-1105.
20. Palui, G.; Avellini, T.; Zhan, N.; Pan, F.; Gray, D.; Alabugin, I.; Mattoussi, H., Photoinduced Phase Transfer of Luminescent Quantum Dots to Polar and Aqueous Media. *Journal of the American Chemical Society* 2012, 134, 16370-16378.
21. Artemyev, M., Resonance energy transfer in conjugates of semiconductor nanocrystals and organic dye molecules. *Journal of Nanophotonics* 2012, 6.
22. Agudelo-Morales, C. E.; Galian, R. E.; Perez-Prieto, J., Pyrene-Functionalized Nanoparticles: Two Independent Sensors, the Excimer and the Monomer. *Analytical Chemistry* 2012, 84, 8083-8087.
23. Bai, J.-M.; Zhang, L.; Liang, R.-P.; Qiu, J.-D., Graphene Quantum Dots Combined with Europium Ions as Photoluminescent Probes for Phosphate Sensing. *Chemistry-a European Journal* 2013, 19, 3822-3826.
24. Nedosekin, D. A.; Sarimollaoglu, M.; Galanzha, E. I.; Sawant, R.; Torchilin, V. P.; Verkhusha, V. V.; Ma, J.; Frank, M. H.; Biris, A. S.; Zharov, V. P., Synergy of photoacoustic and fluorescence flow cytometry of circulating cells with negative and positive contrasts. *Journal of Biophotonics* 2013, 6, 425-434.
25. Chakravarthy, K. V.; Davidson, B. A.; Helinski, J. D.; Ding, H.; Law, W.-C.; Yong, K.-T.; Prasad, P. N.; Knight, P. R., Doxorubicin-conjugated quantum dots to target alveolar macrophages and inflammation. *Nanomedicine-Nanotechnology Biology and Medicine* 2011, 7, 88-96.
26. Hong, J.; Pei, D.; Guo, X., Quantum dot-Eu3+ conjugate as a luminescence turn-on sensor for ultrasensitive detection of nucleoside triphosphates. *Talanta* 2012, 99, 939-943.
27. Jiang, G.; Susha, A. S.; Lutich, A. A.; Stefani, F. D.; Feldmann, J.; Rogach, A. L., Cascaded FRET in Conjugated Polymer/Quantum Dot/Dye-Labeled DNA Complexes for DNA Hybridization Detection. *Acs Nano* 2009, 3, 4127-4131.
28. Cywinski, P. J.; Moro, A. J.; Ritschel, T.; Hildebrandt, N.; Loehmannsroeben, H.-G., Sensitive and selective fluorescence detection of guanosine nucleotides by nanoparticles conjugated with a naphthyridine receptor. *Analytical and Bioanalytical Chemistry* 2011, 399, 1215-1222.

29. Cywinski, P. J.; Moro, A. J.; Löhmannsröben H.G., Cyclic GMP recognition using ratiometric QD-fluorophore conjugate nanosensors. *Biosensors&Bioelectronics* 2014, 52, 288–292.
30. Charbonniere, L. J.; Hildebrandt, N., Lanthanide complexes and quantum dots: A bright wedding for resonance energy transfer. *European Journal of Inorganic Chemistry* 2008, 3241-3251.
31. Kadjane, P.; Starck, M.; Camerel, F.; Hill, D.; Hildebrandt, N.; Ziessel, R.; Charbonniere, L. J., Divergent Approach to a Large Variety of Versatile Luminescent Lanthanide Complexes. *Inorganic Chemistry* 2009, 48, 4601-4603.
32. Lin, C.-A. J.; Sperling, R. A.; Li, J. K.; Yang, T.-Y.; Li, P.-Y.; Zanella, M.; Chang, W. H.; Parak, W. J., Design of an amphiphilic polymer for nanoparticle coating and functionalization. *Small* 2008, 4, 334-341.
33. Fernandez-Argueelles, M. T.; Yakovlev, A.; Sperling, R. A.; Luccardini, C.; Gaillard, S.; Medel, A. S.; Mallet, J.-M.; Brochon, J.-C.; Feltz, A.; Oheim, M.; Parak, W. J., Synthesis and characterization of polymer-coated quantum dots with integrated acceptor dyes as FRET-based nanoprobes. *Nano Letters* 2007, 7, 2613-2617.
34. Zhang, F.; Lees, E.; Amin, F.; Gil, P. R.; Yang, F.; Mulvaney, P.; Parak, W. J., Polymer-Coated Nanoparticles: A Universal Tool for Biolabelling Experiments. *Small* 2011, 7, 3113-3127.
35. Geidel, C.; Schmachtel, S.; Riedinger, A.; Pfeiffer, C.; Mullen, K.; Klapper, M.; Parak, W. J., A General Synthetic Approach for Obtaining Cationic and Anionic Inorganic Nanoparticles via Encapsulation in Amphiphilic Copolymers. *Small* 2011, 7, 2929-2934.
36. Niebling, T.; Zhang, F.; Ali, Z.; Parak, W. J.; Heimbrodt, W., Excitation dynamics in polymer-coated semiconductor quantum dots with integrated dye molecules: The role of reabsorption. *Journal of Applied Physics* 2009, 106.

ADVANCED FUNCTIONAL MATERIALS
www.afm-journal.de

Materials Views
www.MaterialsViews.com

# Photostimulated Au Nanoheaters in Polymer and Biological Media: Characterization of Mechanical Destruction and Boiling

*Dominik Hühn, Alexander Govorov, Pilar Rivera Gil, and Wolfgang J. Parak**

**Agglomerated gold nanoparticle clusters embedded in polyelectrolyte films are optically excited, which results in local ablation of material from the polyelectrolyte films and in some cases leads to the formation of a gas bubble. Evidence is given that this process is mediated by superheating of the medium around the excited gold nanoparticle clusters. This process is highly dependent on the medium used. Besides the boiling point, salt and proteins in the medium also affect the formation of gas bubbles. These data demonstrate that the type of medium must be considered when describing light-mediated heating of gold nanoparticle clusters, which are fixed in a matrix surrounded by medium.**

## 1. Introduction

Gold nanoparticles (Au NPs) hold great promise for biological applications.[1–4] This promise goes back to the fact that they present a strong absorption band in the visible to NIR region, which is the origin of the observed red to purple colors of gold NPs in solution. This absorption band results from the collective oscillation of the conduction-band electrons (the so-called electron gas) in resonance with the frequency of the incident electromagnetic field and is known as surface plasmon resonance (SPR) absorption. The influence of shape and interparticle distance is, in general, even greater than that of size. While a single absorption band is present for spherically symmetric gold NPs, multiple absorption bands correlated with their various axes appear for nonspherical ones; this is the case for gold nanorods which possess two different resonance modes due to electron oscillation across and along the long axis of the nanorod that are commonly labelled the transverse and longitudinal modes.[5] Of special relevance is the tuning of the SPR absorption through the modulation of the distance between neighboring NPs, which is usually afforded by means of encapsulation with an insulating layer, made, for example, of silica or organic capping agents.[6–8] In this fashion the interparticle spacer can screen the dipole–dipole interparticle interactions in such a way that the collective optical properties can be modulated between those of the bulk metal and those of individual NPs. Upon optical excitation at the SPR frequency significant amounts of energy can be pumped into the conduction electrons. Electron lattice coupling results in transfer of this energy from the electrons to the crystal lattice,[9–12] from where it is dissipated as heat to the local environment.[11,13–15] In this way gold NPs can be considered as a light-controlled nano-oven.[10,16] Photogenerated local heat has been used, for example, to directly destroy local tissue,[17–20] to melt matrices and thus open containers to release molecules to the local environment,[21–26] to break molecular bonds,[27–29] and to weld tissue.[30] Arguably biological applications of photoinduced heating take place in biological environments,[31] which involves the presence of salts, proteins, etc. While the processes of photoinduced heating have been investigated in detail concerning absorption,[32–34] relaxation of the excited electron gas,[35] and dissipation to basic continua such as water or ice,[10,36–38] the influence of the composition of the surrounding medium has not been fully elucidated to date because of the complexity of interactions between inorganic elements (e.g., Au NPs) and biological systems.[17] The understanding of nanostructure–biosystem interactions is especially important since the potential and current use of Au NP heaters implies thermal and physical contact of NPs with biological media such as tissue, blood, etc. In the present study we investigated the influence of the composition of the fluidic media, including biological fluids (serum, growth medium, etc.), around Au NPs on light-induced heating of polymer matrices. For this purpose agglomerates of Au NPs were embedded in polymer films created by layer-by-layer (LbL) assembly.[39] Layers were locally destroyed by photoinduced heating of the embedded Au NPs. Hereby the influence of the composition of the aqueous solution above and within the polymer films was investigated.

D. Hühn, Dr. P. Rivera Gil, Prof. W. J. Parak
Fachbereich Physik and WZMW
Philipps-Universität Marburg
Renthof 7, 35032 Marburg, Germany
E-mail: wolfgang.parak@physik.uni-marburg.de
Prof. A. Govorov
Department of Physics and Astronomy
Ohio University
Athens, Ohio 45701, USA

DOI: 10.1002/adfm.201101134

## 2. Strategy and Theoretical Expectations

### 2.1. Materials

Poly(allylamine hydrolchloride) (PAH; ref 283223, $M_w$ = 56 kDa), poly(fluorescein isothiocyanate allylamine hydrochloride) ($PAH_{FITC}$, ref 630209, $M_w$ = 56 kDa, ratio PAH:FITC

50:1), poly(sodium 4-styrenesulfonate) (PSS, ref 243051, $M_w$ = 70 kDa), albumin from bovine serum (BSA, ref A9647, $M_w$ = 66 kDa), albumin–fluorescein isothiocyanate conjugate ($BSA_{FITC}$, ref A9771, $M_w$ = 66 kDa, ratio FITC:BSA 7:1), glycerol (ref G8773), minimum essential medium eagle (basal medium, ref M4655), and penicillin–streptomycin (ref P4333) were purchased from Sigma-Aldrich (Germany). The polyelectrolytes PAH (or $PAH_{FITC}$) and PSS were dissolved in 0.5 M NaCl solution. The concentration of PAH or $PAH_{FITC}$ was 1.872 mg $mL^{-1}$ and the concentration of PSS was 4.124 mg $mL^{-1}$, to give an equal number of charged groups present in solution. After dissolution the pH was adjusted to 6.5 by addition of HCl or NaOH. $BSA_{FITC}$ was dissolved in pure water with a concentration of 0.5 mg $mL^{-1}$. Growth medium for cell culture was made by combination of basal medium with 10% fetal bovine serum (serum, ref S 0615, Biochrom), 1% penicillin–streptomycin, and 1% L-glutamine (ref 25030-024, Invitrogen). Lime-soda-glass slides (ref H868.1), NaCl (cellpure, ref HN00.2), methanol (ref 8388.5), ethanol (ref T171.2), 2-propanol (ref 7343.1), toluene (ref 9558.3), *N*,*N*-dimethylformamide (DMF, ref 6251.2), and monoethylene glycol (MEG, ref 6881.2) were purchased from Roth. Au NPs (15 nm core diameter, citrate-coated, ref EMGC15) were purchased from British Biocell International. All solutions were based on three-stage purified water (R = 18.2 MΩ·cm at 25 °C, Milli-Q Academic, Millipore).

### 2.2. Sample Preparation and Characterization

Multilayered thin films on glass slides were prepared by the LbL deposition technique.[40] Glass slides were cleaned first by sonication for 30 minutes at 60 °C in a water/ethanol mixture (3:7) with 1% KOH, and then subsequently washed exhaustively with pure water. This procedure ensured negatively charged surfaces. For polymer films without proteins the pretreated glass slides were dipped for 5 minutes into $PAH_{FITC}$ solution, which resulted in attachment of $PAH_{FITC}$ to the surface and inversion of the surface charge. The glass slides were then subsequently dipped for 5 minutes into PSS solution, whereupon PSS adsorbed and restored the original charge. After each immersion an intermediate washing step was performed to remove unbound material. Upon repetition of the PAH and PSS adsorption steps, processed multilayers with the architecture $(PAH_{FITC}/PSS)_n$ were grown. To embed $BSA_{FITC}$ into the polymer film, the LbL procedure was applied as described above. However instead of $PAH_{FITC}$ unlabeled PAH solution was used. $BSA_{FITC}$ was added as an intermediate layer between PAH and PSS by incubation of the PAH terminated surface with 1 ml of the $BSA_{FITC}$ solution. Due to the negative charge of BSA (isoelectric point: 4.7) at neutral pH the proteins adsorb onto the positively charged surface. PSS is believed to stabilize layer growth by completing the negatively charged layer. This procedure led to the architecture $(PAH/BSA_{FITC}+PSS)_n$. To embed aggregated Au NP clusters the procedure was repeated as for embedding of BSA, substituting aggregated Au NP clusters for BSA. For this purpose the Au NPs first had to be aggregated. Au NPs (c ≈ 2 nM in water) were mixed with the same volume of 0.5 M NaCl. As soon as the NaCl solution had been added the Au NPs started to aggregate (color changed from red to bluish) and the solutions had to be used for integration into the polyelectrolyte layers within several minutes, whereby the incubation time depended on the desired grade of aggregation. It is believed that Au clusters still carry enough charge to be adsorbed onto the PAH terminated layer even though they become agglomerated by screening of charged citrate molecules. In addition to electrostatic attraction, van der Waals attraction in close proximity to the surface might enhance stable incorporation of Au NP clusters.[41] Samples with incorporated Au NPs finally consisted of three layers of Au NP clusters and ten layers of $BSA_{FITC}$ in-between PAH and PSS. As the same Au solution was taken for all three layers, different sizes of clusters were embedded (the Au NP agglomerates still were growing while the subsequent layers were assembled). Thus, the final architecture of these samples was $(PAH/Au+PSS)_3(PAH/BSA_{FITC}+PSS)_{10}$. Multilayer growth of polyelectrolyte films was quantified by fluorescence measurements using a Fluorolog FL3-22 from Horiba Jobin Yvon (excitation wavelength: 495 nm) equipped with a solid sample holder with fine angle adjustment on dried samples. Hereby addition of each fluorescent layer ($PAH_{FITC}$ or $BSA_{FITC}$) of the fluorescent samples $(PAH_{FITC}/PSS)_n$, $(PAH/BSA_{FITC}+PSS)_n$, $(PAH/Au/PSS)_3(PAH/BSA_{FITC}+PSS)_{10}$ was observed after every PSS step. After preparation all samples were stored in Rotilabo®-slide tubes (ref KL89.1) from Roth at 4 °C. Before measurements, samples were dried in a nitrogen stream.

### 2.3. Microscope Set-Up

Light irradiation experiments on the polyelectrolyte samples were carried out with a microscope set-up consisting of an upright Axiotech microscope from Zeiss (Germany) equipped with an additional continuous wave near-infrared (NIR) laser diode emitting at 830 nm. The NIR laser beam was coupled into the microscope using a beam splitter (2P-Strahlenteiler 725 DCSPXR, ref F33-725, AHF Analysentechnik) and was focused by changing the working distance with an *x*–*y* stage (**Figure 1**). The polyelectrolyte samples were placed on a micrometer-resolution motorized *x*–*y*–*z* stage (SMI, Luigs & Neuman Feinmechanik und Elektrotechnik GmbH, Germany) in the focus of the microscope. As microscope imaging was operated in reflection, small silicon wafers served as the mirror below the polyelectrolyte sample. The microscope was furthermore equipped with several filters. Transmission, green fluorescence (Filtersatz 09, excitation BP 450–490, beam splitter FT 515, emission LP 515, ref 488009-9901-000, Zeiss Germany), and red fluorescence (Filtersatz 00, excitation BP 530–585, beam splitter FT 600, emission LP 615, ref 488000-0000-000, Zeiss Germany) were investigated. Filters were mounted into a filter bar that had to be shifted manually. In transmission mode a 100 W white-light halogen lamp (HAL-100, Zeiss Germany) served as the light source. For fluorescence observations a mercury-vapor lamp (HBO-100, Zeiss Germany) was used. The light beam for transmission and fluorescence illumination and the NIR laser beam for the excitation of the Au NPs were focused onto the polyelectrolyte sample with a water immersion objective (W Plan-Apochromat 63x/1.0 Ph3, ref 441471-9910-000, Zeiss Germany). Images were recorded with a charge-coupled device (CCD) true-color camera (MRc AxioCam,

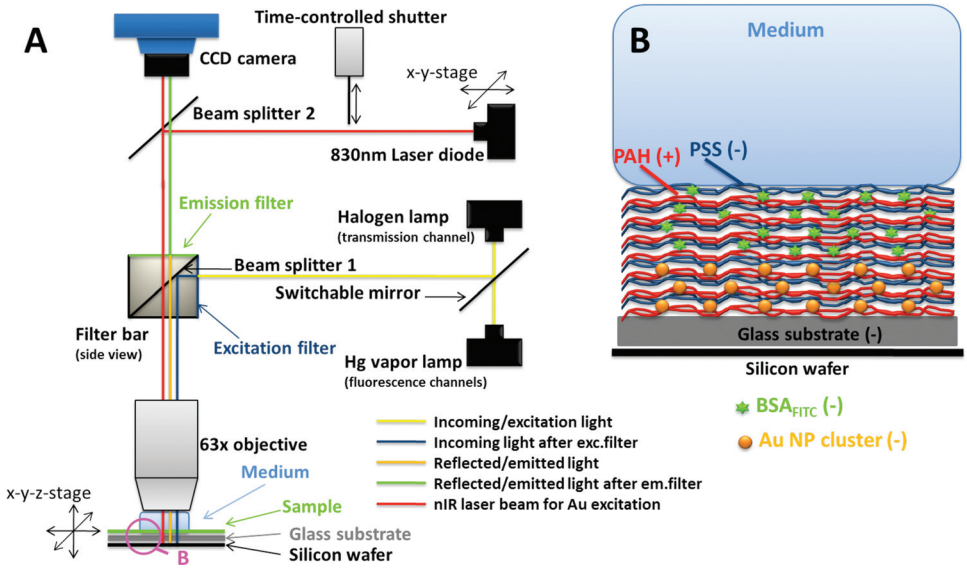


**Figure 1.** Experimental set-up. A) An 830 nm NIR laser is coupled into an inverted microscope via beam splitter #2. In parallel the illumination for transmission or fluorescence is coupled with beam splitter #1. In this way a laser spot of a few micrometers can be generated on a sample in the focus of a 63x objective (cf. Figure 2), as well as illuminating the sample in the viewing area of the objective. Light reflected from or originating from fluorescence of the sample is imaged after having passed appropriate filters with a CCD camera. B) The sample consists of Au NP clusters embedded in a polymer film which has been assembled by LbL deposition on a glass slide, placed on top of a silicon wafer, which acts as mirror. As the thickness of one polyelectrolyte layer is around 1 nm[51] and the diameter of one Au NP cluster is 0.1–10 µm; the scheme is not drawn to scale. The sample is immersed in medium, which is varied within this work between different buffers.

Zeiss Germany) and further analyzed with the AxioVision software (Rel. 4.6, Zeiss Germany). Part of the NIR laser light was absorbed by the optical components of the microscope set-up. Therefore the laser intensity in the focal plane was determined with a power meter (PM100 display unit with S130A slim sensor, Thorlabs). The NIR laser was completed with a self-constructed shutter system, which allowed control over the excitation of the polyelectrolyte samples. For NIR excitation of the sample a 150 µL drop of medium solution was put on top of the dried polyelectrolyte films. The lens of the water objective immersed this drop and the distance in-between sample and lens was adjusted until the sample was focused. The NIR laser spot was aimed at single Au clusters in the polyelectrolyte samples, which were then exposed by opening the shutter for 1 second (**Figure 2**). Transmission and fluorescence images of the polyelectrolyte layers were taken before and after NIR exposure. Upon NIR exposure of the $(PAH/Au+PSS)_3(PAH/BSA_{FITC}+PSS)_{10}$ samples, part of the polyelectrolyte layers around the excited Au NP cluster had been removed, which appeared as black hole in the green fluorescence channel, and a gas bubble had formed (**Figure 3**). For each experiment the cross-sectional area $A_{cluster}$ of the excited Au NP cluster before excitation, the area of the resulting hole in the polyelectrolyte film $A_{hole,}$ and the cross-section $A_{bubble}$ of the gas bubble after excitation were determined from the recorded transmission and fluorescence images (**Figure 4**). For different experiments the laser power $P_{laser}$ and the medium on top of the polyelectrolyte film were varied.

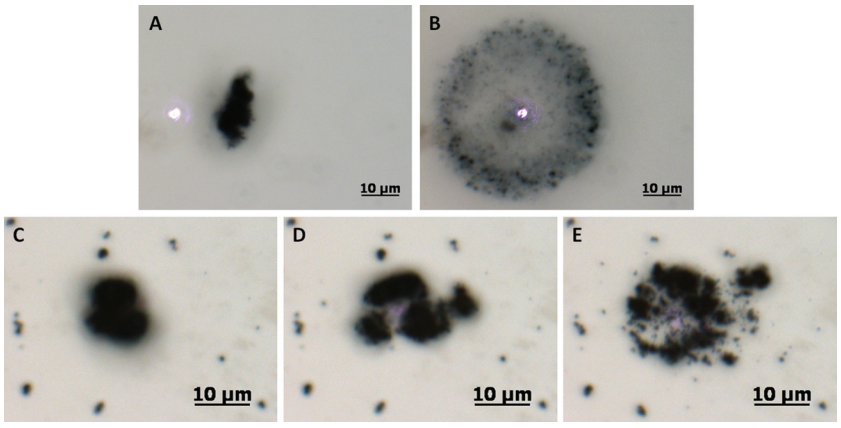


**Figure 2.** Mechanical disintegration of Au NP clusters upon NIR illumination. A) Illumination of a site next to an Au NP cluster leads to no effect. B) When the NIR laser spot ($P_{laser}$ = 10 mW) is aimed at the same Au NP cluster as in (A) the cluster disintegrates mechanically and the Au NPs are spread upon switching on the laser. C–E) In the case of lower laser powers ($P_{laser}$ = 4 mW) illumination of the cluster causes fragmentation of the cluster instead of complete disintegration.

### 2.4. Boiling Point, Surface Tension, and Viscosity Measurements

Basic properties of the medium above the polyelectrolyte film such as boiling point, surface tension, and viscosity were determined.

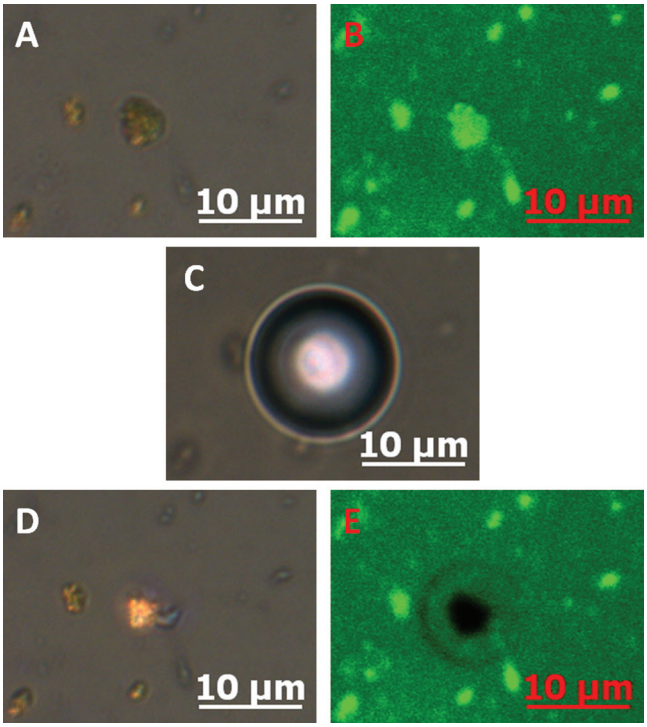


**Figure 3.** A polyelectrolyte film with integrated Au NP clusters (geometry $(PAH/Au+PSS)_3(PAH/BSA_{FITC}+PSS)_{10}$) is shown in A) phase-contrast and B) fluorescence mode as imaged with the objective as in the microscopy set-up shown in Figure 1. Au NP clusters appear brighter compared to the background in the phase-contrast image. The fluorescence originates from the $BSA_{FITC}$ which is integrated into the polymer film. C) Upon excitation for 1 s a vapor bubble appears, which is shown directly after the shutter is closed, where the bubble reached its maximum cross-sectional area. After the bubble has disappeared a hole remains in the polymer film around the excited Au NP cluster, as can be seen in D) phase-contrast and E) fluorescence images. The phase-contrast image suggests that part of the Au NP cluster remain at the original position, whereas the fluorescence image demonstrates that the polyelectrolyte film including the incorporated BSA has been locally removed.

For determination of the boiling point, media were heated on a hot plate while measuring the equilibrated temperature when boiling. In the cases of serum and growth medium a boiling point could not be determined as coagulation occurred before an equilibrated temperature was reached. The surface tension was measured by pulling an aluminum ring, wetted in a sufficient amount of medium, out of the medium.[42] Thereupon a nearly cylindrical thin film of medium was formed in-between the ring and the medium surface. From the applied force at the point where the film collapsed, the surface tension could be calculated. The viscosity was measured following the law of Hagen–Poiseuille.[42] A fixed amount of medium was stored in a reservoir, from where it could run vertically downwards through a thin glass capillary into a collection beaker. From the time until the medium had completely passed through the capillary and the comparison of surface levels in the reservoir and the collection beaker before and after the flow, the viscosity could be calculated.

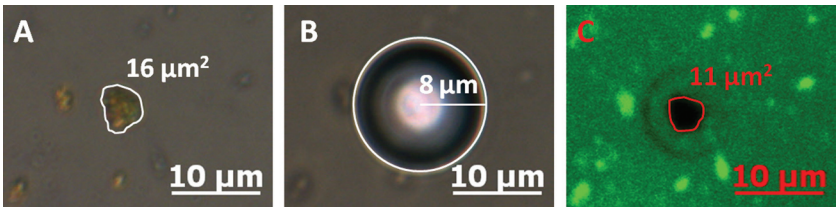


**Figure 4.** From the experimental observations shown in Figure 3 the following parameters are extracted. A) The cross-sectional area $A_{cluster}$ of the excited Au NP cluster before excitation. B) The cross-section $A_{bubble}$ of the gas bubble immediately after excitation, derived from the radius $r_{bubble}$ with $A_{bubble} = \pi \cdot r_{bubble}^2$, and C) the area of the resulting hole in the polyelectrolyte film $A_{hole}$.

### 2.5. Theoretical Modeling

In **Figure 5** we have depicted a simple model to estimate the temperature in our system. First of all, we notice that the laser-beam diameter ($d_{beam} \approx$ µm) is smaller than the typical diameter of Au NP aggregates (≈few µm). For further estimates, we will assume the Au NP cluster diameter to be $d_{cluster}$ = 3–8 µm. A cluster effective dielectric function ($\varepsilon_{eff}$) can be written using the Maxwell–Garnett equation:[43]

$$\varepsilon_{eff} = \varepsilon_0 \frac{\varepsilon_{NP}(1+2\alpha) - \varepsilon_0(2\alpha - 2)}{\varepsilon_0(2+\alpha) + \varepsilon_{NP}(1-\alpha)} \quad (1)$$

where $\varepsilon_{NP}$ and $\varepsilon_0$ are the dielectric functions of metal (the Au NPs) and voids. Voids are filled mostly with surfactant molecules (the citrate capping around the Au NPs) and we assume that $\varepsilon_0 = 2$ (polymer); $\varepsilon_{NP}$ is taken for Au from the tables.[44] In Equation (1), $\alpha$ is a filling factor that will be taken as 0.43 (Au NP spheres have ca. 1 nm surface-to-surface distance due to the citrate capping on the NP surface, which acts as spacer). Since $d_{beam} < d_{cluster}$, an approach of geometric optics can be employed for estimates. Using the above effective dielectric function, we see that clusters with $d_{cluster}$ = 3–8 µm are not transparent to the beam. At an excitation wavelength of 830 nm, the decay length for the light penetrating the effective medium is ≈2 µm. Assuming that the laser beam strikes a flat surface of an effective material (Au NPs and voids), the power absorbed by the cluster will be given by Equation 2:

$$P_{absorbed} = P_{laser} \cdot (1 - R) \quad (2)$$

where $P_{laser}$ is the incident laser power, $R = |\sqrt{\varepsilon_{eff}} - \sqrt{\varepsilon_{med}}|^2 / |\sqrt{\varepsilon_{eff}} + \sqrt{\varepsilon_{med}}|^2$ is the reflection coefficient, and $\varepsilon_{med}$ is a dielectric constant of a medium (Figure 5). Using the above effective-medium approach and taking $\varepsilon_{med}$ = 1.8–2 (water, polymer, or a biological medium), we see that the absorption of light by the cluster is very efficient: $A = (1 - R) \approx 0.95$. Now we look at the thermal part of the problem. A heated cluster is located on a boundary of two media, fluid medium above and glass below (Figure 5). By assuming that the cluster of Au NPs is spherical and located at the boundary of the two media, we write an estimate (Equation 3) for the temperature at the outer surface of a spherical cluster under steady illumination:[13]

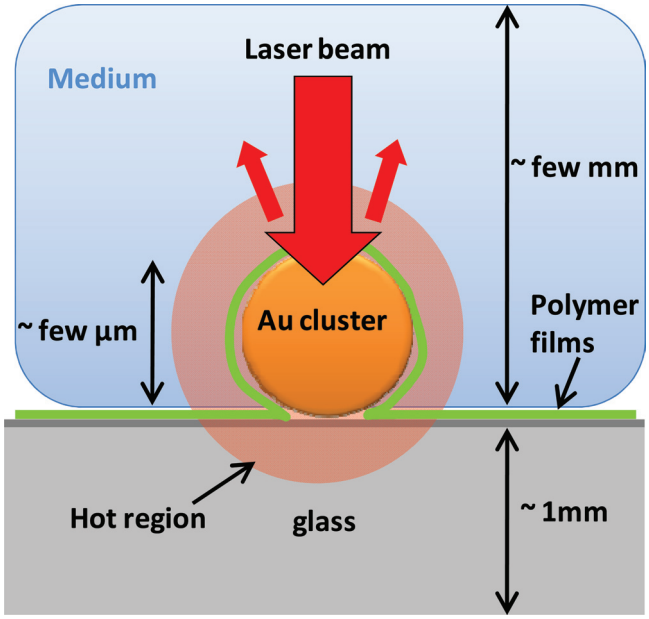


**Figure 5.** Geometry used for the theoretical modeling.

$$T = T_{\text{room}} + \Delta T \approx T_{\text{room}} + \frac{P_{\text{absorbed}}}{2\pi k_{\text{av}} d_{\text{cluster}}} = T_{\text{room}} + \frac{P_{\text{laser}}\ (1 - R)}{2\pi k_{\text{av}} d_{\text{cluster}}} \tag{3}$$

where $k_{\text{av}} = (k_{\text{glass}} + k_{\text{med}})/2$ is an averaged thermal conductivity of the neighboring media. Typical numbers for thermal materials parameters are the following: $k_{\text{glass}} \approx 1$ W mk$^{-1}$ and $k_{\text{med}} \approx k_{\text{water}} = 0.6$ W mk$^{-1}$. We note that the above approximation for $k_{\text{med}}$ is quite reliable for many biological media.[45] Then, we obtain the following numerical result (Equation 4) for the temperature at the outer surface of the Au NP cluster:

$$T = 20\,^{\circ}\text{C} + 189\,^{\circ}\text{C}\frac{P_{\text{laser [mW]}}}{d_{\text{cluster [µm]}}} \tag{4}$$

where $P_{\text{laser}}$ [mW] is the incident power in mW and $d_{\text{cluster}}$ [µm] is the diameter of an Au NP cluster in µm.

## 3. Results and Discussion

### 3.1. Mechanical Manipulation of Au NP Clusters upon Excitation

Optical excitation of Au NPs leads to heating of the particles and imposes momentum by means of an optical force.[41,46,47] Hereby resonant and off-resonant excitation has to be distinguished. As we used Au NP clusters instead of single Au NPs in the present study, a sharp plasmon resonance frequency as present for single particles no longer existed. Due to the broad absorption band[48] which also contains the applied laser wavelength, both effects (heat generation and translational motion) have to be considered as being responsible for the following effects. In Figure 2 excitation of one Au NP cluster (without being embedded in a polyelectrolyte film) is demonstrated. Note that NIR excitation was at 830 nm, whereas the surface plasmon resonance of individual Au NPs (diameter: 15 nm) is at 520 nm. Light is absorbed only due to the fact that the Au NPs have been aggregated into clusters (Figure SI.4, Supporting Information). As can be seen in Figure 2 the excitation of Au NP clusters led to a mechanical explosion of the clusters. This effect depended on the excitation power $P_{\text{laser}}$. Mechanical disintegration of clusters was observed at rather high powers (ca. 10 mW). For lower powers (≤4 mW) this effect decreased. Instead of complete disintegration, clusters were rather split into fragments. No effect was typically observed for powers smaller than 2 mW or when the laser was applied to a site where no cluster was present.

### 3.2. Local Disintegration of Polyelectrolyte Films upon Heating of Embedded Au NP Clusters

Optical excitation of Au NP clusters immobilized in polyelectrolyte films caused local destruction of the polyelectrolyte films mediated by disintegration/fragmentaion of the Au NP clusters, see Figure 3. In the following all experiments refer to the geometry $(\text{PAH/Au+PSS})_3(\text{PAH/BSA}_{\text{FITC}}\text{+PSS})_{10}$ of the polyelectrolyte multilayers. Optical excitation of an Au NP cluster with water as medium on top of the polyelectrolyte film caused the formation of a vapor bubble which stayed localized at the cluster site and decreased with time, as well as creating a remaining black hole in the green fluorescent polymer film around the heated cluster. For other media these observations could be different as, for example, in the case of using growth medium or serum on top of the polyelectrolyte film, when almost no bubbles could be observed. In Figure 4 the three parameters which were extracted out of each excitation experiment are depicted: The cross-sectional area $A_{\text{cluster}}$ of the Au NP cluster before it had been excited, the cross-section $A_{\text{bubble}}$ of the gas bubble which had been formed during excitation, and the area $A_{\text{hole}}$ of the resulting hole in the fluorescent polyelectrolyte film. It has to be pointed out that quantification of these experimental parameters was not always straightforward. Only spherical objects were interpreted as a bubble whereas non-spherical moving structures at the border of a cluster during an excitation might have been caused by mechanical interference of debris of the locally destroyed polyelectrolyte film. Heating of Au NP clusters is a cooperative effect and generated heat strongly depends on the cluster size.[16] The bigger the Au NP cluster the more thermal energy is locally produced,; this induces bigger bubbles and holes in the poylmer film. We thus normalized the cross-section of the bubbles and the size of the hole in the polymer film to the size of the excited Au NP cluster: $A_{\text{bubble}}/A_{\text{cluster}}$, $A_{\text{hole}}/A_{\text{cluster}}$. Phenomenological data show that the polyelectrolyte films were efficiently effected by optical excitation of the integrated Au NP clusters. The shape of the disturbed area, i.e., the hole in the polymer film, was mostly determined by the shape of the Au NP cluster before excitation. An often-seen phenomenon was the formation of a green border of greater fluorescence around the black hole after excitation, which indicated that film material had been mechanically pushed away (Figure SI.13, Supporting Information). In many other cases the black hole was surrounded by another ring of

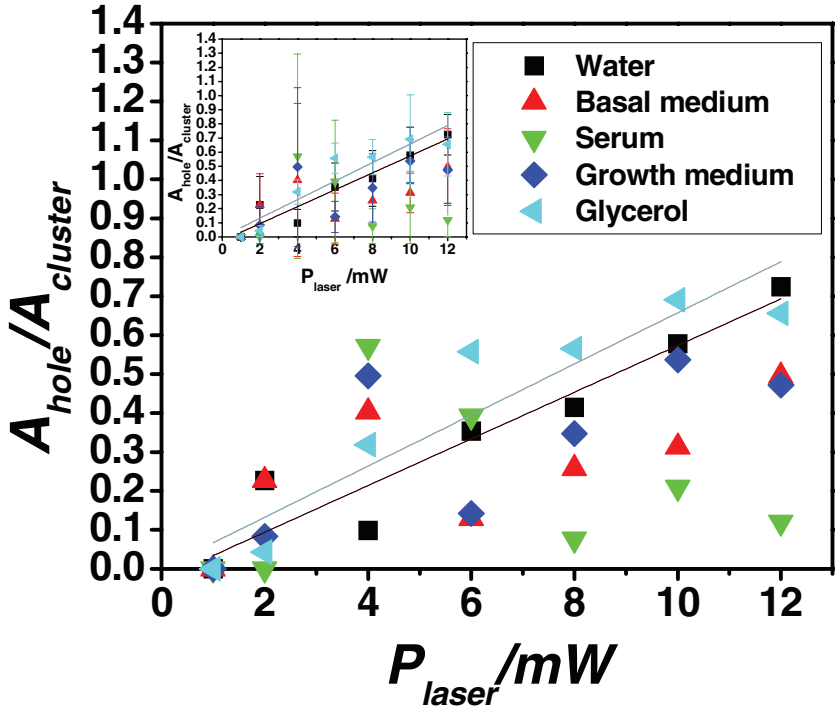


**Figure 6.** $A_{hole}$, normalized to $A_{cluster}$, is plotted $P_{laser}$ which had been focused to the Au NP cluster for 1 s for excitation of the Au NPs, cf. Figure 4. Experiments were performed with different media on top of the polyelectrolyte films: water, basal medium, serum, growth medium, and glycerol. The linear fits serve as guides to the eye indicating the trend observed for water and glycerol. Error bars are shown in the inset.

lower fluorescence (Figure 3E). We can only estimate that this ring originates from the boundary of a vapor bubble at the polyelectrolyte surface. Controls made by optically exciting areas of the polymer films in which no Au NP cluster was found did not result in the formation of a hole in the film and no bubbles could be observed. Therefore the effects are related to the presence of Au NP clusters and we can exclude that the black holes originated from bleaching of the FITC in the polymer film. The size of the hole depended on the laser power. In the case of water on top of the polyelectrolyte film it was found that the black hole area as well as the bubble cross-section increased almost linearly with the applied laser power, except for at lower powers ($P_{laser} \leq 4$ mW). Films might be destroyed either by melting of the polyelectrolytes, by mechanical force imposed by the disintegrating expanding Au NP clusters, or by mechanical stress upon the bubble formation, which will be discussed in more detail later on.

### 3.3. Analysis of the Creation of a Hole in the Polymer Film at Locations of Optically Excited Au NP Clusters

In the following an excitation series with water, basal medium, serum, growth medium, and glycerol as medium on top of the polymer film is discussed. The area of the black hole (normalized to the Au NP cluster size) $A_{hole}/A_{cluster}$ as created at the illuminated Au NP cluster (1 s excitation) is plotted versus $P_{laser}$ (Figure 4 and **Figure 6**). As the borders of the black holes were barely visible at low illumination powers and for the glycerol- and serum-containing media, experiments were repeated several times to get meaningful mean values. For water and glycerol a clear trend towards bigger holes upon increasing laser power can be observed. In the case of glycerol the borders around the black hole in the polymer film appeared in bright green in the fluorescence channel, which indicates the presence of $BSA_{FITC}$-labeled polymer material originating from the area from which the polymer had been removed. In the other media (basal medium, growth medium, serum) no direct correlation between the size of the hole in the polymer film and the laser power was obvious.

### 3.4. Analysis of the Creation of a Bubble Adjacent to Optically Excited Au NP Clusters

In the case of water, excitation of an Au NP cluster with laser powers above 4 mW always resulted in the formation of a bubble adjacent to the cluster. This formation was also observed with water which had been degassed prior to experiments. In the case of basal medium only in some cases bubbles appeared, which resulted in a smaller mean bubble size (the mean value also comprises the results in which no bubble had formed, i.e., with bubble size 0). Within the standard deviation for water and basal medium one can conclude that an almost constant bubble size was present for various laser powers (6–12 mW) (**Figure 7**A). For lower laser powers below 4 mW the bubble size decreased rapidly to zero. Considering the probability $n_{bubble}$ with which bubbles appeared upon illumination (Figure 7B) one can describe the result for water as "all-or-nothing-response" with a threshold of around 4 mW, as for powers above 4 mW a bubble arose during each excitation ($n_{bubble} = 1$), whereas at 2 mW no more bubbles could be observed ($n_{bubble} = 0$). For basal medium a bubble probability of ca. 20% was found between 4 mW and 12 mW. For the rest of the media no bubbles were created upon excitation of the Au NP clusters (Figure 7B). As basal medium contains around 150 mM of various salts (mainly NaCl) we speculated that differences in bubble appearance upon excitation of Au NP clusters might be influenced by ion concentration in the medium. Presence of ions screens the negative charges on the surface of Au NPs and of the polyelectrolytes which could change the geometry in the Au NP clusters (such as the average Au NP–Au NP distance). For this purpose a series of excitation of polymer films with Au NP clusters with water with variable NaCl concentration in the medium was performed (Figure 7C). Clearly the average bubble size decreased upon increasing NaCl concentration. At $P_{laser} = 12$ mW no bubbles could be observed anymore when the NaCl concentration has been increased to 1 M. However, the concentration of various salts (mainly NaCl) in

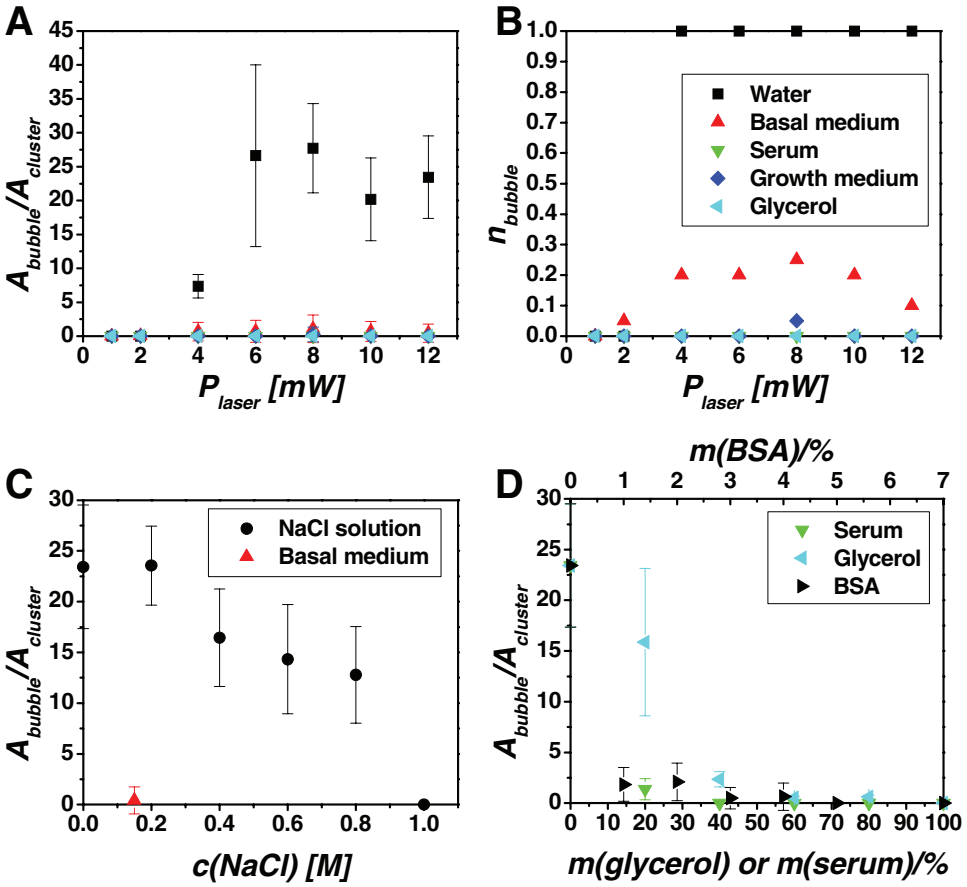


**Figure 7.** A) $A_{bubble}$, normalized to $A_{cluster}$, is plotted versus $P_{laser}$, which had been focused to the Au NP cluster for 1 s for excitation of the Au NPs, cf. Figure 4. Data points correspond to the same experiments as reported in Figure 6. Experiments were performed with different media on top of the polyelectrolyte films: water, basal medium, serum, growth medium, and glycerol (legend is the same as in (B)). In the cases where no bubble appeared $A_{bubble}$ was taken as zero. As in the case of basal medium only sometimes bubbles appeared (cf. (B)) the mean bubble size is much smaller than is the case with water. B) As can be seen in (A), for several media bubbles barely occurred (i.e., $A_{bubble} = 0$). For this reason in (B) $n_{bubble}$ is plotted for different media and excitation powers. $n_{bubble} = 1$ would refer to a situation in which in each case of illumination a bubble had appeared, and $n_{bubble} = 0$ to the case where in no case of illumination any bubble had appeared. C) The same experiment as described in (A) was performed, but with NaCl solution of different concentrations $c_{NaCl}$ on top of the polyelectrolyte film. For all excitations we used $P_{laser} = 12$ mW. As reference also basal medium (with a salt concentration of 0.15 M) was used. D) The same experiment as described in (A) was performed, but with water as medium, to which variable amounts (in percent mass) of BSA, glycerol, or serum had been added. For all excitations we used $P_{laser} = 12$ mW. Comparable contents of proteins in the medium led to comparable average bubble sizes. The axes represent the assumption that serum is composed of 7% proteins.

basal medium, where only bubbles with a small average size appear, is only 150 mM. In contrast the frequency of bubble formation in water with 150 mM NaCl is at best slightly reduced. Though basal medium also comprises some other ions besides $Na^+$ and $Cl^-$ at lower concentration (also divalent ones) the data presented in Figure 7C indicate that presence of salt is not the predominant factor which hinders formation of bubbles upon optical excitation of Au NP clusters. We suppose that bubbles arise upon superheating around excited Au NP clusters, whereby the medium is heated to a temperature higher than its boiling point. For this to happen the medium has to be free of nucleation sites. In case of pure Milli-Q water nucleation sites may be rare enough, which leads the water to form a metastable "superheated" state, and finally causes an explosionlike vaporization. In media containing more "ingredients," more nucleation sites may be present to prevent superheating and thus avoid the explosive appearance of vapor bubbles. Especially in the case of serum, the content of proteins might suppress the appearance of vapor bubbles because there are sufficient nucleation sites on the one hand and locally coagulating material on the other. Therefore another excitation series was performed to verify the influence of protein content in the medium (Figure 7D). Aqueous mixtures of bovine serum albumin (BSA) and serum served as medium and the same trend could be observed considering the normalized bubble size. The axes were chosen like this as serum is supposed to be composed of 7% from proteins (100% serum $\wedge_=$ 7% BSA). When considering glycerol, which was taken as a viscous medium for comparison, one observes that increasing viscosity might not be the crucial factor for a decreased average bubble size. To further elucidate the role of the medium for bubble formation we performed similar excitation experiments with Au NP clusters in polymer films with additional media (**Figure 8**). The media were selected to allow understanding of how parameters like boiling

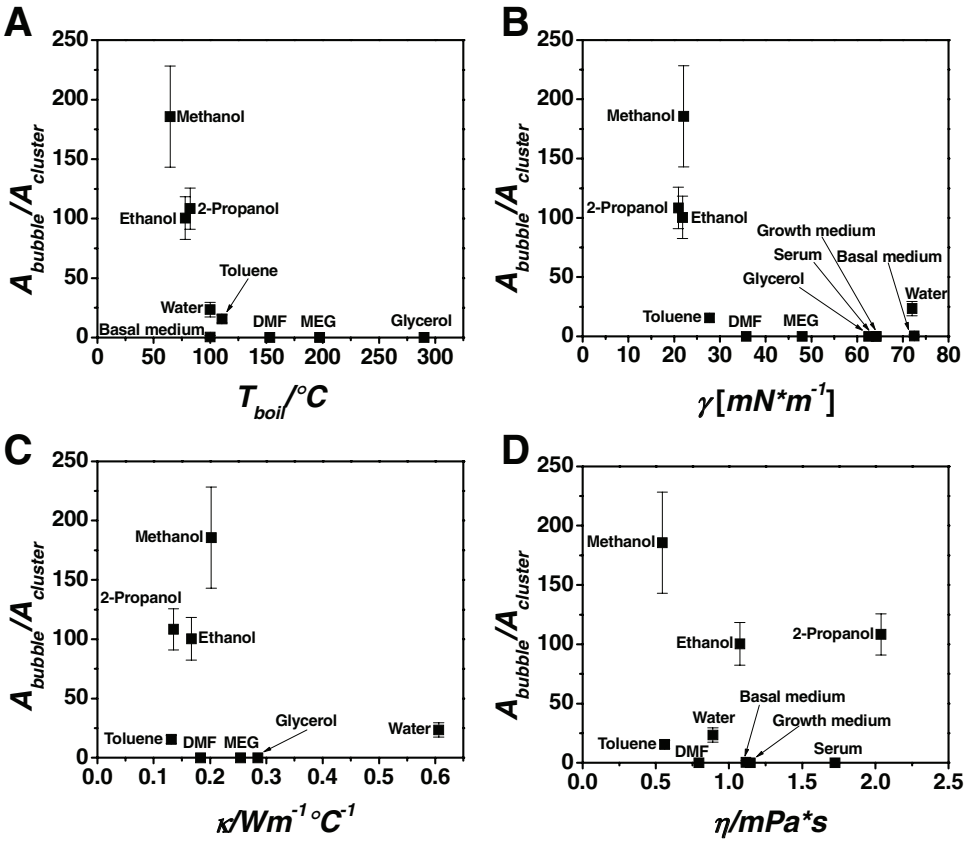


**Figure 8.** $A_{bubble}$ upon laser illumination, normalized to $A_{cluster}$, is plotted versus A) $T_{boil}$, B) $\gamma$ at 25 °C, C) $\kappa$, and D) $\eta$ of different media on top of the polyelectrolyte film. Au NP clusters were hereby illuminated with $P_{laser} = 12$ mW for 1 s, cf. Figure 4. Experiments were performed with different media on top of the polyelectrolyte films: water, methanol, ethanol, 2-propanol, toluene, DMF, MEG, glycerol, basal medium, serum, and growth medium. In the case of serum and growth medium (which contains 10% serum) no boiling point could be determined, as the proteins in solution coagulated upon heating. Also the thermal conductivity was not determined for these two media. In (D) glycerol and MEG are not displayed for clarity due to their high $\eta$ values.

point $T_{boil}$, surface tension $\gamma$, thermal conductivity $\kappa$, and viscosity $\eta$ influence the formation of vapor bubbles. As supposed, superheating might be the reason for the appearance of bubbles as the dependence on the boiling point leads to a clear trend for different media with a threshold of $T_{boil}$ between 110 °C and 150 °C (Figure 8A). No bubbles could be observed above a boiling point of 150 °C. This result, however, does not automatically mean that for these media the boiling point is not reached, as thermal energy is permanently transported away from the Au NP cluster, which may avoid local superheating. Basal medium, however, has a boiling point below the indicated threshold, so here another explanation has to be found. Indeed the impurity of media (salt and other contents) might be the crucial parameter as discussed below. In Figure 8C the dependence of bubble formation on the thermal conductivity of the medium (which is the parameter which quantifies the heat transportation capability) is plotted. $\kappa$ is of the same order of magnitude (0.1 – 0.3 $W \cdot K^{-1} \cdot m^{-1}$) for all media except water. However, no clear trend can be observed in the bubble size versus thermal conductivity relation. At any rate, low thermal conductivity seems to be beneficial for local superheating if the boiling point is low enough. The dependence of the bubble size on the surface tension of the medium is shown in Figure 8B. For most media the surface tension increases almost linearly with the boiling point, which results in a comparable profile: decreasing bubble size with increasing surface tension, similar to decreasing bubble size with increasing boiling point. Water, however, does not fit in this scheme. Water has a rather high surface tension due to its high polarity and exhibits strong molecular interaction. No dependence of the bubble size on the viscosity of the medium was found (Figure 8D). This result leaves the boiling point of the medium as the most influential parameter for bubble size upon local optical excitation of Au NP clusters, but it does not, however, explain the fact that addition of salt reduces formation of bubbles as addition of salt (e.g., NaCl) leads to an increase in $T_{boil}$ that is still below the found threshold in Figure 8A. By following Raoult's law together with the Clausius–Clapeyron equation, the extent of boiling point elevation can be calculated to be $\Delta T_{boil} \approx 6.3$ °C for a concentration of 6.14 M, which corresponds to the maximum solubility of NaCl in water. As discussed above, the addition of salt could affect the geometry of the polymer layers and the Au NP clusters. Salt could reduce the interparticle distance in the Au NP clusters, which, however, should lead to more bubbles upon increased NaCl concentration (there is more heat generation among closely spaced NPs[16]), which is in contrast to the

experimental data. Thus, as Au NPs had been agglomerated to clusters before incorporation in the polyelectrolyte films, the addition of more salt may not induce more agglomeration. However, salt may also affect the layer geometry. Salt can affect the charged sites of the layers, such that the competitive ion pairing between the oppositely charged layers and the respective counterion reduces the binding force between layers.[49] Thus permeability for molecules out of the layers could be higher when salt is present,[50] which might increase the content of nucleation sites above the LbL film. As the influence of salt still does not explain the results obtained with serum-containing media still another effect must play a role. Proteins in serum containing medium coagulate before the boiling point of the medium is reached. Coagulated proteins could act as further nucleation sites, which would thus prevent superheating and the formation of big gas bubbles.

### 3.5. Results of Theoretical Modeling

With Equation (4) from the theoretical model we now can estimate the cluster surface temperature for clusters with $d_{cluster}$ = 3–8 μm. We now see that the temperature achieves 100 °C for the following laser powers $P_{laser}$: 1.3 ($d_{cluster}$ = 3 μm) and 3.4 mW ($d_{cluster}$ = 8 μm). Active boiling of water in the experiments starts at ca. 4 mW (Figure 7). This power corresponds to ca. 114 °C ($d_{cluster}$ = 8 μm) and ca. 270 °C ($d_{cluster}$ = 3 μm). The above numbers for the temperature are greater than 100 °C which is not surprising since it is expected that the boiling process starts under the superheated conditions.[38] We therefore see that our simple model for the local temperature gives numbers that are in reasonable agreement with the experimental findings. Finally, we comment that the formation of holes in the polymer film in our experiments begins at $P_{laser} \approx 2$ mW. The above temperature estimates are actually valid for the maximum temperature outside the polymer film, at the water–polymer boundary. For a spherical heated object under steady-state conditions (i.e., under continuous illumination) the temperature outside Equation (3) is given by the total power generated ($P_{absorbed}$) and by the thermal conductivity ($k_{av}$) of the surrounding matrix. Note that Equation (3) does not include the thermal conductivity of the polymer film. The temperature inside the polymer and the Au NP cluster can be higher since the polymer film can create a thermal barrier for heat flow. Indeed, polymer films may have a poor thermal conductivity that will result in a strong overheating effect and in destruction of the polymer film at relatively low laser powers.

## 4. Conclusions

Light-induced heating of polymer-matrix-embedded Au NP clusters in complex media is influenced by several parameters. The formation of a gas bubble of evaporated medium is directly connected to the boiling point of the medium. Salt in the medium may affect the geometry of the polymer matrix leading to reduced gas-bubble sizes. Most important, complex media involving, for example, proteins also reduce formation of gas bubbles, which is speculated to be due to an increased number of nucleation sites which prevent superheating. These results are of great importance to biologically motivated release experiments. For light-triggered release of molecules from polymer films bubble suppression would be welcome as this would reduce mechanical stress. Bubble formation upon heating inside cells could, for example, kill cells.[24] We believe that experiments in this area are positively influenced by the fact that protein-containing media are present inside cells. This study thus helps to optimize the experimental conditions (for example laser power versus Au NP cluster size) for such biologically related release experiments (as, for example, drug delivery) in cells.

## Supporting Information

Supporting Information is available from the Wiley Online Library or from the author.

## Acknowledgements

This work was supported by the BMBF (Eranet grant Nanosyn) to WJP. The authors are grateful to Dr. Miguel A. Correa-Duarte for inspiring technical discussions.

Received: May 19, 2011
Revised: October 4, 2011
Published online: November 17, 2011

[1] C. M. Cobley, J. Y. Chen, E. C. Cho, L. V. Wang, Y. N. Xia, *Chem. Soc. Rev.* **2011**, *40*, 44.
[2] P. K. Jain, I. H. El-Sayed, M. A. El-Sayed, *Nano Today* **2007**, *2*, 18.
[3] P. K. Jain, X. Huang, I. H. El-Sayed, M. A. El-Sayad, *Plasmonics* **2007**, *2*, 107.
[4] R. A. Sperling, P. Rivera_Gil, F. Zhang, M. Zanella, W. J. Parak, *Chem. Soc. Rev.* **2008**, *37*, 1896.
[5] J. Perez-Juste, I. Pastoriza-Santos, L. M. Liz-Marzan, P. Mulvaney, *Coord. Chem. Rev.* **2005**, *249*, 1870.
[6] A. C. Templeton, J. J. Pietron, R. W. Murray, P. Mulvaney, *J. Phys. Chem. B* **2000**, *104*, 564.
[7] M. A. Correa-Duarte, N. Sobal, L. M. Liz-Marzan, M. Giersig, *Adv. Mater.* **2004**, *16*, 2179.
[8] V. Salgueirino-Maceira, F. Caruso, L. M. Liz-Marzan, *J. Phys. Chem. B* **2003**, *107*, 10990.
[9] P. K. Jain, W. Qian, M. A. El-Sayed, *J. Phys. Chem. B* **2006**, *110*, 136.
[10] A. O. Govorov, H. H. Richardson, *Nano Today* **2007**, *2*, 30.
[11] G. Baffou, R. Quidant, C. Girard, *Appl. Phys. Lett.* **2009**, *94*, 153109.
[12] J. Zhu, Z. Sun, J. J. Li, J. W. Zhao, *Eur. Phys. J. B* **2010**, *78*, 311.
[13] A. O. Govorov, W. Zhang, T. Skeini, H. Richardson, J. Lee, N. A. Kotov, *Nanoscale Res. Lett.* **2006**, *1*, 84.
[14] H. H. Richardson, Z. N. Hickman, A. O. Govorov, A. C. Thomas, W. Zhang, M. E. Kordesch, *Nano Lett.* **2006**, *6*, 783.
[15] H. H. Richardson, M. T. Carlson, P. J. Tandler, P. Hernandez, A. O. Govorov, *Nano Lett.* **2009**, *9*, 1139.
[16] C. Hrelescu, J. Stehr, M. Ringler, R. A. Sperling, W. J. Parak, T. A. Klar, J. Feldmann, *J. Phys. Chem. C* **2010**, *114*, 7401.
[17] L. R. Hirsch, R. J. Stafford, J. A. Bankson, S. R. Sershen, B. Rivera, R. E. Price, J. D. Hazle, N. J. Halas, J. L. West, *Proc. Natl. Acad. Sci. U. S. A.* **2003**, *100*, 13549.
[18] D. P. O'Neal, L. R. Hirsch, N. J. Halas, J. D. Payne, J. L. West, *Cancer Lett.* **2004**, *209*, 171.

[19] X. Huang, P. Jain, I. El-Sayed, M. El-Sayed, *Lasers in Medical Science* **2007**, *23*, 217.
[20] X. Huang, I. H. El-Sayed, W. Qian, M. A. El-Sayed, *J. Am. Chem. Soc.* **2006**, *128*, 2115.
[21] B. Radt, T. A. Smith, F. Caruso, *Adv. Mater.* **2004**, *16*, 2184.
[22] A. G. Skirtach, C. Dejugnat, D. Braun, A. S. Susha, W. J. Parak, H. Möhwald, G. B. Sukhorukov, *Nano Lett.* **2005**, *5*, 1371.
[23] A. G. Skirtach, A. M. Javier, O. Kreft, K. Köhler, A. P. Alberola, H. Möhwald, W. J. Parak, G. B. Sukhorukov, *Angew. Chem. Int. Ed.* **2006**, *45*, 4612.
[24] A. Muñoz_Javier, P. d. Pino, M. Bedard, A. G. Skirtach, D. Ho, G. Sukhorukov, C. Plank, W. J. Parak, *Langmuir* **2009**, *24*, 12517.
[25] E. V. Skorb, A. G. Skirtach, D. V. Sviridov, D. G. Shchukin, H. Mohwald, *ACS Nano* **2009**, *3*, 1753.
[26] D. V. Volodkin, N. Madaboosi, J. Blacklock, A. G. Skirtach, H. Mohwald, *Langmuir* **2009**, *25*, 14037.
[27] J. Stehr, C. Hrelescu, R. A. Sperling, G. Raschke, M. Wunderlich, A. Nichtl, D. Heindl, K. Kürzinger, W. J. Parak, T. A. Klar, J. Feldmann, *Nano Lett.* **2008**, *8*, 619.
[28] M. J. Kogan, N. G. Bastus, R. Amigo, D. Grillo-Bosch, E. Araya, A. Turiel, A. Labarta, E. Giralt, V. F. Puntes, *Nano Lett.* **2006**, *6*, 110.
[29] N. G. Bastus, M. J. Kogan, R. Amigo, D. Grillo-Bosch, E. Araya, A. Turiel, A. Labarta, E. Giralt, V. F. Puntes, *Mater. Sci. Eng. C* **2007**, *27*, 1236.
[30] A. M. Gobin, D. P. O'Neal, D. M. Watkins, N. J. Halas, R. A. Drezek, J. L. West, *Lasers Surg. Med.* **2005**, *37*, 123.
[31] Z. Krpetic, P. Nativo, V. See, I. A. Prior, M. Brust, M. Volk, *Nano Lett.* **2010**, *10*, 4549.
[32] M. M. Alvarez, J. T. Khoury, T. G. Schaaff, M. N. Shafigullin, I. Vezmar, R. L. Whetten, *J. Phys. Chem. B* **1997**, *101*, 3706.
[33] S. Link, M. A. El-Sayed, *J. Phys. Chem. B* **1999**, *103*, 4212.
[34] P. K. Jain, K. S. Lee, I. H. El-Sayed, M. A. El-Sayed, *J. Phys. Chem. B* **2006**, *110*, 7238.
[35] B. Palpant, Y. Guillet, M. Rashidi-Huyeh, D. Prot, *Gold Bull.* **2008**, *41*, 105.
[36] D. Lapotko, *Int. J. Heat Mass Transfer* **2009**, *52*, 1540.
[37] L. Francois, M. Mostafavi, J. Belloni, J. A. Delaire, *Phys. Chem. Chem. Phys.* **2001**, *3*, 4965.
[38] V. Kotaidis, C. Dahmen, G. v. Plessen, F. Springer, A. Plech, *J. Chem. Phys.* **2006**, *124*, 1.
[39] G. Decher, B. Lehr, K. Lowack, Y. Lvov, J. Schmitt, *Biosens. Bioelectron.* **1994**, *9*, 677.
[40] G. Decher, *Science* **1997**, *277*, 1232.
[41] A. S. Urban, A. A. Lutich, F. D. Stefani, J. Feldmann, *Nano Lett.* **2010**, *10*, 4794.
[42] W. Walcher, in *Praktikum der Physik*, 9th ed., Vieweg&Teubner, Wiesbaden, Germany **2009**.
[43] T. C. Choy, in *Effective Medium Theory: Principles and Applications*, Oxford University Press, Oxford, **1999**.
[44] E. D. Palik, in *Handbook of Optical Constants of Solids*, Academic Press, New York, **1985**.
[45] A. J. Welch, M. J. C. van Gemert, in *Optical-Thermal Response of Laser-Irradiated Tissue*, Plenum Press, New York **1995**.
[46] M. J. Guffey, N. F. Scherer, *Nano Lett.* **2010**, *10*, 4302.
[47] M. Schwagler, C. Nowak, J. Hoffmann, W. Schartl, *J. Phys. Chem. C* **2009**, *113*, 15124.
[48] M. F. Bedard, D. Braun, G. B. Sukhorukov, A. G. Skirtach, *ACS Nano* **2008**, *2*, 1807.
[49] S. T. Dubas, J. B. Schlenoff, *Macromolecules* **1999**, *32*, 8153.
[50] G. Ibarz, L. Dähne, E. Donath, H. Möhwald, *Adv. Mater.* **2001**, *13*, 1324.
[51] G. Decher, J. Schlenoff, in *Multilayer Thin Films: Sequential Assembly of Nanocomposite Materials*, 1st ed., Wiley VCH, Weinheim, **2002**.

JOURNAL OF NANOBIOTECHNOLOGY

RESEARCH Open Access

# Light triggered detection of aminophenyl phosphate with a quantum dot based enzyme electrode

Waqas Khalid[1], Gero Göbel[2], Dominik Hühn[1], Jose-Maria Montenegro[1], Pilar Rivera-Gil[1], Fred Lisdat[2] and Wolfgang J Parak[1*]

**Abstract**

An electrochemical sensor for *p*-aminophenyl phosphate (*p*APP) is reported. It is based on the electrochemical conversion of 4-aminophenol (4AP) at a quantum dot (QD) modified electrode under illumination. Without illumination no electron transfer and thus no oxidation of 4AP can occur. *p*APP as substrate is converted by the enzyme alkaline phosphatase (ALP) to generate 4AP as a product. The QDs are coupled via 1,4-benzenedithiol (BDT) linkage to the surface of a gold electrode and thus allow potential-controlled photocurrent generation. The photocurrent is modified by the enzyme reaction providing access to the substrate detection. In order to develop a photobioelectrochemical sensor the enzyme is immobilized on top of the photo-switchable layer of the QDs. Immobilization of ALP is required for the potential possibility of spatially resolved measurements. Geometries with immobilized ALP are compared versus having the ALP in solution. Data indicate that functional immobilization with layer-by-layer assembly is possible. Enzymatic activity of ALP and thus the photocurrent can be described by Michaelis- Menten kinetics. *p*APP is detected as proof of principle investigation within the range of 25 μM - 1 mM.

## Introduction

Colloidal quantum dots (QDs), which are fluorescent semiconductor nanoparticles, have recently brought impact to various disciplines, as has been highlighted in various review articles [1-5]. QDs have been recently discussed also as new building blocks for the construction of electrochemical sensors [6-12]. Upon optical illumination (below the wavelength of the first exciton peak QDs have a a continuous absorption spectrum, with a local maximum at the exciton peak [13]) electron hole pairs are generated inside QDs. Due to these charge carriers electrons can be transferred to or from the QDs. QDs thus can be oxidized/reduced and can serve as light-controlled redox active element and can be integrated in electrochemical signal chains [9,14-16]. The key advantage hereby is that the redox reaction of the QD surface can be virtually switched on and off by light. QD have been also used as elements of signal transduction of enzymatic reactions [17,18].

In the present work we wanted to apply QDs as light-controlled redox active element for the enzymatic detection of *p*-aminophenyl phosphate (*p*APP) with alkaline phosphatase (ALP). ALP is a widely used enzyme in bioanalysis as it has a high turnover rate and broad substrate specificity [19]. The enzyme is particularly interesting as label for immunoassays [20,21]. Very sensitive substrate recycling schemes have been also reported [22,23]. Four different groups of substrates are known for ALP: i) ß-glycerophosphate and hexose phosphate [24-26], ii) phenyl phosphate [27,28] and ß-naphthyl phosphate [29], iii) *p*-nitrophenyl phosphate [30] and phenolphthalein diphosphate [31,32], 4-methyl-umbellipheryl phosphate [33] and *p*-aminophenyl phosphate (*p*APP) [34], and iv) phosphoenol pyruvate [35]. Electrochemical detection has been reported for a number of ALP substrates [36,37], in particular for phenyl phosphate. However, *p*APP is claimed to be a better substrate for ALP than phenyl phosphate, as its product 4-aminophenol (4AP) is more easily oxidizable than phenol, which is the product of phenyl phosphate, as it does not foul the electrode even at higher concentrations, and as it has a rather

* Correspondence: wolfgang.parak@physik.uni-marburg.de
[1]Fachbereich Physik and WZMW, Philipps Universität Marburg, Germany
Full list of author information is available at the end of the article

reversible electrochemical behavior [34]. For this reason we chose *p*APP as substrate in the present study. Readout of the enzymatic reaction was performed with the QD-modified electrode [6]. We hereby put particular interest in the way of immobilization of ALP on the electrode. In previous work the enzymes were suspended in the solution above the sensor electrode [6,9]. Here we go a step further and directly immobilize the enzyme on the QD-modified electrode. This was done in order to investigate whether a specific enzymatic reaction can be coupled with a photoinitiated reaction at a QD modified electrode in a way that the recognition element is integrated with the transducer. The potential advantage of light-triggered detection would be the possibility of spatially resolved detection [38-41]. Only at the illuminated parts of the electrode a photocurrent signal is induced. By having different enzymes immobilized at different regions of the electrode they could be selectively addressed by illumination. Thus, two key elements of this study are the following. First, instead of using enzymes in solution as in previous studies we demonstrate that enzymatic reactions can also be followed when enzymes are immobilized on the sensor surface, which is a requirement for potential spatially resolved analysis. Second, we investigate how the way of immobilization influences the sensing properties.

## Materials and Methods

Materials: CdS QDs were grown via thermal decomposition of precursors under the presence of organic surfactant molecules following published procedures [42]. 1,4-benzenedithiol (BDT) was purchased from TCI Europe, Belgium. Chloroform, toluene, methanol, acetone, ethanol, sodium sulfide (nanohydrate), alkaline phosphatase (from bovine intestinal mucosa type VII S), 4-nitrophenyl phosphate disodium hexahydrate, 4-aminophenol (4AP), phosphate buffer, sodium poly(styrene sulfonate) (PSS, $M_w$ = 56,000), poly(allylamine hydrochloride) (PAH, $M_w$ = 70,000), and potassium ferri/ferro cyanide were purchased from Sigma Aldrich and used without further purification. All aqueous solutions were prepared using 18 MΩ ultra purified water. The electrochemical measurement cells and electronics have been described in a previous publication [43] and comprised a home built potentiostat, an Ag/AgCl reference electrode (#MF 2078 RE-6 from BASi, UK), and a lock-in amplifier (EG&G Princeton Applied Research model # 5210). Illumination was done with a xenon lamp (PTI model A-1010 arc lamp housing, UXL-75XE Xenon Lamp from USHIO, powered by PTI LPS-220) modulated by an optical chopper (Scitec instruments).

Immobilization of QDs: CdS QDs were immobilized on top of gold electrodes following a previously published protocol [43], cfg. Figure 1. First, the gold electrodes (Au film evaporated on glass chips) were cleaned by sonication toluene for five minutes. For cleaning the cyclic voltammetry (CV) of the gold electrode was performed in 1 M NaOH for 20 minutes within the potential limits of -0.8 V < U < +0.2 V, and later in 0.5 M $H_2SO_4$ for 30 minutes within the potential limits of -0.2 V < U < 1.6 V (the CV curves are shown in Additional File 1). After cleaning, the gold electrodes were placed in a solution of 50 mM BDT dissolved in toluene for 24 hours. This resulted in a self assembled monolayer of BDT on the gold surface due to formation of thiol-gold bonds. In the next step CdS QDs dissolved in toluene (typically with a first exciton peak around 380 nm, concentration around 140 μM) were spin coated at a speed of 6000 rpm on top of the BDT coated gold electrodes. After spin coating the gold electrodes were rinsed twice with toluene to remove the excess of QDs.

Confirmation of QDs immobilization: Immobilization of CdS QDs on top of the Au electrodes was performed with current measurements. CVs were recorded before and after immobilization of BDT and QDs on top of gold electrodes with $Fe^{3+}/Fe^{2+}$ as redox couple in solution [43]. While on bare gold electrodes the typical oxidation and reduction currents could be observed these were not visible in the case of gold electrodes coated with BDT and QDs (see Additional File 1 for data). Alternatively current at fixed bias voltage was recorded for gold electrodes before and after immobilization of BDT and QDs, while illumination was switched on and off. In the case of QDs present on top of the Au electrode a photocurrent could be measured under illumination (date are shown in Additional File 1)

Solubilized versus immobilized enzymes: In order to observe the enzymatic reaction of ALP and *p*APP the enzyme ALP was either directly added to the bath solution (S) or immobilized on top of the QDs layer (I). All geometries are depicted in Figure 2. In the simplest case ($S_0$) the Au electrodes with spin coated QDs layer were directly used without further modification. For the next geometry ($S_1$) a polyelectrolyte layer of PAH was coated on top of the CdS QDs layer mediated by electrostatic attraction by immersing the QDs coated Au electrode in a solution of PAH for 5 minutes (0.02 M monomer concentration, pH = 6.5, 0.5 M NaCl) [43,44]. Unbound excess PAH was removed by rinsing. PAH is positively charged. We speculate that the QDs layer is not tight so that PAH is attracted by the negatively charged underlying BDT monolayer. Stability after rinsing confirmed stable deposition of PAH. To this configuration a second polyelectrolyte layer ($S_2$) of PSS could be added by immersing the PAH coated QDs-Au electrode ($S_1$) for 5 minutes in a solution of PSS (0.02 M monomer concentration, pH = 6.5, 0.5 M NaCl), followed by a rinsing

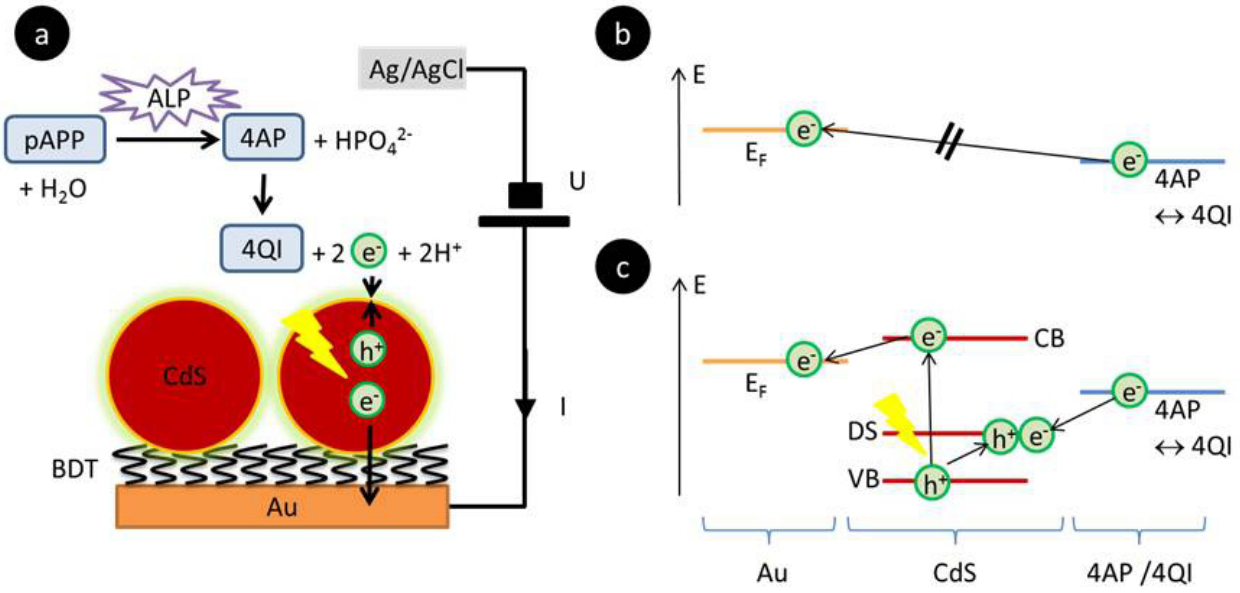


**Figure 1 Detection principle and redox schemes**. a) Sketch of the detection scheme. A bias voltage U is applied to a Au electrode versus an Ag/AgCl reference electrode in the bath solution. The Au electrode is coated with CdS QDs which are attached via a BDT layer. *p*APP is in solution degraded by ALP to 4AP. Upon illumination of the QDs electron hole pairs are generated. This leads to oxidation of 4AP to 4QI on the QD surface, whereby electrons are transferred to the QD. Electrons are passed to the Au electrode and can be detected as oxidation current I. b) Without QDs as redox mediator oxidation of 4AP can't happen in case the bias potential U is not positive enough. Energy levels E are shown. For oxidation the Fermi level $E_F$ of the Au electrode would need to be lower than the energy level at which electrons upon oxidation of 4AP are released. c) Illuminated QDs can act as redox mediator. Defect states (DS) at the QD surface (which are energetically above the valance band VB) prevent light generated electron hole pairs from immediate recombination. In this way electrons resulting from the oxidation of 4AP to 4QI can be transferred to the DS of the QD. In turn electrons from the conduction band (CB) can be drained via the BDT layer to the gold electrode, which is detected as oxidation/photocurrent.

step to remove unbound PSS. PSS is negatively charged and thus electrostatically attracted by the PAH layer [44]. In all three geometries ($S_0$, $S_1$, $S_2$) ALP was added directly to the solution on top of the electrode without any direct attachment. We also tried to directly immobilize ALP on the electrodes. For this purpose QDs coated Au electrodes were first modified with a PAH layer, leading to a positively charged surface ($S_1$). To this negatively charged ALP [45,46] was added by 5 minutes immersion in a solution of ALP (120 units/ml, pH = 7.8, 10 mM phosphate buffer). Attachment of ALP to PAH was mediated by electrostatic interaction ($I_1$). In order to increase the amount of immobilized ALP, the coating procedure was repeated ($I_2$). The electrodes with one layer of ALP were immersed again for 5 minutes in a solution of PAH, followed by rinsing, and then for 5 minutes in a solution of ALP followed by rinsing. This step-wise multilayer assembly mediated by electrostatic interaction [44] lead to two layers of ALP on top of the QD coated Au electrodes. Layer-by-layer assembly was confirmed with fluorescence labeled polyelectrolytes (data see Additional File 1).

Electrochemical measurements of dose-response curves: A constant bias voltage U was applied and the base line photocurrent $I_0$ was measured in phosphate buffer solution (pH 7.8) by switching illumination on and off with mechanical shutter, see Figure 3. Then the electrochemical cell was rinsed twice and a known amount of 4AP (product of ALP) or *p*APP (substrate for ALP) was added and the photocurrent I was measured again. Also hereby illumination was switched on and off several times with a mechanical shutter. For the next measurement the cell was again rinsed twice, an increasing amount of 4AP or *p*APP was added, and the photocurrent I was measured while switching on and off the illumination. With this procedure the response in photocurrent $\Delta I(c) = I(c) - I_0$ to different concentrations of 4AP or *p*APP was determined, see Figure 3. The resulting dose-response curves are plotted in Figures 4-5. It has to be noted that after each excitation there is a slight decrease in photocurrent, which we have previously ascribed to degradation of the QDs layer [43]. Polyelectrolyte layers above the QDs layer have been demonstrated to increase stability [43].

## Results and Discussion

Detection of 4AP and sensor principle: First we have investigated whether the CdS modified gold electrode

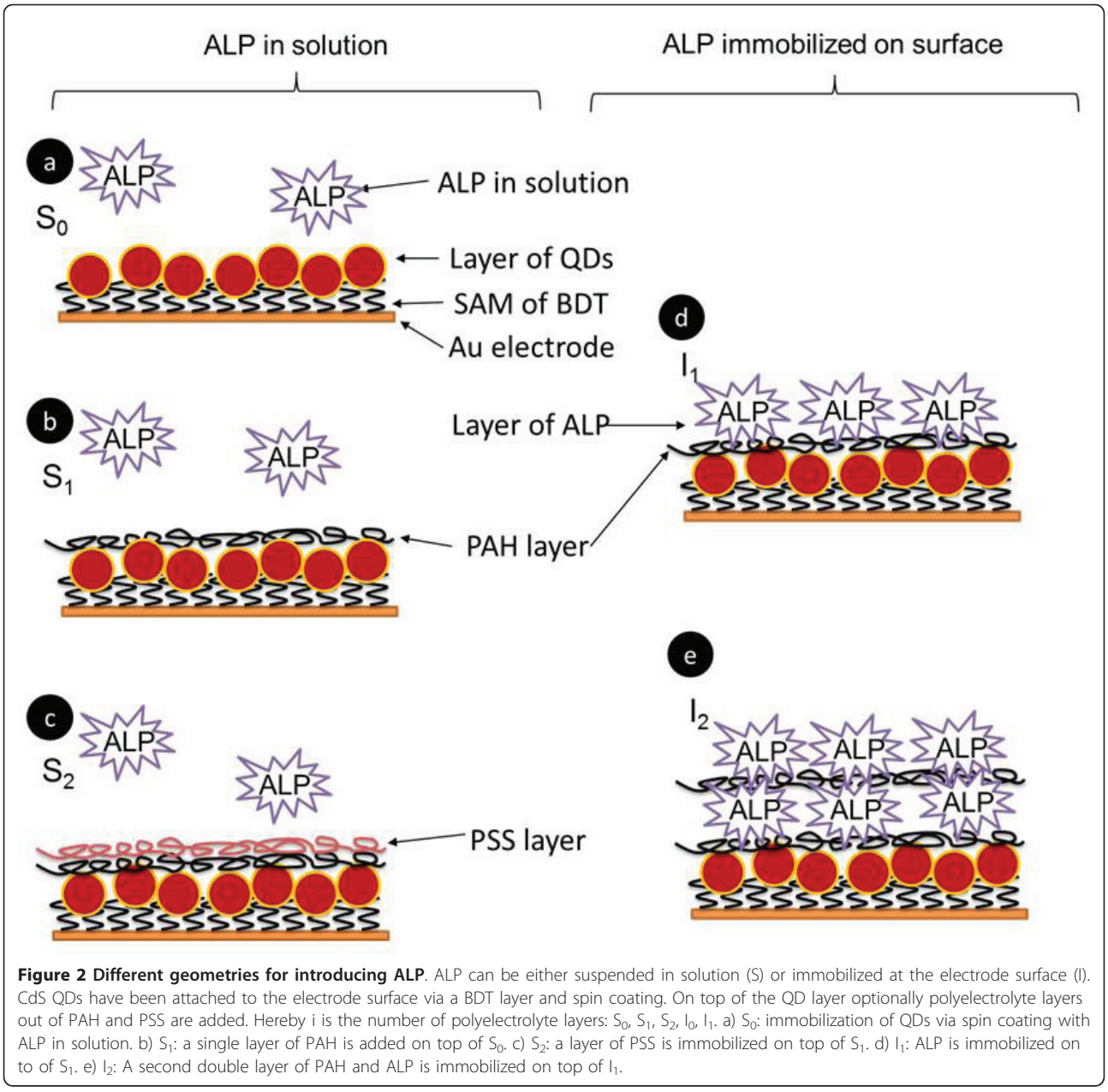


**Figure 2 Different geometries for introducing ALP**. ALP can be either suspended in solution (S) or immobilized at the electrode surface (I). CdS QDs have been attached to the electrode surface via a BDT layer and spin coating. On top of the QD layer optionally polyelectrolyte layers out of PAH and PSS are added. Hereby i is the number of polyelectrolyte layers: $S_0$, $S_1$, $S_2$, $I_0$, $I_1$. a) $S_0$: immobilization of QDs via spin coating with ALP in solution. b) $S_1$: a single layer of PAH is added on top of $S_0$. c) $S_2$: a layer of PSS is immobilized on top of $S_1$. d) $I_1$: ALP is immobilized on to of $S_1$. e) $I_2$: A second double layer of PAH and ALP is immobilized on top of $I_1$.

can be used as transducer to the analysis of 4AP - the reaction product of ALP reaction. For this purpose the electrode potential U was varied and the current I was measured under pulsed illumination. A clear response of the photocurrent to the presence of 4AP was found indicating that the QDs electrode provides a suitable surface for 4AP oxidation (cfg. Figure 3). Since the electrochemical behavior of 4AP is well known, the reaction is shown in Figure 6.

A maximum of photocurrent was detected for an applied bias potential of +200 mV against Ag/AgCl, 3M KCL (data are shown in Additional File 1). For this reason all following measurements were performed at fixed bias U = +200 mV. On the basis of the sensitivity of the QD electrode for 4AP, we wanted to construct a photoelectrochemical sensor. A sketch of our sensor concept is depicted in Figure 1. In presence of ALP *p*APP is hydrolyzed to 4AP and $HPO_4^{2-}$ (cfg. Figure 7) which is subsequently converted at the electrode under illumination.

The actual sensor electrode was composed out of QDs which were coupled via a 1,4-benzenedithiol (BDT) layer on top of a gold film electrode. A bias voltage U = +200 mV was applied and the corresponding current I

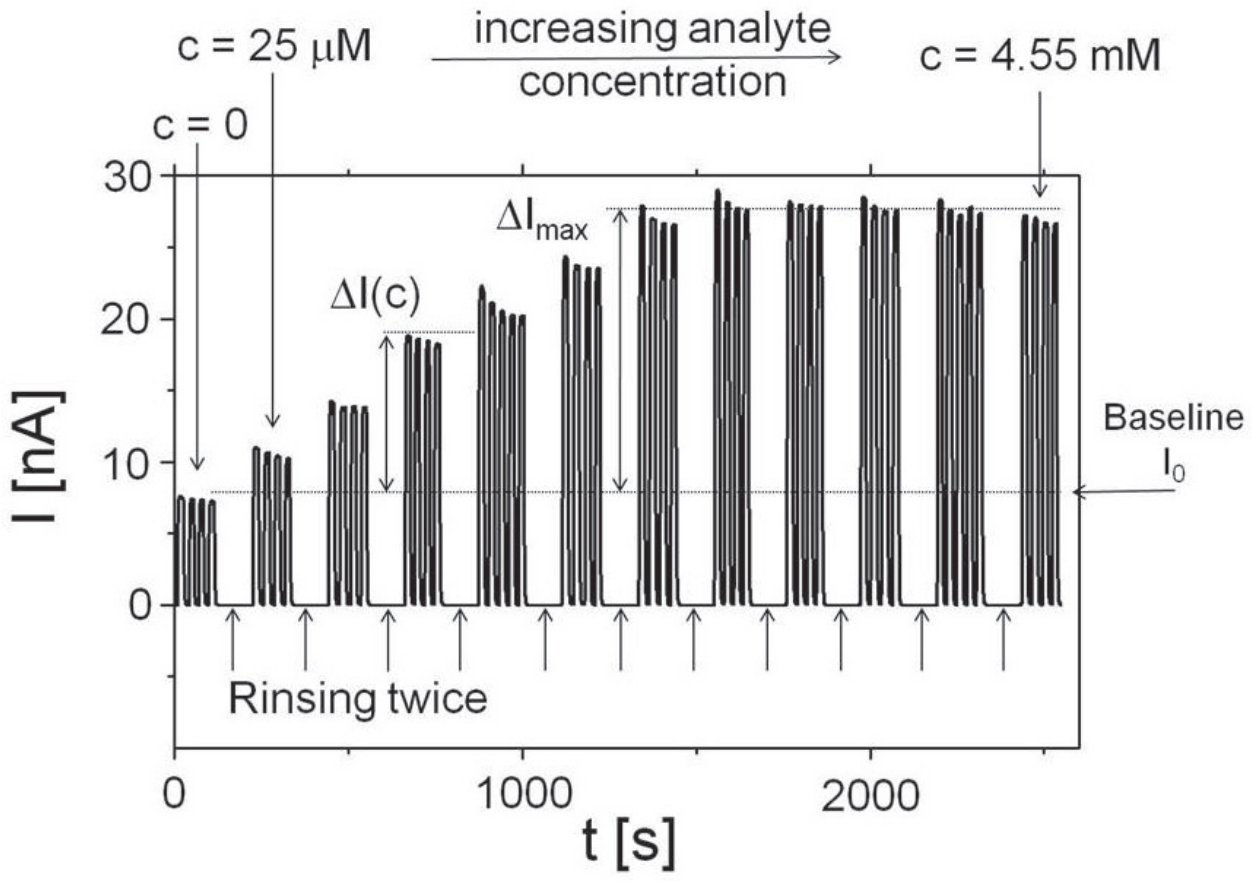


**Figure 3 Detection principle of dose response curves**. A constant bias U = +200 mV is applied and current I is detected. Hereby illumination is switched on and off with a shutter. During the periods without illumination no current can flow. The base line current $I_0$ is detected. After 2 rinsing steps analyte is added (in this case 4AP dissolved in 25% methanol and 75% phosphate buffer at pH 5, geometry $S_o$) and the respective photocurrent I is recorded in phosphate buffer with final pH = 7.8. This process is repeated while successively adding more analyte (in the present example 4AP concentration was increased from 25 µM to 4.55 mM). The respective oxidation current response ΔI(c) for each analyte concentration c is derived by subtracting the base line $I_0$ from the detected photocurrent I(c). The dose response curve for the present example is displayed in Figure 4a.

was recorded. Upon illumination of the QDs, electron-hole pairs were generated. Electron transfer could take place in between CdS QDs and the 4AP/QI - redox couple in solution and in between the QDs and the electrode. Thus, the QDs could be used as a light-triggered interlayer to transfer electrons from the redox couple, present in solution to the electrode. The energetical situation of the electron transfer pathway is depicted in Figure 1b/c. 4AP could be only oxidized to 4QI if the two released electrons could be transferred to an energetically lower level. In case the bias U applied to a gold electrode was not positive enough (i.e. its Fermi level was above the energy of the 4AP/4QI redox couple), no oxidation of 4AP could occur (cfg. Figure 1b). However, if at the same bias illuminated QDs were used oxidation of 4AP was possible (cfg. Figure 1c). Upon illumination, electrons in the QDs were excited from the valence band (VB) to the conduction band (CB), resulting in electrons ($e^-$) and holes ($h^+$). The holes were trapped in defect states (DS) [47] at the surface of the QDs. 4AP could now be oxidized to 4QI upon transferring the electrons to the QDs where they recombined with the holes. In turn, electrons were transferred from the CB of the QDs to the gold electrode, thus creating an oxidation current I.

In order to realize this signal chain in a sensor format (with the potential possibility of spatially resolved detection) the enzyme needed to be immobilized on the photosensitive electrode. The layer by layer approach in depositing protein molecules is a very favorable technique since it allows control on the deposited amount in one layer but also in the whole assembly by the number of deposition steps [48,49]. In order to deposit ALP, the positively charged polyelectrolyte PAH was used here.

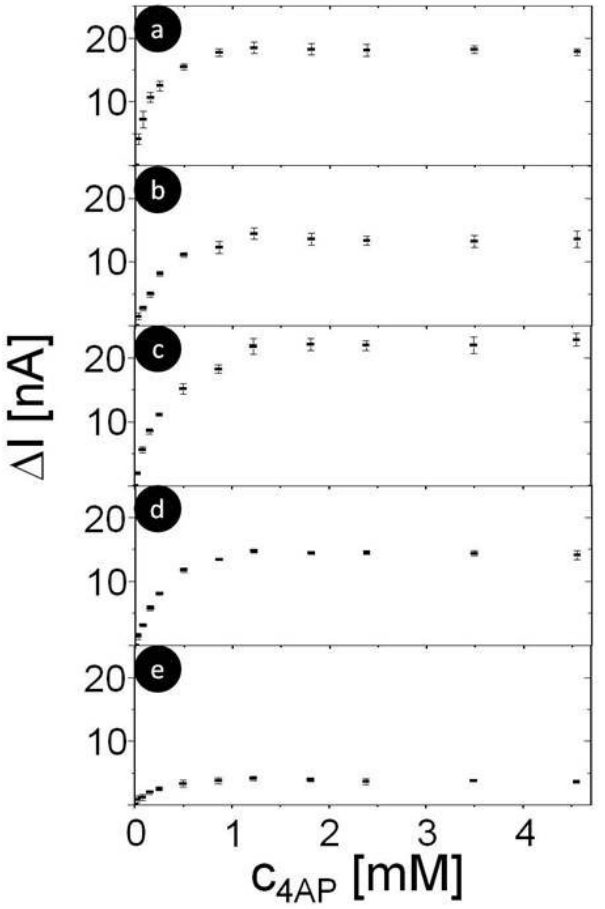


**Figure 4 Dose response curve for detection of 4AP (originally dissolved in 25% methanol and 75% phosphate buffer pH 5) as recorded in phosphate buffer pH 7.8 at bias potential of +200 mV for geometries a) $S_0$, b) $S_1$, c) $S_2$, d) $I_1$, e) $I_2$.** The resulting photocurrent I is plotted versus the concentration c of 4AP.

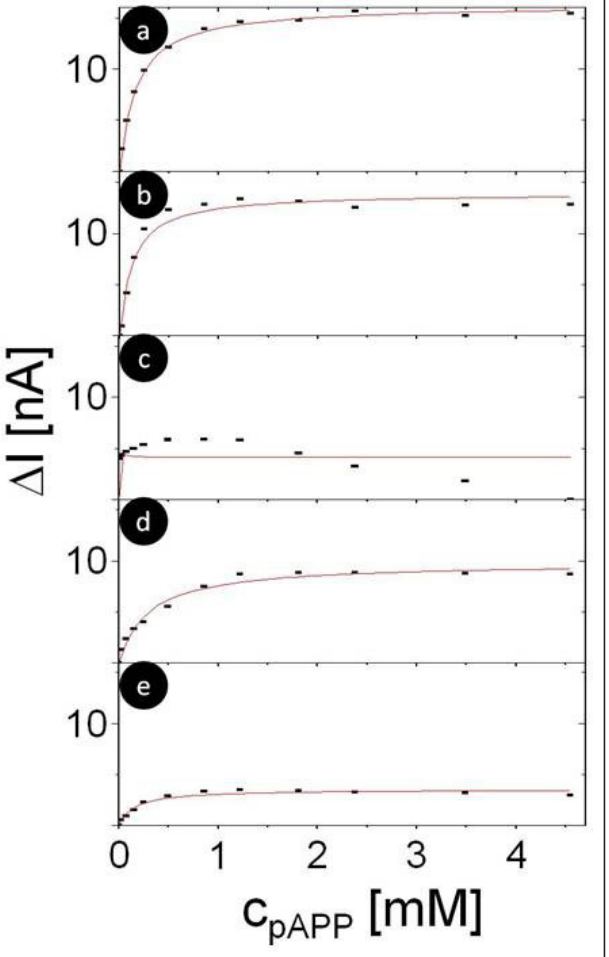


**Figure 5 Dose response curve for detection of *p*APP as recorded in phosphate buffer pH 7.8 at bias potential of +200 mV under the presence of ALP (120 units per 2 ml in case of geometry S) for geometries a) $S_0$, b) $S_1$, c) $S_2$, d) $I_1$, e) $I_2$.** The resulting photocurrent I is plotted versus the concentration c of *p*APP. The solid line in each of the curves indicates a fit with the Michaelis-Menten equation. Values are displayed in Table 1

We have investigated ALP as a monolayer but also as bilayer. In order to mimic the influence of the charge situation we have studied the effect of the polyelectrolyte alone on the sensing behavior. Figure 2 summarizes the different systems which have been analyzed on the way to a sensing electrode. To ensure high sensitivity for 4AP detection, the influence of protein and polyelectrolyte interlayers on the photocatalytic oxidation of 4AP were investigated. The oxidation current for different 4AP concentrations was determined for all 5 geometries shown in Figure 2. For each geometry a dose response curve was generated, see Figure 4. Data demonstrate that the concentration of 4AP can be reasonably detected within the ranges of 25 μM to around 1.5 mM. For 4AP concentrations larger than 1.5 mM the photocurrent response is saturated for all geometries. However, there was a significant difference in the maximum response of the oxidation current. The maximum photocurrents $\Delta I_{max}$ at saturation are displayed in Table 1. For geometry $S_2$ the higher current probably might be due to electrostatic attraction of negatively charged PSS and 4AP. For geometry $I_2$ the photocurrent response is smaller than for the other geometries (Figure 4e). This might be ascribed to a rather dense assembly of ALP with PAH hindering 4AP to reach the QDs modified electrode. At any rate, the data show that the polyelectrolyte used and the immobilized protein still allow the conversion of the reaction product of ALP. Thus another important precondition for the sensor construction seems to be fulfilled.

Detection of *p*-aminophenyl phosphate: As an experimental complication it has to be pointed out that *p*APP has limited stability, since *p*APP decomposes slowly in

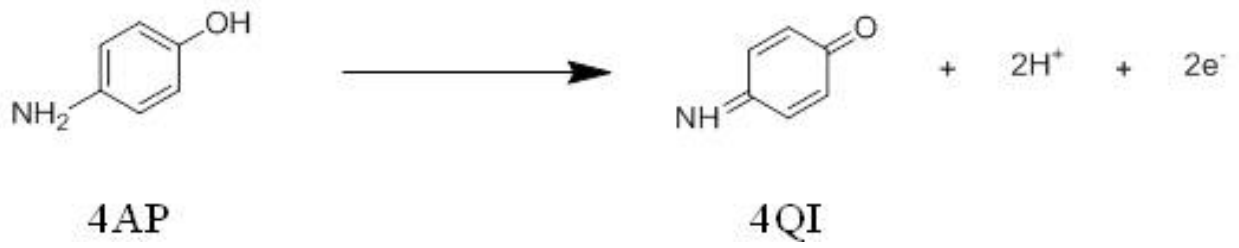


**Figure 6 Oxidation reaction of 4-aminophenol (4AP) to 4-quinoneimine (4QI)**.

alkaline solution [50]. In order to be sure to test the enzyme activity on the CdS electrode, *p*APP has also been investigated with the 3 different geometries given in Figure 2 (without the enzyme). Only a very small response of about 1-2 nA was obtained (cfg. Table 1 and Additional File 1). This is an order of magnitude lower than the response to 4AP and ensured specific detection of the substrate *p*APP by the enzymatic conversion as will be shown in the following. In a first step, the enzymatic reaction of ALP with *p*APP causing the production of 4AP was investigated with the enzyme in solution. As has been shown above this is possible, as there is response of the photocurrent to the product 4AP, but barely to the substrate *p*APP. As shown in Figure 5 a-c the enzymatic reaction could be detected for all the 3 geometries in which the enzyme was free in solution, as indicated in Figure 2. However, there were significant differences in the response curves. In contrast to the detection of 4AP alone (geometry $S_0$) the response in geometry $S_2$ for *p*APP in the conversion with ALP is small, probably due to a depletion of the substrate near the electrode because of electrostatic repulsion.

In a final step the enzyme has been immobilized in a single and double layer as depicted in Figure 2d and 2e. By this method, the biospecific recognition element is part of the device and no substances have to be added to the solution despite the molecule to be detected (here *p*APP). In the case of geometry $I_2$ the maximum photocurrent response is relatively low (Figure 5e). This corresponds directly to the control experiments in which 4AP has been detected directly (Figure 4e). The ALP/polyelectrolyte layers seem to hinder diffusion of 4AP to the QDs surface. Immobilization of ALP also reduces the steepness of the dose-response curve (*cf.* Figure 5a,b versus Figure 5d). Nevertheless, for electrodes with a single layer of ALP fixed with the polyelectrolyte PAH a very well defined response to the enzyme substrate is obtained. This shows that the concept of a photobioelectrochemical sensor can be realized with the example of ALP. Sensitivity for 4AP detection could be provided in the range from 25 μM to 1.5 mM (*cf.* Figure 3, in all geometries shown, addition of 25 μM clearly triggered a response in the photocurrent). We want to point out that the aim of this paper was not the development for a practical sensor for direct *p*APP detection in real samples, but rather to demonstrate the proof of concept for a photo-triggered enzyme sensor (of the first generation). In order to further analyze the response behavior quantitatively, the dose response curves were fitted with the Michaelis-Menten equation, cfg. Eq. 1 [51]. Hereby we assumed that the rate of the enzymatic reaction v was proportional to the oxidation current I, and thus $v/v_{max} = \Delta I/\Delta I_{max}$, whereby $v_{max}$ is the maximum reaction rate and $K_M$ is the Michaelis-Menten constant, *cf.* Eq. 1. Values are given in Table 1.

$$\Delta I/\Delta I_{max} = c\,(p\mathrm{APP}) \,/\, (K_M + c\,(p\mathrm{APP})) \quad (1)$$

In literature $K_M$ values of 0.48 mM [52] and 0.056 mM [53] have been reported, which are in the same

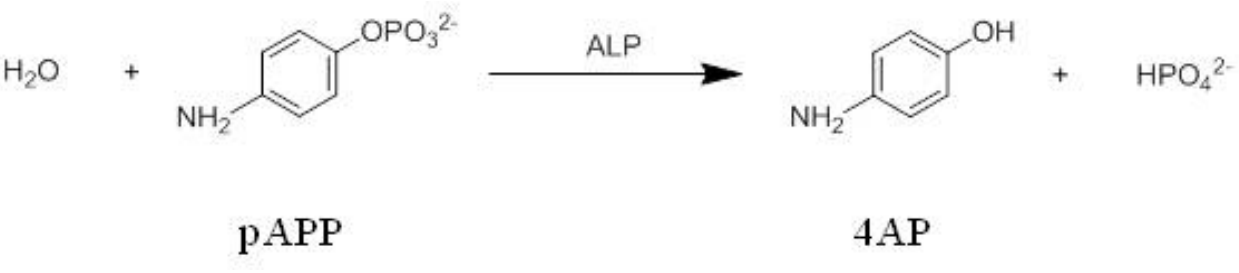


**Figure 7 Hydrolysis reaction of *p*-aminophenol phosphate to 4-aminophenol catalyzed with alkaline phosphatase**.

**Table 1 Oxidation currents for the different geometries**

| Geometry | $\Delta I_{max}$ [nA] direct detection of 4AP | $\Delta I_{max}$ [nA] direct detection of *p*APP | $\Delta I_{max}$ [nA] enzymatic reaction | $K_M$ [mM] |
|---|---|---|---|---|
| $S_0$ | 18.4 | 2.1 | 16.3 | 0.16 |
| $S_1$ | 14.4 | 2.1 | 14.0 | 0.12 |
| $S_2$ | 21.8 | - | - | - |
| $I_1$ | 14.8 | - | 9.8 | 0.29 |
| $I_2$ | 4.1 | - | 3.5 | 0.15 |

Maximum oxidation currents are recorded for different geometries $S_0$, $S_1$, $S_2$, $I_1$, $I_2$ as recorded in phosphate buffer with pH = 7.8. Data are shown for detection of 4AP (cfg. Figure 4), *p*APP (cfg. Additional File 1), and detection of 4AP after enzymatic degradation of *p*APP with ALP (cfg. Figure 5). In the case of the enzymatic reaction also the Michaelis-Menten constant $K_M$ is given.

order of magnitude as the values detected in our work with the enzyme in solution. For the sensor configuration developed ($I_1$) a larger value can be derived from the experiments. It has to be pointed out that in the case of the polyelectrolyte -fixed enzyme the $K_M$ value has to be considered as apparent $K_M$ value since here the concentration of half maximum conversion rate is influenced by the immobilization [54]. Comparison of the $\Delta I_{max}$ values as obtained for direct detection of 4AP (Figure 4) and detection of 4AP after enzymatic degradation of *p*APP to 4AP shows that both oxidation signals (detected at the same geometry and provided abundance of enzyme) are quite similar. This is in good agreement with the detection principle proposed.

In summary the developed sensor as illustrated in Figure 2d by immobilizing the ALP via the polyelectrolyte PAH, provides the proof of principle for a detection system for the enzyme substrate *p*APP. The analytical performance with a detection regime within the concentration range from 0.025 to 1 mM is relatively poor, so that the here presented device has to be seen as a proof of principle demonstrator rather than as an applicable sensor.

## Conclusions

A light controlled bioelectrochemical sensor for *p*APP has been demonstrated. By using QDs as interlayer on gold, 4AP could be oxidized and thus detected via a corresponding photocurrent in case the QDs were illuminated. Enzymes could be functionally immobilized on the sensor surface. This provides the basis for future spatially resolved measurements [40] by selectively illuminating and reading-out only the area of interest of an electrode which is non-structured, but modified with different immobilized enzyme systems. The approach presented here allows for observing enzymatic reactions which yield 4AP as product. We have demonstrated this for the substrate *p*APP and the enzyme ALP. A crucial point for such measurements is to ensure high local enzyme concentration and specificity for the detection of the enzymatic product. By using a polyelectrolyte layer of PAH, the enzyme ALP could be immobilized on the electrode surface, retaining enzymatic activity. However, polyelectrolyte layers can also hinder diffusion of the molecule to be detected 4AP to the QD surface, thus hindering detection. For this reason permeability of the polyelectrolyte layers has been studied here for the respective molecule.

## Additional material

**Additional file 1: Supporting information: Cleaning of gold electrodes**. Immobilization of QDs on the electrode surface. Confirmation of QDs immobilization. Detection of 4-aminophenol and *p*-aminophenyl phosphate (*p*APP). Immobilization of ALP in polyelectrolyte layers on top of the QDs layer. Set-up for the detection of fotocurrents [55-57].

**Acknowledgements**
This work was supported by the German Research Foundation (DFG, grants PA 794/3-1, LI706/2-1).

**Author details**
[1]Fachbereich Physik and WZMW, Philipps Universität Marburg, Germany. [2]Biosystems Technology, University of Applied Sciences Wildau, Wildau, Germany.

**Authors' contributions**
WK, GG, DH and JMM: performed experiments and analyzed data. PRG: designed experiments and analyzed data. FL and WJP: designed experiments and wrote manuscript. All authors read and approved the final manuscript.

**Competing interests**
The authors declare that they have no competing interests.

Received: 18 August 2011 Accepted: 7 October 2011
Published: 7 October 2011

**References**

1. Wang C, Gao X, Su XG: **In vitro and in vivo imaging with quantum dots.** *Analytical And Bioanalytical Chemistry* 2010, **397**:1397-1415.
2. Pinaud F, Clarke S, Sittner A, Dahan M: **Probing cellular events, one quantum dot at a time.** *Nature Methods* 2010, **7**:275-285.
3. Resch-Genger U, Grabolle M, Cavaliere-Jaricot S, Nitschke R, Nann T: **Quantum dots versus organic dyes as fluorescent labels.** *Nat Meth* 2008, **5**:763.
4. Zhang F, Ali Z, Amin F, Riedinger A, Parak WJ: **In vitro and intracellular sensing by using the photoluminescence of quantum dots.** *Analytical And Bioanalytical Chemistry* 2010, **397**:935-942.
5. Parak WJ, Pellegrino T, Plank C: **Labelling of cells with quantum dots.** *Nanotechnology* 2005, **16**:R5-R25.

6. Stoll C, Kudera S, J.Parak W, Lisdat F: **Quantum Dots on Gold:Electrodes For Photoswitchable Cytochrome c Electrochemistry.** *SMALL* 2006, **2**:741-743.
7. Katz E, Zayats M, Willner I, Lisdat F: **Controlling the direction of photocurrents by means of CdS nanoparticles and cytochrome c-mediated biocatalytic cascades.** *Chemical Communications* 2006, 1395-1397.
8. Stoll C, Gehring C, Schubert K, Zanella M, Parak WJ, Lisdata F: **Photoelectrochemical signal chain based on quantum dots on gold–Sensitive to superoxide radicals in solution.** *Biosensors and Bioelectronics* 2008, **24**:260-265.
9. Schubert K, Khalid W, Yue Z, Parak WJ, Lisdat F: **Quantum-Dot-Modified Electrode in Combination with NADH-Dependent Dehydrogenase Reactions for Substrate Analysis.** *Langmuir* 2010, **26**:1395-1400.
10. Liu Q, Lu XB, Li J, Yao X, Li JH: **Direct electrochemistry of glucose oxidase and electrochemical biosensing of glucose on quantum dots/carbon nanotubes electrodes.** *Biosensors & Bioelectronics* 2007, **22**:3203-3209.
11. Wang Z, Xu Q, Wang HQ, Yang Q, Yu JH, Zhao YD: **Hydrogen peroxide biosensor based on direct electron transfer of horseradish peroxidase with vapor deposited quantum dots.** *Sensors And Actuators B-Chemical* 2009, **138**:278-282.
12. Tang LH, Zhu YH, Yang XL, Sun JJ, Li CZ: **Self-assembled CNTs/CdS/dehydrogenase hybrid-based amperometric biosensor triggered by photovoltaic effect.** *Biosensors & Bioelectronics* 2008, **24**:319-323.
13. Bawendi MG, Steigerwald ML, Brus LE: **The quantum mechanics of large semiconductor clusters ("quantum dots").** *Annu Rev Phys Chem* 1990, **41**:477-496.
14. Kucur E, Riegler J, Urban GA, Nann T: **Determination of quantum confinement in CdSe nanocrystals by cyclic voltammetry.** *Journal of Chemical Physics* 2003, **119**:2333-2337.
15. Ehlert O, Tiwari A, Nann T: **Quantum confinement of the thermodynamic functions for the formation of electrons and holes in CdSe nanocrystals.** *Journal Of Applied Physics* 2006, **100.**
16. Kucur E, Bucking W, Arenz S, Giernoth R, Nann T: **Heterogeneous charge transfer of colloidal nanocrystals in ionic liquids.** *Chemphyschem* 2006, **7**:77-81.
17. Niemeyer CM: **Functional hybrid devices of proteins and inorganic nanoparticles.** *ANGEW CHEM INT EDIT* 2003, **42**:5796-5800.
18. Willner I, Basnar B, Willner B: **Nanoparticle-enzyme hybrid systems for nanobiotechnology.** *Febs Journal* 2007, **274**:302-309.
19. Bagel O, Limoges B, Schollhorn B, Degrand C: **Subfemtomolar determination of alkaline phosphatase at a disposable screen-printed electrode modified with a perfluorosulfonated ionomer film.** *Analytical Chemistry* 1997, **69**:4688-4694.
20. Nistor C, Emneus J: **An enzyme flow immunoassay using alkaline phosphatase as the label and a tyrosinase biosensor as the label detector.** *Analytical Communications* 1998, **35**:417-419.
21. Kreuzer MP, O'Sullivan CK, Guilbault GG: **Alkaline phosphatase as a label for immunoassay using amperometric detection with a variety of substrates and an optimal buffer system.** *Analytica Chimica Acta* 1999, **393**:95-102.
22. Campas M, Olteanu MG, Marty JL: **Enzymatic recycling for signal amplification: Improving microcystin detection with biosensors.** *Sensors And Actuators B-Chemical* 2008, **129**:263-267.
23. Wollenberger U, Schubert F, Scheller FW: **Biosensor For Sensitive Phosphate Detection.** *Sensors And Actuators B-Chemical* 1992, **7**:412-415.
24. Bodansky A: **Phosphatase studies II. Determination of serum phosphatase. Factors influencing the accuracy of the determination.** *Journal Of Biological Chemistry* 1933, **101**:93-104.
25. Shinowara GY, Jones LM, Reinhart HL: **The estimation of serum inorganic phosphate and " acid" and " alkaline" phosphatase activity.** *Journal Of Biological Chemistry* 1942, **142**:921-933.
26. Tietz NW, Green A: **Automated Procedure For Determination Of Phosphorus + Alkaline Phosphatase (Bodansky) In Serum.** *Clinica Chimica Acta* 1964, **9**:392-&.
27. Kind PRN, King EJ: **Estimation Of Plasma Phosphatase By Determination Of Hydrolysed Phenol With Amino-Antipyrine.** *Journal Of Clinical Pathology* 1954, **7**:322-326.
28. King EJ, Armstrong AR: **A convenient method for determining serum and bile phosphatase activity.** *Canadian Medical Association Journal* 1934, **31**:376-381.
29. Seligman AM, Chauncey HH, Nachlas MM, Manheimer LH, Ravin HA: **The Colorimetric Determination Of Phosphatases In Human Serum.** *Journal Of Biological Chemistry* 1951, **190**:7-15.
30. Bessey OA, Lowry OH, Brock MJ: **A Method For The Rapid Determination Of Alkaline Phosphatase With 5 Cubic Millimeters Of Serum.** *Journal Of Biological Chemistry* 1946, **164**:321-329.
31. Fischl J, Segal S, Rabiah S: **Microdetermination Of Phosphatases Employing Phenolphthalein Diphosphate As Substrate.** *Clinical Chemistry* 1967, **13**:941.
32. Huggins C, Talalay P: **Sodium Phenolphthalein Phosphate As A Substrate For Phosphatase Tests.** *Journal Of Biological Chemistry* 1945, **159**:399-410.
33. Fernley HN, Walker PG: **Kinetic Behaviour Of Calf-Intestinal Alkaline Phosphatase With 4-Methylumbelliferyl Phosphate.** *Biochemical Journal* 1965, **97**:95.
34. Tang HT, Lunte CE, Halsall HB, Heineman WR: **P-Aminophenyl Phosphate - An Improved Substrate For Electrochemical Enzyme-Immunoassay.** *Analytica Chimica Acta* 1988, **214**:187-195.
35. Fischer F, Siebert G: **Optischer Test Zur Bestimmung Der Alkalischen Phosphate Im Serum.** *Klinische Wochenschrift* 1961, **39**:202.
36. McNeil CJ, Higgins IJ, Bannister JV: **Amperometric Determination Of Alkaline-Phosphatase Activity - Application To Enzyme-Immunoassay.** *Biosensors* 1987, **3**:199-209.
37. Wehmeyer KR, Halsall HB, Heineman WR, Volle CP, Chen IW: **Competitive Heterogeneous Enzyme-Immunoassay For Digoxin With Electrochemical Detection.** *Analytical Chemistry* 1986, **58**:135-139.
38. McConnell HM, Owicki JC, Parce JW, Miller DL, Baxter GT, Wada HG, Pitchford S: **The Cytosensor Microphysiometer: Biological Applications of Silicon Technology.** *Science* 1992, **257**:1906-1912.
39. Licht S, Myung N, Sun Y: **A Light Addressable Photoelectrochemical Cyanide Sensor.** *Analytical Chemistry* 1996, **68**:954-959.
40. Parak WJ, Hofmann UG, Gaub HE, Owicki JC: **Lateral Resolution of Light Addressable Potentiometric Sensors: An Experimental and Theoretical Investigation.** *Sensors and Actuators A* 1997, **63**:47-57.
41. George M, Parak WJ, Gerhardt I, Moritz W, Kaesen F, Geiger H, Eisele I, Gaub HE: **Investigation of the spatial resolution of the light-addressable potentiometric sensor (LAPS).** *Sensors and Actuators A* 2000, **83**:149-249.
42. Kudera S, Carbone L, Casula MF, Cingolani R, Falqui A, Snoeck E, Parak WJ, Manna L: **Selective growth of PbSe on one or both tips of colloidal semiconductor nanorods.** *Nanoletters* 2005, **5**:445-449.
43. Yue Z, Khalid W, Zanella M, Abbasi AZ, Pfreundt A, Rivera_Gil P, Schubert K, Lisdat F, Parak WJ: **Evaluation of quantum dots applied as switchable layer in a light-controlled electrochemical sensor.** *Analytical and Bioanalytical Chemistry* 2010, **396**:1095-1103.
44. Decher G: **Fuzzy nanoassemblies: Toward Layered Polymeric Multicomposites.** *Science* 1997, **277**:1232-1237.
45. Latner AL, Parsons ME, Skillen AW: **Isoelectric Focusing Of Human Liver Alkaline Phosphatase.** *Biochemical Journal* 1970, **118**:299.
46. Xie Q, Alpers DH: **The two isozymes of rat intestinal alkaline phosphatase are products of two distinct genes.** *Physiological Genomics* 2000, **3**:1-8.
47. Wuister SF, Donega CD, Meijerink A: **Influence of thiol capping on the exciton luminescence and decay kinetics of CdTe and CdSe quantum.** *Journal of Physical Chemistry B* 2004, **108**:17393-17397.
48. Decher G, Schlenoff J: *Multilayer Thin Films: Sequential Assembly of Nanocomposite Materials* Wiley VCH; 2002.
49. Lisdat F, Dronov R, Mohwald H, Scheller FW, Kurth DG: **Self-assembly of electro-active protein architectures on electrodes for the construction of biomimetic signal chains.** *Chemical Communications* 2009, 274-283.
50. Gil EP, Tang HT, Halsall HB, Heineman WR, Misiego AS: **Competitive Heterogeneous Enzyme-Immunoassay For Theophylline By Flow-Injection Analysis With Electrochemical Detection Of Para-Aminophenol.** *Clinical Chemistry* 1990, **36**:662-665.
51. Hommes FA: **Integrated Michaelis-Menten Equation.** *Archives Of Biochemistry And Biophysics* 1962, **96**:28.
52. Gehring AG, Brewster JD, Irwin PL, Tu SI, Van Houten LJ: **1-Naphthyl phosphate as an enzymatic substrate for enzyme-linked immunomagnetic electrochemistry.** *Journal Of Electroanalytical Chemistry* 1999, **469**:27-33.
53. Thompson RQ, Barone GC, Halsall HB, Heineman WR: **Comparison Of Methods For Following Alkaline-Phosphatase Catalysis - Spectrophotometric Versus Amperometric Detection.** *Analytical Biochemistry* 1991, **192**:90-95.

54. Neugebauer S, Stoica L, Guschin D, Schuhmann W: **Redox-amplified biosensors based on selective modification of nanopore electrode structures with enzymes entrapped within electrodeposition paints.** *Microchimica Acta* 2008, **163**:33-40.
55. Bauer CG, Eremenko AV, EhrentreichForster E, Bier FF, Makower A, Halsall HB, Heineman WR, Scheller FW: **Zeptomole-detecting biosensor for alkaline phosphatase in an electrochemical immunoassay for 2,4-dichlorophenoxyacetic acid.** *Analytical Chemistry* 1996, **68**:2453-2458.
56. Frew JE, Foulds NC, Wilshere JM, Forrow NJ, Green MJ: **Measurement Of Alkaline-Phosphatase Activity By Electrochemical Detection Of Phosphate-Esters - Application To Amperometric Enzyme-Immunoassay.** *Journal Of Electroanalytical Chemistry* 1989, **266**:309-316.
57. Neumann H, Vanvreed M: **An Improved Alkaline Phosphatase Determination With P-Nitrophenyl Phosphate.** *Clinica Chimica Acta* 1967, **17**:183-187.

doi:10.1186/1477-3155-9-46
**Cite this article as:** Khalid *et al.*: Light triggered detection of aminophenyl phosphate with a quantum dot based enzyme electrode. *Journal of Nanobiotechnology* 2011 **9**:46.

# Ion Transport Through Polyelectrolyte Multilayers

Susana Carregal-Romero, Philipp Rinklin, Susanne Schulze, Martin Schäfer, Andrea Ott, Dominik Hühn, Xiang Yu, Bernhard Wolfrum,* Karl-Michael Weitzel,* Wolfgang J. Parak*

Polyelectrolyte multilayer (PEM) films and capsules loaded with ion-sensitive fluorophores can be used as ion-sensors for many applications including measurements of intracellular ion concentration. Previous studies have shown the influence of the PEM films/shells on the specific response of encapsulated ion-sensitive fluorophores. PEM shells are considered as semipermeable barriers between the environment and the encapsulated fluorophores. Parameters such as the time response of the encapsulated sensor can be affected by the porosity and charge of the PEM shell. In this study, the time response of an encapsulated pH-sensitive fluorophore towards pH changes in the surrounding environment is investigated. Furthermore, the conductance of PEM films for potassium ions is determined.

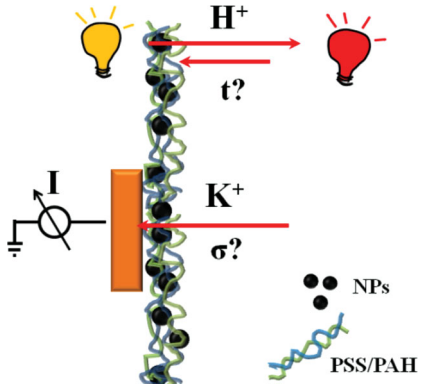


## 1. Introduction

Polyelectrolyte multilayer (PEM) films (i.e., planar geometry) and capsules (i.e., spherical geometry) produced by layer-by-layer (lbl) self assembly methods have become popular materials in applications such as filtration,[1] drug delivery,[2,3] and sensors.[4,5] Concerning sensing, one strategy is based on embedding analyte-sensitive fluorophores in the cavity of PEM capsules. In particular, this can be achieved by linkage of the analyte-sensitive fluorophores to big macromolecules such as dextran, which can be entrapped in the inner cavities of the capsules.[5] Upon encapsulation of the modified analyte-sensitive fluorophore, the fluorescence emission of the capsules will change depending on the analyte concentration. Thus, the analyte concentration can be determined via fluorescence read-out.[5] The PEM shell hereby acts as a semi-permeable membrane. PEM capsules must be porous enough to allow free diffusion of analyte molecules into the capsules where they can be detected. In contrast, their pores must be small enough to prevent the leakage of the analyte-sensitive fluorophores bound to macromolecules out of the capsules. Thus this detection principle is limited to small analytes, such as ions or small molecules like urea or $CO_2$, which can traverse the PEM shell.[6,7] Diffusion of ions or small molecules in a porous medium depends on the permeability.[8] The permeability of PEM shells can be tuned by

S. Carregal-Romero, A. Ott, D. Hühn, X. Yu, W. J. Parak
Fachbereich Physik, Philipps Universität Marburg, Marburg, Germany
E-mail: wolfgang.parak@physik.uni-marburg.de
S. Carregal-Romero
BIONAND, Centro Andaluz de Nanomedicina y Biotecnología, Málaga, Spain
P. Rinklin, B. Wolfrum
Institute of Bioelectronics PGI-8/ICS-8, JARA-FIT, Forschungszentrum, Jülich, Jülich, Germany
E-mail: b.wolfrum@fz-juelich.de
S. Schulze, M. Schäfer, K.-M. Weitzel
Fachbereich Chemie, Philipps Universität Marburg, Marburg, Germany
E-mail: weitzel@chemie.uni-marburg.de
W. J. Parak
CIC Biomagune, San Sebastian, Spain

*Macromol. Rapid Commun.* **2013**, DOI: 10.1002/marc.201300571

modification of several parameters during their assembly: i) Porosity of PEM shells depends on the chemical structure of the polyelectrolytes.[9] ii) The increase of the number of polyelectrolyte layers decreases the permeability of the shell.[10] iii) The introduction of additional building blocks such as nanoparticles (NPs) in-between the polyelectrolyte layers changes permeability of the PEM shells.[11] iv) Parameters such as temperature and ionic strength during the lbl assembly process also affect the final pore size of the PEM shell.[12,13] Furthermore, besides the assembly process, changes in the environment of already assembled PEM shells are also of importance and can temporarily or permanently modify their permeability due to the shrinking or swelling of the capsule. The swelling/shrinking of capsules depends on the nature of the polyelectrolytes, the number of bilayers, and the charge of the terminating layer. The environmental parameters that can affect the permeability are: i) temperature,[14,15] ii) changes of pH,[16–18] iii) changes of the redox state,[19] iv) changes in the polarity of the solvent,[20] and v) changes of the ionic strength.[21,22]

In the following, the transport of small ions as example of analyte molecules through PEM shells will be discussed. Due to their charge, ions can interact electrostatically with the PEM shell, in contrast to uncharged analytes. Understanding the ion transport through PEM shells is important for several applications especially for PEM capsules based ion-sensors. As already mentioned PEM capsules based on ion-sensitive fluorophores entrapped in the inner cavity have been successfully used as ion-sensors for $Na^+$, $K^+$, $Cl^-$ and $H^+$ "in test tube"[5,23] and in vitro.[23–26] In this context, even multiplexed ion-sensing was demonstrated by using quantum dots (QDs) acting as barcodes.[27] These sensors can only work in case ions from the analyte solution or cellular environment can diffuse through the PEM shell and thus reach the encapsulated ion-sensitive fluorophores. Therefore, for further applications it is necessary to gain a better understanding of the parameters that affect the ion transport in these systems. Here in particular the temporal resolution, i.e., how fast ions can traverse the PEM shells and the possibility to determine absolute ion concentrations, i.e., if the ion concentration inside and outside the PEM shells is the same, are of importance. Concerning static equilibria and due to effects related to the Donnan potential, the ion concentration inside capsules in general differs from the bulk concentration.[22,28–31] Dynamic equilibria (transport processes) have been described in terms of ion diffusion and ion conductance. Ghostine et al. for example calculated diffusion coefficients of ferricyanide through a PEM shell using steady-state electrochemistry.[32] They observed an increase of the ion mobility as the temperature and the charge increased. Currently established concepts for determining ion conductivity of solid materials include impedance spectroscopy (IS),[33–35] the radiotracer diffusion technique (RD),[36] and pulsed field gradient nuclear magnetic resonance (PFG-NMR).[37–39] IS relies on the ability to have two electrodes in contact with the sample, which in the case of nanoscale samples raises the problem of electrical short circuits. RD and PFG-NMR do not use electrodes but cannot be easily applied to nanoscale samples either. The ideal technique for measuring ion transport through ultra-thin samples would be based on a setup with a single sample electrode contact. Such a new technique, termed low energy bombardment induced ion transport (BIIT) has been recently developed and demonstrated to be widely applicable.[40–42]

This work first tries to address the question how fast ions from the bulk can reach the ion-sensitive fluorophores embedded in the capsule cavity. For this purpose we measured the time response of encapsulated pH-sensitive fluorophores, which gives an upper limit for the response time of ion-sensitive dyes entrapped within PEM capsules. Second ion conductivity (in the case of potassium) through PEM membranes has been investigated experimentally. As the presence of NPs within the PEM shells is an important tool for adding new functionalities to the capsules such as magnetic guidance and barcoding,[27,43] we have also studied the influence of the presence of gold NPs in PEM films on their ion conductivity.

## 2. Results and Discussion

### 2.1. Synthesis of PEM Capsules with Embedded pH-sensitive Fluorophores

PEM capsules with the pH indicator seminaphtharhodafluor (SNARF) in their cavity and with and without polymer coated magnetic NPs ($\gamma$-$Fe_2O_3$, 31 $\pm$ 6 nm core diameter)[44,45] in their shell were synthesized according to standard procedures by lbl assembly of poly(sodium 4-styrenesulfonate) (PSS) and poly(allylamine hydrochloride) (PAH).[26,45] Some characterization data of the capsules are reported in Figure 1. SNARF is a pH-sensitive fluorophore which emits at two different wavelengths.[46] The ratio of the intensities of the two emission peaks depends on the pH value of the environment. In acidic media SNARF emits light more in the yellow at 583 nm and in alkaline ones more in the red at 627 nm.

### 2.2. Estimation of the Diffusion Time of Ions into PEM Capsules

For the study of the time response of encapsulated SNARF as pH-sensitive fluorophore the PEM capsules were modified with magnetic NPs. The PEM capsules were exposed to a time-dependent pH concentration profile, while meas-

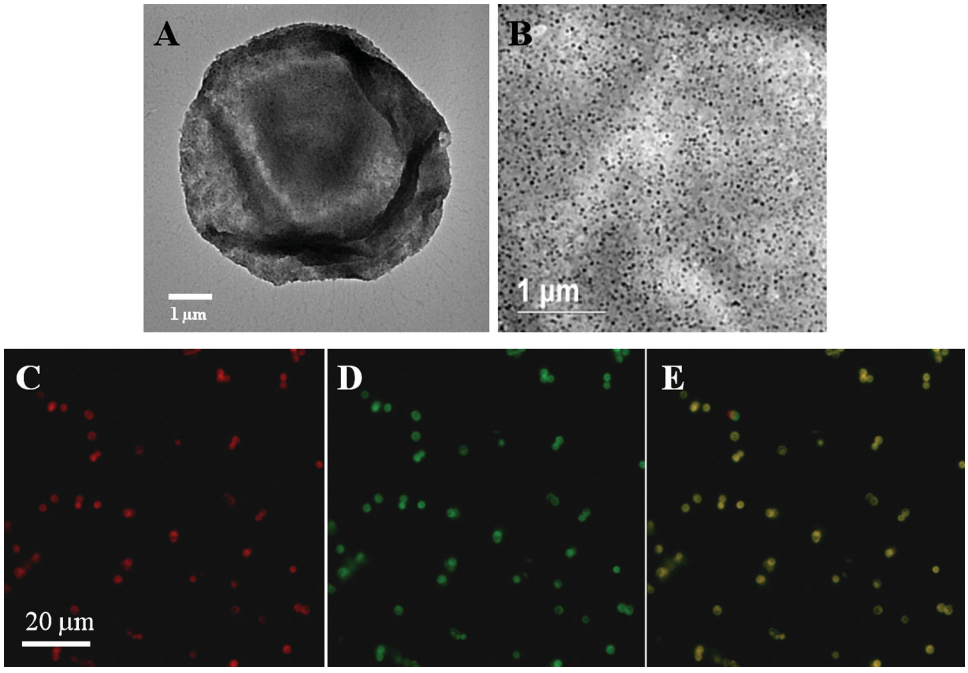


*Figure 1.* (A) Transmission electron microscopy (TEM) image of a PEM capsule loaded with γ-$Fe_2O_3$ NPs in its PEM wall (without SNARF in its cavity). (B) Image of the same capsule with higher resolution in order to demonstrate the distribution of the magnetic NPs. (C-E) Confocal microscopy images (red, "green" channel + overlay) of PEM capsules with magnetic NPs in their walls, and with the ratiometric dye SNARF in their cavity. Please note that SNARF actually emits in the red and in the yellow. However, for presentation purposes the yellow emission is depicted in green in false color mode. The composition of the walls of these magnetic PEM capsules was $(PSS/PAH)_2$γ-$Fe_2O_3$ $(PSS/PAH)_2$. SNARF was linked to dextran ($M_w$ = 10 kDa) in order to prevent leakage of the dye from the capsule cavity.[26] The ratio of the emission intensities in the "green" and red channel can be used to calculate the local pH value.[23]

uring the fluorescence response ($I_y$) in real-time. We used a microfluidic channel with two inlets and a single outlet to generate a dynamic pH gradient (see Figure 2). The channel was molded using polyolefin polymer (POP). To load the channel with magnetic pH-sensitive PEM capsules, a suspension of the capsules (≈7 × $10^4$ $mL^{-1}$) was flushed through the channel and capsules (with embedded magnetic NPs) were trapped at the top of the channel via a magnetic field.[47] The capsules did not deform during the magnetic trapping and kept their spherical shape (see the Supporting Information). Afterwards, two different pH-buffered solutions (10 mM of 2-(*N*-morpholino)ethanesulfonic acid

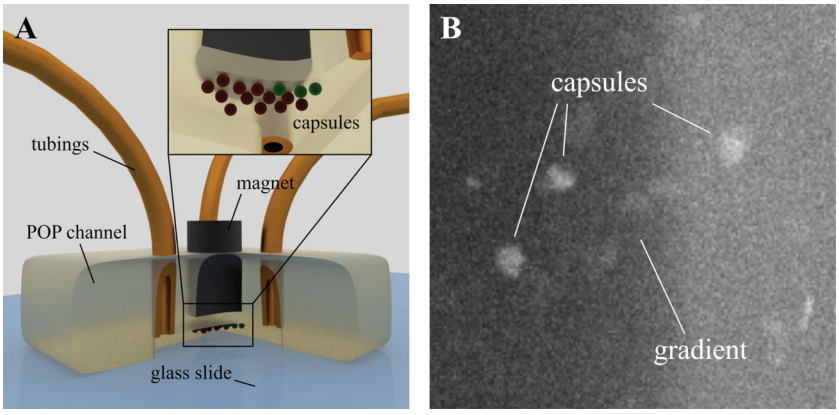


*Figure 2.* A) Microfluidic channel coupled to a fluorescence microscope where the PEM capsules are magnetically trapped at the top of the channel. Two solutions (1, 2) with different concentrations of protons ($c_1$, $c_2$) and pressure ($p_1$, $p_2$) are mixed producing a gradient that can be moved perpendicular to the direction of the gradient plane by ($p_1$, $p_2$) modification. B) Fluorescence image of $(PSS/PAH)_2$γ-$Fe_2O_3$ $(PSS/PAH)_2$ capsules trapped in the microfluidic channel in the vicinity of a static gradient (TRIS buffer adjusted to pH 9 on the left and MES buffer adjusted to pH6 labeled with TRITC on the right).

(MES) and 1 mM of tris(hydroxymethyl)aminomethane (TRIS) adjusted to pH 6 and pH 9, respectively) were pumped into the individual microchannel inlets using a pressure controlled fluidic system. By applying alternating pressures of 100 and 300 mbar at each inlet, the pH gradient could be rapidly moved from one side of the fluidic chamber to the other. The change in fluorescence of the SNARF in the capsules induced by the gradient's switching was recorded with an emCCD camera mounted to an inverted fluorescence microscope. The interframe time for the recording was set to 26.6 ms. For each measurement two pulses of pH 6 and pH 9 (duration: 10 s each) were applied and the intensity traces of individual capsules were extracted from the recorded image sequence. In order to increase the time resolution of the set-up, only one filter was used and thus the microscope registered intensity changes only of the yellow emission channel ($I_y$). In this way, at acidic pH = 6 the emission $I_y$ of the capsules is higher than at basic pH = 9. The increase/decrease of such emission was measured while pH buffers (pH = 6 and 9) were exchanged. To correlate the capsules' switching behavior with that of the gradient, control measurements were performed using the above mentioned solutions and pressure protocols with tetramethylrhodamine isothiocyanate (TRITC) added to the pH 6 buffer.

The time it takes for ions (in this case $H^+$) to diffuse into the PEM capsules was estimated from the temporal change in fluorescence during exposure to the switching pH gradient in the microfluidic system. Therefore, we analyzed the recorded fluorescence intensity traces $I_y(t)$ of each capsule after switching from pH 6 to pH 9 and vice versa. Figure 3 shows a typical response after switching the concentration from pH 6 to pH 9. An offset was added to set the lower average steady-state fluorescence signal to 0. The horizontal lines indicate the levels at which 25%, 50% and 75% of the expected intensity change had occurred. To evaluate the response speed we derived the time it takes for the fluorescence change to reach a 25% threshold of the target value (at least 3 standard deviations of the root mean square (RMS) noise). This can be seen as the onset of unambiguous detection for the pH concentration measurements. To obtain a full response curve, the recorded intensity signal has to be deconvoluted with the concentration profile of the gradient. However, this would require exact knowledge of the time-dependent concentration distribution, for example by solving the combined Navier-Stokes and convection diffusion equations with the proper boundary conditions. Thus only an upper limit for the response time can be derived by assuming a step-like concentration profile of the gradient. From the recorded intensity traces of the individual capsules, we thus obtain a half time response of 163 ± 64 ms for the switch from pH 6 to pH 9 and 213 ± 114 ms for the switch from pH 9 to pH 6 (n = 8). The discrepancy for the two switching directions could be explained by inhomogeneities and the finite width of the actual concentration gradient at the channel surface. Another possible explanation could be related with the degree of ionization of the PAH layer. At pH 9 the ammonium groups of PAH are more deprotonated than at pH 6 and the loopy conformation of PAH in this conditions could decrease the permeation of $H^+$ through the capsule shell. In this way, the time response of the sensor capsule would be higher when the shift is from higher to lower pH than the contrary as it was observed in our experiment. It is known that the pH can affect the permeation of different ions such as $Na^+$, therefore it could also affect the permeation of $H^+$.[22] Nevertheless, the results yield a good estimate for an upper boundary of the response time of encapsulated SNARF to pH. The half time response of SNARF free in solution has been studied by fluorescent spectrophotometry using a stopped-flow mixing accessory that decreases the response time of the fluorescent spectrophotometer to 1 ms and the mixing time up to 8 ms. Chen et al. reported a response time of around 50 ms for SNARF free in solution and for switching from pH 2 to pH 10.[48] Therefore, the charged PEM shell increases the upper limit of the half time response for encapsulated SNARF as pH-sensor to 100-150 ms. Chen et al. also observed an increase of 10 ms in the time response of SNARF encapsulated in a nanoreactor made of calcium phosphate and phosphatidylcholine liposomes. The different nature of the SNARF carriers could explain the discrepancies. Nevertheless, the time response of SNARF encapsulated in PEM capsules is enough for many in vitro pH detection applications.[25,49] The effect of the PEM shell needs to be taken into account when using techniques that require higher temporal resolution.[50] It should be considered that proton transport or even diffusional transport of small ions in water occurs on a much faster time scale (*e.g.* 0.5 ms for a typical diffusion constant of $1.0 \cdot 10^{-9}$ $m^2/s$ at a diffusion length of 1 µm considering 1D diffusion),[51] which is the size range of one PEM capsule.

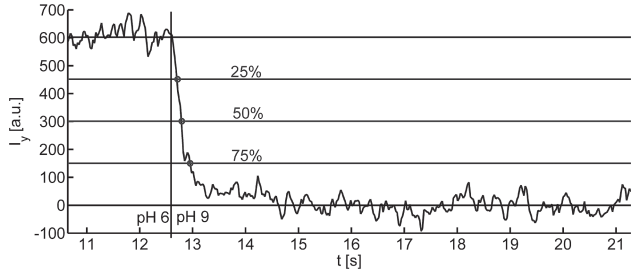


*Figure 3.* Fluorescence response measurements of PEM capsules loaded with 10 kDa SNARF-dextran in real-time. The selected filter set (excitation 440-490 nm, beam splitter 510 nm and emission 525-625 nm) records the emission $I_y(t)$ of the acidic form (pH 6) of SNARF. The vertical line indicates the time at which pH was switched from pH = 6 to pH = 9.

### 2.3. Estimation of the Ion Conductivity of Planar PEM Films

Finally, we studied the ion conductivity of planar PEM films, first without NPs trapped in between the polyelectrolyte layers. In a second measurement, the influence of the NPs on the ion conductivity was investigated. Application of PFG-NMR to the PEM films as investigated in this work is not straight forward, since the layers are in general prepared on a substrate. As it was mentioned, trying to detect the ion conductivity through these films with the help of impedance spectroscopy requires contact with two electrodes, which can easily induce short-circuits in the case of ultra-thin layers. As a consequence, we employ another technique, the recently developed bombardment induced ion transport (BIIT).[40–42] The pivotal aspect of this approach is that there is only the contact between one single electrode and the sample of interest needed for measuring the direct ion current through the film. The ion transport in the sample is induced by shining an ion beam on the front side of the sample, which leads to the adsorption of ions there. Adjusting the kinetic energy of the ions allowed us to create a well-defined surface potential and eventually gives rise to a potential and a concentration gradient across the sample. The ion transport was then detected by measuring the current induced on the backside electrode.

We have investigated the ionic conductivity of PEM films consisting of sixteen bilayers of (PAH/PSS) with and without gold NPs within the film, $(PAH/PSS)_{16}$ and $(PAH/PSS)(PAH/Au\ NPs/PSS)_{15}$ respectively, by means of the BIIT technique. The layers were prepared by the lbl technique according to a previously published protocol.[52] directly on a copper plate that was premodified with a monolayer of 3-mercaptopropionic acid, which at the same time served as the backside electrode required in BIIT (see the Supporting Information). The first layer of 3-mercaptopropionic acid was necessary to have a negative surface charge and start the lbl assembly.[53] The layers were bombarded by a continuous potassium ion beam with energies ranging between thermal conditions and about 10 eV. The current of the primary $K^+$ beam was typically 5 nA. In the experiment, the backside current was measured as a function of the ion beam potential which in turn determines the surface potential.

Our measurements indicate that the conductance of the $(PAH/PSS)_{16}$ membranes with and without Au NPs was of the order of $G = 1 \cdot 10^{-9}$ S; see Figure 4. Combined

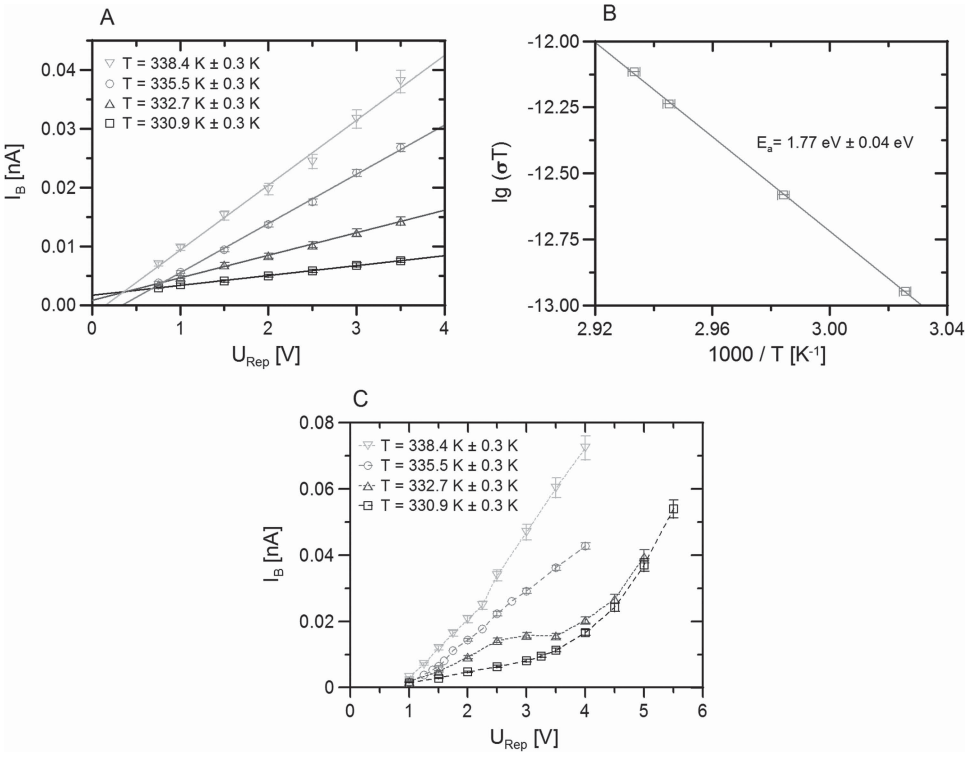


*Figure 4.* A) Backside current $I_B$ in the PEM film based on $(PAH/PSS)_{16}$ without NPs as a function of the repeller voltage $U_{Rep}$ at different temperatures. B) Arrhenius plot of the temperature dependence of the ionic conductivity σ in a polyelectrolyte multilayer film of PSS and PAH. The slope of the linear regression to the BIIT data is included, leading to the activation energy $E_a$. C) Backside current $I_B$ of the PEM film based on $(PAH/PSS)(PAH/Au\ NPs/PSS)_{15}$ as a function of the repeller voltage.

with the area hit by the ion beam and the actual thickness of the membranes this leads to a conductivity of approximately $10^{-12}$ S/m. Much higher conductivities have been reported in the literature for e.g. protons in PEM films. However those measurements were carried out in aqueous conditions.[54,55] Here, the BIIT experiment was carried out under high vacuum conditions ($10^{-9}$ mbar), so the membranes are most likely free of water. Our results agree with previously reported conductivities for similar PEM films of PSS/PAH in low hydration conditions. Direct current (DC) conductivities for (PSS/PAH) films were reported to be in the range of $10^{-12}$ S/m.[54,55] De et al. studied the dependence between humidity and ion conductivity in polyelectrolyte complexes for two different cations ($Na^+$ and $Cs^+$).[56] The water content within the PEM matrix was found to increase almost linearly while the DC ion conductivity increased exponentially with increasing humidity. Water molecules are responsible for the ion hydration as well as for the lowering of the energy barrier of the ion transport. Therefore, the conductivity and the activation energy for the ion transport obtained by the BIIT technique were expected to be lower and higher respectively than the ones obtained at higher ambient pressure.[57]

Despite the conductivities of both films with and without NPs being on the same order of magnitude, the current-voltage characteristics are fundamentally different (cf. Figure 4A,C). For the film without NPs, the observed backside current increased linearly with the applied voltage, indicating an Ohm's law like behavior. A similar behavior can be found for ion conducting glasses[41] and is most likely induced by the high number of mobile carriers inside the film prior to the ion bombardment. By contrast, the films with NPs clearly show a non-linear current-voltage characteristic indicating that more than one transport mechanism has to be considered. The presence of the NPs induces additional grains and thus grain boundaries such that competing conduction path ways arise. Depending on the given conditions such as the temperature and the applied voltage, the charge transport might work more efficiently either through the film material or along the grain boundaries. Finally one can probably not categorically rule out the possibility of electronic conductivity (as opposed to ionic conductivity) in the film with NPs. As a result, the current-voltage characteristics show linear and power law regimes as well as plateaus in the conductivity for one single temperature at different applied voltages. Thus, the temperature dependence of the conductivity is more complicated when NPs are present such that the activation energy in terms of an Arrhenius behavior cannot be derived. In contrast, the conductivity of the $(PAH/PSS)_{16}$ films made without NPs exhibits a simple Arrhenius behavior such that a well-defined activation energy of $1.77 \pm 0.04$ eV could be determined.

## 3. Conclusions

In conclusion, PEM shells around encapsulated ion-sensitive fluorophores act as semi-permeable barrier between the ion-sensitive fluorophores and the surrounding media. This barrier probably increases the response time of the ion-sensitive fluorophores. In the case of SNARF as example of a pH-sensitive fluorophore the response time was found to be below 500 ms, which is acceptable for many studies involving the analysis of the kinetics of cellular pH changes. Studies of the ion (here $K^+$) conductivity of PEM films have shown that films with and without NPs possess the same $K^+$ conductance in the order of $G = 1 \cdot 10^{-9}$ S meaning that the presence of gold NPs does not significantly affect the ion conductivity of the PEM shell. However the presence of gold NPs within the shell modified subtle details of the current-voltage characteristics of the PEM shell. The BIIT approach applied in this work has hardly any intrinsic thickness limitation. As such, the current experiment is considered to provide a proof of principle which paves the road to the investigation of even thinner films.

## Supporting Information

Supporting Information is available from the Wiley Online Library or from the authors.

Acknowledgements: This work was partly funded by the German Research Foundation (DFG grant PA 794/15-1 to WJP). X. Yu acknowledges a Chinese government scholarship (CSC).

Received: July 26, 2013; Revised: August 31, 2013; Published online: DOI: 10.1002/marc.201300571

[1] Z. Liu, Y. Yi, J. Gauczinski, H. Xu, M. Schönhoff, X. Zhang, *Langmuir* **2011**, *27*, 11806.
[2] S. Park, S. H. Bhang, W.-G. La, J. Seo, B.-S. Kim, K. Char, *Biomaterials* **2012**, *33*, 5468.
[3] M. Ochs, S. Carregal-Romero, J. Rejman, K. Braeckmans, S. C. De Smedt, W. J. Parak, *Angew. Chem. Int. Ed.* **2013**, *52*, 695.
[4] Z. Guanghong, X. Yibo, G. Jian, W. Zhiqiang, Z. Xi, *Langmuir* **2010**, *26*, 15022.
[5] L. L. del Mercato, A. Z. Abbasi, W. J. Parak, *Small* **2011**, *7*, 351.
[6] L. I. Kazakova, L. I. Shabarchina, G. B. Sukhorukov, *PhysChemChemPhys* **2011**, *13*, 11110.
[7] M. Wang, V. Janout, S. L. Regen, *Chem. Commun.* **2013**, *49*, 3576.

[8] K. Scott, S. Pilditch, M. Mamlouk, *J. Appl. Electrochem.* **2007**, *37*, 1245.
[9] L. L. del Mercato, G. Maruccio, P. P. Pompa, B. Bochicchio, A. M. Tamburro, R. Cingolani, R. Rinaldi, *Biomacromolecules* **2008**, *9*, 796–803.
[10] A. S. Angelatos, A. P. Johnston, Y. Wang, F. Caruso, *Langmuir* **2007**, *23*, 4554.
[11] W. Yuan, Z. Lu, C. M. Li, *J. Mater. Chem.* **2011**, *21*, 5148.
[12] C. Dejugnat, K. Kohler, M. Dubois, G. B. Sukhorukov, H. Mohwald, T. Zemb, P. Guttmann, *Adv. Mater.* **2007**, *19*, 1331.
[13] W.-F. Dong, S. Liu, L. Wan, G. Mao, D. G. Kurth, H. Möhwald, *Chem. Mater.* **2005**, *17*, 4992.
[14] K. Köhler, H. Möhwald, G. B. Sukhorukov, *J. Phys. Chem. B* **2006**, *110*, 24002.
[15] M. Prevot, C. Déjugnat, H. Möhwald, G. B. Sukhorukov, *ChemPhysChem* **2006**, *7*, 2497.
[16] P. M. Biesheuvel, T. Mauser, G. B. Sukhorukov, H. Möhwald, *Macromolecules* **2006**, *39*, 8480.
[17] T. Mauser, C. Déjugnat, G. B. Sukhorukov, *J. Phys. Chem. B* **2006**, *110*, 20246.
[18] D. Halozan, C. Déjugnat, M. Brumen, G. B. Sukhorukov, *J. Chem. Info. Modeling* **2005**, *45*, 1589.
[19] Y. Ma, W.-F. Dong, M. A. Hempenius, H. Möhwald, G. J. Vancso, *Nat. Mater.* **2006**, *5*, 724.
[20] A. A. Antipov, G. B. Sukhorukov, *Adv. Colloid Interface Sci.* **2004**, *111*, 49.
[21] K. Köhler, P. M. Biesheuvel, R. Weinkamer, H. Möhwald, G. B. Sukhorukov, *Phys. Rev. Lett.* **2006**, *97*, 188301/1.
[22] L. Krasemann, B. Tieke, *Langmuir* **2000**, *16*, 287.
[23] O. Kreft, A. Muñoz Javier, G. B. Sukhorukov, W. J. Parak, *J. Mater. Chem.* **2007**, *17*, 4471.
[24] M. Semmling, O. Kreft, A. Muñoz Javier, G. B. Sukhorukov, J. Käs, W. J. Parak, *Small* **2008**, *4*, 1763.
[25] P. Rivera Gil, M. Nazarenus, S. Ashraf, W. J. Parak, *Small* **2012**, *8*, 943.
[26] S. Carregal-Romero, M. Ochs, P. Rivera Gil, C. Ganas, A. M. Pavlov, G. B. Sukhorukov, W. J. Parak, *J. Controlled Release* **2012**, *159*, 120.
[27] L. L. del Mercato, A. Z. Abbasi, M. Ochs, W. J. Parak, *ACS Nano* **2011**, *5*, 9668.
[28] G. B. Sukhorukov, M. Brumen, E. Donath, H. Möhwald, *J. Phys. Chem. B* **1999**, *103*, 6434.
[29] D. Halozan, G. B. Sukhorukov, M. Brumen, E. Donath, H. Möhwald, *Acta Chimica Slovenica* **2007**, *54*, 598.
[30] D. Halozan, U. Riebentanz, M. Brumen, E. Donath, *Colloids Surf., A* **2009**, *342*, 115.
[31] H. Ohshima, *J. Colloid Interface Sci.* **2008**, *323*, 92.
[32] R. A. Ghostine, J. B. Schlenoff, *Langmuir* **2011**, *27*, 8241.
[33] B. Roling, C. Martiny, S. Bruckner, *Phys. Rev. B* **2001**, *63*, 214203/1.
[34] K. Funke, R. D. Banhatti, *Solid State Ionics* **2006**, *177*, 1551.
[35] J. C. Dyre, P. Maass, B. Roling, D. L. Sidebottom, *Rep. Prog. Phys.* **2009**, *72*, 046501/1.
[36] H. Mehrer, *Z. Phys. Chem.* **2009**, *223*, 1143.
[37] S. Arumugam, J. Shi, D. P. Tunstall, C. A. Vincent, *J. Phys.: Condens. Matter* **1993**, *5*, 153.
[38] A. R. Waldeck, A. J. Lennon, B. E. Chapman, P. W. Kuchel, *J. Chem. Soc., Faraday Trans.* **1993**, *89*, 2807.
[39] J. Kösters, M. Schönhoff, N. A. Stolwijk, *J. Phys. Chem. B* **2013**, *117*, 2527.
[40] M. Schäfer, K.-M. Weitzel, *PhysChemChemPhys* **2011**, *13*, 20112.
[41] P. V. Menezes, J. Martin, M. Schäfer, H. Staesche, B. Roling, K.-M. Weitzel, *PhysChemChemPhys* **2011**, *13*, 20123.
[42] S. Schulze, M. Schäfer, A. Greiner, K.-M. Weitzel, *PhysChem-ChemPhys* **2013**, *15*, 1481.
[43] B. Zebli, A. S. Susha, G. B. Sukhorukov, A. L. Rogach, W. J. Parak, *Langmuir* **2005**, *21*, 4262.
[44] T. Hyeon, S. S. Lee, J. Park, Y. Chung, H. Bin Na, *J. Am. Chem. Soc.* **2001**, *123*, 12798.
[45] A. Z. Abbasi, L. Gutierrez, L. L. del Mercato, F. Herranz, O. Chubykalo-Fesenko, S. Veintemillas-Verdaguer, W. J. Parak, M. P. Morales, J. M. Gonzalez, A. Hernando, P. de la Presa, *J. Phys. Chem. C* **2011**, *115*, 6257.
[46] K. J. Buckler, R. D. Vaughan-Jones, *Pflügers Arch. Euro. J. Physiol.* **1990**, *417*, 234.
[47] P. del Pino, A. Munoz-Javier, D. Vlaskou, P. Rivera Gil, C. Plank, W. J. Parak, *Nano Lett.* **2010**, *10*, 3914.
[48] Y.-C. Chen, A. Ostafin, H. Mizukami, *Nanotechnology* **2010**, *21*, 215503/1.
[49] D. Morgan, M. Capasso, B. Musset, V. V. Cherny, E. Rios, M. J. S. Dyer, T. E. DeCoursey, *Proc. Natl. Acad. Sci. USA* **2009**, *106*, 18022.
[50] F.-M. Boldt, J. Heinze, M. Diez, J. Petersen, M. Börsch, *Anal. Chem.* **2004**, *76*, 3473.
[51] E. Kätelhön, K. J. Krause, P. S. Singh, S. G. Lemay, B. Wolfrum, *J. Am. Chem. Soc.* **2013**, *135*, 8874.
[52] D. Hühn, A. Govorov, P. Rivera Gil, W. J. Parak, *Adv. Funct. Mater.* **2012**, *22*, 294.
[53] M. M. Sung, K. Sung, C. G. Kim, S. S. Lee, Y. Kim, *J. Phys. Chem. B* **2000**, *104*, 2273.
[54] M. F. Durstock, M. F. Rubner, *Langmuir* **2001**, *17*, 7865.
[55] Y. Akgöl, C. Hofmann, Y. Karatas, C. Cramer, H.-D. Wiemhöfer, M. Schönhoff, *J. Phys. Chem. B* **2007**, *111*, 8532.
[56] S. De, C. Cramer, M. Schönhoff, *Macromolecules* **2011**, *44*, 8936.
[57] C. Cramer, S. De, M. Schönhoff, *Phys. Rev. Lett.* **2011**, *107*, 028301/1.

Pharmacological Research 62 (2010) 115–125

Contents lists available at ScienceDirect

Pharmacological Research

journal homepage: www.elsevier.com/locate/yphrs

Review

# Nanopharmacy: Inorganic nanoscale devices as vectors and active compounds

Pilar Rivera Gil*, Dominik Hühn, Loretta L. del Mercato, Daniel Sasse, Wolfgang J. Parak

*Fachbereich Physik and Wissenschaftliches Zentrum für Materialwissenschaften, Philipps Universität Marburg, Renthof 7, 35037 Marburg, Germany*

ARTICLE INFO

*Article history:*
Received 28 December 2009
Received in revised form 14 January 2010
Accepted 15 January 2010

*Keywords:*
Inorganic nanoparticles
Market
Nanoscale medicines
Nanopharmacy
Pharmaceutical preparations
Medical devices

ABSTRACT

In this review we would like to aim at pharmaceuticals engineered on the nanoscale, i.e. pharmaceuticals where the nanomaterial plays the pivotal therapeutic role or adds additional functionality to the previous compound. Those cases would be considered as nanopharmaceuticals. The development of inorganic systems is opening the pharmaceutical nanotechnology novel horizons for diagnosis, imaging and therapy mainly because of their nanometer-size and their high surface area to volume ratios which allow for specific functions that are not possible in the micrometer-size particles. This review will focus on pharmaceutical forms that are based on inorganic nanoparticles where the nanosize of the inorganic component provides unique characteristics to the pharmaceutical form. Several examples of these systems that are either in pre-clinical investigation and under examination by the Food and Drug Administration (FDA) or that have been already approved by the FDA and are in clinical practice today like Gastromark®, NanoTherm®, Colloidal Gold for Lateral Flow tests, HfO-NPs, BioVant™ will be described and reviewed.


**Contents**



## 1. The era of Nanoscience

Nanotechnologies are nowadays gaining in commercial use. After almost thirty years of basic and applied research, the number of commercial products advertised as containing nanoparticles (NPs) is increasing rapidly. Within all the fields to which nanotechnology can be applied, the medical field is one of the prominent directions which attract continuous investment and financial support. Nanomedicine could be defined as the application of nanotechnology to health care [1] [2] or more concretely, the use of nanoscale or nanostructured materials in medicine that according to their structure have unique medical effects [3]. Nanomedicine involves nanomaterials in a submicron size range of a few to a few hundreds of nanometers which are on purpose designed to

* Corresponding author.
*E-mail address:* pilar.riveragil@physik.uni-marburg.de (P. Rivera Gil).

1043-6618/$ – see front matter © 2010 Elsevier Ltd. All rights reserved.
doi:10.1016/j.phrs.2010.01.009

result in new medical effects due to their unique physico-chemical properties that differ from their macroscopic counterparts. These materials also require novel manufacturing and characterization techniques. Different applications of Nanomedicine within the health care include the use of NPs (i) as active pharmaceutical ingredient (API), where the main role is played by the nanomaterial, i.e. for the purpose of therapy, diagnostics, imaging; (ii) as vectors (a solid carrier that introduces the active ingredient into a recipient or host organism) or with an *enabling* function. In the latest application, the NPs add a new functionality to the pre-existing product, e.g. NPs for target delivery or as biomaterials.

Based on the definition of Nanomedicine and that of Pharmacy (science concerned with the preparation, dispensing and effective use of pharmaceuticals), in this review we would referred to Nanopharmacy as an interdisciplinary science concerned with the preparation, dispensing and effective use of nanoscale-based pharmaceuticals, i.e. active compounds used in the treatment, cure, prevention or diagnosis of diseases. A proposed definition describes nanopharmacy as "*decreasing the particle size of sparingly soluble drugs down to nanometric regime and conjugation with appropriate excipients*" [4]. However, in this review we would like to aim at pharmaceuticals engineered on the nanoscale, i.e. pharmaceuticals where the nanomaterial plays the pivotal therapeutic role or adds additional functionality to the previous compound. Those cases would be considered as nanopharmaceuticals. The most common nanopharmaceutical forms today are organic platforms that include polymeric NPs and dendrimers, liposomes and other lipid assemblies, and engineered viral NPs mostly for drug/gene delivery applications [5]. Nevertheless, the development of inorganic systems is opening the pharmaceutical nanotechnology novel horizons for diagnosis, imaging and therapy mainly because of their nanometer-size and their *high surface* area to *volume ratios* which allow for specific functions that are not possible in the micrometer-size particles [6,7].

This review will focus on pharmaceutical preparations that are based on inorganic NPs where the nanosize of the inorganic component provides unique characteristics to the pharmaceutical form. Several examples of these systems that are either in pre-clinical investigation and under examination by the Food and Drug Administration (FDA) or that have been already approved by the FDA and are in clinical practice today like Gastromark®, NanoTherm®, Colloidal Gold for Lateral Flow tests, will be described and reviewed.

## 2. Physical, biochemical and biological properties of inorganic nanoparticles

### 2.1. Iron oxide nanoparticles (FeO-NPs)

FeO-NPs are commonly composed of an inorganic magnetic core and a biocompatible surface coating that provides chemical stability under physiological conditions, dispersibility in aqueous solution, and reduced toxicity [8–10]. Inorganic cores of 4–15 nm size made up of iron oxides such as magnetite ($Fe_3O_4$) or maghemite ($\gamma$-$Fe_2O_3$) dominate the field of biomedical applications due to their superior stability and the lower toxicity compared to other metal oxides [11,12]. FeO-NPs can naturally be broken down within the Fe-metabolism in the spleen and liver and due to their small size are more difficult to recognize by the immune system [13–15]. When the particle has only one magnetic domain (like in case of small NPs) thermal excitations can flip the direction of magnetization in relation to the particle axis at temperatures higher than the so called blocking temperature. Thus, superparamagnetic NPs (SPIOs) show no magnetism above the blocking temperature in the absence of an external magnetic field, as their respective magnetizations are randomly oriented. This is termed the superparamagnetic state [16]. A magnetic field can effectively magnetize the particles, as the magnetic moments of the particles are oriented in this field. When the field is removed the magnetization disappears completely, unlike in larger particles or bulk material in which residual magnetism (also known as remanence) can be observed. Depending on the sort of magnetic field applied, SPIOs exhibit different properties useful for medical applications, i.e. (i) as heat-producing agents for treatment or (ii) as contrast agents for imaging. (i) When exposed to varying magnetic fields created by alternating currents (AC) SPIOs heat up. The underlying heating mechanisms by which the field energy is converted into thermal energy depends on the magnetic properties of the particles and thus on their size [17]. Hysteresis heating under AC magnetic fields can only be observed in ferro- or ferri-magnetic materials, but not in superparamagnetic particles [17]. The heat originated by SPIOs is produced because the magnetic moments align under the influence of the magnetic field (but the particles as a whole do not physically rotate) and relax to their equilibrium orientation when the field is turned off. This effect is referred to as Néel relaxation [17]. During cyclic alignment energy is dissipated. In contrast, heating by physical rotation of the particle as a whole is referred to as Brownian rotation and possible in both cases [17]. SPIOs show remarkably higher specific absorption rates (SAR [W/g], the measure of the heat generating capacity of the magnetic substance in the alternating magnetic field) than larger particles. Thus, by applying the right quantity of field energy and for the right time heat can be efficiently produced to cause thermal-mediated cell death. This makes SPIOs a good alternative for clinical applications of hyperthermia, in particular for cancer therapy [18]. (ii) When exposed to static magnetic fields SPIOs are magnetized, which creates a local magnetic field gradient. This finally leads to improved signals for the visibility of the internal structure where the NPs are accumulated. Diagnostic imaging in principle depends on the signal contrast between normal and pathologic tissue: the higher the signal contrast, the more advantageous the conditions for resolving anatomic structures and pathologic changes. In general, contrast agents can mark selective regions such as the gastrointestinal tract, for example to enhance the distinction from other adjacent organs and tissues [20]. In essence, MR image contrast is mainly due to distinct spin relaxation times of different types of tissue and the local proton density. The spin is a fundamental quantum mechanical property, which has no classical analogue and is therefore not exactly illustrative. As a basic concept, the spin can be perceived as a vector that points in a respective direction. Within the MRI scanner a strong, static magnetic field causes the nuclear spins of hydrogen protons to precess around an axis parallel to the magnetic field lines. The precessing spins are like small magnets that orientate themselves on the sides of a cone parallel or antiparallel to the field lines. For energetic reasons, nuclei with parallel orientation predominate and create a constant magnetization. The precession frequency of the spins (Larmor frequency) depends on the strength of the applied field, and because the field is applied with a spatial gradient, the precession frequency of the spins depends on their position within the field. A transverse radio frequency (RF, an electromagnetic wave) pulse, tuned to the protons Larmor frequency of a certain layer within the magnetic gradient field, is used to deflect the spins, and thereby the magnetization is tilted. The magnetization can be decomposed into a component along field lines of the static magnetic field (longitudinal magnetization), and a perpendicular component (transverse magnetization). After the perturbation through the RF pulse both the longitudinal and the transverse magnetization relax independently to their state of equilibrium by spin–lattice and spin–spin interaction, respectively. The realignment of the magnetic moments induces small voltages in

surrounding inductors that are monitored to obtain the MR image. The time constants of the longitudinal (T1) and transverse (T2) relaxation are tissue specific and can additionally be altered by the accumulation of contrast agent in tissue [21]. The SPIOs cause local field gradients within a magnetic field that strongly reduce both T1 and T2 relaxation times [14]. How much the proton relaxation rate is increased by a contrast medium is described by its relaxivity, which is the reciprocal of the relaxation time [14]. The relaxivity further depends on temperature, field strength and solvent [22]. Conventional contrast agents rely on paramagnetic metal (usually gadolinium) chelates that primarily shorten the T1 relaxation of the regions nearby [23]. They are called positive contrast agents because they increase the signal intensity in T1-weighted sequences and thus appear bright [22]. Free $Gd^{3+}$ is acutely toxic, but the tolerance of gadolinium chelates is basically excellent [24]. However, nephrogenic systemic fibrosis was recently associated with gadolinium-containing contrast agents in patients with severe renal impairment [25]. Depending on the diagnostic question, the contrast medium is either orally administered or directly injected into veins, arteries or joints to make, e.g. the brain, kidney, liver, blood vessels or the gastrointestinal tract and potential damages visible. In many cases, pathology can be diagnosed by varied signal enhancement kinetics [26]. As an example, hypervascular tumor tissue is often seen to enhance earlier than normal tissue, thus the tumor-to-normal tissue contrast is transiently increased [27]. Nowadays, novel formulations can be found in the market that are based on SPIOs that, unlike conventional contrast agents, provide T2 pronounced contrast enhancement by shortening T2 relaxation times [22,28,29]. The crystalline FeO cores coated with dextran (in ferumoxide and ferumoxtran) or siloxane (in ferumoxsil) [30] are referred to as "negative contrast agents" because they originate shorter T2 times that appear dark in T2 weighted images. The mean crystal diameters of particles used for MRI (volume weighted distribution) are listed in the range of 4.6–5.6 nm for ferumoxides, 4.3–6.2 nm for ferumoxtran and 7.9–9.5 nm for ferumoxsil. Differences in the values depend on the measurement technique and the definition of "mean", i.e. number average, surface area weighted or volume weighted average diameter [30]. Therefore, within a magnetic field SPIOs are able to create local inhomogeneities what makes them suitable for MRI applications [14].

### 2.2. Gold nanoparticles (Au-NPs)

The synthesis and functionalization of inorganic colloidal Au-NPs comprises well-known reproducible methods [31–33] which makes these NPs suitable for commercial purposes. Au-NPs show high colloidal stability upon wrapping the inorganic Au core within a shell of stabilizing molecules that also acts as an anchor for further functionalization upon attachment of biomolecules [34]. Au-NPs have unique optical properties due to their nanometer size [35]. Au-NPs are able to strongly absorb light if the corresponding frequency matches with their surface plasmon resonance (SPR) frequency. This absorption band causes the color of a colloidal Au-NP solution. The SPR frequency is mainly influenced by shape and size of the Au-NPs. For example 20 nm Au-NPs typically absorb at about 520 nm what causes the (observable by eye) red color of the solution. SPR is basically a collective oscillation of the free electron gas in the metal upon stimulation [36]. On a NP surface such a stimulus leads to the formation of evanescent surface waves with longitudinal electronic oscillations parallel to the metal surface. Coupling of the electron gas to the atomic lattice transfers the absorbed energy from the electron gas to the crystal lattice (resistive heating). Finally the heat diffuses into the surrounding medium [37–41]. These photothermal properties of Au-NPs make them suitable for medical applications related to temperature-sensitive phenomena. Examples comprise the removal of tissue, such as endometrial ablation, the destruction of tumors by increasing the temperature of the cancerous cells to lethal levels, as done in hyperthermia or thermal ablation [42,43]. Therefore pharmaceutical preparations that support these therapies (mostly auxiliary therapies) are very promising in the field of nanopharmacy.

Because gold is a noble metal and therefore slack of chemical reactions it causes almost no inherent toxicity, though several aspects of cytotoxicity have to be verified. The nanoscopic dimensions could cause cytotoxic effects if Au-NPs are taken up and stored by cells, considering the fact that nano-sized gold particles may turn into effective catalysts also depending on their shape [44]. Of course also different properties like cell type [45,46], surface chemistry (including functionalized Au-NPs by side chains) [47], and Au-NP size [48] influence the cytotoxic behavior. How Au-NPs interact with cells, cell compartments and especially DNA has been investigated in several studies. *In vitro* studies agree that the most favorable reason for cytotoxicity is concentration-dependent [49,50]. In the case of the interaction of Au-NPs with DNA, there are two dominant reasons. On one hand NPs with the right size (about 1.4 nm) match nearly with that of the major DNA grooves and on the other hand gold as the most electronegative metal easily attracts to those grooves due to their negative environment. Thereby small Au-NPs cause a strong toxicity towards different cell lines as opposed to 18–20 nm Au-NPs [51]. Recently, *in vivo* studies confirmed size-dependent toxicity [52,53]. Besides also the form of uptake might play a role, thus oral ingestion and injection showed different safety profiles [54,55]. Regarding the studies concerning cytotoxicity of Au-NPs one can say that this important factor is not explored enough yet and that their use should be always considering the possibility of potential cytotoxicity.

### 2.3. Hafnium oxide ($HfO_2$) nanoparticles (HfO-NPs)

Hf is an inert transition element corrosion resistant and with a high melting point that forms a stable crystalline oxide which tends to be insoluble in water. The low ionization energy values (the least required energy to release a single electron from the atom into vaccum) for Hf together with its low electronegativity (ability to draw electrons relative to other elements) make this metal easily ionizable and thus a good electron donor upon light irradiation. Due to these physicochemical properties, HfO appears as a potent oxidant agent that could be useful for redox-related medical applications as radiotherapy. The mechanism underlying the action of Hf for radiotherapy is explained as follows. When X-rays are absorbed by HfO, the Hf atoms become ionized and can act as electron donors, which can create free radicals. In the same direction, when excited HfO particles relax to the ground state, they emit UV light [56], which in turn can produce free radicals. In this way, X-ray excitation of HfO in contact with water and oxygen can produce reactive oxygen species (ROS). These include free radical and non-radical reactive intermediates such as $O_2^-$, $OH^-$, and $H_2O_2$. In biological environment, high concentrations of these reactive metabolites are able to cause cell death [57]. Although, HfO has been mainly investigated as thin films [58,59], inorganic microparticles made of hafnium germinate and HfO as by-products with excellent X-ray absorption properties due to their high density have also been described recently [60]. However, neither the crystalline structure, nor the size distribution, nor the stability in solution of these particles, is yet well controlled. Then they strongly vary on the synthesis procedures, which are not yet well characterized.

### 2.4. Calcium phosphate nanoparticles (CaP-NPs)

Calcium phosphate is one of the principle building blocks of hard tissues in the body such as bones, teeth and tendons [61]. Moreover

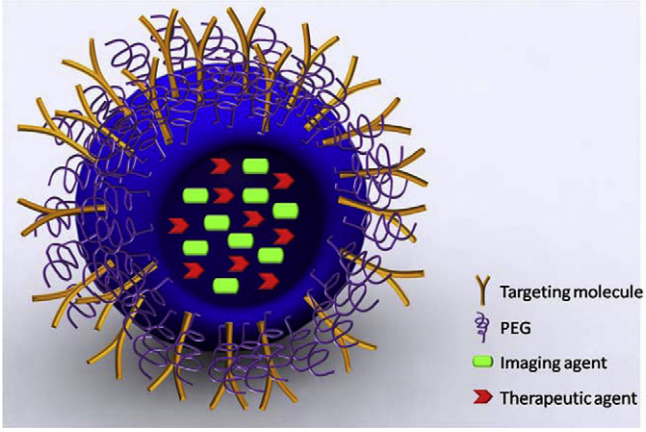


**Fig. 1.** Schematics of a multifunctional CaP-NP for both imaging and drug delivery. Imaging agents (green) and active therapeutic agents (red) can be encapsulated within the matrix of the particle whereas low-fouling molecules (i.e. polyethylene glycol (PEG)) and targeting molecules (antibodies or other recognition agents) can be functionalized onto the particle surface. Figure adapted from reference [67] (For interpretation of the references to color in this figure legend, the reader is referred to the web version of the article).

its biodegradation products, $Ca^{2+}$ and $PO_4^{3-}$, are found in relatively high concentrations (about 1–5 mM) in the bloodstream [62,63]. Because of their natural occurrence, CaP-NPs are classified as biocompatible and safe systems by the FDA [61] and are widely used in pharmaceutical technology [64–68]. Nevertheless, World Health Organization and the European Pharmacopoeia recommend their use at concentrations lower than 1.3 mg of calcium per dose [69], probably because even small concentrations of calcium might disrupt the delicate chemical balance of the organism. The synthesis of CaP-NPs can be performed by using a wide variety of precipitation strategies [70–73]. However, the major part of these procedures produces particles with diameters above 100 nm and with some agglomeration [71,72]. Because the formation of CaP-NPs occurs during a precipitation reaction, the active agent (hydrophilic or hydrophobic) can be easily encapsulated within the CaP matrix of the particle by simply adding it during the particle formation process [68,74]. However, special attention must be taken by selecting the precipitation strategy, since composition and adsorption properties of CaP-NPs must be highly controlled in order to obtain a safety calcium/phosphorus molar ratio and enough cargo entrapped, respectively [69]. Encapsulation preserves not only the pharmacological activity of the cargo from biological degradations, but also reduces the potential toxicity of the cargo versus non-target sites during circulation within the body. CaP formulations are typically highly stable in physiological conditions over extended times (several weeks) [67]. The release mechanism of encapsulated material is mainly based on the pH-dependent solubility of CaP-NPs. In fact, the CaP embedding matrix is relatively insoluble at physiological pH (pH 7.4) and becomes increasingly soluble below pH 6 [64,65,68,75,76]. The pH changes occurring during cellular uptake, lead to dissolution of CaP-NPs and subsequent release of encapsulated agents [74]. In this way, it can be concluded that CaP-NPs appear as a promising carrier (Fig. 1) due to their biocompatibility and their ability to use the natural environment of the cell to release the cargo without the necessity of an external trigger.

## 3. Inorganic nanoparticles as API

In this section, some pharmaceutical preparations that make use of the above introduced NPs that are already marketed or under clinical studies will be described and referred to their medical applications.

### 3.1. In vivo imaging—FeO-NPs formulations for MRI

The clinical use of SPIOs is most advanced in the field of MRI. MR images are obtained by measuring the relaxation of hydrogen spins. Contrast agents (like FeO-NPs) can strongly influence the relaxation of nearby hydrogen spins. Upon a strong, static magnetic field the magnetic moments of the nuclei of the hydrogen atoms are aligned to the magnetic field. Then the precessing of the spins is disturbed upon radio frequency pulses, after which the spins can finally relax to their original orientation. This re-alignment of the magnetic moments induces currents in conduction coils which are the signals detected by MR tomography. FeO-NPs have gained market maturity [3]. Approved contrast agents based on SPIOs are currently used to improve imaging of abdominal structures (GastroMARK®/Lumirem® and Abdoscan®). The median diameter (coating included) of FeO-NPs is greater than 50 nm. GastroMARK (ferumoxil, agent: AMI-121) is an aqueous suspension intended for oral administration, with particle sizes reported between 200 and 400 nm. However these values correspond to the overall size of the FeO formulation and not to the inorganic core, which is in the range of a few nanometers. After administration, GastroMARK flows through and darkens the bowel, which makes it easier to distinguish the intestinal loops from adjacent tissues and organs, as pancreas and anterior kidney. Other SPIO-based contrast agents approved for the imaging of the liver and spleen like Endorem/FERIDEX I.V. and Resovist has been currently removed from the market. One of the limitations of FeO-NPs is that they tend to suffer from strong problems of aggregation during the synthesis as well as inside the cells. Therefore, special attention must be taken to control the colloidal and chemical stability of FeO-NPs in different environments. This involves for example low/high pH and interaction with blood-occurring proteins. The contrast enhancement of NPs is strongly affected by size, surface properties and degree of aggregation [85].

Another example of FeO-NPs being currently developed as blood pool agents for vascular angiography and for lymph node imaging are the ultra small superparamagnetic iron oxide nanoparticles (USPIOs) with diameters less than 50 nm [14]. The most advanced formulation in this field seems to be Sinerem®, an USPIO-based contrast agent developed for tumor detection in lymph nodes. In 2007, Guerbet (www.guerbet.com) withdrew its marketing authorization application for Sinerem®, whose efficiency could not be demonstrated statistically.

### 3.2. Thermal cancer therapy—FeO-NPs formulations for hyperthermia

Thermal cancer therapy is basically the use of heat from different sources, such as electromagnetic waves or ultrasound, to kill tumor cells mainly by means of cytoplasmic and membrane protein denaturation [86]. The idea of hyperthermia as the artificially induced elevation of temperature above the therapeutic threshold of 41 °C up to 46 °C inside the body exists since decades [18,87]. Hyperthermia is usually applied in combination with other therapies like chemotherapy or radiotherapy [88]. The underlying mechanism of thermal radiosensitization is that heat produces vasodilatation (increase in the diameter of the vessels) and subsequent reduction of the velocity of the blood flow in order to maintain the flux constant as well as raising the pressure in the vessel. In case of tumor tissue connected to the blood supply by their own vessels, the resulting low velocity and differences in pressure favors the gas exchange between the extracellular and the intratumoral space and could lead to higher $O_2$ levels in the hypoxic cancerous tissue, thus increasing the efficacy of the radiotherapy (see Section 3.4). Similarly, chemosensitization occurs due to the increased delivery of the

chemotherapeutic drug. However, these two processes only occur in the first phase of the hyperthermia (<43 °C). When the temperature increases to lethal levels (>43 °C), the hyperthermia can starve out the tumor cells by raising the hypoxia and the acidosis of the tumor because of a decreased blood flow [86]. Recently, superficial hyperthermia as a palliative therapy for solid surface and subsurface tumors was approved by the FDA (www.bsdmedical.com). However this technology based on the simple application of heat is limited to the location and depth of the tumor and by the side effects related to the direct heating upon tissue. The use of NPs could help to overcome these problems. In the field of nanotechnology both Au and FeO-NPs can be aimed at hyperthermia [89–92]. Au-NPs can be heated by absorption of light, whereby the absorbed light energy is converted into thermal energy. Upon exposure of FeO-NPs to alternating magnetic fields, heat is generated by Néel relaxation and Brownian rotation [10,93]. SPIOs show remarkable higher SAR than the larger particles show [18]. Ideally, biofunctionalized NPs can be targeted (via passive or active targeting) to the tumor, where they accumulate. If now an external stimulus is applied the temperature of cells close to the particles is raised faster than that of more distant cells. In this way cells in the vicinity of the particles can be selectively killed and a reduction of the exposure time of the organism to the external stimuli is achieved. Nevertheless, hyperthermia by photoinduced heating of Au-NPs will work best for tissue close to the skin since the light intensity diminishes among penetration. For deeper tissues heating with magnetic particles is favorable. On one hand, the magnetic fields are more difficult to focus than the light beam, thus unnecessarily exposing the healthy tissue to heat. On the other hand, the overall increase in the temperature stimulates the immune system which could help fighting against the tumor.

In the field of nanotechnology, MagForce Nanotechnologies GmbH (Berlin) (www.magforce.de) with their technology currently in the final phases of clinical trials seems to be pioneers in this field. NanoTherm® magnetic fluid is an aqueous colloidal dispersion of FeO-NPs (≈111 mg/ml Fe concentration). The FeO-NPs are synthesized in magnetite phase ($Fe_3O_4$). The resulting NPs have an average size that ranges from 10 to 15 nm and the cores are coated with aminosilanes. NanoTherm® is currently under clinical studies within Phase I (feasibility studies) or Phase II (efficacy studies) for esophageal cancer and various local recurring or residual tumors or for malignant brain tumors (glioblastoma multiforme) and prostate carcinomas, respectively. The NPs are brought to the tumor by instillation (lat. *instillare = to drip*) which implies the slow administration of the liquid (3–10 ml) drop by drop with the help of a cannula. The tumor cells can incorporate the NPs upon exposure of the tumor tissue to the solution. Now the magnetic field applicator is positioned around the overheating region (around 20 cm) and a spool current of 100 kHz oscillating cycle continuously adjustable from 100 to 500 A is applied. In response the NPs generate heat (Fig. 2). Since the SAR of the NPs is known, the exact quantity of magnetic fluid necessary for a thermotherapy procedure can be determined. Thus, the magnetic energy conversion into heat can be calculated from the density distribution which is measured in a computer tomography. However, high SAR values are pivotal for an effective energy transfer under clinical conditions because the strength and the frequency of the applied magnetic AC field are (clinically and technically) limited [17]. Furthermore, differences in thermal conductivity among the tissues or inhomogeneous distribution of the NPs within the tissue could result in very non-uniform heat (temperature) distribution and thus inefficiency of the technique since the thermal dose and the clinical outcome are significantly correlated. Additionally, hyperthermic cell death can be disrupted if the temperature increase is not maintained high and long enough to enter the exponential phase (>43 °C) where irreversible cytotoxicity is induced [86]. Possible reasons are because of applying inadequate exposure times (too short) or due to thermoresistance, i.e. increase and decrease of the temperature above the threshold for irreversible damage between different heat shocks originate a thermotolerance [94].

### 3.3. Photothermal cancer therapy—gold shell NPs for thermal ablation

Both, hyperthermia and thermal ablation are therapies related to the use of heat as a way of action to kill pathophysiological tissue. The difference relies mainly on the range of rising temperature applied. Whereas hyperthermia is associated with temperatures between 41 and 46 °C where the cells are more sensitive to other therapies, thermal ablation involves higher temperature raising up to 70–80 °C that causes irreparable damage to the cells [95]. Thermal ablation whereby a needle attached to an electrode is positioned into a tumor has been studied in many forms, including microwaves, radiofrequencies, laser irradiation, and high-intensity focused ultrasound [91]. Depending on the size of the tumor, thermal ablation can itself be the primary therapy or an auxiliary therapy to the traditional ones, i.e. surgery, chemo- and radiotherapy. The so-called Plasmonic Photothermal Therapy makes use of the physico-chemical properties of Au-NPs and has been found to be orders of magnitude more intense and powerful in tumor destruction than conventional phototherapy (irradiation of diseased tissue without NPs) [96]. Au-NPs-based formulations make use of different forms of laser excitation (near infrared, NIR or visible light) to cause a light-to-heat energy conversion [97–99]. By tuning the shape of the NPs, the excitation wavelengths can be shifted to the NIR region of the light spectrum which is more

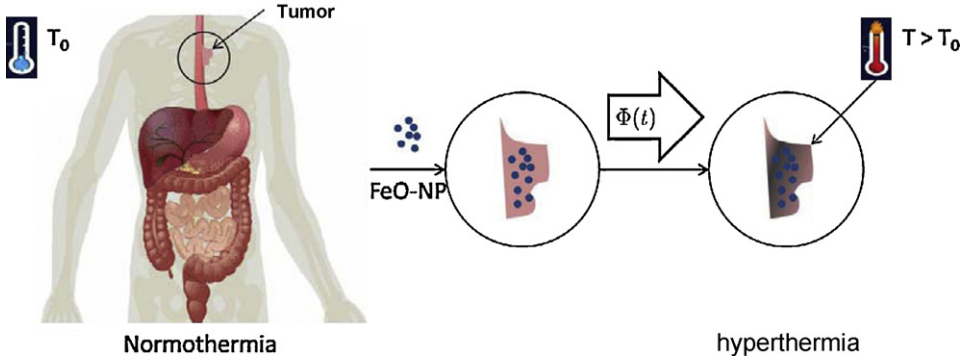


**Fig. 2.** FeO-NPs-induced hyperthermia for cancer therapy. FeO-NPs (blue dots) are brought to the tumor site (esophageal cancer). An alternating magnetic field ($\Phi$ ($t$)) of sufficient strength is applied to heat up the particles via the conversion of magnetic field energy to thermal energy. Thus, a permanent energy flow into the surrounding tissue, that irreversibly increases the temperature to lethal levels can be obtained resulting in hyperthermal-induced cell death (the necrotic tumor tissue is represented in black color) (For interpretation of the references to color in this figure legend, the reader is referred to the web version of the article).

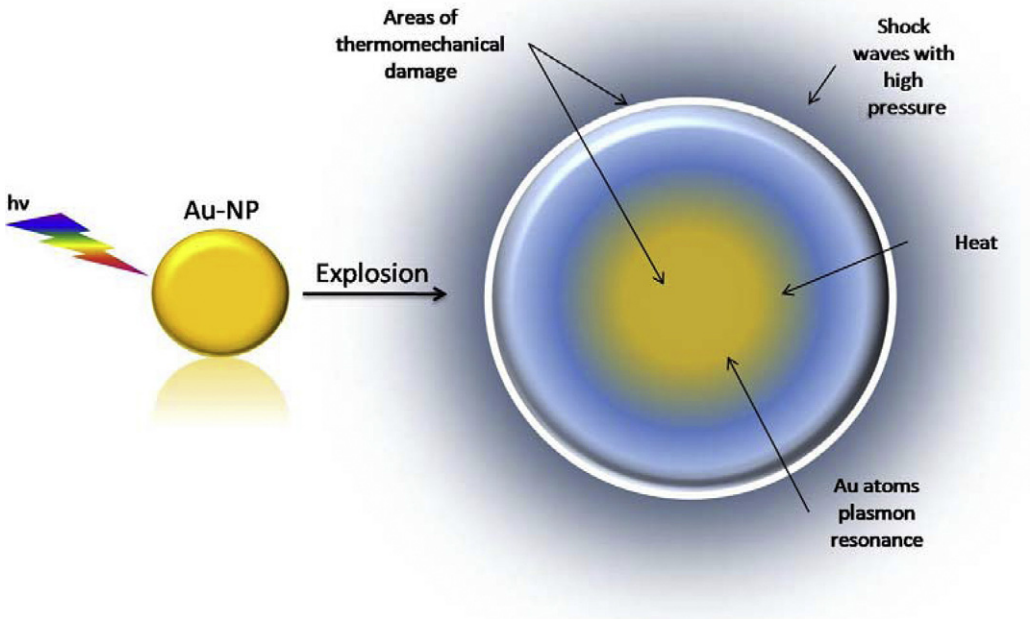


**Fig. 3.** Photo-induced thermomechanical damage mediated by Au-NPs. Light ($h\nu$) irradiation of Au-NPs induces thermal explosion. Upon absorption of light, Au-NPs transfer the energy into heat which is then transported by the water-based medium to the surrounding areas. The increase in the temperature of water causes vapor bubbles that can mechanically damage the surrounding medium due to the formation of pressure waves with the elevated temperatures obtained by heating the Au-NPs. Figure adapted from reference [102].

permeable in tissue compared to light of smaller wavelengths. Combining thermal ablation and the photothermal properties of Au-NPs, Nanospectra Biosciences (www.nanospectra.com) developed a core-shell intravenous formulation (AuroShell) for particle assisted laser ablation of solid tumors which is currently the subject of a clinical pilot study concerning refractory and/or recurrent tumors of the head and neck. AuroShell consists of a silica core (80–150 nm) with an Au shell of 10–20 nm that has been PEGylated (functionalized with poly(ethylene)glycol, PEG). PEG was presumably used to increase the colloidal stability of the NPs in the blood stream. The uptake of the AuroShell NPs by tumor cells after intravenous injection underlies the enhanced permeability and retention effect (EPR) concerning solid tumors. For irradiation a laser probe gets inserted into the solid tumor and upon excitation of the Au-NPs the tumor cells are intended to be destroyed. The main advantage of this NP-based device relies on the ability to localize the heating in the tumor where the NPs are located and therefore to shorten the time of irradiation applied. However, as thermal ablation, it is a localized destructive technique and this limits the number and the size of the tumors that can be treated. Furthermore, this system is a matter of unspecific/non-controllable way of delivery that makes use of the intrinsic properties of tumors to accumulate the NPs [100] and therefore with the associated disadvantages of accumulation of the NPs in healthy tissue. This undesired effect could be abrogated by controlling the accumulation of the NPs via active targeting or if possible by direct injection of the NPs to the tumor site. Despite active or passive targeting, it would be possible that the diffusion of the heat from the NPs to the surrounding environment does not reach all areas of the tumor, since the temperature elevation compared to the surrounding medium decreases reciprocally with $1/r$ ($r$ = distance to the NP center) [101]. Therefore not all the cancer cells will be destroyed. Another possibility that could enhance/supplement thermal ablation mediated by Au-NPs is offered by the use of light induced thermal explosion of Au-NPs enabled by short laser pulses. For this a strongly absorbing target has to generate heat more rapidly than the heat can diffuse away in the surrounding medium. The effect of explosion would lead to the formation of air/water vapor bubbles and acoustic or shock waves which cause an intense mechanical damage of the surrounding cancer tissue (Fig. 3). This method promises also the protection of healthy tissue due to the sensitive adjustability of parameters like the laser pulse duration and wavelength [102].

### 3.4. Ionizing radiation cancer therapy—radiotherapy with HfO-NPs

Radiation therapy is hereby referred to as the treatment of diseases (e.g. cancer) with ionizing radiation, such as X-rays. It involves the formation of ROS, i.e. free radicals or non-radical reactive metabolites of the ionized/excited molecules, that leads to (programmed) cell death (necrosis/apoptosis) [103]. In oncology, radiotherapy is mainly used with curative intent (as an adjuvant treatment that follows the primary therapy, normally surgery, when the risk for relapse is high or concomitantly to other therapies) or for palliation. One of the major limitations of radiotherapy is the low levels of molecular oxygen (state called hypoxia) present in the tumor tissue. Oxygen is a potent radiosensitizer that induces the formation of ROS upon its reduction by ionized/excited molecules (i.e. water, metals). Vascular abnormalities or intratumoral pressure gradients are parameters involved in generating a hypoxic environment underlying solid tumors that adversely influences the outcome of radiotherapy [104]. HfO-NPs (nbtxr3) represent another example of inorganic NPs as therapeutic sources in this case for radiotherapy. Nbtxr3 NPs are synthesized by Nanobiotix (www.nanobiotix.com) [60] for the treatment of radiosensitive and radioresistant tumors. These NPs are still under pre-clinical development and not even yet validated for clinical trials. Nbtxr3 consists of a suspension of inert crystalline NPs of hafnium oxide with an average size of 70 nm, stabilized in water with a coating agent. The formulation is for injection directly at the tumor site. Due to their inert nature, the NPs do not cause any chemical reaction unless

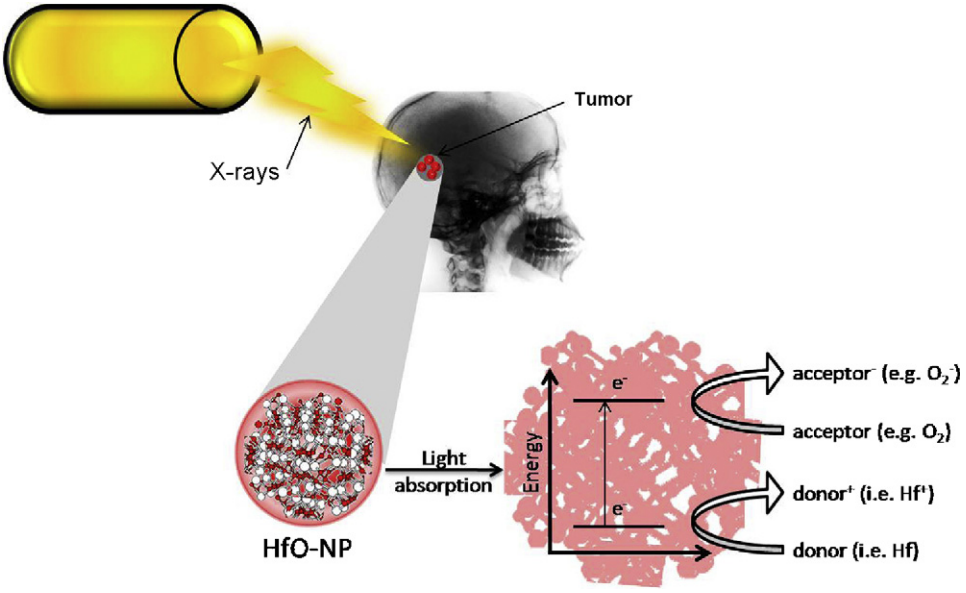


**Fig. 4.** Radiotherapy based on HfO-NPs. Water soluble HfO (red and white, respectively)-NPs are directly injected to and thus localized at the tumor site (e.g. brain tumor). Radiotherapy based on HfO-NPs depends on the ability of Hf atoms to ionize surrounding tissue by the absorption of X-rays (For interpretation of the references to color in this figure legend, the reader is referred to the web version of the article).

they are ionized with an external beam of X-rays. Once injected intratumorously, the interaction between the X-rays and the NPs results in ionization (Fig. 4). This promotes the composition of free radicals, which ultimately kill the tumor cells. Probably Nanobiotix tries to make use of HfO-NPs to mimic the action of oxygen in order to overcome the hypoxia-associated decreased radiosensitivity and therefore to increase the effectiveness of a given dose of ionizing radiation. HfO-NPs would then serve as radiosensitizers agents to sensitize tumor cells to radiation. The main advantage of this system relies in the ability to diminish the exposure time of the organism to the ionizing radiation and to accumulate in the target tumor tissue higher levels of radiation due to the increased absorption by the NPs. Nevertheless, the still unsolved problem is that water molecules also strongly absorb X-rays and therefore the healthy tissue is also exposed to free radicals. Furthermore like in other kinds of radiotherapy, the dose delivered to the patient should be verified with *in vivo* measurements in order to control the amount of energy imparted to or absorbed by the body and to avoid unnecessary harm to health. This should be taken into special account when involving NPs in the treatment. Inhomogeneous distribution of the particles within the tumor could lead to non-uniform patterns of energy deposition.

## 4. Inorganic NPs as vectors or with an *enabling* function

In this section some inorganic NPs-based formulations as carriers to guide the active ingredient into a recipient or host organism, with an *enabling* function to add a new functionality or as implantable biomaterials will be described.

### *4.1. In vitro diagnosis—lateral flow devices based on fluorogenic Au-NPs conjugated to specific antibodies (Abs)*

The system in this chapter consists of Au-NPs conjugated to Abs for the detection of molecules *in vitro*. Though this system fits better into the definition of medical device (as a diagnostic agent) and not on the definition of pharmaceutical preparation, it is a very well established application of Au-NPs on the market and thus interesting to describe. It is also worthy to mention that although the heart of the system could be considered being the Abs as the detection component, the Au-NPs also play a pivotal role as signal generator and read out device. Since strictly thought the Au-NPs are the carriers for the Abs, we have decided to classify this device under chapter 4 (inorganic NPs as vectors).

Lateral flow assays are also known as immunochromatographic strip tests. Lateral flow devices are based on a strip format that uses (nitro)cellulose, paper or a plastic support to detect a single or multiple analytes based on fluid migration or capillary action. A great variety of lateral flow devices for the detection of analytes under circumstances where a rapid test is required can be found in the market rapid test is required. They are easy and quickly to read out but they are not the most sensitive devices. The principle works upon an antigen-Ab binding in a sort of sandwich immunoassay. Therefore, two different Abs that are able to detect distinct epitopes of an analyte molecule are used (e.g. for pregnancy, drugs). One is immobilized in a line onto a nitrocellulose membrane. The other one is labeled with a signal (e.g. color) generator (e.g. Au-NPs) and positioned within a glass fiber membrane. The latter is dissolved upon exposure with the test analyte (antigen) in an aqueous solution. The newly created complex (Au-NP-Ab-analyte) flows along the substrate upon capillary forces until the analyte becomes detected when reaching the line/zones on the nitrocellulose membrane pretreated with the immobilized Abs. In positive samples, there is a high accumulation of immobilized complexes, and the line/zone exhibits a colored band due to the coupling of plasmons in nearby Au-NPs [105] that is easily detectable with the eyes. It consists of an on/off test for qualitative measurements. However, quantitatively results can be obtained by determining the optical density via scanning photometry or charge coupled device (CCD). To give an example, Nymox Pharmaceutical Corporation developed a commercially available lateral flow test for recent smoke exposure called TobacAlert™. The analyte to be tested is in this case cotinine, a metabolite of nicotine ("cotinine" is an anagram of "nicotine"). The test strip works upon the above mentioned principle with the extension that not only one site is equipped with the immobilized antibody, but several "traps" are placed on the strip one behind the other. Thus, the Au-NP-Ab-analyte complex flows further on if a trap is satisfied and therefore the smoke exposure corresponds to the number of labeled traps. As mentioned before, the main disadvantage of these assays is their reduced sensitiv-

ity. Hereby a compromise is found between sensitivity and fast response. Another critical point would be the lack of control of the number of attached Abs to the colored reagent (Au-NPs) and thus the possibility of a falsely negative result (e.g. if a lot of analyte binds to an insufficient amount of Au-NPs). This is the current operation procedure that should be improved towards enhanced sensitivity, i.e. optimization of the selected Ab and the raw material that affect the flow rate of the complex and thus the time of interaction with the immobilized Ab.

### 4.2. Delivery systems—CaP-NPs (a) for drug delivery and (b) as implantable biomaterials

(a) Binding of a pharmaceutical to a particulate drug delivery system is a strategy widely investigated to induce sustained drug delivery [106,107]. Bioceramics, such as CaP, represent an interesting class of materials suitable for the use as carriers for drugs, non-viral gene delivery, antigens, enzymes, and proteins. Moreover, CaP can be produced at a low cost and are simple to manufacture (see Section 2.4). So far the use of CaP as drug carrier for localized pharmaceutical treatments has been demonstrated by injections [108] or surgical placement of disks, pellets or particulates [109]. Thanks to the localized release of drugs from these CaP-based systems, low concentrations of drugs were required compared to the typically high concentrations required in the bloodstream and other organs to achieve therapeutic outcomes. Nowadays several companies are working to develop CaP particulate systems suitable for clinical applications. BioSante Pharmaceuticals Company (www.biosantepharma.com) announced in august 2009 the development of a novel therapeutic drug delivery platform (BioAir™/BioOral™) based on the CaP nanotechnology. BioAir™/BioOral™ are formulations for delivering proteins via buccal and pulmonary routes using biodegradable CaP-NPs as basis (a carrier, composed of one or more excipients, for the active substance(s) in semi-solid and solid preparations) for controlled drug release of proteins and peptides. Thanks to the improved bioavailability and to the encapsulation of the cargo within a carrier, less protein is needed per dose. The Company completed pre-clinical tests showing that biodegradable CaP-NP basis enhance and extend the hypoglycemic effect of proteins when administered subcutaneously, buccally and pulmonarily. It is expected that CaP NPs might be used to deliver different types of proteins, such as human Factor IX for hemophiliacs, Interferon alpha-2b for chronic hepatitis B treatment, a1-antitrypsin for the prophylaxis of venous thromboembolism, and peptides. However, the successful use of nanosized CaP particles as drug carrier for localized treatment strongly depends on the ability to efficiently load and release the drug in a controlled manner. Moreover, it is also imperative that the drug released is chemically active and effective over a long period of time. Thus, additional efforts must be made to avoid a "burst" release profile of the drug which is due to the naturally occurring degradation of CaP compounds in the body which would strongly interfere with the kinetics of cargo release and thus effectiveness of the drug.

(b) CaP biomaterials became the most interesting artificial bone grafts when bioglass (CaP containing glass) and hydroxyapatite ceramics (HA) were found to be osteoconductive (in the 1970s–1980s). So far, the main goals in this task have consisted of adding additional properties, such as osteoinductivity, resorbability, simplicity of handling and mechanically resistance, in order to implement CaP biomaterials according to the clinical requirements. However, recently a different approach which is based on the use of CaP as particulate formulation has been suggested by the company Angstrom Medica Inc. (www.angstrommedica.com) for creating structural, injectable, and programmable medical devices that can act standing alone or as a carrier for pharmokinetic agents and orthobiologic materials. The formulation NanOss™ is a highly osteoconductive biomaterial able to remodel over time into human bone with applications in sports medicine, trauma, spine and general orthopedics markets. In biomaterial science osteoconduction means bone formation towards implants from host bone bed as well as guided bone formation on material surfaces resulting in bone binding. The details of the process used to create NanOss™ are currently a trade secret. However, the company has developed a new process for forming nanostructured CaP utilizing a patented precipitation process. The result is a precipitate of CaP nanocrystals with a predetermined size, shape, and composition. The nanocrystals are then combined into building blocks that are ultimately used to assemble complex devices whose morphology is inspired to the most commonly used devices in orthopedic surgery. Because the main goal in several fields of nanotechnology for biomedical application is to create novel materials able to mimic the functions of the naturally occurring materials, the strategy based on this formulation appears to be quite promising. In fact, the key properties of these CaP-based devices are that they are bioactive and that they reproduce the shape and the size of the bones. Moreover they are able to induce bone cell attachment and proliferation. All these properties combined together allow for using these Ca-NPs as implantable systems for directing the growth of the body cells around the nanocrystal matrixes. These cells are then able to engulf the NPs, break them down and remodel them into real bone. It is clear that particulate implants whose activities are based on the above described mechanism, represent ideal devices because once injected into the target-damaged tissue they turn into the integral part of the future regenerated bone. Due to their natural occurrence, CaP nanoparticulate systems are very well tolerated and easily absorbed and might constitute a good alternative as implantable bioresorbable materials to the classic bioscaffolds [110,122,123].

### 4.3. Vaccination—CaP-NPs as vaccine adjuvants

Adjuvants (immune potentiators or immunomodulators) are used to improve the immune response to vaccine antigens against an infectious disease. The incorporation of adjuvants into vaccine formulations is aimed at enhancing, accelerating and prolonging the specific immune response towards the desired response to vaccine antigens. The main routes by which different kinds of adjuvants exert their activities include: (i) presentation of the antigen, i.e. adsorbants and particulate adjuvants, emulsions; (ii) immune potentiation/modulation, i.e. microbial, synthetic and endogenous adjuvants, mineral salts (aluminium hydroxide (Al) or CaP gels); (iii) the protection of the antigen from degradation and elimination, i.e. emulsions; (iv) targeting to specific cells, i.e. T-helper cells 2 (T-lymphocytes against bacterial infection). In case of the commonly used adjuvants based on mineral salts (i.e. Al or CaP gels), they are associated to the vaccine by adsorption processes and are able to enhance the immunogenicity of the vaccine by promoting the formation of an inflammatory focus at the site of injection, which is a disadvantage if it ends up in an allergic reaction. A novel adjuvant formulation based on CaP technology takes advantage of the biofriendly nature of CaP and the nanotechnology to make CaP-based nanocarriers that incorporate the antigen molecules in their interior. In this system, the vaccine/adjuvant association is mainly encapsulation and the mechanism of action is achieved by protecting the antigen from degradation [69,108,111,112]. Thus, a higher local tolerance is achieved. Furthermore, a common problem for adjuvants lies in the ineffectiveness against immunogenic-weak antigens, i.e. recombinant proteins or viruses. In this context, CaP-NPs have demonstrated to enhance vaccine immune responses to viral antigens as well [108]. Additionally, CaP-NPs based adjuvants are easy to manufacture on an industrial scale, and show

less variation in quality and physicochemical properties between batches than the aluminum compounds [113,114]. Together with the introduction of BioAir™/BioOral™, BioSante Pharmaceuticals also announced novel vaccine adjuvants (BioVant™) based on the CaP nanotechnology. A synthetic analog of CaP is used as a basis for BioVant™ to build a CaP-NP-adjuvanted matrix for vaccines against different viruses. Pre-clinical studies have demonstrated that the system elicits positive immune response to vaccines and may sustain higher antibody levels over a longer period than both aluminum-formulated vaccines and non-adjuvanted vaccines leading to the use of lower vaccine dosage, while maintaining or improving effectiveness and offering an improved safety profile. However, these results are based on pre-clinical trials and BioSante's achievements in this area are still on a research and development level. In particular, the BioVant formulation is in Phase I development under the U.S. Food and Drug Administration (FDA) SPA (Special Protocol Assessment). Remarkably, both the geometry and the mechanism of action of this system are poorly understood and the company does not bring clearness, especially regarding the association vaccine/adjuvant, which directly influences the efficiency of vaccination. The main advantage of the NP-based systems relies on the ability of nanotechnology to enhance the uptake of vaccine/adjuvant formulations by appropriate cells through manipulation of their surface chemistry.

## 5. Conclusions

Materials on the nanosize scale have unique characteristics compared to their macrosized counterparts that derivate from their nanosize. Additionally, because of their enormous surface area relative to their total volume only NPs are able to produce a large number of binding sites between cells and target molecules. The coating of the inorganic crystal mainly confer the NPs stability in water solutions [115] but can also be used to functionalize the surface of the NPs with different biomolecules for different purposes [116]. For example, for *in vivo* applications PEG (poly(ethylene glycol)) molecules increase the colloidal stability and reduce recognition of the NPs by the mononuclear-phagocyte system due to their low-fouling properties (the attachment of unspecific serum protein to the surface of the NPs which will make the NPs easily detectable by the immune system is reduced). Specific molecules like DNA, antibodies, aptamers or ligands (transferring, folic acid) transfer the NPs molecular recognition properties to detect target cells or cellular components [117,118]. Other kind of chemical functionalities like cell penetrating peptides are postulated to allow the internalized NPs to escape from the intracellular compartment where they are trapped [119–121]. Although inorganic NPs are foreign bodies and potentially immunogenic, their small sizes (below 100 nm) confine them a sort of acute protection against recognition by the mononuclear-phagocyte system and thus, clearance from the organism is delayed. Furthermore, an elevate number of NPs can accumulate inside cells [121] thus increasing the efficiency of their function. Despite the incoming potential of NPs in the field of medicine and pharmacy, NPs also have their limitations (as described in this review) and therefore should not be considered as a panacea. NPs are rather novel tools to increment the pre-existing tool kit for diagnosis and treatment of diseases and they are not necessarily aimed at substituting current methods.

## Acknowledgement

This project was supported by the European Union (grant NANOGNOSTICS).

## References

[1] Farokhzad OC, Langer R. Nanomedicine: developing smarter therapeutic and diagnostic modalities. Advanced Drug Delivery Reviews 2006;58(14):1456–9.
[2] Riehemann K, Schneider SW, Luger TA, Godin B, Ferrari M, Fuchs H. Nanomedicine-challenge and perspectives. Angewandte Chemie-International Edition 2009;48(5):872–97.
[3] Wagner V, Dullaart A, Bock AK, Zweck A. The emerging nanomedicine landscape. Nature Biotechnology 2006;24(10):1211–7.
[4] Nagare S, Sagawa J, Senna M. Chemical and structural properties of drug-protein nanocomposites prepared by pulsed laser deposition from conjugated targets. Journal of Nanoparticle Research 2006;8(1):37–42.
[5] Cho K, Wang X, Nie S, Chen Z, Shin DM. Therapeutic nanoparticles for drug delivery in cancer. Clinical Cancer Research 2008;14(5):1310–6.
[6] Nie SM, Xing Y, Kim GJ, Simons JW. Nanotechnology applications in cancer. Annual Review of Biomedical Engineering 2007;9:257–88.
[7] Zhang F, Zulqurnain A, Amin F, Feltz A, Oheim M, Parak WJ. Ion and pH sensing with colloidal nanoparticles—the influence of surface charge on sensing and colloidal properties. Chemistry and Physics Chemical Journal, in press.
[8] Shubayev VI, Pisanic TR, Jin SH. Magnetic nanoparticles for theragnostics. Advanced Drug Delivery Reviews 2009;61(6):467–77.
[9] Sun C, Lee J, Zhang M. Magnetic nanoparticles in MR imaging and drug delivery. Advanced Drug Delivery Reviews 2008;60(11):1252–65.
[10] Pankhurst QA, Connolly J, Jones SK, Dobson J. Applications of magnetic nanoparticles in biomedicine. Journal of Physics D-Applied Physics 2003;36(13):R167–81.
[11] Wormuth K. Superparamagnetic latex via inverse emulsion polymerization. Journal of Colloid and Interface Science 2001;241(2):366–77.
[12] Tartaj P, Morales M, Veintemillas-Verdaguer S, Gonzalez-Carreno T, Serna C. The preparation of magnetic nanoparticles for applications in biomedicine. Journal of Physics D-Applied Physics 2003;36(13):R182–97.
[13] Sun C, Lee JSH, Zhang M. Magnetic nanoparticles in MR imaging and drug delivery. Advanced Drug Delivery Reviews 2008;60(11):1252.
[14] Corot C, Robert P, Idee JM, Port M. Recent advances in iron oxide nanocrystal technology for medical imaging. Advanced Drug Delivery Reviews 2006;58(14):1471–504.
[15] Ferrucci JT, Stark DD. Iron-oxide enhanced Mr-imaging of the liver and spleen—review of the 1St-5 years. American Journal of Roentgenology 1990;155(5):943–50.
[16] Lu AH, Salabas EL, Schuth F. Magnetic nanoparticles: synthesis, protection, functionalization, and application. Angewandte Chemie-International Edition 2007;46(8):1222–44.
[17] Mornet S, Vasseur S, Grasset F, Duguet E. Magnetic nanoparticle design for medical diagnosis and therapy. Journal of Materials Chemistry 2004;14(14):2161–75.
[18] Jordan A, Scholz R, Wust P, Fahling H, Felix R. Magnetic fluid hyperthermia (MFH): cancer treatment with AC magnetic field induced excitation of biocompatible superparamagnetic nanoparticles. Journal of Magnetism and Magnetic Materials 1999;201:413–9.
[20] Fretz CJ, Stark DD, Metz CE, Elizondo G, Weissleder R, Shen JH, et al. Detection of hepatic metastases—comparison of contrast-enhanced Ct, unenhanced mr imaging, and iron-oxide enhanced Mr imaging. American Journal of Roentgenology 1990;155(4):763–70.
[21] Weishaupt D, Köchli VD, Marincek B. How does MRI work. second edition Berlin, Germany: Springer-Verlag; 2006.
[22] Rohrer MP, Bauer HP, Mintorovitch JP, Requardt MP, Weinmann H-JP. Comparison of magnetic properties of MRI contrast media solutions at different magnetic field strengths [Article] 2003. Investigative Radiology 2005;40(November (11)):715–24.
[23] Bellin M, Webb J, Van der Molen A, Thomsen H, Morcos S. ESUR, and, safety of MR liver specific contrast media. European Radiology 2005;15(8):1607–14.
[24] Bellin MF. MR contrast agents, the old and the new. European Journal of Radiology 2006;60(3):314–23.
[25] Broome DR. Nephrogenic systemic fibrosis associated with gadolinium based contrast agents: a summary of the medical literature reporting. European Journal of Radiology 2008;66(2):230–4.
[26] Weinmann HJ, Ebert W, Misselwitz B, Schmitt-Willich H. Tissue-specific MR contrast agents. European Journal of Radiology 2003;46(1):33–44.
[27] Ito K. Hepatocellular carcinoma: conventional MRI findings including gadolinium-enhanced dynamic imaging. European Journal of Radiology 2006;58(2):186–99.
[28] Shapiro M, Atanasijevic T, Faas H, Westmeyer G, Jasanoff A. Dynamic imaging with MRI contrast agents: quantitative considerations. Magnetic Resonance Imaging 2006;24(4):449–62.
[29] Wang Y-XJ, Hussain SM, Krestin GP. Superparamagnetic iron oxide contrast agents: physicochemical characteristics and applications in MR imaging. European Radiology 2001;11:2319–31.
[30] Jung C, Jacobs P. Physical and chemical-properties of superparamagnetic iron-oxide MR contrast agents—ferumoxides, ferumoxtran, ferumoxsil. Magnetic Resonance Imaging 1995;13(5):661–74.
[31] Brust M, Walker M, Bethell D, Schiffrin DJ, Whyman R. Synthesis of thiol-derivatised gold nanoparticles in a two-phase liquid–liquid system. Journal of Chemical Society, Chemical Communications 1994;1994:801–2.
[32] Templeton AC, Wuelfing WP, Murray RW. Monolayer-protected cluster molecules. Accounts of Chemical Research 2000;33(1):27–36.

[33] Turkevich J, Stevenson PC, Hillier J. A study of the nucleation and growth processes in the synthesis of colloidal golde. Journal of Discussion Faraday Society 1951:55–75.
[34] Sperling RA, Rivera_Gil P, Zhang F, Zanella M, Parak WJ. Biological applications of gold nanoparticles. Chemical Society Reviews 2008;37(9):1896–908.
[35] Sonnichsen C, Franzl T, Wilk T, von Plessen G, Feldmann J. Plasmon resonances in large noble-metal clusters. New Journal of Physics 2002, 4.
[36] Lal S, Link S, Halas NJ. Nano-optics from sensing to waveguiding. Nature Photonics 2007;1(11):641–8.
[37] Kreibig U, Genzel L. Optical absorption of small metallic particles. Surface Science 1985;156(2):678–700.
[38] Alvarez MM, Khoury JT, Schaaff TG, Shafigullin MN, Vezmar I, Whetten RL. Optical absorption spectra of nanocrystal gold molecules. Journal of Physical Chemistry B 1997;101(19):3706–12.
[39] Eustis S, El-Sayed MA. Why gold nanoparticles are more presious than pretty gold: noble metal surface plasmon resonance and its enhancement of the radiative and nonradiative properties of nanocrystals of different shapes. Chemical Society Reviews 2006;35:209–17.
[40] Ghosh SK, Pal T. Interparticle coupling effect on the surface plasmon resonance of gold nanoparticles: from theory to applications. Chemical Reviews 2007;107:4797–862.
[41] Skirtach AG, Karageorgiev P, De_Geest BG, Pazos-Perez N, Braun D, Sukhorukov GB. Nanorods as wavelength-selective absorption centers in the visible and near-infrared regions of the electromagnetic spectrum. Advanced Materials 2008;20:506–10.
[42] Zharov VP, Mercer KE, Galitovskaya EN, Smeltzer S. Photothermal nanotherapeutics and nanodiagnostics for selective killing of bacteria targeted with gold nanoparticles. Biophysical Journal 2006;90:619–27.
[43] Chen J, Wang D, Xi J, Au L, Siekkinen A, Warsen A, et al. Immuno gold nanocages with tailored optical properties for targeted photothermal destruction of cancer cells. Nano Letters 2007;7(5):1318–22.
[44] Chithrani BD, Ghazan AA, Chan CW. Determining the size and the shape dependence of gold nanoparticle uptake into mammalian cells. Nano Letters 2006;6(4):662–8.
[45] Patra HK, Banerjee S, Chaudhuri U, Lahiri P, Dasgupta AK. Cell selective response to gold nanoparticles. Nanomedicine-Nanotechnology Biology and Medicine 2007;3(2):111–9.
[46] Shukla R, Bansal V, Chaudhary M, Basu A, Bhonde RR, Sastry M. Biocompatibility of gold nanoparticles and their endocytotic fate inside the cellular compartment: a microscopic overview. Langmuir 2005;21: 10644–54.
[47] Goodman CM, McCusker CD, Yilmaz T, Rotello VM. Toxicity of gold nanoparticles functionalized with cationic and anionic side chains. Bioconjugate Chemistry 2004;15(4):897–900.
[48] Pan Y, Neuss S, Leifert A, Fischler M, Wen F, Simon U, et al. Size-dependent cytotoxicity of gold nanoparticles. Small 2007;3(11):1941–9.
[49] Qu Y, Lü X. Aqueous synthesis of gold nanoparticles and their cytotoxicity in human dermal fibroblasts–fetal. Biomedical Materials 2009;4:1–5.
[50] Pernodet N, Fang XH, Sun Y, Bakhtina A, Ramakrishnan A, Sokolov J, et al. Adverse effects of citrate/gold nanoparticles on human dermal fibroblasts. Small 2006;2(6):766–73.
[51] Tsoli M, Kuhn H, Brandau W, Esche H, Schmid G. Cellular uptake and toxicity of Au55 clusters. Small 2005;1(8–9):841–4.
[52] Chen Y-S, Hung Y-C, Liau I, Huang GS. Assessment of the in vivo toxicity of gold nanoparticles. Nanoscale Research Letters 2009;4:858–64.
[53] Bar-Ilan O, Albrecht RM, Fako VE, Furgeson DY. Toxicity assessments of multisized gold and silver nanoparticles in Zebrafish embryos. Small 2009;5(16):1897–910.
[54] Davis P. Gold therapy in the treatment of rheumatoid arthritis. Canadian Family Physician 1988;34:445–52.
[55] Semmler-Behnke M, Kreyling WG, Lipka J, Fertsch S, Wenk A, Takenaka S, et al. Biodistribution of 1.4-and 18-nm gold particles in rats. Small 2008;4(12):2108–11.
[56] Levy L, Hochepied JF, Balencie J, Prasad PN, Bergey EJ. X-ray and/or UV activable particles, their preparation and their therapeutic or diagnostic uses, in European Patent Office, E.P. Office, Editor; 2008.
[57] Novo E, Parola M. Redox mechanisms in hepatic chronic wound healing and fibrogenesis. Fibrogenesis Tissue Repair 2008;1(1):5.
[58] Vittadello M, Negro E, Lavina S, Pace G, Safari A, Di Noto V. Vibrational studies and properties of hybrid inorganic-organic proton conducting membranes based on nafion and hafnium oxide nanoparticles. Journal of Physical Chemistry B 2008;112(51):16590–600.
[59] Rauwel E, Clavel G, Willinger MG, Rawel P, Pinna N. Non-aqueous routes to metal oxide thin films by atomic layer deposition. Angewandte Chemie-International Edition 2008;47(19):3592–5.
[60] Balencie J, Levy L, Hochepied JF. Synthesis of hafnium gen-nanate (HfGeO4) by co-precipitation routes. Thin Solid Films 2007;515(16):6298–301.
[61] Dorozhkin SV, Epple M. Biological and medical significance of calcium phosphates. Angewandte Chemie-International Edition 2002;41(17):3130–46.
[62] Wang S, McDonnell EH, Sedor FA, Toffaletti JG. pH effects on measurements of ionized calcium and ionized magnesium in blood. Archives of Pathology and Laboratory Medicine 2002;126(8):947–50.
[63] Alberts B, Johnson A, Lewis J, Raff M, Roberts K, Walter P. Molecular biology of the cell. fifth edition New York: Garland Science; 2008.
[64] Roy I, Mitra S, Maitra A, Mozumdar S. Calcium phosphate nanoparticles as novel non-viral vectors for targeted gene delivery. International Journal of Pharmaceutics 2003;250(1):25–33.
[65] Maitra A. Calcium phosphate nanoparticles: second-generation nonviral vectors in gene therapy. Expert Review of Molecular Diagnostics 2005;5(6):893–905.
[66] Muddana HS, Morgan TT, Tabouillot T, Adair JH, Butler PJ. Single molecule fluorescence techniques to evaluate calcium phosphate nanoparticles as potential drug carriers. Biorheology 2008;45(1–2):134–134.
[67] Altınoğlu EI, Russin TJ, Kaiser JM, Barth BM, Eklund BC, Kester M, et al. Near-infrared emitting fluorophore-doped calcium phosphate nanoparticles for in vivo imaging of human breast cancer. ACS Nano 2008;2:2075–84.
[68] Kester M, Heakal Y, Fox T, Sharma A, Robertson GP, Morgan TT, et al. Calcium phosphate nanocomposite particles for in vitro imaging and encapsulated chemotherapeutic drug delivery to cancer cells. Nano Letters 2008;8(12):4116–21.
[69] Jiang DP, Premachandra GS, Johnston C, Hem SL. Structure and adsorption properties of commercial calcium phosphate adjuvant. Vaccine 2004;23(5):693–8.
[70] Sadasivan S, Khushalani D, Mann S. Synthesis of calcium phosphate nanofilaments in reverse micelles. Chemistry of Materials 2005;17(10):2765–70.
[71] Bisht S, Bhakta G, Mitra S, Maitra A. pDNA loaded calcium phosphate nanoparticles: highly efficient non-viral vector for gene delivery. International journal of pharmaceutics 2005;288(1):157–68.
[72] Welzel T, Radtke I, Meyer-Zaika W, Heumann R, Epple M. Transfection of cells with custom-made calcium phosphate nanoparticles coated with DNA. Journal of Materials Chemistry 2004;14(14):2213–7.
[73] Tang RK, Wang LJ, Nancollas GH. Size-effects in the dissolution of hydroxyapatite: an understanding of biological demineralization. Journal of Materials Chemistry 2004;14(14):2341–6.
[74] Morgan TT, Muddana HS, Altinoglu EI, Rouse SM, Tabakovic A, Tabouillot T, et al. Encapsulation of organic molecules in calcium phosphate nanocomposite particles for intracellular imaging and drug delivery. Nano Letters 2008;8(12):4108–15.
[75] Panyam J, Labhasetwar V. Biodegradable nanoparticles for drug and gene delivery to cells and tissue. Advanced Drug Delivery Reviews 2003;55(3):329–47.
[76] Prakash KH, Kumar R, Ooi CP, Cheang P, Khor KA. Apparent solubility of hydroxyapatite in aqueous medium and its influence on the morphology of nanocrystallites with precipitation temperature. Langmuir 2006;22(26):11002–8.
[85] Tromsdorf UI, Bigall NC, Kaul M, Bruns OT, Nikolic MS, Mollwitz B, et al. Size and surface effects on the MRI relaxivity of manganese ferrite nanoparticle contrast agents. Nanoletters 2007;7(8):2422–7.
[86] Hildebrandt B, Wust P, Ahlers O, Dieing A, Sreenivasa G, Kerner T, et al. The cellular and molecular basis of hyperthermia. Critical Reviews in Oncology Hematology 2002;43(1):33–56.
[87] Choi MR, Stanton-Maxey KJ, Stanley JK, Levin CS, Bardhan R, Akin D, et al. A cellular Trojan horse for delivery of therapeutic nanoparticles into tumors. Nano Letters 2007;7(12):3759–65.
[88] Westermann AM, Jones EL, Schem BC, van der Steen-Banasik EM, Koper P, Mella O, et al. First results of triple-modality treatment combining radiotherapy, chemotherapy, and hyperthermia for the treatment of patients with stage IIB, III, and IVA cervical carcinoma. Cancer 2005;104(4): 763–70.
[89] Wang CG, Chen J, Talavage T, Irudayaraj J. Gold nanorod/$Fe_3O_4$ nanoparticle "Nano-Pearl-Necklaces" for simultaneous targeting. dual-mode imaging, and photothermal ablation of cancer cells. Angewandte Chemie-International Edition 2009;48(15):2759–63.
[90] Huff TB, Tong L, Zhao Y, Hansen MN, Cheng JX, Wei A. Hyperthermic effects of gold nanorods on tumor cells. Nanomedicine 2007;2(1):125–32.
[91] Huang XH, Jain PK, El-Sayed IH, El-Sayed MA. Determination of the minimum temperature required for selective photothermal destruction of cancer cells with the use of immunotargeted gold nanoparticles. Photochemistry and Photobiology 2006;82(2):412–7.
[92] Lowery AR, Gobin AM, Day ES, Halas NJ, West JL. Immunonanoshells for targeted photothermal ablation of tumor cells. International Journal of Nanomedicine 2006;1(2):149–54.
[93] Hiergeist R, Andrä W, Buske N, Hergt R, Hilger I, Richter U, et al. Application of magnetite ferrofluids for hyperthermia. Journal of Magnetism and Magnetic Materials 1999;201:420–2.
[94] Wust P, Hildebrandt B, Sreenivasa G, Rau B, Gellermann J, Riess H, et al. Hyperthermia in combined treatment of cancer. Lancet Oncology 2002;3(8):487–97.
[95] Lepock JR. Cellular effects of hyperthermia: relevance to the minimum dose for thermal damage. International Journal of Hyperthermia 2003;19(3):252–66.
[96] Huang X, Jain P, El-Sayed I, El-Sayed M. Plasmonic photothermal therapy (PPTT) using gold nanoparticles. Lasers in Medical Science 2007;23(3):217–28.
[97] Schwartz JA, Shetty AM, Price RE, Stafford RJ, Wang JC, Uthamanthil RK, et al. Feasibility study of particle-assisted laser ablation of brain tumors in orthotopic canine model. Cancer Research 2009;69(4):1659–67.
[98] O'Neal DP, Hirsch LR, Halas NJ, Payne JD, West JL. Photo-thermal tumor ablation in mice using near infrared-absorbing nanoparticles. Cancer Letters 2004;209(2):171–6.

[99] Hirsch LR, Stafford RJ, Bankson JA, Sershen SR, Rivera B, Price RE, et al. Nanoshell-mediated near-infrared thermal therapy of tumors under magnetic resonance guidance. Proceedings of the National Academy of Science of the United States of America 2003;100(23):13549–54.
[100] Rivera_Gil P, Parak WJ. Composite nanoparticles take aim at cancer. ACS Nano 2008;2(11):2200–5.
[101] Govorov AO, Richardson HH. Generating heat with metal nanoparticles. Nano Today 2007;2(1):30–8.
[102] Letfullin RR, Joenathan C, George TF, Zharov VP. Laser-induced explosion of gold nanoparticles: potential role for nanophotothermolysis of cancer. Nanomedicine 2006;1(4):473–80.
[103] West JD, Marnett LJ. Endogenous reactive intermediates as modulators of cell signaling and cell death. Chemical Research in Toxicology 2006;19(2):173–94.
[104] Harrison LB, Chadha M, Hill RJ, Hu K, Shasha D. Impact of tumor hypoxia and anemia on radiation therapy outcomes. Oncologist 2002;7(6):492–508.
[105] Sonnichsen C, Reinhard BM, Liphardt J, Alivisatos AP. A molecular ruler based on plasmon coupling of single gold and silver nanoparticles. Nature Biotechnology 2005;23(6):741–5.
[106] Ghosh P, Han G, De M, Kim CK, Rotello VM. Gold nanoparticles in delivery applications. Advanced Drug Delivery Reviews 2008;60(11):1307–15.
[107] Polyak B, Friedman G. Magnetic targeting for site-specific drug delivery: applications and clinical potential. Expert Opinion on Drug Delivery 2009;6(1):53–70.
[108] He Q, Mitchell AR, Johnson SL, Wagner-Bartak C, Morcol T, Bell SJD. Calcium phosphate nanoparticle adjuvant. Clinical and Diagnostic Laboratory Immunology 2000;7(6):899–903.
[109] Mizushima Y, Ikoma T, Tanaka J, Hoshi K, Ishihara T, Ogawa Y, et al. Injectable porous hydroxyapatite microparticles as a new carrier for protein and lipophilic drugs. Journal of Controlled Release 2006;110(2):260–5.
[110] El-Ghannam A. Bone reconstruction: from bioceramics to tissue engineering. Expert Review of Medical Devices 2005;2(1):87–101.
[111] Frayssinet P, Ciocca D, Rouquet N. Calcium phosphate powder for cancer vaccination. Bioceramics 20(Pts 1 and 2) 2008:361–63, p. 1207–10.
[112] Joyappa DH, Kumar CA, Banumathi N, Reddy GR, Suryanarayana VVS. Calcium phosphate nanoparticle prepared with foot and mouth disease virus P1-3CD gene construct protects mice and guinea pigs against the challenge virus. Veterinary Microbiology 2009;139(1–2):58–66.
[113] Feldkamp JR, White JL, Hem SL. Effect of surface charge and particle size on gel structure of aluminum hydroxycarbonate gel. Journal of Pharmaceutical Sciences 1982;71(1):43–6.
[114] Kreuter J, Haenzel I. Mode of action of immunological adjuvants: some physicochemical factors influencing the effectivity of polyacrylic adjuvants. Infection and Immunity 1978;19(2):667–75.
[115] Pellegrino T, Manna L, Kudera S, Liedl T, Koktysh D, Rogach AL, et al. Hydrophobic nanocrystals coated with an amphiphilic polymer shell: a general route to water soluble nanocrystals. Nanoletters 2004;4(4):703–7.
[116] Sperling RA, Pellegrino T, Li JK, Chang WH, Parak WJ. Electrophoretic separation of nanoparticles with a discrete number of functional groups. Advanced Functional Materials 2006;16(7):943–8.
[117] Parak WJ, Pellegrino T, Micheel CM, Gerion D, Williams SC, Alivisatos AP. Conformation of oligonucleotides attached to gold nanocrystals probed by gel electrophoresis. Nano Letters 2003;3(1):33–6.
[118] Farokhzad OC, Cheng J, Teply BA, Sherifi I, Jon S, Kantoff PW, et al. Targeted nanoparticle-aptamer bioconjugates for cancer chemotherapy in vivo. PNAS 2006;103(16):6315–20.
[119] Rudolph C, Plank C, Lausier J, Schillinger U, Muller RH, Rosenecker J. Oligomers of the arginine-rich motif of the HIV-1 TAT protein are capable of transferring plasmid DNA into cells. Journal Of Biological Chemistry 2003;278(13):11411–8.
[120] de la Fuente JM, Berry CC. Tat peptide as an efficient molecule to translocate gold nanoparticles into the cell nucleus. Bioconjugate Chemistry 2005;16(5):1176–80.
[121] Nativo P, Prior IA, Brust M. Uptake and intracellular fate of surface-modified gold nanoparticles. ACS Nano 2008;2(8):1639–44.
[122] Boccaccini AR, Blaker JJ. Bioactive composite materials for tissue engineering scaffolds. Expert Review of Medical Devices 2005;2(3):303–17.
[123] Wlodarski KH, Wlodarski PK, Galus R. Bioactive composites for bone regeneration. Review. Ortopedia, Traumatologia, Rehabilitacja 2008;10(3):201–10.

Review in Advance first posted online on February 28, 2013. (Changes may still occur before final publication online and in print.)

# Multiplexed Sensing and Imaging with Colloidal Nano- and Microparticles

Susana Carregal-Romero,[1,2] Encarnación Caballero-Díaz,[1,3] Lule Beqa,[1] Abuelmagd M. Abdelmonem,[1] Markus Ochs,[1] Dominik Hühn,[1] Bartolome Simonet Suau,[3] Miguel Valcarcel,[3] and Wolfgang J. Parak[1]

[1]Fachbereich Physik and WZMW, Philipps Universität Marburg, Marburg 35043, Germany; email: susana.carregal@physik.uni-marburg.de, wolfgang.parak@physik.uni-marburg.de

[2]BIONAND, Centro Andaluz de Nanomedicina y Biotecnología, Málaga 29590, Spain

[3]Department of Analytical Chemistry, Campus de Rabanales, University of Córdoba, Córdoba 14071, Spain



Annu. Rev. Anal. Chem. 2013. 6:53–81

The *Annual Review of Analytical Chemistry* is online at anchem.annualreviews.org

This article's doi: 10.1146/annurev-anchem-062012-092621



## Keywords

multifunctional colloidal nanoparticles, analyte recognition, bar-coding, multiplexing

## Abstract

Sensing and imaging with fluorescent, plasmonic, and magnetic colloidal nano- and microparticles have improved during the past decade. In this review, we describe the concepts and applications of how these techniques can be used in the multiplexed mode, that is, sensing of several analytes in parallel or imaging of several labels in parallel.

## 1. INTRODUCTION

During the past decade, the use of colloidal nano- and microparticles in biological sciences has attracted a great deal of attention. They have long been used as contrast agents for imaging (1–3) and transducers for molecular sensing (4). Materials developed for these purposes range from single nanoparticles (NPs) and microparticles to complex hybrid nano- and microstructures. Nanoengineering allows for the integration of different functionalities into a single carrier system. Examples of multifunctional composites include the recently described nanocomposites based on silica, silver, and gold NPs (AuNPs), which have applications in photodynamic therapy, photothermolysis, and IR detection (5). Our review focuses on the use of inorganic NPs as building blocks of multifunctional composites on the nano- and micrometer scales, and on their applications in biosensing and diagnostics. After briefly introducing the main detection modes, we discuss why and how the assembly of individual NPs into multifunctional composites allows for multiplexing. Multiplexed sensing and imaging mean that several analytes can be detected in parallel and that different types of particles can be imaged simultaneously. Finally, we discuss some issues and new challenges concerning sensing and imaging involving hybrid materials based on inorganic NPs.

## 2. DETECTION MODES

In sensing and imaging applications, NPs are used to provide readout. In sensing applications, the transduction principle, which provides readout in the presence of a specific analyte, can depend on either direct interaction between the NP and the analyte or interaction between the analyte and another entity supported on the NP, which then interacts with the NP. The NP ultimately changes the signal for readout in the presence of the analyte. In the case of imaging, NPs are typically used as markers that provide contrast (and thus readout) for different imaging techniques. Readout is usually based on optical, electrical, or magnetic detection, as we discuss in detail below. However, naturally there are also other detection schemes, such as detection with X-rays (6), radioactivity (7), or mass changes (8); we do not focus on those techniques in this review.

### 2.1. Optical Detection

The principle of optical detection is based on the interaction between continuous or pulsed light and the sample to be analyzed. This interaction causes changes in the initial incident light wave in terms of frequency, amplitude, phase, polarization state, or time dependence. **Figure 1** summarizes some of the phenomena that are useful for analysis; these phenomena may occur when incident light interacts with a sample of dispersed colloidal particles (9). In general, transmission, elastic and inelastic scattering, and absorption processes can occur. In the case of transmission, light passes through the object and is normally affected in terms of amplitude or intensity. In the case of scattering phenomena, the interaction between light and the particles changes the direction of the incident light wave. However, following elastic scattering, the energy of the incident light, and thus the wavelength, remains unchanged. The Rayleigh and Mie theories describe typical particle-based scattering for small (<5-nm) and large (>5-nm) particles, respectively. In contrast, following inelastic scattering, the energy of the incident light, and thus the wavelength, changes. The inelastic scattering process (Raman scattering) is especially important for colloidal particles. The interaction between the incident light and the sample modifies the energy of the internal (typically rotational or vibronic) states of the particle, and the scattered light has either higher or lower energy, termed anti-Stokes or Stokes scattering, respectively. For luminescent particles, other interesting processes, such as the emission of light, may occur. This phenomenon is based

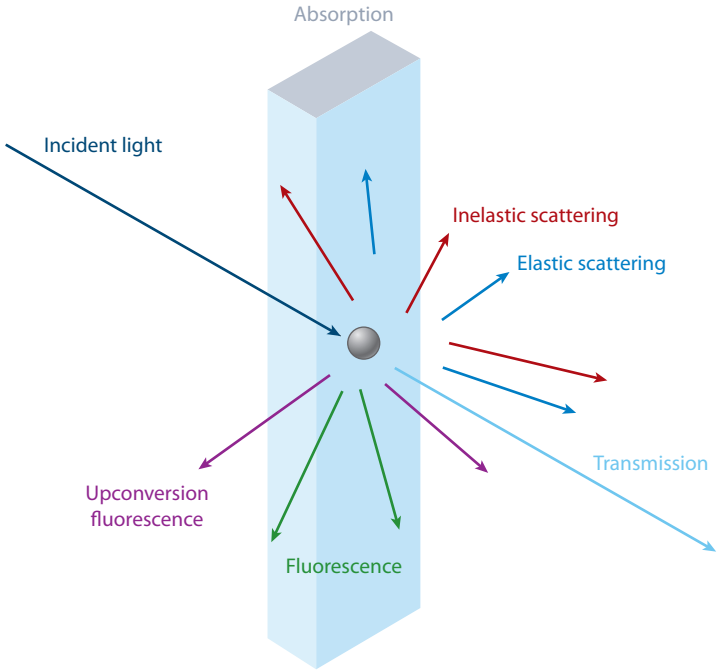


**Figure 1**

Possible interactions between a particle and light.

on the excitation of energetic states by the charge carrier's absorption of the incident wave energy, which in general is possible only if the incident wave is in resonance with the excited electronic state. The light that is reemitted following relaxation of the excited states to the ground states is termed fluorescence if the emitted light is less energetic than the incident light (more conventional process) and upconversion fluorescence if the emitted light is more energetic (less conventional process). Other parts of the energy can be converted into heat. This nonradiative energetic contribution is referred to as absorption, which does not lead to the emission of light, and whereby the energy remains in the sample.

Various techniques exist for the optical detection of particles on the basis of the above-mentioned mechanisms. Hereafter, we distinguish between plasmonic (10) and fluorescent (11) particles (12).

NPs of several metals, such as platinum, copper, gold, and silver, or alloys such as $Cu_{2-x}Se$, demonstrate surface plasmon resonance (SPR) due to the collective oscillation of the free electrons stimulated by incident light of an appropriate wavelength (13); they are therefore referred to as plasmonic NPs. This property has been exploited in many analytical techniques for sensing and imaging.

1. Localized surface plasmon resonance (LSPR) spectroscopy benefits from the high sensitivity of the plasmon resonance to changes in the local refractive index, and it can be applied to both individual NPs and periodic arrays of NPs. The light scattered by individual plasmonic NPs, for example, can be detected with dark-field microscopy (14). Plasmon resonance wavelength and intensity can be modified by the temporal or irreversible presence of an analyte (bound or adsorbed) on the NP surface. LSPR is a very sensitive tool for quantitative analyte analysis (15), allowing for even single-molecule detection (16, 17).

2. Colorimetric sensors are also based on LSPR techniques, but they were developed on the basis of the visible color changes that plasmonic NPs undergo in the presence of a target analyte that triggers the agglomeration (or redispersion) of an assembly of NPs (18). Although similar concepts have previously been used (19), the breakthrough in this technique was achieved by target DNA–mediated agglomeration of oligonucleotide-modified AuNPs, as introduced by the Mirkin group (4). In that study, the presence of target DNA was observed by the naked eye following a color change of a AuNP solution from red to blue. This concept has been further extended and has led to, for example, the development of scanometric sensors for DNA strands according to the specific binding of oligonucleotide-functionalized AuNPs in a DNA array. The change of color due to analyte recognition was further amplified through the addition of a silver layer onto the AuNPs. This process causes visible darkening of the array surface only in the presence of a complementary target (20). Colorimetric detection of analytes via analyte-induced agglomeration of plasmonic NPs is currently used for many different analytes (21, 22).
3. Surface-enhanced Raman spectroscopy (SERS) benefits from the intense electromagnetic field generated on some plasmonic nanostructures due to their LSPRs. Applications of this technique are expanding because of the possibility of ultrasensitive molecule detection without the need for special preparation of the sample. Imaging and sensing can be achieved with SERS labels in close contact with plasmonic NPs (23–26).
4. The nonradiative decay of plasmons can produce a localized increase of temperature on the plasmonic NP surface that can be exploited for imaging. Relevant techniques include photothermal microscopy (27, 28) and photoacoustic tomography (29, 30).

Fluorescence microscopy, spectroscopy, and flow cytometry are among the most powerful tools for imaging and analytical detection of molecules and ions. Several types of fluorescent particles can be used for sensing and imaging applications.

1. Quantum dots (QDs), namely semiconductor NPs, with tunable light emission. QDs composed by atoms in groups II–VI (CdSe, CdS, etc.) have been studied largely because of their higher stability against oxidation or agglomeration in biological fluids, compared with those of other semiconductor materials (31, 32). However, QDs based on silicon or carbon are more interesting for biological applications due to their reduced toxicity. Efforts to synthesize, stabilize, and use silicon and carbon QDs as contrast agents and sensors are under way in clinical applications (33–36).
2. Noble-metal clusters. Silver NPs or AuNPs with diameters less than 2 nm do not exhibit SPR, but they can present fluorescence owing to their molecule-like properties (37, 38). Such small NPs can be used as fluorescent labels within multifunctional nanostructures or individually if they are properly stabilized.
3. Upconversion NPs and complexes. Based mostly on lanthanide-doped materials, these materials are promising for in vivo imaging. Their range of excitation/emission wavelengths can be tuned to the near-IR region, in which tissue produces minimal absorption and scattering of light. Moreover, they have low cytotoxicity, a long lifetime, and a narrow emission bandwidth (39, 40).
4. Inorganic NPs acting as passive carriers. These NPs can accumulate organic dyes and bioluminescent or chemiluminescent molecules either on the surface of or within a particle (41).
5. Polymeric nanomatrices acting as passive carriers. Photonic explorers for bioanalysis with biologically localized embedding (PEBBLE) sensors are a prominent example. They can be loaded with several dyes, permitting ratiometric sensor preparation and multiplexing (42).

6. Microbeads and microcapsules. Due to their size, they can be simultaneously loaded with both organic dyes and fluorescent NPs. Multitasking can be readily achieved with such materials (43, 44).

Detection based on fluorescent particles depends on the physicochemical process involved in the modification of the emitted light upon analyte–particle interaction. The main applied concepts for fluorescence detection include the following.

1. Readout based on analyte-sensitive fluorophores. The presence of the analyte can directly modify the emission of the fluorophore (45).
2. Readout based on the quenching of QD fluorescence through the proximity of another NP, such as a AuNP (46).
3. Readout based on photoinduced electron-transfer (PET) sensors. They consist of one fluorescent species attached to a recognition group that acts as a quencher in the unbound dark state. The binding of the recognition component with the analyte (normally metal cations and protons) cancels the electron transfer and dequenches the fluorophore (47).
4. Readout based on Förster resonance energy transfer (FRET) between two fluorophores. Often, QDs act as donors and transfer energy to an analyte-sensitive fluorophore that acts as an acceptor, but FRET in which the QDs are acting as the acceptors can occur (48). The lifetime of and the response to analytes of the acceptor fluorophore are modified due to the presence [within a short (<10-nm) distance] of the donor fluorophore.
5. Readout based on chemiluminescence resonance energy transfer (CRET). In CRET, a chemiluminescent probe is the donor; it excites the acceptor fluorophore, which can be a dye or a particle. The chemiluminescent probe should be analyte sensitive and should be formed by two species that react to produce emission of light only in the presence of the analyte (49).
6. Readout based on bioluminescence resonance energy transfer (BRET). Bioluminescent proteins are efficient energy donors for QDs (50). Because CRET and BRET processes do not need light excitation, their sensitivity is high.

## 2.2. Electrical Detection

Electrical detection modes deal mainly with NPs that conduct electricity, such as noble metals or semiconductors, which are typically supported by a flat electrode (51, 52). However, oxide NPs and hybrid multifunctional NPs have also been used as electrochemical sensors and biosensors. The function of the NPs in such sensors varies not only according to the nature of the NP but also on the basis of how the analyte is detected. Luo et al. (53) provide some important examples of the functions of NPs in electrical sensors: (*a*) The NPs are reactants themselves (54), (*b*) they are catalysts of electrochemical reactions (55), (*c*) they provide an appropriate surface for immobilization of biomolecules (e.g., analyte receptors) (56), (*d*) they improve or vary the conductivity between the analyte receptor and the electrode (57, 58), (*e*) they enhance electron-transfer processes (59), and (*f*) they perform labeling (60). The four main electroanalytical categories of detection involving NPs are (*a*) classic potentiometry (which involves potential measurements) (61), (*b*) coulometry (by measuring current, the amount of matter transformed during the electrolysis reaction is calculated) (62), (*c*) amperometry (wherein ions are detected on the basis of current measurements) (54), and (*d*) voltammetry (in which current measurements are performed while the potential is changed) (55). Electrochemical biosensing is often applied to the detection of biomolecules such as enzymes, antigens, and DNA, which are responsible for specifically recognizing the analyte and, in the case of enzymes, for converting the analyte in the signal that is actually detected (such

as electrons, $H^+$, and $H_2O_2$). Many comprehensive reviews summarizing the most significant improvements in nanomaterial-based electrical biosensing have been published, and we recommend reading them for further information (63, 64).

Hybrid systems that mix optical and electrical measurements for analyses involving NPs have been performed. Electrochemical-LSPR biosensors have been developed for label-free detection of peptide toxins through the use of core-shell NP arrays (65). The substrate comprised silica NPs used as the core and a thin gold film used as the shell, which simultaneously acted as a working electrode and an LSPR sensor. The binding of the peptide toxin melittin to the hybrid electrode was optically detected by LSPR, and the membrane-disturbing properties were assessed electrochemically (65). In the case of fluorescent NPs, optical excitation can be used to modulate the electrochemical signal. The illumination of QDs, immobilized on an electrode, generates charge carriers (electrons and holes) and gives rise to a photocurrent. This detection scheme has been employed in, for instance, the light-triggered electrochemical detection of aminophenyl phosphate (66).

### 2.3. Magnetic Detection

Functionalized magnetic nanoparticles (MNPs) are widely used for sensing and imaging in the context of magnetic resonance (MR) (67–69). When used as targeted contrast agents, molecules or functional groups on the MNP surface bind the targeted molecules, first producing local inhomogeneities in the applied magnetic field that affect the proton spin precession (decreasing the relaxation time) within the target molecules and then increasing the contrast. These changes in relaxation times have been extensively utilized for high-sensitivity detection. For example, a recently published study used polymerase chain reaction detection, which normally requires fluorescence readout methods (70).

Magnetic relaxation switches are MR-based assays that are associated with different spin–spin relaxation times between the dispersed and agglomerated states of MNPs (71). SQUIDs (superconducting quantum interference devices) have been used for sensing on the basis of the change of the relaxation magnetic moment in the presence or absence of the corresponding analyte (72). Moreover, magnetoresistance can be also applied to magnetic sensing (73). In this case, the change of the sensor's electrical resistance is measured following analyte binding in the presence of a magnetic field. Superparamagnetic NPs are normally used as magnetic field concentrators, but they need to be functionalized with a molecule that specifically binds the corresponding analyte. Proteins, DNA, and enzyme reactions have been detected with this technique, given that it is one of the most sensitive magnetic sensing methods (71, 74).

## 3. MULTIPLEXED SENSING

Analyte detection involving colloidal NPs often requires the use of multifunctional NPs. In this context, the simplest sensing system would be formed by NPs that produce or enhance a signal (which can be detected optically, electrically, magnetically, etc.), coated with a recognition element such as an antibody or an analyte-sensitive fluorophore. Multianalyte sensing could be achieved simply by producing similarly functionalized NPs with different recognition elements according to the respective analytes and with individually resolved readout (for example, by different wavelengths in the case of optical readout). However, practical problems, such as cross-reactivity between analytes to different recognition elements involving limited selectivity, signal overlap of the different readouts, and limitations related to the NP functionalization, have to be considered. Not only does multiplexed detection reduce costs, sample volume, and assay time,

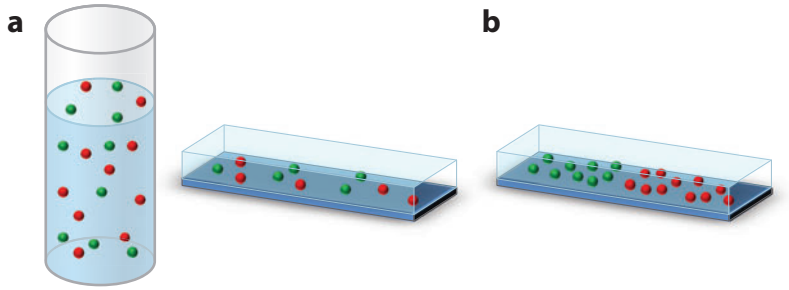


**Figure 2**

Classification of sensors on the basis of multifunctional particles. (*a*) Particles are dispersed in solution, and following analyte binding, readout can be performed in solution or on a planar surface, where sensor particles are randomly distributed. (*b*) Readout is based on structured surfaces on which the particles are bound to specific locations.



but it is convenient for the analysis of real samples, such as blood or river water, in which many different analytes can interfere with the signal of a specific sensor. Therefore, there is increasing interest in developing multiplexed sensors that can substitute individual analyte-detection assays, such as enzyme-linked immunosorbent assays (ELISAs) for tumor markers (75).

In this section, we discuss some recent nanotechnology strategies applied to multiplexed sensing. There are two different approaches: assays based on particles in suspension and assays based on planar arrays. Advantages of the use of particle sensors in suspension include (*a*) the higher surface-to-volume ratio for receptor conjugation and target analyte binding; (*b*) the better accessibility of the analyte to the sensing surface, given that sensor particles move in solution similarly to the analyte; and (*c*) the possibility of incorporation in vivo by targeted delivery. This approach also has some drawbacks: (*a*) Particles in suspension are normally less sensitive (i.e., have higher detection limits) than planar array sensors; (*b*) their stability and reusability are often lower; (*c*) multiplexing due to spatial separation is more easily achieved for planar arrays of NPs; and (*d*) in the case of in vivo sensing, one must take into account the fact that NPs may stay in the body for a long time and thus have cytotoxic effects. We describe two scenarios: sensing based on dispersed particles in solution and sensing based on particles associated with planar arrays. In the first case, readout is typically carried out without the particles having to be ordered on specific positions; in other words, the particles are randomly dispersed in solution (after the binding of the analyte) or are randomly associated with a surface (without order). In the second case, readout is based on structured surfaces on which the particles are bound to specific locations (**Figure 2**).

## 3.1. Multiplexed Sensors Based on Dispersed Particles in Solution

For multiplexed detection in solution, particles must be designed to carry receptors for specific analytes. Also required are the corresponding transducer and an encoding scheme for use in determining which receptor is emitting the signal (76). In this section, we focus on optical readout because it is the most frequently used technique for multiplexed sensing with dispersed particles.

Multiplexing can be achieved by spectral, spatial, and temporal separation of the readout originated from different particles (which are sensitive to different analytes) (77). Before we describe the different principles for multiplexed sensing, we note that in all sensing applications involving particle-based sensors, one must be aware that the analyte concentration close to the (sensitive) particle surface in general differs from that in bulk (76). This problem can be easily understood

with the following examples. First, in the case of ion detection, electrostatic interaction between the corresponding ion and the particle surface occurs when the particles are charged. Debye–Hückel–based screening on the particle charge with counterions thus involves ion concentrations close to the particle surface (where the actual detection takes place) that are different from those in bulk (78–80). Second, in the case of protein detection, one has to be aware that proteins often (nonspecifically) adsorb to the surface of particles, forming the so-called protein corona (81, 82). Thus, the protein concentration at particle surfaces is generally higher than in bulk. Third, the sensing element (for example, an analyte-sensitive fluorophore bound to the particle) can be influenced by the particle. If the sensing element, the actual probe, is bound inside a (porous) particle or to the particle surface, then the particle impregnates a different environment to the probe. The environment near the particle can be, for example, more apolar than the surrounding aqueous solution, which can affect the response of the probe (83). One must therefore be aware that what particle-based sensors actually detect are local analyte concentrations, not bulk concentrations.

In case the spectrally resolved readout is based on fluorescent particles, multiplexing can be performed by using a set of particles emitting at different wavelengths, whereby the fluorescence readout of each particle-based sensor is sensitive to one analyte species. Spectrally resolved fluorescence measurements allow several analytes to be detected in parallel. The most significant problem with this approach is spectral overlap of the fluorescence from different particles. QDs are better suited to this purpose than particles that are decorated or filled with organic fluorophores, given that the emission spectra of QDs are generally narrower and do not have a red tail (1). For example, investigators have simultaneously detected enzymatic activity from two different enzymes by using a simple assay procedure based on QDs with distinct emission spectra (46). The enzymatic biomarkers uPA protease and Her2 kinase were detected at concentrations that were clinically relevant for the determination of breast cancer prognosis by use of two differently functionalized QDs with different emission spectra. The first QD dequenched following enzymatic degradation (**Figure 3*a*,*b***). FRET occurred between the second QD (donor) and an organic dye (acceptor) when the residue of the enzymatic reaction was bound to a specific antibody functionalized with organic dyes on the surface of the QD (**Figure 3*c*,*d***). Another example, also based on various QD emissions, involves a direct multiplexed sensor for $Ag^{+}$ and $Hg^{2+}$. The QDs were functionalized with different nucleic acids that specifically bound $Ag^{+}$ or $Hg^{2+}$ (84). Thereafter, the presence of these ions in solution caused the formation of $Ag^{+}$–cytosine or $Hg^{2+}$–thymine complexes and resulted in QD electron-transfer quenching.

Multiplexed, spectrally resolved optical readout can also take place with plasmonic NPs because the LSPR depends on the size and shape of the plasmonic NPs (85). Thus, plasmons of different types of NPs can be recorded at different wavelengths. This property has been used to create a multiplexed LSPR sensor involving gold nanorods (AuNRs) with different aspect ratios (86). In this study, the ratio between the length and the thickness of the rods determined the respective readouts. NRs with different aspect ratios were modified with recognition molecules for various analytes. The binding of the analytes to the different AuNRs can shift the plasmon band position and modify its extent. In this context, investigators have carried out parallel detection of three different cell-surface markers and detection of two different types of bacteria (87, 88). Although these sensors can detect only a few different analytes in parallel (given that the plasmonic peaks are relatively broad and thus suffer from spectral overlap), they are interesting because of their simple design and ease of use.

The principles discussed above are based on ensemble measurements that allow for simultaneous readout. Each particle is responsible for the detection of one analyte, giving rise to the corresponding signals at different wavelengths. Thus, readout can be spectrally resolved. However, there is an alternative way to read out particles one by one; in other words, readout can

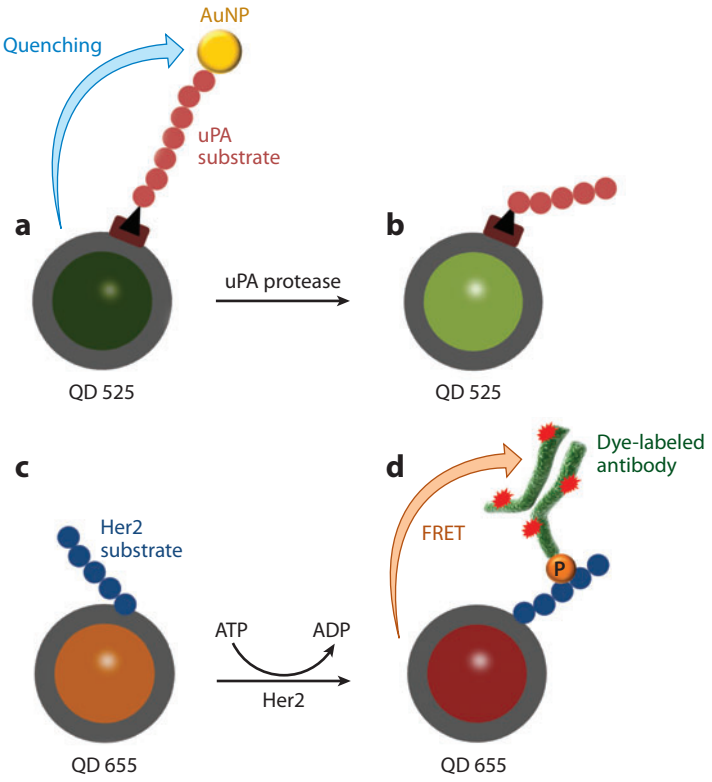


**Figure 3**

A multiplexed sensor for uPA protease and Her2 kinase. (*a*,*b*) The protease sensor is based on the quenching of quantum dots (QDs) emitting at 525 nm (*a*) and further dequenching in the presence of uPA that cleaves the substrate and releases the gold nanoparticles (AuNPs) responsible for the quenching. AuNPs absorb light very efficiently due to their surface plasmon resonance (*b*). (*c*,*d*) The kinase sensor is based on Förster resonance energy transfer (FRET) from QDs emitting at 655 nm to organic dyes that label the antibody bound to the analyte on the surface of the QDs following an enzymatic reaction. Modified from Reference 46 with permission.

be spatially resolved. In this case, spectral overlap does not pose a problem because the particles are spatially separated and readout can be correlated with individual particles (77). To read out particles one by one in solution, one can use either flow cytometry or microscopy.

In this context, there are two readout strategies both based on bar-coding. In the first strategy, analyte-sensitive readout can be combined with a bar code. The bar code identifies the analyte for each optical readout. Consider, for example, a class of fluorophores that are sensitive to $Na^+$ and another class sensitive to $K^+$ and that the emission spectra of both types of fluorophores overlap. If two types of particles that make up either the $Na^+$- or $K^+$-sensitive fluorophores, along with a corresponding bar code, are produced, then one can classify each particle by first reading the bar code, which reveals whether the fluorescence from the analyte-sensitive fluorophore corresponds to $Na^+$ or $K^+$ (77). QDs are very useful for the production of fluorescent bar codes due to their narrow emission band. Compared with that of organic dyes, the emission of different QD species can be better spectrally resolved, so more codes can be generated. For instance, the inner cavities of porous microparticles (polyelectrolyte capsules) were loaded with analyte-sensitive fluorophores, and the surfaces of the fluorophores were tagged with a QD-based fluorescence bar code. This

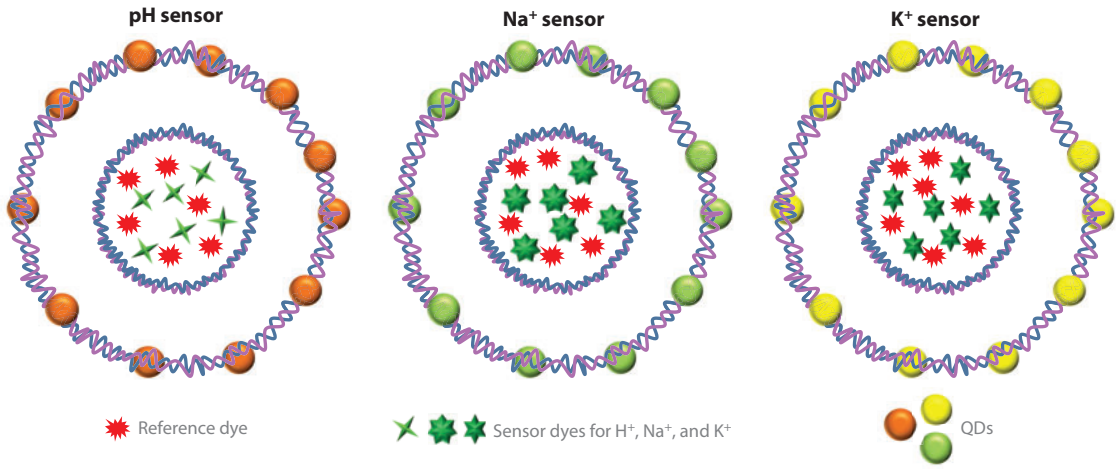


**Figure 4**

Simplified scheme of multiplexed sensors for $H^+$, $Na^+$, and $K^+$ based on quantum dot (QD) bar codes. Ion-sensitive dyes are encapsulated, together with a reference dye, in a permeable multiple-shell structure within the capsule to enable ratiometric measurements. The emission of the specific ion sensors may overlap, but the bar codes made with the different QDs allow for discrimination between signals.

system allowed three ions ($H^+$, $Na^+$, and $K^+$) to be detected in parallel, despite the spectral overlap of the analyte-sensitive fluorophores (**Figure 4**) (44).

The second bar code–based strategy is based not on active sensing (i.e., there is no molecule or particle of which the readout is altered following binding of the analyte), but on passive detection. On the basis of molecular recognition, analyte molecules in solution are tagged with a bar code; that is, bar codes need to be modified with analyte receptors. Consider a scenario in which different viruses are to be detected in solution. Antibodies for the different viruses would be modified with different bar codes. By observing one by one the conjugates that form (as mentioned above in the context of flow cytometry or with microscopy), one can identify the different viruses. An important example is a multiplexed sensor for five different genetic biomarkers (human immunodeficiency virus, malaria, hepatitis B, hepatitis C, and syphilis) developed by Giri et al. (43). These authors encoded microbeads with QDs of different emission wavelengths and intensities to produce a library of bar codes for multiplexed detection; this library exceeded the limit of 100 useful bar codes of similar systems involving organic dyes instead of QDs. The bar-coded particle bound the biomarker without causing any change in its fluorescent emission. A universal fluorescent probe that binds all biomarkers was used to discriminate between the unbound bar codes and the analyte–bar-coded particles. Only when there was colocalization between the emission of the bar code and the universal probe was the analyte bound to the bar code. Readout was performed with flow cytometry (**Figure 5**).

SERS-encoded NPs are a promising alternative to bar-coding (89). Particles should contain organic molecules (SERS reporters) in close contact with or bound to the plasmonic surfaces, providing the signature of the particle (90). The particle should be separately functionalized with an analyte receptor (91). Due to the uncountable number of molecules, each of which has specific vibrational spectra, a multiplexed sensor based on SERS-encoded NPs can be considered limitless. However, the number of codes that can be experimentally produced is restricted by several factors involved in the synthesis of multifunctional particles, such as the binding of the SERS reporter

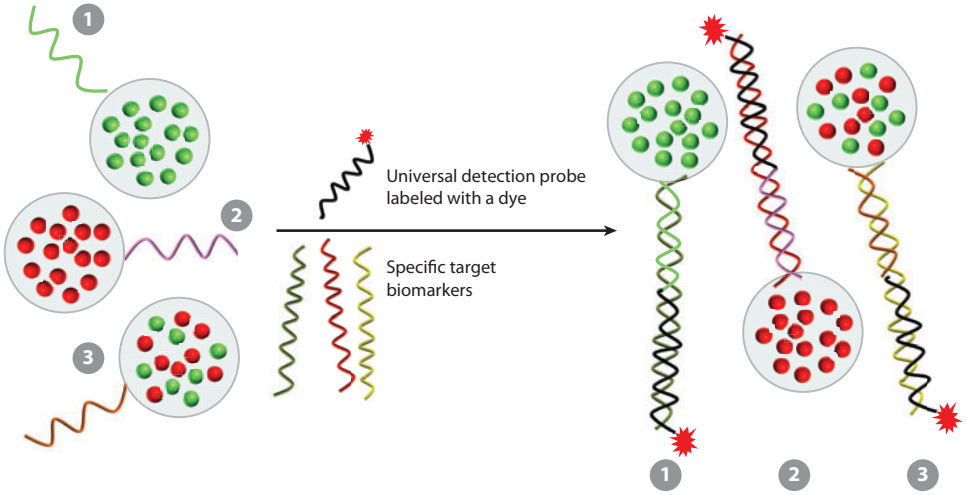


**Figure 5**

Microbeads labeled with different mixtures of quantum dots for multiplexed biomarker detection. Each sensor is functionalized with a capture DNA strand (steps ❶ through ❸). In solution, hybridization occurs between the specific target biomarkers and the universal detection probe. The universal labeled probe is used to differentiate between bar codes bound to the biomarkers and free ones. Finally, the sample is analyzed by flow cytometry, in which each particle is analyzed individually.

on the metallic surface, the insufficient field enhancement necessary to raise the SERS signal up to detectable levels, and the stability of the particles. Many examples of the synthesis of encoded NPs for SERS sensing in solution exist (92, 93) but the multiplexed sensing of a large number of analytes is still in its infancy, so more universal strategies for the SERS-encoding and detection should be performed. In vivo multiplexed sensing has been demonstrated only recently (94).

Another example involves plasmonic NPs assembled on a surface for the design of SERS-based multiplexed sensing platforms (95). So-called sandwich-type DNA coated silver NPs arrays have been used to specifically hybridize various DNA strands labeled with different SERS probes (96). Multiplexing can take place because different SERS labels can conveniently be spectrally resolved (**Figure 6**); thus, no structuring of the surface is required. The number of DNA strands that can be detected in parallel is limited by the number of SERS labels that can bind DNA and by the length of the DNA strand (with sufficient enhancement of the Raman signal, which depends on the number of labels and the distance between the labels and the surface). The creation of hot spots following DNA hybridization has also been exploited in multiplexed SERS-based sensors involving sandwich-type DNA arrays to reach a DNA detection limit of 10 pM (97).

Encoded hybrid materials can help improve the number of analytes detected in parallel, as discussed in the previous section. However, if a second encoding scheme is added to multifunctional NPs, then the number of parallel detected analytes can be multiplied. This idea was introduced by Wang et al. (98), who recently produced a hybrid system based on AuNRs coated with $SiO_2$ and encoded with different QDs with different emission and SERS labels. The resulting immunoassay has great potential for multiplexing.

In addition to spectral and spatial discrimination, temporal resolution of different optical sensors can also be performed. In the case of fluorescent particles, analyses of luminescence lifetime and the intensity-to-lifetime ratio allow for discrimination between signals that may be spectrally overlapped (99, 100). Sensors based on lifetime measurements of QDs exist (101),

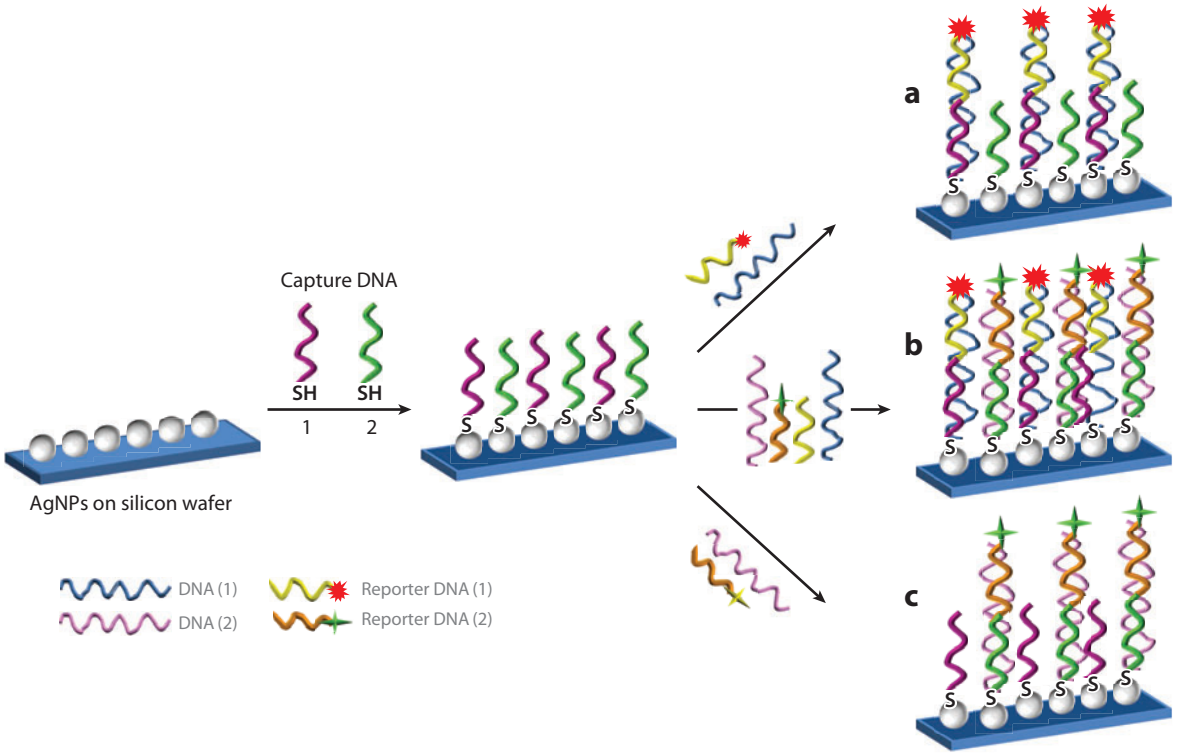


**Figure 6**

A multiplexed DNA sensor based on silver nanoparticles (AgNPs) deposited on silicon wafers and functionalized with thiolated DNA (1 and 2) strands for the specific hybridization of DNA (1) and DNA (2) and the corresponding surface-enhanced Raman spectroscopy–labeled DNA reporters. (*a*) Only DNA (1) in solution. (*b*) A mixture of DNA (1) and DNA (2) in solution. (*c*) Only DNA (2) in solution. Abbreviation: SH, thiol group termination. Modified from Reference 96 with permission.

but to the best of our knowledge, multiplexed sensors based on lifetime measurements are still uncommon. Techniques such as fluorescence lifetime imaging microscopy (FLIM) will probably extend the use of temporal discrimination in optical biosensing. Recently, cellular viscosity was studied with fluorescent ratiometry and FLIM (102), and multiplexed sensing is likely to evolve in this direction by simultaneously taking advantage of several measurements, either spectral and temporal or spatial and temporal (103). An example of a promising technique in multiplexing wherein lifetime and spectral measurements of fluorophores can reveal information about analyte binding involves multiplexed FRET assays. If FRET occurs, not only the emission intensity and wavelength of the donor and acceptor fluorophore but also the lifetime can be changed (Section 2). Multiplexed FRET assays for biosensing have been developed on the basis of (*a*) FRET from luminescent lanthanide complexes to several different QDs (acceptors) following molecular recognition (104) or (*b*) FRET from several QDs (donors) to organic dyes for the detection of DNA (105).

Although most of the examples of multifunctional NPs used for multiplexed sensing in solution involve optical detection, there are remarkable examples that mix several detection modes. These include magnetofluorescent nanoparticles, which can be used for flow cytometry and diagnostic MR detection (106, 107).

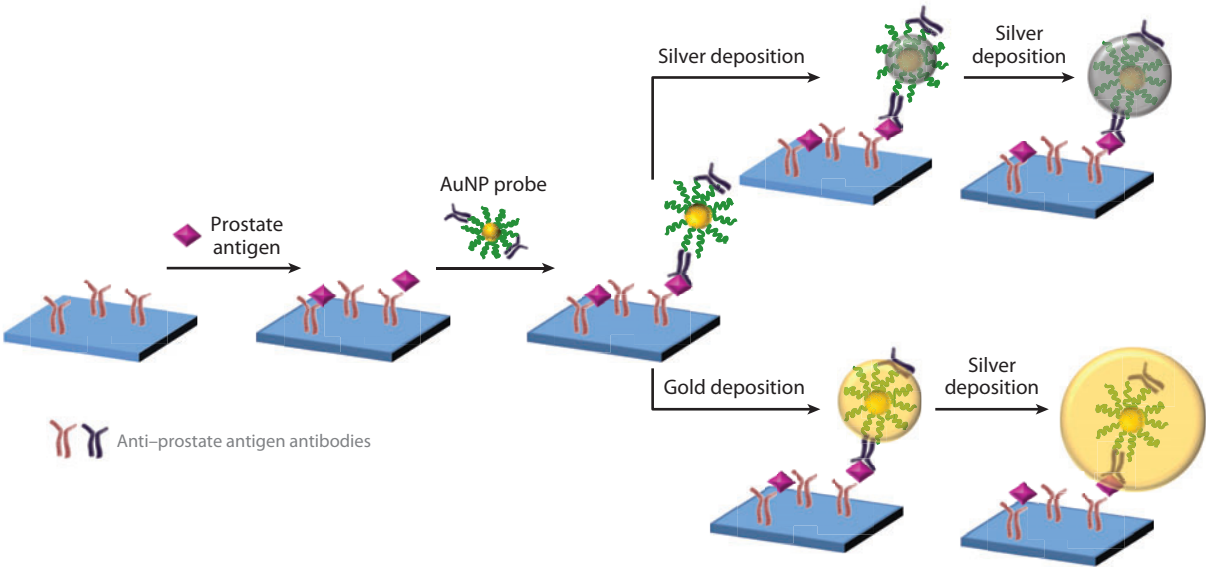


**Figure 7**

A scanometric immunoassay. Abbreviation: AuNP, gold nanoparticle. Modified in part from Reference 116.

## 3.2. Multiplexed Sensors Based on Particles Associated with Planar Arrays

Planar arrays, composed mainly of metallic and semiconductor NPs and arrays of biomolecules such as DNA and antibodies that bind NPs, have been extensively studied for use in NP-based optical or electrical biosensors (108–110). Multiplexed sensing with NPs associated with (typically planar) arrays can easily be performed because of the possibility of positional encoding (111). The general idea is to detect various analytes at different positions of the (generally structured) array. In this section, we discuss recent examples of multiplexed sensors based on NP planar arrays.

**3.2.1. Localized surface plasmon resonance spectroscopy.** LSPR-based multiplexed sensors detect, for example, changes in interparticle distance; modification of the refractive index; and changes in color in the LSPR of NPs due to the presence of analytes, whose individual signal can be differentiated by specific receptors, normally DNA or antibodies (112–114). Colorimetric assays can be produced through functionalization of a microstructure chip with different antibodies in different regions. The addition of a solution with antigen produces specific antibody–antigen binding, and depending on the amount of antigen, the response in color (and absorbance) may differ. This method is sensitive and specific. Endo et al. (115) applied this method to eight different proteins. In a similar approach, investigators modified the above-mentioned scanometric assay by using antibodies instead of DNA microarrays and electroless deposition of gold instead of silver. The light was thereby scattered by antibody–oligonucleotide hybrid AuNPs, and the amplification of the signal was greater than that of precedent scanometric assays due to gold deposition (**Figure 7**). The assay detected very low concentrations of different proteins, in this case in serum, without the need to trap of the analyte in solution with two differently labeled NPs. This process eliminated several steps from the production of the multiplexed sensors (116). Note that scanometric assays are US Food and Drug Administration–approved detection methods for biological samples. Therefore, they are among the most-studied and most widely used methods for multiplexed analyses involving NPs.

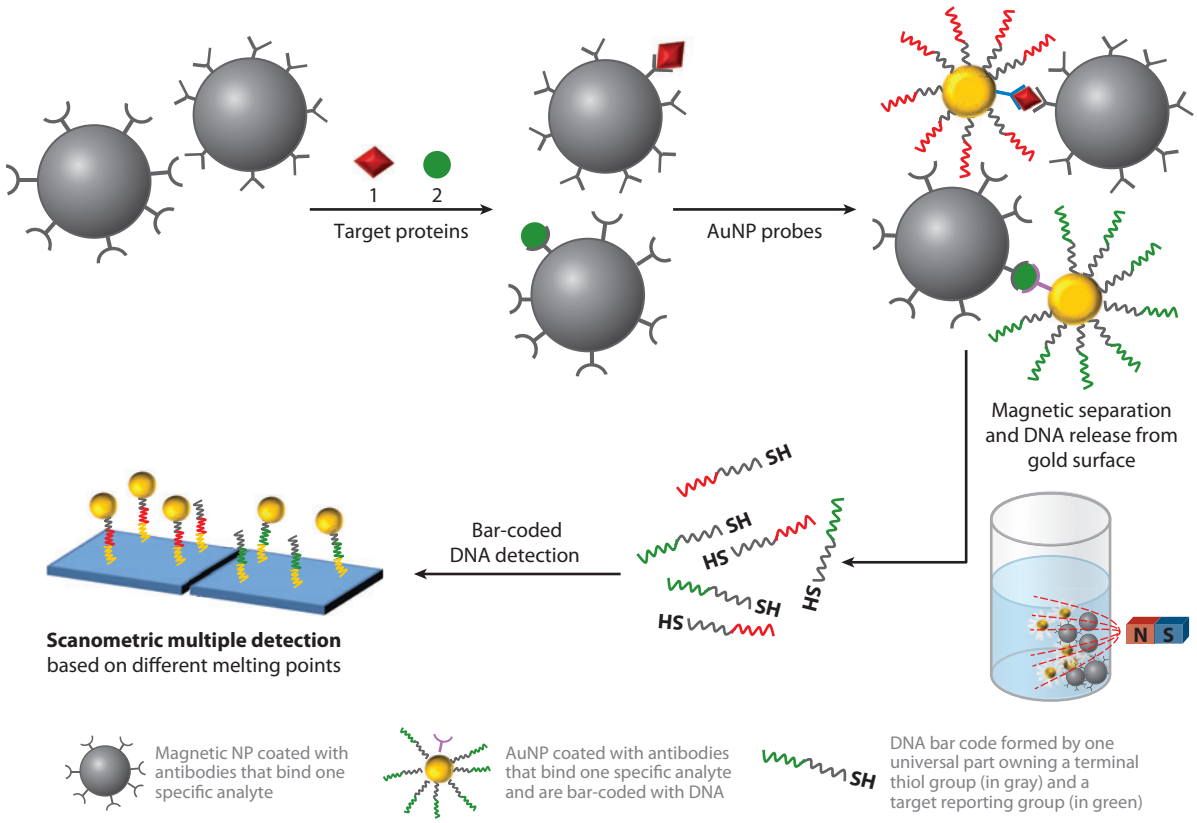


**Figure 8**

A bio-bar-coded gold nanoparticle (AuNP) assay for multiplexed protein detection. Scanometric detection also involves a silver coating to improve sensitivity (not shown for simplicity). Abbreviation: SH, thiol group termination. Modified from Reference 117 with permission.

In addition to direct arrangement of the NPs via recognition of the analyte on the array surface, NPs that have captured an analyte can also be arranged via bar codes. Bar codes can be made, for example, with biological molecules. An interesting example is a multiplexed sensor based on bio-bar-coded AuNPs and scanometric detection (involving colorimetric detection) (117). The analytes—in this case, protein cancer markers—are trapped by two different types of NPs, DNA bar-coded AuNPs and MNPs, which have different antibodies that bind the same protein in different epitopes. Magnetic separation is applied after the analytes are trapped in solution by the antibodies bound to the surface of the MNPs. The DNA used as a bar code is then released from the gold surface and quantified in a scanometric detector (LSPR-based detection). Again, the detector involves (smaller) AuNPs and a silver-layer coating that significantly amplified the signal and reduced the detection limits. **Figure 8** depicts this multiplexed sensor, which is very sensitive and specific. However, it requires many functionalization steps for numerous different NPs.

Recently, copper-capped silica particles have been used to develop a cost-effective optical setup on disposable chips capable of multiplexed sensing of biomolecules; the chips have a detection limit of 10 fM. The assay is based on measurable changes in the refractive index in the presence of analytes (in this case, different DNA strands), which arise from the LSPR of the copper layer deposited on the silica NPs (118). The combination of LSPR refractive-index sensing and the

well-known ELISA assay has led to the development of another colorimetric multiplexed sensor with single-molecule sensitivity. This new technique takes advantage of the amplification of the shift of the LSPR scattering maximum following an enzymatic reaction that allows for the detection of one or a few enzymes (119). The authors have not yet applied this new approach to multianalyte analyses, but due to the sensor configuration and the results from single-particle analyses, multiplexing is highly anticipated, along with the development of nonfluorescence single-molecule ELISA assays.

**3.2.2. Electrochemical immunosensors and immunoassays.** Electrochemical immunosensors and immunoassays (EIIs) are electrochemical sensors in which antibody–antigen interactions occur on an electrochemical transducer (in immunosensors) or the immunological material is immobilized on a solid support, such as a nanomaterial. Following sandwich or competitive immunoreactions, the solid support containing the immunological material is attached to the transducer surface (in immunoassays) (120). EIIs are excellent candidates for multianalyte analysis in terms of clinical diagnosis, in which the biological agents to be detected are present in very low concentrations (121). Multiplexed analysis can be performed in EIIs when the sensing electrodes are sufficient separated to prevent signal interference (cross talk) between neighboring electrodes. Very low analyte concentrations can be detected through amplification of the antibody–antigen interaction transduction signal with labels such as enzymes or NPs (122). NPs can have different functions within the sensor (Section 2.2), such as trapping analytes and improving the transducer surface for better antibody adhesion.

Interesting examples of EIIs involving multifunctional NPs have recently been provided (60, 123). Mani et al. (124) produced a multiplexed sensor for four different oral cancer biomarkers that can be used with clinical samples. These authors achieved ultralow detection (5–50 fg $ml^{-1}$) on the basis of amperometric measurements. In another study, magnetic nanobeads were functionalized with both an antibody to capture a specific analyte and horseradish peroxidase to amplify the signal during the detection on the planar electrode. In the first step of the detection, the magnetic beads functionalized with specific antibodies captured the corresponding analyte due to antibody–antigen interactions; then, these magnetic nanobeads were magnetically separated from the solution. The second step of the detection involved the binding of a second antibody with the corresponding antigen on a planar electrode. This time, the second antibody bound to another epitope of the same antigen, and the unbound magnetic nanobeads were washed out. Multiplexing was achieved through the use of several electrodes in parallel (125). **Figure 9** depicts this multiplexed sensor.

AuNP arrays are useful in immunoassays for several reasons. First, they increase the electrode surface area. Second, they facilitate the attachment of numerous antibodies due to the easy functionalization of gold surfaces. The production of high-AuNP-coverage electrodes depends on both the stabilizing molecule on the gold surface and the electrode surface. Often, it is necessary to coat the electrode with a layer of molecules that increase the adhesion of the AuNP. For example, positively charged polyelectrolytes such as PDDA [poly(diallyldimethylammonium chloride)] can be used to increase the AuNP's adhesion. Similar electrodes have been produced for multiplexed protein detection by use of carbon nanotube arrays, but their detection limits, reproducibility, and stability were lower than those of the AuNPs arrays (124, 126, –127).

Multiplexing, as discussed above, is based on the use of an array of differently functionalized electrodes. Geometrically, the number of electrodes that can be used in parallel is limited (128). However, as an alternative to electrode arrays, spatial resolution and, thus, multiplexing capability can be achieved by use of a light pointer in connection with a semiconducting electrode surface to select defined points on an electrode surface (129–131). The light pointer creates a local

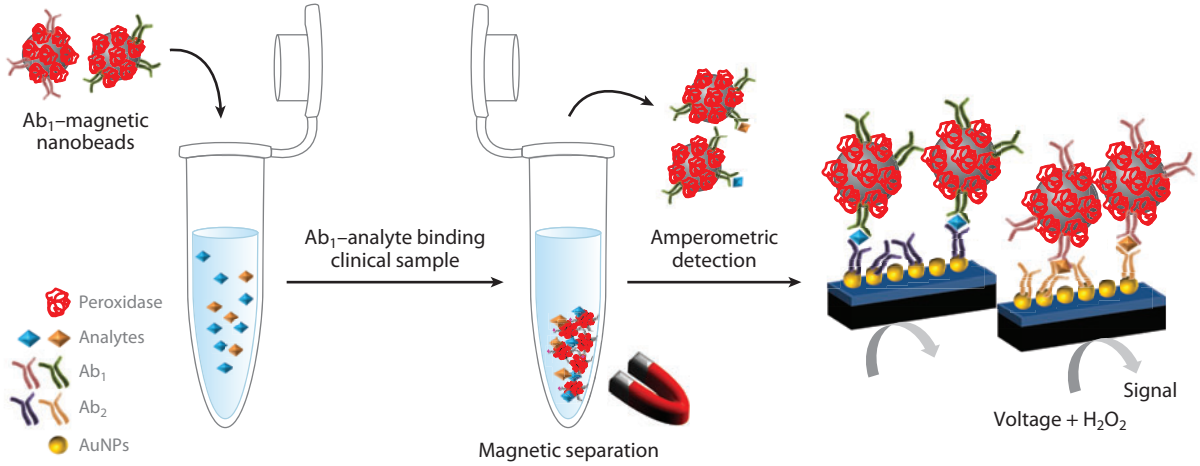


**Figure 9**

A gold nanoparticle (AuNP) array functionalized with antibodies ($Ab_2$) for the ultrasensitive detection of cancer biomarkers. The sensor also contains magnetic beads labeled with antibodies ($Ab_1$) and horseradish peroxidase for amplification and biomarker capture. Multiplexing is achieved through parallel detection in different electrodes.

photocurrent whose amplitude is influenced by local redox reactions on the electrode surface. The semiconductor layer can be constructed from QDs (57, 58). The first observations of enzymatic reactions have already been reported (55, 66, 132, 133). Although multiplexed analysis has not yet been practically demonstrated, its spatial resolution capability clearly demonstrates its potential.

**3.2.3. Giant magnetoresistive sensors.** Giant magnetoresistive (GMR) sensors are a promising and low-cost alternative for the detection of proteins and nucleic acids. In the former case, antibodies arrays must be prepared beforehand to specifically capture the corresponding analyte. Functionalized MNPs in solution that bind the same antigen are used to detect the presence of an analyte by measuring the small changes in resistance due to the binding event in the presence of a magnetic field. Multiplexed sensors have been developed using this technique, but their reproducibility and sensitivity remain compromised in extended sensing applications with real and untreated samples (134–138).

There are many other examples of the use of NP arrays or NPs as labels in immunoassays, such as chemiluminescence imaging immunoassays involving horseradish peroxidase and AuNPs (139). New strategies for multiplexing with planar arrays are continually being introduced due to their significant possibilities in multifunctional NP synthesis and the application of new materials, such as fluorescent nano–graphene oxide and ensemble aptamers instead of more specific DNAs for analyte recognition (140).

## 4. MULTIMODAL IMAGING

In recent years, many applications of NPs to bioimaging and diagnosis have been developed (141–143). The most important example is undoubtedly the use of MNPs in magnetic resonance imaging (MRI) (144–147). However, many other NP applications are expected to find clinical use in the near future. Advances in colloidal chemistry have enabled "à la carte" design of multifunctional particles. By combining elements such as radioactive isotopes, QDs (31, 148), and organic dyes in the same nanostructure or microparticle, one can easily obtain

multimodal nano- or microcomposites. The use of multimodal labels is necessary to overcome the limits of any single technique, such as spatial resolution or bleaching. Cheon & Lee (149) explored these ideas on the basis of multimodal imaging probes consisting of MNPs with further functionalities, namely radionuclides enabling positron emission tomography and fluorescent moieties for optical tracking. These probes can be modified with anchor molecules such as antibodies, peptides, DNA, and RNA, permitting the investigators to address specific targets.

Liong et al. (150) provided an example of advantageous MNP-based multimodal systems. These authors applied multifunctional iron oxide–mesoporous silica NPs that were detectable both optically and by MRI. They rendered the particles suitable for live-cell imaging and therapeutic purposes by targeting them specifically to human cancer cells. Moreover, those particles were simultaneously used to deliver hydrophobic anticancer drugs (or other molecules) into cells.

Nahrendorf et al. (151) investigated a comparable trimodal imaging system comprising MRI (iron oxide core), PET sensors (chelator ligand complexing the radiotracer $Cu^{64}$), and fluorescence (VivoTag-680$^{TM}$) that enabled in vivo studies of the detection of macrophage markers, specifically, the detection of inflammatory atherosclerosis. Given the lower required concentration of NPs and their higher target-to-background ratio, the authors found this technique especially relevant for clinical use. The production of nano- or microprobes for multimodal imaging in vivo can be difficult, mainly because of targeting issues (152, 153), the colloidal stability and purity of the probes, the retention time in vivo (154), the long-term stability of the signal, degradability, possible toxicity, and the clearance mechanisms of the probes in humans. Degradation over the long term and dissolution of the nanoprobes within the body are very difficult to avoid, in particular in the case of corrosive NP materials such as CdSe or silver. Regarding in vivo applications, the use of toxic materials (e.g., radiotracers) or materials that deliver toxic ions during dissolution (e.g., CdSe QDs) should be minimized. Nevertheless, in specific instances, the lack of a diagnosis would be worse for the patient than the risk posed by the probe itself (e.g., a PET sensor).

Several types of multimodal particle platforms exist. On the NP level, for example, polymer-coated NPs purified with gel electrophoresis and size-exclusion chromatography fulfill most of the above-mentioned requirements (80, 155). They are very stable and pure (156–158); their size is reasonably small; and in the size range longest blood circulation time (10–100 nm) (159), the surface charge can be varied (160), the polymer shell itself does not impose enhanced cytotoxicity (161), and the polymer protecting the core can be loaded with functional entities (162). For these NPs, the inorganic core can be used as the first label (for example, it can be made magnetic, fluorescent, or radioactive), and the second label can be incorporated within the amphiphilic polymer that stabilizes the NP surface (155, 157, 158). Both labels are thereby protected from the biological environment, which helps improve signal stability and leaves the NP surface free for further functionalization by, for instance, cell-penetrating peptides, molecular receptors, or molecules that improve cell circulation such as poly(ethylene glycol) (154). **Figure 10** presents examples of such probes.

Fluorescent microscopy can be conveniently combined with SERS imaging through the incorporation of dyes, SERS probes, and even surface-enhanced resonance Raman scattering (SERRS)-active labels in the same multifunctional particle. Core-shell particles made from a gold core and an organosilica shell are good platforms for the simultaneous entrapment of fluorophores and SERS probes. Cui et al. (163) produced ~100-nm-diameter core-shell particles loaded with fluorescein isothiocyanate and malachite green isothiocyanate (green dye and SERS label). In a further demonstration of multiplexing, the authors synthesized similar particles with fluorescein isothiocyanate and X-rhodamine-5-(6)-isothiocyanate (green dye and SERRS label) (**Figure 11*a***). Multimodal imaging in living cells was thereby demonstrated with these two differently labeled types of particles.

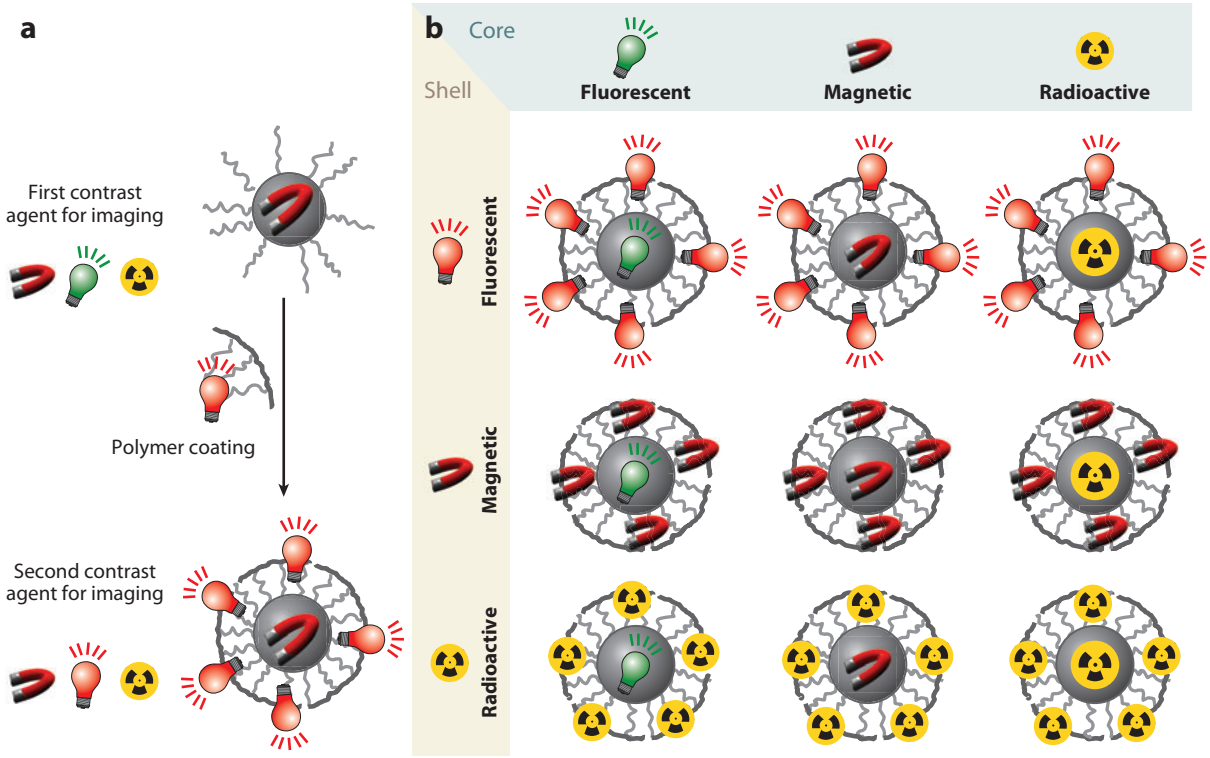


**Figure 10**

Strategy to produce multifunctional nanoparticles (NPs) for dual imaging. (*a*) Inorganic cores (*gray*) can be synthesized with different materials that are magnetic, fluorescent, or radioactive. Organic molecules are stabilized the NP surface following core synthesis. The cores are coated with an amphiphilic polymer that makes them water soluble. The amphiphilic polymer is loaded prior to coating with the second label (fluorophore, radioactive atom, etc.), and the final NP is double labeled. (*b*) Table including the possibilities of NPs for dual imaging based on polymer-coated NPs.

Currently, SERS imaging is limited by light penetration. NPs can be detected at a maximum depth of 1 cm (164). The combination of SERS with techniques such as spatially offset Raman spectroscopy could pave the way for clinical detection because the depth can be increased to up to 5 cm (165). In SERS applications and, more importantly, in bioimaging, the metallic surface of the NPs should be protected with an appropriate shell that hinders the adsorption of molecular species that could interfere with the vibrational code of the SERS probe. Silica shells have been used primarily for SERS applications and for multimodal imaging based on colloidal NPs because of their (*a*) reduced agglomeration, (*b*) biocompatibility, (*c*) optical transparency, (*d*) tunable porosity, (*e*) chemical inertness, and (*f*) ease of further functionalization (166). **Figure 11** shows several examples of multimodal NP imaging probes built up with silica shells and different inorganic cores. Not only do silica shells act as protective shells, but also they can be loaded with fluorophores, SERS and SERRS labels, or other NPs (**Figure 11*a***). For example, the surface of $Fe_3O_4$@$SiO_2$ core-shell particles was further functionalized with AuNRs for in vivo MRI and IR imaging (167). Also, more than two imaging modalities can be used within one NP (**Figure 11*c***). Hwang et al. (41) have produced quadruple-labeled particles by first coating cobalt ferrite NPs with a silica shell entrapping rhodamine B isothiocyanate and then functionalizing the silica surface with an organic dye. The bioluminescent protein luciferase was added as a third label and radioactive $^{68}GaCl_3$ as

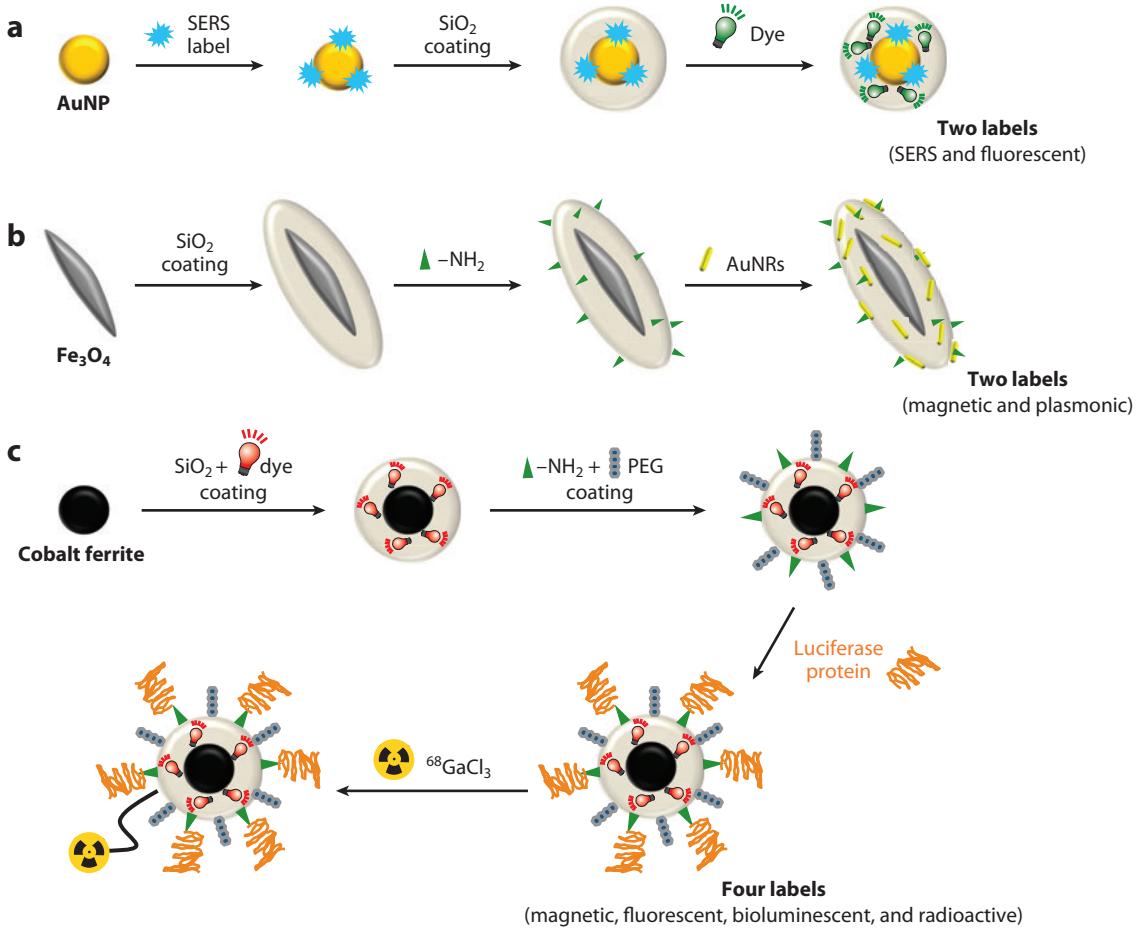


**Figure 11**

Different multimodal nanoparticle (NP) probes made with core-shell particles involving silica coating. (*a*) Particles for surface-enhanced Raman spectroscopy (SERS) and fluorescence imaging. Gold nanoparticles (AuNPs) are coated with a silica layer that entraps both the SERS probe and the fluorophore. Image adopted from Cui et al. (163). (*b*) Particles for in vivo magnetic resonance imaging and IR thermal imaging. $Fe_3O_4$ ellipsoids are coated with silica and gold nanorods (AuNRs). Image adapted from Ma et al. (167). (*c*) Quadruple imaging based on a magnetic core coated with a silica shell embedding a fluorophore, and further silica surface functionalization with a bioluminescent protein and a radioactive isotope. Abbreviation: PEG, poly(ethylene glycol). Data adapted from Hwang et al. (41).

the fourth. These particles were successfully used in five in vivo imaging techniques: fluorescence, bioluminescence, BRET, positron emission tomography, and MRI. The same authors monitored in vivo and in vitro uptake in target cells of similar particles that were functionalized with specific aptamers with fluorescent microscopy, radioactive detection, and MRI (168).

Silica shells have also helped produce lanthanide-based multifunctional NPs. Upconverting NPs are interesting for multimodal imaging due to their special 4f electron structure, their rich optical and magnetic properties, their biocompatibility, and the tunability of their emission wavelength (169). More importantly, the upconversion of light due to anti-Stokes emission significantly minimized the background and simplified the discrimination of the signal from the target tissues or cells, compared with other optical techniques. Core-shell trimodal particles involving silica shells

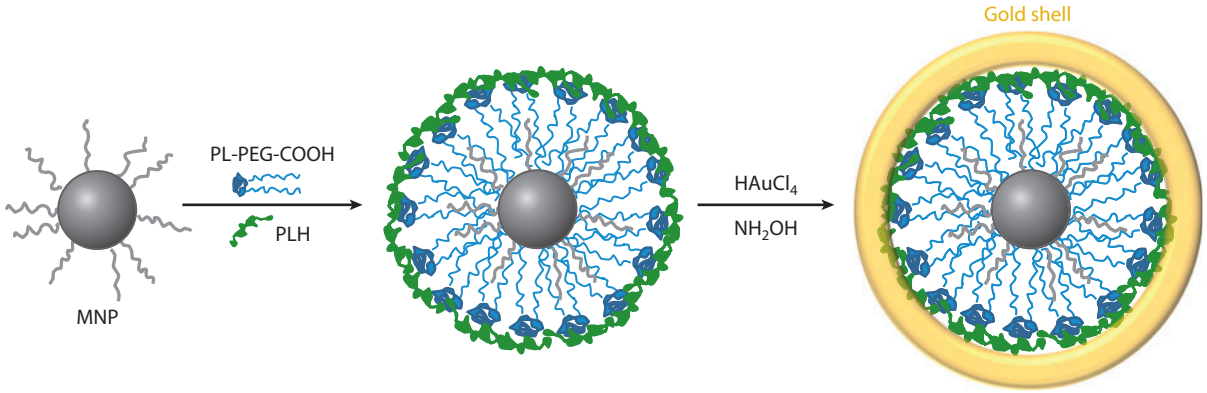


**Figure 12**

Core-shell iron oxide–gold nanoparticles. Magnetic nanoparticles (MNPs) were initially stabilized with oleic acid (*gray*), then coated with phospholipid–poly(ethylene glycol) (PL-PEG)-COOH and polyhistidine (PLH) to form a gold layer through the reduction of the salt $HAuCl_4$ by $NH_2OH$ on the particle surface.

have recently been produced for X-ray computed tomography, MRI, and fluorescence imaging, demonstrating their suitability for further in vitro and in vivo applications (170, 171).

Multifunctional particles can also extend the application of certain imaging techniques, such as for magnetophotoacoustic (MPA) imaging. MPA imaging is based on the synergy of magnetomotive ultrasound, photoacoustic, and ultrasound imaging. It is a noninvasive technique that can be applied in diagnosis. To this end, Jin et al. (172) recently introduced a new class of core-shell NPs made from an iron oxide core and a gold shell separated by phospholipid–poly(ethylene) glycol and a layer of polyhistidine (**Figure 12**). Due to the hybrid nature of these NPs, their contrast, resolution, and sensitivity obtained in ultrasound imaging were acceptable. Otherwise, the technique is not yet good enough in terms of contrast, although it remains interesting due to its resolution at reasonable depths, nonionizing nature, cost-effectiveness, and portability. Moreover, the particles can be imaged with electron microscopy, MRI, and scattering-based techniques.

Multilayer polyelectrolyte capsules are promising candidates for multimodal imaging because they can simultaneously incorporate several labels that are spatially separated. In Section 3.1, we describe bar-coded capsules for multiplexed analysis (44). Multimodal imaging can be easily achieved in the same manner by combining organic labels with inorganic NPs that act as contrast agents. In addition to optical detection with fluorescence microscopy, the magnetic properties of capsules loaded with superparamagnetic NPs are suitable for MRI (173). Moreover, Johnston et al. (174) have demonstrated that it is possible to control the binding and uptake of such capsules on target cells by antibody labeling.

## 5. IMAGING AND SENSING

Many multifunctional NPs can be used for either imaging or sensing. The classical example is iron oxide–based NPs, which are useful in MRI as negative-contrast agents (image darkening) and in magnetoresistive immunoassays as nanotags (134, 144). However, there are fewer examples of particles that can be applied simultaneously to in vivo or in vitro imaging and sensing. The application of multifunctional particles for such purposes could lead to great advances in diagnosis. The size of NPs is similar to that of ribosomes and some proteins; therefore, NPs may be able to simultaneously detect and localize changes in biomolecule or ion concentrations that are related

to many diseases. In this context, nanoprobes based on organic polymers have been used to simultaneously image and estimate local concentrations of $O_2$ in vitro (175, 176). Moreover, polymer matrices such as PEBBLE nanosensors have incorporated several fluorophores for imaging and ratiometric determination of in vitro ion concentrations (177). Rare earth–doped NPs have been used as in vitro and in vivo luminescent tags and temperature sensors (178, 179). Recently, SERS nanotags were simultaneously employed to image and detect cancer biomarkers in vivo (94).

Another alternative, similar to PEBBLE sensors, is the nanostructured production of polymer microcapsules that simultaneously incorporate NPs and fluorophores that are sensitive to different analytes (44, 180). In vitro experiments to estimate pH changes in cells have been performed, but given the feasibility for multifunctionalization involving bar-coding, antibody functionalization, and ratiometric measurements, many future applications involving simultaneous imaging and sensing are likely (44, 174, 181).



## 6. OUTLOOK

This review describes many strategies for multiplexed sensing and multimodal imaging involving multifunctional nano- and microparticles. Although interesting examples have been published, most of these techniques have not yet been used for detection with real samples, such as blood serum, or for in vivo imaging. Some of these sensing techniques still lack reproducibility. With regard to in vitro detection, DNA arrays, for example, have been successfully used for multiplexed sensing of various analytes. However, the values obtained for the analyte concentrations are often only informative and not quantitative. Antibody arrays are promising substitutes for DNA arrays because they can detect, in the case of gene expression, proteins directly from protein–antigen interactions, so quantification should be easier to perform. However, the use of antibodies for analyte trapping or recognition poses certain problems. The epitope where antibody–antigen binding takes part is only a small part of the analyte, and antibodies often aberrantly bind epitopes of nontargeted analytes. Some of the examples discussed above regarding antibody arrays involve several antibody–antigen binding events to reduce cross-reactivity. New amplification methods are currently being developed to improve sensitivity by improving analyte–receptor interaction specificity, as is the case in applications of orthogonal chemistries to diagnosis and imaging (107, 182). Particle stability (76) still poses a problem for in vivo applications such as particle-based sensors and contrast agents for imaging. Circulation within the bloodstream and further uptake in target tissues remain the most critical challenges for nanomedicine (183).

## DISCLOSURE STATEMENT

The authors are not aware of any affiliations, memberships, funding, or financial holdings that might be perceived as affecting the objectivity of this review.

## ACKNOWLEDGMENTS

Parts of our work were supported by DFG (Germany; grant PA794/11-1 to W.J.P.) and the European Commission (a nanognostics grant to W.J.P.). We acknowledge technical discussions with Dr. Gaëlle Charron.

## LITERATURE CITED

1. Bruchez MJ, Moronne M, Gin P, Weiss S, Alivisatos AP. 1998. Semiconductor nanocrystals as fluorescent biological labels. *Science* 281:2013–16

2. Chan WCW, Nie S. 1998. Quantum dot bioconjugates for ultrasensitive nonisotopic detection. *Science* 281:2016–18
3. Alivisatos AP. 2004. The use of nanocrystals in biological detection. *Nat. Biotechnol.* 22:47–51
4. Elghanian R, Storhoff JJ, Mucic RC, Letsinger RL, Mirkin CA. 1997. Selective colorimetric detection of polynucleotides based on the distance-dependent optical properties of gold nanoparticles. *Science* 277:1078–81
5. Khlebtsov B, Panfilova E, Khanadeev V, Bibikova O, Terentyuk G, et al. 2012. Nanocomposites containing silica-coated gold–silver Nanocages and Yb-2,4-dimethoxyhematoporphyrin: multifunctional capability of IR-luminescence detection, photosensitization, and photothermolysis. *Am. Chem. Soc. Nano* 5:7077–89
6. Jakhmola A, Anton N, Vandamme TF. 2012. Inorganic nanoparticles based contrast agents for X-ray computed tomography. *Adv. Healthc. Mater.* 1:413–31
7. Judenhofer MS, Wehrl HF, Newport DF, Catana C, Siegel SB, et al. 2008. Simultaneous PET-MRI: a new approach for functional and morphological imaging. *Nat. Med.* 14:459–65
8. Ross P, Hall L, Smirnov I, Haff L. 1998. High level multiplex genotyping by MALDI-TOF mass spectrometry. *Nat. Biotechnol.* 16:1347–51
9. Kotov N. 2011. Bioimaging: The only way is up. *Nat. Mater.* 10:903–4
10. Jans H, Huo Q. 2012. Gold nanoparticle–enabled biological and chemical detection and analysis. *Chem. Soc. Rev.* 41:2849–66
11. Freeman R, Willner I. 2012. Optical molecular sensing with semiconductor quantum dots (QDs). *Chem. Soc. Rev.* 41:4067–85
12. Jimenez de Aberasturi D, Montenegro JM, Ruiz de Larramendi I, Rojo T, Klar TA, et al. 2012. Optical sensing of small ions with colloidal nanoparticles. *Chem. Mater.* 24:738–45
13. Scotognella F, Della Valle G, Kandada ARS, Dorfs D, Zavelani-Rossi M, et al. 2011. Plasmon dynamics in colloidal $Cu_{2-x}Se$ nanocrystals. *Nano Lett.* 11:4711–17
14. McFarland AD, Van Duyne RP. 2003. Single silver nanoparticles as real-time optical sensors with zeptomole sensitivity. *Nano Lett.* 3:1057–62
15. Rodríguez-Lorenzo L, de la Rica R, Álvarez-Puebla RA, Liz-Marzán LM, Stevens MM. 2012. Plasmonic nanosensors with inverse sensitivity by means of enzyme-guided crystal growth. *Nat. Mater.* 11:604–7
16. Claridge SA, Schwartz JJ, Weiss PS. 2011. Electrons, photons, and force: quantitative single-molecule measurements from physics to biology. *Am. Chem. Soc. Nano* 5:693–729
17. Ament I, Prasad J, Henkel A, Schmachtel S, Soennichsen C. 2012. Single unlabeled protein detection on individual plasmonic nanoparticles. *Nano Lett.* 12:1092–95
18. Saha K, Agasti SS, Kim C, Li X, Rotello VM. 2012. Gold nanoparticles in chemical and biological sensing. *Chem. Rev.* 112:2739–79
19. Leuvering JHW, Thal P, Vanderwaart M, Schuurs A. 1981. A sol particle agglutination assay for human chorionic gonadotropin. *J. Immunol. Methods* 45:183–94
20. Taton TA, Mirkin CA, Letsinger RL. 2000. Scanometric DNA array detection with nanoparticle probes. *Science* 289:1757–60
21. Zhao W, Chiuman W, Lam JCF, McManus SA, Chen W, et al. 2008. DNA aptamer folding on gold nanoparticles: from colloid chemistry to biosensors. *J. Am. Chem. Soc.* 130:3610–18
22. Beqa L, Singh AK, Khan SA, Senapati D, Arumugam SR, Ray PC. 2011. Gold nanoparticle–based simple colorimetric and ultrasensitive dynamic light scattering assay for the selective detection of Pb(II) from paints, plastics, and water samples. *Am. Chem. Soc. Appl. Mater. Interfaces* 3:668–73
23. Aldeanueva-Potel P, Correa-Duarte MA, Álvarez-Puebla RA, Liz-Marzán LM. 2010. Free-standing carbon nanotube films as optical accumulators for multiplex SERRS attomolar detection. *Am. Chem. Soc. Appl. Mater. Interfaces* 2:19–22
24. Álvarez-Puebla RA, Agarwal A, Manna P, Khanal BP, Aldeanueva-Potel P, et al. 2011. Gold nanorods 3D supercrystals as surface enhanced Raman scattering spectroscopy substrates for the rapid detection of scrambled prions. *Proc. Natl. Acad. Sci. USA* 108:8157–61
25. Song J, Zhou J, Duan H. 2012. Self-assembled plasmonic vesicles of SERS-encoded amphiphilic gold nanoparticles for cancer cell targeting and traceable intracellular drug delivery. *J. Am. Chem. Soc.* 134:13458–69

26. Tsoutsi D, Montenegro JM, Dommershausen F, Koert U, Liz-Marzán LM, et al. 2011. Quantitative surface-enhanced Raman ultradetection of atomic inorganic ions: the case of chloride. *Am. Chem. Soc. Nano* 5:7539–46
27. Boyer D, Tamarat P, Maali A, Lounis B, Orrit M. 2002. Photothermal imaging of nanometer-sized metal particles among scatterers. *Science* 297:1160–63
28. Lasne D, Blab GA, Berciaud S, Heine M, Groc L, et al. 2006. Single nanoparticle photothermal tracking (SNaPT) of 5-nm gold beads in live cells. *Biophys. J.* 91:4598–604
29. Dreaden EC, Alkilany AM, Huang X, Murphy CJ, El-Sayed MA. 2012. The golden age: gold nanoparticles for biomedicine. *Chem. Soc. Rev.* 41:2740–79
30. Ku G, Zhou M, Song S, Huang Q, Hazle J, Li C. 2012. Copper sulfide nanoparticles as a new class of photoacoustic contrast agent for deep tissue imaging at 1,064 nm. *Am. Chem. Soc. Nano* 6:7489–96
31. Michalet X, Pinaud FF, Bentolila LA, Tsay JM, Doose S, et al. 2005. Quantum dots for live cells, in vivo imaging, and diagnostics. *Science* 307:538–44
32. Jamieson T, Bakhshi R, Petrova D, Pocock R, Imani M, Seifalian AM. 2007. Biological applications of quantum dots. *Biomaterials* 28:4717–32
33. Erogbogbo F, Yong K-T, Roy I, Xu G, Prasad PN, Swihart MT. 2008. Biocompatible luminescent silicon quantum dots for imaging of cancer cells. *Am. Chem. Soc. Nano* 2:873–78
34. Erogbogbo F, Chang C-W, May JL, Liu L, Kumar R, et al. 2012. Bioconjugation of luminescent silicon quantum dots to gadolinium ions for bioimaging applications. *Nanoscale* 4:5483–89
35. Fowley C, McCaughan B, Devlin A, Yildiz I, Raymo FM, Callan JF. 2012. Highly luminescent biocompatible carbon quantum dots by encapsulation with an amphiphilic polymer. *Chem. Commun.* 48:9361–63
36. Dong Y, Wang R, Li G, Chen C, Chi Y, Chen G. 2012. Polyamine-functionalized carbon quantum dots as fluorescent probes for selective and sensitive detection of copper ions. *Anal. Chem.* 84:6220–24
37. Lin CAJ, Yang TY, Lee CH, Huang SH, Sperling RA, et al. 2009. Synthesis, characterization, and bioconjugation of fluorescent gold nanoclusters toward biological labeling applications. *Am. Chem. Soc. Nano* 3:395–401
38. Huang S, Pfeiffer C, Hollmann J, Friede S, Chen JJ-C, et al. 2012. Synthesis and characterization of colloidal fluorescent silver nanoclusters. *Langmuir* 28:8915–19
39. Hilderbrand SA, Shao F, Salthouse C, Mahmood U, Weissleder R. 2009. Upconverting luminescent nanomaterials: application to in vivo bioimaging. *Chem. Commun.* 2009:4188–90
40. Wang F, Banerjee D, Liu Y, Chen X, Liu X. 2010. Upconversion nanoparticles in biological labeling, imaging, and therapy. *Analyst* 135:1839–54
41. Hwang DW, Ko HY, Kim S-K, Kim D, Lee DS, Kim S. 2009. Development of a quadruple imaging modality by using nanoparticles. *Chem. Eur. J.* 15:9387–93
42. Park EJ, Brasuel M, Behrend C, Philbert MA, Kopelman R. 2003. Ratiometric optical PEBBLE nanosensors for real-time magnesium ion concentrations inside viable cells. *Anal. Chem.* 75:3784–91
43. Giri S, Sykes EA, Jennings TL, Chan WCW. 2011. Rapid screening of genetic biomarkers of infectious agents using quantum dot barcodes. *Am. Chem. Soc. Nano* 5:1580–87
44. del Mercato LL, Abbasi AZ, Ochs M, Parak WJ. 2011. Multiplexed sensing of ions with barcoded polyelectrolyte capsules. *Am. Chem. Soc. Nano* 5:9668–74
45. del Mercato LL, Abbasi AZ, Parak WJ. 2011. Synthesis and characterization of ratiometric ion-sensitive polyelectrolyte capsules. *Small* 7:351–63
46. Lowe SB, Dick JAG, Cohen BE, Stevens MM. 2012. Multiplex sensing of protease and kinase enzyme activity via orthogonal coupling of quantum dot–peptide conjugates. *Am. Chem. Soc. Nano* 6:851–57
47. Marin MJ, Galindo F, Thomas P, Russell DA. 2012. Localized intracellular pH measurement using a ratiometric photoinduced electron-transfer-based nanosensor. *Angew. Chem. Int. Ed.*51:9657–61
48. Algar WR, Wegner D, Huston AL, Blanco-Canosa JB, Stewart MH, et al. 2012. Quantum dots as simultaneous acceptors and donors in time-gated Förster resonance energy transfer relays: characterization and biosensing. *J. Am. Chem. Soc.* 134:1876–91
49. Freeman R, Liu X, Willner I. 2011. Chemiluminescent and chemiluminescence resonance energy transfer (CRET) detection of DNA, metal ions, and aptamer–substrate complexes using Hemin/G-quadruplexes and CdSe/ZnS quantum dots. *J. Am. Chem. Soc.* 133:11597–604

50. Xia Z, Xing Y, So MK, Koh AL, Sinclair R, Rao J. 2008. Multiplex detection of protease activity with quantum dot nanosensors prepared by intein-mediated specific bioconjugation. *Anal Chem* 80:8649–55
51. Maltez–da Costa M, de la Escosura-Muñiz A, Nogués C, Barrios L, Ibáñez E, Merkoçi A. 2012. Simple monitoring of cancer cells using nanoparticles. *Nano Lett.* 12:4164–71
52. Yáñez-Sedeño P, Pingarrón JM, Riu J, Rius FX. 2010. Electrochemical sensing based on carbon nanotubes. *Trends Anal. Chem.* 29:939–53
53. Luo X, Morrin A, Killard AJ, Smyth MR. 2006. Application of nanoparticles in electrochemical sensors and biosensors. *Electroanalysis* 18:319–26
54. Xu J-J, Luo X-L, Du Y, Chen H-Y. 2004. Application of $MnO_2$ nanoparticles as an eliminator of ascorbate interference to amperometric glucose biosensors. *Electrochem. Commun.* 6:1169–73
55. Khalid W, Helou ME, Murböck T, Yue Z, Montenegro J-M, et al. 2011. Immobilization of quantum dots via conjugated self-assembled monolayers and their application as a light-controlled sensor for the detection of hydrogen peroxide. *Am. Chem. Soc. Nano* 5:9870–76
56. Ko JW, Woo J-M, Jinhong A, Cheon JH, Lim JH, et al. 2011. Multi-order dynamic range DNA sensor using a gold decorated SWCNT random network. *Am. Chem. Soc. Nano* 5:4365–72
57. Stoll C, Kudera S, Parak WJ, Lisdat F. 2006. Quantum dots on gold:electrodes for photoswitchable cytochrome *c* electrochemistry. *Small* 2:741–43
58. Katz E, Zayats M, Willner I, Lisdat F. 2006. Controlling the direction of photocurrents by means of CdS nanoparticles and cytochrome *c*–mediated biocatalytic cascades. *Chem. Commun.* 2006:1395–97
59. Hočevar SB, Wang J, Deo RP, Musameh M, Ogorevc B. 2005. Carbon nanotube modified microelectrode for enhanced voltammetric detection of dopamine in the presence of ascorbate. *Electroanalysis* 17:417–22
60. Liu B, Zhang B, Cui Y, Chen H, Gao Z, Tang D. 2011. Multifunctional gold-silica nanostructures for ultrasensitive electrochemical immunoassay of streptomycin residues. *Am. Chem. Soc. Appl. Mater. Interfaces*3:4668–76
61. Zelada-Guillén GA, Sebastián-Avila JL, Blondeau P, Riu J, Rius FX. 2012. Label-free detection of *Staphylococcus aureus* in skin using real-time potentiometric biosensors based on carbon nanotubes and aptamers. *Biosens. Bioelectron.* 31:226–32
62. Zhang J, Song S, Zhang L, Wang L, Wu H, et al. 2006. Sequence-specific detection of femtomolar DNA via a chronocoulometric DNA sensor (CDS): effects of nanoparticle-mediated amplification and nanoscale control of DNA assembly at electrodes. *J. Am. Chem. Soc.* 128:8575–80
63. Wang J. 2005. Nanomaterial-based electrochemical biosensors. *Analyst* 130:421–26
64. Willner I, Willner B, Tel-Vered R. 2011. Electroanalytical applications of metallic nanoparticles and supramolecular nanostructures. *Electroanalysis* 23:13–28
65. Hiep HM, Endo T, Saito M, Chikae M, Kim DK, et al. 2008. Label-free detection of melittin binding to a membrane using electrochemical-localized surface plasmon resonance. *Anal. Chem.* 80:1859–64
66. Khalid W, Göbel G, Hühn D, Montenegro JM, Rivera Gil P, et al. 2011. Light triggered detection of aminophenyl phosphate with a quantum dot based enzyme electrode. *J. Nanobiotechnol.* 9:46
67. Pankhurst QA, Connolly J, Jones SK, Dobson J. 2003. Applications of magnetic nanoparticles in biomedicine. *J. Phys. D* 36:R167–81
68. Colombo M, Carregal-Romero S, Casula MF, Gutiérrez L, Morales MP, et al. 2012. Biological applications of magnetic nanoparticles. *Chem. Soc. Rev.* 41:4306–34
69. Moros M, Pelaz B, López-Larrubia P, García-Martin ML, Grazú V, de la Fuente JM. 2010. Engineering biofunctional magnetic nanoparticles for biotechnological applications. *Nanoscale* 2:1746–55
70. Alcantara D, Guo Y, Yuan H, Goergen CJ, Chen HH, et al. 2012. Fluorochrome-functionalized magnetic nanoparticles for high-sensitivity monitoring of the polymerase chain reaction by magnetic resonance. *Angew. Chem. Int. Ed.* 51:6904–7
71. Koh I, Josephson L. 2009. Magnetic nanoparticle sensors. *Sensors* 9:8130–45
72. Hathaway HJ, Butler KS, Adolphi NL, Lovato DM, Belfon R, et al. 2011. Detection of breast cancer cells using targeted magnetic nanoparticles and ultra-sensitive magnetic field sensors. *Breast Cancer Res.* 13:R108
73. Gaster RS, Xu L, Han S-J, Wilson RJ, Hall DA, et al. 2011. Quantification of protein interactions and solution transport using high-density GMR sensor arrays. *Nat. Nanotechnol.* 6:314–20

74. Perez JM, Josephson L, O'Loughlin T, Högemann D, Weissleder R. 2002. Magnetic relaxation switches capable of sensing molecular interactions. *Nat. Biotechnol.* 20:816–20
75. Wang Y, Fang F, Shi C, Zhang X, Liu L, et al. 2012. Evaluation of a method for the simultaneous detection of multiple tumor markers using a multiplex suspension bead array. *Clin. Biochem.* 45:1394–98
76. Rivera-Gil P, Jimenez de Aberasturi D, Wulf V, Pelaz B, del Pino P, et al. 2012. The challenge to relate the physicochemical properties of colloidal nanoparticles to their cytotoxicity. *Acc. Chem. Res.* In press. doi:10.1021/ar300039j
77. Abbasi AZ, Amin F, Niebling T, Friede S, Ochs M, et al. 2011. How colloidal nanoparticles could facilitate multiplexed measurements of different analytes with analyte-sensitive organic fluorophores. *Am. Chem. Soc. Nano* 5:21–25
78. Zhang F, Ali Z, Amin F, Feltz A, Oheim M, Parak WJ. 2010. Ion and pH sensing with colloidal nanoparticles: influence of surface charge on sensing and colloidal properties. *ChemPhysChem* 11:730–35
79. Riedinger A, Zhang F, Dommershausen F, Röcker C, Brandholt S, et al. 2010. Ratiometric optical sensing of chloride ions with organic fluorophore–gold nanoparticle hybrids: a systematic study of distance dependency and the influence of surface charge. *Small* 6:2590–97
80. Zhang F, Lees E, Amin F, Rivera-Gil P, Yang F, et al. 2011. Polymer-coated nanoparticles: a universal tool for biolabelling experiments. *Small* 7:3113–27
81. Cedervall T, Lynch I, Lindman S, Berggård T, Thulin E, et al. 2007. Understanding the nanoparticle–protein corona using methods to quantify exchange rates and affinities of proteins for nanoparticles. *Proc. Natl. Acad. Sci. USA* 104:2050–55
82. Jiang X, Weise S, Hafner M, Röcker C, Zhang F, et al. 2010. Quantitative analysis of the protein corona on FePt nanoparticles formed by transferrin binding. *J. R. Soc. Interface* 7:S5–13
83. Amin F, Yushchenko DA, Montenegro JM, Parak WJ. 2012. Integration of organic fluorophores in the surface of polymer-coated colloidal nanoparticles for sensing the local polarity of the environment. *ChemPhysChem* 13:1030–35
84. Freeman R, Finder T, Willner I. 2009. Multiplexed analysis of $Hg^{2+}$ and $Ag^{+}$ ions by nucleic acid functionalized CdSe/ZnS quantum dots and their use for logic gate operations. *Angew. Chem. Int. Ed.* 48:7818–21
85. Jin R, Cao Y, Mirkin CA, Kelly KL, Schatz GC, Zheng JG. 2001. Photoinduced conversion of silver nanospheres to nanoprisms. *Science* 294:1901–3
86. Yu C, Irudayaraj J. 2007. Multiplex biosensor using gold nanorods. *Anal. Chem.* 79:572–79
87. Yu C, Nakshatri H, Irudayaraj J. 2007. Identity profiling of cell surface markers by multiplex gold nanorod probes. *Nano Lett.* 7:2300–6
88. Wang C, Irudayaraj J. 2008. Gold nanorod probes for the detection of multiple pathogens. *Small* 4:2204–8
89. Fernández-López C, Mateo-Mateo C, Álvarez-Puebla RA, Pérez-Juste J, Pastoriza-Santos I, Liz-Marzán LM. 2009. Highly controlled silica coating of PEG-capped metal nanoparticles and preparation of SERS-encoded particles. *Langmuir* 25:13894–99
90. Abalde-Cela S, Aldeanueva-Potel P, Mateo-Mateo C, Rodríguez-Lorenzo L, Álvarez-Puebla RA, Liz-Marzán LM. 2010. Surface-enhanced Raman scattering biomedical applications of plasmonic colloidal particles. *J. R. Soc. Interface* 7:S435–50
91. Raez J, Blais DR, Zhang Y, Álvarez-Puebla RA, Bravo-Vasquez JP, et al. 2007. Spectroscopically encoded microspheres for antigen biosensing. *Langmuir* 23:6482–85
92. Sanles-Sobrido M, Exner W, Rodríguez-Lorenzo L, Rodríguez-Gonzalez B, Correa-Duarte MA, et al. 2009. Design of SERS-encoded, submicron, hollow particles through confined growth of encapsulated metal nanoparticles. *J. Am. Chem. Soc.* 131:2699–705
93. Kim K, Lee YM, Lee HB, Shin KS. 2009. Silver-coated silica beads applicable as core materials of dual-tagging sensors operating via SERS and MEF. *Am. Chem. Soc. Appl. Mater. Interfaces* 1:2174–80
94. Maiti KK, Dinish US, Samanta A, Vendrell M, Soh K-S, et al. 2012. Multiplex targeted in vivo cancer detection using sensitive near-infrared SERS nanotags. *Nano Today* 7:85–93
95. Sanchez-Iglesias A, Aldeanueva-Potel P, Ni WH, Pérez-Juste J, Pastoriza-Santos I, et al. 2010. Chemical seeded growth of Ag nanoparticle arrays and their application as reproducible SERS substrates. *Nano Today* 5:21–27

96. Jiang ZY, Jiang XX, Su S, Wei XP, Lee ST, He Y. 2012. Silicon-based reproducible and active surface-enhanced Raman scattering substrates for sensitive, specific, and multiplex DNA detection. *Appl. Phys. Lett.* 100:203104
97. Kang T, Yoo SM, Yoon I, Lee SY, Kim B. 2010. Patterned multiplex pathogen DNA detection by Au particle–on–wire SERS sensor. *Nano Lett.* 10:1189–93
98. Wang Z, Zong S, Li W, Wang C, Xu S, et al. 2012. SERS-fluorescence joint spectral encoding using organic-metal-QD hybrid nanoparticles with a huge encoding capacity for high-throughput biodetection: putting theory into practice. *J. Am. Chem. Soc.* 134:2993–3000
99. Nagl S, Wolfbeis OS. 2007. Optical multiple chemical sensing: status and current challenges. *Analyst* 132:507–11
100. Grabolle M, Kapusta P, Nann T, Shu X, Ziegler J, Resch-Genger U. 2009. Fluorescence lifetime multiplexing with nanocrystals and organic labels. *Anal. Chem.* 81:7807–13
101. Ruedas-Rama MJ, Orte A, Hall EAH, Alvarez-Pez JM, Talavera EM. 2011. Quantum dot photoluminescence lifetime–based pH nanosensor. *Chem. Commun.* 47:2898–900
102. Peng X, Yang Z, Wang J, Fan J, He Y, et al. 2011. Fluorescence ratiometry and fluorescence lifetime imaging: using a single molecular sensor for dual mode imaging of cellular viscosity. *J. Am. Chem. Soc.* 133:6626–35
103. Kim J-H, Patra CR, Arkalgud JR, Boghossian AA, Zhang J, et al. 2011. Single-molecule detection of $H_2O_2$ mediating angiogenic redox signaling on fluorescent single-walled carbon nanotube array. *Am. Chem. Soc. Nano* 5:7848–57
104. Geissler D, Charbonnière L, Ziessel R, Butlin N, Löhmannsröben HG, Hildebrandt N. 2010. Quantum dot biosensors for ultrasensitive multiplexed diagnostics. *Angew. Chem. Int. Ed.* 49:1396–401
105. Freeman R, Liu X, Willner I. 2011. Amplified multiplexed analysis of DNA by the exonuclease III–catalyzed regeneration of the target DNA in the presence of functionalized semiconductor quantum dots. *Nano Lett.* 11:4456–61
106. Haun JB, Devaraj NK, Marinelli BS, Lee H, Weissleder R. 2012. Probing intracellular biomarkers and mediators of cell activation using nanosensors and bioorthogonal chemistry. *Am. Chem. Soc. Nano* 5:3204–13
107. Peterson VM, Castro CM, Lee H, Weissleder R. 2012. Orthogonal amplification of nanoparticles for improved diagnostic sensing. *Am. Chem. Soc. Nano* 6:3506–13
108. Shipway AN, Katz E, Willner I. 2000. Nanoparticle arrays on surfaces for electronic, optical, and sensor applications. *ChemPhysChem* 1:18–52
109. Katz E, Willner I. 2004. Integrated nanoparticle-biomolecule hybrid systems: synthesis, properties, and applications. *Angew. Chem. Int. Ed.* 43:6042–108
110. Ferguson JA, Steemers FJ, Walt DR. 2000. High-density fiber-optic DNA random microsphere array. *Anal. Chem.* 72:5618–24
111. Pregibon DC, Toner M, Doyle PS. 2007. Multifunctional encoded particles for high-throughput biomolecule analysis. *Science* 315:1393–96
112. Zamborini FP, Bao L, Dasari R. 2012. Nanoparticles in measurement science. *Anal. Chem.* 84:541–76
113. Mayer KM, Hafner JH. 2011. Localized surface plasmon resonance sensors. *Chem. Rev.* 111:3828–57
114. He S, Liu K-K, Su S, Yan J, Mao X, et al. 2012. Graphene-based high-efficiency surface-enhanced Raman scattering–active platform for sensitive and multiplex DNA detection. *Anal. Chem.* 84:4622–27
115. Endo T, Kerman K, Nagatani N, Hiepa HM, Kim D-K, et al. 2006. Multiple label-free detection of antigen–antibody reaction using localized surface plasmon resonance–based core-shell structured nanoparticle layer nanochip. *Anal. Chem.* 78:6465–75
116. Kim D, Daniel WL, Mirkin CA. 2009. Microarray-based multiplexed scanometric immunoassay for protein cancer markers using gold nanoparticle probes. *Anal. Chem.* 81:9183–87
117. Stoeva SI, Lee J-S, Smith JE, Rosen ST, Mirkin CA. 2006. Multiplexed detection of protein cancer markers with biobarcoded nanoparticle probes. *J. Am. Chem. Soc.* 128:8378–79
118. Kim D-K, Yoo S-M, Park T-J, Yoshikawa H, Tamiya E-I, et al. 2011. Plasmonic properties of the multispot copper-capped nanoparticle array chip and its application to optical biosensors for pathogen detection of multiplex DNAs. *Anal. Chem.* 83:6215–22

119. Chen S, Svedendahl M, Van Duyne RP, Kaell M. 2011. Plasmon-enhanced colorimetric ELISA with single molecule sensitivity. *Nano Lett.* 11:1826–30
120. Skladal P. 1997. Advances in electrochemical immunosensors. *Electroanalysis* 9:737–45
121. Wilson MS, Nie W. 2006. Electrochemical multianalyte immunoassays using an array-based sensor. *Anal. Chem.* 78:2507–13
122. Akter R, Rahman MA, Rhee CK. 2012. Amplified electrochemical detection of a cancer biomarker by enhanced precipitation using horseradish peroxidase attached on carbon nanotubes. *Anal. Chem.* 84:6407–15
123. Lai G, Yan F, Wu J, Leng C, Ju H. 2011. Ultrasensitive multiplexed immunoassay with electrochemical stripping analysis of silver nanoparticles catalytically deposited by gold nanoparticles and enzymatic reaction. *Anal. Chem.* 83:2726–32
124. Mani V, Chikkaveeraiah BV, Patel V, Gutkind JS, Rusling JF. 2009. Ultrasensitive immunosensor for cancer biomarker proteins using gold nanoparticle film electrodes and multienzyme–particle amplification. *Am. Chem. Soc. Nano* 3:585–94
125. Malhotra R, Patel V, Chikkaveeraiah BV, Munge BS, Cheong SC, et al. 2012. Ultrasensitive detection of cancer biomarkers in the clinic by use of a nanostructured microfluidic array. *Anal. Chem.* 84:6249–55
126. Chikkaveeraiah BV, Bhirde A, Malhotra R, Patel V, Gutkind JS, Rusling James F. 2009. Single-wall carbon nanotube forest arrays for immunoelectrochemical measurement of four protein biomarkers for prostate cancer. *Anal. Chem.* 81:9129–34
127. Zarei H, Ghourchian H, Eskandari K, Zeinali M. 2012. Magnetic nanocomposite of anti-human IgG/COOH-multiwalled carbon nanotubes/$Fe_3O_4$ as a platform for electrochemical immunoassay. *Anal. Biochem.* 421:446–53
128. George M, Parak WJ, Gaub HE. 2000. Highly integrated surface potential sensors. *Sens. Actuators B* 69:266–75
129. Hafeman DG, Parce JW, McConnell HM. 1988. Light-addressable potentiometric sensor for biochemical systems. *Science* 240:1182–85
130. Lundström I, Erlandsson R, Frykman U, Hedborg E, Spetz A, et al. 1991. Artificial "olfactory" images from a chemical sensor using a light-pulse technique. *Nature* 352:47–50
131. Parak WJ, Hofmann UG, Gaub HE, Owicki JC. 1997. Lateral resolution of light addressable potentiometric sensors: an experimental and theoretical investigation. *Sens. Actuators A* 63:47–57
132. Tanne J, Schafer D, Khalid W, Parak WJ, Lisdat F. 2011. Light-controlled bioelectrochemical sensor based on CdSe/ZnS quantum dots. *Anal. Chem.* 83:7778–85
133. Schubert K, Khalid W, Yue Z, Parak WJ, Lisdat F. 2010. Quantum dot–modified electrode for the detection of NAD-dependent dehydrogenase reactions. *Langmuir* 26:1395–400
134. Li Y, Srinivasan B, Jing Y, Yao X, Hugger MA, et al. 2010. Nanomagnetic competition assay for low-abundance protein biomarker quantification in unprocessed human sera. *J. Am. Chem. Soc.* 132:4388–92
135. Mak AC, Osterfeld SJ, Yu H, Wang SX, Davis RW, et al. 2010. Sensitive giant magnetoresistive–based immunoassay for multiplex mycotoxin detection. *Biosens. Bioelectron.* 25:1635–39
136. Osterfeld SJ, Yu H, Gaster RS, Caramuta S, Xu L, et al. 2008. Multiplex protein assay based on real-time magnetic nanotag sensing. *Proc. Natl. Acad. Sci. USA* 105:20637–40
137. Hall DA, Gaster RS, Osterfeld SJ, Murmann B, Wang SX. 2010. GMR biosensor arrays: Correction techniques for reproducibility and enhanced sensitivity. *Biosens. Bioelectron.* 25:2177–81
138. Hall DA, Gaster RS, Osterfeld SJ, Murmann B, Wang SX. 2011. GMR biosensor arrays: correction techniques for reproducibility and enhanced sensitivity. *Biosens. Bioelectron.* 25:2177–81
139. Zong C, Wu J, Wang C, Ju H, Yan F. 2012. Chemiluminescence imaging immunoassay of multiple tumor markers for cancer screening. *Anal. Chem.* 84:2410–15
140. Pei H, Li J, Lv M, Wang J, Gao J, et al. 2012. A graphene-based sensor array for high-precision and adaptive target identification with ensemble aptamers. *J. Am. Chem. Soc.* 134:13843–49
141. He X, Wang K, Cheng Z. 2010. In vivo near-infrared fluorescence imaging of cancer with nanoparticle-based probes. *Wiley Interdiscip. Rev. Nanomed. Nanobiotechnol.* 2:349–66
142. Rivera-Gil P, Parak WJ. 2008. Composite nanoparticles take aim at cancer. *Am. Chem. Soc. Nano* 2:2200–5

143. Peteiro-Cartelle J, Rodríguez-Pedreira M, Zhang F, Rivera-Gil P, del Mercato LL, Parak WJ. 2009. One example on how colloidal nano- and microparticles could contribute to medicine. *Nanomedicine* 4:967–79
144. Weissleder R, Moore A, Mahmood U, Bhorade R, Benveniste H, et al. 2000. In vivo magnetic resonance imaging of transgene expression. *Nat. Med.* 6:351–55
145. Alexiou C, Arnold W, Hulin P, Klein RJ, Renz H, et al. 2001. Magnetic mitoxantrone nanoparticle detection by histology, X-ray and MRI after magnetic tumor targeting. *J. Magn. Magn. Mater.* 225:187–93
146. Morales MP, Bomati-Miguel O, de Alejo RP, Ruiz-Cabello J, Veintemillas-Verdaguer S, O'Grady K. 2003. Contrast agents for MRI based on iron oxide nanoparticles prepared by laser pyrolysis. *J. Magn. Magn. Mater.* 266:102–9
147. Harisinghani MG, Barentsz J, Hahn PF, Deserno WM, Tabatabaei S, et al. 2003. Noninvasive detection of clinically occult lymph-node metastases in prostate cancer. *N. Engl. J. Med.* 348:2491–99
148. Wang C, Gao X, Su XG. 2010. In vitro and in vivo imaging with quantum dots. *Anal. Bioanal. Chem.* 397:1397–415
149. Cheon J, Lee J-H. 2008. Synergistically integrated nanoparticles as multimodal probes for nanobiotechnology. *Acc. Chem. Res.* 41:1630–40
150. Liong M, Lu J, Kovochich M, Xia T, Ruehm SG, et al. 2008. Multifunctional inorganic nanoparticles for imaging, targeting, and drug delivery. *Am. Chem. Soc. Nano* 2:889–96
151. Nahrendorf M, Zhang HW, Hembrador S, Panizzi P, Sosnovik DE, et al. 2008. Nanoparticle PET-CT imaging of macrophages in inflammatory atherosclerosis. *Circulation* 117:379–87
152. Altınoğlu EI, Russin TJ, Kaiser JM, Barth BM, Eklund BC, et al. 2008. Near-infrared emitting fluorophore–doped calcium phosphate nanoparticles for in vivo imaging of human breast cancer. *Am. Chem. Soc. Nano* 2:2075–84
153. Kumar R, Roy I, Ohulchanskky TY, Vathy LA, Bergey EJ, et al. 2010. In vivo biodistribution and clearance studies using multimodal organically modified silica nanoparticles. *Am. Chem. Soc. Nano* 4:699–708
154. Lipka M, Semmler-Behnke M, Sperling RA, Wenk A, Takenaka S, et al. 2010. Biodistribution of PEG-modified gold nanoparticles following intratracheal instillation and intravenous injection. *Biomaterials* 31:6574–81
155. Ali Z, Abbasi AZ, Zhang F, Arosio P, Lascialfari A, et al. 2011. Multifunctional nanoparticles for dual imaging. *Anal. Chem.* 83:2877–82
156. Sperling RA, Pellegrino T, Li JK, Chang WH, Parak WJ. 2006. Electrophoretic separation of nanoparticles with a discrete number of functional groups. *Adv. Funct. Mater.* 16:943–48
157. Fernández-Argüelles MT, Yakovlev A, Sperling RA, Luccardini C, Gaillard S, et al. 2007. Synthesis and characterization of polymer-coated quantum dots with integrated acceptor dyes as FRET-based nanoprobes. *Nano Lett.* 7:2613–17
158. Corato RD, Quarta A, Piacenza P, Ragusa A, Figuerola A, et al. 2008. Water solubilization of hydrophobic nanocrystals by means of poly(maleic anhydride-*alt*-1-octadecene). *J. Mater. Chem.* 18:1991–96
159. Sperling RA, Liedl T, Duhr S, Kudera S, Zanella M, et al. 2007. Size determination of (bio-)conjugated water-soluble colloidal nanoparticles—a comparison of different techniques. *J. Phys. Chem. C* 111:11552–59
160. Geidel C, Schmachtel S, Riedinger A, Pfeiffer C, Müllen K, et al. 2011. A general synthetic approach for obtaining cationic and anionic inorganic nanoparticles via encapsulation in amphiphilic copolymers. *Small* 7:2929–34
161. Lehmann AD, Parak WJ, Zhang F, Ali Z, Röcker C, et al. 2010. Fluorescent-magnetic hybrid nanoparticles induce a dose-dependent increase in proinflammatory response in lung cells in vitro correlated with intracellular localization. *Small* 6:753–62
162. Lin C-AJ, Sperling RA, Li JK, Yang T-Y, Li P-Y, et al. 2008. Design of an amphiphilic polymer for nanoparticle coating and functionalization. *Small* 4:334–41
163. Cui Y, Zheng XS, Ren B, Wang R, Zhang J, et al. 2011. Au@organosilica multifunctional nanoparticles for the multimodal imaging. *Chem. Sci.* 2:1463–69

164. McQueenie R, Stevenson R, Benson R, MacRitchie N, McInnes I, et al. 2012. Detection of inflammation in vivo by surface-enhanced Raman scattering provides higher sensitivity than conventional fluorescence imaging. *Anal. Chem.* 84:5968–75
165. Stone N, Kerssens M, Lloyd GR, Faulds K, Graham D, Matousek P. 2011. Surface enhanced spatially offset Raman spectroscopic (SESORS) imaging—the next dimension. *Chem. Sci.* 2:776–80
166. Guerrero-Martinez A, Pérez-Juste J, Liz-Marzán LM. 2012. Recent progress on silica coating of nanoparticles and related nanomaterials. *Adv. Mater.* 22:1182–95
167. Ma M, Chen H, Chen Y, Wang X, Chen F, et al. 2012. Au capped magnetic core/mesoporous silica shell nanoparticles for combined photothermo-/chemo-therapy and multimodal imaging. *Biomaterials* 33:989–98
168. Hwang DW, Ko HY, Lee JH, Kang H, Ryu SH, et al. 2012. A nucleolin-targeted multimodal nanoparticle imaging probe for tracking cancer cells using an aptamer. *J. Nucl. Med.* 51:98–105
169. Wang F, Deng R, Wang J, Wang Q, Han Y, et al. 2011. Tuning upconversion through energy migration in core-shell nanoparticles. *Nat. Mater.* 10:968–73
170. Xia A, Chen M, Gao Y, Wu D, Feng W, Li F. 2012. $Gd^{3+}$ complex-modified $NaLuF_4$-based upconversion nanophosphors for trimodality imaging of NIR-to-NIR upconversion luminescence, X-ray computed tomography and magnetic resonance. *Biomaterials* 33:5394–405
171. Xing H, Bu W, Zhang S, Zheng X, Li M, et al. 2012. Multifunctional nanoprobes for upconversion fluorescence, MR and CT trimodal imaging. *Biomaterials* 33:1079–89
172. Jin Y, Jia C, Huang S-W, O'Donnell M, Gao X. 2010. Multifunctional nanoparticles as coupled contrast agents. *Nat. Commun.* 1:41
173. Abbasi AZ, Gutierrez L, del Mercato LL, Herranz F, Chubykalo-Fesenko O, et al. 2011. Magnetic capsules for NMR imaging: effect of magnetic nanoparticles spatial distribution and aggregation. *J. Phys. Chem. C* 115:6257–64
174. Johnston APR, Kamphuis MMJ, Such GK, Scott AM, Nice EC, et al. 2012. Targeting cancer cells: controlling the binding and internalization of antibody-functionalized capsules. *Am. Chem. Soc. Nano* 6:6667–74
175. Kondrashina AV, Dmitriev RI, Borisov SM, Klimant I, O'Brien I, et al. 2012. A phosphorescent nanoparticle–based probe for sensing and imaging of (intra)cellular oxygen in multiple detection modalities. *Adv. Func. Mater.* In press
176. Fercher A, Borisov SM, Zhdanov AV, Klimant I, Papkovsky DB. 2011. Intracellular $O_2$ sensing probe based on cell-penetrating phosphorescent nanoparticles. *Am. Chem. Soc. Nano* 5:5499–508
177. Si D, Epstein T, Lee Y-EK, Kopelman R. 2012. Nanoparticle PEBBLE sensors for quantitative nanomolar imaging of intracellular free calcium ions. *Anal. Chem.* 84:978–86
178. Vetrone F, Naccache R, Zamarrón A, Juarranz de la Fuente A, Sanz-Rodríguez F, et al. 2010. Temperature sensing using fluorescent nanothermometers. *Am. Chem. Soc. Nano* 4:3254–58
179. Dong B, Cao B, He Y, Liu Z, Li Z, Feng Z. 2012. Temperature sensing and in vivo imaging by molybdenum sensitized visible upconversion luminescence of rare-earth oxides. *Adv. Mater.* 24:1987–93
180. Carregal-Romero S, Ochs M, Parak WJ. 2012. Nanoparticle-functionalized microcapsules for in vitro delivery and sensing. *Nanophotonics* 1:171–80
181. Rivera-Gil P, Nazarenus M, Ashraf S, Parak WJ. 2012. pH Sensitive capsules as intracellular optical reporters for monitoring lysosomal pH changes upon stimulation. *Small* 8:943–48
182. Yang KS, Budin G, Reiner T, Vinegoni C, Weissleder R. 2012. Bioorthogonal imaging of aurora kinase A in live cells. *Angew. Chem. Int. Ed.* 51:6598–603
183. Pelaz B, Jaber S, Jimenez de Aberasturi D, Wulf V, de la Fuente JM, et al. 2012. The state of nanoparticle-based nanoscience and biotechnology: progress, promises, and challenges. *Am. Chem. Soc. Nano.* 6:8468–83

JOURNAL OF THE ROYAL SOCIETY Interface

rsif.royalsocietypublishing.org

Review

**Cite this article:** Pfeiffer C, Rehbock C, Hühn D, Carrillo C, de Aberasturi DJ, Merk V, Barcikowski S, Parak WJ. 2014 Interaction of colloidal nanoparticles with their local environment: the (ionic) nanoenvironment around nanoparticles is different from bulk and determines the physico-chemical properties of the nanoparticles. *J. R. Soc. Interface* 20130931.
http://dx.doi.org/10.1098/rsif.2013.0931

Received: 11 October 2013
Accepted: 27 November 2013

**Subject Areas:**
nanotechnology

**Keywords:**
colloids, screening, ion distribution

**Authors for correspondence:**
Stephan Barcikowski
e-mail: stephan.barcikowski@uni-due.de
Wolfgang J. Parak
e-mail: wolfgang.parak@physik.uni-marburg.de

†These authors contributed equally to this study.

Royal Society Publishing

# Interaction of colloidal nanoparticles with their local environment: the (ionic) nanoenvironment around nanoparticles is different from bulk and determines the physico-chemical properties of the nanoparticles

Christian Pfeiffer[1,†], Christoph Rehbock[2,†], Dominik Hühn[1], Carolina Carrillo[1], Dorleta Jimenez de Aberasturi[1], Vivian Merk[2], Stephan Barcikowski[2] and Wolfgang J. Parak[1]

[1]Fachbereich Physik, Philipps Universität Marburg, Marburg, Germany
[2]Center for Nanointegration Duisburg-Essen (CENIDE), University of Duisburg-Essen, Essen, Germany

The physico-chemical properties of colloidal nanoparticles (NPs) are influenced by their local environment, as, in turn, the local environment influences the physico-chemical properties of the NPs. In other words, the local environment around NPs has profound impact on the NPs, and it is different from bulk due to interaction with the NP surface. So far, this important effect has not been addressed in a comprehensive way in the literature. The vicinity of NPs can be sensitively influenced by local ions and ligands, with effects already occurring at extremely low concentrations. NPs in the Hückel regime are more sensitive against fluctuations in the ionic environment, because of a larger Debye length. The local ion concentration hereby affects the colloidal stability of the NPs, as it is different from bulk owing to Debye Hückel screening caused by the charge of the NPs. This can have subtle effects, now caused by the environment to the performance of the NP, such as for example a buffering effect caused by surface reaction on ultrapure ligand-free nanogold, a size quenching effect in the presence of specific ions and a significant impact on fluorophore-labelled NPs acting as ion sensors. Thus, the aim of this review is to clarify and give an unifying view of the complex interplay between the NP's surface with their nanoenvironment.

## 1. Introduction

The potential impact of colloidal nanoparticles (NPs) on the environment is topic of ongoing discussions [1]. The scenario of intended exposure (e.g. fertilizers [2–4], antimicrobial agents [5–7], removal of contaminants [8–10] and clinical use [11–15]), as well as unintended exposure (e.g. contamination [16] and general uptake by all types of organisms [17–20]) has been analysed in a large body of work. These studies clearly point out that in fact NPs have impact on the environment, whether intended or unintended. However, besides such global impact of NPs on their environment, in a less spectacular way they also influence the physico-chemical properties of their local environment. Likewise, the local environment impacts the physico-chemical properties of the NPs. In this way, there is a subtle interaction between the surface of NPs and their local environment, which affects the physico-chemical properties of both. Important physico-chemical parameters of NP surfaces are for example charge, and hydrophobicity [21]. They are influenced by the local environment (e.g. the surface charge of NPs may depend on the local pH), as the NPs influence themselves the local environment (e.g. accumulations of ions and proteins from bulk



[A10]1

owing to local charge and hydrophobicity patterns). In the following, this will be explained with the example of two major compounds of biological fluids: proteins and salts.

Because many proteins are charged, repulsive interaction between proteins and NPs (for like-charged NPs and proteins) or electrostatic attraction (for oppositely charged NPs and proteins) can occur [22,23]. NP surfaces may also contain local hydrophilic/hydrophobic patterns that cause protein adsorption [24,25]. This layer of adsorbed proteins to the surface of NPs has been termed protein corona [26,27]. Continuing our aforementioned argument, the formation of the protein corona (i.e. interaction between NPs and proteins [28]) affects both, the NPs, as well as their local environment. Adsorbed proteins clearly change two key parameters of NPs: their hydrodynamic diameter [29,30] and in many cases also their colloidal stability [31–33]. On the other hand, also the NPs may affect (some types of) adsorbed proteins, in particular via structural changes, which may lead to dysfunction of the proteins [34–36]. In addition, owing to local charge and hydrophobicity [37] effects associated with the NP surface, there is a higher local protein concentration present on the NP surface (the corona) than in bulk, and thus high NP concentrations can deplete bulk solutions from proteins. Adsorption of proteins to NPs can be experimentally assessed with a variety of different methods, some of which are specific to the NP nature. One example is size measurements of the NPs [38–40]. The more protein molecules are adsorbed on the NP surface, the bigger the size of each NP becomes [29,41,42]. In the case of highly colloidal stable NPs with narrow size distribution, it was shown that in solutions with only one type of protein (such as for example human bovine serum [29,43] or transferrin [30,44]) adsorbed proteins under saturation conditions form a monolayer on top of the NP surface. Often, interaction of proteins with NPs is unwanted and thus needs to be circumvented. Protein adsorption to surfaces is for example reduced by controlled pre-saturation of the surface with serum albumin, which blocks adsorption spots and thus reduces adsorption of other proteins. The PEGylation (poly(ethylene glycol), PEG) of NPs is also used as a general and effective approach to reduce non-specific binding of proteins to NPs [45].

Also interaction of salt and NPs has an effect on the NPs, as well as on the local concentration of the ions (from the dissociated salt). The surface charge of NPs plays also an important role on the stabilization of NPs. In order to prevent agglomeration by van der Waal's attraction, NPs need to be stabilized either by electrostatic or by steric repulsion [46–48]. In the case of electrostatically stabilized NPs, the NPs with likewise charged surfaces repel each other and thus are dispersed. Salt in solution screens the charge on the NP surface (basically in first order by the Debye–Hückel effect [49]), and thus typically leads to colloidal instability at high concentrations, followed by agglomeration [50–54]. While this screening effect (e.g. the effect of the local ion concentration on the colloidal stability of NPs) is reported plentifully in the literature, another consequence of the same effect is less widely reported, but not less relevant. In case, the charge on the surface of the NPs is screened by counter ions, there is a higher and lower concentration of ions with the opposite and the same sign of charge around the NPs compared with bulk, respectively. Thus, the NPs change their local environment, and ion concentrations at the NP surface are different from bulk [55–57]. Local ion concentrations around NP surfaces can be measured using for instance ion-sensitive fluorophores [55–57]. The theoretical analysis however is not as straightforward. When interactions of ions with the curved nanoenvironment of NPs are generally discussed, most applied models, e.g. the DLVO theory [58,59] are based on continuum effects considering ions as point charges [60]. However, effects considering the nature of the used ions, namely *specific* ion effects, are often disregarded, though they may be of high importance for example for the colloidal stability of the NPs. These effects have long been known for example in biological systems, in which they are responsible for the well-known Hofmeister effect [61–64], describing stabilization and precipitation tendencies in proteins. Another example is the well-known fact that specific adsorption and monolayer formation of anions occurs in flat charged gold surfaces dipped in electrolytes [65–69]. Hence, ion-specific effects must not be ignored when the nanoenvironment of NPs is studied, particularly at low salinities in case the previously discussed screening of charges described by continuum models is not dominant. Changes in the ion concentration around the surface of NPs have profound effect on ion-sensitive NPs, as instead of the bulk ion concentration the local ion concentration is determined [55–57].

Thus, interaction of ions and proteins with NPs affects both the ions and proteins as well as the NPs. In the following, we will focus on the case of ions.

## 2. Non-specific effects of ion-induced nanoenvironments on the synthesis and stability of ligand-free metal nanoparticles

The nanoenvironment of charged NPs has been extensively studied for a long time. Generally, the model of the electrochemical 'double layer' by Stern [70,71] which describes a fixed layer of surface charges (the Helmholtz model [72]), and a continuous diffuse layer of counter-ions (the Gouy–Chapman model [73–75]) is used in this context. The thickness of this diffuse layer, and hence the nanoscopic vicinity of the NPs, is highly dependent on the solution's ionic strength and may be characterized by the Debye parameter ($\kappa$) or its reciprocal value, the Debye screening length ($\kappa^{-1}$). In a classical DLVO model [58,59], which considers dissolved ions as point charges, $\kappa^{-1}$ decreases with increasing ionic strength ($I$[$M$], which is a function of the concentration of all ions: $I = 1/2 \sum_i z_i^2 c_i$, where $z_i$ is the valence of ions of species $i$, and $c_i$ [$M$] the respective concentration of these ions). This leads to a screening of surface charges accompanied by a reduction of the electrostatic stability and induces NP agglomeration owing to dominant van der Waal's attraction. Next to these frequently described effects, the nanoenvironment also affects the electrophoretic mobility ($\mu$ [$m^2V^{-1}s^{-1}$]) of NPs and hence related values, such as the zeta-potential ($\zeta$ [V]), a parameter of outmost importance when judging NP stabilities in colloidal science [76]. The main parameters in this context are the ionic strength, influencing the Debye parameter ($\kappa$ [$m^{-1}$]), and the NP radius ($r_c$ [m]). Based on these values, the best representation of the correlation between $\mu$ and $\zeta$ may be given by the Smoluchowski formula [77] for the nanoenvironment of larger NPs at high ionic strengths ($\kappa \times r_c \gg 1$) and by the Hückel equation [78] for low ionic strengths and small NPs ($\kappa \times r_c \ll 1$). In the intermediate regime, the Henry function $f_H(\kappa \times r_c)$ may be used [79]. Please note that we are referring

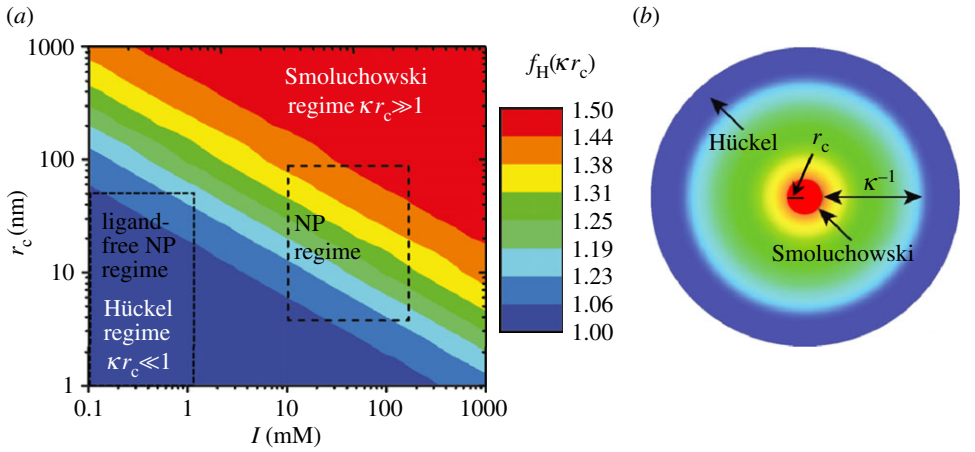


**Figure 1.** (*a*) Scheme showing different models for the determination of the electrophoretic mobility of bare NPs for different ionic strengths *I* and NP radii $r_c$ (referring to the geometrical radii of the inorganic NP materials). The colour indicates the Henry factor $f_H$, which defines the relationship between the bare mobility $\mu$ and resulting zeta-potential $\zeta$, with higher zeta-potentials at given mobility in the Hückel regime. Note that $f_H$ changes with the distance from the NP surface. (*b*) Shows the two-dimensional distribution of the Debye layer thickness $\kappa^{-1}$ (adapted from Doane *et al.* [76]).

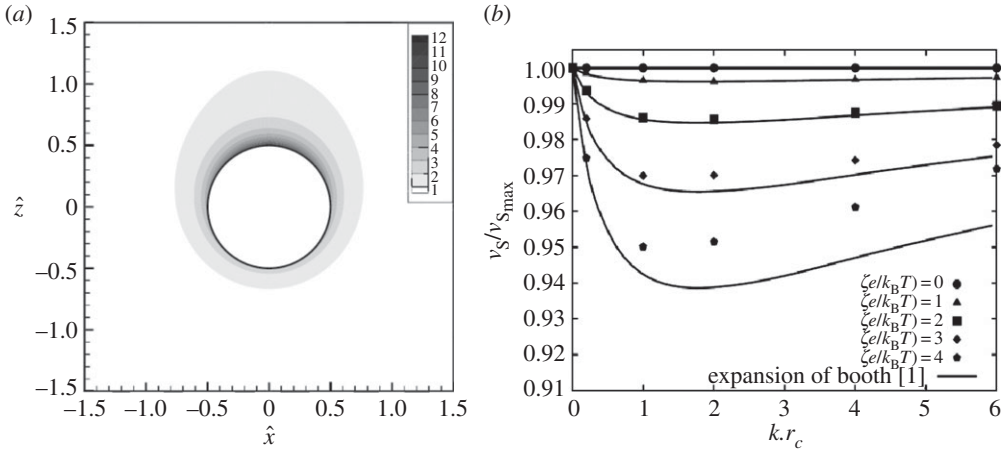


**Figure 2.** Distortion of the ionic nanoenvironment during centrifugation and effect on the sedimentation velocity $v_S$ at different zeta-potentials $\zeta$. (*a*) Distribution of counter-ions around an NP in the *x*–*z* plane at $\kappa \times r_c = 2$, $\zeta e/k_BT = 3$, and a fluidic Reynolds number of $Re_f = 4.45 \times 10^{-2}$ (100 000 g). (*b*) Normalized sedimentation velocity $v_S/v_{S_{max}}$ at different $\kappa \times r_c$ and $(\zeta e/k_BT)$ values (adapted from Keller *et al.* [85]).

to (geometrical) particle radii $r_c$, not to hydrodynamic radii $r_h$ [21]. A more detailed discussion of the different models can be found in a review article recently published by Doane *et al.* [80]. Figure 1 shows the different regimes dependent on NP radius $r_c$ and ionic strength *I*. With the zeta-potential $\zeta$ being inversely proportional to the Henry factor, zeta-potentials of an NP at a given mobility $\mu$ are up to 50% higher ($f_H = 1.5$) in the Hückel regime. NPs synthesized by wet chemistry methods typically bear charge and mobility properties in the intermediate regime (marked in figure 1) between Smoluchowski and Hückel [76], whereas colloids with low ionic strength, e.g. physically prepared colloidal NPs [81–84], are often located in the Hückel regime, being more sensitive for local changes or fluctuations in the ionic environment as a result of the larger Debye length $\kappa^{-1}$. Note that ion adsorption to the surface of NPs results in a non-continuum ionic strength regime around the NPs, causing a gradient in the Henry factor. In ideal conditions (no drag force, very low or very high fluid Reynolds numbers), the two-dimensional distribution of the Henry factor around the NP is symmetric.

Next to external electrical fields, the symmetric vicinity of an NP may also be altered by gravitational forces as they are found during centrifugation. A detailed understanding of this process and its correlation with ionic strength, *g*-force and zeta-potential may help to elucidate the sedimentation process and might contribute to controlling agglomeration processes occurring during centrifugation. Recent simulation experiments conducted by Keller *et al.* [85] revealed that the counter-ion cloud found in the vicinity of the NPs is deformed at high *g*-forces (figure 2*a*). This leads to a local electric field which causes a reduction in the sedimentation velocity $v_S$ [m s$^{-1}$]. This process is highly dependent on the present zeta-potential $\zeta$ and the ionic strength *I*. This correlation is depicted in figure 2*b*, where $\zeta$ is shown as the dimensionless factor $\zeta e/k_BT$, where *e* is the elemental charge ($e = 1.602 \times 10^{-19}$C), $k_B$ is the Boltzmann factor ($k_B = 1.380 \times 10^{-23}$ J K$^{-1}$), and *T* [K] is the temperature of the solution. In that context, a factor of 1 at room temperature ($T = 298$ K) is equivalent to a zeta-potential of 26 mV. The ionic strength is plotted as the factor $\kappa \times r_c$, where a value of 2 is equivalent to an ionic strength of $1.04 \times 10^{-6}$ M at a particle radius of $r_c = 3 \times 10^{-7}$ m.

The preceding examples clearly demonstrate that the continuous, ion-induced nanoenvironment can remarkably alter the physical properties of NPs and may have a severe influence on colloidal chemistry. These effects are meant to be particularly pronounced at ligand-free particles, which hence could

[A10]3

provide a sufficiently sensitive system to study such effects. However, in the above described examples, the ions were only considered as point charges and ion-specific effects were not yet considered [60]. The point of ion specificity is further addressed in the following paragraph.

## 3. Specific effects of ion-induced nanoenvironments on the synthesis and stability of ligand-free metal nanoparticles

The specific impact of ions on bare noble metal surfaces has been widely studied for decades, e.g. for gold electrodes in the presence of different electrolytes. A significant accumulation and adsorption of the halogens $Cl^-$, $Br^-$ and $I^-$, and hence changes of the nanoenvironment have been reported and verified by several methods, including atomic force microscopy [68], X-ray diffraction analysis [67], scanning tunnelling microscopy [66] and surface enhanced Raman scattering [65]. Additionally, it has been known for a very long time that bare gold surfaces dipped in pure water suppositionally collect a negative surface charge owing to accumulation of $OH^-$ [69]. Another example of specific ion interactions is the Hofmeister effect, which has been known since the nineteenth century [62]. It was first discovered in the field of protein precipitation [61,63,64], but was successfully applied to other fields, ranging from simple physical effects on electrolytes to colloidal dispersions and macromolecules [86]. This effect is based on the fact that ions may be classified into chaotropic (soft) and kosmotropic (hard) based on their stabilization of biomolecules and their interactions with surfaces. The nature of these effects is not yet fully understood but it is believed that it may be related to the polarizability of the ions [87,88]. While chaotropic ions have a diffuse charge distribution, they may interact with hydrophobic surfaces, whereas kosmotropic ions with a high surface charge density are repelled. Other findings seem to indicate that the structure of the water molecules found on their surface may be of paramount importance. While water molecules close to kosmotropic ions are highly ordered, chaotropic ions are known to alter their surrounding water shell [89–91]. Hence, ions may lose their hydrate shell and become chemisorbed on hydrophobic surfaces, which is not possible for densely hydrated kosmotropic anions [92]. Even though ion-specific effects have been discussed for a very long time, a detailed examination and transfer of these effects to the nanoenvironment of NPs has long been neglected owing to the unavailability of appropriate test systems. NPs obtained from gas-phase synthesis are barely available in colloidal state owing to their strong agglomeration tendencies and hence undefined surface areas [93,94]. On the other hand, ion-induced interactions with metal surfaces are screened in the presence of surface ligands such as citrate [95] negating a study of these effects with chemically synthesized NPs. In this case, ion–NP interactions in the nanoenvironment are dominated by the nature of the organic ligands, which is thoroughly discussed in the next paragraph. Most recently, the availability of ligand-free colloidal NPs synthesized by the quickly emerging field [82,96] of pulsed laser ablation in liquid [83,84,97,98] has significantly stimulated this research, whereas particularly gold colloids were extensively studied [96,99,100]. Owing to this emerging synthesis route, ultrapure curved NP surfaces are nowadays available which enable studies of NP–ion interactions in the Hückel regime at extremely low ionic strengths [31,101]. These effects will be thoroughly reviewed in the following and complemented by some recent findings. Basically, these effects can be subdivided into (i) ion effects, and (ii) pH effects though in many experiments this influence cannot be clearly distinguished.

### 3.1. Ion effects

When it comes to interactions of NPs with electrolytes, generally, a destabilization owing to the well-known screening of surface charges is predominantly discussed in the literature [46]. However, when totally ligand-free gold and silver, NPs were first laser-synthesized in the presence of electrolytes, stabilization occurred in the presence of NaCl [102,103]. More extensive studies with different electrolytes at varying salinities revealed that these effects are anion-specific, occurring only with chaotropic anions ($Cl^-$, $Br^-$, $I^-$, $SCN^-$), whereas kosmotropic anions ($F^-$, $SO_4^{2-}$) did not induce a stabilizing effect. For $NO_3^-$, the findings in the literature are inconsistent. While generally a destabilizing effect is reported for gold [95,103], at lower ionic strengths [101] and for silver [102], however, stabilization was found. It is believed that this ion adsorption significantly alters the NP's nanoenvironment, as the ions transfer their charges to the NP surface and hence increase electrostatic stabilization (figure 3*a*). These findings seem to indicate that Hofmeister effects, thoroughly described in the preceding paragraph, may also appear on curved gold interfaces. A Hofmeister series of anions for this system could be deferred, by successfully correlating the stability of gold colloids to the polarizability of the anions present during synthesis [101] (figure 3*b*). Interestingly, these effects already occur in highly diluted electrolytes in a micromolar to millimolar concentration range [31,101,102]. Specific accumulation of chaotropic anions in the nanoenvironment of NPs does not only affect colloidal stability, it also interferes with the growth mechanism of ligand-free NPs. As a result, these ions induce a size quenching effect during NP growth which was reported for gold [31,97,103] and silver NPs [102,104–106]. This means that in a micromolar concentration regime increasing ionic strengths significantly reduce NP size and their NP size distribution. It was recently proposed that size reduction in highly diluted electrolytes is directly related to the NP surface area, which can be electrostatically stabilized by the available anions [31]. A summary of the different anions and their stabilizing and size quenching effects on ligand-free gold and silver NPs is summarized in table 1. Table 1 clearly shows the suitability of anions for size quenching of ligand-free nanoparticles. Consecutively, comments are provided when ambiguous effects were reported for different ions. For example, for HCl, different stabilizing effects were found dependent on the used ionic strength (concentration) and for gold and silver nanoparticles (material). Additionally, table 1 provides literature for a more detailed study, sorted by the metals (Au, Ag) studied.

### 3.2. pH effects

The influence of pH on the nanoenvironment of ligand-free colloidal metal (M) NPs is mostly due to oxidation of surface atoms and a pH-dependent equilibrium between $M–O^-$/$M–OH$ and $M–OH/MOH_2^+$ species, respectively. This has

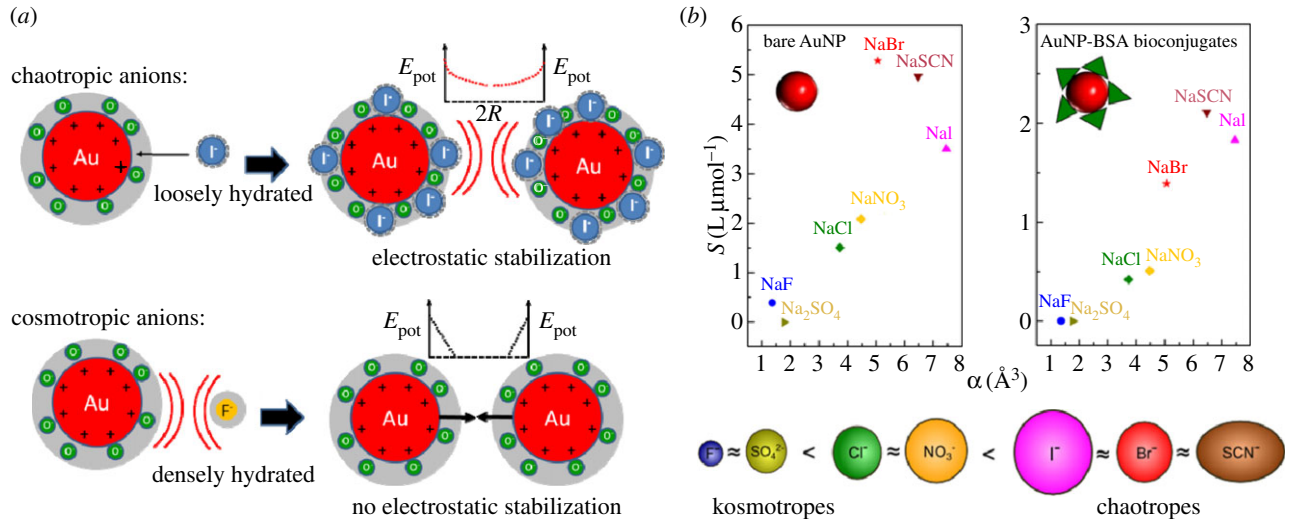


**Figure 3.** (*a*) Ion-specific interactions of chaotropic and kosmotropic anions in the nanoenvironment of gold NPs. The graph shows the dependence of the repulsive potential energy Epot in dependence of the surface-to-surface distance 2*R* between adjacent NPs. (*b*) Colloidal stability as indicated by the slope *S* of the polydispersity index from UV–Vis spectroscopy, in dependence of the polarizability α of the anion, for bare Au NPs without ligand and Au NPs coated with bovine serum albumin (BSA). The resulting Hofmeister series for gold NPs is shown. Adapted from Merk *et al.* [101], to which we also refer for more details.

**Table 1.** Specific effects of different ions on the stability and size quenching of ligand-free Au and Ag NPs. (Signs in brackets indicate limitations or ambivalent effects found by different researchers including comments regarding possible reasons).

| ion | stabilization | size quenching | reference |
|---|---|---|---|
| $F^-$ | — | — | Au [101] |
| $Cl^-$ | (+)/(−) | (+)/(−) | Au [31,83,95,101,103] |
| | concentration | concentration | Ag [102,104–106] |
| $Br^-$ | ++ | + | Au [31,101] |
| $I^-$ | (++) NP etching | + | Au [95,101] |
| $SCN^-$ | ++ | + | Au [101] |
| $NO_3^-$ | (−)/(+) | (−)/(+) | Au [95,101,103] |
| | concentration | concentration | Ag [102] |
| $SO_4^{2-}$ | — | — | Au [31,101] |
| $PO_4^{3-}$ | + | + | Au [31] |
| $NaH_2PO_4$/ $Na_2HPO_4$ | + | + | Au [31] |
| $OH^-$ | + | (+)/(−) | Au [103] |
| | | concentration | |
| HCl | (−)/(+) | (−)/(+) | Au [103] |
| | concentration, material | concentration, material | Ag [102] |
| $S_2O_3^{2-}$ | — | — | Ag [102] |

been quantitatively described in the case of $SiO_2$ and $Al_2O_3$ surfaces by the site-binding model used for solid-state based ion-sensitive sensors [107–111]. At low pH, the surface can be charged positively by the adsorption of protons ($MOH_2^+$), whereas it will be negatively charged at high pH owing to depletion of protons ($M–O^-$). The equilibrium of the reaction $M–O^- + 2\,H^+ \leftrightarrow M–OH + H^+ \leftrightarrow MOH_2^+$ is described by the law of mass action by the respective $pK_a$ ($=-\log(K_a)$) values $K_{a1} = c(M–O^-) \times c(H^+)/c(M–OH)$ and $K_{a2} = c(M–OH) \times c(H^+)/c(MOH_2^+)$. Both equilibria depend on pH ($=-\log(c(H^+))$). In this way, the surface charge and hence the electrostatic stability reaches a minimum close to the isoelectric point (p*I*) at pH = p*I* [112]. This effect was frequently observed for metal oxide NPs such as ZnO [113,114], $TiO_2$ [115] and $Al_2O_3$ [116], where larger NPs owing to agglomeration were predominantly formed close to the p*I* value of the respective NP species. It is important to note that with metal oxides, e.g. for $Al_2O_3$, different hydroxide species may form. Dependent on the pH, the NPs were equilibrated, and hence different p*I* values may be found [117] The p*I* values of exemplary NP species are shown in table 2. As the presence of surface hydroxide is obvious in metal oxides, they are also found in the case of gold NPs obtained from physical synthesis routes such as laser ablation in liquid. X-ray photoelectron spectroscopy measurements confirmed that these NPs possess partially oxidized surfaces (3.3–6.6% of $Au^+$ and $Au^{3+}$) [101,120]. Fourier transform infrared spectroscopy

[A10]5

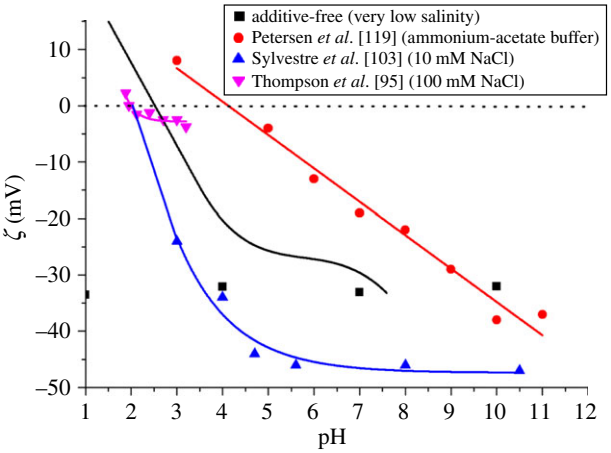


**Figure 4.** Ion effects on the isoelectric points of gold NPs. Zeta-potential $\zeta$ of ligand-free NPs at different pH values for the determination of the isoelectric point, as adapted from [95,103,119] as well as unpublished data.

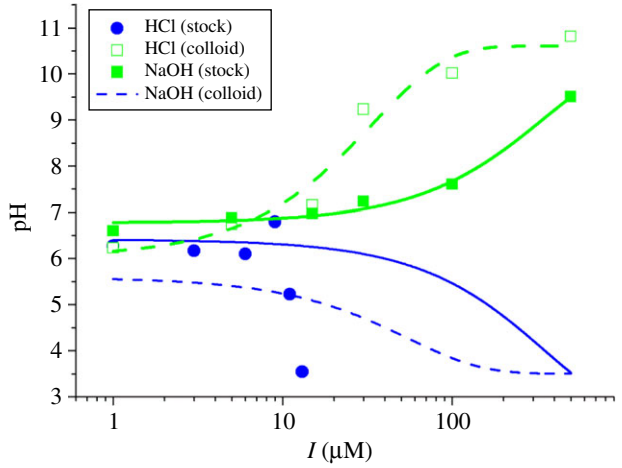


**Figure 5.** The buffer effect of charged NP surfaces. The pH values of ligand-free gold NP suspensions as synthesized in the presence of NaOH and HCl at varying concentrations of the respective acid (HCl) and base (NaOH; solid lines) are plotted versus the ionic strength *I* of the solution. As comparison the pH of the NaOH and HCl stock solutions was monitored as well (dashed lines).

**Table 2.** Charge equilibrium in the nanoenvironment (pH at the isoelectric points (pI)) of exemplary ligand-free colloidal NPs.

| NP species | isoelectric point (p*I*) | reference |
|---|---|---|
| $TiO_2$ | 6 | [115] |
| ZnO | 9 | [113] |
| $Al_2O_3$ | 8.6 (acidic equilibration) | [117] |
| | 5.3 (alkaline equilibration) | |
| AuPt | (7) indirect method | [118] |
| Au | 2–2.5 (4.5) | [95,103,119] |

measurements verified the presence of Au–O bonds on the surface [103]. An indirect verification of a p*I* value in ligand-free noble metal systems was recently found for $Au_{50}Pt_{50}$–alloy NPs which were laser-ablated at different pHs. Here, a steep increase in NP size owing to agglomeration processes was found at pH < 7 [118]. A titration of ligand-free gold NPs in order to determine the p*I* value was performed for NPs obtained from gas-phase synthesis [95] and laser ablation in liquid [103,119] by monitoring the zeta-potential at different pH values. In all cases, stabilization was found for more alkaline pH. The results from three different references and recently obtained experimental data are summarized in figure 4. In our experiments, totally additive-free gold NPs were titrated with HCl, fitted with a fourth-order polynomial, whereas linear extrapolation was used in order to determine the p*I* value. Note that Thompson *et al.* [95] originally measured the electrophoretic motility, which was transferred to the zeta-potential for better comparability, applying Smoluchowski's equation [77].

These data clearly show that additive-free gold NPs possess an isoelectric point at pH = 2.5. These findings slightly deviate from p*I*-values reported in the literature by Thompson *et al.* [95] (p*I* = 2) and Sylvestre *et al.* [103] (p*I* = 2.2). These differences may be due to high concentrations of chloride (100 and 10 mM) present during their experiments, whereas in the additive-free sample chloride, solutions with three orders of magnitude lower salinities (93 μM) were applied. As it was described in the preceding paragraph, chloride may specifically adsorb on gold NP surfaces, which increases the negative surface charge of the NPs. Naturally, in these samples, more protons are necessary for charge compensation, and the isoelectric point is reached at a more acidic pH. Completely different results were obtained by Petersen *et al.* [119] where a p*I* of 4.5 was found. These deviations may be due to the fact that a system of $CH_3COOH/NH_3$ was used for pH adjustment. On the one hand, this approach eliminates ion effects but on the other hand, another organic ligand is added and a $CH_3COO^-/CH_3COOH$ buffer system is formed, influencing the solution's pH. This high diversity of findings clearly illustrates that to further examine the influence of varying pH on the nanoenvironment of ligand-free gold NPs, additional ion effects need to be minimized and hence the ionic strength has to be reduced. To this end, we recently prepared NPs by pulsed laser ablation in liquid in the presence of NaOH and HCl at concentrations from 1 to 500 μM. In both cases, a significant growth quenching causing size reduction of the NPs was found compared with products synthesized in water. In case of HCl, this is most likely due to the stabilizing effect of $Cl^-$, blocking the gold seed's crystal growth preventing further growth. In the observed concentration regime, this effect seems to compensate the destabilization by protons reported for higher HCl concentrations [103]. For NaOH, the deprotonation of surface Au–OH groups, and the increased abundance of surface charges is the most probable cause for reduced NP size and stabilization, which is in accordance with data from literature [103]. The most interesting effect, however, was observed when the pH of the stock solution (just diluted HCl or NaCl), and the NP-containing solution was monitored during this experiment (figure 5). It was found that the pH of both NP-containing solutions synthesized in the presence of HCl and NaOH remained stable at around 6.5 up to a concentration of 30 μM, leading to a significant deviation from pH values found in the stock solution. For higher concentrations, the pH significantly deviated from the value of 6.5, though the measured values were still considerably different from the stock solutions. These findings seem to indicate that ligand-free gold NPs work as a buffer in highly diluted electrolytes, totally stabilizing the pH at 6.5 up to a proton surplus, as well as a proton deficiency of 30 μM. Apparently, the nanoenvironment of the

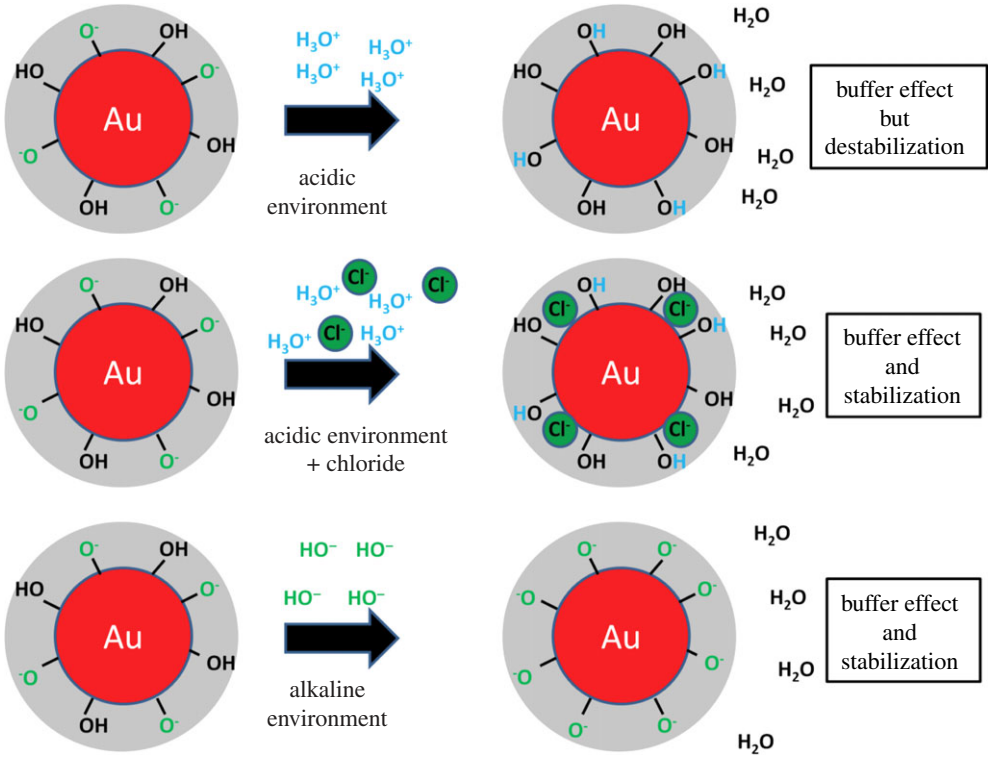


**Figure 6.** Buffer effect caused by the nanoenvironment of gold NPs in acidic and alkaline bulk environment.

gold NPs accumulates protons from acidic solutions and emits protons to an alkaline environment probably by changing the Au–$O^-$/Au–OH ratio, significantly affecting the pH of the bulk solution. This fundamental effect, that the NPs themselves and their nanoenvironment work as a buffer system, significantly affecting the bulk solution, is often neglected when working with NPs. The underlying concept is illustrated in figure 6. As a result, in 1 ml of the examined gold NP solution with an average NP core radius $r_c$ of 4 nm and a mass concentration of 100 µg $ml^{-1}$, there are roughly $2.2 \times 10^{17}$ gold surface atoms present, which can accumulate and emit about 30 nmol of $H^+$, which is equal to $1.8 \times 10^{16}$ $H^+$ ions. Consequently, about 8% of the surface atoms take part in this buffering reaction, which is in good accordance with the literature stating that up to 6.6% of the gold surface is oxidized [101,120] and hence may carry an Au–OH or $AuO^-$ group. In conclusion, a buffer capacity of 0.77 nmol $(H^+)/cm^2$(gold NP surface) is reached, which is very low compared with conventional buffers, though this comparison only considers pure continuum states of the environment. By contrast, the observed buffer effect is directly caused by the Gouy–Chapman layer in the nanoscopic vicinity of the NPs. Hence, such effects might be relevant in highly pH-sensitive reactions at low concentrations.

## 4. Effects of ion-induced nanoenvironments on the stability and the nanoenvironment of ligand-coated nanoparticles

While the concepts as described above for ligand-free metal NPs, in general, are true also for ligand-coated NPs, the situation becomes more complex. This is due to the hybrid nature of ligand-coated NPs, which besides the inorganic core also comprise an organic (ligand-)coating [21]. Now, ions in solution will be in equilibrium with several entities, not only with the originally bare NP surface of the inorganic core but also with the ligand shell, which itself can comprise different parts. In the important case of carboxylic acids as ligand, there will be the pH-dependent equilibrium $-COO^- + H^+ \leftrightarrow -COOH$ with $K_a = c(-COO^-) \times c(H^+)/c(-COOH)$. In the case of complex carboxylic acids several $pK_a$ values can exist, which can be determined by titration experiments [121]. In case the pH is smaller than the $pK_a$ value, the NP surface is losing its charge and predominantly comprises $-COOH$ groups, as $pK_a - pH = -\log(c(-COO^-)/c(-COOH))$. Thus, the NPs lose their colloidal stability and start to agglomerate. At alkaline solution $pH \gg pK_a$, the NP's surface on the other hand is saturated with negative charge $c(-COO^-)$ and the NPs are colloidal stable. The situation can change with other ligands, for example with positively charged ones [122]. In the case of amino terminated ligands $-NH_2 + H^+ \leftrightarrow -NH_3^+$, the NPs are charged at low, acidic pH ($-NH_3^+$, $pH \ll pK_a$), as $pK_a - pH = -\log(c(-NH_2)/c(-NH_3^+))$. In the case of high $pH \gg pK_a$, the NPs are uncharged ($-NH_2$) and thus will lose their colloidal stability. Consequently, as described before for ligand-free NPs also in the case of ligand-coated NPs, the local pH can (though not automatically) determine the surface charge of the NPs, whereby the dependence is given by the nature of the ligand. In contrast to ligand-free NPs, ligand-coated NPs can be also made with ligands comprising a permanent charge (e.g. ammonium salts, which are fully dissociated and thus permanently charged), which then have a pH-independent surface charge [53]. Most important, these NPs can be stabilized also with macromolecular ligands, such as PEG, which provides colloidal stability via steric repulsion. In this way, ligands on the NP surface introduce higher flexibility in achieving (pH-independent) colloidal stability, in particular via permanently charged ligands and/or ligands providing steric repulsion. As for ligand-free NPs, besides the charge directly associated with the NP surface (now here in particular to the ligand shell), also ligand-coated NPs comprise a diffusive cloud of charge

[A10]7

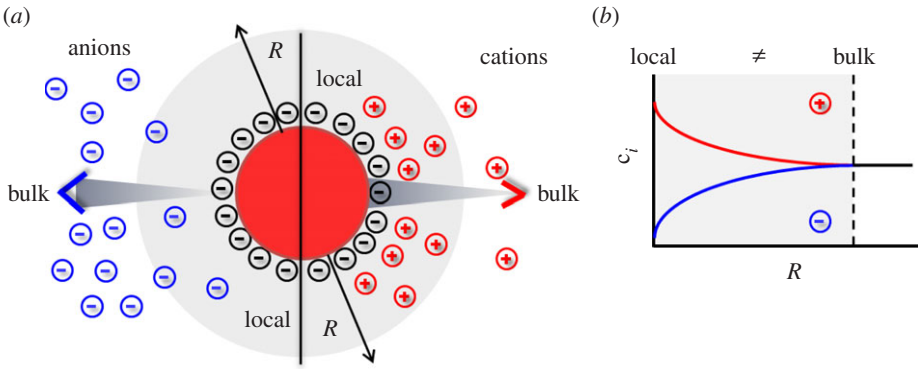


**Figure 7.** The concentration of ions at the surface of an NP is different from the respective bulk concentration. (*a*) In the case of negatively charged NPs (e.g. NPs with $-COO^-$ ligands) owing to Debye–Hückel screening there will be a local depletion and accumulation of anions and cations, respectively, close to the NP's surface. (*b*) The graph demonstrates schematically that the concentration $c_i$ of ions of different species depends on the distance $R$ from the NP surface, and is different from bulk close to NP surfaces.

by attracted counter ions according to the Gouy–Chapman model. Thus, in a similar way, the use of charged NPs produces changes in the concentration of charged species in a solution. For negatively charged NP surfaces (e.g. $COO^-$ stabilized NPs), there is a local depletion of negatively charged analytes (i.e. anions such as $OH^-$ or $Cl^-$), and a local accumulation of positively charged analytes (i.e. cations such as $Na^+$ or $H^+$; figure 7*a*, [55]). Please note that these effects are absolutely non-specific and only depend on charge and valency of the ions. There will be a screening effect by oppositely charged ions, but in case several different ions are present all of them contribute. In the case, $Na^+$ ions are present, less $H^+$ is attracted to the surface of negatively charged NPs [55]. The opposite scenario will occur in the case positively charged NPs are involved [55,56]. Coming back to our main statement, this means that the local ion concentration close to the NP surface will be different from the bulk concentration (figure 7*b*), i.e. NPs influence their environment. This fact has severe effects on sensing with NPs, which will be discussed later. In the same way, this screening effect owing to the adsorption of counter-ions, together with the pH-dependent surface charge of the ligand shell, determines the colloidal stability of the NPs, i.e. the nanoenvironment affects the physico-chemical properties of the NP surface.

Unfortunately, a detailed theoretical description of the ion distribution around ligand-coated NPs is not as straight forward as for ligand-free NPs. This is due to their hybrid nature. Already, the question where the NP surface begins cannot be clearly answered [21]. The ligand shell, in general, is not homogeneous. A practical system for example can comprise hydrophobic surfactant molecules, surrounded by an amphiphilic polymer, with an additional shell of PEG [57]. This ligand shell is not completely rigid, i.e. one cannot exactly determine where the transition from one layer to the next layer (e.g. the polymer PEG interface) is located. Even the final hydrodynamic radii $r_h$ underlie much larger distributions than the original core radius $r_c$. Thus, models describing the different parts of the ligand shell would need to consider distributions of respective different layers. Fortunately, distributions are not as smeared out as one may expect, as for example indicated by fluorescence resonance energy transfer measurements which revealed a relatively narrow distribution of fluorophores attached to the polymer shell around fluorescent NPs [123]. Different layers of the ligand shell can also interact in different manners with ions. Long PEG chains, for example, chelate ions such as $Na^+$ or $K^+$, and thus change the surface charge of the NPs [124]. All these effects make theoretical predictions about the quantitative ion distribution around ligand-coated NPs complicated. The starting point of such theoretical descriptions very often uses the Poisson–Boltzmann equation. It can be solved within numerical or analytical approximations as was shown for a charged hard sphere within an electrolyte solution in various studies [125–130]. More accurate models assume a permeable soft shell, e.g. consisting of a polyelectrolyte layer, around the hard sphere to approximate a potential ligand shell, although the detailed conformation of that shell is not considered [131–133]. More recent approaches are based on Monte Carlo simulations and the classical density functional theory (DFT). These allow for the consideration of the intrinsic ion volume and moreover for the treatment of the solvent molecules as third fraction of individual components instead of a dielectric continuum [134,135]. The DFT moreover offers the possibility to consider volume displacement effects by potential ligands such as PEG attached to the NP surface [136–138].

From an experimental approach, ion-sensitive fluorophores attached to NPs are a feasible strategy to probe ion concentrations close to NP surfaces. Such fluorophores change their emission, usually the intensity of emission, dependent on the concentration of the respective ion. However, most convenient are ion-sensitive fluorophores with ratiometric detection schemes, in which not absolute intensities need to be detected, but the intensities of the emissions at two different wavelengths are compared [56,139]. This can be achieved either by fluorophores with two emission peaks [140] or by combining an ion-sensitive fluorophore which emits at one wavelength with a reference fluorophore which emits at another wavelength [56,141,142]. Thus, in order to determine the ion concentration profile around NPs, ion-sensitive fluorophores (and the reference fluorophores) need to be immobilized at different distances R to the NP surface. This can be conveniently done by using molecular spacers such as DNA [143–145] or PEG [55–57]. In order to obtain spacers providing controlled distances R, the trick lies in saturating the NP surface. In this way, the spacers are stretched (instead of forming statistical coils) and thus have defined conformation [146]. The confirmation of only a few spacer molecules per NP is in general not known. In the case of flexible spacers, they might be partly wrapped around the NP surface, or they might be dangling in solution [146]. However, in the case the NP surface is saturated with attached spacer molecules, they all will adopt similar geometry and thus lead to defined distances *R*.

[A10]8

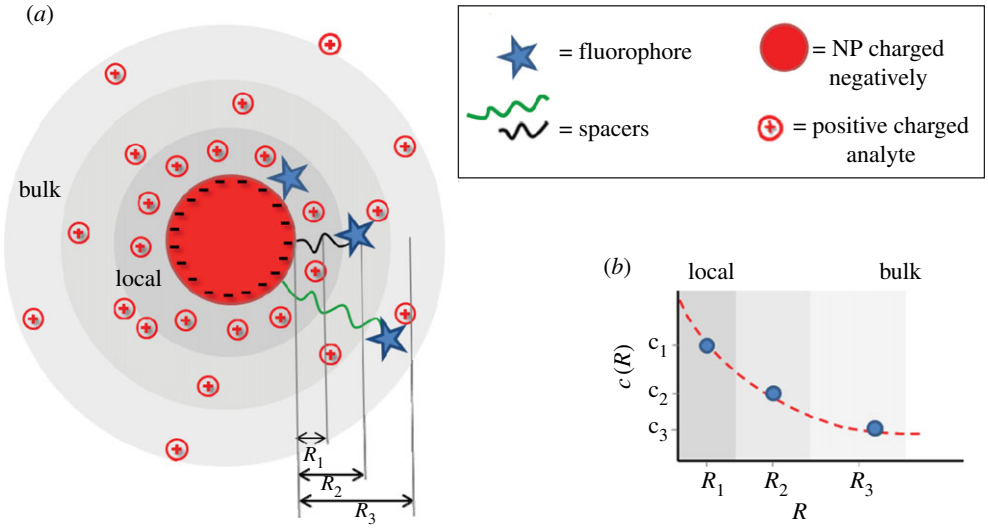


**Figure 8.** Scheme for measuring the distribution of ions with concentration $c(R)$ in dependence of the distance $R$ to the NP surface.

Fluorophores can be linked to the end of the spacer molecules [147,148], and by using spacers with different molecular weight the average distance between fluorophores and the NP surface can be tuned [143,149,150]. This principle has been applied to sense local $H^+$ [55,57] and $Cl^-$ [56] concentrations. According to figures 7 and 8 for negatively charged NPs, higher $H^+$ and lower $Cl^-$ concentrations were found close to the NP surface when compared with bulk. Thus, the response curves of the ion-sensitive fluorescence readout are shifted in the case the fluorophores are attached close to the NP surface. In the case of long enough spacers, the fluorophores are sufficiently far away from the NP surface, and thus bulk readout is obtained. This implicates that for all NP-based sensing applications one must consider that the actual environment of the NPs where the measurement takes place is different from bulk, e.g. ion concentrations at the NP surface are different from bulk values.

## 5. Conclusion

The local environment of NPs has profound interaction with the surface of NPs, which induce that the physico-chemical properties of both, the environment and the surface can be mutually altered. The surface of NPs creates a special local environment, with different properties compared with the bulk. Owing to different repulsion/adsorption effects local molecular concentrations around the NP, surface can be quite different from bulk concentrations. This has strong effects on NP-based sensors, as those probe concentrations of the local environment, and not from the bulk. In the other direction, the surface charge of NPs is determined by the presence of ions in the local nanoenvironment. Via reaction with ligands or even with the bare NP surface, this regulates the surface charge of NPs and thus also their colloidal stability. These effects may be particularly pronounced when they are studied in highly pure ligand-free systems. Here, next to continuum effects, ion-specific interactions occur in the particle's nanoenvironment which may significantly alter particle properties such as stability and may even affect the composition of the bulk phase.

Acknowledgements. D.J. acknowledges a PhD fellowship for the Basque Country, Spain.

Funding statement. This work was supported by the DFG (graduate research school 1782 to W.J.P. and the project REPROTOX within priority programme SPP1313 to S.B.). C.C. acknowledges a postdoctoral fellowship from the Alexander von Humboldt Foundation.

## References

1. Pelaz B, Charron G, Pfeiffer C, Zhao YL, de la Fuente JM, Liang XJ, Parak WJ, del Pino P. 2013 Interfacing engineered nanoparticles with biological systems: anticipating adverse nanobio interactions. *Small* **9**, 1573–1584. (doi:10.1002/smll.201201229)
2. Singh D, Kumar S, Singh SC, Lal B, Singh NB. 2012 Applications of liquid assisted pulsed laser ablation synthesized TiO2 nanoparticles on germination, growth and biochemical parameters of brassica oleracea var. capitata. *Sci. Adv. Mater.* **4**, 522–531. (doi:10.1166/sam.2012.1313)
3. Corradini E, de Moura MR, Mattoso LHC. 2010 A preliminary study of the incorparation of NPK fertilizer into chitosan nanoparticles. *Express. Polymer Lett.* **4**, 509–515. (doi:10.3144/expresspolymlett.2010.64)
4. Khodakovskaya MV, de Silva K, Biris AS, Dervishi E, Villagarcia H. 2012 Carbon nanotubes induce growth enhancement of tobacco cells. *ACS Nano* **6**, 2128–2135. (doi:10.1021/nn204643g)
5. Perelshtein I *et al.* 2013 Chitosan and chitosan-ZnO-based complex nanoparticles: formation, characterization, and antibacterial activity. *J. Mater. Chem. B* **1**, 1968–1976. (doi:10.1039/c3tb00555k)
6. Chernousova S, Epple M. 2013 Silver as antibacterial agent: ion, nanoparticle, and metal. *Angew. Chem. Int. Ed.* **52**, 1636–1653. (doi:10.1002/anie.201205923)
7. Hajipour MJ, Fromm KM, Ashkarran AA, Aberasturi DJd, Larramendi IRd, Rojo T, Serpooshan V, Parak WJ, Mahmoudi M. 2012 Antibacterial properties of nanoparticles. *Trends Biotechnol.* **30**, 499–511. (doi:10.1016/j.tibtech.2012.06.004)
8. Ojea-Jimenez I, Lopez X, Arbiol J, Puntes V. 2012 Citrate-coated gold nanoparticles as smart scavengers for mercury(II) removal from polluted waters. *ACS Nano* **6**, 2253–2260. (doi:10.1021/nn204313a)
9. Venkatanarasimhan S, Raghavachari D. 2013 Epoxidized natural rubber-magnetite nanocomposites for oil spill recovery. *J. Mater. Chem. A* **1**, 868–876. (doi:10.1039/c2ta00445c)

10. Zhu Q, Tao F, Pan Q. 2010 Fast and selective removal of oils from water surface via highly hydrophobic core-shell Fe2O3@C nanoparticles under magnetic field. *ACS Appl. Mater. Interfaces* **2**, 3141–3146. (doi:10.1021/am1006194)
11. Arvizo RR, Bhattacharyya S, Kudgus RA, Giri K, Bhattacharya R, Mukherjee P. 2012 Intrinsic therapeutic applications of noble metal nanoparticles: past, present and future. *Chem. Soc. Rev.* **41**, 2943–2970. (doi:10.1039/c2cs15355f)
12. Parveen S, Misra R, Sahoo SK. 2012 Nanoparticles: a boon to drug delivery, therapeutics, diagnostics and imaging. *Nanomedicine* **8**, 147–166. (doi:10.1016/j.nano.2011.05.016)
13. Garcia-Bennett A, Nees M, Fadeel B. 2011 In search of the holy grail: folate-targeted nanoparticles for cancer therapy. *Biochem. Pharmacol.* **81**, 976–984. (doi:10.1016/j.bcp.2011.01.023)
14. Al-Jamal WT, Kostarelos K. 2011 Liposomes: from a clinically established drug delivery system to a nanoparticle platform for theranostic nanomedicine. *Acc. Chem. Res.* **44**, 1094–1104. (doi:10.1021/ar200105p)
15. Peteiro-Cartelle J, Rodríguez-Pedreira M, Zhang F, Gil PR, Mercato LLd, Parak WJ. 2009 One example on how colloidal nano- and microparticles could contribute to medicine. *Nanomedicine* **4**, 967–979. (doi:10.2217/nnm.09.84)
16. Batley GE, Kirby JK, McLaughlin MJ. 2013 Fate and risks of nanomaterials in aquatic and terrestrial environments. *Acc. Chem. Res.* **46**, 854–862. (doi:10.1021/ar2003368)
17. Peters R *et al*. 2012 Presence of nano-sized silica during in vitro digestion of foods containing silica as a food additive. *ACS Nano* **6**, 2441–2451. (doi:10.1021/nn204728k)
18. Zhang P, Ma YH, Zhang ZY, He X, Zhang J, Guo Z, Tai RZ, Zhao YL, Chai ZF. 2012 Biotransformation of ceria nanoparticles in cucumber plants. *ACS Nano* **6**, 9943–9950. (doi:10.1021/nn303543n)
19. Hernandez-Viezcas JA *et al*. 2013 In situ synchrotron X-ray fluorescence mapping and speciation of $CeO_2$ and ZnO nanoparticles in soil cultivated soybean (glycine max). *ACS Nano* **7**, 1415–1423. (doi:10.1021/nn305196q)
20. Hoecke KV, Schamphelaer KACD, Ali Z, Zhang F, Elsaesser A, Rivera_Gil P, Parak WJ, Smagghe G, Janssen CR. 2013 *In vitro* ecotoxicity and uptake of polymer coated gold nanoparticles. *Nanotoxicology* **7**, 37–47. (doi:10.3109/17435390.2011.626566)
21. Rivera Gil P *et al*. 2013 The challenge to relate the physicochemical properties of colloidal nanoparticles to their cytotoxicity. *Acc. Chem. Res.* **46**, 743–749. (doi:10.1021/ar300039j)
22. Fu FN, Fuller MP, Singh BR. 1993 Use of fourier-transform infrared attenuated total reflectance spectroscopy for the study of surface-adsorption of proteins. *Appl. Spectrosc.* **47**, 98–102. (doi:10.1366/0003702934048451)
23. Peng ZG, Hidajat K, Uddin MS. 2004 Adsorption of bovine serum albumin on nanosized magnetic particles. *J. Colloid Interface Sci.* **271**, 277–283. (doi:10.1016/j.jcis.2003.12.022)
24. Verma A, Uzun O, Hu YH, Hu Y, Han HS, Watson N, Chen SL, Irvine DJ, Stellacci F. 2008 Surface-structure-regulated cell-membrane penetration by monolayer-protected nanoparticles. *Nat. Mater.* **7**, 588–595. (doi:10.1038/nmat2202)
25. Hung A, Mwenifumbo S, Mager M, Kuna JJ, Stellacci F, Yarovsky I, Stevens MM. 2011 Ordering surfaces on the nanoscale: implications for protein adsorption. *J. Am. Chem. Soc.* **133**, 1438–1450. (doi:10.1021/ja108285u)
26. Cedervall T, Lynch I, Lindman S, Berggård T, Thulin E, Nilsson H, Dawson KA, Linse S. 2007 Understanding the nanoparticle-protein corona using methods to quantify exchange rates and affinities of proteins for nanoparticles. *Proc. Natl Acad. Sci. USA* **104**, 2050–2055. (doi:10.1073/pnas.0608582104)
27. Linse S, Cabaleiro-Lago C, Xue W-F, Lynch I, Lindman S, Thulin E, Radford SE, Dawson KA. 2007 Nucleation of protein fibrillation by nanoparticles. *Proc. Natl Acad. Sci. USA* **104**, 8691–8696. (doi:10.1073/pnas.0701250104)
28. Lynch I, Dawson KA. 2008 Protein-nanoparticle interactions. *Nano Today* **3**, 40–47. (doi:10.1016/S1748-0132(08)70014-8)
29. Röcker C, Pötzl M, Zhang F, Parak WJ, Nienhaus GU. 2009 A quantitative fluorescence study of protein monolayer formation on colloidal nanoparticles. *Nat. Nanotechnol.* **4**, 577–580. (doi:10.1038/nnano.2009.195)
30. Jiang X, Weise S, Hafner M, Röcker C, Zhang F, Parak WJ, Nienhaus GU. 2010 Quantitative analysis of the protein corona on FePt nanoparticles formed by transferrin binding. *J. R. Soc. Interface* **7**, S5–S13. (doi:10.1098/rsif.2009.0272.focus)
31. Rehbock C, Merk V, Gamrad L, Streubel R, Barcikowski S. 2013 Size control of laser-fabricated surfactant-free gold nanoparticles with highly diluted electrolytes and their subsequent bioconjugation. *Phys. Chem. Chem. Phys.* **15**, 3057–3067. (doi:10.1039/c2cp42641b)
32. Gebauer JS, Malissek M, Simon S, Knauer SK, Maskos M, Stauber RH, Peukert W, Treuel L. 2012 Impact of the nanoparticle-protein corona on colloidal stability and protein structure. *Langmuir* **28**, 9673–9679. (doi:10.1021/la301104a)
33. Kittler S *et al*. 2010 The influence of proteins on the dispersability and cell-biological activity of silver nanoparticles. *J. Mater. Chem.* **20**, 512–518. (doi:10.1039/b914875b)
34. Shemetov AA, Nabiev I, Sukhanova A. 2012 Molecular interaction of proteins and peptides with nanoparticles. *ACS Nano* **6**, 4585–4602. (doi:10.1021/nn300415x)
35. Deng ZJ, Liang M, Toth I, Monteiro MJ, Minchin RF. 2012 Molecular interaction of poly(acrylic acid) gold nanoparticles with human fibrinogen. *ACS Nano* **6**, 8962–8969. (doi:10.1021/nn3029953)
36. Goy-Lopez S, Juarez J, Alatorre-Meda M, Casals E, Puntes VF, Taboada P, Mosquera V. 2012 Physicochemical characteristics of protein-NP bioconjugates: the role of particle curvature and solution conditions on human serum albumin conformation and fibrillogenesis inhibition. *Langmuir* **28**, 9113–9126. (doi:10.1021/la300402w)
37. Amin F, Yushchenko DA, Montenegro JM, Parak WJ. 2012 Integration of organic fluorophores in the surface of polymer-coated colloidal nanoparticles for sensing the local polarity of the environment. *ChemPhysChem* **13**, 1030–1035. (doi:10.1002/cphc.201100901)
38. Fatin-Rouge N, Starchev K, Buffle J. 2004 Size effects on diffusion processes within agarose gels. *Biophys. J.* **86**, 2710–2719. (doi:10.1016/S0006-3495(04)74325-8)
39. Sperling RA, Liedl T, Duhr S, Kudera S, Zanella M, Lin C-AJ, Chang WH, Braun D, Parak WJ. 2007 Size determination of (bio-) conjugated water-soluble colloidal nanoparticles: a comparison of different techniques. *J. Phys. Chem. C* **111**, 11 552–11 559. (doi:10.1021/jp070999d)
40. Bell NC, Minelli C, Tompkins J, Stevens MM, Shard AG. 2012 Emerging techniques for submicrometer particle sizing applied to stober silica. *Langmuir* **28**, 10 860–10 872. (doi:10.1021/la203419y)
41. Lees EE, Gunzburg MJ, Nguyen T-L, Howlett GJ, Rothacker J, Nice EC, Clayton AHA, Mulvaney P. 2008 Experimental determination of quantum dot size distributions, ligand packing densities, and bioconjugation using analytical ultracentrifugation. *Nano Lett.* **8**, 2883–2890. (doi:10.1021/nl801629f)
42. Monopoli MP, Walczyk D, Campbell A, Elia G, Lynch I, Bombelli FB, Dawson KA. 2011 Physical-chemical aspects of protein corona: relevance to in vitro and in vivo biological impacts of nanoparticles. *J. Am. Chem. Soc.* **133**, 2525–2534. (doi:10.1021/ja107583h)
43. Maffre P, Nienhaus K, Amin F, Parak WJ, Nienhaus GU. 2011 Characterization of protein adsorption onto FePt nanoparticles using dual-focus fluorescence correlation spectroscopy. *Beilstein J. Nanotechnol.* **2**, 374–383. (doi:10.3762/bjnano.2.43)
44. Mahmoudi M *et al*. 2013 Temperature: the ?ignored? factor at the nanobio interface. *ACS Nano* **7**, 6555–6562. (doi:10.1021/nn305337c)
45. He Q, Zhang J, Shi J, Zhu Z, Zhang L, Bu W, Guo L, chen Y. 2010 The effect of PEGylation of mesoporous silica nanoparticles on nonspecific binding of serum proteins and cellular responses. *Biomaterials* **31**, 1085–1092. (doi:10.1016/j.biomaterials.2009.10.046)
46. Pellegrino T, Kudera S, Liedl T, Javier AM, Manna L, Parak WJ. 2005 On the development of colloidal nanoparticles towards multifunctional structures and their possible use for biological applications. *Small* **1**, 48–63. (doi:10.1002/smll.200400071)
47. Zhang X, Servos MR, Liu J. 2012 Ultrahigh nanoparticle stability against salt, pH, and solvent with retained surface accessibility via depletion stabilization. *J. Am. Chem. Soc.* **134**, 9910–9913. (doi:10.1021/ja303787e)
48. Ravikumar C, Kumar S, Bandyopadhyaya R. 2012 Aggregation of dextran coated magnetic nanoparticles in aqueous medium: experiments and

Monte Carlo simulation. *Colloids Surf. A, Physicochem. Eng. Aspects* **403**, 1–6. (doi:10.1016/j.colsurfa.2012.02.007)

49. Debye P, Hückel E. 1923 Zur Theorie der Elektrolyte. *Phys. Z* **24**, 185–206.
50. Huynh KA, Chen KL. 2011 Aggregation kinetics of citrate and polyvinylpyrrolidone coated silver nanoparticles in monovalent and divalent electrolyte solutions. *Environ. Sci. Technol.* **45**, 5564–5571. (doi:10.1021/es200157h)
51. Li X, Lenhart JJ, Walker HW. 2012 Aggregation kinetics and dissolution of coated silver nanoparticles. *Langmuir* **28**, 1095–1104. (doi:10.1021/la202328n)
52. Gebauer JS, Treuel L. 2011 Influence of individual ionic components on the agglomeration kinetics of silver nanoparticles. *J. Colloid Interface Sci.* **354**, 546–554. (doi:10.1016/j.jcis.2010.11.016)
53. Hühn D *et al*. 2013 Polymer-coated nanoparticles interacting with proteins and cells: focusing on the sign of the net charge. *ACS Nano* **7**, 3253–3263. (doi:10.1021/nn3059295)
54. Caballero-Díaz E, Pfeiffer C, Kastl L, Rivera-Gil P, Simonet B, Valcárcel M, Jiménez-Lamana J, Laborda F, Parak WJ. 2013 The toxicity of silver nanoparticles depends on their uptake by cells and thus on their surface chemistry. *Particle Particle Syst. Charact*. (doi:10.1002/ppsc.201300215)
55. Zhang F, Ali Z, Amin F, Feltz A, Oheim M, Parak WJ. 2010 Ion and pH sensing with colloidal nanoparticles: influence of surface charge on sensing and colloidal properties. *ChemPhysChem* **11**, 730–735. (doi:10.1002/cphc.200900849)
56. Riedinger A, Zhang F, Dommershausen F, Röcker C, Brandholt S, Nienhaus GU, Koert U, Parak WJ. 2010 Ratiometric optical sensing of chloride ions with organic fluorophore – gold nanoparticle hybrids: a systematic study of distance dependency and the influence of surface charge. *Small* **6**, 2590–2597. (doi:10.1002/smll.201000868)
57. Zhang F, Lees E, Amin F, Rivera Gil P, Yang F, Mulvaney P, Parak WJ. 2011 Polymer-coated nanoparticles: a universal tool for biolabelling experiments. *Small* **7**, 3113–3127. (doi:10.1002/smll.201100608)
58. Derjaguin B, Sidorenkov G. 1941 Thermoosmosis at ordinary temperatures and its analogy with the thermomechanical effect in helium II. *C. R. Acad. Sci.* **32**, 622–626.
59. Verwey EJW, Overbeek JTG. 1948 *Theory of the stability of lyophobic colloids*. Amsterdam, The Netherlands: Elsevier.
60. Ninham BW. 1999 On progress in forces since the DLVO theory. *Adv. Colloid Interface Sci.* **83**, 1–17. (doi:10.1016/S0001-8686(99)00008-1)
61. Bauduin P, Nohmie F, Touraud D, Neueder R, Kunz W, Ninham BW. 2006 Hofmeister specific-ion effects on enzyme activity and buffer pH: Horseradish peroxidase in citrate buffer. *J. Mol. Liq.* **123**, 14–19. (doi:10.1016/j.molliq.2005.03.003)
62. Hofmeister F. 1888 Zur Lehre von der Wirkung der Salze - Zweite Mittheilung. *Arch. Exp. Pathol. Pharm* **24**, 247–260. (doi:10.1007/BF01918191)
63. Medda L, Barse B, Cugia F, Bostrom M, Parsons DF, Ninham BW, Monduzzi M, Salis A. 2012 Hofmeister challenges: ion binding and charge of the BSA protein as explicit examples. *Langmuir* **28**, 16 355–16 363. (doi:10.1021/la3035984)
64. Vrbka L, Jungwirth P, Bauduin P, Touraud D, Kunz W. 2006 Specific ion effects at protein surfaces: a molecular dynamics study of bovine pancreatic trypsin inhibitor and horseradish peroxidase in selected salt solutions. *J. Phys. Chem. B* **110**, 7036–7043. (doi:10.1021/jp0567624)
65. Gao P, Weaver MJ. 1986 Metal adsorbate vibrational frequencies as a probe of surface bonding – halides and pseudohalides at gold electrodes. *J. Phys. Chem.* **90**, 4057–4063. (doi:10.1021/j100408a045)
66. Magnussen OM, Ocko BM, Wang JX, Adzic RR. 1996 *In situ* X-ray diffraction and STM studies of bromide adsorption on Au(111) electrodes. *J. Phys. Chem.* **100**, 5500–5508. (doi:10.1021/jp953281j)
67. Magnussen OM, Ocko BM, Adzic RR, Wang JX. 1995 X-ray-diffraction studies of ordered chloride and bromide monolayers at the Au(111)-solution interface. *Phys. Rev. B* **51**, 5510–5513. (doi:10.1103/PhysRevB.51.5510)
68. Biggs S, Mulvaney P, Zukoski CF, Grieser F. 1994 Study of anion adsorption at the gold-aqueous solution interface by atomic-force microscopy. *J. Am. Chem. Soc.* **116**, 9150–9157. (doi:10.1021/ja00099a033)
69. Verwey EJW, De Boer JH. 1936 Surface oxide films. *Recueil Des Travaux Chimiques Des Pays-Bas* **55**, 675–687. (doi:10.1002/recl.19360550806)
70. Stern O. 1924 Zur Theorie der Elektrolytischen Doppelschicht. *Z. Elektr.* **30**, 508–516.
71. Rhee IH, Dzombak DA. 1998 Surface complexation Gouy–Chapman modeling of binary and ternary cation exchange. *Langmuir* **14**, 935–943. (doi:10.1021/la9700331)
72. Helmholtz H. 1879 Studien über elektrische Grenzschichten. *Wiedemanns Anal. Phys. Chem.* **7**, 337–382.
73. Chapman DL. 1913 A contribution to the theory of electrocapillarity. *Philos. Mag.* **25**, 475–481.
74. Gouy M. 1909 Sur la constitution de la charge electrique a la surface d'un electrolyte. *C.R. Acad. Sci.* **149**, 654–657.
75. Gouy M. 1910 Sur la constitution de la charge electrique a la surface d'un electrolyte. *J. Phys.* **9**, 457–468.
76. Doane TL, Chuang CH, Hill RJ, Burda C. 2012 Nanoparticle zeta-potentials. *Acc. Chem. Res.* **45**, 317–326. (doi:10.1021/ar200113c)
77. Smoluchowski M. 1906 Zur kinetischen Theorie der Brownschen Molekularbewegung und der Suspensionen. *Ann. Phys.* **21**, 756–780. (doi:10.1002/andp.19063261405)
78. Hückel E. 1924 Die Kataphorese der Kugel. *Phys. Z* **25**, 204–210.
79. Henry DC. 1931 The cataphoresis of suspended particles. I. the equation of cataphoresis. *Proc. R. Soc. Lond. A* **133**, 106–129. (doi:10.1098/rspa.1931.0133)
80. Doane TL, Burda C. 2012 The unique role of nanoparticles in nanomedicine: imaging, drug delivery and therapy. *Chem. Soc. Rev.* **41**, 2885–2911. (doi:10.1039/c2cs15260f)
81. Baersch N, Jakobi J, Weiler S, Barcikowski S. 2009 Pure colloidal metal and ceramic nanoparticles from high-power picosecond laser ablation in water and acetone. *Nanotechnology* **20**, 445603. (doi:10.1088/0957-4484/20/44/445603)
82. Barcikowski S, Compagnini G. 2013 Advanced nanoparticle generation and excitation by lasers in liquids. *Phys. Chem. Chem. Phys.* **15**, 3022–3026. (doi:10.1039/c2cp90132c)
83. Amendola V, Meneghetti M. 2013 What controls the composition and the structure of nanomaterials generated by laser ablation in liquid solution? *Phys. Chem. Chem. Phys.* **15**, 3027–3046. (doi:10.1039/c2cp42895d)
84. Zeng HB, Du XW, Singh SC, Kulinich SA, Yang SK, He JP, Cai WP. 2012 Nanomaterials via laser ablation/irradiation in liquid: a review. *Adv. Funct. Mater.* **22**, 1333–1353. (doi:10.1002/adfm.201102295)
85. Keller F, Feist M, Nirschl H, Dorfler W. 2010 Investigation of the nonlinear effects during the sedimentation process of a charged colloidal particle by direct numerical simulation. *J. Colloid Interface Sci.* **344**, 228–236. (doi:10.1016/j.jcis.2009.12.032)
86. Lo Nostro P, Ninham BW. 2012 Hofmeister phenomena: an update on ion specificity in biology. *Chem. Rev.* **112**, 2286–2322. (doi:10.1021/cr200271j)
87. Tavares FW, Bratko D, Blanch HW, Prausnitz JM. 2004 Ion-specific effects in the colloid-colloid or protein-protein potential of mean force: Role of salt-macroion van der Waals interactions. *J. Phys. Chem. B* **108**, 9228–9235. (doi:10.1021/jp037809t)
88. dos Santos AP, Levin Y. 2012 Ions at the water–oil interface: interfacial tension of electrolyte solutions. *Langmuir* **28**, 1304–1308. (doi:10.1021/la204036e)
89. Collins KD. 1997 Charge density-dependent strength of hydration and biological structure. *Biophys. J.* **72**, 65–76. (doi:10.1016/S0006-3495(97)78647-8)
90. Collins KD. 2004 Ions from the Hofmeister series and osmolytes: effects on proteins in solution and in the crystallization process. *Methods* **34**, 300–311. (doi:10.1016/j.ymeth.2004.03.021)
91. Manciu M, Ruckenstein E. 2003 Specific ion effects via ion hydration: I. Surface tension. *Adv. Colloid Interface Sci.* **105**, 63–101. (doi:10.1016/S0001-8686(03)00018-6)
92. Kolb DM, Franke C. 1989 Surface-states at the metal electrolyte interface. *Appl. Phys. A, Mater. Sci. Process.* **49**, 379–387. (doi:10.1007/BF00615020)
93. Gutsch A, Muhlenweg H, Kramer M. 2005 Tailor-made nanoparticles via gas-phase synthesis. *Small* **1**, 30–46. (doi:10.1002/smll.200400021)
94. Kruis FE, Fissan H, Peled A. 1998 Synthesis of nanoparticles in the gas phase for electronic, optical and magnetic applications – a review. *J. Aerosol Sci.* **29**, 511–535. (doi:10.1016/S0021-8502(97)10032-5)


[A10]11

95. Thompson DW, Collins IR. 1992 Electrical-properties of the gold aqueous-solution interface. *J. Colloid Interface Sci.* **152**, 197–204. (doi:10.1016/0021-9797(92)90019-I)
96. Menendez-Manjon A, Barcikowski S. 2011 Hydrodynamic size distribution of gold nanoparticles controlled by repetition rate during pulsed laser ablation in water. *Appl. Surf. Sci.* **257**, 4285–4290. (doi:10.1016/j.apsusc.2010.12.037)
97. Amendola V, Meneghetti M. 2009 Laser ablation synthesis in solution and size manipulation of noble metal nanoparticles. *Phys. Chem. Chem. Phys.* **11**, 3805–3821. (doi:10.1039/b900654k)
98. Semaltianos NG. 2010 Nanoparticles by laser ablation. *Crit. Rev. Solid State Mater. Sci.* **35**, 105–124. (doi:10.1080/10408431003788233)
99. Tilaki RM, Zad AI, Mahdavi SM. 2007 The effect of liquid environment on size and aggregation of gold nanoparticles prepared by pulsed laser ablation. *J. Nanoparticle Res.* **9**, 853–860. (doi:10.1007/s11051-006-9143-0)
100. Kabashin AV, Meunier M. 2003 Synthesis of colloidal nanoparticles during femtosecond laser ablation of gold in water. *J. Appl. Phys.* **94**, 7941–7943. (doi:10.1063/1.1626793)
101. Merk CVR, Rehbock C, Becker F, Hagemann U, Nienhaus H, Barcikowski S. 2013 Non-DLVO stabilization of surface-free, plasmonic gold nanoparticles: the effect of Hofmeister's anions. *Langmuir*. Q2
102. Siskova K, Vlckova B, Turpin PY, Fayet C. 2008 Ion-specific effects on laser ablation of silver in aqueous electrolyte solutions. *J. Phys. Chem. C* **112**, 4435–4443. (doi:10.1021/jp076680a)
103. Sylvestre JP, Poulin S, Kabashin AV, Sacher E, Meunier M, Luong JHT. 2004 Surface chemistry of gold nanoparticles produced by laser ablation in aqueous media. *J. Phys. Chem. B* **108**, 16 864–16 869. (doi:10.1021/jp047134+)
104. Srnova I, Prochazka M, Vlckova B, Stepanek J, Maly P. 1998 Surface-enhanced Raman scattering-active systems prepared from Ag colloids laser-ablated in chemically-modified aqueous media. *Langmuir* **14**, 4666–4670. (doi:10.1021/la9707540)
105. Bae CH, Nam SH, Park SM. 2002 Formation of silver nanoparticles by laser ablation of a silver target in NaCl solution. *Appl. Surf. Sci.* **197**, 628–634. (doi:10.1016/S0169-4332(02)00430-0)
106. Prochazka M, Mojzes P, Stepanek J, Vlckova B, Turpin PY. 1997 Probing applications of laser ablated Ag colloids in SERS spectroscopy: Improvement of ablation procedure and SERS spectral testing. *Anal. Chem.* **69**, 5103–5108. (doi:10.1021/ac970683+)
107. Bousse L, Rooij NFd, Bergveld P. 1983 The influence of counter-ion adsorption on the $\psi_0$/pH characteristics of insulator surfaces. *Surf. Sci.* **135**, 479–496. (doi:10.1016/0039-6028(83)90237-6)
108. Bousse L, Mostarshed S. 1991 The zeta potential of silicon nitride thin films. *J. Electroanal. Chem.* **302**, 269–274. (doi:10.1016/0022-0728(91)85046-R)
109. Raiteri R, Martinoia S, Grattarola M. 1996 pH-dependent charge density at the insulator-electrolyte interface probed by a scanning force microscope. *Biosens. Bioelectron.* **11**, 1009–1017. (doi:10.1016/0956-5663(96)87660-3)
110. van Hal REG, Eijkel JCT, Bergveld P. 1995 A novel description of ISFET sensitivity with the buffer capacity and double-layer capacitance as key parameters. *Sensors Actuators B, Chem.* **24–25**, 201–205. (doi:10.1016/0925-4005(95)85043-0)
111. Healy TW, Chan D, White LR. 1980 Colloidal behaviour of materials with ionizable group surfaces. *Pure Appl. Chem.* **52**, 1207–1219. (doi:10.1351/pac198052051207)
112. Parks GA. 1965 The isoelectric points of solid oxides, solid hydroxides, and aqueous hydroxo complex systems. *Chem. Rev.* **65**, 177–198. (doi:10.1021/cr60234a002)
113. Liufu S, Xiao H, Li Y. 2004 Investigation of PEG adsorption on the surface of zinc oxide nanoparticles. *Powder Technol.* **145**, 20–24. (doi:10.1016/j.powtec.2004.05.007)
114. He C, Sasaki T, Usui H, Shimizu Y, Koshizaki N. 2007 Fabrication of ZnO nanoparticles by pulsed laser ablation in aqueous media and pH-dependent particle size: an approach to study the mechanism of enhanced green photoluminescence. *J. Photochem. Photobiol. A Chem.* **191**, 66–73. (doi:10.1016/j.jphotochem.2007.04.006)
115. Sugiyama M, Okazaki H, Koda S. 2002 Size and shape transformation of $TiO_2$ nanoparticles by irradiation of 308-nm laser beam. *Jpn J. Appl. Phys. Part 1 Regular Pap. Short Not. Rev. Pap.* **41**, 4666–4674. (doi:10.1143/JJAP.41.4666)
116. Al-Mamun SA, Nakajima R, Ishigaki T. 2013 Tuning the size of aluminum oxide nanoparticles synthesized by laser ablation in water using physical and chemical approaches. *J. Colloid Interface Sci.* **392**, 172–182. (doi:10.1016/j.jcis.2012.10.027)
117. Gulicovski JJ, Cerovic LS, Milonjin SK. 2008 Point of zero charge and isoelectric point of alumina. *Mater. Manuf. Process.* **23**, 615–619. (doi:10.1080/10426910802160668)
118. Zhang JM, Oko DN, Garbarino S, Imbeault R, Chaker M, Tavares AC, Guay D, Ma DL. 2012 Preparation of PtAu alloy colloids by laser ablation in solution and their characterization. *J. Phys. Chem. C* **116**, 13 413–13 420. (doi:10.1021/jp302485g)
119. Petersen S, Barchanski A, Taylor U, Klein S, Rath D, Barcikowski S. 2011 Penetratin-conjugated gold nanoparticles - design of cell-penetrating nanomarkers by femtosecond laser ablation. *J. Phys. Chem. C* **115**, 5152–5159. (doi:10.1021/jp1093614)
120. Muto H, Yamada K, Miyajima K, Mafune F. 2007 Estimation of surface oxide on surfactant-free gold nanoparticles laser-ablated in water. *J. Phys. Chem. C* **111**, 17 221–17 226. (doi:10.1021/jp075582m)
121. Charron G, Hühn D, Perrier A, Cordier L, Pickett CJ, Nann T, Parak WJ. 2012 On the use of pH titration to quantitatively characterize colloidal nanoparticles. *Langmuir* **28**, 15 141–15 149. (doi:10.1021/la302570s)
122. Geidel C, Schmachtel S, Riedinger A, Pfeiffer C, Müllen K, Klapper M, Parak WJ. 2011 A general synthetic approach for obtaining cationic and anionic inorganic nanoparticles via encapsulation in amphiphilic copolymers. *Small* **7**, 2929–2934. (doi:10.1002/smll.201100509)
123. Yakovlev AV *et al*. 2009 Wrapping nanocrystals with an amphiphilic polymer preloaded with fixed amounts of fluorophore generates FRET-based nanoprobes with a controlled donor/acceptor ratio. *Langmuir* **25**, 3232–3239. (doi:10.1021/la8038347)
124. Sperling RA, Pellegrino T, Li JK, Chang WH, Parak WJ. 2006 Electrophoretic separation of nanoparticles with a discrete number of functional groups. *Adv. Funct. Mater.* **16**, 943–948. (doi:10.1002/adfm.200500589)
125. Hoskin NE. 1953 Solution to the Poisson–Boltzmann equation for the potential distribution in the double layer of a single spherical colloidal particle. *Trans. Faraday Soc.* **49**, 1471–1477. (doi:10.1039/tf9534901471)
126. Brenner SL, Roberts RE. 1973 Variational solution of Poisson–Boltzmann equation for a spherical colloidal particle. *J. Phys. Chem.* **77**, 2367–2370. (doi:10.1021/j100639a001)
127. White LR. 1977 Approximate analytic solution of the Poisson-Boltzmann equation for a spherical colloidal particle. *J. Chem. Soc. Faraday Trans. II* **73**, 577–596. (doi:10.1039/f29777300577)
128. Ohshima H, Healy TW, White LR. 1982 Accurate analytic expressions for the surface-charge density surface-potential relationship and double-layer potential distribution for a spherical colloidal particle. *J. Colloid Interface Sci.* **90**, 17–26. (doi:10.1016/0021-9797(82)90393-9)
129. Ohshima H. 2004 Potential distribution around a charged spherical colloidal particle in a medium containing its counterions and a small amount of added salts. *Colloid Polym. Sci.* **282**, 1185–1191. (doi:10.1007/s00396-004-1072-9)
130. Zhou S, Zhang G. 2012 Approximate analytic solution of the nonlinear Poisson–Boltzmann equation for spherical colloidal particles immersed in a general electrolyte solution. *Colloid Polym. Sci.* **290**, 1511–1526. (doi:10.1007/s00396-012-2683-1)
131. Lopez-Garcia JJ, Horno J, Grosse C. 2001 Numerical solution of the Poisson–Boltzmann equation for suspended charged particles surrounded by a charged permeable membrane. *Phys. Chem. Chem. Phys.* **3**, 3754–3760. (doi:10.1039/b101701m)
132. Ohshima H. 2003 Potential distribution around a polyelectrolyte-coated spherical particle in a salt-free medium. *J. Colloid Interface Sci.* **268**, 429–434. (doi:10.1016/j.jcis.2003.08.020)
133. Ohshima H. 2008 Donnan potential and surface potential of a spherical soft particle in an electrolyte solution. *J. Colloid Interface Sci.* **323**, 92–97. (doi:10.1016/j.jcis.2008.03.021)
134. Patra CN. 2009 Molecular solvent model of spherical electric double layers: a systematic study by Monte Carlo simulations and density functional theory. *J. Phys. Chem. B* **113**, 13 980–13 987. (doi:10.1021/jp907790t)
135. Patra CN. 2010 Structure of spherical electric double layers containing mixed electrolytes: a systematic

study by Monte Carlo simulations and density functional theory. *J. Phys. Chem. B* **114**, 10 550–10 557. (doi:10.1021/jp1042975)

136. Wu JZ, Li ZD. 2007 Density-functional theory for complex fluids. *Annu. Rev. Phys. Chem.* **58**, 85–112. (doi:10.1146/annurev.physchem.58.032806.104650)
137. Yu YX, Wu JZ, Gao GH. 2004 Density-functional theory of spherical electric double layers and zeta potentials of colloidal particles in restricted-primitive-model electrolyte solutions. *J. Chem. Phys.* **120**, 7223–7233. (doi:10.1063/1.1676121)
138. Rex S, Zuckermann MJ, Lafleur M, Silvius JR. 1998 Experimental and Monte Carlo simulation studies of the thermodynamics of polyethyleneglycol chains grafted to lipid bilayers. *Biophys. J.* **75**, 2900–2914. (doi:10.1016/S0006-3495(98)77732-X)
139. Arduini M, Mancin F, Tecilla P, Tonellato U. 2007 Self-organized fluorescent nanosensors for ratiometric $Pb^{2+}$ detection. *Langmuir* **23**, 8632–8636. (doi:10.1021/la700971n)
140. Page LE, Zhang X, Jawaid AM, Snee PT. 2011 Detection of toxic mercury ions using a ratiometric CdSe/ZnS nanocrystal sensor. *Chem. Commun.* **47**, 7773–7775. (doi:10.1039/c1cc11442e)
141. Doussineau T, Smaihi M, Mohr GJ. 2009 Two-dye core/shell zeolite nanoparticles: a new tool for ratiometric pH measurements. *Adv. Funct. Mater.* **19**, 117–122. (doi:10.1002/adfm.200800718)
142. Ali Z *et al*. 2011 Multifunctional nanoparticles for dual imaging. *Anal. Chem.* **83**, 2877–2882. (doi:10.1021/ac103261y)
143. Obliosca JM, Wang P-C, Tseng F-G. 2012 Probing quenched dye fluorescence of Cy3-DNA-Au-nanoparticle hybrid conjugates using solution and array platforms. *J. Colloid Interface Sci.* **371**, 34–41. (doi:10.1016/j.jcis.2011.12.026)
144. Diaz JA, Grewer DM, Gibbs-Davis JM. 2012 Tuning ratios, densities, and supramolecular spacing in bifunctional DNA-modified gold nanoparticles. *Small* **8**, 873–883. (doi:10.1002/smll.201101922)
145. Chhabra R, Sharma J, Wang H, Zou S, Lin S, Yan H, Lindsay S, Liu Y. 2009 Distance-dependent interactions between gold nanoparticles and fluorescent molecules with DNA as tunable spacers. *Nanotechnology* **20**, 485201. (doi:10.1088/0957-4484/20/48/485201)
146. Pellegrino T, Sperling RA, Alivisatos AP, Parak WJ. 2007 Gelelectrophoresis of gold-DNA nanoconjugates. *J. Biomed. Biotechnol.* **2007,** 1–9. (doi:10.1155/2007/26796)
147. Shenoy D, Fu W, Li J, Crasto C, Jones G, DiMarzio C, Sridhar S, Amiji M. 2006 Surface functionalization of gold nanoparticles using hetero-bifunctional poly(ethylene glycol) spacer for intracellular tracking and delivery. *Int. J. Nanomed.* **1**, 51–57. (doi:10.2147/nano.2006.1.1.51)
148. Liu W, Howarth M, Greytak AB, Zheng Y, Nocera DG, Ting AY, Bawendi MG. 2008 Compact biocompatible quantum dots functionalized for cellular imaging. *J. Am. Chem. Soc.* **130**, 1274–1284. (doi:10.1021/ja076069p)
149. Dulkeith E, Ringler M, Klar TA, Feldmann J, Javier AM, Parak WJ. 2005 Gold nanoparticles quench fluorescence by phase induced radiative rate suppression. *Nanoletters* **5**, 585–589. (doi:10.1021/nl0480969)
150. Nagatoishi S, Nojima T, Galezowska E, Gluszynska A, Juskowiak B, Takenaka S. 2007 Fluorescence energy transfer probes based on the guanine quadruplex formation for the fluorometric detection of potassium ion. *Anal. Chim. Acta* **581**, 125–131. (doi:10.1016/j.aca.2006.08.010)